ARO 25143.19-MS-A

(2)

CONTROLLING FUNDAMENTALS IN HIGH-ENERGY HIGH-RATE PULSED POWER MATERIALS PROCESSING OF POWDERED TUNGSTEN, TITANIUM ALUMINIDES, AND COPPER-GRAPHITE COMPOSITES

Principal Investigators: Harris L. Marcus and William F. Weldon
Co-Investigators: Chadee Persad, Zwy Eliezer and David Bourell

Center for Materials Science and Engineering & Center for Electromechanics

The University of Texas at Austin
Austin, Texas

October 1990

UTCMSE-90-02
Final Technical Report

Army Research Office
Contract DAAL 0387-K-0073

Final Technical Report
Contract DAAL 0387-K-0073
The University of Texas at Austin
Reporting Period: June 1, 1987 - August 31, 1990

CONTROLLING FUNDAMENTALS IN HIGH-ENERGY HIGH-RATE PULSED POWER MATERIALS PROCESSING OF POWDERED TUNGSTEN, TITANIUM ALUMINIDES, AND COPPER-GRAPHITE COMPOSITES

Principal Investigators

Harris L. Marcus
Professor of Mechanical Engineering
Director of Center for
Materials Science and Engineering

William F. Weldon
Professor of Mechanical & Electrical Engineering
Director of Center for Electromechanics

Report Number: UTCMSE-90-02

REPORT DOCUMENTATION PAGE

1a. REPORT SECURITY CLASSIFICATION Unclassified	1b. RESTRICTIVE MARKINGS
2a. SECURITY CLASSIFICATION AUTHORITY	3. DISTRIBUTION/AVAILABILITY OF REPORT Approved for public release; distribution unlimited.
2b. DECLASSIFICATION/DOWNGRADING SCHEDULE	
4. PERFORMING ORGANIZATION REPORT NUMBER(S)	5. MONITORING ORGANIZATION REPORT NUMBER(S) ARO 25143.19-MS-A
6a. NAME OF PERFORMING ORGANIZATION Center for Materials Science and Engineering & Center for Electromechanics, The University of Texas at Austin. 6b. OFFICE SYMBOL (If applicable)	7a. NAME OF MONITORING ORGANIZATION U. S. Army Research Office
6c. ADDRESS (City, State, and ZIP Code) Austin, TX 78712.	7b. ADDRESS (City, State, and ZIP Code) P. O. Box 12211 Research Triangle Park, NC 27709-2211
8a. NAME OF FUNDING/SPONSORING ORGANIZATION U. S. Army Research Office 8b. OFFICE SYMBOL (If applicable)	9. PROCUREMENT INSTRUMENT IDENTIFICATION NUMBER DAAL03-87-K-0073
8c. ADDRESS (City, State, and ZIP Code) P. O. Box 12211 Research Triangle Park, NC 27709-2211	10 SOURCE OF FUNDING NUMBERS PROGRAM LEMENT NO. / PROJECT NO. / TASK NO. / WORK UNIT ACCESSION NO.

11 TITLE (Include Security Class) CONTROLLING FUNDAMENTALS IN HIGH-ENERGY HIGH-RATE PULSED POWER MATERIALS PROCESSING OF POWDERED TUNGSTEN, TITANIUM ALUMINIDES, AND COPPER-GRAPHITE COMPOSITES [FINAL REPORT, UNCLASSIFIED.]

12. PERSONAL AUTHOR(S) C. PERSAD, H. L. MARCUS, D. L. BOURELL, Z. ELIEZER, W. F. WELDON.

13a. TYPE OF REPORT	13b. TIME COVERED	14 DATE OF REPORT (Year, Month, Day)	15. PAGE COUNT
FINAL REPORT	FROM 87 JUN 01 TO 90 AUG 31	90 OCT 31	315

16 SUPPLEMENTARY NOTATION The view, opinions and/or findings contained in this report are those of the author(s) and should not be construed as an official Department of the Army position, policy, or decision, unless so designated by other documentation.

17. COSATI CODES		
FIELD	GROUP	SUB-GROUP

18. SUBJECT TERMS (Continue on reverse if necessary and identify by block number) (SEE BLOCK 18 ENTRY OVERLEAF)

19 ABSTRACT (Continue on reverse if necessary and identify by block number)

(SEE BLOCK 19 ENTRY OVERLEAF)

20 DISTRIBUTION/AVAILABILITY OF ABSTRACT ☐ UNCLASSIFIED/UNLIMITED ☐ SAME AS RPT ☐ DTIC USERS	21 ABSTRACT SECURITY CLASSIFICATION Unclassified
22a NAME OF RESPONSIBLE INDIVIDUAL	22b. TELEPHONE (Include Area Code) / 22c OFFICE SYMBOL

18. SUBJECT TERMS
(BASED UPON MATERIALS RESEARCH SOCIETY KEYWORDS BY TOPIC GUIDELINES)

A. **SYNTHESIS:** chemical synthesis, powder metallurgy, self-propagating high-temperature synthesis, sintering, sol-gel.

B. **PROCESSING:** bonding, extrusion, forging, welding.

C. **MATERIAL TYPE:** alloys-intermetallic, ceramics, composites, glasses-metallic, metals, superconductors.

D. **MATERIAL FORM:** colloidal, laminate, mixture, polycrystal, powder.

E. **ANALYSIS TECHNIQUES:** Auger electron spectroscopy, computer simulation, differential thermal analysis, hardness testing, optical metallography, scanning electron microscopy, scanning/transmission electron microscopy, transmission electron microscopy, x-ray diffraction.

F. **PROPERTY STUDIED:** electrical properties, mechanical properties, tribology, crystallographic structure, phase transformation, diffusion.

* Powder metallurgy,
* Tungsten alloys,
* Titanium aluminide,
* Copper alloys
* Graphite

19. ABSTRACT

This study was conducted to determine the controlling fundamentals in the high-energy high-rate (1 MJ in 1s) processing of metal powders. This processing utilizes a large electrical current pulse to heat a pressurized powder mass. The current pulse was provided by a homopolar generator. Simple short cylindrical shapes were consolidated so as to minimize tooling costs. Powders were subjected to current densities of 5 kA/cm2 to 25 kA/cm2 under applied pressures ranging from 70 MPa to 500 MPa. Disks with diameters of 25 mm to 70 mm, and thicknesses of 1 mm to 10 mm were consolidated. Densities of 75% to 99% of theoretical values were obtained in powder consolidates of tungsten, titanium aluminides, copper-graphite, and other metal-ceramic composites. Extensive microstructural characterization was performed to follow the changes occuring in the shape and microstructure of the various powders. The processing science has at its foundation the control of the duration of elevated temperature exposure during powder consolidation. The goal was a fuller understanding of the interrelated electrical, thermal and mechanical interactions that occur during the observed rapid densification.Three major densification mechanisms were observed. These were: plastic flow at elevated temperature in single-phase systems such as tungsten; plastic flow of a minor low-temperature phase in a two phase non-interacting system such as tungsten-copper; and liquid-phase-assisted densification via the production of a small quantity of liquid within the consolidated mass. The process appears particularly well-matched to the elevated temperature, solid state consolidation of powders of metals, and of metal-matrix composites such as copper + graphite, in which exothermic reactions are absent. With the continued maturation of the now commercially available homopolar generator pulsed power sources, the materials processing technology flowing from this research will find specialized niches in the production of components that fully exploit its potential for single-residence conversion of powders to finished parts. High performance sliding electrical contacts provide one example of such a process-product match in which technology transfer is now imminent.

1. FOREWORD

This is the final report of work completed under DARPA/ARO Contract **DAAL 0387-K-0073,** [June 1, 1987 - August 31, 1990], to perform research on the controlling fundamentals of High-energy High-rate materials processing using pulsed power sources. The work was performed by the Center for Materials Science and Engineering, and the Center for Electromechanics, Bureau of Engineering Research, The University of Texas at Austin, Austin, TX 78712.

Special materials were provided for this research by outside laboratories. Tungsten powders were received from Los Alamos National Laboratories, NM. (H. Sheinberg), and from GTE. Titanium aluminide powders (γ-TiAl and α_2-Ti_3Al-based) were provided by Ralph Anderson's group at Pratt and Whitney, FL.

Project monitors were E. Farnum, DARPA, and A. Crowson, ARO.

2. TABLE OF CONTENTS

3. LIST OF TABLES, FIGURES, AND APPENDICES

Appendices

4A. STATEMENT OF THE PROBLEM STUDIED

The objective of this three-year effort was to develop an understanding of the controlling fundamentals in high-energy high-rate materials processing using pulsed power. The primary powder materials systems selected for study were tungsten, titanium aluminide, and copper-graphite. Other systems were investigated to define specific niches where this type of processing could be advantageously applied.

4B. SUMMARY OF THE MOST IMPORTANT RESULTS

INTRODUCTION

This final report is a summary and compilation of published research results. The research was funded by DARPA and monitored by ARO. The research was aimed at understanding the con ˋlling fundamentals in high-energy high-rate powder processing. In this process, pressurized conductive powders are densified by the Joule (I^2R) heating obtained from a current pulse. The large current pulse is provided by the discharge of a Homopolar Generator (HPG).

This section summarizes the findings of the research into the controlling fundamentals in High-Energy High-Rate Processing. In section 4.1, the processing method is compared to the global set of powder consolidation processes. In section 4.2, its historical development is traced. In section 4.3, the methodology associated with the application of the technique in laboratory research is described. In section 4.4, the observed mechanisms that control densification are discussed. Factors pertinent to the evolution of this process into a manufacturing technology are indicated in section 4.6. In section 4.7, results obtained on specific materials systems are described.

4.1 Comparison with Other Processes

Efficient densification of metallic powders can be achieved by the simultaneous application of temperature and pressure. Uniaxial vacuum hot pressing, hot isostatic pressing, and hot large-strain deformation processing such as powder rolling and powder extrusion which exploit this approach are well-established processes for making fully dense materials from powder.

High-energy High-rate processing for powder consolidation belongs to the group of processes in which electrical energy is dissipated within the powder mass to cause a rise in temperature. When combined with pressure application, this process leads to rapid densification.

In powder consolidation, the pressure-assisted densification processes have been differentiated by the magnitude, duration, and directionality of the applied pressure.

Table 4.1. A comparison of pressure-assisted densification processes [1].

PROCESS	MAGNITUDE (GPa)	DURATION (s)	DIRECTIONALITY OF LOADING
Hot pressing	0.01-0.03	10^3-10^4	Uniaxial
Hot Isostatic Pressing	0.10-0.30	10^3-10^4	Isostatic
Hot Extrusion	0.10-1.00	10^2-10^4	Complex
HEHR	0.10-0.50	1-10	Uniaxial
Explosive	10-100	$\sim 10^{-6}$	Complex

Table 4.1 provides a comparison of several of the mature powder consolidation processes with the High-Energy High-Rate (HEHR) Process. It is observed that a key feature of the HEHR process is the short duration of the time at elevated temperature. By careful matching of a pressure application profile to the temperature developed within the powder mass, efficient pressure-assisted densification can be obtained by plastic flow.

Appendix A-1 provides an overview of the metallurgical approach to the application of pulsed power to materials processing. The interaction time and power density mapping of a variety of materials processes are mapped in Figure 1. Overlaid is the regime labelled PPP1 in which most of this research was performed. PPP2 is the regime for capacitor-bank powered consolidation. Less conductive materials such as the YBCO superconductor powders were processed in this regime [see Appendix G-2 for details].

From a metallurgical standpoint, the manipulation of time-at-temperature is the common approach to control of transformations. Figure 2 indicates the potency of HEHR processing in controlling transformations by limiting the time at elevated temperature.

Appendix A-2 discusses some of the engineering aspects associated with implementation of this type of processing.

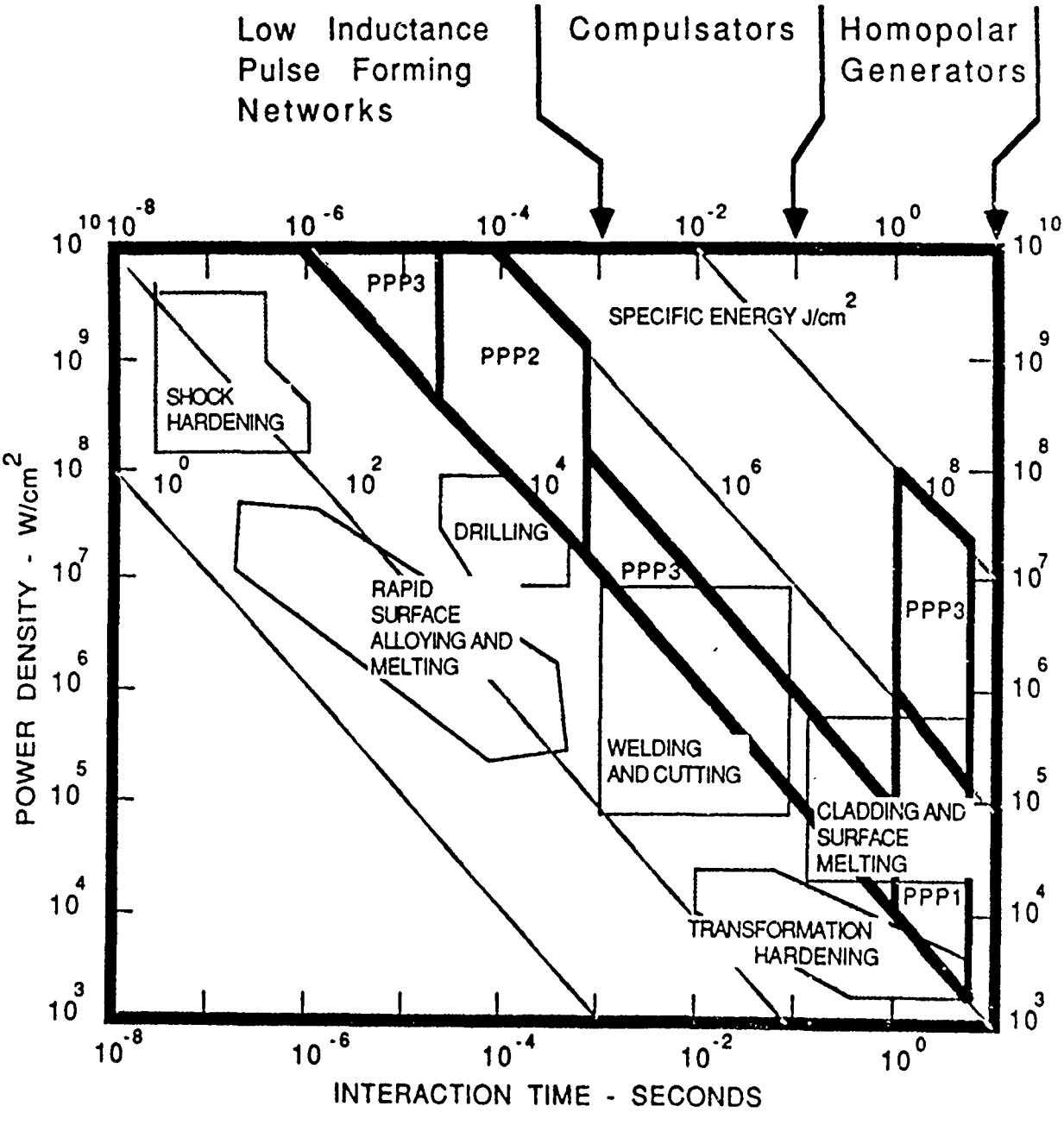

Figure 1. A power density versus interaction time plot indicating the fields of HEHR processing research. PPP1 and PPP2 indicate the fields in which this HEHR processing research was performed. PPP3 is the regime for pulsed power sources now under development.

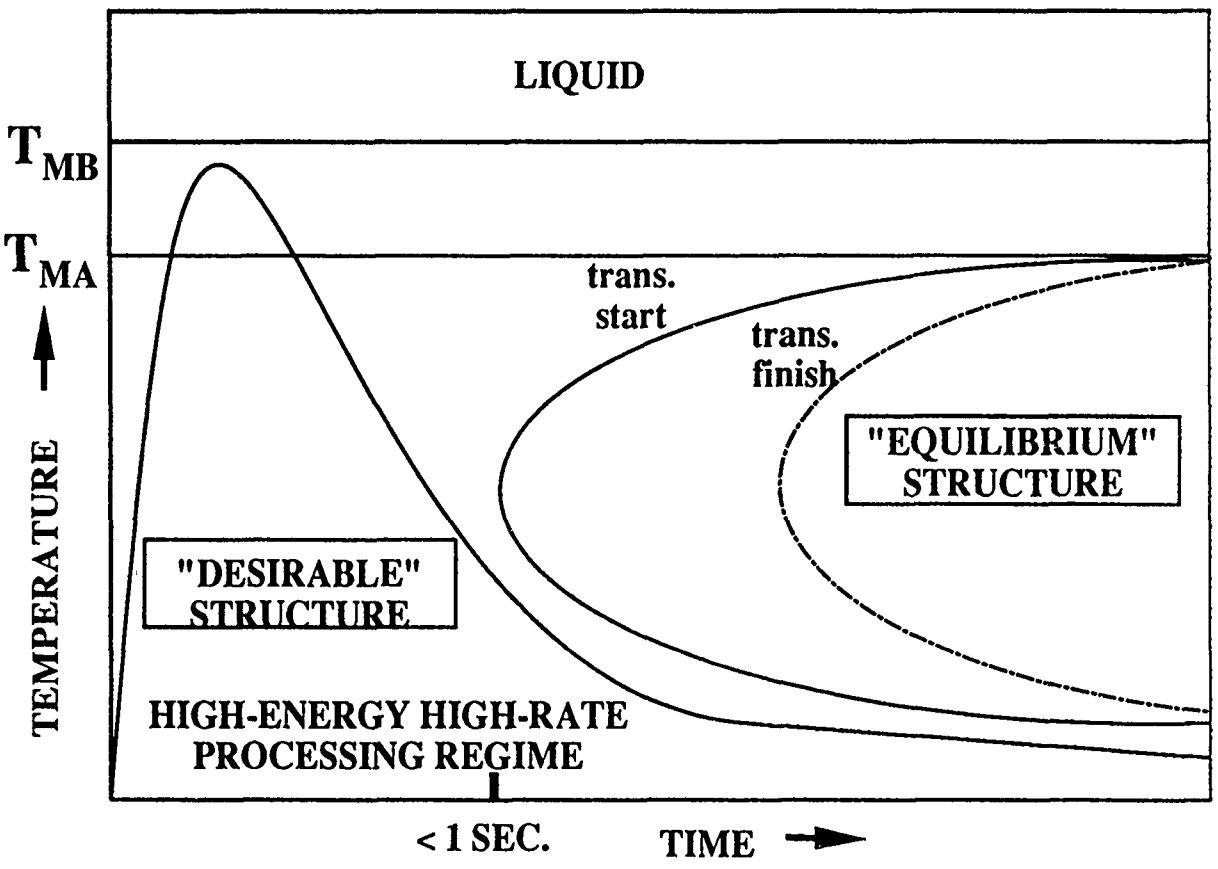

Figure 2. A TTT diagram demonstrates the potential advantage of HEHR consolidation in maintaining non-equilibrium structures. A profile for a two-phase powder assemblage is shown thermally pulsed with a short (< 1 s) high temperature exposure.

4.2 Historical Background

Powder-based metallic materials and metal-ceramic composites can be produced by a variety of methods including the use of large electrical currents. For over fifty years it has been known that the direct electrical resistance heating of conductive metallic powder materials can cause densification. The mechanism by which this densification proceeds is material specific and is related to time at temperature during processing. The interest in the use of electrical current for heating of powders has been sporadic [2-5] and has been handicapped by the absence of a well-matched power source.

Over the last decade, devices for the production of pulsed electrical power have enjoyed a developmental thrust. In particular, homopolar generators (HPG) based upon the Faraday disk have been successfully engineered and commercialized [6]. The availability of these machines as pulsed power sources has fostered the development of novel powder processing approaches for metals and metal-ceramic composites.

At the University of Texas at Austin, powder processing powered by a homopolar generator has been developed as a high-energy high-rate (HEHR) materials processing technique [7]. The '1 MJ in 1s' pulsed energy delivery from a 10 MJ HPG has been employed in a wide-ranging series of processing experiments, including welding, billet heating, and powder consolidation.

4.3 Experimental Apparatus

In laboratory research, the two key components in the apparatus are a powder heating source and a powder pressurization source. These are shown schematically in Figure 3 in conjunction with the die. The powder mass is maintained under pressure in the die between two electrodes which also deliver the electrical current for heating.

As indicated earlier the powder heating occurs by pulsed Joule Heating [proportional to the product of the square of the current and the resistance of the powder mass (I^2R)]. The heating source is therefore a high current delivery system - a Homopolar generator. The basic principles of these rotating electrical machines as pulsed power supplies have been discussed and compared to other pulsed power systems by Weldon [8]. For powder consolidation, these machines are capable of delivering high stored energies via currents at 10^6 Ampere levels. Their low voltage (< 100V) is sufficient for the processing of most metallic-conducting systems.

The pressure is provided by a hydraulic press with 100 ton capacity. By incorporating customized accumulators and timers into a basic system, it was possible to increase the pressure at a time during the temperature cycle corresponding to the peak temperature, thus obtaining plastic-flow induced densification at minimum flow stress. While the system employed in this research was based upon preset values of pressure vs time, a fast-response system with feed-back based upon changes in resistivity of the powder mass may be easily engineered into a system for a specific industrial application. An example of the clear changes in resistivity during the processing of metallic glass powders is presented in Figure 4 and discussed in Appendix E-3.

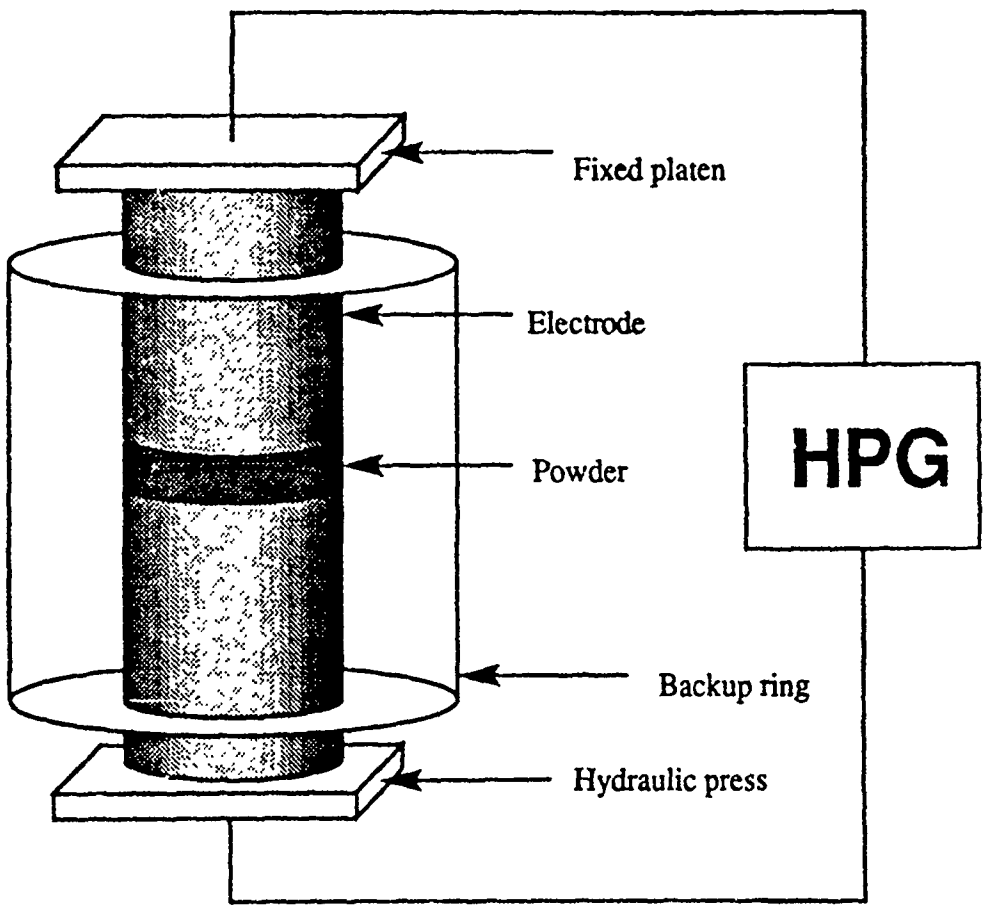

Figure 3. Schematic of HEHR consolidation processing apparatus.

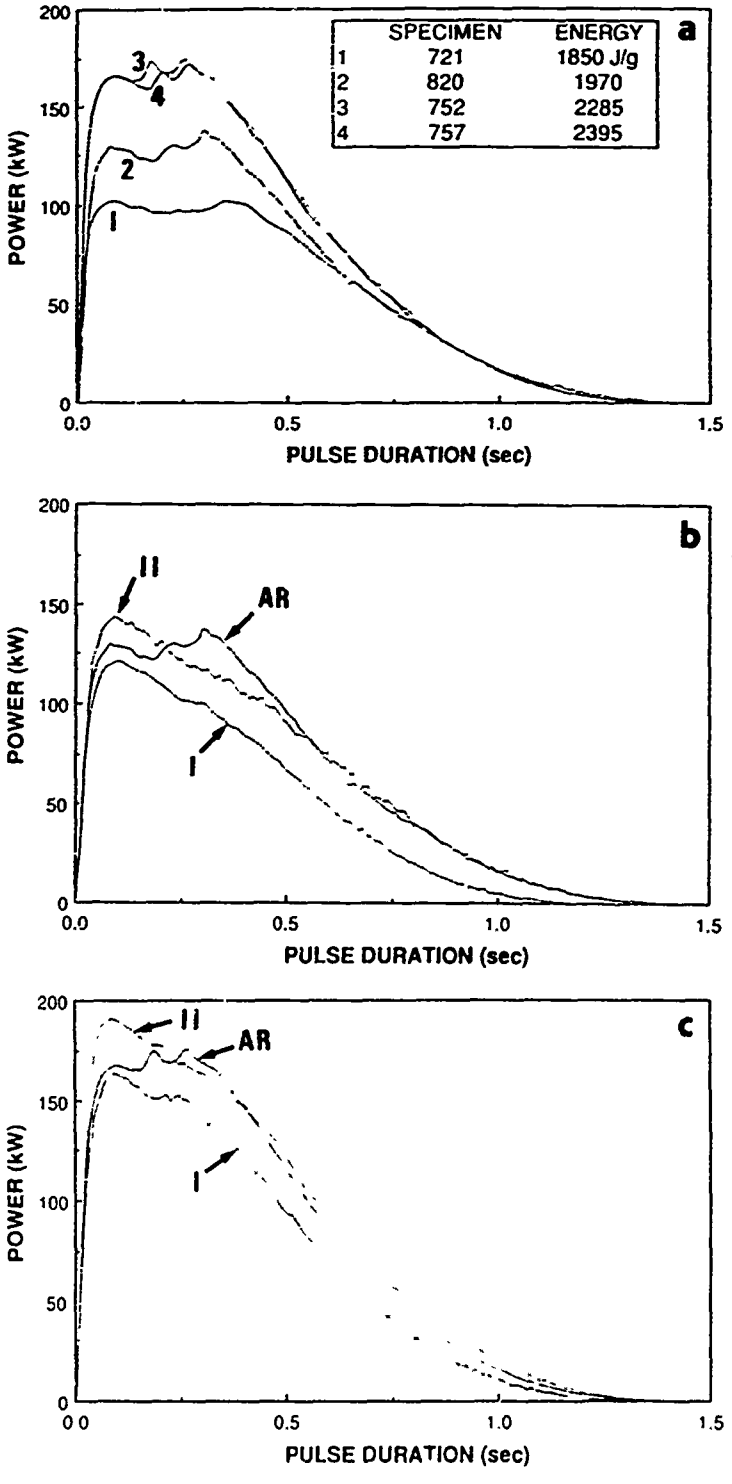

Figure 4. Power spectra of the (a) as-received powder consolidates, (b) low (<2000 J/g) input energy samples #820 (AR), #766 (I), #824 (II) and (c) high (>2000 J/g) input energy samples #757 (AR), #765 (I), #827 (II). Metallic glass powders in various stages of crystallization show sensitive responses to energy input based upon their electrical resistivities, see Appendix E-3 for a detailed discussion.

4.4 Densification Mechanisms

Different material-specific mechanisms were observed to operate in the single-residence conversion of loose powders into a consolidated mass of near full density. Three broad classes are distinguished: (i) single-phase systems processed in the solid state, eg. W, (ii) two-phase systems in which deformation occurs preferentially in the lower strength phase, eg., W-Cu, (iii) multiphase systems in which a transient liquid phase is formed during processing either by a solid→liquid phase change of one constituent, or by the formation of a reaction product with lower melting temperature than the parent phases, eg., W-Ni, W-Ni-Fe + B_4C. Most of this research was conducted with systems in which the materials were maintained in the solid state, and in which the densification occured by plastic-flow. This type of HEHR processing is essentially a single-residence closed-die powder forging operation in which the elevated exposure temperature is limited to very short times.

From a materials synthesis standpoint, the processing of multi-phase systems in which new liquid phases are produced offers many exciting possibilities. From an engineering standpoint however, the containment of liquids at high pressures requires considerably more effort in die design and in the selection of die materials that resist attack by liquid metals. One interesting approach to this problem is to utilize the liquid formed in an exfiltration mode. In this method a controlled volume of liquid is formed well within the hot pressurized mass and forced outward in all directions becoming solid again before it can exit from the consolidated mass.

4.6 Towards a Manufacturing Technology

HEHR powder processing is still a research laboratory technique awaiting industrial deployment. The vehicle for such deployment is expected to be a product which utilizes the technique at its full potential. Two such products are now under consideration, both of which have origins in this research. These are a high-speed, high-current sliding electrical contact based on copper-graphite, and a wear-resistant mining tool based upon cemented tungsten carbide. Both of these attempt to exploit a unique feature of HEHR processing: the ability to consolidate powders and to bond the consolidate onto a wrought mandrel all in the same process.

4.7 Specific Materials Systems

The focus of the program has been an experimental effort to define processing/ microstructure/property relationships. Although the emphasis was on understanding the processing science, several materials systems of varying complexity were studied.

Three major materials systems were studied: tungsten; titanium aluminides; and copper-graphite composites. The highlights of the results are given here. Details are provided in the published papers which are appended. Table 4.2 is a compilation of the many materials systems that were investigated and the sources in which the results are documented.

Table 4.2. Materials Systems Studied in this Research and Published Sources

MATERIALS SYSTEM	PUBLISHED SOURCE
Al-SiC	Appendix G-3, Appendix G-4
TiAl	Appendix C-2, Appendix C-3
Ti_3Al	Appendix C-1, Appendix C-2, Appendix C-3
Fe-Si-B	Appendix E-1
Co-Fe-B	Appendix G-5
Ni-Mo-Fe-B	Appendix E-2, Appendix E-3
Cu-C	Appendix D-1, Appendix D-2, Appendix D-3
Cu-W	Appendix F-2
Cu-W-WC-C	Appendix F-4
$YBa_2Cu_3O_{7-x}$	Appendix G-2
W	Appendix B-1, Appendix B-2, Appendix B-3, Appendix B-4
W-Ni	Appendix B-3
W-Cu	Appendix D-3
W-Nb	Appendix B-3
W-Ni-Fe + B_4C	Appendix B-1, Appendix B-2, Appendix B-3

In the case of the tungsten processing, a fully integrated approach was developed that included the synthesis of ultrafine metallic powders from oxide precursors. These ultrafine powders provided excellent matching to the process since the resistance of the powder mass constituted therefrom had a large constriction resistance contribution. This particle-size controlled component of the resistance improved the efficiency with which the powder mass could be heated, and allowed the achievement of the high temperatures necessary for tungsten consolidation. Results are detailed in Appendix B-1 to B-4.

The initial effort on the titanium aluminides examined the processability of γ-TiAl powders, and of Nb-stabilized Ti_3Al. Because of their inherent low ductility, the γ-TiAl disks produced were always cracked, often in a radial pattern. Crack-free disks of Nb-stabilized Ti_3Al were produced at near-full density. The latter composition was then employed as an intermetallic matrix and reinforced with ceramic powders such as SiC, TiB_2 and AlN. The interfaces produced in these systems showed a variety of reaction products indicating that these reinforcements were not stable at high temperatures. An effort to produce a composite of TiAl dispersed in Ti_3Al matrix showed a more stable interface. Details are given in Appendix C-1 to C-3.

The effort on copper-graphite composites was aimed at the consolidation of fully dense material from elemental copper and carbon powders. It was anticipated that such binderless consolidation would allow these materials, as sliding electrical contacts, to surpass the 200m/s barrier that had been observed in conventionally processed materials which contained Pb-Sn additives. This performance objective was met by the materials consolidated by this method [9]. A continuing program funded by the State of Texas is now underway to commercialize this class of materials for high performance sliding electrical contact applications.

Other significant efforts were in the areas of metallic glass processing [see Appendix E] and in the area of solid armatures/electrotribology [see Appendix F]. The effort on metallic glasses led to the discovery of a new eta-boride phase, (see Appendix E-2), and the understanding of the influence of degree of crystallinity upon the heat evolved during processing and its effect on the microstructure of HEHR consolidated material (Appendix E-3). The solid armatures/electrotribology area provided interesting insights into how materials respond to large pulsed currents in electromagnetic launch technology and contributed to the understanding of the possibilities in multi-phase materials processing using pulsed power. These insights have also produced some new initiatives aimed at the development of specially tailored materials for these high performance electrotribological applications (for example, see Appendix F-4).

Summary

This study was conducted to determine the controlling fundamentals in the high-energy high-rate (1 MJ in 1s) processing of metal powders. This processing utilizes a large electrical current pulse to heat a pressurized powder mass. The current pulse was provided by a homopolar generator. Simple short cylindrical shapes were consolidated so as to minimize tooling costs. Powders were subjected to current densities of 5 kA/cm2 to 25 kA/cm2 under applied pressures ranging from 70 MPa to 500 MPa. Disks with diameters of 25 mm to 70 mm, and thicknesses of 1 mm to 10 mm were consolidated. Densities of 75% to 99% of theoretical values were obtained in powders of tungsten, titanium aluminides, copper-graphite, and other metal-ceramic composites. Extensive microstructural characterization was performed to follow the changes occuring in the shape and microstructure of the various powders. The processing science has at its foundation the control of the duration of elevated temperature exposure during powder consolidation. The goal was a fuller understanding of the interrelated electrical, thermal and mechanical interactions that occur during the observed rapid densification.Three major densification mechanisms were observed. These were: plastic flow at elevated temperature in single-phase systems such as tungsten; plastic flow of a minor low-temperature phase in a two phase non-interacting system such as tungsten-copper; and liquid-phase-assisted densification via the production of a small quantity of liquid within the consolidated mass. The process appears particularly well-matched to the elevated temperature, solid state consolidation of powders of metals, and of metal-matrix composites such as copper + graphite, in which exothermic reactions are absent. With the continued maturation of the now commercially available homopolar generator pulsed power sources, the materials processing technology flowing from this research will find specialized niches in the production of components that fully exploit its potential for single-residence conversion of powders to finished parts. High performance sliding electrical contacts provide one example of such a process-product match in which technology transfer is now imminent.

4C. LIST OF PUBLICATIONS AND TECHNICAL REPORTS

1. H. L. Marcus, D. L. Bourell, Z. Eliezer, C. Persad and W. Weldon, "High-Energy High-Rate Materials Processing," Journal of Metals, Vol. 39, No. 12, Dec. 1987,pp. 6-10.

2. G. Elkabir, C. Persad, H. L. Marcus, and T. A. Aanstoos, "High-Energy High-Rate Consolidation of Aluminum- Silicon Carbide Composites", Proceedings of the Ninth Annual Discontinuously Reinforced MMC Working Group Meeting, Park City, UTAH, January 1987, (MMCIAC No. 000695), MMCIAC, Santa Barbara, CA, 1988, pp. 363-386.

3. C. J. Lund, C. Persad, Z. Eliezer, D. Peterson, and J. Hahne, "Composite Solid Armatures for Railguns", J. H. Gully (ed.), Paper #13 in Proceedings of the 3rd International Conference on Current Collectors, Austin, TX, November 1987.

4. M. J. Wang, C. Persad, Z. Eliezer, and W. F. Weldon, "High-Energy/High-Rate Consolidation of Copper-Graphite Composite Brushes for High-Speed, High-Current Applications", J. H. Gully (ed.), Paper #20 in Proceedings of the 3rd International Conference on Current Collectors, Austin, TX, November 1987.

5. Y. W. Kim, D. L. Bourell, and C. Persad, "Consolidation of Metallic Glass Ribbons using Electric Discharge Welding", Metall. Trans., Vol. 19A, June 1988, pp 1634-1638.

6. M. E. Fine, D. L. Bourell, Z. Eliezer, C. Persad, and H. L. Marcus, "Basic Principles for Selecting Phases for High Temperature Metal Matrix Composites: Interfacial Considerations" Scripta Met., 22, June 1988, pp. 907-910.

7. Y. W. Kim, L. Rabenberg, and D. L. Bourell, "Identification of an eta-Boride Phase as a Crystallization Product of a NiMoFeB Amorphous Alloy", Journal Mater. Res. 3(6), November/December 1988, pp. 1336-1341.

8. C. Persad, S. J. Lee, D. R. Peterson, J. S. Swinnea, M. Schmerling, K. M. Ralls, H. L. Marcus and H. Steinfink, "Consolidation of Powders of the Oxide Superconductor $YBa_2Cu_3O_x$ by High-Energy High-Rate Processing", Proceedings of the World Congress on Superconductivity, Houston, TX, February, 1988, C. G. Burnham & R. Kane (eds), Vol. VIII of World Scientific Series on PROGRESS IN HIGH TEMPERATURE SUPERCONDUCTIVITY, World Scientific Publishers, Teaneck, NJ, 1988, pp 460-475.

9. Z. Eliezer, M. J. Wang, C. Persad, and J. H. Gully, "A Novel Processing Technique for Metal/Ceramic Composites", in Ceramic Developments, C. C. Sorrell and B. Ben-Nissan (eds.), Materials Science Forum, Vol. 34-36, Trans. Tech. Publ., Switzerland, (1988) pp 505-509.

10. C. Persad, S. Raghunathan, B. H. Lee, D. L. Bourell, Z. Eliezer and H. L. Marcus, "High-Energy High-Rate Processing of High-Temperature Metal-Matrix Composites", Proceedings of the MRS Symposium on High Performance Composites, Reno, NV, April 1988, published as MRS Symposia Proc. Vol. 120, F. D. Lemekey, A. G. Evans, S. Fishman, and J. R. Strife (eds.), MRS, Pittsburgh, PA, 1988, pp 23-28.

11. C. Persad, D. R. Peterson, and R. C. Zowarka, "Composite Solid Armature Consolidation by Pulse Power Processing: A Novel Homopolar Generator Application in EML Technology", IEEE Trans. on MAgnetics, January 1989, pp 429-432.

12. C. Persad, C. J. Lund, Z. Eliezer, D. Peterson, J. Hahne, and R. C. Zowarka, "Wear of Conductors in Railguns: Metallurgical Aspects", IEEE Trans. on Magnetics, January 1989, pp 433-437.

13. H. L. Marcus, C. Persad, Z. Eliezer, D. L. Bourell, and W. F. Weldon, "High-Energy High-Rate Processing of Composites", Proceedings of the Tenth Annual Discontinously Reinforced MMC Working Group Meeting, Park City, Utah, January 1988, (MMCIAC No. 000696), MMCIAC, Santa Barbara, CA, 1989, pp 235-259.

14. C. Persad, S. Raghunathan, A. Manthiram, M. Schmerling, D. L. Bourell, Z. Eliezer, H. L. Marcus, and W. F. Weldon, "Manufacturing Metallurgy of Tungsten: A Novel Integrated Powder Metallurgy Approach", IIE/OAS/SwRI Proceedings of the Tenth Inter-American Conference on Materials Technology, April, 1989, San Antonio, TX, Volume II, Section 30, pp 33-39.

15. H. M. Tello, C. Persad, H. L. Marcus and D. L. Bourell, "High-Energy High-Rate Deformation Processing of Aluminum-Silicon Carbide Composites", IIE/OAS/SwRI Proceedings of the Tenth Inter-American Conference on Materials Technology, April, 1989, San Antonio, TX, Volume II, Section 30, pp 27-31.

16. W. F. Weldon and T. A. Aanstoos, "Single Residency Sintering and Consolidation of Powder Metal Alloys, Intermetallics, and Composites by Pulsed Homopolar Generator Discharge", Journal of Mechanical Working Technology, 20 (1989) 353-363.

17. C. Persad, B. H. Lee, C. J. Hou, Z. Eliezer, and H. L. Marcus, "Microstructure/ Processing Relationaships in High-Energy High-Rate Consolidated Powder Composites of Ti_3Al + TiAl", MRS Symposium Proceedings, Vol. 133: "High Temperature Ordered Intermetallic Alloys III", edited by C. T. Liu, A. I. Taub, N. S. Stoloff, and C. C. Koch, MRS, Pittsburgh, PA, 1989, pp 717-722.

18. Y. W. Kim, D. L. Bourell and C. Persad, "High Energy-High Rate Powder Processing of a Rapidly-Quenched Quaternary Alloy, $Ni_{56.5}Mo_{23.5}Fe_{10}B_{10}$", Materials Science and Engineering, A123, 1990, pp. 99-115.

19. C. Persad, S. Raghunathan, A. Manthiram, M. Schmerling, D. L. Bourell, Z. Eliezer, and H. L. Marcus, "Development and Control of Microstructure in P/M Tungsten by Synthesis and Reduction of Tungsten Trioxide Gels", Solid State Powder Processing, A. H. Clauer and J. J. de Barbadillo, eds., TMS, Warrendale, PA, 1990, pp. 357-364.

20. Z. Eliezer, B.-H. Lee, C. J. Hou, C. Persad, and H. L. Marcus, "Matrix-Reinforcement Interface Characteristics of (Ti_3Al + Nb)-Based Powder Composites, Consolidated by High-Energy High-Rate Processing", in Metal & Ceramic Matrix Composites: Processing, Modeling & Mechanical Behavior, R. B. Bhagat, A. H. Clauer, P. Kumar, and A. M. Ritter, eds., TMS, Warrendale, PA, 1990, pp. 401-412.

21. G. Elkabir, C. Persad and H. L. Marcus,"Electrical Characteristics of High Energy-High Rate Consolidated Metal Matrix Composites", Journal of Composite Materials, in press.

22. S. K. Raghunathan, C. Persad, D. L. Bourell and H. L. Marcus, "High-energy, High-rate Consolidation of Tungsten and Tungsten-based Composite Powders", Materials Science and Engineering, A131 (1990) in press.

23. H. L. Marcus, D. L. Bourell, Z. Eliezer, C. Persad, and W. F. Weldon, "Synthesis and High Energy High Rate Processing of Ultrafine Grained Tungsten", Proceedings of BTI Advanced Armor/Anti-Armor Materials Program Review, in pres 1990.

24. Z. Eliezer, C. Persad, S.C. Sparks, D. Moore, M. Schmerling, J. Gully, and R. Carnes "Advanced Composite Materials for High-Performance Electrotribological Applications", paper presented at ASM International's Conference on Tribology of Composite Materials, Oak Ridge, TN, May 2, 1990 and submitted to ASM Proceedings.

25. C. Persad, M. Schmerling, Z. Eliezer, R. Carnes, and J. Gully, "Nanosized Structures in Cu-W-WC-C Composites for Electrotribological Applications", paper submitted to Proceedings of the TMS Northeast Conference on High Performance Composites, Morristown, NJ, June 1990.

26. M. J. Wang, Z. Eliezer and C. Persad, "High-Energy/High-Rate Powder Consolidation of Straight Copper-Graphite Composites for Hogh-Speed, High-current Sliding Contact Applications", submitted to Wear, 1990.

4D. LIST OF SCIENTIFIC PERSONNEL

Faculty and Staff

1. H. L. Marcus
2. Z. Eliezer
3. D. L. Bourell
4. C. Persad
5. M. Schmerling
6. S. Swinnea
7. R. J. Allen
8. T. A. Aanstoos
9. W. F. Weldon

Students

1. C. J. Lund (Grad. Res. Asst.)
2. S. Raghunathan (Grad. Res. Asst.)
3. S. J. Lee (Grad. Res. Asst.)
4. M. J. Wang (Grad. Res. Asst.)
5. H. Tello (Undergrad. Res. Asst. till May 1988, then Grad. Res. Asst.)
6. L. Govea (Grad. Res. Asst.)
7. A. de Jesus (Grad. Res. Asst.)
8. Y. W. Kim (Grad. Res. Asst.)
9. G. Elkabir (Grad. Res. Asst.)
10. B. H. Lee (Grad. Res. Asst.)

11. U. Lakshminarayan (Grad. Res. Asst.)
12. C. Jan Hou (Grad. Res. Asst.)
13. S. Cheng (Undergrad. Res. Asst.)
14. V. Martinez (Undergrad. Res. Asst.)
15. R. Rice (Undergrad. Res. Asst.)

Degrees Granted

1. G. Elkabir, PhD, August 1987
2. Y. W. Kim, PhD, December 1987
3. C. J. Lund, MS, December 1987
4. S. Raghunathan, MS, August 1988
5. S. J. Lee, PhD.,December 1988
6. M. J. Wang, PhD., December 1988
7. U. Lakshminarayan, MS, May 1989
8. B. H. Lee, MS, May 1989
9. H. Tello, MS, August 1989
10. S. Sparks, MS, May 1990.

5. BIBLIOGRAPHY

1. C. A. Kelto, E. E. Timm, A. J. Pyzik, Ann. Rev. Mat. Sci. 1989, 19: 527-550.

2. G. F. Taylor, Apparatus for Making Hard Metal Compositions, U. S. Patent 1,896,844, February 1933.

3. F. V. Lenel, J. of Metals, 1955, 7, 158.

4. S. Isserow, Impulse Resistance Sintering of Compounds for Armor, AMMRC-TR 73-43, 1973.

5. C. Persad, H. L. Marcus and W. F. Weldon, High-Energy High-Rate Pulsed Power Processing of Materials by Powder Consolidation and by Railgun Deposition, UTCMSE-87-02, March 1987, Gov. Reports Index # 732,954, NTIS Code AD-A179 289/4/GAR PC A07/MF A01.

6. J. H. Gully, T. A. Aanstoos, K. Nalty and W. A. Walls, IEEE Trans. Mag., 1986, 22, 1489.

7. H. L. Marcus, D. L. Bourell, Z. Eliezer, C. Persad and W. F. Weldon, JOM, 1987, 39, 6-10.

8. W. F. Weldon, "Pulsed Power Packs a Punch, IEEE Spectrum, Vol. 22 No. 3 (1985), pp 59-66.

9. R. Laughlin, J. Gully, M. Spann, W. F. Weldon, "Continous Duty Current Collection", Final Technical Report, Wright-Patterson Air Force Base Contract F33615-86-C2673, June, 1990.

APPENDIX A

PROCESSING OVERVIEWS

A-1. High-Energy High-Rate Materials Processing

A-2. Single Residency Sintering and Consolidation of Powder Metal Alloys, Intermetallics, and Composites by Pulsed Homopolar Generator Discharge

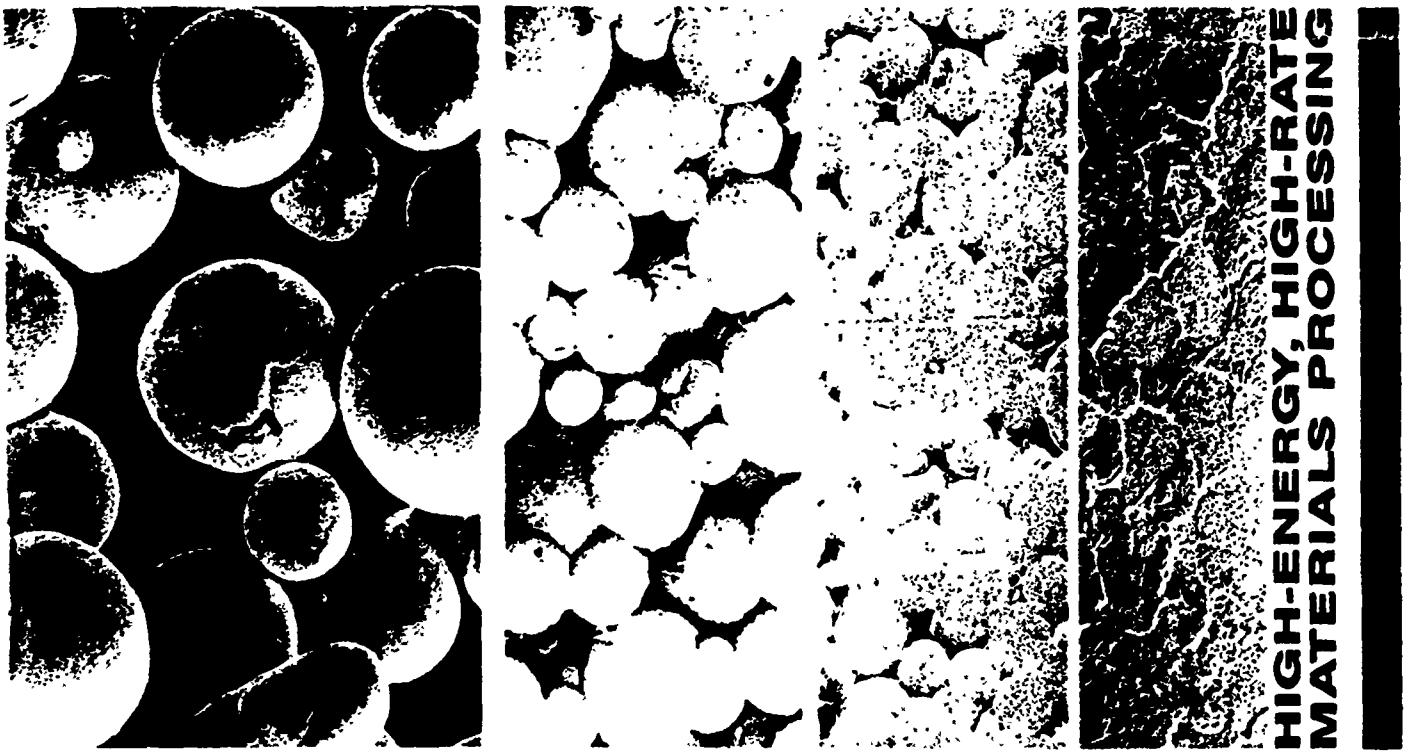

HIGH-ENERGY, HIGH-RATE MATERIALS PROCESSING

High-energy, high-rate processing, driven by fast discharging stored energy devices, offers new potential for producing materials that are otherwise difficult to create, and for the secondary processing of materials such as those derived from the rapid solidification technologies.

H.L. Marcus, D.L. Bourell, Z. Eliezer, C. Persad and W. Weldon
University of Texas at Austin

The consolidation microstructures of molybdenum alloy TZM PREP powders processed in about one second at increasing energy inputs up to 4,300 kJ/kg.

INTRODUCTION

During the development of kinetic energy machinery at the Center for Electromechanics at the University of Texas, it became apparent that the devices are potentially exciting sources of energy for high-energy, high-rate (HEHR) processing. The availability of the pulsed energy sources allowed exploratory programs in butt welding of heavy cross sections of metals, high-rate billet heating, powder consolidation, coating of mixed materials and localized heating. The key result of the exploratory work was that HEHR processing offers several unique processing advantages, with the potential of creating interesting materials not easily produced in other ways. Nevertheless, the technique holds its own set of processing problems that must be solved before becoming commercially competitive.

FUNDAMENTALS

The availability of pulsed power, high-energy kinetic energy storage devices offers an opportunity to perform a wide range of experiments. The power density/interaction time plot shown in Figure 1 gives the regimes where the processing has the most potential. Processing approaches can be divided between direct and indirect techniques.

The discussed studies were performed using a 10 MJ homopolar generator as the pulsed power processing energy source. The homopolar generator is an electric machine that converts stored rotational kinetic energy into electric energy using the Faraday effect. A low-voltage, high-current device, it is an excellent power supply for applications that require short-time, high-energy pulses.[1] Coupling of the homopolar generator to an inductor allows production of current pulse widths down to tens of microseconds. Small-scale experiments are powered by capacitor banks linked into fast, low-impedance, pulse-forming networks. Taken together, these pulse sources offer a variety of processing possibilities with short-time power densities of up to 10^{10} W cm^{-2} over large areas, with interaction times of 10^{-5} to several seconds. Figure 1 shows the operational fields of these pulse power systems as superimposed on a broad materials processing map.

Direct Processing

Direct processes rely on converting stored energy into megampere level electrical currents and passing these currents through the materials in a prescribed manner in terms of pulse time and current distribution, in conjunction with other processes such as application of pressure

Time-Temperature-Transformation (TTT) concepts provide the basis for a fundamental understanding of the potential advantages of the direct pulsed power processing. Because of the inherent control of the times to reach peak temperature, of the order

of the interaction times shown in Figure 1, the duration at the temperature developed can be held to relatively short times. This regime limits the conversion of metastable phases to their equilibrium counterparts and can be well below that required for grain growth even in simple single-phase systems. Depending upon the method of applying the pulsed power, the temperature rise time can be from 10 microseconds to one second. By using a pulsed preheat or postheat in conjunction with the high-temperature pulse, more detailed microstructural control in the workpiece can be expected. A conceptual TTT diagram for a two-component powder system with a pulsed power processing thermal cycle is shown in Figure 2. The example represented by Figure 2 is a transient liquid phase, A, leading to full densification of an A + B blend. A and B could be refractory metals with melting temperatures such that $T_{MA} < T_{MB}$ (e.g., Mo and W, or Nb and W). This could be considered a high-temperature brazing process where no low-temperature materials are involved. Alternatively, for a system with component B alone, it represents fast heating to just below T_{MB}, in consolidating a powder for example. For single component systems with heating rate dependent phase transformations, the HEHR pulsed power processing could allow the phase transformation to proceed in a desired manner. For example, consolidation of metallic glass particulates would allow the final state of crystallization to be controlled. In a microcrystalline solid with processing-dependent metastable phases, controlled pulse power processing could permit a range of structures to be produced by controlling the processing parameters.

The TTT diagram also indicates other regimes of powder consolidation potential for the HEHR pulsed power processing. The primary consideration is that the consolidation processing allows both the introduction of the power and the application of externally applied stresses. The ability to go to very high homologous temperatures would allow deformation to take place at much lower stresses and at much higher rates. This can then lead to more complete consolidation without the primary microstructural changes that would normally take place when processing for extended times at the elevated temperature. In addition, the higher temperature could also serve as the starting point for in-

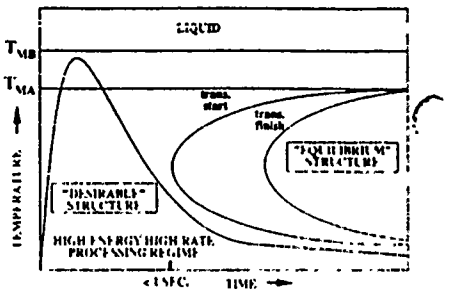

Figure 2. A TTT diagram demonstrates the potential advantage of HEHR consolidation in producing non-equilibrium structures. A two-phase powder assemblage is shown thermally cycled in a short (< 1 s) time exposure.

place extrusion or hot forging of the consolidated material to enhance the properties. This secondary processing that, in many cases, will be required to obtain acceptable mechanical properties, would also be done on a cold wall basis with minimum time at temperature.

Consolidation can range from a green compact to a cast condition depending on the relationship between specific energy input and the applied stress. This and the information suggested by Figures 1 and 2 is the basis of HEHR pulsed power processing. Figure 3 shows the fineness of structure which can be obtained with this method of consolidation. In Figure 3a, prior particle boundaries are evident in a compact consolidated with low energy input by a powder forging mechanism. With high energy input, a finely distributed hard boride phase becomes evident (Figure 3b). The fineness of structure maintained by HEHR processing contributes to the increased comparative hardness: HRC 46-47, hot isostatic pressing (HIP'ing); HRC 47-50, hot extrusion; HRC 55-60, HEHR processing. Additionally, HEHR processing can produce densities comparable to HIP'ing and hot extrusion.[4]

Direct processes require that the power, in terms of electrical current, be placed at the appropriate region of the processed material to obtain the desired properties and microstructure throughout the workpiece. For example, the ability to concentrate a major fraction of the energy into a thin segment of the material using a very short electrical current pulse, which behaves as a very high frequency current (skin effect), allows localized phase and grain structure changes to take place without changing the bulk of the material. Case hardening via skin effect experiments on 1040 steel has been demonstrated as well as skin heating of copper, leading to grain growth and lower strength.[5]

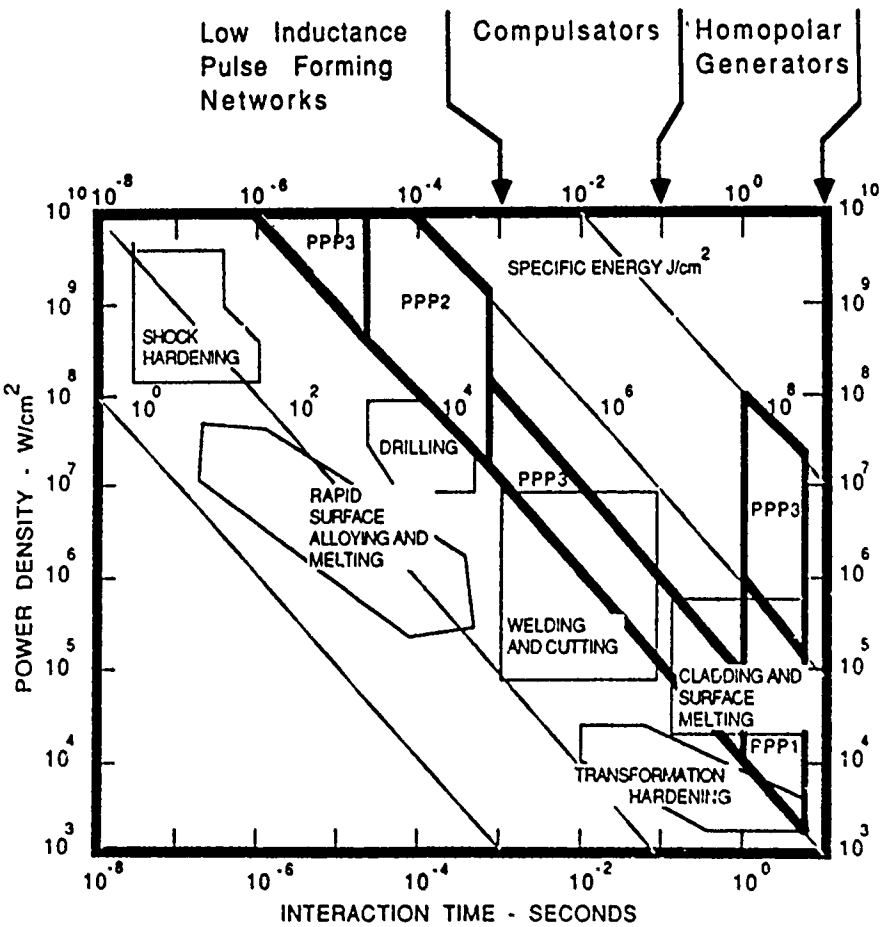

Figure 1. A power density versus interaction time plot indicating the fields of HEHR processing research. PPP1 and PPP2 indicate the fields of current exploratory HEHR processing research. PPP3 is the regime for pulsed power sources now under development.

Indirect Processing

Indirect HEHR processing approaches involve the delivery of the power into a secondary process that then causes the material processing to proceed. Figure 4 shows the general experimental scheme associated with railgun processing. The HEHR processing power source applies current through the rails and accelerates the material as a plasma, possibly transporting with it liquid droplets and/or solid particles at very high velocities. This material is then directed at a substrate. The velocities reached, which can be greater than 10 km/s, then induce interactions between the propelled materials and the substrate. The velocities make it possible for a thin layer of the interface between the substrate and the deposited material to be either locally implanted or mechanically mixed to form a graded interface. Multiple deposits offer the potential of a wide range of chemically graded, layered surface coatings. General surface modification is a possibility of this technique.

The railgun approach is also the basis for shock loading HEHR processing. In this case, the accelerated projectile operates as a shock loading ram that impacts the materials to be processed. This offers the possibility of consolidation of nonconducting materials as well as the potential for inducing very high pressure stable phase transformations comparable to explosive loading approaches.

The third indirect HEHR processing approach involves application of large induced magnetic field forces associated with the large currents in the process. These magnetic-related forces have the potential to be used for various deformation processing methods, including localized deformation and the consolidation of nonconductors.

POWDER CONSOLIDATION

HEHR processing is a potentially useful approach to powder consolidation for two reasons. The first is that the speed associated with the processing offers the opportunity to maintain the fine microstructure associated with the original powders in the consolidated material. This fine structure could be either a non-equilibrium microstructure or a fine grain or subgrain structure. The second is that the heating is concentrated at the interfaces of the conducting particles. This acts as a self-limiting heating region due to the resistivity increase at the interface shunting the current. In addition, the containment die operates in a cold wall configuration which serves to assist in accelerated cooling after the current is removed. Special advances in enhanced cooling are also required to optimize this approach. As schematically shown in Figure 2, the ability to complete the processing in times shorter than the transformation times or with little growth of the transformed phases allows investigation of a wide range of materials consolidation processes.

Process Control

One feature of consolidation using the homopolar generator is that the consolidation sequence can be monitored through in-process data. In metallic glasses, for example, the as-received powder consolidation power spectra show three peaks. The first peak arises from initial consolidation between powders that causes reduced contact resistance and an accompanying reduction of power. The powder then undergoes the first crystallization with the associated exothermic reaction. This reduces the material's specific resistivity and induces higher current from the still-discharging homopolar generator. This in turn results in a second peak on the power spectrum. The third peak has a similar origin as the second peak, only due to the second crystallization. The exothermic reaction of crystallization acts as another heat source for final consolidation. Therefore, it is proposed that to accomplish metallic glass compaction with minimal degradation of the initial powder microstructure, current should be cut off using a closed loop control process that initiates a by-pass current path interlocked with discharge controlling devices after the first power peak. Other materials systems have shown similar characteristics.

Refractory Molybdenum Alloy

TZM PREP powders have proven difficult to consolidate by conventional methods. In particular, HIP'ing at 1600°C at 30 ksi for three hours has not produced full densification. Densification was a vital aspect of this work. Densification of TZM powder to about 99% of the theoretical density without extensive melting has been accomplished, making the process unique.[6] For TZM PREP, the trends indicate that density increases with increasing energy input and applied pressure. Figure 5a shows a representative structure of TZM PREP powder consolidated at 4300 kJ kg and 270 MPa. High density is obtained with no visible evidence of melting. Densification at the higher specific energy inputs (~9000 kJ/kg) may have been accelerated by local interparticle-interface melting.

The fracture study showed all of the failures to be by brittle cleavage as was the case for the HIP'ed material. There did not appear to be any grain boundary fracture, even in the highly dense regions. Powder particle shape outlines were distinguishable to varying degrees in the consolidated product. The inhomogeneity of the as-received powders masked the effect of the processing on grain growth. However, there was little evidence of melting and no massive grain growth. Also, there was no evidence of coarsening in the carbides of the consolidated samples. Both high- and low-input energy samples has Mo_2C and TiC particles of the same size.

Nickel-Based Metallic Glass

Metallic glasses created in thin sections at cooling rates of ~ 10^6 K/s pose peculiar secondary processing problems. The structure stability is so fragile that most practical consolidation approaches to make thicker sections utilizing elevated temperature and pressure lead to significant degeneration in structure. Deserting

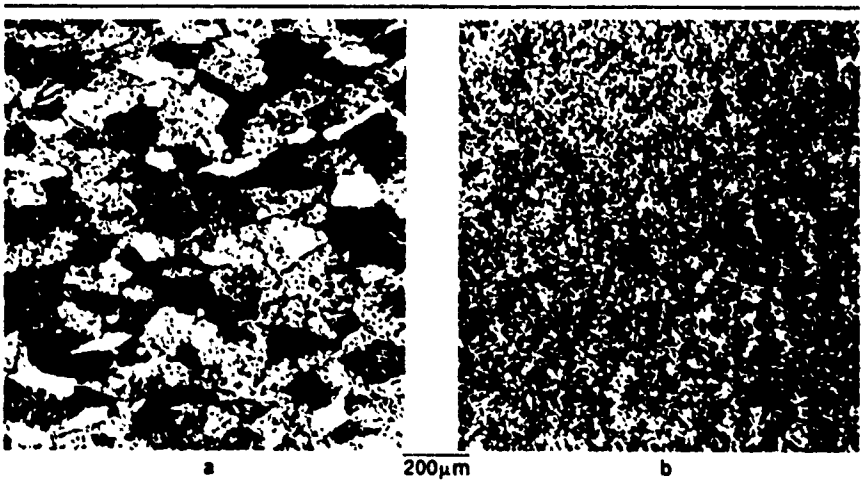

Figure 3 Structure comparisons of METGLAS® 7025 produced by HEHR consolidation (a) Low energy input (700 kJ/kg) and (b) high energy input (6600 kJ/kg)

the pristine objective of amorphous bulk materials, a more pragmatic approach has been espoused which involves the derivation of microcrystalline materials by controlled processing of metallic glass powders. The HEHR processing applied to consolidation of metallic glass powders is based on this approach. Macrostructure of as-consolidated samples from as-received metallic glass powder shows a heterogeneous structure along the axial dimension. There is nugget formation in the middle of the sample where high temperatures are generated due to high contact resistance and the exothermic reactions of crystallization. This processing problem may be solved by controlling local current density in the compact.

Heat treatment after consolidation at 700°C for 50 hours produced an ordered phase (Ni_2Mo) which precipitated on twin boundaries and increased the hardness about 20% over as-consolidated material. This ordered phase becomes metastable and disappears after further heat treatment. A new transformed phase forms, eta boride, which is fcc with a large lattice parameter (a = 1.08 nm). This new phase has not been reported by researchers who consolidated HIP'ed or hot extruded METGLAS® 7025 heat treated to the same condition. A very stable Ni_2Mo ordered phase and the P or sigma TCP phases have been found with the same heat treatment as that of this study. It is not clear whether or not the ordered phase acts as a precursor for new phase formation. There might be a metastable compositional fluctuation in the Ni-Mo solid solution during consolidation, which can subsequently transit to an ordered phase or to the new phase with post-consolidation heat treatment. The detailed phase transformation evolution is still under investigation.

Tribological Applications

HEHR processing was applied to the development of high-temperature tribological materials that cannot be produced by conventionalmeans. Tribological graphite-containing components are generally based on a metal matrix with the graphite particles bonded to the matrix by a low-temperature binder. While such solid lubricated materials perform satisfactorily at low temperatures, they fail at high temperatures. It has been clearly shown that the failure at high temperatures, consists of melting of the low-temperature binder due to extremely high interface temperatures. For higher temperature applications, a new consolidation method is required. Such a method would provide the wetting of graphite by copper or other elements in the absence of a low-temperature binder.

HEHR processing has the potential for the manufacture of such high-temperature tribological materials.[7] The very high current developed at the copper-graphite interface during consolidation may induce local melting of copper resulting in a very high degree of geometrical conformability. At the same time, the short holding times at high temperatures reduces the problems associated with possible oxidation at the interface as well as in bulk. Figure 5b shows a Cu-11 wt.% flake graphite consolidate. Relatively uniform high densities are obtained, assisted by the internal lubrication effect of the graphite. The tribological behavior of this material is presently being evaluated using a high-speed brush tester. The nature of the interfacial interaction can be tailored to a certain extent by choosing the optimal electrical current waveform, and by varying the energy input and the applied pressure.

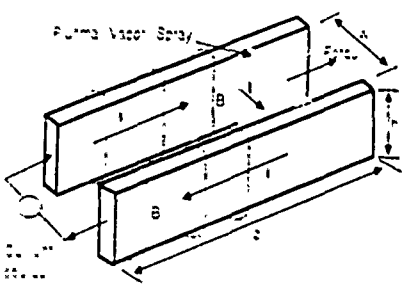

Figure 4. A schematic of the railgun processing concept. Shown are the rails, the conducting charge and the power source.

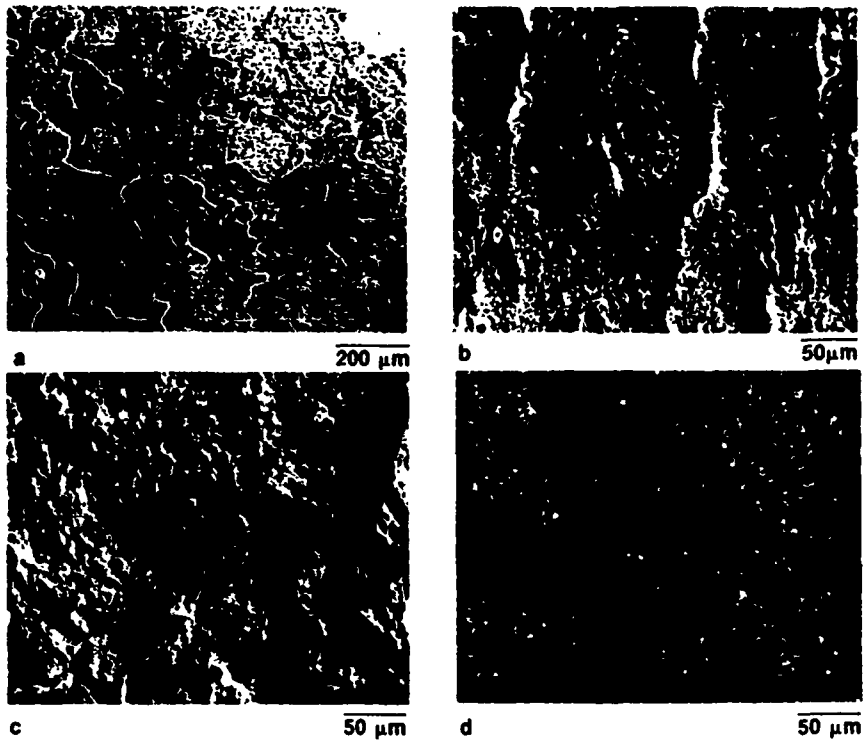

Figure 5. Representative microstructures produced by HEHR consolidation. (a) TZM PREP material, (b) copper 11 w/o graphite tribological material, (c) an SEM fractograph of tungsten blended with nickel, iron and boron carbide and (d) titanium aluminide (Ti_3Al).

Metal Matrix Composites

Several metal matrix composites (MMC) have been investigated using HEHR processing. The aim of these studies was to determine the relationship between the specific energy input into the powder during consolidation and the resulting microstructures and interface structures.[8] The bonding which occurs during consolidation by this technique stems from pulse-resistive heating which is produced at interparticle interfaces.

Air-atomized aluminum alloy powders were processed either separately or combined with SiC powders. A series of samples were consolidated varying the specific energy input from a value of 400 kJ/kg up to 2,500 kJ/kg. To date, Al/SiC discontinuous composites with densities up to 99% of the theoretical density were made in processing times of about one second. Several Al MMC systems were successfully consolidated with various types and grades of discontinuous SiC reinforcement both whisker and particulate) in volume fractions up to 30%. Graphite enriched β-SiC enabled an increase in the volume fraction of the ceramic reinforcing phase due to better electrical conductivity associated with the graphite on the surfaces.

A direct correlation was determined between the density, hardness and tensile fracture stress, and the specific energy input. The ductility and fracture properties of the MMC are very limited due to limited plastic deformation associated with the processing of these materials. The bonding between the SiC and the Al matrix appears to be good, based on transmission electron microscopy and Auger electron spectroscopy fracture studies. A 10 nm thick contiguous oxide phase at the interface between the two components was observed, and the fine microstucture and grain size maintained. The carbon-rich SiC featured interface fracture within the carbon layer.

Superconductors

The new class of high-temperature superconducting oxides pose formidable materials processing challenges in their conversion into useful bulk forms because of the inherent friability of the $YBa_2Cu_3O_x$ powders. Toward this end, HEHR processing has been employed to consolidate bulk monoliths and composite disks from these powders by employing discharges from both a capacitor bank and a homopolar generator. The homopolar generator discharges have been shown to produce high-density compacts with T_c values onsetting in excess of 80K. The relatively slow hompolar discharge did lead to phase modifications.

The research is addressing the kinetics of oxygen de-intercalation of these materials. The potential virtue of this approach lies in the possibility of limiting the duration of the high temperature exposure to a sufficient degree for densification but not long enough to seriously affect the state of oxidation of the copper. Secondary processing combined with consolidating research is also being initiated.

Tungsten

Tungsten processing by powder metallurgy techniques, including electrical resistance sintering, has been studied extensively. It is usual to use liquid phase sintering to produce many of the commercial "heavy metal" alloys, and the sintering kinetics of these materials are well understood. However, there is very little work on pure tungsten. Processing of pure tungsten poses peculiar problems due to the high processing temperature requirements and the difficulties in die containment. These difficulties notwithstanding, it has been demonstrated that pure tungsten powders can be partially powder-forged, and the nature of the surface oxide on the densification characteristics is being assessed. It appears that energy density/pressure combinations in excess of 5000 kJ/kg·at 300 MPa are necessary to produce dense compacts. These high-energy densities are now under study. In addition, a tungsten alloy MMC has been made. A scanning electron micrograph of a fracture surface of a tungsten, iron, nickel alloy mixed with boron carbide as a composite is shown in Figure 5c.

Titanium Aluminides

Titanium aluminides (TiAl, Ti_3Al) are currently considered as potential high-temperature components because of their specific properties combined with excellent high-temperature properties. A study is underway to evaluate the possibility of successful consolidation of titanium aluminides from RSR powders via HEHR processing. Two-inch diameter disks were consolidated from 50 grams of powder under pressures ranging from 15 to 45 ksi. At intermediate energy inputs, virtually full density was obtained by a powder forging mechanism. To date, it has been observed that Ti_3Al is easier to consolidate than TiAl, probably because of more efficient energy coupling to the homopolar generator pulse. Figure 5d shows the microstructure of a dense compact of Ti_3Al. Densification by powder forging is evident as is retention of the original grain structure within each powder particle.

RAILGUN DEPOSITION AND COATINGS

Railgun deposition is a powerful tool for synthesis of novel surface structures. Unique possibilities extend to combining rapid solidification and consolidation in a single in-situ process to produce desirable fine structures. The material to be deposited—in the plasma, gas, liquid or solid state—is accelerated electromagnetically in a railgun and deposited on a substrate. The flexibility of a material deposition process depends upon the ease and degree of independence with which three sub-processes are controlled. These are: the creation of the deposit species, the transport of these species, and the response of the substrate.

Railgun deposition in its current stage of development utilizes pulse power in species creation and in species transport. The devices used for this purpose are an exploding foil device and a railgun, respectively. In the novel configurations used in recent work, these devices have been coupled into systems which allow control of the phase and dimensions of the deposit species. In one configuration, plasma/vapor species derived from a foil explosion are accelerated in a railgun and condensed onto a substrate. The mode of nucleation depends on the species type(s) and the substrate. Interactions between substrate materials and deposit species govern the nature of the interface. One example of a system consists of co-deposited alumina + titania condensed as a <100 nm coating. Immiscible systems such as Mo + Cu have been vapor quenched into 100 nm crystalline mixtures. Particulate deposition systems involving molten and solid particles have also been processed. Systems such as Mo + MoS_2 and graphite have been assessed for tribological applications.[9]

A complex blend of interdependent process variables controls railgun deposition. These may be divided into four major categories: power and energy levels of the pulse, character of deposit material, substrate surface state and bulk thermophysical properties, and operating geometry and environmental conditions. By applying materials science fundamentals, the approach has the possibility to implement processing regimes which will yield materials within a prescribed structure/property band.

ACKNOWLEDGEMENTS

The research described in this paper was partially supported under the DARPA/NADC Contract, N6 2269-85-C-0222 and the DARPA/ARO Contract, DAAL03-87-K-0073. The authors would like to acknowledge the many contributions of Dennis Peterson and Ted Aanstoos of the Center for Electromechanics, as well as Professor L. Rabenberg, Dr. Michael Schmerling and the many graduate students in The Center for Materials Science and Engineering who have contributed to this research.

References

1 W F Weldon, *IEEE Spectrum* 22, No 3 1985, p 59
2 G.B. Grant, W.M Featherston R E Keith, W F. Weldon, H G Rylander and H H Woodson *Welding Journal*, 58 (1979) pp 24-26
3 J.B Walters and T.A. Aanstoos, *Metal Progress*, April 1985, p 25
4 S K Das and D Raybould, Fifth Int Conf on Rapidly Quenched Metals, Paper N67 Wurzburg, Germany September, 1984
5 C Persad and D R Peterson *IEEE Trans on Magnetics* Vol 22, November 1986 pp 1658-1661
6 D R Ervin, D L Bourell C Persad and L Rabenberg *Journal of Materials Science and Engineering* in press
7 K C Owen, M J Wang, C Persad and Z Eliezer, *Wear* 120 No 1 (1987), p 177
8 H L Marcus, L Rabenberg L D Brown G Elkabir and Y M Cheong, *ICCM VI ECCM 2*, ed F L Matthews et al Elsevier Applied Science Publisher Ltd, London 1987 p 2459
9 C J Lund C Persad and Z Eliezer *Wear* No 2 (1987), p 251

If you want more information on this subject please circle reader service card number 65.

Journal of Mechanical Working Technology, 20 (1989) 353-363
Elsevier Science Publishers B.V., Amsterdam - Printed in The Netherlands

SINGLE RESIDENCY SINTERING AND CONSOLIDATION OF POWDER METAL ALLOYS, INTERMETALLICS, AND COMPOSITES BY PULSED HOMOPOLAR GENERATOR DISCHARGE

W. F. Weldon and T. A. Aanstoos

Center for Electromechanics, The University of Texas at Austin, 10,100 Burnet Road Bldg. 133, Austin, Texas 78758-4497 (USA)

SUMMARY

Utilizing inertial energy storage the homopolar generator (HPG) is capable of delivering multimegawatt, megampere current pulses into resistive or inductive loads with high efficiency.(1) Such HPG's have been used for many years as power supplies for research in pulsed processing of metal alloy components and systems. Most of these processes rely on extremely rapid thermal excursions in the workpiece(s) caused by resistive heating during the current pulse. A new application of pulsed HPG's that carries great promise is homopolar pulse consolidation (HPC) of powder metal alloys or components.(2) In HPC, powder metal constituents are loaded into a thermally and electrically insulated die, then precompacted to an initial pressure. The "rams" of the compaction press are also the electrodes for homopolar discharge current. While in single residency, the powder compact is heated uniformly by HPG discharge current, sintering occurs, and consolidation is accomplished by hydraulic control of the consolidation press. The process is completed in approximately one sec, with unaided cooling to room temperature on the order of 100 sec, depending on compact mass. Microstructural control is closely tied to beginning particle size and distribution. Traditionally unsinterable alloys have been consolidated using HPC. Novel intermetallic alloys and phases have been produced. Cermets and other composites can be produced, as long as the continuous matrix is conductive. New tooling designs allow for controlled atmospheres, near-net shapes, and automated manufacturing.

INTRODUCTION

The Center for Electromechanics at The University of Texas at Austin (CEM-UT) has investigated novel pulsed electric generators since 1972. Chief among these is the iron-core (ferromagnetic) pulsed homopolar generator (HPG).(1) The homopolar effect, discovered and described by Michael Faraday in the 1830's, is characterized by a voltage gradient generated in a conducting rotor that spins in a uniform magnetic field. The open circuit voltage thus created is given by:

$$v = \frac{\omega\phi}{2\pi}$$

where ω is angular speed in radians per second, and ϕ is magnetic flux in Webers. Typically, HPG's are low voltage, low internal impedance devices. In a pulsed HPC

energy stored in the rotor due to its angular velocity is converted into electric energy in an external circuit as the reacting torque brakes the rotor to a reduced speed, or to a stop. The electric current pulse is characterized by a rapid rise to peak (approximately 50-100 ms), followed by a first order exponential decay to zero, over a pulsewidth of from 0.5 to two or more seconds. Depending on generator parameters and external circuit characteristics, with an HPG of 1 t mass, this pulse can be greater than one megampere peak current with an average power of tens of megawatts.

CEM-UT has developed and operated numerous HPG's for a wide range of applications.(3) Because of the high available power, HPG's are ideal sources for rapid joule heating of resistive workpieces. For this reason, along with their reliability and ease of operation and control, HPG's have been studied as pulsed power supplies for various industrial applications, including homopolar pulsed welding and homopolar pulsed heating .(4) A 10 MJ, disk type, pulsed HPG system at CEM-UT (figure 1) has been dedicated to such pulsed processing research since 1976. This is the system in which sintering and consolidation of powder metal (PM) alloys, in single residency, is currently under development.

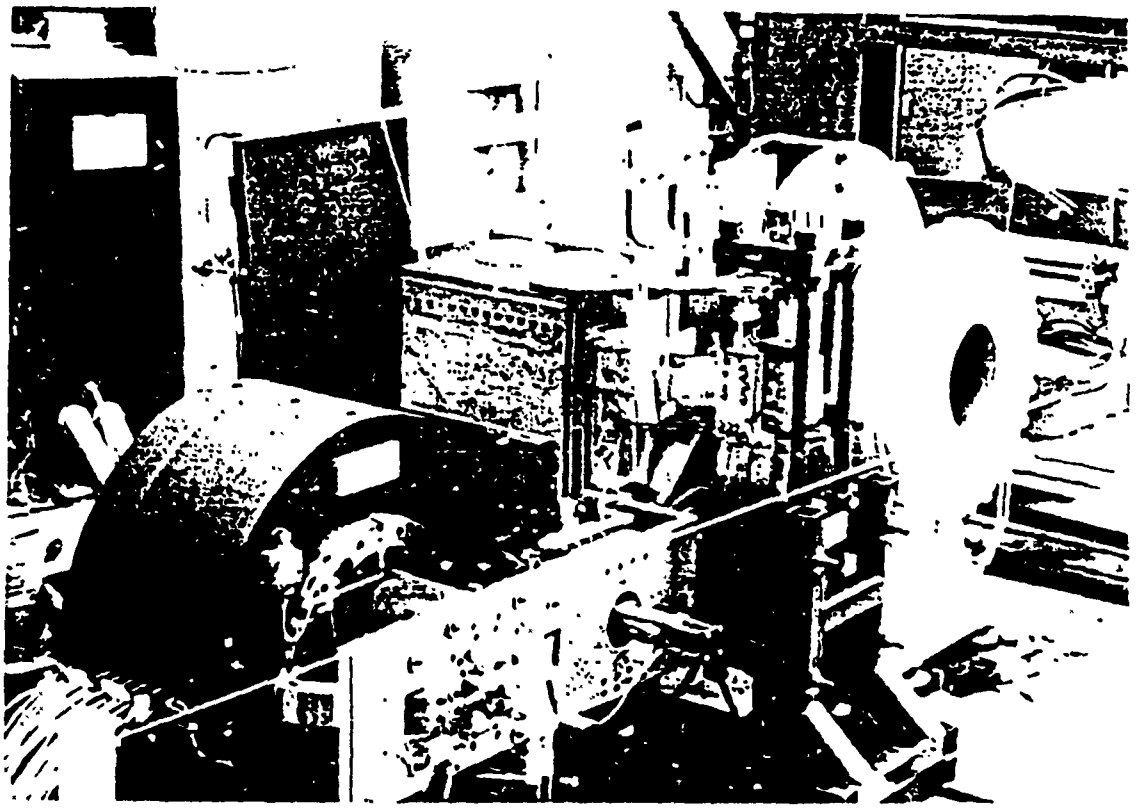

Figure 1. 10 MJ Homopolar Generator Research System at CEM-UT

BACKGROUND

Conventionally, PM alloys are processed into monolithic shapes by a series of process steps that usually involves pre-compaction, sintering, pressing, subsequent hot and/or cold working, and "healing" to reduce residual porosity. Final consolidation of finished parts is accomplished normally by hot isostatic pressing, during which the workpiece is held at elevated temperature and pressure for as long as hours. Sintering refers to the diffusion-driven process by which precompacted "green" products, under application of heat and pressure, consolidate as nucleation and growth occur between neighboring powder particles. The driving potential for this solid state phase transformation is the free surface energy associated with the total powder particle surface area in the compact. The sintering process represents the largest energy requirement in conventional PM processing.(5)

For this reason, researchers since World War II have concentrated their efforts on developing solid state, direct heating sintering processes as a means of reducing PM costs while improving productivity. Some of these high energy rate processes use "activation" of the powder through chemistry and morphology control;(6) most rely on joule heating of the powder by electric current. Jones, Cremer, and Ross independently studied the application of welding power supplies to direct sintering and compaction of PM parts in the late 1940's.(7) Regulated alternating current was tested as a sintering power supply at Rensselaer Polytechnic Institute shortly thereafter.(ibid) A Japanese process was licensed to the Lockheed Corporation in the late 1960's for a process called "spark" sintering, in which alternating and direct current were staged independently (and simultaneously) for the production of beryllium-copper parts and tungsten rod and wire.(8) These processes produced parts ranging from 5.0 to 23.0 cm in diameter that required from 3.0 to 19.4 kA/cm^2 current density for times ranging from tens of minutes to tens of seconds. Spark sintering has produced parts as large as 31.8 kg. All these processes involve multiple step procedures, including, in most cases, post-sintering work to increase density, or heat treatment.

In the 1970's, researchers at The University of Texas at Austin (Chou, et al) investigated single residency sintering and consolidation of copper-graphite composites under direct heating by nickel-iron battery discharge.(9) In these experiments, low voltage battery pulses were conducted through the rams of a double acting die at relatively modest current densities (276 A/cm^2). The low power available from the battery bank necessitated consolidation times in excess of 30 s; however, densities in excess of 93% were achieved with good mechanical and tribological properties as compared to similar composites consolidated by conventional processes. This research indicated that the HPG, with higher available current and power than batteries, as well as lower source impedance, would be a suitable power supply for sintering.

HOMOPOLAR PULSE CONSOLIDATION

Homopolar pulsed consolidation (HPC) is a process whereby the discharge current from a pulsed HPG is conducted through a compacted PM load, under pressure, such that the pressurizing rams are also the conducting electrodes for the discharge current (figure 2). A ceramic lining in the bore of the die serves to insulate, electrically and thermally, the compact from the surrounding structure. The PM product is loaded into the die at ambient conditions and pressurized to a state in which interparticle resistance favors very rapid microwelding of particles upon initiation of HPG current. This is where HPC departs from traditional direct means of sintering and consolidation. Because the HPG discharge pulse is unidirectional, the skin effect, or depth of penetration, associated with high frequency alternating current, is minimized or eliminated, resulting in uniform current distribution in the cross section of the compact (assuming uniform pressure distribution within the die). Thus heat generation and resulting temperature excursions are uniform and the resulting sintering reaction, being very rapid, is essentially adiabatic. The volumetric change associated with consolidation is compensated by fast response hydraulic control of the consolidation press, such that applied pressure remains relatively constant during the transition. Therefore, consolidation of the PM part is accelerated by plastic deformation of the powder particles, greatly reducing the time required for conventional consolidation processes. Radial thermal gradients within the die are controlled by conventional powder press considerations to reduce sidewall effects on axial pressure distribution, and the thermal characteristics of the ceramic lining. Axial thermal gradients can be regulated by choice of electrode or interelectrode spacer material such that the thermal boundary conditions in the axial direction do not represent a heat source or sink to the compact. Because of the rapid thermal excursion, both in heating and cooling, final microstructure is linked closely to beginning particle size and distribution, making tailored as-consolidated properties achievable. If post-consolidation heat treatment is necessary for physical property control, this can be accomplished in-residency by post-pulsing of the HPG via field excitation control based on preset values or temperature feedback signals. In general, controlled atmospheres are not required because of the short process duration, but purged or evacuated conditions do not present significant design problems. Material handling between initial compaction and final part ejection is minimized or eliminated.

The HPC system is represented schematically in figure 3. An iron core pulsed HPG is motored externally (generally by closed loop hydraulic drive systems) to a discharge speed appropriate for the mass of PM load material. Upon freewheel (coasting) of the rotor and excitation of the magnetic field, the external circuit is closed by actuation of the sliding contacts or a discrete making switch. The subsequent discharge current pulse delivers high-rate energy to the compact by direct (joule)

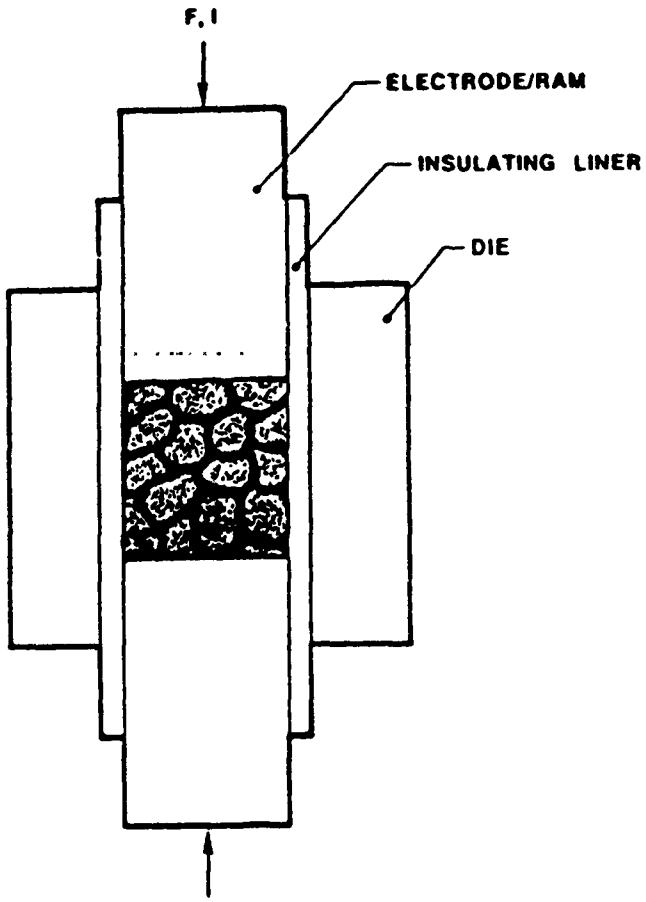

Figure 2. Schematic of HPC Die

heating, and sintering occurs rapidly. Displacement sensors track the consolidation of the compact and pressure regulators are used to control the hydraulic press. In-situ temperature measurements within the compact are accomplished by fiber-optic isolated thermocouple leads so that the magnetic and radio frequency fields associated with current passage through the compact do not cause interference. Process parameters recorded include compact pressure, voltage, current, temperature, and axial consolidation, as well as HPG operational parameters.

RESEARCH RESULTS

A wide range of materials, from lightweight aluminum-ceramic alloys to refractory alloys, has been consolidated by HPC with very promising results.(10) It is apparent that any material mixture can be heated and consolidated by this process as long as the continuous matrix through the compacted mixture is conductive. As-consolidated mechanical properties usually depend, in addition to processing parameters, on prior powder particle conditions and environments.

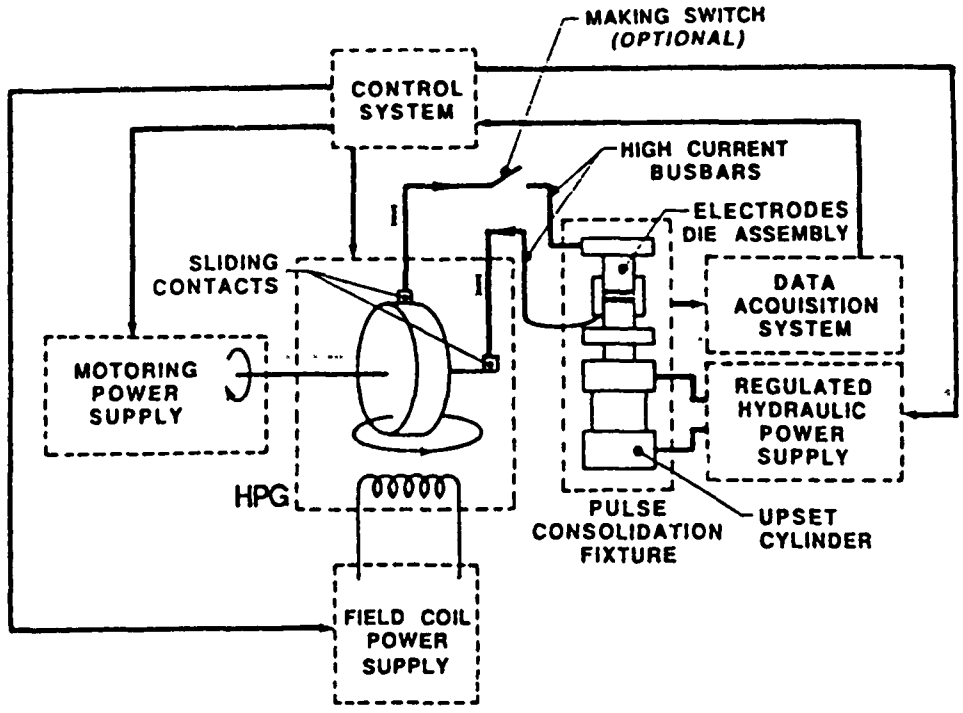

Figure 3. Homopolar Pulse Consolidation System Schematic

Aluminum Alloys

Numerous aluminum alloys have been tested in HPC, most notably ALCOA X7091™.(11) As-consolidated density in this alloy reached 98% of theoretical without localized melting. Also, numerous SiC-reinforced aluminum alloys have been studied. These composites, being cermets, heat and consolidate more readily than does pure aluminum, because of their nigher resistivity and lower thermal diffusivity. However, as with similar materials consolidated by other means, post-consolidation hot or warm work is required to restore room temperature ductility. A typical as-consolidated aluminum compact is shown in figure 4.

Copper-Graphite

Extensive research has been conducted in the processing and applications for copper-graphite alloys at CEM-UT since Chou's battery powered experiments. Wang, et al, have developed a copper-graphite HPC alloy that is chemically similar to available commercial grades, but with greatly improved mechanical properties.(12) Recent data suggest that this material, beacause of good electrical, thermal, and tribological properties, may be a suitable sliding contact material for next-generation pulsed power generators. Figure 5 shows a typical copper-graphite HPC compact.

Molybdenum Alloys

The amorphous PM alloy NiMoFeB (METGLAS 7025™) has been studied using HPC. Although in the bulk of the finished compact (approximately 4.5 cm diameter by 1 cm length) amorphosivity was not conserved, a highly dense microcrystalline

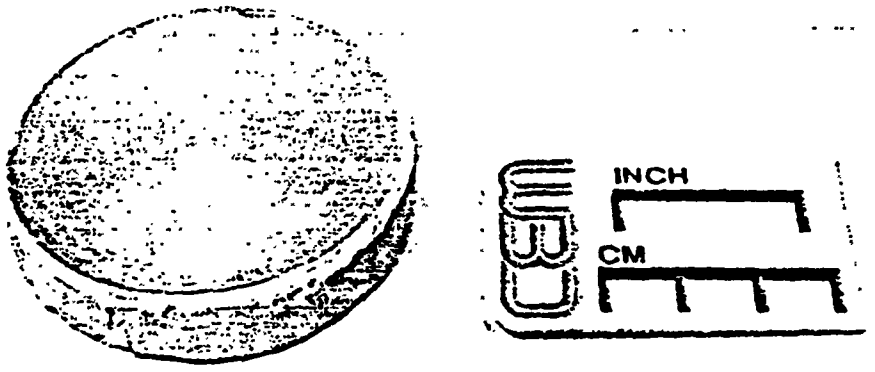

Figure 4. Aluminum HPC Compact

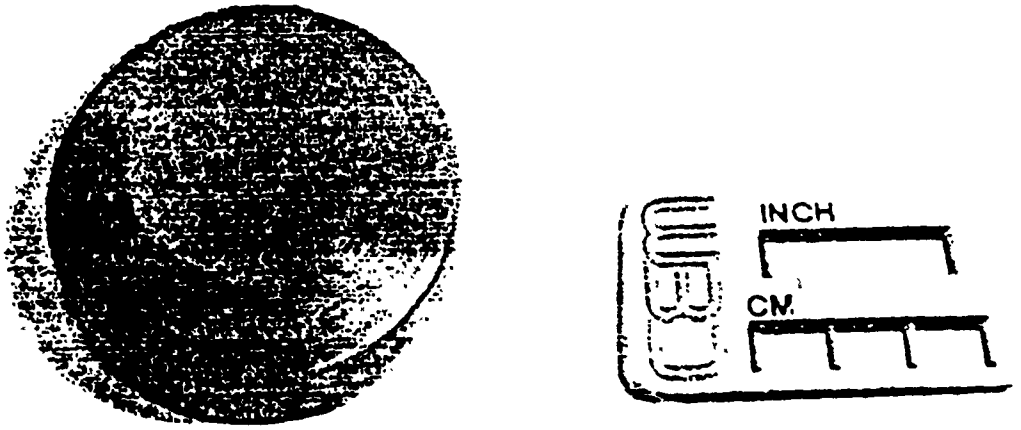

Figure 5. Copper-Graphite HPC Compact

structure was produced. This structure represents a new room-temperature metastable phase, named the η-Boride phase, which had not been observed in this alloy previously.(13) Such a compact is shown in figure 6. Another alloy of tungsten, zirconium, and molybdenum, (TZM PREP) was investigated. In the coarse, oxidized form, this PM product has proven difficult to consolidate by conventional means. After HPC, without special process control, this alloy shows very good density and a stable μ-phase

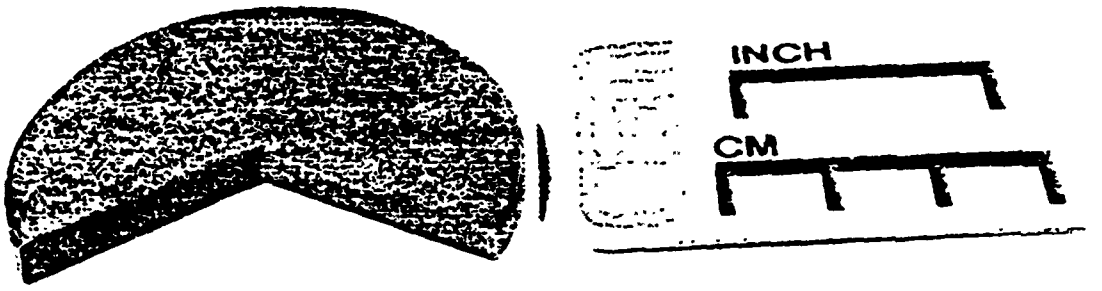

Figure 6. METGLAS 7025™ HPC Compact

Tungsten Alloys

HPC compacts of tungsten with nickel, cobalt, copper, or niobium alloying elements have been produced with good density and other properties.(2) However, pure tungsten is difficult to consolidate because of adverse die interactions at the very high temperatures and pressures required for the sintering reaction (approximately 3000C and 300 MPa). Furthermore, aggregation of powder particles below approximately 100 m size can result in non-uniform density and degraded mechanical properties of the compact. In addition, sintering of tungsten to near-theoretical density by conventional means requires hours in controlled atmospheres.(14) Recent data at CEM-UT suggests that a novel pre-processing technique for tungsten particles, combined with HPC, can result in very uniform tungsten parts of high density that have mechanical properties (specifically hardness) significantly higher than conventionally produced pure tungsten parts. Research is continuing into this application.

MANUFACTURING WITH HPC

Implementation of HPC into a manufacturing plant in the near term is feasible. The required power supplies and auxiliary equipment are commercially available, and the tooling and fixturing required are essentially designed from conventional mechanical, electronic, and hydraulic components.

Capabilities

Research results indicate that compact masses of 1.0 kg can be consolidated per 10 MJ of HPG capacity per operational cycle (one discharge per operational cycle). Industrially rated, actively cooled HPG's are available that can operate at full energy on a 5 min duty cycle.(15) To date, most HPC compacts have been cylindrical or disk coupons for research analysis. These are produced in ceramic lined, quick release diesets (figure 7) that are approximately 2.5 times the diameter of the finished compact. It is anticipated that prismatic, or constant section, shapes can be formed by HPC with special tooling design. Thus near-net shapes, such as turbine bladeforms, are probably feasible. Furthermore, consolidated PM parts can be joined to monolithic parts during consolidation. Figure 8 shows a copper disk bonded to an HPC-produced tungsten-iron alloy.

Cost and Productivity

On a per Joule basis, iron core HPG's represent the most economical reusable energy storage and pulsed power supply available. Capacitor banks, for example, are more costly by a factor of 5-10, while occupying as much as 10-100 times the volume, for an equivalent stored energy.

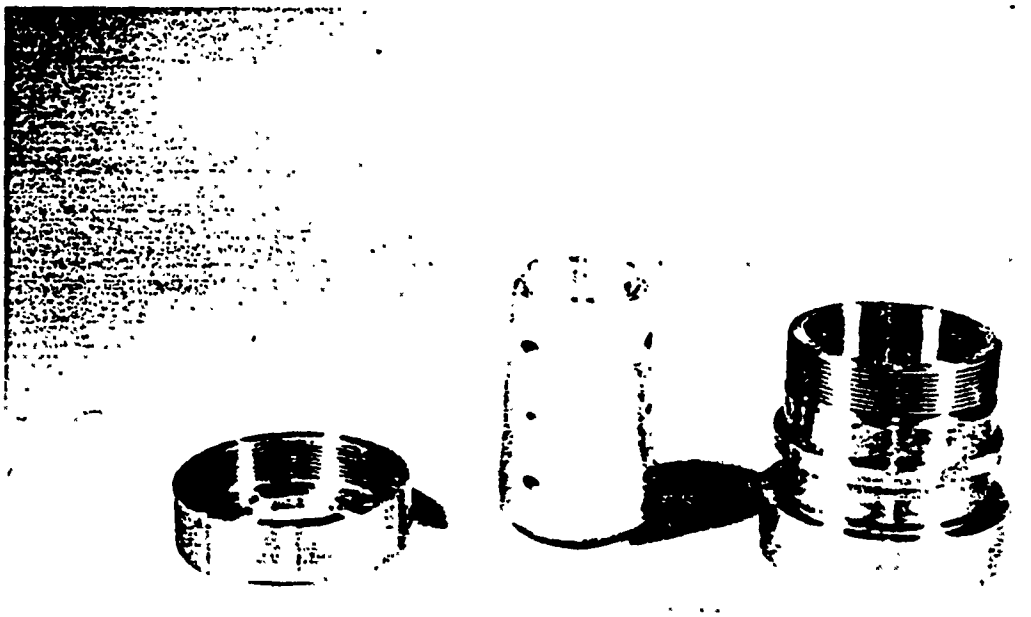

Figure 7. Quick Release HPC Dieset

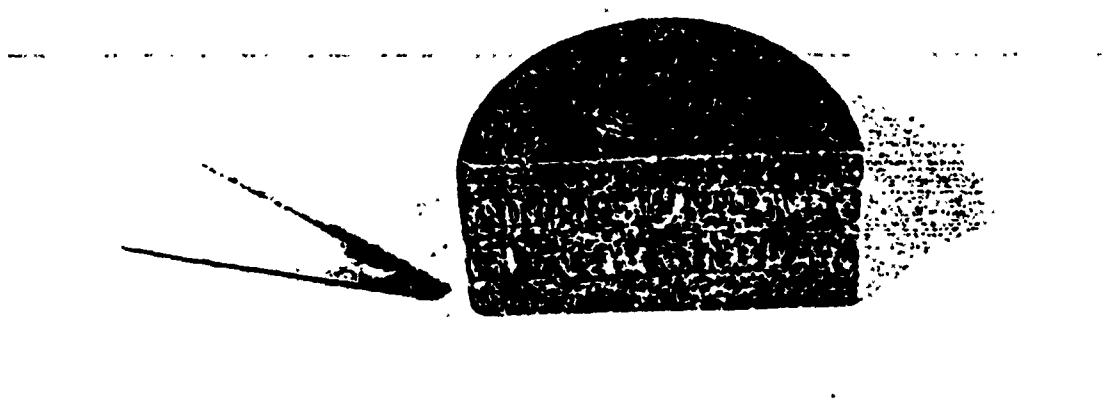

Figure 8. Copper-Tungsten Alloy HPC Joint

Operational costs for HPG's are also low. Motoring to speed is accomplished at modest power levels (200-500 kW); auxiliary power requirements may total to an equivalent number. Total energy cost per cycle for a 10 MJ unit might therefore approach $0.10, depending on local utility rates. Furthermore, because the high power discharge is accomplished off-line, no demand rates for high power surges are incurred.

CONCLUSIONS

The Center for Electromechanics at The University of Texas at Austin has applied pulsed iron core homopolar generators to a rapid, single residency process for compacting, sintering, and consolidating powder metal alloys and composites. Many materials, from lightweight to refractory alloys, can be consolidated with this process with high density and excellent properties. Consolidation time is very short compared to conventional powder metal processing techniques. Near-net shapes can be consolidated, and joints between consolidated and monolithic parts can be accomplished. Homopolar generators are economical, reliable, and inexpensive to operate.

ACKNOWLEDGMENTS

Fundamental research support for the work presented here was provided by the Texas Atomic Energy Research Foundation. Specific research was sponsored by DARPA/NADC Contract Number N6 2269-85-C-0222, DARPA/ARO Contract

Number DAALO3-7-8-0073, and the Texas Advanced Technology Projects The contributions and support of Professor H. L. Marcus and Dr. C. Persad, and the staff at the Center for Materials Science And Engineering, The University of Texas at Austin are gratefully acknowledged.

REFERENCES

1. S. A. Nasar and H. H. Woodson, "Storage and Transfer of Energy for Pulsed Power Applications," Sixth Suymposium on Engineering Problems in Fusion Research, San Diego, CA, November 18-21, 1975.
2. H. L. Marcus, D. L. Bourell, Z. Eliezer, C. Persad, and W. F. Weldon, "High-Energy, High-Rate Materials Processing," Journal of Metals, No. 12, pp 6-10, December 1987.
3. J. H. Gully, T. A. Aanstoos, K. E. Nalty, and W. A. Walls, "HPG Operating Experience at CEM-UT, IEEE Transactions on Magnetics, Volume Mag-22, No. 6, pp 1489-1494, November 1986.
4. T. A. Aanstoos and J. B. Walters, (Parker Kinetic Designs, Inc.) "Welding and Billet Heating with Homopolar Generators," Metal Progress, April 1986
5. E. Lardner, 1981 Powder Metallurgy Group Meeting, Powder Metallurgy, No. 4, 1981.
6. M. M. Ristic (ed.). "Sintering-New Concepts," Proceedings of the 4th Inernational Round Table Conference on Sintering, Dubrovnik, Yugoslavia, September 5-10, 1977, Elsevier Scientific Publishing Company, 1979.
7. F. V. Lenel. "Resistance Sintering Under Pressure," Journal of Metals, V. 203 No. 1, January, 1955.
8. R. W. Boesel, et al. "Spark Sintering Tames Exotic P/M Products," Materials Engineering, October 1969.
9. J. M. Chou, "Electrical Resistance Sintering of Motor/Generator Brushes Under Pressure," Master's Thesis, The University of Texas at Austin.
10. W. F. Weldon, H. L. Marcus, and C. Persad, "High Energy, High Rate, Pulsed Power Processing of Materials by Powder Consolidation and by Railgun Deposition", The Naval Air Development Center and Center for Materials Science and Engineering.
11. G. Elkabir, et al. "Microstructure and Mechanical Properties of High Energy Rate P/M Processed Aluminum Alloy X7091," 1986 TMS Annual Meeting, New Orleans, Louisiana, March 2-6, 1986.
12. M J. Wang, C. Persad, and Z. Eliezer, Center for Materials Science and Engineering, W. F. Weldon, Center for Electromechanics, "High Energy/High-Rate Consolidation of Copper Graphite Composite Brushes for High Speed, High Current Applications," 1987 Current Collector Conference, Austin, TX, November 16-17, 1988.
13. T. W. Kim, et al. "Identification of an n-Boride Phase as a Crystallization Product of a NiMoFe Amorphous Alloy," publication pending.
14. H. H. Hausner. Handbook of Powder Metallurgy, Chemical Publishing Co. Inc., New York, New York, 1973.
15. M. A. Pichot, et al., "Design of a 15 Megajoule Industrial Homopolar Generator," 5th IEEE Pulsed Power Conference, Arlington, Virginia, 1985

APPENDIX B

TUNGSTEN PROCESSING

B-1. Manufacturing Metallurgy of Tungsten: A Novel Integrated Powder Metallurgy Approach

B-2. Development and Control of Microstructure in P/M Tungsten by Synthesis and Reduction of Tungsten Trioxide Gels

B-3. High-energy, High-rate Consolidation of Tungsten and Tungsten-based Composite Powders

B-4. Synthesis and High Energy High Rate Processing of Ultrafine Grained Tungsten

MANUFACTURING METALLURGY OF TUNGSTEN : A NOVEL INTEGRATED POWDER METALLURGY APPROACH

C. Persad, S. Raghunathan, A. Manthiram,
M. Schmerling, D. L. Bourell, Z. Eliezer, H.L. Marcus,
Center for Mat. Science and Engineering, The University of Texas,
Austin, TX 78712.
and W. F. Weldon , Center for Electromechanics, The University of
Texas, Austin, TX 78712.

ABSTRACT

Two principal technologies underpin the P/M manufacturing metallurgy of tungsten: powder production and powder consolidation. The powder metallurgy approach employed in this study offers the specific advantages associated with fine-grained microstructure. In the consolidation step, in which a '1MJ in 1s' high electrical energy pulse is used, the duration of the exposure to elevated temperature is minimized. However, the potential advantage of this consolidation technique could only be obtained by control of the powder production phase. A research effort targeting fine microstructure by integrating the powder production and powder consolidation phases was undertaken. Tungsten trioxide gels produced from acidic solutions of sodium tungstate were the precursor materials for hydrogen reduction to produce submicron metallic tungsten particles. Temperature and pH control in the gel producing step lead to the nucleation and controlled growth of tungsten trioxide particles down to 50 nm size. Aquagels and alcogels were reduced in copper and in alumina boats in a stream of dry hydrogen at 1123K for 3600s to yield 100nm metallic tungsten particles. These particles were subsequently consolidated to produce dense, fine-grained (~200 nm) compacts. Liquid-phase-assisted consolidation was compared in the hard-metal composite W-Ni-Fe + B_4C - a cobalt-free WC analog.

INTRODUCTION

The manufacturing metallurgy of tungsten has been driven by the expanding uses of the metal. Tungsten and high-tungsten alloys have found extensive use in metalworking machinery, mining machinery, and in electrical and lighting equipment. These end use categories accounted for over 80% of the 1985 US consumption of 8.2×10^{6} kg.(1). Tungsten has the highest melting point of metallic elements, T_m = 3410 °C, and a high density of 19.3 gm/cm^3. These and other unique physical properties, and high hardness contribute to the demand for the metal in new applications (1).

Important tungsten minerals include wolframite, (FeMn) WO_4; and scheelite, $CaWO_4$. Wolframite is converted to tungstic acid , H_2WO_4 (= hydrated tungsten trioxide, $WO_3 . H_2O$), by first fusing it with sodium carbonate at 1000 °C to produce soluble sodium tungstate, which is then acidified. Scheelite treated with hydrochloric acid produces calcium chloride and insoluble tungstic acid.

The possibilities of manipulating the form in which the tungsten trioxide is precipitated were explored in this study. Crystalline and colloidal forms are possible. Among the latter forms are sols and gels. A sol is a solid dispersed in a liquid, a gel is liquid dispersed in a solid (2). The aquagel consists of water dispersed in a fine three-dimensional network of non-crystalline tungsten trioxide. The solid network occupies 1-10% of the total volume depending upon the sizes of the individual particles.

The conversion of a primary aquagel to an aerogel by critical point drying, and the use of this aerogel as a precursor for the production of fine metallic tungsten powders are the novel features of this work. By producing such a fine powder for consolidation by High-Energy High-Rate (HEHR) Processing, this work exploits one of the fundamental features of HEHR Processing, namely, the control of time-at-temperature transformations.

In this simple, single- phase refractory metal system the key metallurgical feature is grain size. Maintaining submicron grain size in consolidated tungsten opens up new possiblities for novel secondary processing such as by superplastic forming, and for new applications such as hypervelocity sliding electrical contacts (3).

The complex tungsten-based composite material selected for study presents a sharp contrast. A completely different group of high temperature applications utilizing high hot hardness is anticipated for the cobalt-free substitutes for WC + Co composites. The B_4C -reinforced W-Ni-Fe composites are a prototypical system (4,5). The hot hardness of the 2.5 B_4C - 97.5 W-Ni-Fe [95.0 W - 3.5 Ni - 1.5 Fe] is 10 to 20% higher than the premium grade of WC + Co at 1073K. When produced by hot pressing at 1733K, the B_4C is fully reacted and phases with a variety of chemistries are produced. These include graphite, tungsten carbide, and Fe-Ni and W-B-C phases. Further analysis revealed the onset of the series of reactions to be at 1173K (4).

EXPERIMENTAL PROCEDURE

Materials

Gel-based W

The source material for tungsten in this study was crystalline sodium tungstate, supplied by the Alfa Products Div'n of Morton Thiokol. Reagent grade hydrochloric acid was used for acidification of sodium tungstate.

W-Ni-Fe/B_4C

The tungsten-based composite was supplied as a premixed powder blend by Los Alamos National Laboratories, NM. The metallic matrix elemental powders W:Ni:Fe were mixed in a mass ratio of 93:5:2. The mass of B_4C was 1.3 or 1.65 percent of the total composite mass, corresponding to a volume fraction of 8% or ~10%. Detailed characteristics of such powder blends have been reported previously by Sheinberg (5).

Preparation of Tungsten Trioxide

Tungsten trioxide was prepared in crystalline and in gel forms by the controlled acidification of sodium tungstate. Control of pH and temperature led to the synthesis of the material in gel form using 0.25N hydrochloric acid at 298K. The first step in the preparation of the tungsten trioxide gel was the dissolution of sodium tungstate in a dilute 0.1N hydrochloric acid at room temperature. This solution was further acidified until streaks of the white tungstic acid gel were observed. Upon further acidification, a light yellow gel was precipitated in a sodium chloride solution. The gel was then filtered and washed in flowing distilled water. The simple chemical reaction is:

$$Na_2WO_4 + 2HCl \longrightarrow WO_3 \cdot H_2O + 2NaCl \quad (1)$$

A number of gels were prepared using fifty-gram batches of sodium tungstate. Some preparations of the aquagel were converted into alcogels by an alcohol-for-water substitution. These alcogels were later processed into aerogels by critical point drying using carbon dioxide (6). Samples of the gels were taken for particle size characterization and for thermogravimetric analysis. The remainder was placed in alumina and in copper boats for hydrogen reduction.

Hydrogen Reduction of Gels

Hydrogen reduction was performed by flowing hydrogen through a 50 mm diameter x 1.2 m long quartz tube containing the gel-filled boats. The tube was placed in a three-zone tube furnace operated at 1123K. A hydrogen flow rate of 40 ml/min. was maintained for 1 hour to achieve complete reduction.

Processing

Advances in kinetic energy storage devices have opened up a new approach to powder processing of refractory metals and high-temperature composites. The processing consists of internal heating of a customized powder by a fast electrical discharge of a homopolar generator. The high-energy high-rate "1MJ in 1s" pulse permits rapid heating of a conducting powder in a cold wall die. This short time at temperature approach offers the opportunity to control phase transformations and the degree of microstructural coarsening not readily possible using standard powder processing approaches.

The underlying fundamental approaches to high-energy high-rate processing have been described elsewhere (7). The general details of the experimental apparatus and the pulse characteristics have also been reported(8). The technique has been employed previously in the processing of the refractory metal alloy, Mo-TZM, as well as Al-SiC, Cu-Graphite, and $(Ti,Nb)_3Al$-SiC composites (7-11).

In this study, 50g quantities of the gel-based tungsten or of the composite powder blends were loaded into insulated die cavities between copper or tungsten electrodes. Pressures between 210 and 420 MPa were applied, and the compacts were rapidly heated by a homopolar generator pulse discharge. Disks with diameters of 25 mm or 30 mm were produced. Specific energy inputs ranged from 2000 kJ/kg to 7000 kJ/kg.

Microstructure Evaluation

Standard metallographic procedures were employed in the preparation of radial cross sections of each of the consolidated materials. Sectioning required the use of water-jet machining. Vickers microhardness measurements were performed at room temperature to determine the degree of microstructural homogeneity.

X-ray diffraction analyses were performed on a Phillips diffractometer fitted with a Cu tube and a graphite monochromator. Powder samples were held onto a glass slide with double-sided adhesive tape. Sufficient powder was used so that no signal was detected from the glass slide.

A JEOL 35M SEM with EDS and WDS capability was employed for powder particle chacterization, densification studies, and to verify the chemical discontinuities associated with the formation of reaction products at the matrix-reinforcement interface in the composite.

A 200 kV JEOL-200CX instrument was used in the TEM studies of the xerogel and the metallic powder product. Drops of a 0.01 percent solution of the alcogel was placed on holey carbon grids and vacuum dried for gel size and contiguity characterization.

RESULTS AND DISCUSSION

The results of each of the several steps studied are presented and discussed. They include controlled synthesis of an oxide gel, conversion of the gel into a desirable form, reduction of the gel, and consolidation of the gel-derived metallic tungsten powders. Together, these represent an integration of the chemical and mechanical metallurgy of tungsten.

The conventional manufacturing metallurgy of tungsten employs chemical decomposition rather than pyro-metallurgy in the extractive metallurgy. This involves the extraction, reduction and purification of the metal oxide from minerals and from low concentration ores. Methods and processes for accomplishing these steps are the subjects of a voluminous patent literature. Systematic and comprehensive reviews are available (12,13).

Gel Preparation, Conversion and Reduction

High-purity tungsten powders with submicrometer particle sizes are obtainable by this preparation -> conversion -> reduction processing sequence. Aerogel forms are particularly well suited precursors for hydrogen reduction. Alcogels may also be reduced under slightly different conditions to produce similar particle sizes. Alcogels are an intermediate product in the critical point drying procedure for tungsten trioxide aquagels.

Thermogravimetric analysis indicated that the aquagel contained ~15 H_2O molecules of which ~13 were in the gel interstices and ~2 were present as water of hydration. TEM observation of vacuum-dried alcogels at 1:10,000 dilution indicated contiguous two-dimensional particle arrays consisting of monosized particles with 50 nm dimensions.

The lower size limits of these gel particles are as yet not determined. However, if indeed these are < 10 nm, and can be converted into crystalline form without coarsening, then the extremely promising work on ductile nanocrystalline metal oxides may be advanced by this route . For example, Karch et al. have shown that nanocrystalline TiO_2 develops room-temperature ductility due to enhanced grain boundary creep originating in short diffusion lengths and increased interfacial diffusivity (14).

$$12\ WO_3 + 3\ H_2 = 3\ W_4O_{11} + 3\ H_2O$$

v
v
v

$$3\ W_4O_{11} + 9\ H_2 = 12\ WO_2 + 9\ H_2O$$

v
v
v

$$12\ WO_2 + 24\ H_2 = 12\ W + 24\ H_2O$$

Fig.1. Schematic sequence of the tungsten trioxide reduction reactions in dry hydrogen at 1123K. In the simplified sequence the possible presence of co-existing non-stoichiometric oxides as intermediate products is disregarded.

Fig.2. TEM photomicrograph of metallic tungsten powder particles made by hydrogen reduction of a tungsten trioxide alcogel. Particle dimensions of ~100 nm are evident.

Free energy and enthalpy chang indicate that magnesium or aluminum ma be more effective exothermal reductant. for the metal oxide (13), however, product purity demands are best met by the use of high-purity hydrogen. The standard sequence of reduction reactions is shown schematically in Figure 1.

The reduction procedure performed at 1123K for 3600s in dry hydrogen yields metallic tungsten. X-ray diffraction studies indicate that the crystalline oxide level is below the detection limit. However, an adsorbed oxygen layer is a potential contaminant due to the large surface area/unit mass of the reduced powders, (estimated value 3-10 m^2/g). Transmission electron microscopy confirms the ~100 nm average dimension of the reduced metallic tungsten particles. Figure 2 is a TEM photomicrograph of a cluster of these particles. The individual particles appear to be single- or bi-crystals.

The factors which affect the post-reduction size of metallic tungsten particles are incorporated into Parsons' empirical equation (15). They include the bulk density of the oxide powder, the particle size of the oxide powder, the reduction time, the bed depth, and the reduction temperature. The refinement in microstructure through the use of 50 nm tungsten trioxide in aerogel form therefore has a strong effect on the reduction kinetics, due to the low bulk density and small particle size.

Consolidation Parameters

The processing parameters used for these initial consolidation experiments on each of these systems were derived from parameter sets previously developed for commercial tungsten powders (16). The inherent assumption is that beyond a set electrical conductivity threshold, the pulse resistive heating under pressure would provide rapid densification. The most identifiable solid state densification mechanism is powder forging. The parameters for the gel-based W were: Applied Pressure = 60 ksi (420 MPa), Specific energy input: 5000 kJ/kg. For the W-Ni-Fe/B_4C system they were: Applied Pressure = 45 - 60 ksi (315 - 420 MPa), Specific energy input: 3000 to 7000 kJ/kg.

Microstructure/Property

Figures 3 and 4 provide typical overviews of the rapidly densified microstructures developed in the gel-based W and in the W-Ni-Fe/B_4C systems respectively.

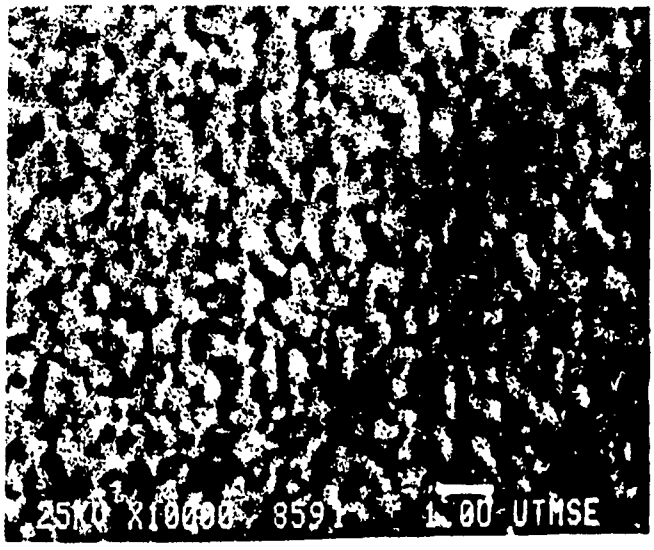

Fig. 3. SEM photomicrograph of a radial cross-section of a gel-based tungsten specimen produced by HEHR powder consolidation with an energy input of 7000 kJ/kg under 420 MPa applied pressure. A uniform consolidated powder particle size of ~200 nm is evident.

The gel-based tungsten was rapidly densified to ~85 % density in a single energy pulse. This densification response may be associated with the increase in total resistance derived from the new numerous interparticle contact resistances. The microstructure is uniform and consists of particles with ~200 nm dimensions. At this stage, the particle size evolution sequence from the oxide gel is: gel particle dimension = ~50 nm; metallic tungsten powder particle size = ~100 nm; consolidated tungsten particle size = ~200 nm.

In this simple single-phase material, the primary microstructural parameters of interest are the fineness and uniformity of the microstructure. The SEM micrograph in Figure 3 indicates that these characteristics are indeed evident in the HEHR powder-consolidation-processed gel-based tungsten.

Microhardness measurements confirm this finding. The average hardness value of 390 VHN_{500} (384 - 404 range) of the ~85% dense tungsten compares favorably with that of conventionally-sintered tungsten, in which values of 90-320 VHN are obtained (17). These values depend upon density, particle size, and degree of cold work. The high hardness observed in the gel-based tungsten may be attributed to the fine scale of the microstructure and its uniformity, and to the strong three-dimensional connectivity developed within the consolidated mass. Post-pulse cooling under an applied pressure may also provide a hardening contribution due to enhanced dislocation density.

In Figure 4, the apparent orientation of the W-Ni-Fe matrix is attributed to flow of the material under pressure during the transient liquid-phase-assisted consolidation. The three microscopic features observed are the B_4C, W and the W-Ni-Fe eutectic.

XRD analyses of the phases present in the high-density processed composite reveal the reaction products to be a series of complex carbides and borides, when sufficient energy is delivered to beginliquid-phase-assisted densification. The lines indexable in a 10 to 80 degree two-theta scan for the W-Ni-Fe/B_4C system after liquid-phase assisted consolidation includes W (110),(200),(211), W_2C (021),(002),(121),(102),(321),(302), FeWB (001),(112), W_2B(110),(002),(200),(211), Fe_3C (101), Fe_6W_6C (660),(822) and Ni_4B_3(211),(410),(403),(013). The intermetallic Fe_7W_6 (119)was also observed. The elemental Fe and Ni were fully reacted. These phases were not observed in the material consolidated completely in the solid state, where the maximum applied pressure of 420 MPa was insufficient to produce full densification.

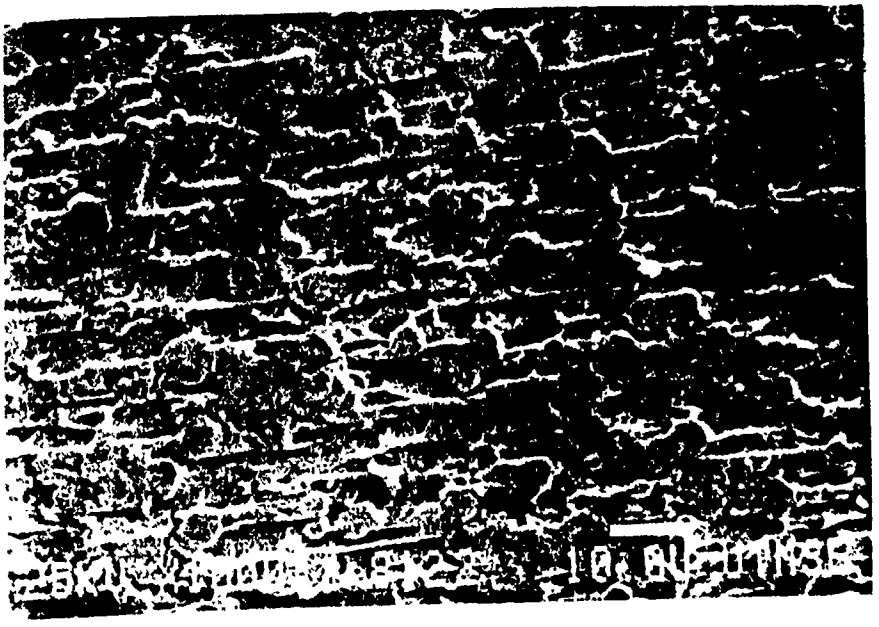

Fig.4. SEM photomicrograph of an etched radial cross-section of a (W-Ni-Fe)/B_4C composite specimen produced with an energy input of 4000 kJ/kg under 420 MPa applied pressure. Full density is obtained by the evident flow of the W-Ni-Fe eutectic matrix.

Several of the carbide-forming reactions are highly exothermic, and once triggered, these reactions which occur at multiple and distributed interface nodes can be expected to maintain the high temperature developed in the early stages of the processing. Indeed this processing cycle then takes on characteristics similar to those observed in Self-Propagating High-Temperature Synthesis of ceramic phases (18). The reaction products so derived effectively transform the nature of the composite material by introducing the attributes of the in-situ composites, in which the reinforcing phases are produced during processing.

ACKNOWLEDGMENT

We thank Haskell Sheinberg of Los Alamos National Laboratories who provided the W-Ni-Fe/B_4C powders. Assistance with HEHR processing was provided by Ted Aanstoos and Jim Allen at CEM-UT. H. Tello and P. C. Trimble assisted in the structure evaluation. This research was supported by DARPA/ARO Contract DAAL03-87-K-0073 and by the Texas Advanced Research Program.

REFERENCES

1. Peter K. Johnson, Trends in the U.S. Tungsten Industry, The Int. J. of Powder Met., Vol. 24, No. 1, 1988, pp. 73-76.

2. F. H. Redmore, Fundamentals of Chemistry,Prentice-Hall. Englewood Cliffs, NJ. 1979. pp. 313-314.

3. C. Persad, D. R. Peterson and R. Zowarka, Composite Solid Armatures by Pulsed Power Processing: A Novel Homopolar Generator Application in EML Technology, IEEE Trans. Magnetics, Jan. 1989, pp.404-408.

4. H. Sheinberg, Int. J. of Refractory and Hard Metals, March 1983, pp.17 - 26.

5. H. Sheinberg, Int. J. of Refractory and Hard Metals, December 1986, pp. 230 - 237.

6. J. Fricke, Aerogels. Springer-Verlag, 1982.

7. H.L.Marcus, D.L.Bourell, Z.Eliezer, C.Persad and W.F. Weldon, High-Energy High-Rate Materials Processing, Journal of Metals, Vol. 39, No. 12, Dec. 1987, pp. 6-10.

8. G.Elkabir, L. Rabenberg, C.Persad and H.L.Marcus , Microstructure and Mechanical Properties of a High Energy Rate P/M Processed Aluminum Alloy, Scripta Met., Vol 20,October 1986, pp. 1411-1416.

9. D. R. Ervin, D. L. Bourell, C. Persad, and L. Rabenberg, Structure and Properties of High Energy, High Rate Consolidated Molybdenum Alloy TZM, J. Mat. Sci. Eng., A102, 1988, pp.25-30.

10. K. C. Owen, M. J. Wang, C. Persad, and Z.Eliezer, Preparation and Tribological Evaluation of Copper-Graphite Composites by High Energy/High Rate Powder Consolidation, Wear, 120 (1987), pp. 117-121.

11. C.Persad, S. Raghunathan, B. -H.Lee, D.L.Bourell, Z. Eliezer and H. L. Marcus, High-Energy High-Rate Processing of High-Temperature Metal-Matrix Composites, Proceedings of the MRS Symposium, Vol. 120, High Temperature High Performance Composites,Reno,NV, April, 1988.

12. K. C. Li and C. Y. Wang. Tungsten. 3rd.ed.. New York: Reinhold, 1955.

13. S. W. H. Yih and C. T. Wang. Tungsten: Sources, metallurgy, properties and application. New York: Plenum, 1979.

14. J. Karch, R. Birringer, and H. Gleiter, Nature,Vol. 330, (1987) p.556.

15. D. S. Parsons, Electrochem. Technol.,V.3 (9/10), , 1965, pp. 280-283.

16. S. Raghunathan, MS Thesis, The University of Texas at Austin, Aug. 1988.

17. N. C. Kothari, Factors Affecting Tungsten-Copper and Tungsten-Silver Electrical Contact Materials, Powder Metallurgy Int., Vol. 14, No. 3, 1982, pp.139-143.

18. J. B. Holt and D. D. Kingman in Emergent Process Methods for High-Technology Ceramics, eds.R. F.Davis, H. Palmour III, and R. L. Porter (Plenum Press,New York, NY, 1984) p. 167.

DEVELOPMENT AND CONTROL OF MICROSTRUCTURE IN P/M TUNGSTEN BY SYNTHESIS AND REDUCTION OF TUNGSTEN TRIOXIDE GELS

C. Persad, S. Raghunathan, A. Manthiram, M. Schmerling,
D.L. Bourell, Z. Eliezer, and H.L. Marcus

Center for Material Science and Engineering
The University of Texas
Austin, TX 78712

Abstract

Tungsten trioxide gels produced from acidic solutions of sodium tungstate have been investigated as precursor materials for submicron metallic tungsten particles. Temperature and pH control in the gel-producing step leads to the nucleation and controlled growth of tungsten trioxide particles down to 50 nm size. Gels of stoichiometric and non-stoichiometric compositions have been studied. 100 nm metallic tungsten particles are obtained through rapid reduction in dry hydrogen. These particles have been consolidated to produce dense, ultrafine-grained compacts. The consolidation is accomplished by use of high-energy high-rate processing driven by a homopolar generator. The consolidation response of these laboratory-synthesized powders has been compared to that of commercial high-purity tungsten powders. X-ray diffraction and electron microscopy were employed in the structure characterization. Microhardness and electrical conductivity were used in the property evaluation. Ultrafine grain sizes (< 2 μm) are retained in the high-energy high-rate consolidated tungsten derived from a gel base. Microhardness is higher than that of commercial wrought materials. Hardness improvement is attributed to the high degree of connectivity and Hall-Petch hardening.

This research was supported by DARPA/ARO Contract DAAL03-87-K-0073 and by the Texas Advanced Research Program Grant # 4357.

Solid State Powder Processing
Edited by A H Clauer and J J deBarbadillo
The Minerals, Metals & Materials Society, 1990

Introduction

A new P/M processing route has been employed to produce ultrafine-grained tungsten. It is obtained by integration of the chemical and the mechanical metallurgy . In this paper we focus on the development and control of powder particle dimensions, with particular emphasis on the preparation and characterization of the precursor species : tungstic acid gels.

Tungsten trioxide is an intermediate product in the conversion of tungsten-bearing ores into tungsten powders. In its hydrated form, also called tungstic acid, it may be prepared as an aquagel. This was demonstrated by Kistler in 1932 (1). A gel structure can be converted into a solid, low-density, highly porous form described as an aerogel (2,3). Such a conversion can be achieved by a series of fluid substitutions in the solid network. An alcohol-for-water substitution converts the aquagel into an alcogel. Later, liquid carbon dioxide replaces the alcohol. When the liquid carbon dioxide is removed by critical point drying, an aerogel results. This aerogel is an uncollapsed, open-structured form of tungsten trioxide with a bulk density of less than ten percent. Tungsten trioxide in aerogel form, containing sub-particles with 50 nm dimensions, provides a highly flexible precursor for efficient reduction to ultrafine tungsten powder.

Powder metallurgy approaches seeking to define fundamental material behavior require materials with well-defined and controlled characteristics. Among these are purity, uniform size, and predictable morphology. Wet chemical processing using sol-gel methods makes the preparation of such powders feasible. In a P/M processing sequence, such powders enable the production of homogeneous compacted preforms, rapid sintering at relatively low temperatures, and novel possibilities for grain growth control, when compared to powders with sizes and size distributions made by conventional methods.

The solid state powder processing described in this study emphasizes the characteristics of tungstic oxide aerogel to metallic tungsten powder conversion, and the subsequent rapid consolidation of this tungsten powder by high-energy, high-rate consolidation processing.

Experimental Procedure

Materials

The starting material for tungsten preparation in this study was crystalline sodium tungstate. It was supplied by the Alfa Products Div'n of Morton Thiokol. Reagent grade hydrochloric acid was used for acidification of sodium tungstate.

Preparation of Tungsten Trioxide

Tungsten trioxide was prepared in crystalline and in gel forms by the controlled acidification of sodium tungstate. Control of pH and temperature led to the synthesis of the material in gel form using 0.25N hydrochloric acid at 298K. The first step in the preparation of the tungsten trioxide gel was the dissolution of sodium tungstate in a dilute 0.1N hydrochloric acid at room temperature. This solution was further acidified until streaks of the white tungstic acid gel were observed. Upon further acidification, a light yellow gel was precipitated in a sodium chloride solution. The gel was then filtered and washed in flowing distilled water. The simple chemical reaction is:

$$Na_2WO_4 + 2HCl \dashrightarrow WO_3 . H_2O + 2NaCl.$$

A number of gels were prepared using fifty-gram batches of sodium tungstate. Some preparations of the aquagel were converted into alcogels by an alcohol-for-water substitution. These alcogels were later processed into aerogels by critical point drying using carbon dioxide. Samples of the gels were taken for particle size characterization and for thermogravimetric analysis. The remainder was placed in alumina and in copper boats for hydrogen reduction.

Hydrogen Reduction of Gels

Hydrogen reduction was performed by flowing hydrogen through a 50 mm diameter x 1.2 m long quartz tube containing the gel-filled boats. The tube was placed in a three-zone tube furnace operated at 1123K. A hydrogen flow rate of 40 ml/min. was maintained for 1 hour to achieve complete reduction.

Powder Consolidation

Advances in kinetic energy storage devices have opened up a new approach to high-energy, high-rate (HEHR) powder processing of refractory metals. The processing consists of internal self-resistance heating of a customized powder by a fast, high-current, electrical discharge of a homopolar generator. The high-energy high-rate "1MJ in 1s" pulse permits rapid heating of a conducting powder in a cold wall die. This short time at temperature approach offers the opportunity to control phase transformations and the degree of microstructural coarsening not readily possible using standard powder processing approaches.

The underlying fundamental approaches to high-energy high-rate processing have been described elsewhere (4). The general details of the experimental apparatus and the pulse characteristics have also been reported (5). The technique has been employed previously in the processing of the refractory metal alloy, Mo-TZM, and for W-Ni-Fe + B_4C, Ni-Mo + MoB_2, Cu-Graphite, and $(Ti,Nb)_3Al$ based composites (4-10).

In this study, 50g quantities of the gel-based tungsten were loaded into insulated die cavities between tungsten electrodes. Pressures between 210 and 420 MPa were applied, and the compacts were rapidly heated by a homopolar generator pulse discharge. Disks with diameters of 25 mm were produced. Specific energy inputs ranged from 2000 kJ/kg to 7000 kJ/kg.

Microstructure Evaluation

Standard metallographic procedures were employed in the preparation of radial cross sections of the consolidated materials. Sectioning required the use of water-jet machining. Vickers microhardness measurements were performed at room temperature to determine the degree of microstructural homogeneity.

X-ray diffraction analyses were performed on a Phillips diffractometer fitted with a Cu tube and a graphite monochromator. Powder samples were held onto a glass slide with double-sided adhesive tape. Sufficient powder was used so that no signal was detected from the glass slide. A JEOL 35C SEM with EDS and WDS capability was employed for powder particle chacterization and for densification studies. A 200 kV JEOL-200CX instrument was used in the TEM studies of the xerogel and the metallic powder product. Drops of a 0.01 percent solution of the alcogel were placed on holey carbon grids and vacuum dried for gel particle size and contiguity characterization.

Results and Discussion

Thermogravimetric analyses of aquagels and alcogels indicate that these gels are fully converted to xerogels at 420 K. There are distinct mass losses associated with evaporation of ethyl alcohol (bp = 352K), the removal of adsorbed and interstitial water, and the loss of water of hydration from the tungstic acid [$WO_3 \cdot x\,H_2O$, ($0.33 < x < 2.0$)]. Post TGA powder X-ray diffraction patterns were compared to the standard pattern obtained for crystalline tungstic acid (CAS # 7783 - 03 - 1, Aldrich Chemical Co., Milwaukee,WI.). Peak broadening was evident in the gel patterns associated with scattering by fine particles.

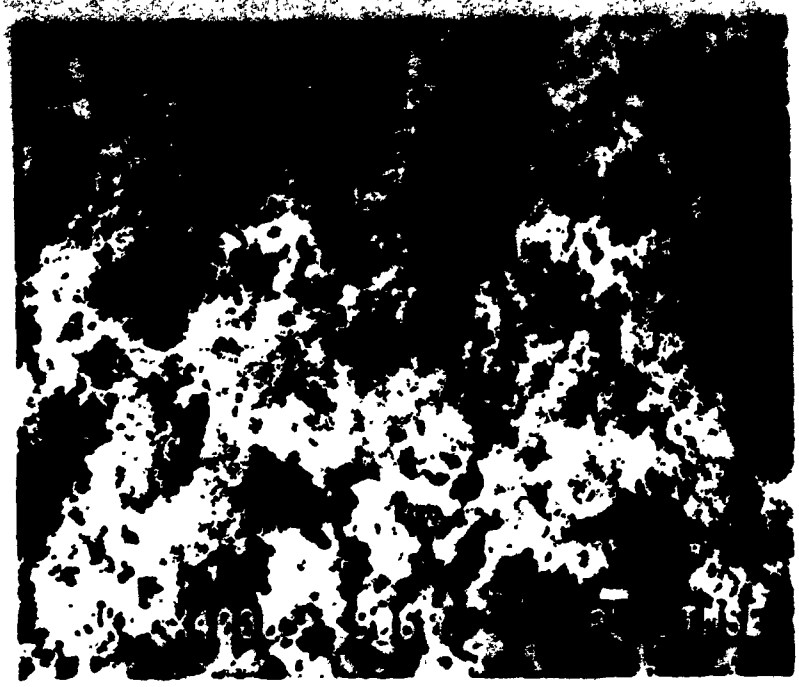

Figure 1- SEM Photomicrograph of a tungstic acid aerogel. Submicron particle clusters are evident in the highly porous microstructure.

Figure 1 shows an SEM photomicrograph of the tungstic acid aerogel. Individual submicron clusters are evident. These clusters are crosslinked into a three-dimensionally continuous structure. The aerogel is extremely fragile, and its low density demands careful handling to avoid breakup.

Hydrogen Reduction

The reduction procedure performed at 1123K for 3600s in dry hydrogen yields metallic tungsten. X-ray diffraction studies indicate that the crystalline oxide level is below the detection limit. However, an adsorbed oxygen layer is a potential contaminant due to the large surface area/unit mass of the reduced powders, (estimated value 3-10 m^2/g). Transmission electron microscopy confirms the ~100 nm average dimension of the reduced metallic tungsten particles.

Figure 2 is a TEM photomicrograph of a cluster of these particles. The individual particles appear to be single- or bi-crystals. The appearance of the metallic tungsten cluster suggests that the reduction mechanism is that described by Cheney (11) as Process 1. This is a gas-solid reaction process that results in tungsten particles nucleated within the precursor oxide skeleton. For these gel precursors, Process 1 appears to be favored over the "vaporization-reduction process", which is the competing reduction process. The detailed characterization of the reduction processes that occur as crystalline tungsten trioxide is converted to metallic tungsten is the subject of numerous studies (12-15), the results of which do not appear to be definitive

The factors which affect the post-reduction size of metallic tungsten particles are incorporated into Parsons' empirical equation (16). They include the bulk density of the oxide powder, the particle size of the oxide powder, the reduction time, the bed depth, and the reduction temperature. The refinement in microstructure through the use of 50 nm tungsten trioxide in aerogel form therefore has a strong effect on the reduction kinetics, due to the low bulk density and small particle size. Furthemore, the ease with which the reducing gas flows through the structure, and the ability to sweep out the water vapor, which is the gaseous reaction product, appear to favor the improved reduction response of these gels.

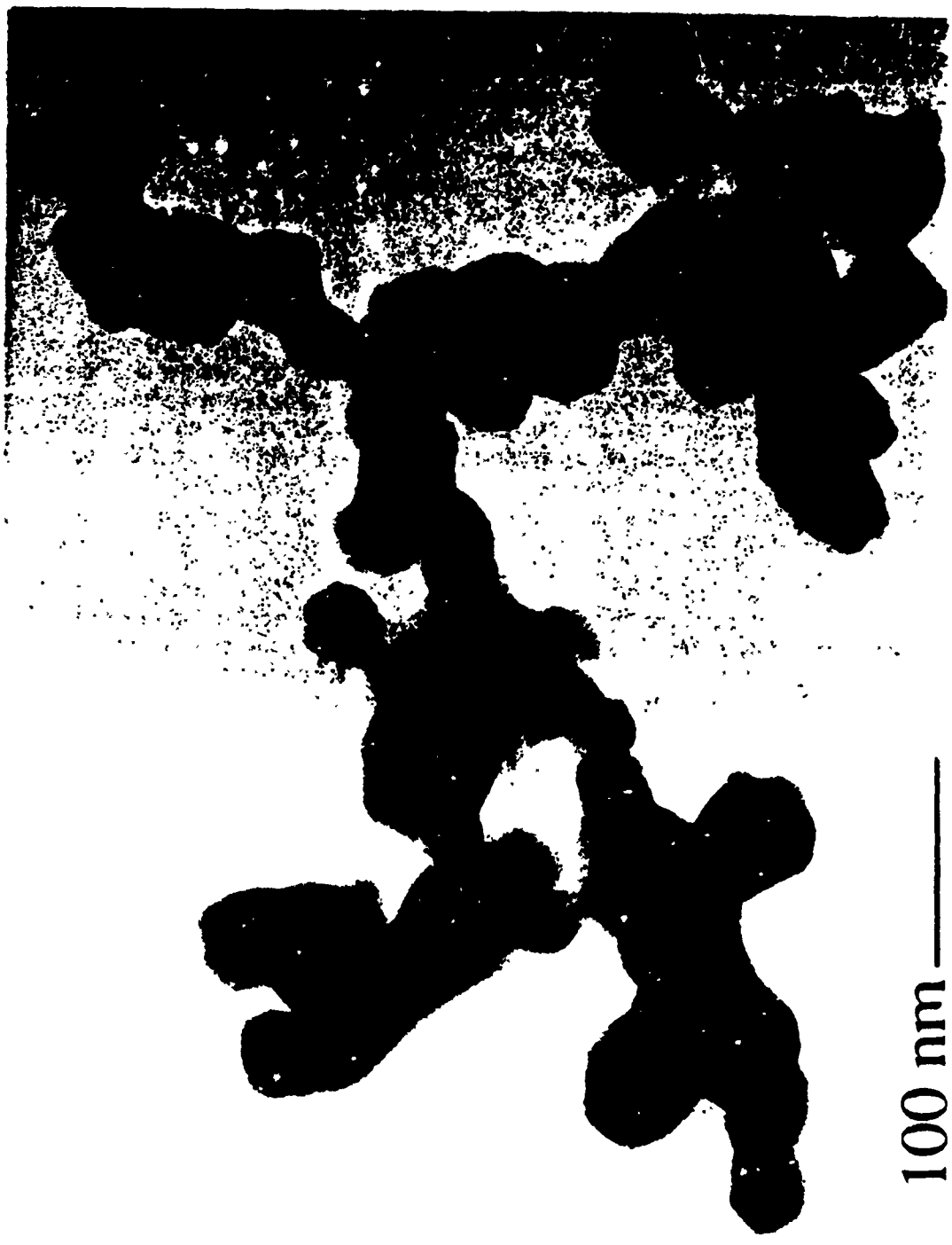

Figure 2- TEM Photomicrograph of metallic tungsten particle cluster obtained by hydrogen reduction (1123K / 3600s) of a tungstic acid gel.

Consolidation Parameters

The processing parameters used for these initial consolidation experiments on each of these systems were derived from parameter sets previously developed for commercial tungsten powders (17). The inherent assumption is that beyond a set electrical conductivity threshold, the pulse resistive heating under pressure would provide rapid densification. The most identifiable solid state densification mechanism is powder forging.

Extrapolations of experimental heating and cooling rate data indicate several features of the thermal history during consolidation. The heating rate is in the 10^3 to 10^4 K/s range, and the peak temperature is ~2500 K. The total time at T > 0.5 Tm is less than 10 s. This duration is largely controlled by the effectiveness of conductive heat extraction fron the surfaces of the consolidated disk through the electrodes to the massive (10 kg) cold copper platens.

Microstructure/Property

The gel-based tungsten was rapidly densified to ~85 % density in a single energy pulse. This densification response may be associated with the increase in total resistance derived from the now numerous interparticle contact resistances. In this simple single-phase material, the primary microstructural parameters of interest are the fineness and uniformity of the microstructure. Microhardness measurements indicate property improvements. The average hardness value of 390 VHN500 (384 - 404 range) of the ~85% average density tungsten compares favorably with that of conventionally-sintered tungsten, in which values of 90-320 VHN are obtained (17). These values depend upon density, particle size, and degree of cold work.

The SEM micrograph in Figure 3 indicates that sufficient connectivity is developed in the HEHR powder-consolidation-processed gel-based tungsten to produce plastic flow. This is evidenced by the curvature of the surface on the perimenter of the hardness impression.The high hardness observed in the gel-based tungsten may be attributed to the fine scale of the microstructure and its uniformity, and to the strong three-dimensional connectivity developed within the consolidated mass. Post-pulse cooling under an applied pressure may also provide a hardening contribution due to enhanced dislocation density.

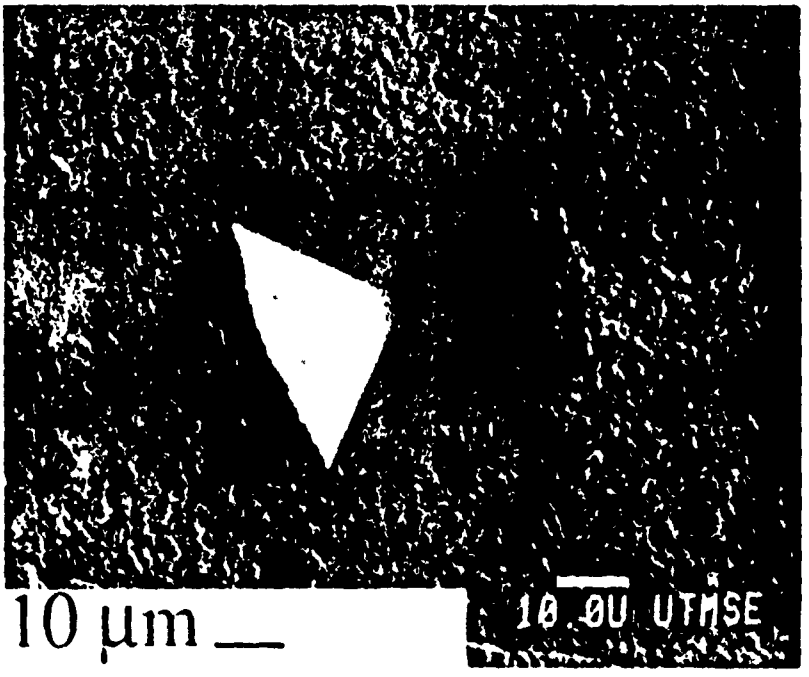

Figure 3- SEM Photomicrograph of a Diamond Pyramid Indenter impression (500g load) in the short-transverse cross-section of a consolidated tungsten disk. The 25mm disk was consolidated to a density of ~85% theoretical by high-energy high-rate powder consolidation processing of powders prepared from tungstic acid gel.

Conclusions

(1) Tungstic acid gels containing 50 nm particles have been prepared by precipitation from a sodium tungstate. Control of pH and temperature permits the synthesis of a gel form rather than a crystalline aggregate.

(2) The tungstic acid aquagel produced by wet chemical processing has been converted to the aerogel form by critical point drying. This dry, open-structured form of tungsten trioxide alters the hydrogen reduction kinetics.

(3) 100 nm tungsten powder particles have been prepared by hydrogen reduction of these tungstic acid gels.

(4) The 100 nm tungsten powder particles made by this method are well-suited to consolidation by pulse self-resistance heating. Tungsten disks consolidated this way have microhardness values higher than conventionally sintered material.

Acknowledgment

Assistance with HEHR processing was provided by Ted Aanstoos and Jim Allen at CEM-UT. H. Tello and P. C. Trimble assisted in the structure evaluation. This research was supported by DARPA/ARO Contract DAAL03-87-K-0073 and by the Texas Advanced Research Program Grant # 4357.

References

1. S. S. Kistler, "Coherent Expanded Aerogels," Journal of Physical Chemistry, 36 (1932), 52-64.

2. J. Fricke, "Aerogels," Scientific American, May 1988, 92-97.

3. J. Fricke, Aerogels - Highly Tenuous Solids with Fascinating Properties, J. of Non-Crystalline Solids, 100 (1988), 169- 173.

4. H.L.Marcus, D.L.Bourell, Z.Eliezer, C.Persad and W.F. Weldon, High-Energy High-Rate Materials Processing, Journal of Metals, 39 (Dec. 1987), 6-10.

5. C. Persad, H. L. Marcus, and W. F. Weldon, " High Energy High Rate Pulsed Power Processing of Materials by Powder Consolidation and by Railgun Deposition", Final Technical Report # UT-CMSE-87-02, March 1987, Gov. Reports Index # 732,954, NTIS Code AD-A179 289/4/GAR PC A07/MF A01.

6. D. R. Ervin, D. L. Bourell, C. Persad, and L. Rabenberg, Structure and Properties of High Energy, High Rate Consolidated Molybdenum Alloy TZM, J. Mat. Sci. Eng., A103 (1988) 25-30.

7. C. Persad, S. Raghunathan, B. -H. Lee, D. L. Bourell, Z. Eliezer and H. L. Marcus, " High -Energy High-Rate Processing ofHigh-Temperature Metal-MatrixComposites," (MRS Symposia Proc. Vol. 120, F. D. Lemkey, A. G Evans, S. Fishman, and J. R. Strife (eds.), MRS, Pittsburgh, PA, 1988), 23 - 28.

8. Y. W. Kim, D L. Bourell, and C. Persad, " Consolidation of Metallic Glass Ribbons using Electric Discharge Welding ", Metallurgical Transactions, Vol. 19A (1988), 1634-1638

9. K. C. Owen, M. J. Wang, C. Persad, and Z.Eliezer, "Preparation and Triboiogical Evaluation of Copper-Graphite Composites by High Energy/High Rate Powder Consolidation," Wear, 120 (1987), 117-121.

10. C. Persad, B. -H. Lee, C. -J. Hou, Z. Eliezer and H. L. Marcus, "Microstructure/ Processing Relationships in High -Energy High-Rate Consolidated Powder Composites of Ti_3Al + TiAl", submitted to Proceedings of the MRS Symposium on High Temperature Ordered Intermetallic Alloys, Boston , MA, November, 1989.

11. R. F. Cheney, " Production of Tungsten, Molybdenum, and Carbide Powders" Metals Handbook Ninth Edition, Volume 7, Powder Metallurgy, ASM, Metals Park, Ohio (1984), 152-159.

12. K. C. Li and C. Y. Wang. Tungsten. 3rd.ed.. New York: Reinhold, 1955.

13. S. W. H. Yih and C. T. Wang. Tungsten: Sources, metallurgy, properties and application. New York: Plenum, 1979.

14. Tao Zheng Ji, "Production of Submicron Tungsten Powder by Hydrogen Reduction of Tungsten Trioxide," (Paper presented at the Third International Tungsten Symposium, Madrid, Spain, May 1985), 108-112.

15. V. K. Sarin, "Morphological Changes Occuring During Reduction of WO_3," Journal of Materials Science, 10 (1975), 593-598.

16. D. S. Parsons, " The Reduction of Tungsten Oxides by Hydrogen", Electrochem. Technology, 3 (1965), 280-283.

17. S. Raghunathan, MS Thesis, The University of Texas at Austin, Aug. 1988.

18. N. C. Kothari, "Factors Affecting Tungsten-Copper and Tungsten-Silver Electrical Contact Materials," Powder Metallurgy Int., 14 (Mar. 1982), 139-143.

Materials Science and Engineering, A131 1990; (XX)-(XX) (XX)

High-energy, High-rate Consolidation of Tungsten and Tungsten-based Composite Powders

S. K. RAGHUNATHAN, C. PERSAD, D. L. BOURELL and H. L. MARCUS

Center for Materials Science and Engineering, The University of Texas at Austin, Austin, TX 78712 (U.S.A.)

(Received May 14, 1990; in revised form July 2, 1990)

Abstract

Tungsten and tungsten-based heavy alloys are well known for their superior mechanical properties at elevated temperatures. However, unalloyed tungsten is difficult to consolidate owing to its very high melting temperature (3683 K). The additions of small amounts of low-melting elements such as iron, nickel, cobalt and copper, facilitate the powder processing of dense heavy alloys at moderate temperatures.

Energetic high-current pulses have been used recently for powder consolidation. In this paper, the use of a homopolar generator as a power source to consolidate selected tungsten and tungsten-based alloys is examined. Various materials were consolidated including unalloyed tungsten, W–Nb, W–Ni, and tungsten heavy alloy with boron carbide. The effect of process parameters such as pressure and specific energy input on the consolidation of different alloy systems is described in terms of microstructure and property relationships.

1. Introduction and background

Many researchers [1–5] have employed electric currents as a heat source to consolidate powders of different alloy systems including tungsten. Greenspan [2] consolidated elemental tungsten powder using current densities ranging from 20 to 47.5 MA m^{-2} to a maximum density of 75% of the theoretical density. Near-theoretical densities were achieved with alloy additions of aluminum and titanium. The processing time was 10 min. A bank of d.c. generators was the power source for these impulse sintering experiments.

The power source used in the present research was a 10 MJ disk-type homopolar generator. The homopolar generator (HPG) is an electric machine that converts rotational kinetic energy into electric energy using the well known Faraday effect. It is a low-voltage, high-current (approximately 300 MA m^{-2}) device that applies high-energy pulses for a very short time [6–8].

High-energy, high-rate (HEHR) consolidation of powders employing the homopolar generator as a power source has definite advantages over conventional powder metallurgy techniques. Since the energy is delivered in a short time (about 1–3 s), this processing technique offers the opportunity to preserve the microstructure associated with the original powders in the consolidated material. Secondly, because of high film and contact resistances and the associated pulse Joule heating effect, the energy deposition is concentrated at the interparticle contacts. Also, the die set-up used in this process operates in a cold wall configuration that assists in accelerated cooling of the compact after the current pulse is discharged.

A wide variety of alloys has been successfully consolidated using this HEHR technique. Among them are Mo–TZM alloy [9], nickel-based metallic glass Metglas® [10], a Cu–graphite metal-matrix composite [11], and Al–SiC metal-matrix composites [12].

2. Experimental procedure

2.1. Consolidation set-up

A schematic sketch of the experimental set-up is given in Fig. 1. The backing ring was used to prevent the spreading of the die liner, which cracks during the application of pressure and subsequent discharge of the pulse. Usually, this backing ring was made of plain carbon or stainless steel. The materials used for sleeves were alumina or borosilicate glass. The electrodes used in this research were usually made from ETP copper or 304 stainless steel. Die inserts, in the

0921-5093/90/$3.50

form of foils or disks, were placed between the electrodes and the compact. The diameter of the insert was equal to that of the electrodes. The inserts were molybdenum, niobium, or stainless steels foils, or molybdenum disks.

The specific energy input (SEI) is the amount of energy in kilojoules per kilogram of the powder mass placed between the electrodes during a consolidation process. This was calculated using oscillographically recorded current and voltage time-traces. The power, at any instant, was calculated as the product of the current and the voltage. The total energy input was obtained as the integral over the total duration of the pulse discharge.

2.2. *Materials*

Powders from different sources were obtained. Particle sizes of the powders and proportion of each constituent in the blend are given in Table 1. Three different tungsten powders were used. Coarse powder, having a minimum particle size of 5 μm and a maximum particle size of 150 μm, was obtained from the Aesar division of Johnson and Matthey Company, MA. This powder was 99.98% pure and was prepared by a proprietary precipitation process [13]. The particles were angular as shown in Fig. 2. Niobium powder was obtained from the Aesar division of Johnson and Matthey Company, MA. This powder was manufactured by a proprietary precipitation process [13]. The minimum particle size was 10 μm and the maximum particle size was 250 μm. This powder was 99.8% pure and was used in pure niobium and W–Nb elemental blends. A scanning electron micrograph is shown in Fig. 3.

The second variety of powder was obtained from Los Alamos National Laboratories, NM.

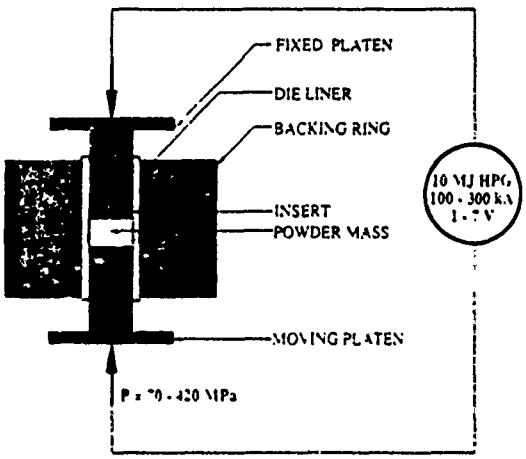

Fig. 1. Schematic diagram of the high-energy, high-rate powder processing set-up

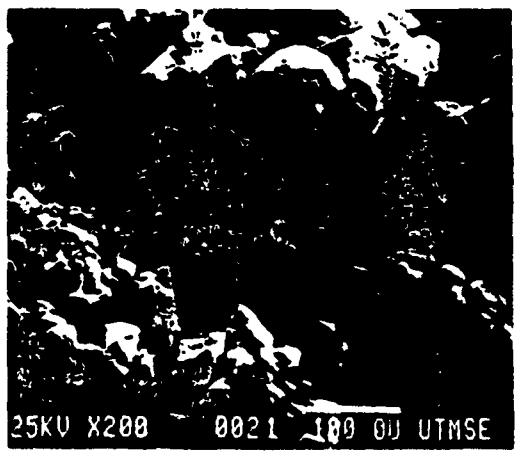

Fig. 2. Scanning electron micrograph of as-received coarse tungsten powder (Aesar). The white bar represents 100 μm.

TABLE 1 Particle size and constitution of the powders used in this research

Material	*Particle size, μm*			*Purity, %*
	Minimum	*Mean*	*Maximum*	
AESAR W	5	–	150	99.98
GTE W	1	3	15	99.9
LANL W	0.5	1.0	1.7	99.8
Nb	10	–	250	99.8
W–Ni–Fe–B_4C	*Prealloyed blend*			
W (93 wt%)	0.8	3	15	
Ni (5 wt%)	1	12	30	
Fe (2 wt%)	2	4	50	
B_4C (0.2 wt%)	1	11	31	

*Not available

Fig. 3. Scanning electron micrograph of as-received niobium powder (Aesar). The white bar represents 100 μm.

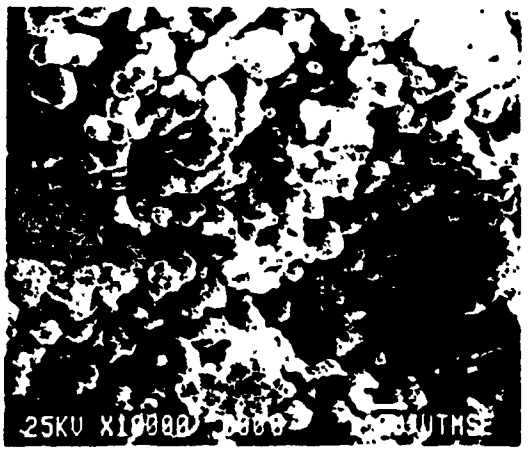

Fig. 4. Scanning electron micrograph of as-received fine tungsten powder (LANL). The white bar represents 1 μm.

The minimum particle size was 0.5 μm and the maximum particle size was 17 μm. The reported purity was 99.9%, minimum. The particles were angular with equiaxed shape as shown in Fig. 4. This powder was deoxidized in hydrogen at 1123 K for 12 h before consolidation and was consolidated in a glove bag with two soft copper disk patches attached to the bag to facilitate the passage of the electric pulse through the powder mass.

The third type of tungsten powder, obtained from GTE Products, was mainly used for consolidating W–Ni alloys. This powder was 99.97% pure. The minimum particle size was 1 μm and the maximum particle size was 15 μm with most of the particles lying in the range 1–4 μm. A

Fig. 5. Scanning electron micrograph of as-received fine tungsten powder (GTE). The white bar represents 1 μm.

scanning electron micrograph of the as-received powder is shown in Fig. 5. Nickel was coated onto this tungsten powder using the method of hydrogen reduction of nickel-nitrate-coated tungsten [14]. A precalculated quantity of hydrous nickel nitrate was mixed with tungsten powder in water and heated to 363–368 K to evaporate the water, thus leaving a nickel nitrate coating on the tungsten powder. The coated powder mass was subsequently reduced in a hydrogen atmosphere at 873 K for 1 h. The resultant alloy powder contained tungsten coated with 1–3 wt.% metallic nickel.

A fourth material consisting of a pre-mixed blend of W–Ni–Fe – B_4C heavy alloy with boron carbide was obtained from Los Alamos National Laboratories, NM. Its constitution is given in Table 1.

2.3 *Characterization and evaluation*

A JEOL 35C scanning electron microscope equipped for energy-dispersive spectroscopy EDS and wavelength-dispersive spectroscopy WDS was used for the preliminary evaluation of the as-received powders, microstructure of the consolidated compacts and fractography. Murakami's etchant was used for revealing the microstructure. X-ray diffraction analysis was performed using a Phillips diffractometer fitted with a copper target, graphite monochromator, and a nickel filter.

The densities of the compacts were determined using both an immersion technique ASME PTC 19.16-65 and lineal analysis of

photomicrographs. The latter method was used when the compacts could not be separated from the electrodes. Densities measured using both techniques of pycnometry were checked for accuracy and were found to be in reasonably good agreement with each other.

Specimens were prepared for hardness evaluation according to ASTM standard E 92-72 [15]. A Wilson Tukon LR® microhardness tester with Vicker's indenter was used to measure hardness values. A load of 0.5 kg was applied.

For fractographic analysis, square rods (2 mm × 2 mm) were machined from the central sections of the consolidated compacts. These specimens were fractured by bending at room temperature. The fractured surfaces were analyzed using scanning electron microscopy. A brief summary of the systems that are discussed with their respective properties is given in Table 2.

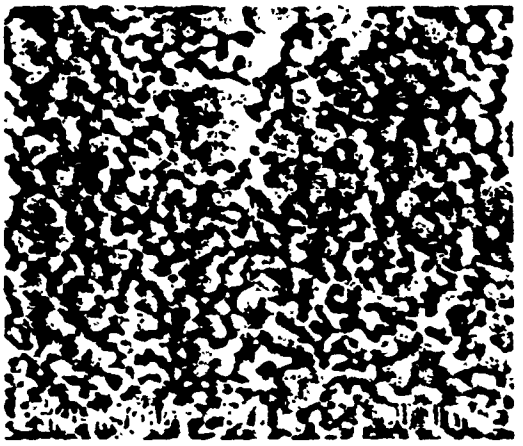

Fig. 6. Scanning electron micrograph of a diametral cross-section of the compact A1 consolidated from deoxidized fine tungsten powder (LANL). This compact was etched with Murakami's reagent. The white bar represents 1 μm.

3. Results

3.1. Microstructure

3.1.1. Pure tungsten

Tungsten compacts were consolidated with either fine or coarse elemental powders. A micrograph of a fine powder compact (A1) is shown in Fig. 6. As is evident from the scanning electron micrograph, some deformation occurred at interparticle contacts; however, there was no substantial densification. The density was measured to be 75% of the theoretical density. The total SEI was 4150 kJ kg^{-1} and the applied pressure was 210 MPa.

The microstructure of the as-received coarse tungsten powder is shown in Fig. 7. The grain size ranged from 5 μm to 100 μm. The compact (A2)

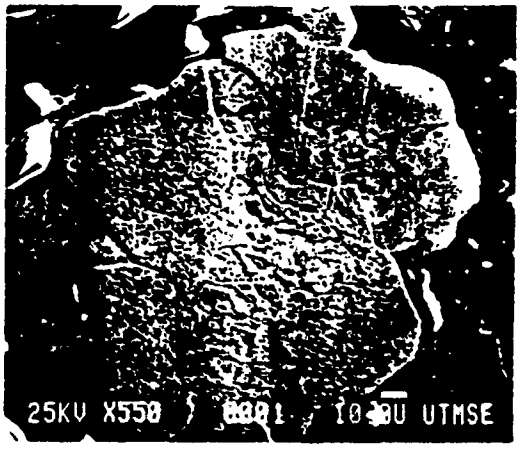

Fig. 7. Microstructure of as-received coarse tungsten powder (Aesar). The etchant used was Murakami's reagent. The white bar represents 10 μm.

TABLE 2 Summary of the systems studied in this research and their respective properties

System	Designation	Powder	Applied pressure MPa	SEI kJ kg	Density	Maximum surface H
W	A1	LANL	210	4150	75	—
W	A2	Aesar	210	7500	78	509
W	A3	Aesar	210	13500	92	400
W-Nb	B1	Aesar	210	10900	82	405
W-Nb	B2	Aesar	210	34000	76	400
W-Ni	C1	GTE	420	142250	98	456
W-Ni	C2	GTE	420	—	97.3	469
W-Ni	C3	GTE	420	—	97	504
W-Ni-Fe + B,C	D1	LANL	420	5800	97	434
W-Ni-Fe + B,C	D2	LANL	210	37400	93	413
W-Ni-Fe + B,C	D3	LANL	210	3000	92.5	424

*Not available.

was processed with coarse tungsten powder at 210 MPa and 750 kJ kg^{-1}. After consolidation, it was apparent that the ends of the compact were infiltrated by copper. The density was measured to be 98%. The compact comprised a central cast region, a particulate-transition region, and a copper-infiltrated end zone.

The micrograph shown in Fig. 8 depicts a magnified image of the cast region, which was at midradius from the center of the compact. This cast region reveals a columnar grain structure after heavy etching. The tungsten particles in the copper-infiltrated region, in Fig. 9, were sintered and surrounded by copper.

Another compact A3 was processed with coarse tungsten powder at 210 MPa and 1800 kJ kg^{-1}. The microstructure at the center of this compact, shown in Fig. 10, revealed that tungsten was not melted and the pores were filled with copper. The density was 92%.

3.1.2. Tungsten–niobium alloy

Tungsten and niobium powders were consolidated using several parameters. A scanning electron micrograph of the 50W–50Nb compact (B1) processed at 210 MPa and 10 900 kJ kg^{-1} is shown in Fig. 11. The light areas are tungsten particles and the darker matrix is niobium. The

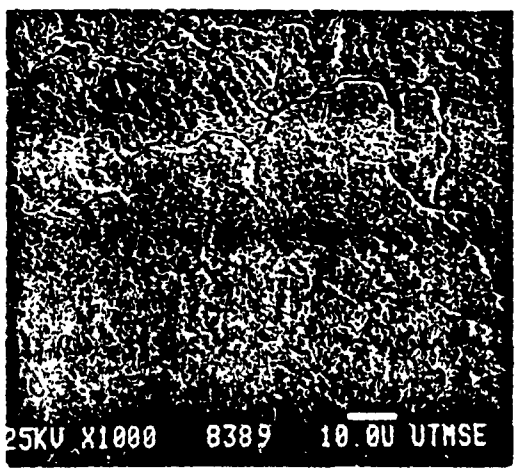

Fig. 8. Microstructure etched with Murakami's reagent of the cast region at midradius from the center of the compact A2 revealing columnar and equiaxed grain structure with copper streams. The white bar represents 10 μm.

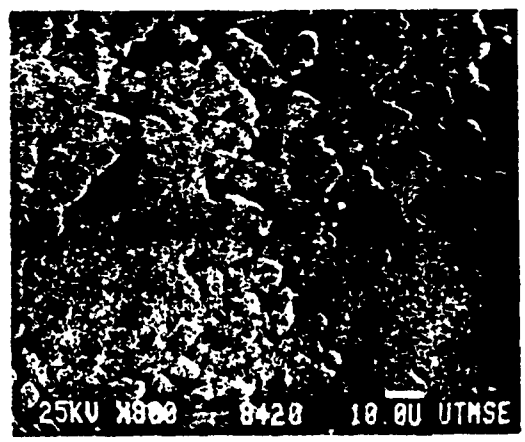

Fig. 10. Microstructure of compact A3 revealing sintered tungsten particles in a copper matrix. The dark phase is copper and the light phase is tungsten. This compact was unetched. The white bar represents 10 μm.

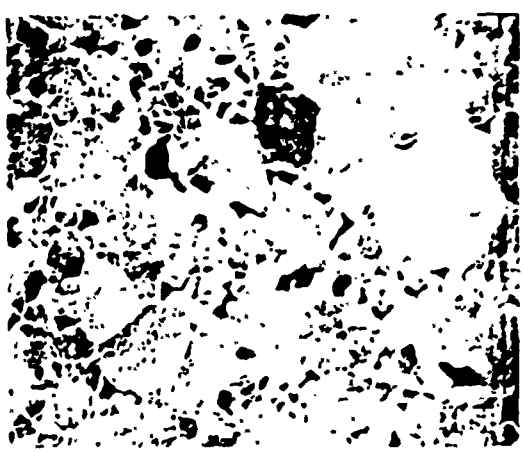

Fig. 9. Microstructure of the copper-infiltrated region adjacent to the edge of the compact A2 etched with Murakami's reagent. The white bar represents 10 μm.

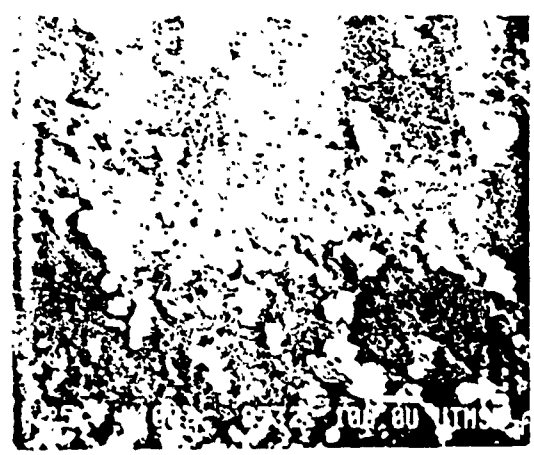

Fig. 11. Microstructure of compact B1, depicting tungsten particles in a niobium matrix. The dark phase is niobium and the light phase is tungsten. This compact was unetched. The white bar represents 10 μm.

niobium appears to have flowed plastically and encapsulated the tungsten particles. The density was 94%. Pores were present at the W–Nb interfaces in all the compacts. Another 50W–50Nb compact (B2), that was processed with copper electrodes instead of stainless steel at a lower energy level (3400 kJ kg^{-1}), reached a density of 76%.

3.1.3. Tungsten–nickel alloy

The amount of nickel coated on GTE tungsten powder in this research was 1, 2, and 3 wt.%. To study the effect of nickel, other parameters such as pressure and discharge rate were maintained constant.

Compact C1 was processed with tungsten powder coated with 3 wt.% Ni, at 420 MPa and 14 250 kJ kg^{-1}. The density of the compact was 98%. The microstructure of the sample revealed isolated nickel pools at the center of the compact. The microstructure of C1 at a nickel-rich area is shown in Fig. 12. The matrix had less nickel at the edge than at the center of the compact.

Another compact in this alloy system (C2) was processed with tungsten powder coated with 2 wt.% Ni. The microstructure of this compact is shown in Fig. 13. The density of the compact was 97.3%.

The third compact C3 was processed with same parameters as C1, except the tungsten powder was coated with 1 wt.% Ni. Nickel pools were absent and nickel was found to be uniformly distributed throughout the compact. The density of the compact was found to be 97% of the theoretical density.

3.1.4. Tungsten heavy alloy + B_4C

These compacts were processed using the prealloyed blend of tungsten, nickel, iron and boron carbide. Compact D1 was processed at 420 MPa and 3810 kJ kg^{-1}. The density was measured to be 97%. The micrograph of this compact is shown in Fig. 14. This micrograph reveals tungsten particles, and the matrix in the form of shear-band-like striations along different directions within the compact. The EDS analysis of the matrix revealed a mixture of tungsten,

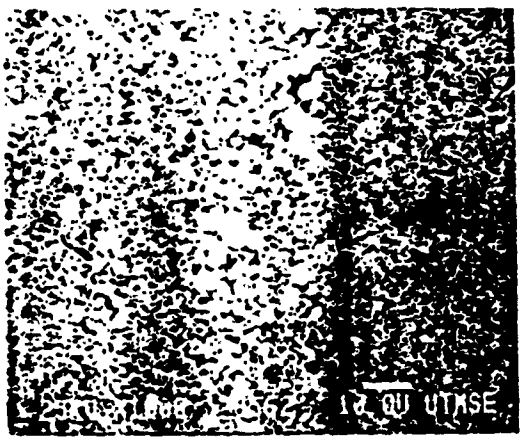

Fig 13. Microstructure of compact C2, revealing largely sintered tungsten particles and nickel at the pores. This compact was unetched. The white bar represents 10 μm

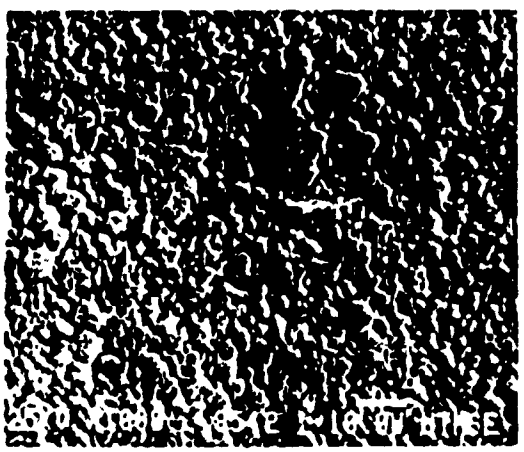

Fig 12. Microstructure of compact C1 revealing sintered tungsten particles in a nickel-rich matrix. The dark phase is nickel and the light, majority, phase is tungsten. This compact was unetched. The white bar represents 10 μm

Fig 14. Microstructure of compact D1 revealing the sintered tungsten particles, the matrix, and the shear-band-like striations. This compact was etched with Murakami's reagent. The white bar represents 100 μm

nickel and iron. The average composition of the matrix obtained from different locations in the matrix was 85.1 wt.% W, 10.3 wt.% Ni, and 4.6 wt.% Fe. Based on X-ray spectroscopy, the phases identified were W, W_2C, FeWB, W_2B, Fe_3C, Fe_4W_6C, and Ni_4B_3. The intermetallic Fe_7W_6 was also observed [16]. The density was 97%.

The other two compacts, D2 and D3, were processed at 210 MPa and 3740 kJ kg^{-1} and 4000 kJ kg^{-1} respectively. These compacts were solid-state sintered since no reaction product could be identified from the X-ray diffraction pattern. Densities of D2 and D3 were 93% and 92.5% respectively.

3.2. *Mechanical properties and fractography*

Hardness values of tungsten ranged from 350 to 500 H_v. The Vickers hardness (0.5 kg) profile of a pure tungsten compact cross-section is shown in Fig. 15(a). The hardness profiles for the tungsten heavy alloy with boron carbide and W–Nb alloy are shown in Figs. 15(b) and 15(c) respectively. From Fig. 15, it is apparent that the hardness values increase from the edge of the compact toward the center. This reveals the inhomogeneity arising from the faster cooling rates on the edges of the compacts, both longitudinally and laterally.

The spread in hardness for tungsten (Fig. 15(a)) and W–Nb (Fig. 15(c)) is not as extensive as was observed in tungsten heavy alloy (Fig. 15(b)). Furthermore, the absolute hardness values for the tungsten compact are comparable with the tungsten components commercially manufactured [17, 18] and the hardness values for W–Nb compacts match the hardness of the niobium phase. The tungsten heavy alloy was processed at significantly less specific energy, which is thought to be the reason for the large hardness gradient.

The variation in the Vickers hardness numbers for coarse tungsten powder compacts, with respect to the specific energy input is shown in Fig. 16. Numbers in the figure denote the average values of the hardness over the entire cross-section of the compacts. From this, it can be seen that the hardness of the coarse tungsten compact increases with the specific energy input to the compact.

The fractograph of coarse tungsten compact A2, processed at 210 MPa and about 7500 kJ kg^{-1}, is shown in Fig. 17. There were three distinct regions, a central-cast region, a particulate-transition region, and a copper-infiltrated region with sintered tungsten particles. In the central cast region, where no prior-particle boundaries were found, the fracture was found to be totally cleavage fracture. In the particulate-transition region, where weak bonding between the particles was found, a crack propagation path was evident. During consolidation, there was also evidence of good plastic deformation, repacking, and reshaping of the particles, as in the case of powder forging. At the edges of the compact, the infiltrated copper matrix failed by ductile fracture, whereas the sintered tungsten particles failed by transgranular cleavage. The fractograph of the pure tungsten compact A3 processed at 210 MPa and 1800 kJ kg^{-1}, also showed ductile failure of the copper matrix and cleavage fracture of tungsten particles. From Fig. 18, necks were found between the sintered tungsten particles.

The fractograph of 50W–50Nb (B2) processed at 210 MPa and 3400 kJ kg^{-1} is shown in Fig. 19. From this figure, porosity is evident. Particles appeared to have sintered only at the asperities. Upon fracture, the interparticle contacts ruptured because of the absence of appreciable bonding.

A densification map denoting the corresponding density for a particular pressure and SEI combination for different systems is given in Fig. 20.

4. Discussion

Compact A2 Fig. 16 was found to contain three zones, a cast region at the center of the compact, a particulate-transition zone next to the cast region, and a copper-infiltrated region with sintered tungsten particles. The sequence of events that occur during the HEHR process are deduced from the above fractograph. Upon discharge of the pulse, the temperature reached the melting temperature of tungsten 3683 K and the center of the compact, the hottest part, was cast. The next region the particulate-transition region on the fractograph was also heated but the maximum temperature was lower than the center of the compact. These particles were plastically forged and partly sintered. As the particulate-transition zone was being sintered, the temperature was sufficient near the copper electrodes for them to melt and infiltrate through the compact, thereby enabling the molten copper to reach the interface between the particulate-transition zone and the copper-infiltrated zone. This resulted in

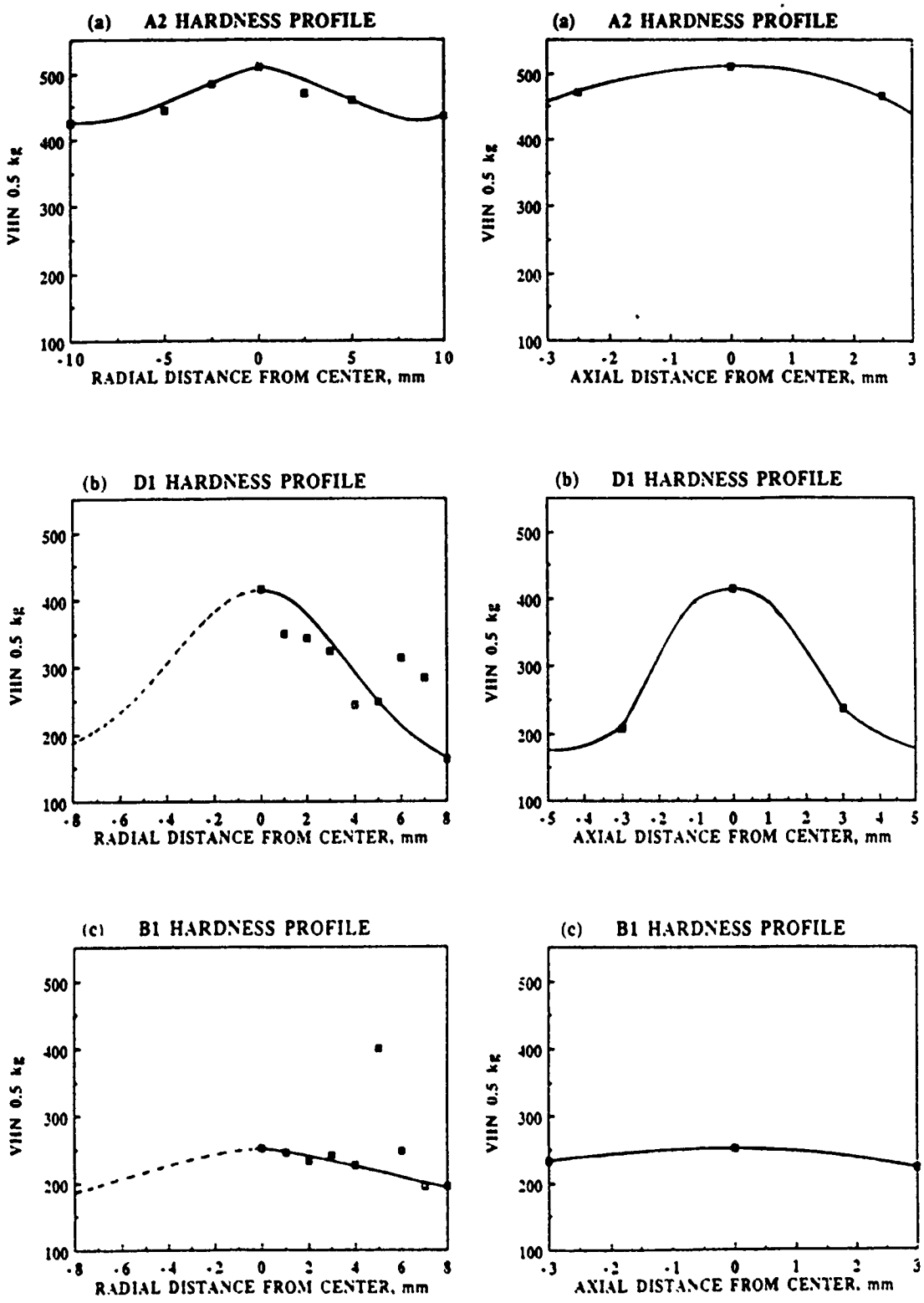

Fig. 15 Vickers hardness profiles for a pure tungsten A2, b tungsten heavy alloy with boron carbide D1, and c tungsten-niobium B1 compacts

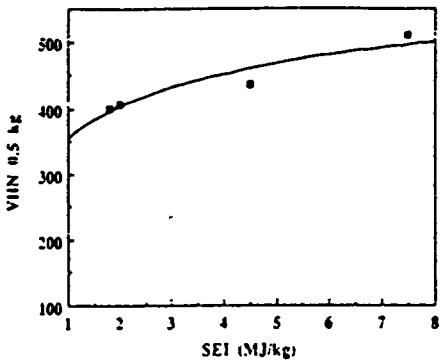

Fig. 16 Influence of the specific energy input on average hardness, in VHN, for compacts consolidated from coarse tungsten powder Aesar .

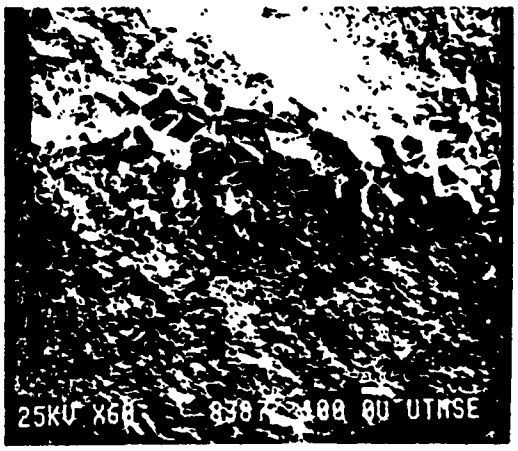

Fig. 17. Fractograph of compact A2 depicting three zones: top, central zast: center, particulate transition; bottom, sintered tungsten particles with copper infiltration The white bar represents 100 μm.

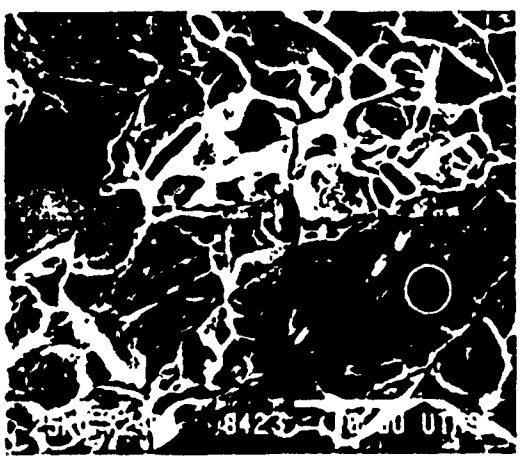

Fig 18 Fractograph of compact showing ductile dimple rupture of copper arrow , and cleavage fracture of sintered tungsten particles circle . The white bar represents 10 μm

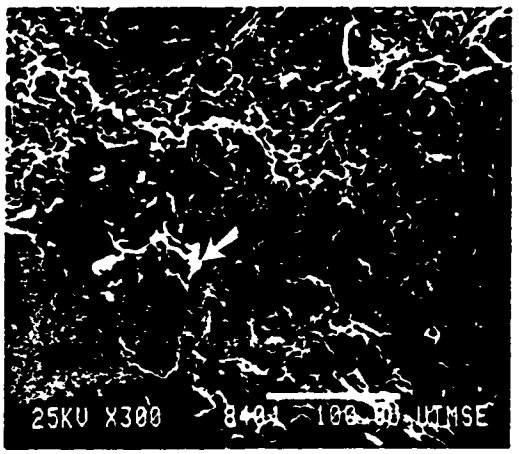

Fig. 19. Fractograph of compact B2 revealing the lack of any appreciable bonding between tungsten particles. The arrow indicates a ductile failure. The white bar represents 100 μm.

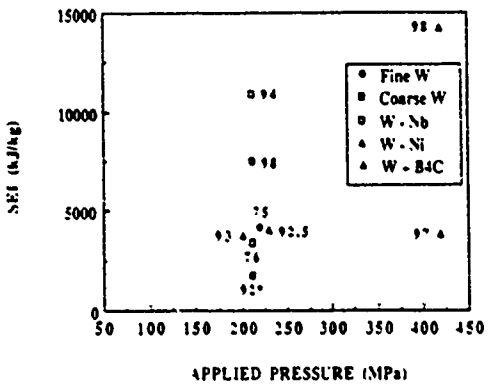

Fig 20 Densification map, shown as variation in density with applied pressure and specific energy input for different systems studied in this research. The density values are given adjacent to the corresponding values of pressure and specific energy input. An asterisk indicates that molten copper infiltrated the compact extensively.

rapid conduction of thermal energy from the then-sintering particulate-transition region, leaving this region just powder forged. In the copper-infiltrated region, the tungsten particles were sintered evident from the necks possibly enhanced by the activator role played by the copper in the mass transport of tungsten [19-21].

No distinct effect of pressure varied from 210 MPa to 420 MPa on the W-Nb compacts was found. However, the density seemed to increase with the increase in specific energy input B1 and B2 .

For the W-3wt.%Ni compact C1 , portions of nickel matrix were isolated as pools, especially at

the center of the compact. This may be due to the tendency of excess liquid to decrease the total number of menisci, resulting in a reduction of the surface free energy. This occurs in the early stages of liquid-phase sintering [22]. Also, the rate of nickel agglomeration is rapid above its melting temperature because liquid nickel can flow along capillaries [23].

With the increase in nickel content from 1 to 2 wt.%, the sintering mechanism changed from W-W to Ni-Ni sintering [24, 25]. Near-theoretical densities were achieved by sintering the compacts at 1773 K for 1 h in hydrogen atmosphere [24, 25]. When these conventional processes are compared with HEHR processing, HEHR processing achieves the same density with virtually no grain growth and the consolidation process is generally complete within 2–3 s.

The tungsten heavy alloy with B_4C is a classic example of liquid-phase sintering and this liquid phase produces a large amount of stress resulting from surface tension [23, 26]. In addition to this inherent pressure, an external pressure is applied in the HEHR process. This has been termed "pressure-assisted liquid-phase sintering". The phase diagrams of the quaternary C–Fe–Ni–W [27] and the ternary Fe–Ni–W [28] alloys are described elsewhere.

Bose *et al.* [29], German *et al.* [30], and Bourguignon and German [31] report that a eutectic, at temperatures slightly over 1708 K, exists in the W–Ni–Fe ternary system. However, no such eutectic seems to exist at that temperature for an Ni:Fe ratio of 7:3 [28]. However, a eutectic does exists at about 1709 K for the Ni–Fe binary alloy system for an Ni:Fe ratio of 7:3 [32]. It is important that this nickel to iron ratio of 7:3 be maintained to eliminate any intermetallic formation between nickel and iron, which tends to embrittle the heavy alloy by segregating along the grain boundaries, thereby resulting in intergranular fracture [30].

In the compact made with W–Ni–Fe – B_4C, a featureless matrix and large grains exist, as has been reported by Sheinberg [33]. The hot hardness of this compact seems to be 10%–20% higher than that of premium-grade conventional WC–Co at 1073 K. The onset of reactions was at 1173 K for fine powders and 1273 K for coarse powders [34].

In compact D1, no boron carbide was found. The elemental iron and nickel powders seemed to have reacted fully, as was reported previously [33] for identical material processed at 1473 K. From the X-ray diffraction pattern, many complex borides and carbides were found. The boron carbide seemed to have reacted completely and the resulting complex borides and carbides were homogeneously dispersed. The matrix was homogeneous with the W:Ni:Fe ratio being approximately the same at different locations in the matrix. This process has the characteristics of "self-propagating high-temperature synthesis" or "SHS" [35]. SHS is a reaction where an exotherm is involved, thereby liberating thermal energy. The liberated heat helps sustain the reaction for a longer time without any external heat input. These reaction products were not observed in compacts D2 and D3, where the constituents seemed to have undergone solid-state consolidation.

5. Conclusions

(1) Consolidation of coarse tungsten (100 μm) to 98% density was achieved using a HEHR processing technique.

(2) There was a distinct increase in the density and hardness of pure tungsten compacts with increase in specific energy input.

(3) There was no definite pressure effect on W–Nb alloys. The density seemed to increase with the specific energy input level.

(4) Tungsten heavy alloy with B_4C was successfully consolidated. At high energy input, various products leading to a "self-sustaining high-temperature synthesis" were identified. At this high energy level, a liquid-phase-assisted consolidation mechanism is operative.

(5) W–Ni alloy systems were consolidated successfully using nickel-coated fine tungsten powders.

Acknowledgments

The authors wish to thank Haskell Sheinberg of Los Alamos National Laboratories for providing tungsten and preblended composite powders. The authors gratefully acknowledge the assistance provided with the HEHR process by Jim Allen and Ted Aanstoos of UT-CEM. M. Schmerling, H. Tello, and S. Cheng assisted in the structural evaluation. This research was supported by DARPA/ARO Contract DAAL03-87-K-0073.

References

1 F. V. Lenel. Resistance sintering under pressure. *J. Met.*, January, 1955) 158–167.

2 J. Greenspan. Impulse resistance sintering of tungsten. *AMMRC TR. 76–32*. September, 1976 (Army Mechanics and Materials Research Center).

3 A-I. Ratchenko *et al.*, Mass transfer and homogenizing in electric-discharge sintering of powder mixture. In M. M. Ristic ed., *Sintering—New Developments*. Elsevier, Amsterdam, 1979, pp. 76–81.

4 D. J. Williams and W. Johnson. Neck formation and growth in high-voltage discharge forming of metal powders. *Powder Metall., 25* 2)(1982) 85–89.

5 M. Shakery *et al.*, Electrical discharge powder compaction. *Powder Metall. Int., 11* (3)(1979) 120–124.

6 H. L. Marcus *et al.*, High-energy, high-rate materials processing. *J. Met., 39* (12)(1987) 6–10.

7 J. B. Walters and T. A. Aanstoos. Welding and billet heating with homopolar generator, *Met. Progr., 127* , 25–28.

8 G. B. Grant *et al.*, *Weld. J., 58* 1979) 24–26.

9 D. R. Ervin, D. L. Bourell, C. Persad and L. Rabenbers. Structure and properties of high-energy, high-rate consolidated molybdenum alloy TZM. *Mater. Sci. Eng., A102* 1988 25–30.

10 Y. W. Kim, D. L. Bourell and C. Persad. High-energy, high-rate powder processing of a rapidly-quenched quaternary alloy, $Ni_{65.5}Mo_{25}Fe_{10}B_{10}$. *Mater. Sci. Eng., A123* 1990 99–115.

11 M. J. Wang *et al.*, High-energy high-rate consolidation of copper-graphite composite brushes for high-speed, high-current applications. In J. H. Gully ed., *Proc. Third Int. Conf. on Current Collectors, Austin, TX, November, 1987*. Paper 20

12 H. L. Marcus *et al.*, in F. C. Matthews, N. C. R. Buskell, J. M. Hodgkinson and J. Norton eds., *Interfaces in Aluminum Metal-Matrix Composites*, Vol. 2, *Proc. Sixth Int. Conf. on Composite Materials, ICCM VI & ECCM 2*. Elsevier, London, 1987, pp 2.459–2.468.

13 L. B. Martin, Aesar Division, Johnson & Matthey Company, Seabrook, NH, private communication, March 1988.

14 C. J. Li and R. M. German. Enhanced sintering of tungsten-phase equilibria effects on properties. *Int. J. Powder Metall. Powder Technol., 20* 2 149–162.

15 *Annual Book of ASTM Standards*, Part 10, ASTM, Philadelphia, PA, 1980, pp 309–319

16 C. Persad *et al.*, High-energy high-rate processing of high-temperature metal-matrix composites. *Mater. Res. Soc. Symp. Proc., 120* , 23–28

17 R. Syre, *Handbook on the Properties of Niobium, Molybdenum, Tantalum, Tungsten and Some of Their Alloys*, NATO Advisory Group for Aeronautical Research and Development, May, 1965.

18 *Aerospace Structural Metals Handbook*, Department of Defense Materials Information Center, March, 1963.

19 A. N. Pilyankevich *et al.*, Special features of failure of the tungsten-copper sintered pseudoalloy. *Sov. Powder Metall. Int., 25* (6)(1986) 516–521.

20 V. N. Panichkina and V. P. Smirnov. Segregation of solutes to the grain boundaries of tungsten-copper pseudoalloys. *Sov. Powder Metall. Int., 25* (4) (1986) 331–333.

21 N. K. Prokushev *et al.*, Kinetics and densification and grain growth of refractory phase grains in the liquid phase sintering of very finely divided tungsten-copper materials. *Sov. Powder Metall Int., 25* (9), 727–733.

22 Y. S. Kwon and D. N. Yoon. The liquid-phase sintering of W-Ni. *Sintering Processes, Materials Science Research*, Vol. 13, Plenum Press, New York, 1980, pp. 203–218.

23 R. M. German. *Liquid Phase Sintering*, Plenum Press, New York, 1985.

24 J. S. Lee and I. H. Moon. The dependence of solid-state sintering of W-Ni powder compact on Ni concentration. *Scr. Metall., 21* 1987 1175–1178.

25 R. M. German. The effect of the binder phase melting temperature on enhanced sintering. *Metall. Trans A, 17* (1986) 903–906.

26 F. V. Lenel. *Powder Metallurgy—Principles and Applications*. MPIF, Princeton, NJ, 1980.

27 A. Gabriel *et al.*, in G. C. Kuczynski *et al.* eds., *Sintering '85*, Plenum Press, New York, 1987, pp 379–393.

28 F. Guillermet and L. Ostlund. Experiments and theoretical study of the phase-equilibria in the Fe-Ni-W system. *Metall. Trans. A, 17* 1986) 1809–1823.

29 A. Bose *et al.*, Test temperature and strain rate effects on the properties of tungsten heavy alloy. *Metall. Trans A, 19* 1988 487–493

30 R. M. German *et al.*, Microstructure limitations of high tungsten content heavy alloys. *J. Met.*, August, 1985 36–39.

31 L. L. Bourguignon and R. M. German. Sintering temperature effects on a tungsten heavy alloy. *Int. J. Powder Metall., 24* 2 1988 115–121.

32 N. V. Agew ed., *Handbook of Binary Metallic Systems*, Vol. II translated from Russian, Israel Program for Scientific Translations, Jerusalem, 1967.

33 H. Sheinberg, Non-conventional tungsten-base hard metal. *Int. J. Refractor. Hard Met.*, March, 1983 17–26.

34 H. Sheinberg, Sintering reactions, structure and properties of cobalt-free non-conventional hard material. *Int J Refractor Hard Met.*, December, 1986 235–237

35 N. D. Corbin *et al.* SHS soli-sintering of materials in the titanium-boron-carbon system. In G. Bruggeman and V. Weiss eds., *Innovations in Materials Processing*, Vol 30, Plenum Press, New York, 1985, pp 337–346

SYNTHESIS
AND
HIGH ENERGY HIGH RATE PROCESSING
OF ULTRAFINE GRAINED TUNGSTEN

H.L. Marcus, D. L. Bourell, Z. Eliezer, C. Persad,
Center for Mat. Sci. and Eng.,
and
W. F. Weldon ,
Center for Electromechanics,
The Univ. of Texas, Austin, TX 78712.

ABSTRACT

High-energy, high-rate processing, driven by fast-discharging stored energy devices, offers new potential for materials science oriented developments. This is evidenced by the tungsten-based research thrust described in this work. Tungsten trioxide gels produced from acidic solutions of sodium tungstate have been investigated as precursor materials for submicron metallic tungsten particles. 100 nm metallic tungsten particles have been obtained through rapid reduction of open-structured aerogel precursors in dry hydrogen. These particles have subsequently been consolidated to produce dense, ultrafine-grained powder compacts. The consolidation step is accomplished by use of high-energy high-rate processing driven by a high current pulse from a homopolar generator. The consolidation response of these laboratory-synthesized powders has been compared to that of commercial high-purity tungsten powders. Binary systems such as W-Cu and W-Mo have also been processed by similar methods. It has been further demonstrated that Cu-W-WC nanosized composite structures for electrotribological applications may be derived from these processing approaches.

This work was supported by DARPA under ARO Contract DAAL 0387-K-0073 and by the Texas Advanced Research Program Grant # 4357.

Nov. 8, 1989, Alexandria, VA.

SYNTHESIS AND HIGH ENERGY HIGH RATE PROCESSING OF ULTRAFINE-GRAINED TUNGSTEN

H. L. MARCUS, D. L. BOURELL, Z. ELIEZER, C. PERSAD,
CENTER FOR MATERIALS SCIENCE AND ENGINEERING,
AND
W. F. WELDON ,

CENTER FOR ELECTROMECHANICS,

THE UNIVERSITY OF TEXAS AT AUSTIN

SUPPORTED BY DARPA/ARO AND TEXAS ARP

IDA, Nov. 8, 1989

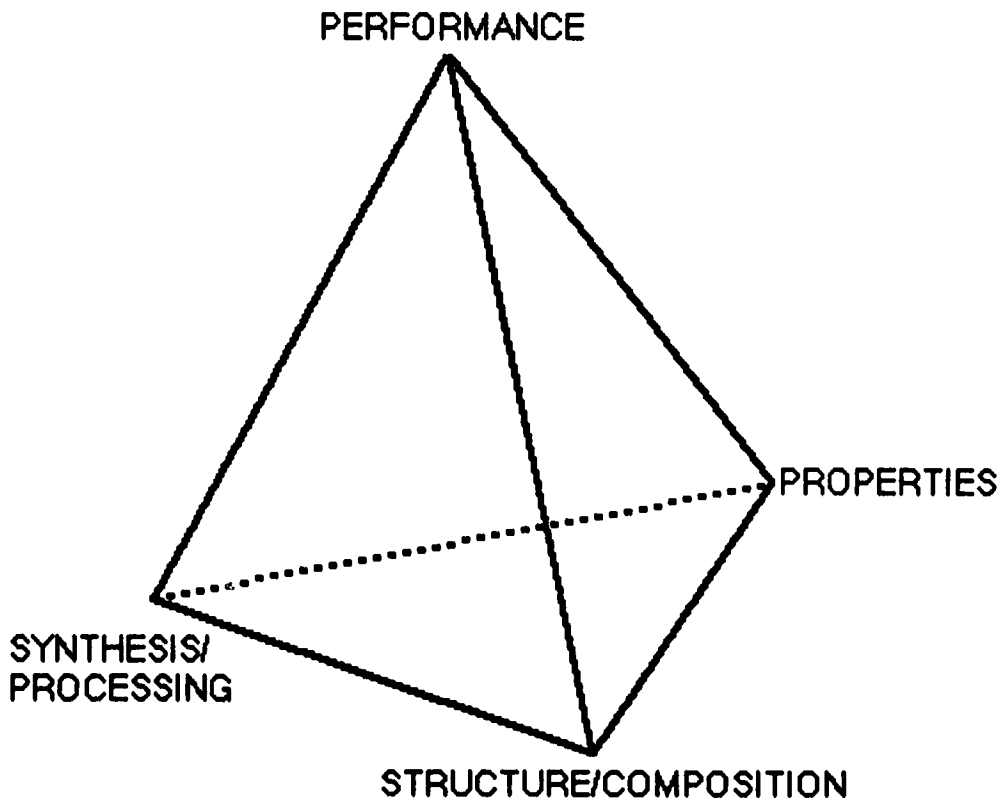
PERFORMANCE
PROPERTIES
SYNTHESIS/
PROCESSING
STRUCTURE/COMPOSITION

OUTLINE

- o HEHR PROCESS
- o W SYNTHESIS
- o PROCESSING
  - > W from gel
  - > W - Cu
  - > W- Mo

MATERIALS

ELEMENTAL: TUNGSTEN: GEL-BASED (100nm)

FINE (0.8 μm)

COARSE

BINARY SYSTEMS: W-Cu

W-Ni

W-Hf

W-Nb

W-Mo.

TERNARY SYSTEMS: W-Ni-Fe

W-Mo-Re

COMPOSITE: W-Ni-Fe + B_4C

HIGH ENERGY HIGH RATE

'1MJ in 1s'

Conversion of
Rotational KE
into Electrical Energy
In the form of a
High Current Pulse

Faraday Disk ---> Homopolar Generator (HPG)

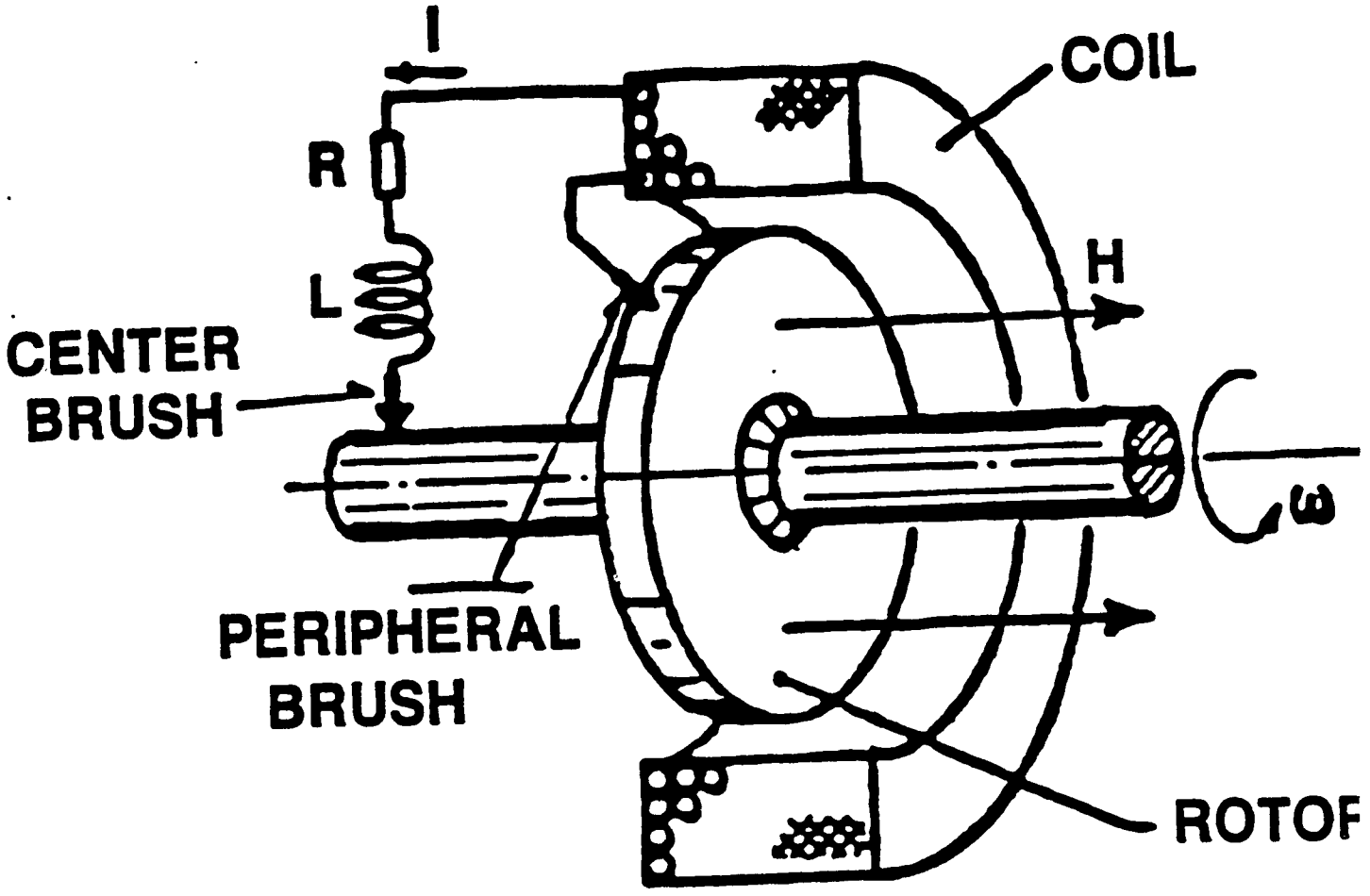
I
COIL
R
L
H
CENTER
BRUSH
ω
PERIPHERAL
BRUSH
ROTOF

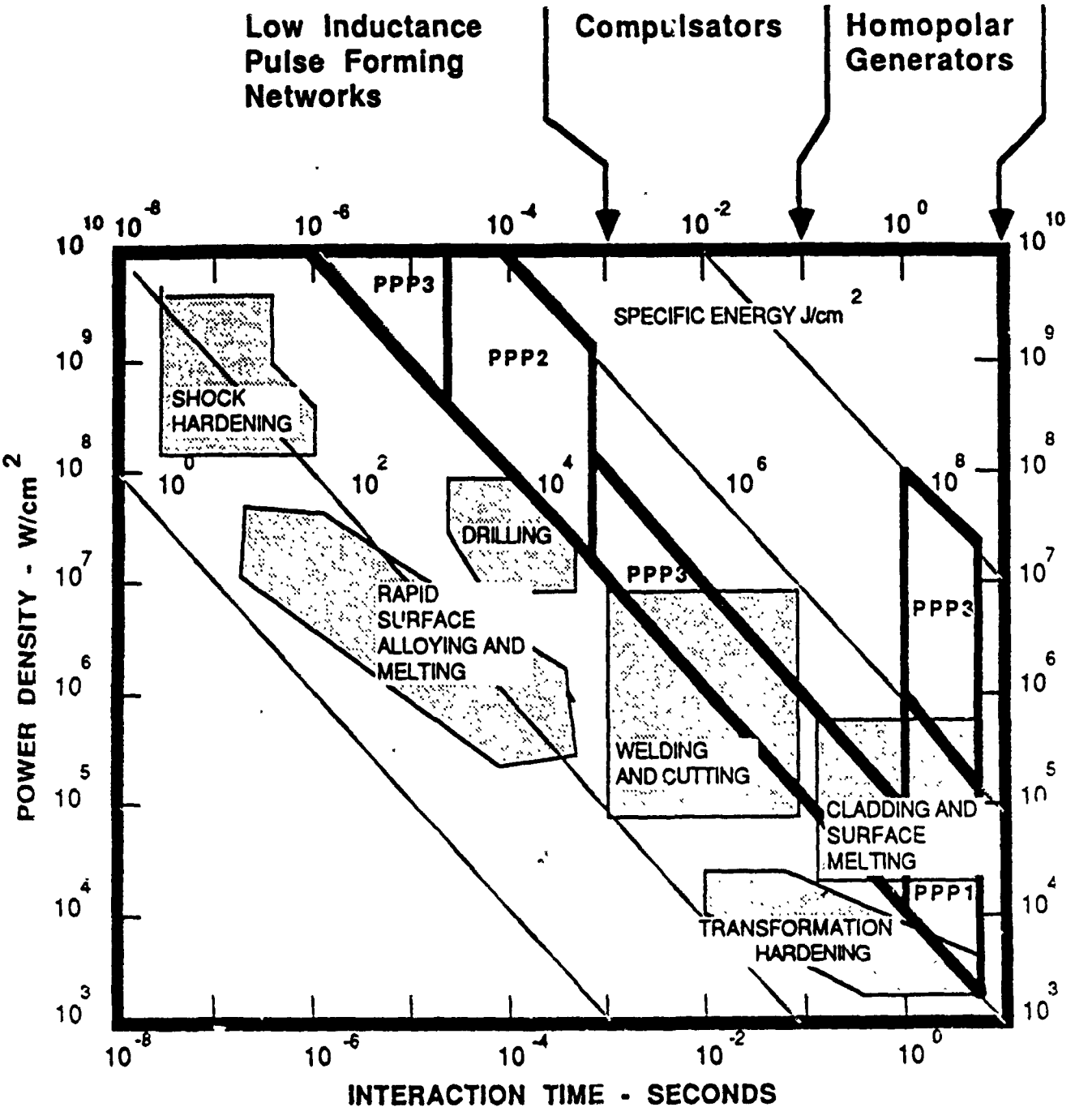
Low Inductance Pulse Forming Networks
Compulsators
Homopolar Generators
SPECIFIC ENERGY J/cm 2
PPP3
PPP2
PPP3
PPP3
PPP1
SHOCK HARDENING
DRILLING
RAPID SURFACE ALLOYING AND MELTING
WELDING AND CUTTING
CLADDING AND SURFACE MELTING
TRANSFORMATION HARDENING
POWER DENSITY - W/cm 2
INTERACTION TIME - SECONDS

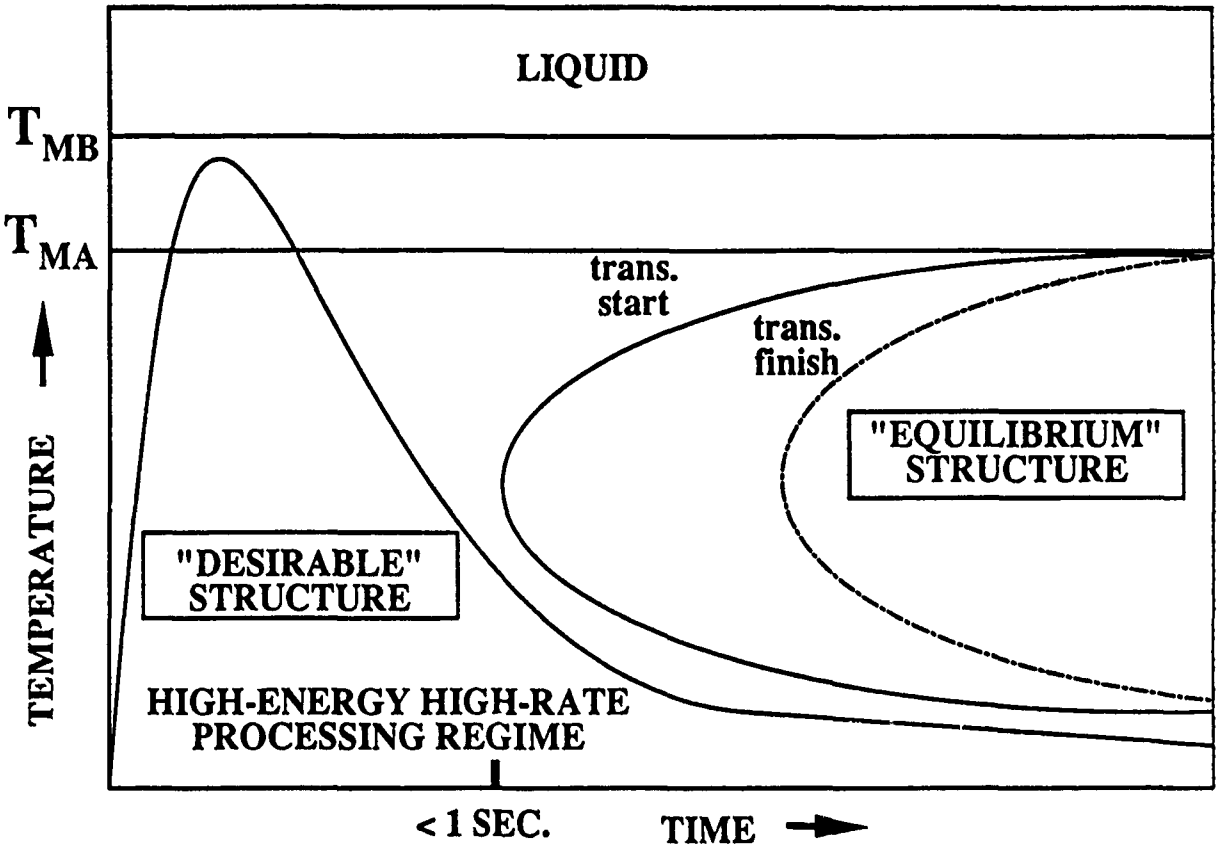
LIQUID
T_{MB}
T_{MA}
trans. start
trans. finish
"EQUILIBRIUM" STRUCTURE
"DESIRABLE" STRUCTURE
HIGH-ENERGY HIGH-RATE PROCESSING REGIME
TEMPERATURE
< 1 SEC.
TIME

POWDER PROCESSABILITY

RESISTIVITY DEPENDENCE

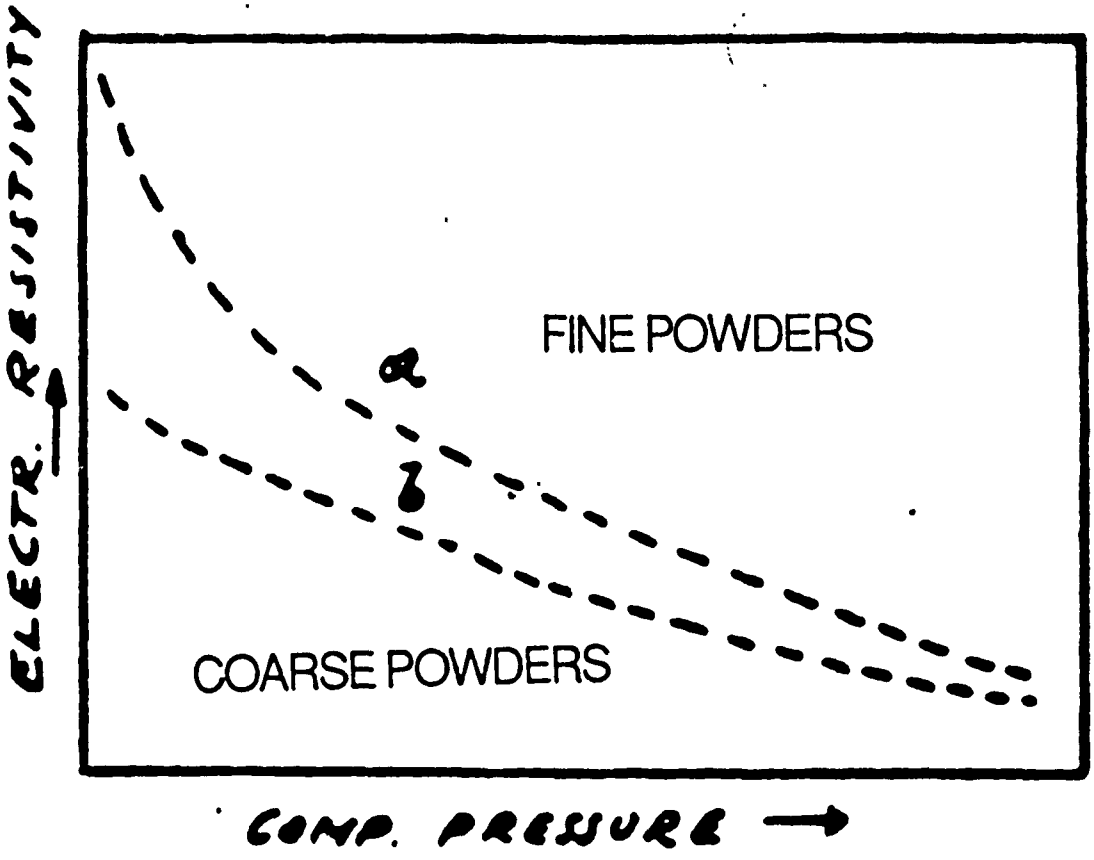

INFLUENCE OF PARTICLE SIZE

MAKING $R_L >> R_S$

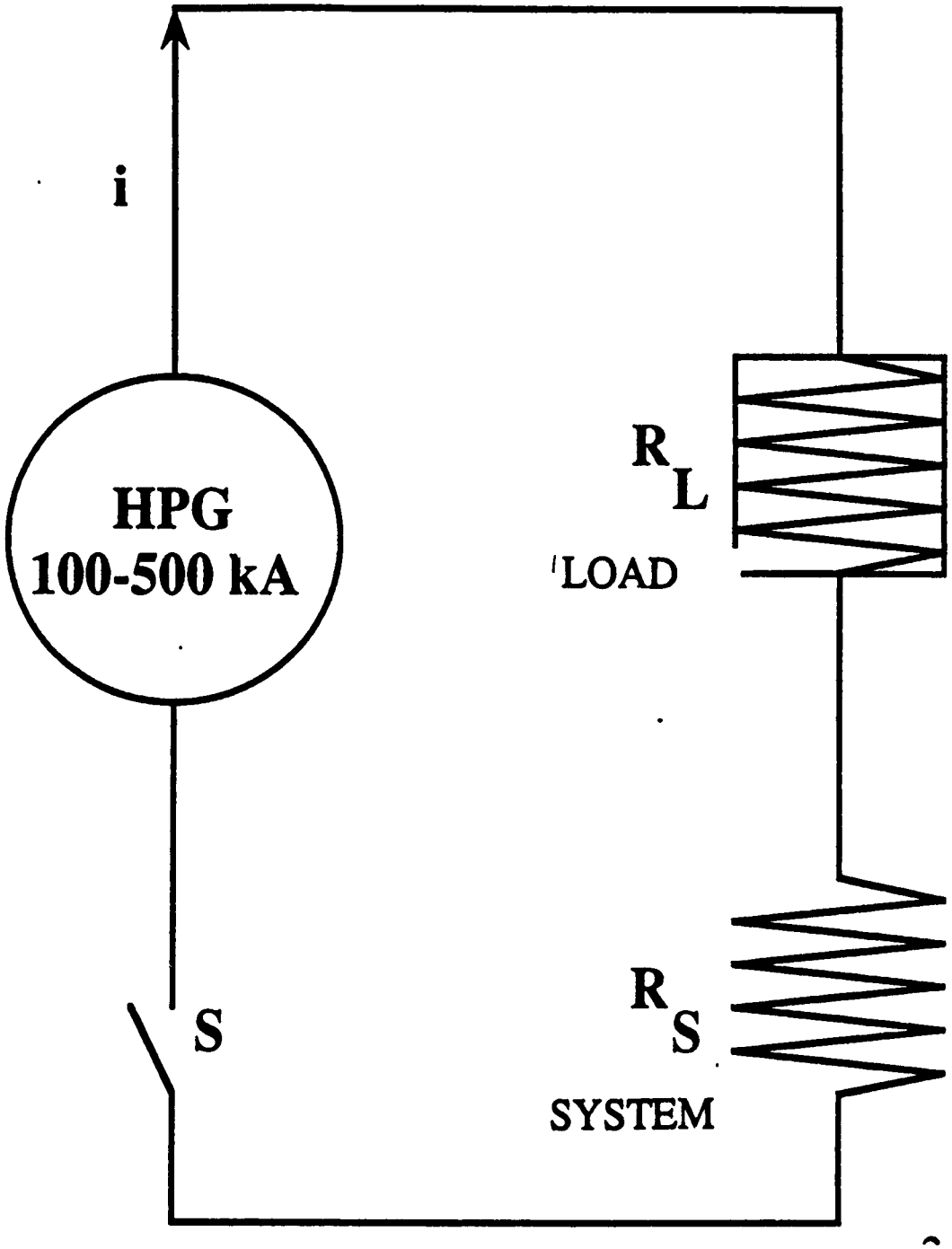

W PROCESSING REQUIRES HIGH TEMP.

HIGH TEMP. ----> LARGE I^2R_L

I IS DETERMINED BY SYSTEM

R_L DEPENDS ON POWDER CHARACTERISTICS

FINE TUNGSTEN POWDERS?

1. No commercial sources of powder < 1μm (1987 -->).

2. Laboratory methods

   - Vapor phase decomposition of WF_6 & WCl_6
   - Freeze-drying of APT
   - Sol-gelroute

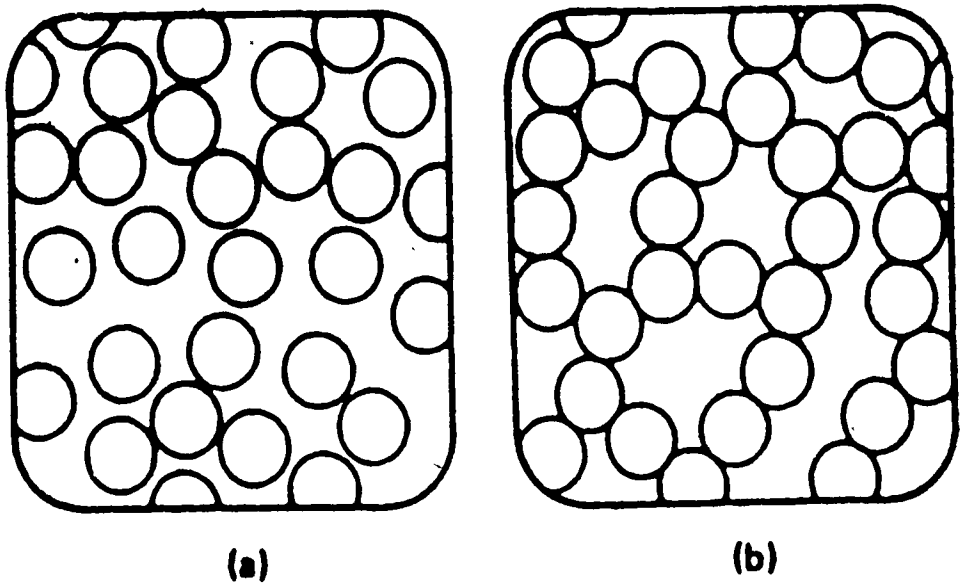

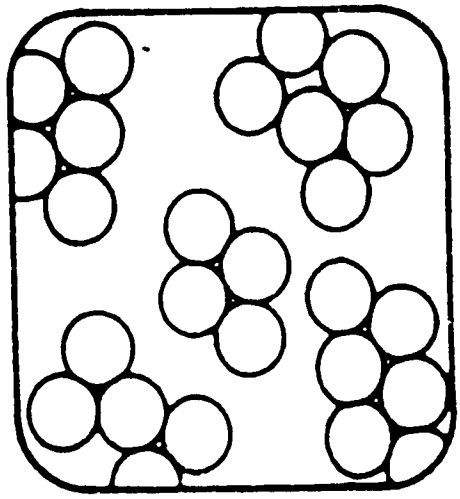

(a), sol; (b), gel; (c), powder

ILER, 1979

Polymerization behavior of silica.

MOST STUDIED GEL

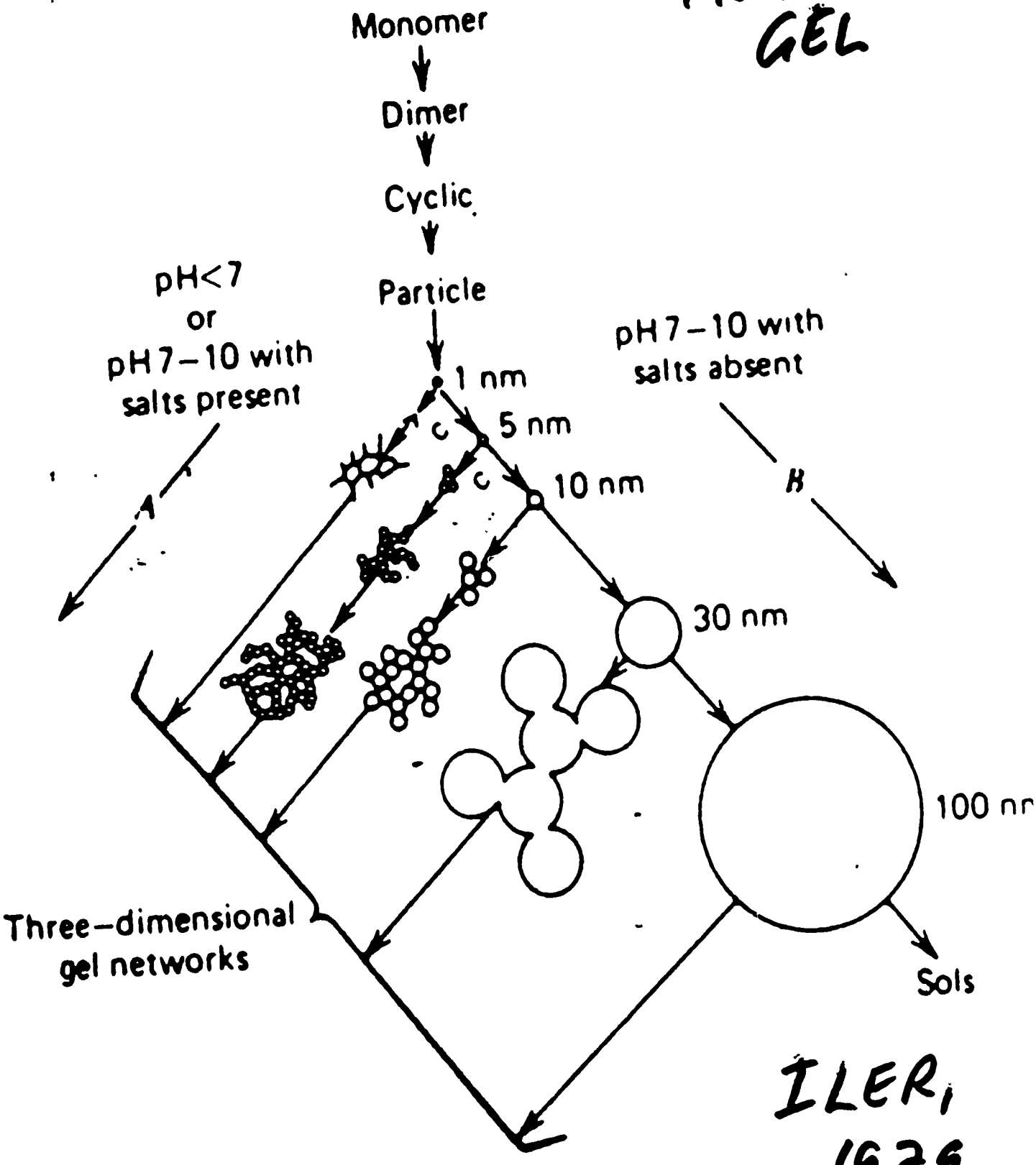

ILER, 1979

TUNGSTEN via P/M
Conventional Method

ORE - TO - POWDER CONVERSION

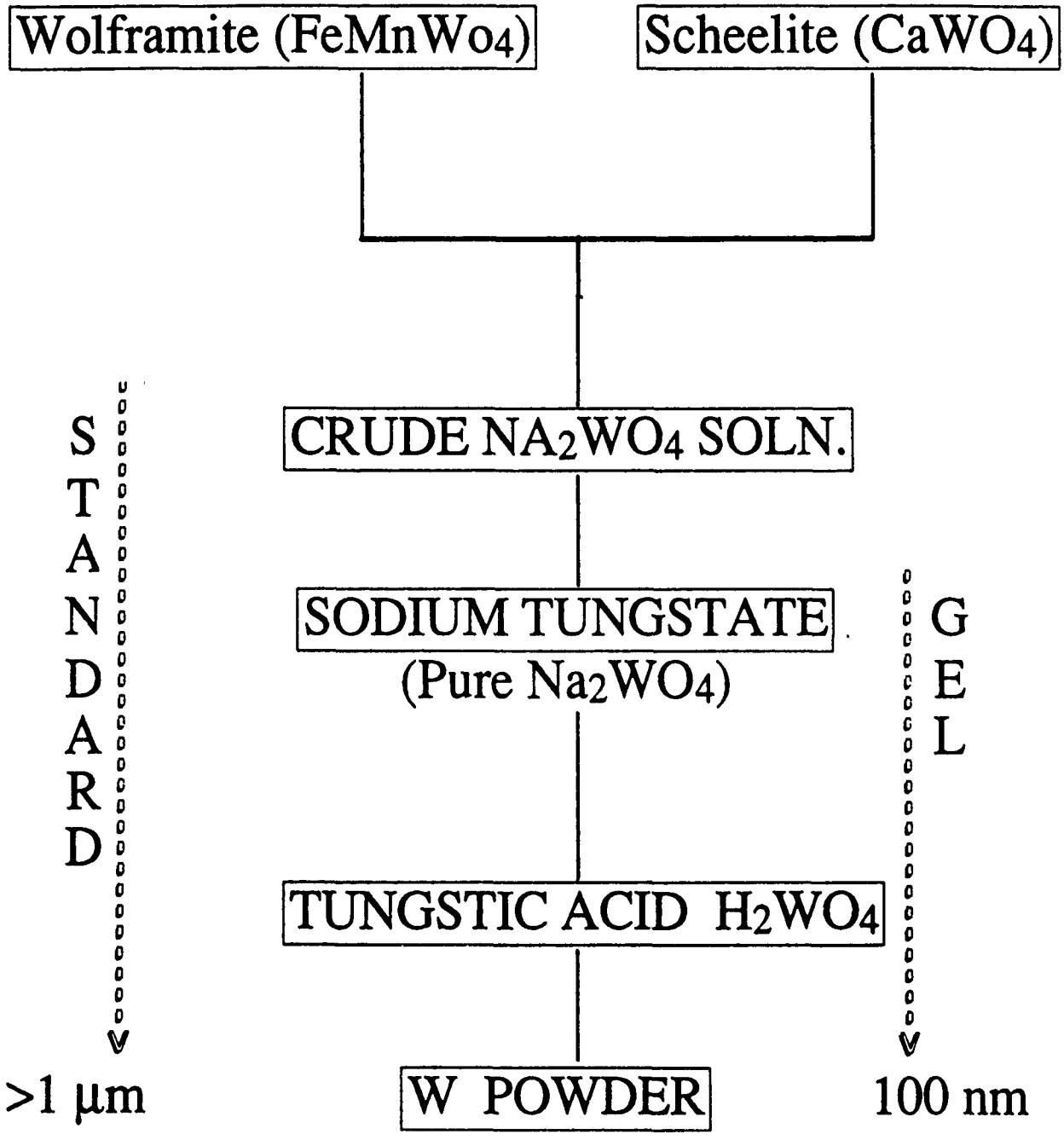

POTENTIAL PRECIPITATION PRODUCTS

1) TUNGSTIC OXIDE MONOHYDRATE (CRYSTALLINE), $WO_3 . H_2O$

> 2N ACID/ 100^0C

2) TUNGSTIC OXIDE DIHYDRATE (CRYSTALLINE), $WO_3 . 2H_2O$

> 0.5 - 2N ACID/ 25^0C

3) COLLOIDAL TUNGSTIC ACID, $WO_3 . nH_2O$, $0.33 < n < 2$

~ 0.25N ACID/ 25^0C

THIS GEL PROCESS

4) SODIUM OCTATUNGSTATE

5) SODIUM TETRATUNGSTATE

SOL-GEL ROUTE

1. Aquagel synthesis
   - Precipitate
   - Filter and wash

2. Gel conversion
   - Aquagel
   - Alcogel
   - Aerogel

3. Gel reduction
   - H_2 at 1073K for 3600s

AEROGEL

REMOVE LIQUID (WITHOUT COLLAPSE)

CRITICAL POINT DRYING

- SURFACE TENSION EFFECTS

- CPD USING CO_2

AEROGEL

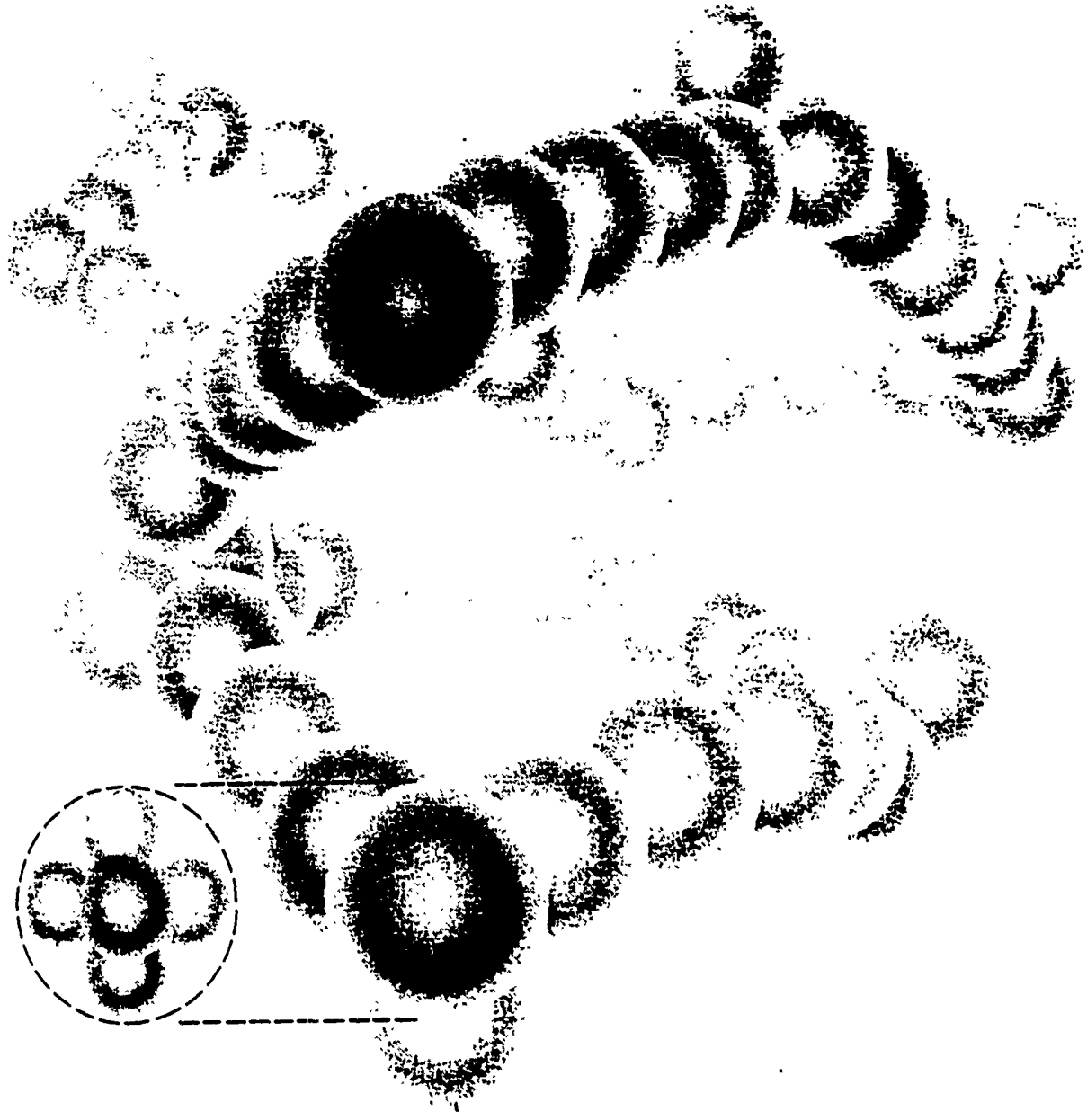

100 nm

FRICKE, 1988

AEROGEL = CPD OF ALCOGEL

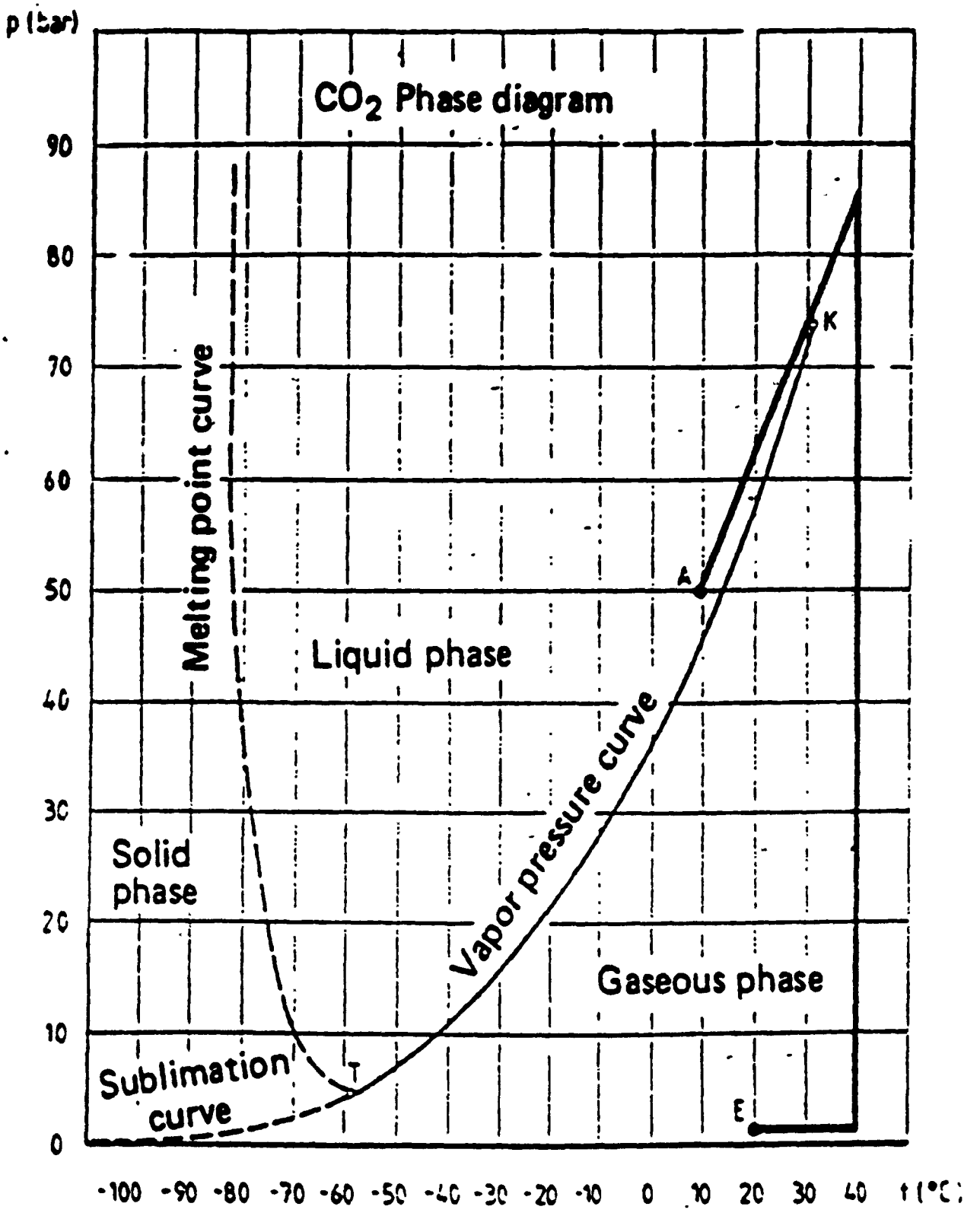

CHEMICAL SYNTHESIS

X-RAY DIFFRACTION

TUNGSTEN TRIOXIDE

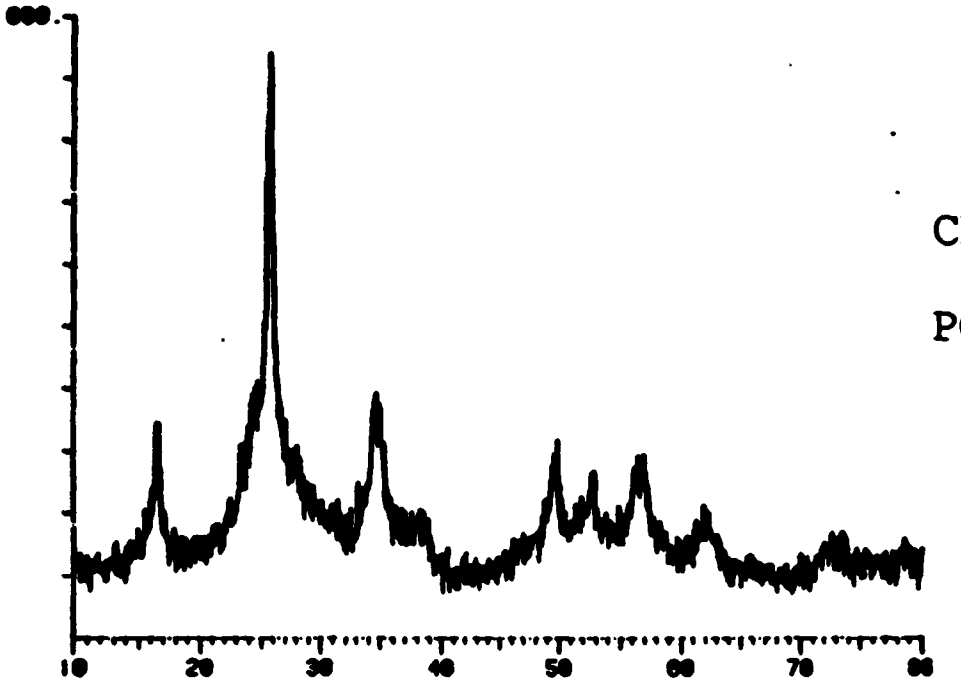

CRYSTALLINE

POWDERS

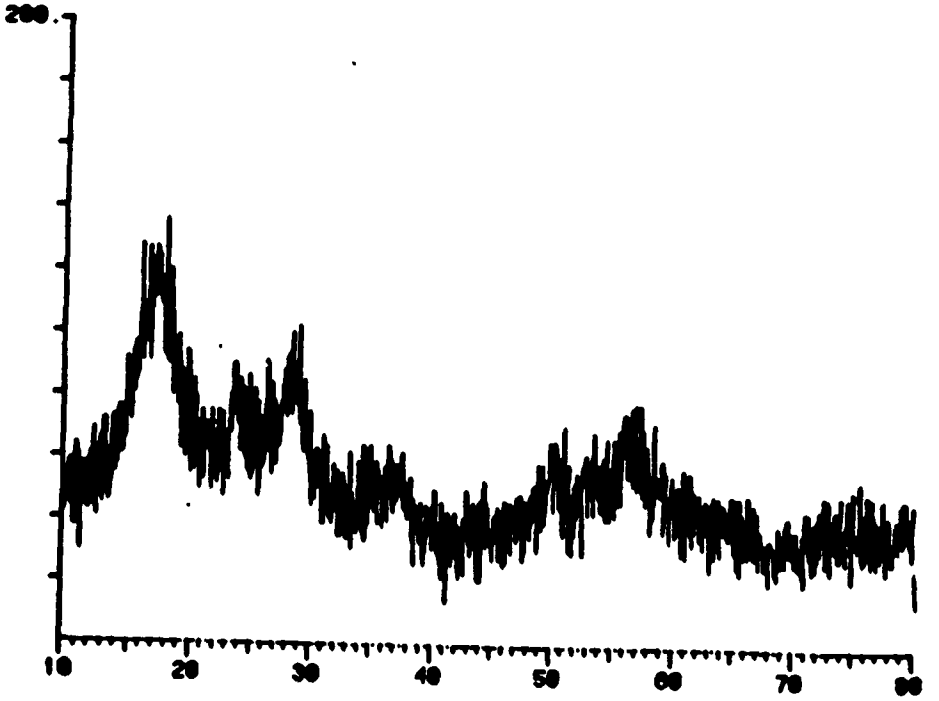

GEL PATTERN

AEROGEL CHARACTERISTICS

1. Reduction kinetics
   - . H_2 flows through
   - . H_2O flows out

2. Connectivity retained

3. Metal Nucleation skeleton

HYDROGEN REDUCTION OF WO_3

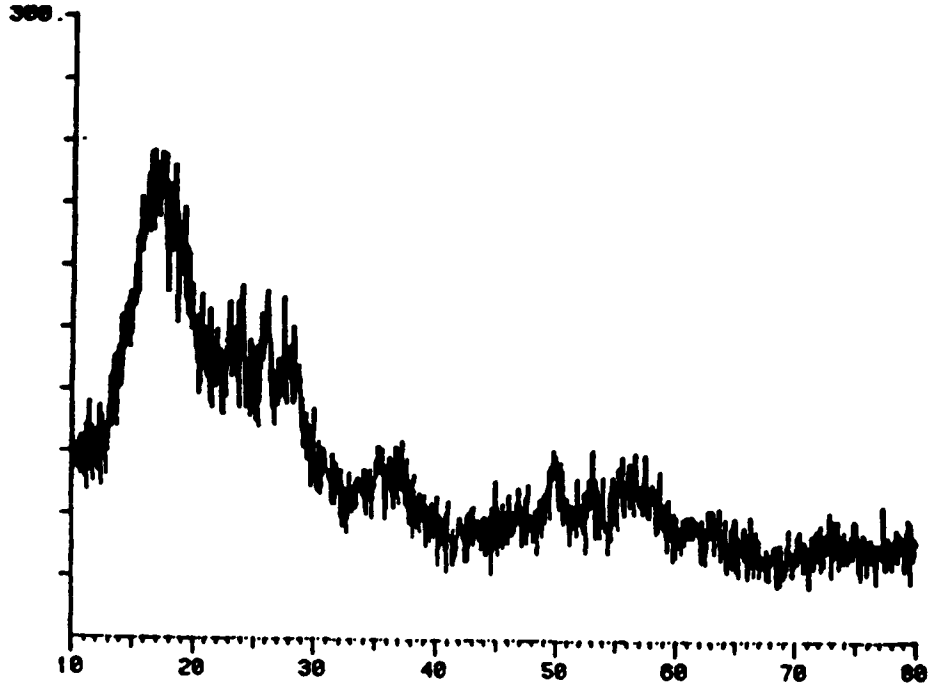

TUNGSTEN

TRIOXIDE

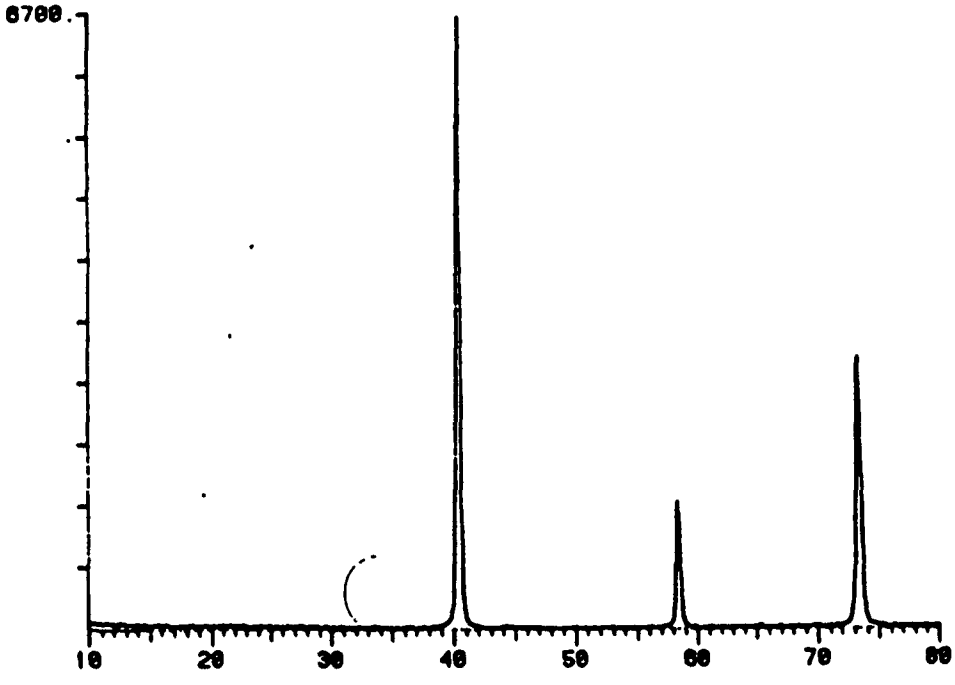

TUNGSTEN -

DRY HYDROGEN

1123K/3600s

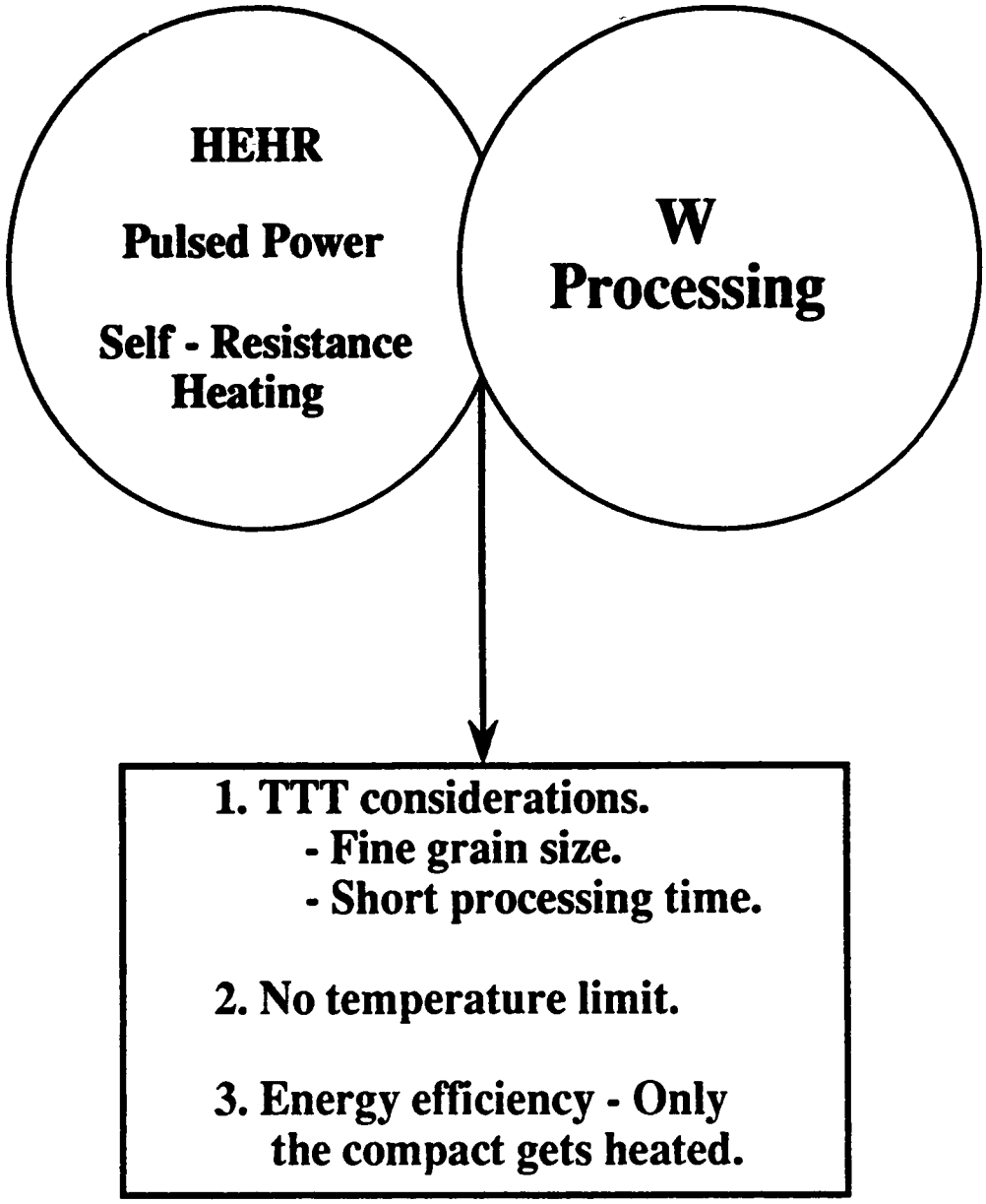
HEHR
Pulsed Power
Self - Resistance Heating
W Processing
1. TTT considerations.
- Fine grain size.
- Short processing time.
2. No temperature limit.
3. Energy efficiency - Only the compact gets heated.

POWDER CONSOLIDATION EXPERIMENTAL EQUIPMENT

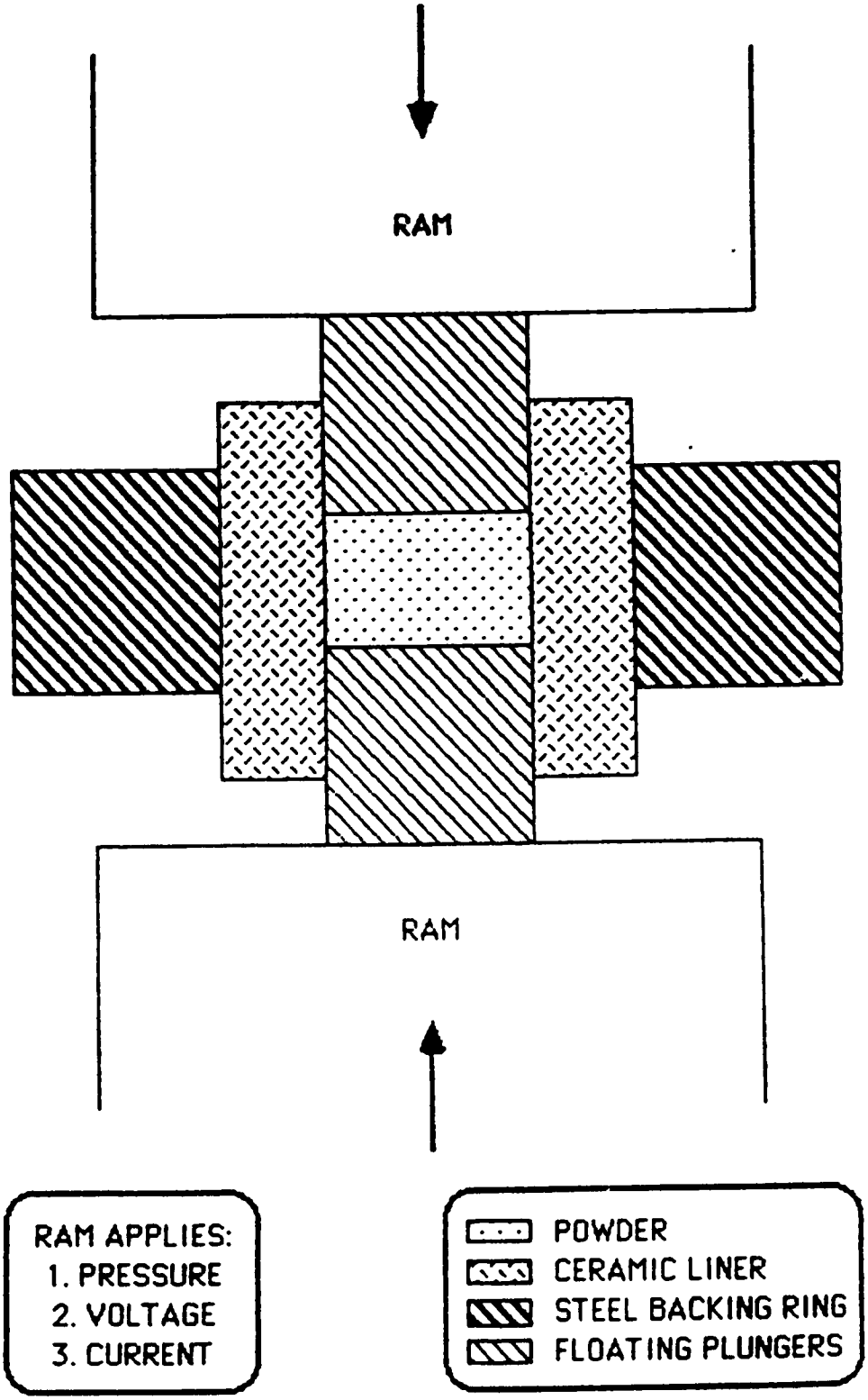

PROCESSING PULSE CHARACTERISTICS

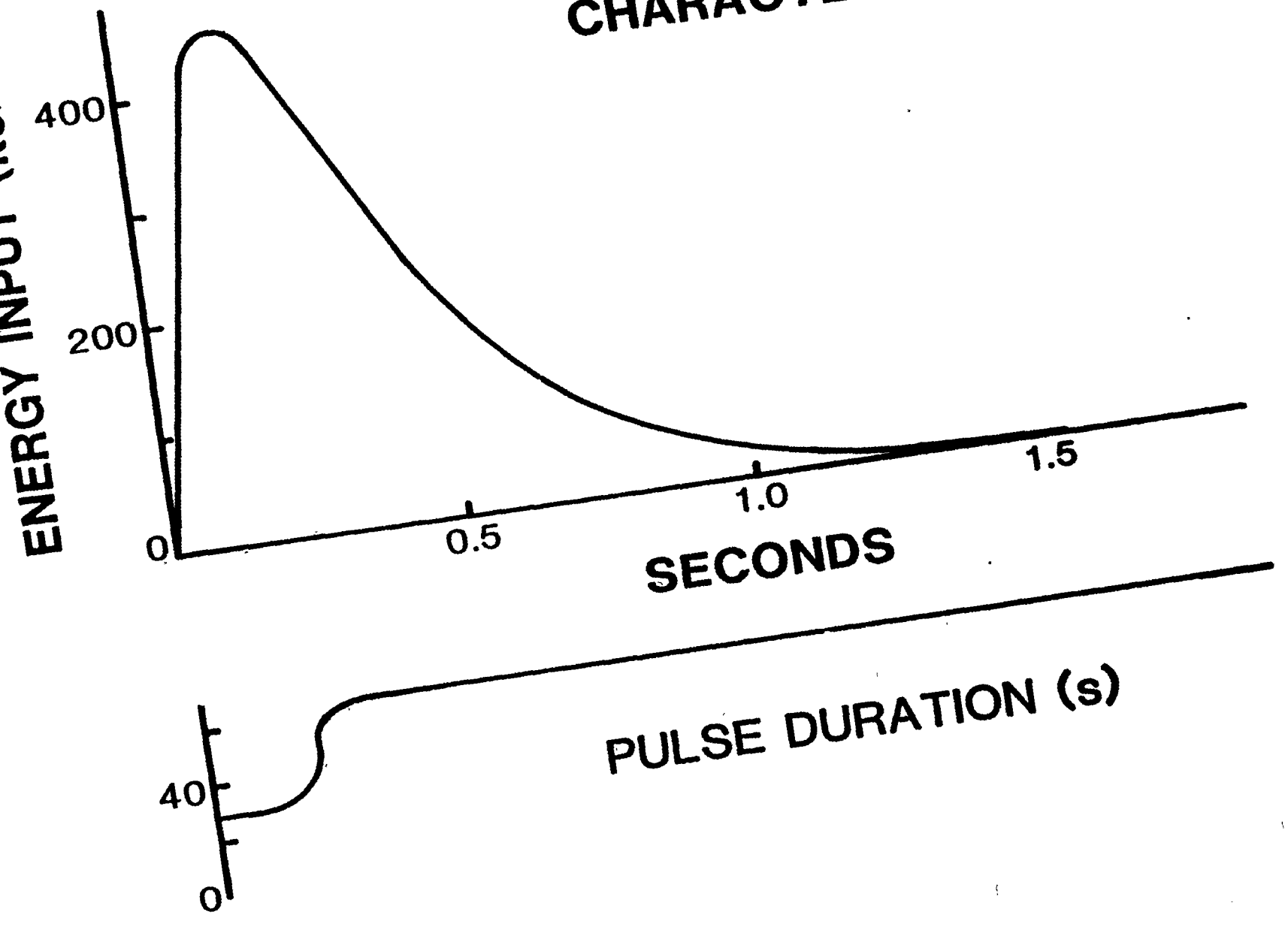

CONSOLIDATED GEL-BASED TUNGSTEN

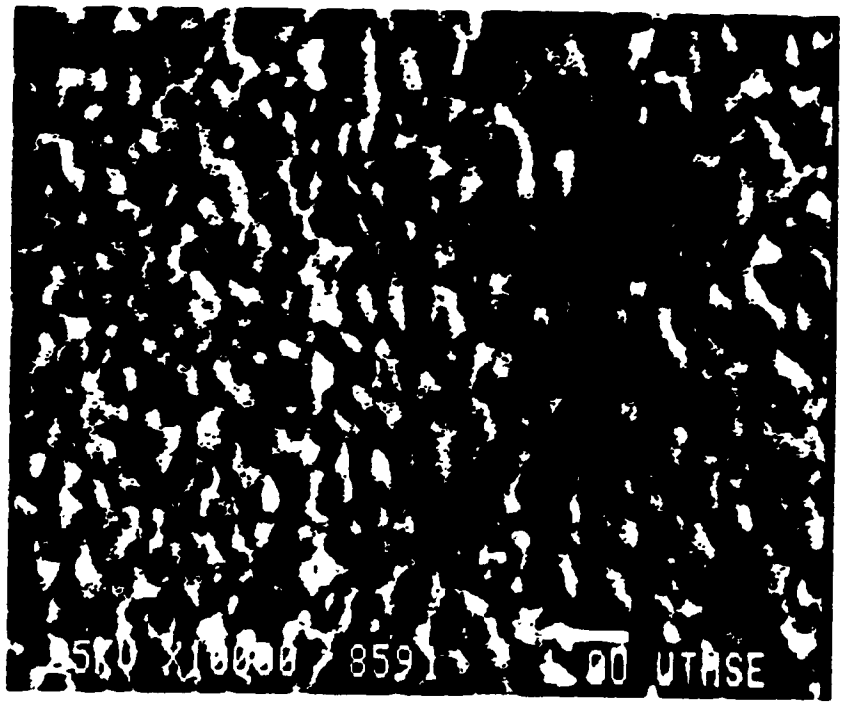

~ 85 % DENSE

TUNGSTEN

STRENGTH VS TEMPERATURE

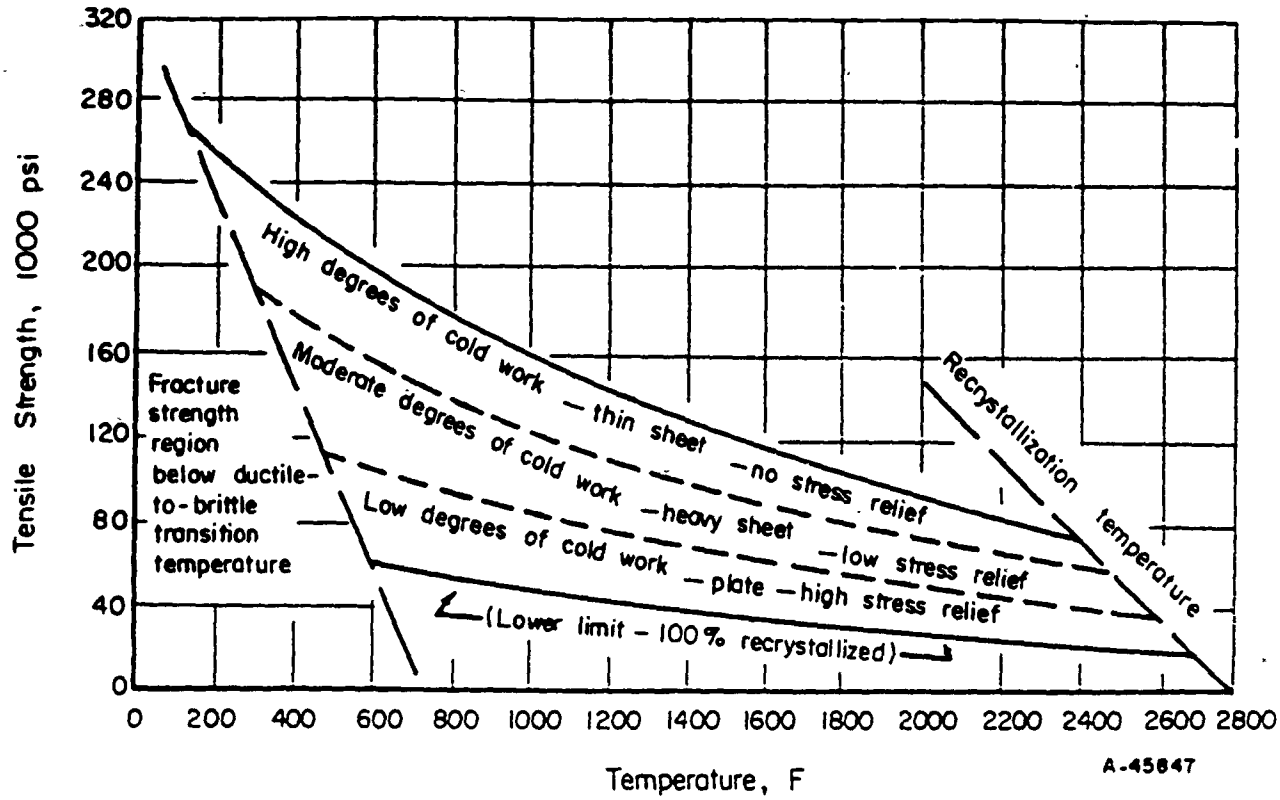

TYPICAL TENSILE-STRENGTH RANGES OF COMMERCIAL-PURITY, POWDER-METALLURGY, TUNGSTEN FLAT-ROLLED PRODUCTS(16)

BATTELLE DMIC REPORT 189,
SEPT. 13, 1963
PP. A40

MICROHARDNESS

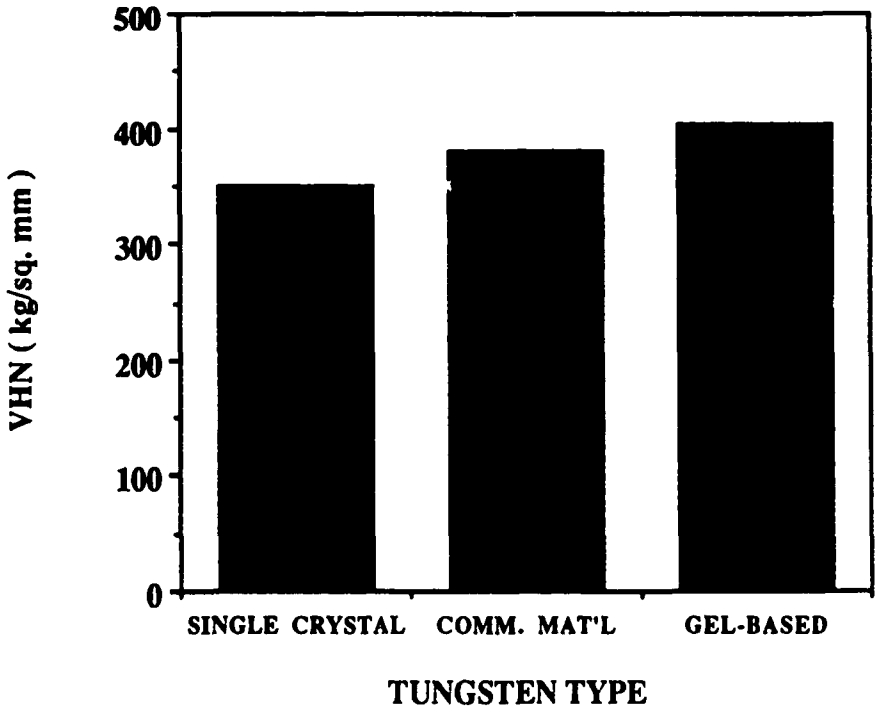

CONSOLIDATED GEL-BASED W

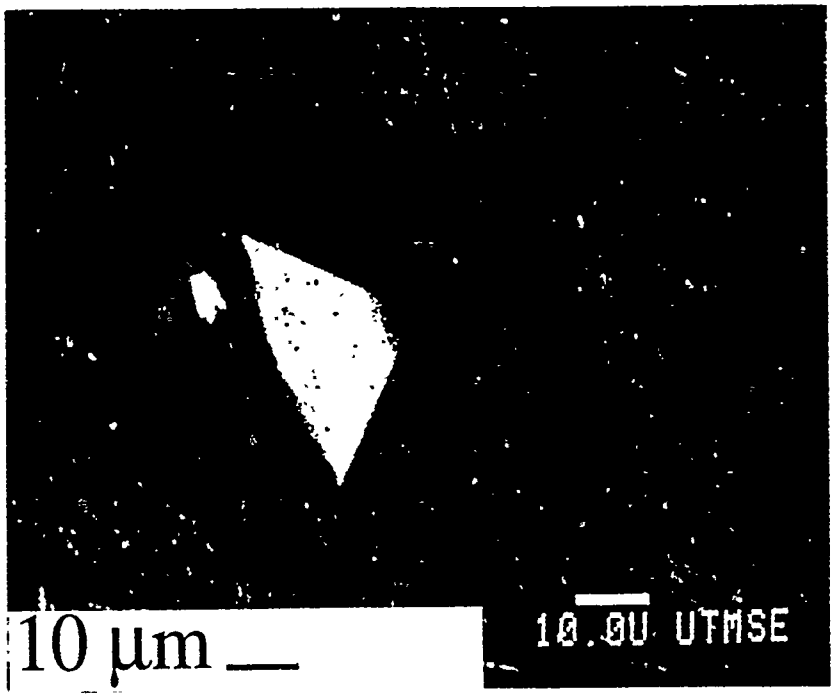

VICKER'S INDENTATION (500g)

CONSOLIDATED GEL-BASED W

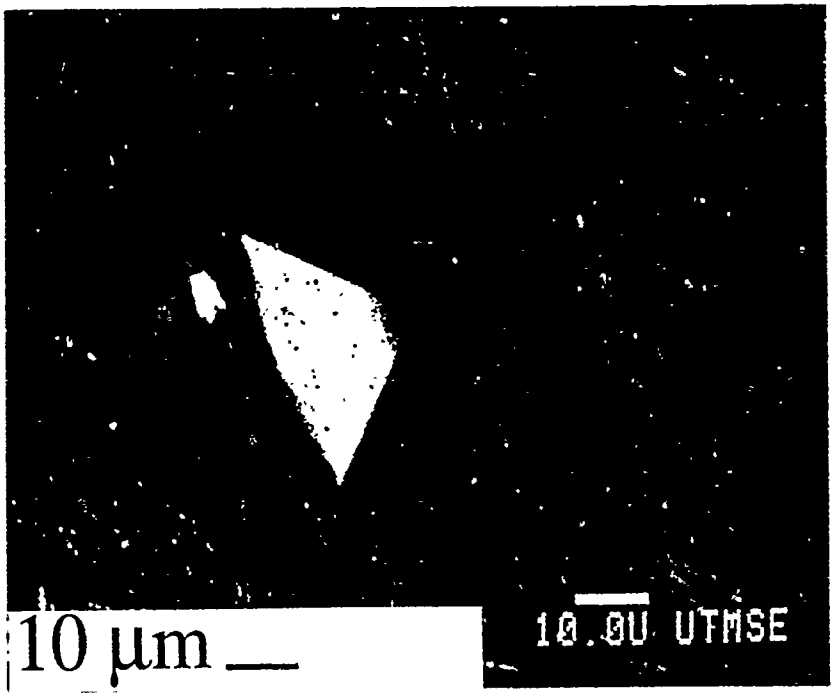

VICKER'S INDENTATION (500g)

TUNGSTEN

HARDNESS VS WORKED STATE

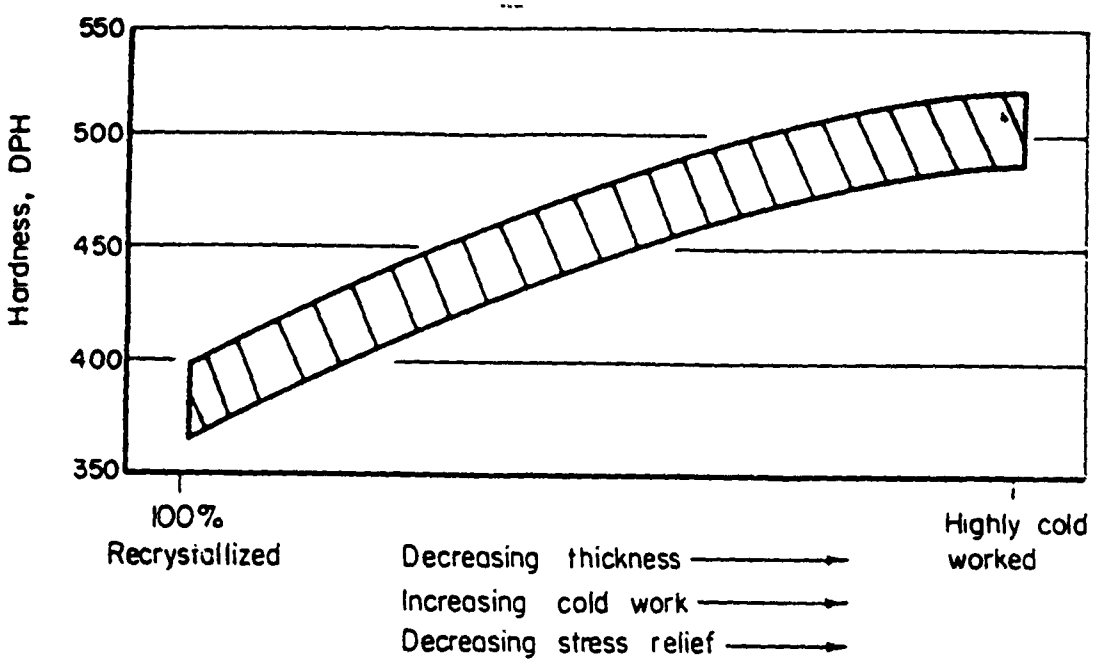

INFLUENCE OF PROCESSING PARAMETERS ON THE HARDNESS OF POWDER-METALLURGY TUNGSTEN FLAT-ROLLED PRODUCTS(16)

BATTELLE DMIC REPORT 189,
SEPT. 13, 1963
PP. A10

SUPERPLASTICITY POTENTIAL

o ultrafine grain sizes
(0.2 to 2 μm)

o grain boundary sliding

o grain growth inhibitors

HIGH SPEED SLIDING CONTACT TYPES

	HIGH SPEED BRUSHES (HPG)	SOLID ARMATURES (EML)
Velocity	> 200 m/s	> 2000 m/s
Current Density	2 kA/cm^2	200 kA/cm^2
Lifetime	1000 Pulses	Single Pulse
Material	Cu-Gr-Sn-Pb Composite	7000 series Aluminum Alloy

INTRODUCTION

APPLICATION OF ELECTRICAL BRUSHES

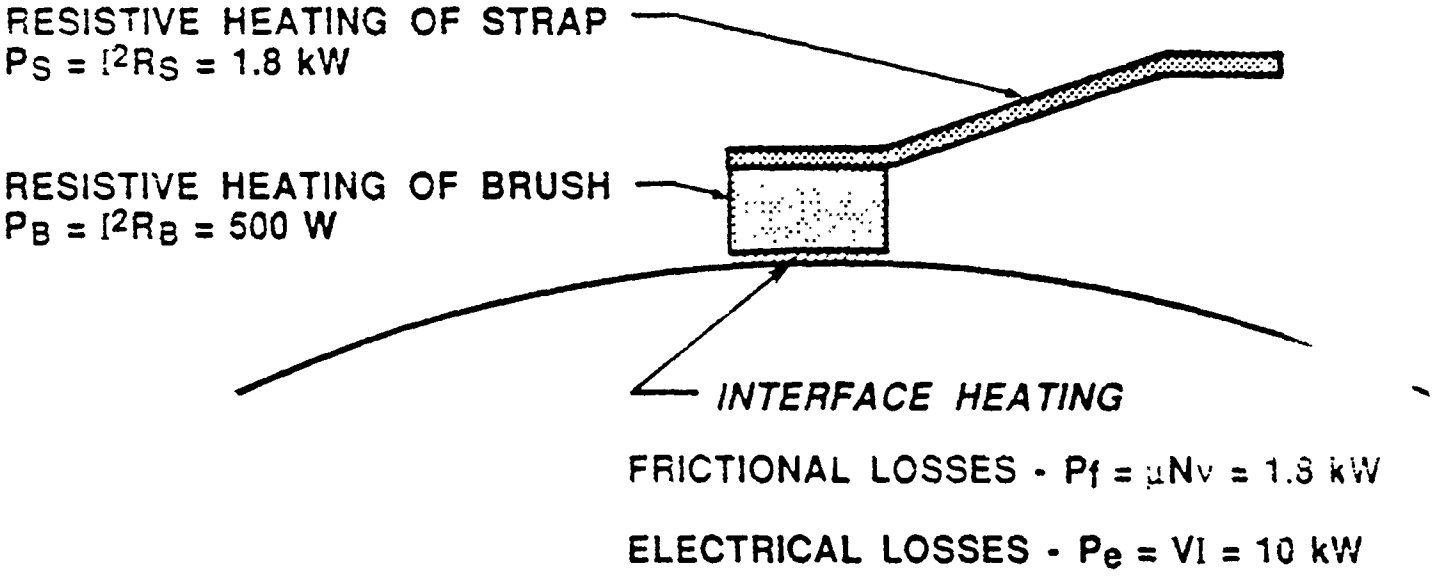

FRICTIONAL LOSSES - $P_f = \mu N v = 1.8$ kW

ELECTRICAL LOSSES - $P_e = VI = 10$ kW

$I = 5$ kA	$V = 2$ V
$v = 200$ m/s	$R_B = 20\ \mu\Omega$
$\mu = 0.2$	$R_S = 72\ \mu\Omega$
$N = 45$ N	

ELECTROMAGNETIC RAILGUN

Electrotribological behavior at > 2 km/s

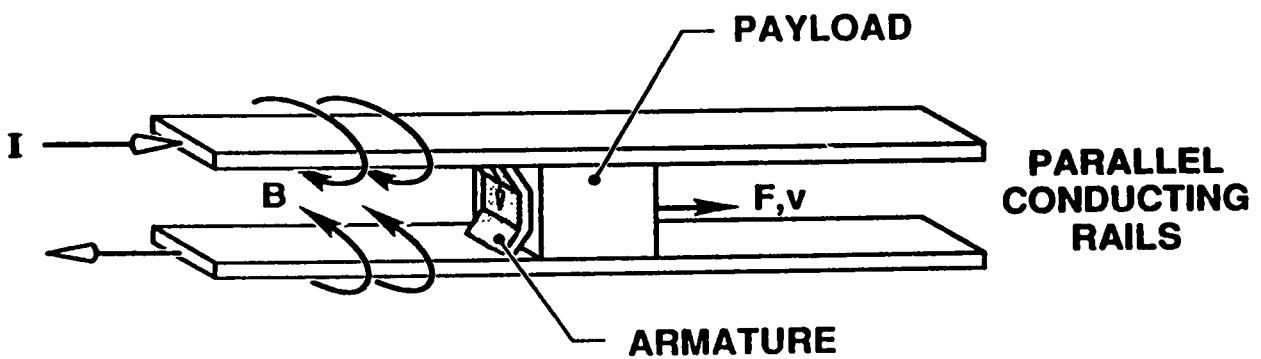

W-CU ELECTRICAL CONTACTS: DENSITY & HARDNESS

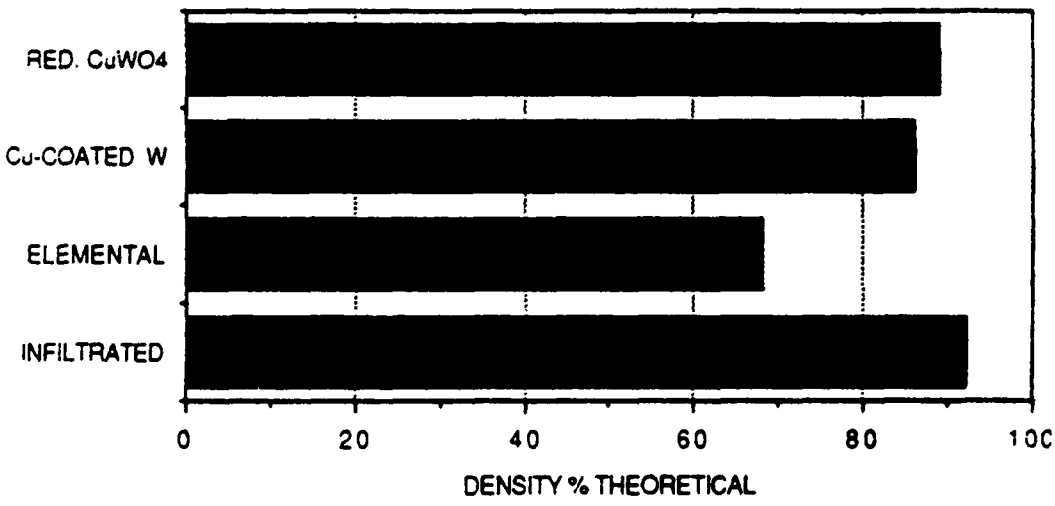

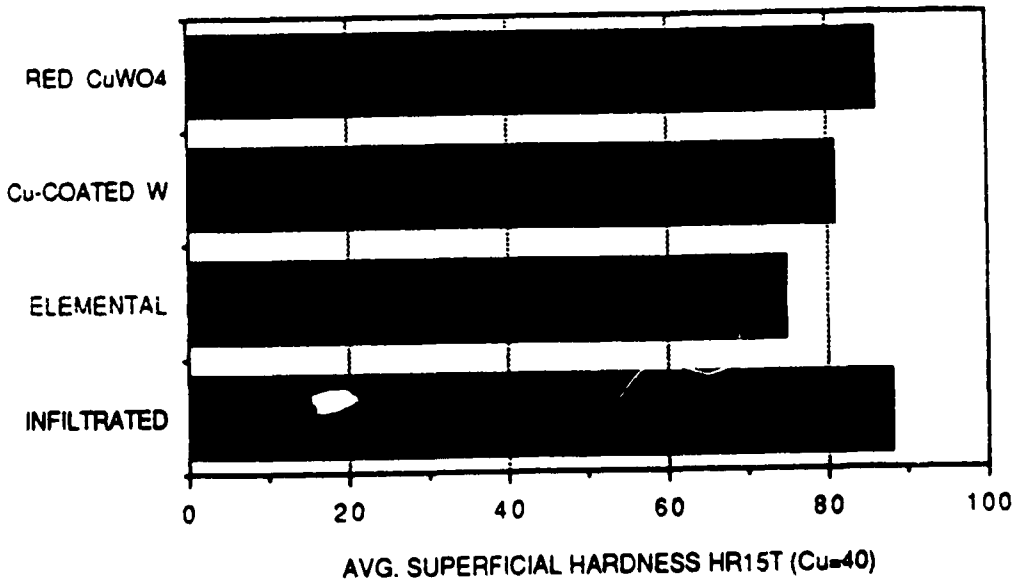

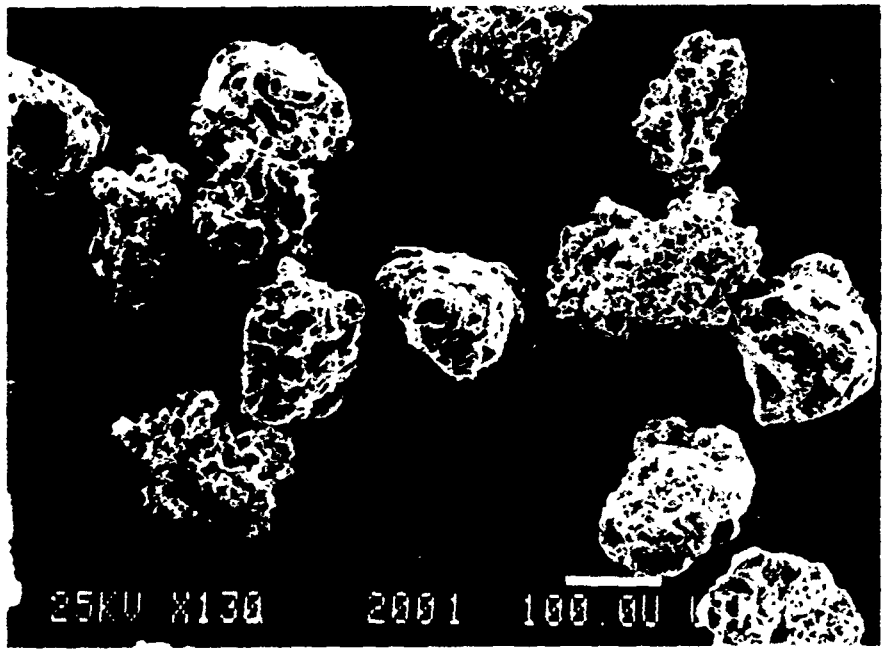

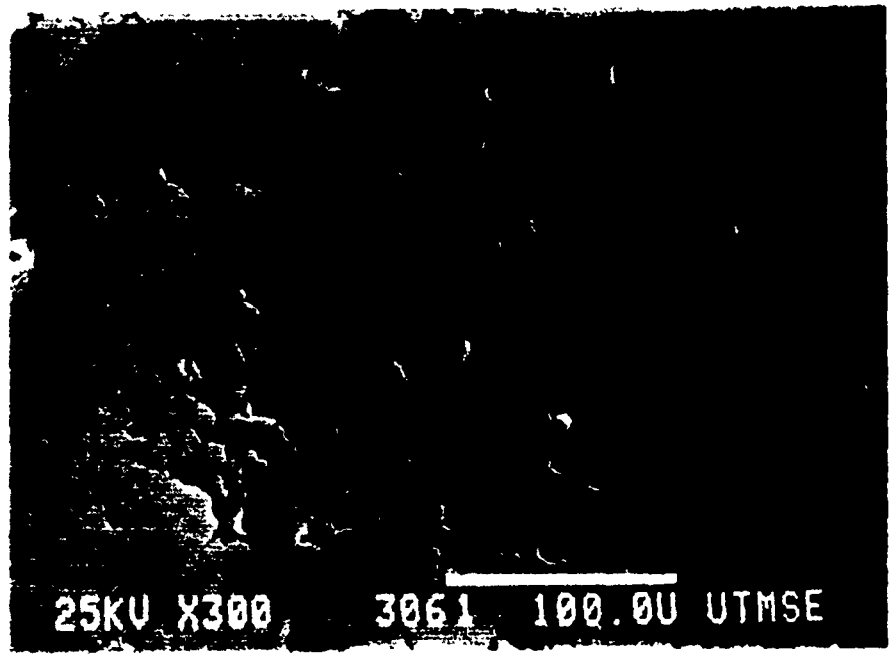

C. Cu-Coated W

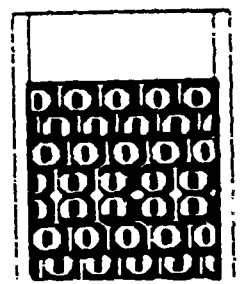

ELECTROTRIBOLOGICAL BEHAVIOR
Cu-COATED TUNGSTEN
(90W/10Cu)

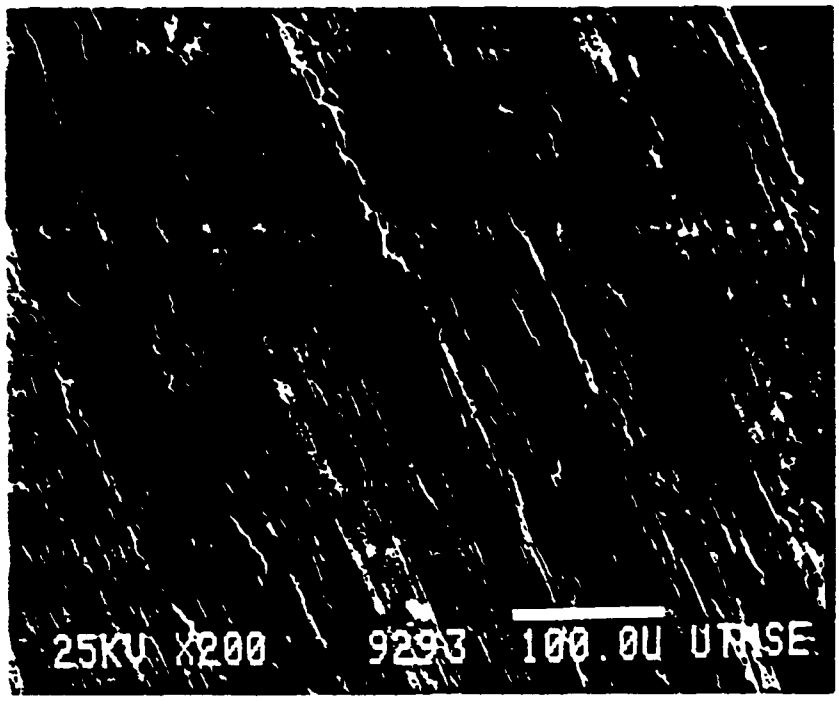

T max. = 560 C.
T avg. = 380 C.

SEM : DIAGONAL WEAR TRACKS
ON SURFACE AFTER HIGH-SPEED TEST.

(IN AIR, UNCOOLED, 100N DOWNFORCE.
RUN FOR 60 s @ 100 m/s WITH ZERO CURRENT,
THEN FOR 30 s @ 100 m/s WITH 1 kA/cm2.)

20 mm x 12.5 mm W-Cu CONTACT
on SMOOTH 4340 STEEL ROTOR.

COPPER-TUNGSTEN PLANAR COMPOSITE

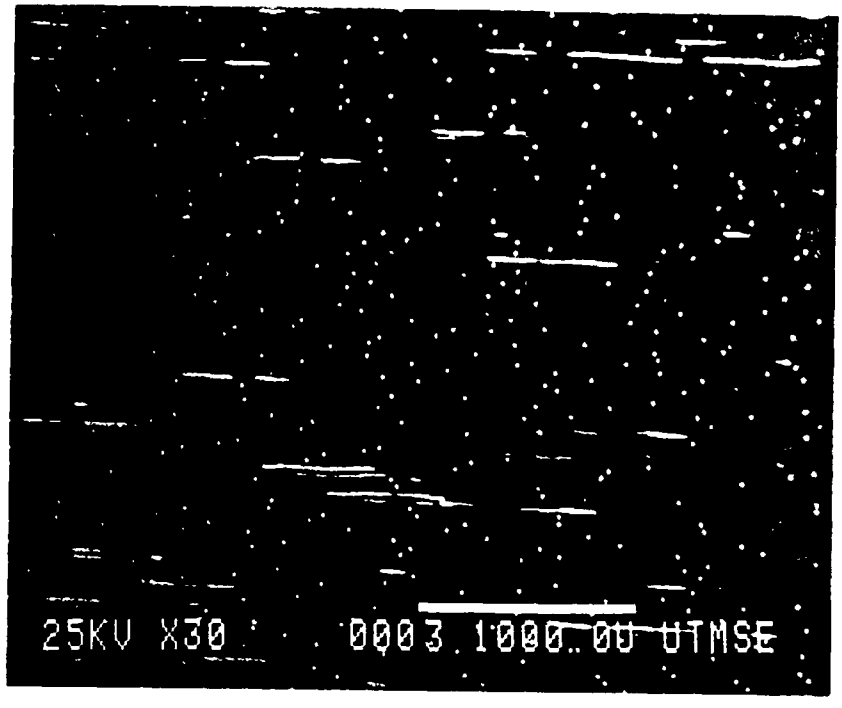

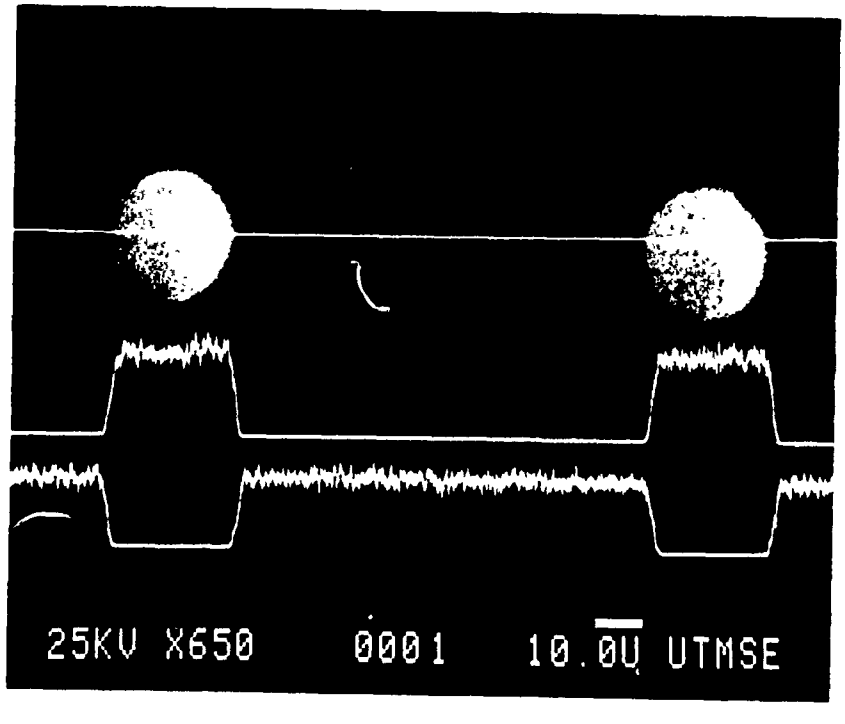

NANOSIZED STRUCTURES FOR ELECTROTRIBOLOGY

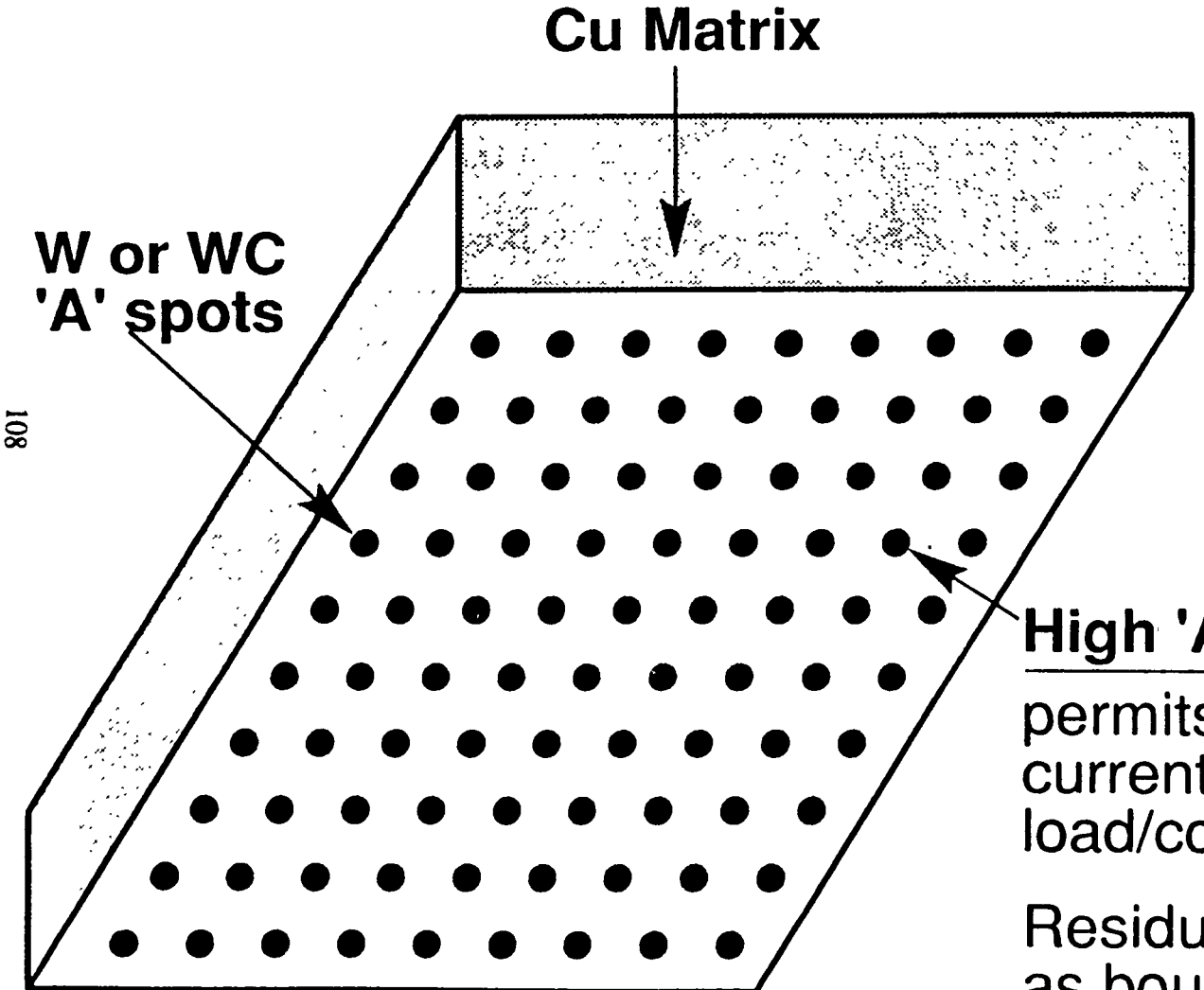

A refractory, nanosized wear-resistant contact layer with a highly conductive bulk substrate should give exceptional electrotribological properties.

High 'A' spot population

permits lower resistance to current flow and decreased load/contact area

Residual graphite acts as boundary lubrication

EXPERIMENTAL PROCEDURE

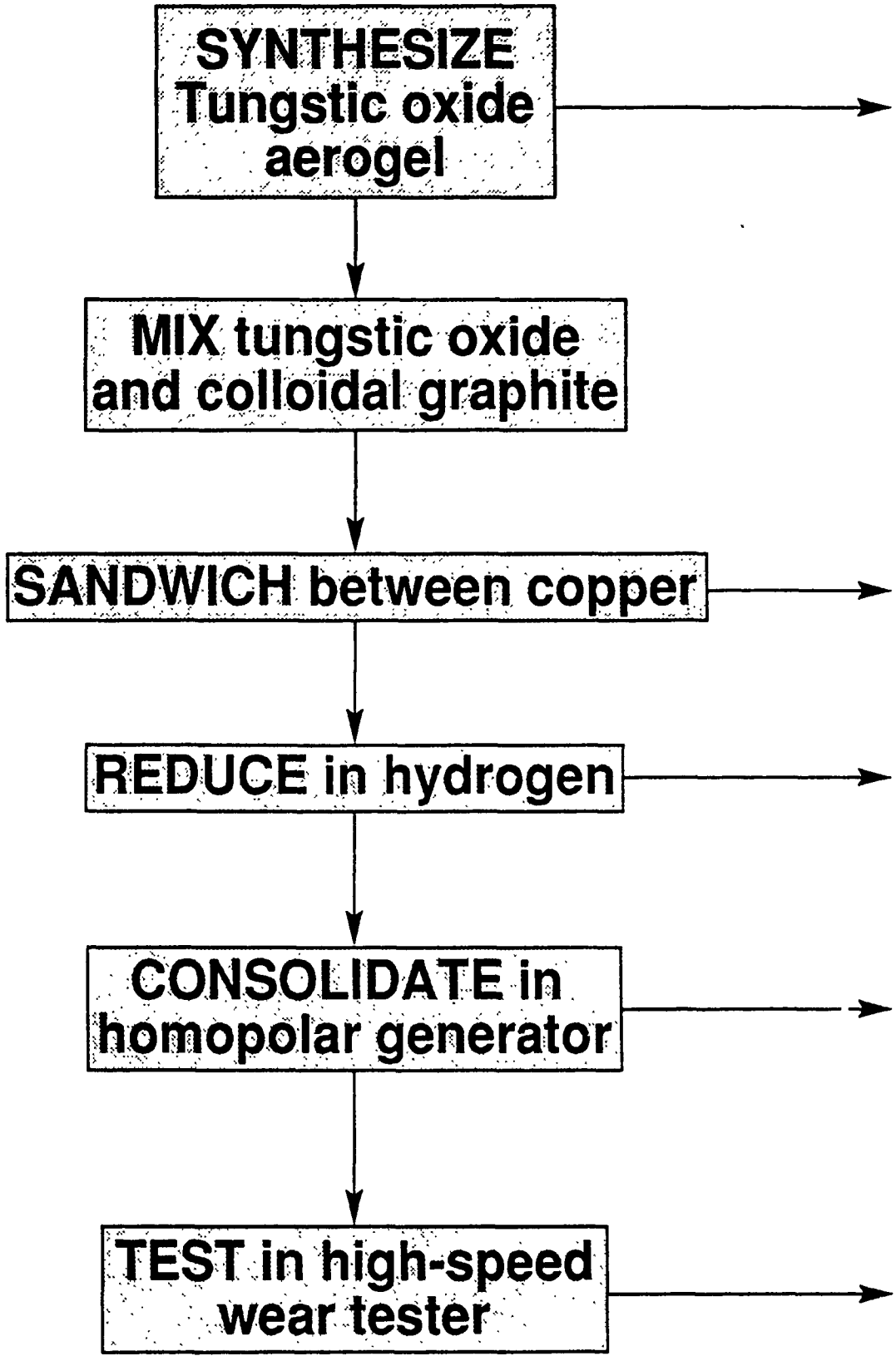

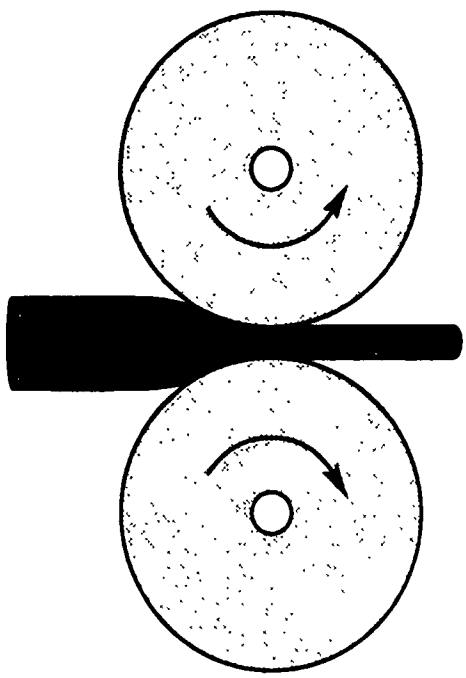

A 1/2 inch copper tube coated on the inside with tungstic oxide/colloidal graphite mixture is rolled to form a sandwich.

CONSOLIDATION SCHEMATIC

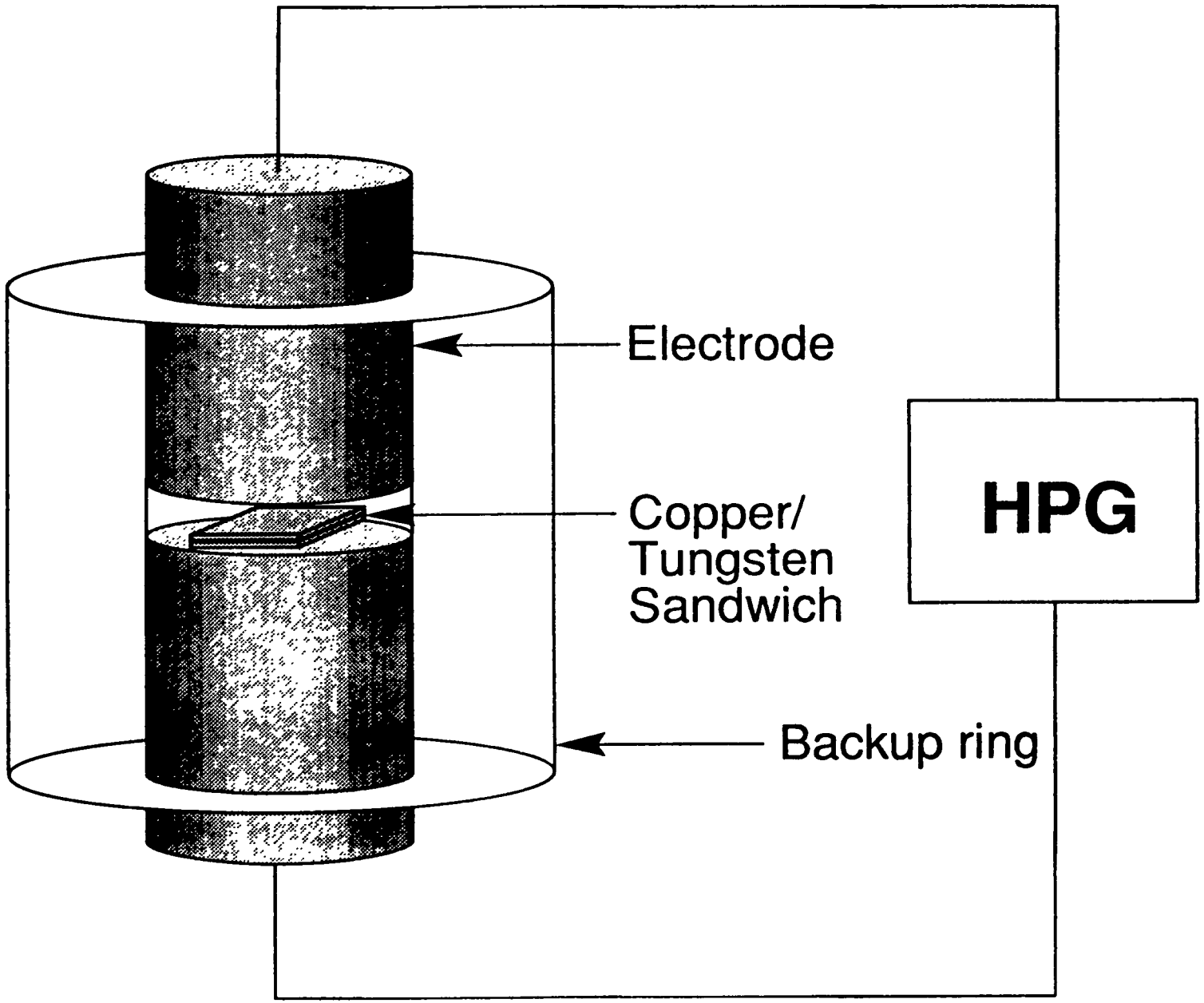

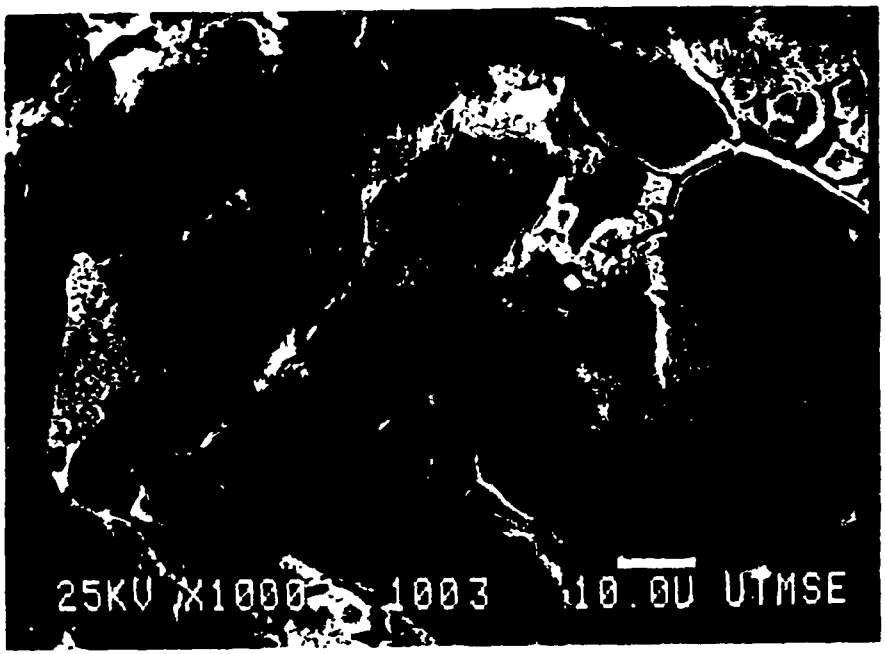

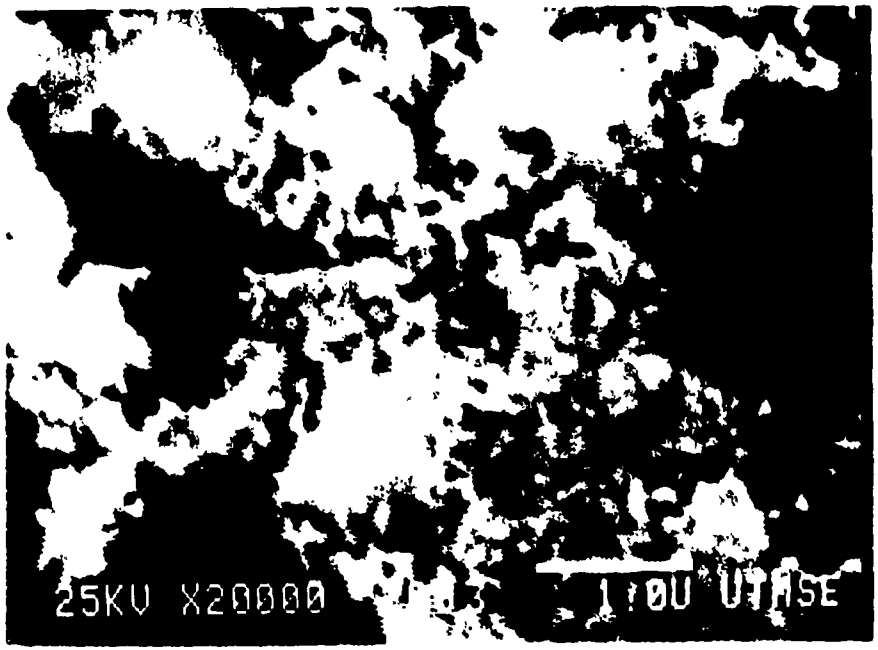

CONSOLIDATED W + C POWDER LAYER EMBEDDED INTO A COPPER SUBSTRATE USING A FAST-RISING, HIGH-CURRENT (95 kA @ 200 ms) PULSE & 280 MPa PRESSURE. SEM PHOTOMICROGRAPHS OF THE SURFACE AFTER CONSOLIDATION SHOWS THE RETENTION OF THE ULTRAFINE STRUCTURE. IN (a) LIGHT PATCHES OF THE GEL-BASED TUNGSTEN ARE CIRCLED IN THE W + C LAYER. IN (b) 100 nm W PARTICLES ARE IMAGED.

W-Ni-Fe/B_4C

AS-RECEIVED

Premixed powder blend

W:Ni:Fe in mass ratio of 93:5:2.

B_4C volume fraction = 8% or 10%.

AFTER CONSOLIDATION

High-density processed composite

by liquid-phase assisted consolidation.

Complex carbides and borides

W_2C , FeWB , W_2B , Fe_3C , Fe_6W_6C , Ni_4B_3

Intermetallic Fe_7W_6

Elemental Fe and Ni fully reacted

Elemental W still dominant phase

New phases not observed in the less-dense

material consolidated completely in the solid state.

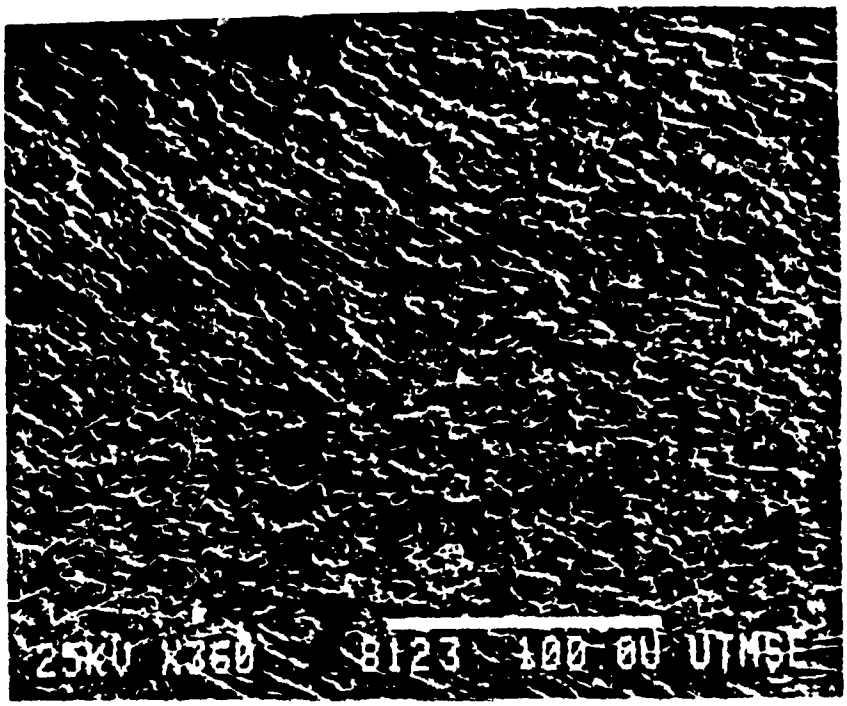

MICROSTRUCTURE OF 93 W-5 NI- 2FE +8 VOL.% B_4C

COMPOSITE (ETCHANT: MURAKAMI'S REAGENT)

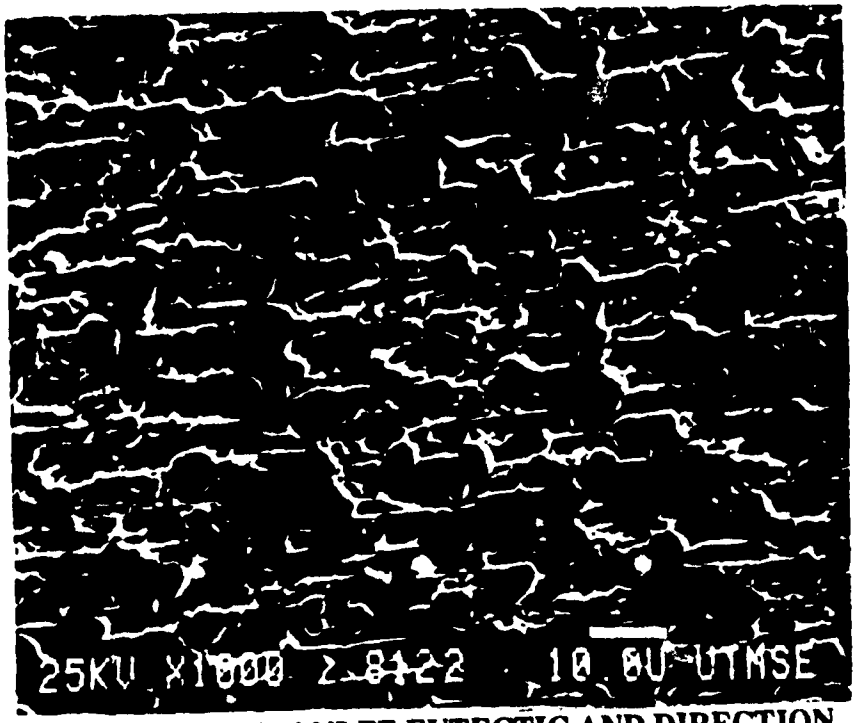

W PARTICLES / W-NI-FE EUTECTIC AND DIRECTION

OF FLOW

SUMMARY

- HEHR PROCESS
- W SYNTHESIS
- PROCESSING
  - > W from gel
  - > W - Cu
  - > W- Mo

APPENDIX C

TITANIUM ALUMINIDE PROCESSING

C-1. High-Energy High-Rate Processing of High-Temperature Metal-Matrix Composites

C-2. Microstructure/ Processing Relationaships in High-Energy High-Rate Consolidated Powder Composites of Ti_3Al + TiAl

C-3. Matrix-Reinforcement Interface Characteristics of (Ti_3Al + Nb)-Based Powder Composites, Consolidated by High-Energy High-Rate Processing

HIGH-ENERGY HIGH-RATE PROCESSING OF HIGH-TEMPERATURE METAL-MATRIX COMPOSITES

C. Persad, S. Raghunathan, B.-H. Lee, D.L. Bourell, Z. Eliezer and H.L. Marcus

Center for Materials Science and Engineering
The University of Texas at Austin,
Austin, Texas 78712.

ABSTRACT

Advances in kinetic energy storage devices have opened up a new approach to powder processing of High Temperature Composites. The processing consists of internal heating of a customized powder blend by a fast electrical discharge of a homopolar generator. The high-energy high-rate "1MJ in 1s" pulse permits rapid heating of a conducting powder in a cold wall die. This short time at temperature approach offers the opportunity to control phase transformations and the degree of microstructural coarsening not readily possible using standard powder processing approaches. This paper will describe the consolidation results of two high temperature composite materials, (W-Ni-Fe)/B_4C and (Ti_3Al+Nb)/SiC. The focus of this study was the identification of the reaction products formed at the matrix/reinforcement interface as a function of input energy and applied stress. Input energies beyond a threshold value for each system were required to produce detectable reaction products. In the (W-Ni-Fe)/B_4C system, the reaction products formed at 4000 kJ/kg input energy under 420 MPa applied stress were a series of complex carbides and borides including W_2C, FeWB, Fe_3C, Fe_6W_6C and Ni_4B_3. The intermetallic Fe_7W_6 was also observed. In the (Ti_3Al+Nb)/SiC system, the reaction products observed at 3400 kJ/kg and 210 MPa were TiC and $TiSi_2$.

INTRODUCTION

The new (Ti_3Al + Nb) - based matrices reinforced with silicon carbide represent a class of high temperature metal matrix composites (MMC) with attractive specific modulus and potential for high temperature service. It has been shown that the (Ti_3Al + Nb) /SiC composites have significantly higher strength/density values over the wrought superalloys in the 560K to 1400K temperature range [1]. These materials are expected to find application in the next generation of high performance aircraft and turbines. The Ti-6Al-4V/SiC MMC shows reduced tensile strength after high temperature exposure. This reduction in strength has been correlated with the formation and growth of deleterious reaction products at the matrix-reinforcement interface [2]. It has been suggested that lowering of the consolidation temperature will result in a reduced amount of reaction product [3]. Similar reaction products may be responsible for the 3 μm thick reacted layer observed in the hot-pressed (Ti_3Al + Nb)/ SiC composites observed by Brindley [1].

A completely different group of high temperature applications utilizing high hot hardness are anticipated for the cobalt-free substitutes for WC + Co composites. The B_4C -reinforced W-Ni-Fe composites are a prototypical system [4,5]. The hot hardness of the 2.5 B_4C - 97.5 W-Ni-Fe [95.0 W - 3.5 Ni - 1.5 Fe] is 10 to 20% higher than the premium grade of WC + Co at 1073K. When produced by hot pressing at 1733K, the B_4C is fully reacted and phases with a variety of chemistries are produced. These include graphite, tungsten carbide, and

Mat. Res. Soc. Symp. Proc. Vol. 120 1988 Materials Research Society

Fe-Ni and W-B-C phases. Further analysis revealed the onset of the series of reactions to be at 1173K [4].

For both these systems an alternative approach to control of the reaction zone is by limiting the duration of the high temperature exposure during processing. This is the thrust of the high-energy high-rate consolidation processing approach applied to these materials systems and described in this paper.

EXPERIMENTAL PROCEDURE

Materials

$(Ti_3Al + Nb)/SiC$

The "Alpha 2" titanium aluminide intermetallic was supplied in powder form by United Technologies Pratt and Whitney Division , FL. These Nb-stabilized compositions were RS processed and were classified to - 80 mesh (< 177 μm).The as-received phase structure of the Alpha 2 composition was determined by XRD and consisted of the Nb-stabilized $\beta + \beta_2$ (bcc structure with B2 ordering).

The SiC particulate was supplied by the Superior Graphite Corp , Grade HSC-ROF95. These +325 mesh (> 44 μm) ß-SiC particulates were deliberately supplied with a graphite-enriched surface layer to enhance local electrical conductivity. This layer extends 1-10 μm below the surface, depending upon particle size (6). The mass of SiC was 20 percent of the total composite mass, corresponding to a volume fraction of 30 %.

$W\text{-}Ni\text{-}Fe/B_4C$

The tungsten-based composite was supplied as a premixed powder blend by Los Alamos National Laboratories, NM. The metallic matrix elemental powders W:Ni:Fe were mixed in a mass ratio of 93:5:2. The mass of B_4C was 1.3 or 1.65 percent of the total composite mass, corresponding to a volume fraction of 8% or 10%. Detailed characteristics of such powder blends have been reported previously by Sheinberg [5].

Processing

Advances in kinetic energy storage devices have opened up a new approach to powder processing of High Temperature Composites. The processing consists of internal heating of a customized powder blend by a fast electrical discharge of a homopolar generator. The high-energy high-rate "1MJ in 1s" pulse permits rapid heating of a conducting powder in a cold wall die. This short time at temperature approach offers the opportunity to control phase transformations and the degree of microstructural coarsening not readily possible using standard powder processing approaches.

The underlying fundamental approaches to high-energy high-rate processing have been described elsewhere [7]. The general details of the experimental apparatus and the pulse characteristics have also been reported[8], and the technique has been employed in the processing of Al-SiC composites [6,9]. In this study, 50g quantities of each of the composite powder blends were loaded into insulated die cavities between copper electrodes. Pressures between 210 and 420 MPa were applied, and the compact was rapidly heated by a homopolar generator pulse discharge. Disks with diameters of 30 mm or 50 mm were produced. Specific energy inputs ranged from 2000 kJ/kg to 7000 kJ/kg.

Microstructure Evaluation

Standard metallographic procedures were employed in the preparation of radial cross sections of each of the consolidated composite materials. The Ti_3Al/SiC required the use of water-jet machining. Vickers microhardness measurements were performed at room temperature to determine the degree of structural homogeneity and to aid in the detection of the reaction zones.

For the (Ti_3Al + Nb)/SiC system, heat treatments of 24h to 96h at 1473K were used to follow the growth of the reaction zone. Unetched and etched cross-sections were examined in an optical microscope fitted with a Nomarski interference contrast system. This permits the polishing relief developed due to phases of different hardnesses to become readily apparent in color micrographs[10]. From such micrographs, average zone width measurements corresponding to each heat treatment were made. These measurements are not absolute values since they are uncorrected for magnification due to random angle sectioning.

X-ray diffraction analyses were performed on a Phillips diffractometer fitted with a Cu tube and a graphite monochromator. The powder samples were held onto a glass slide with double-sided adhesive tape. Sufficient powder was used so that no signal was detected from the glass slide. A JEOL 35M SEM with EDS and WDS capability was employed to verify the chemical discontinuities associated with the formation of reaction products at the matrix-reinforcement interface.

RESULTS AND DISCUSSION

Consolidation Parameters

The processing parameters used for these initial consolidation experiments on each of these composite systems were derived from parameter sets previously developed for the unreinforced matrix materials. The inherent assumption is that beyond a set low electrical conductivity threshold, the pulse resistive heating under pressure would provide rapid densification. The most identifiable solid state densification mechanism is powder forging. Densities greater than 95% of the calculated theoretical values were obtained. The parameters for the (Ti_3Al + Nb)/SiC system were: Applied Pressure = 30 ksi (210 MPa), Specific energy input: 2000 to 4000 kJ/kg. For the W-Ni-Fe/B_4C system they were: Applied Pressure = 45 - 60 ksi (315 - 420 MPa), Specific energy input: 3000 to 7000 kJ/kg.

Microstructure and Chemistry

Figures 1 and 2 provide typical overviews of the rapidly densified microstructures developed in the W-Ni-Fe/B_4C system and the (Ti_3Al + Nb)/SiC system respectively. The metal matrices are well consolidated, and excellent geometric conformability to the darker reinforcing phases is evident in both systems. The reinforcement appears well dispersed.

(Ti_3Al + Nb)/SiC

In Figure 2 from the (Ti_3Al + Nb)/SiC , which was heavily etched in HCl, preferential chemical attack occured at the SiC/matrix interface where a reaction zone was observed. Consolidation appears to have occured in the solid state with the energy input of 3200 kJ/kg under 210 MPa applied pressure. XRD analyses of the phases present in the processed composite reveal the likely reaction products to be TiC and $TiSi_2$. The $TiSi_2$ phase appears to be associated with the regions where localized matrix melting at higher specific energy inputs has occured. The $TiSi_2$ was not observed in the lower energy consolidations.

Phases with corresponding chemistries could be identified in the vicinity of interfaces by EDS in the SEM as shown in Figure 3.The diagonal interface separates a SiC particle (lower half of photo) from the matrix. The light-colored islands on the SiC particle surface are rich in Ti

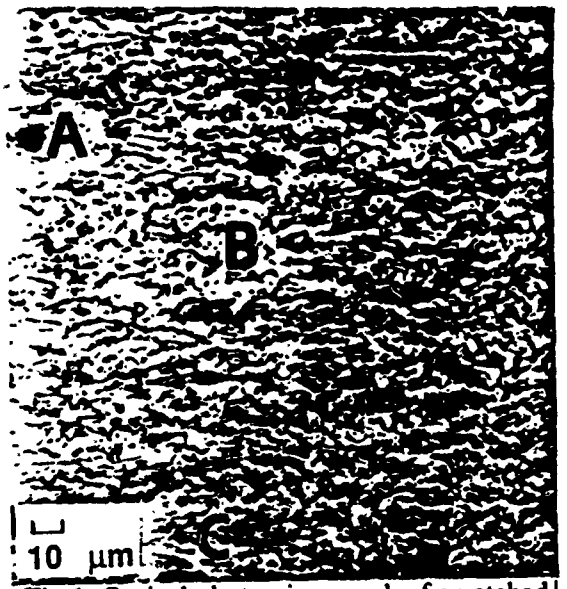

Fig.1. Optical photomicrograph of an etched radial cross-section of a (W-Ni-Fe)/B_4C composite specimen produced with an energy input of 4000 kJ/kg under 420 MPa applied pressure. The macroscopic features are A-B_4C, B-W, and C-W-Ni-Fe eutectic.

Fig.2. SEM photomicrograph of a heavily etched radial cross-section of a (Ti_3Al+Nb)/SiC composite specimen produced with an energy input of 3200 kJ/kg under 210 MPa applied pressure. Tight microencapsulation of the SiC particles is evident.

Fig.3. SEM photomicrograph of an unetched radial cross-section of a (Ti_3Al+Nb)/SiC composite specimen in which localized melting has occured. The region above the diagonal interface is the matrix with dark TiC reaction products. The lower section is a SiC particle on which islands rich in Ti and Si appear as light-colored areas.

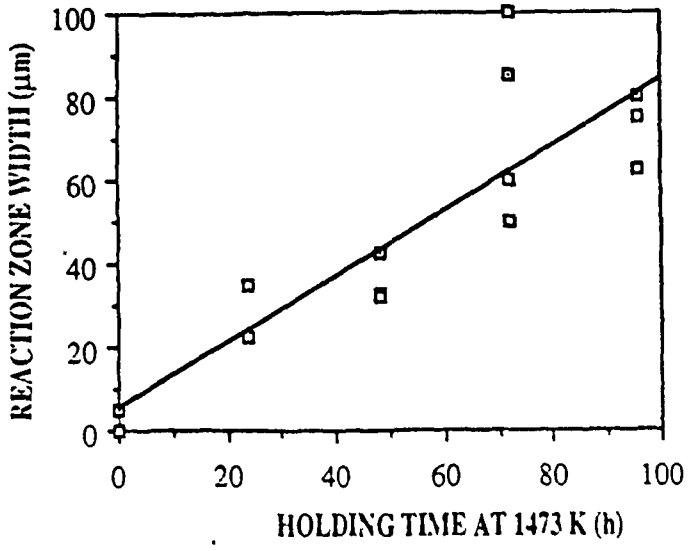

Fig. 4. Average apparent interface reaction zone width measurements corresponding to heat treatments of a (Ti_3Al + Nb)/SiC composite for 24h to 96h at 1473K. These measurements are not absolute values.They are uncorrected for magnification due to random angle sectioning.

and Si and have very little carbon, consistent with the XRD observation of $TiSi_2$. EDS analysis of the dark phases visible above the diagonal interface show these to be TiC.

The multiphase reaction zones were grown by heat treatments at 1473K for 24 to 96h.The apparent width of the reacted layer measured from a series of etched cross-sections is plotted in Figure 4. Additional unidentified phases were produced during these heat treatments. TEM investigations of the phases present are currently underway.

(W-Ni-Fe)/B_4C

In Figure 1, the apparent orientation of the W-Ni-Fe matrix is attributed to flow of the material under pressure during the transient liquid-phase-assisted consolidation. The three microscopic features observed are the B_4C, W and the W-Ni-Fe eutectic.

XRD analyses of the phases present in the high-density processed composite reveal the reaction products to be a series of complex carbides and borides,when sufficient energy is delivered to induce liquid-phase assisted consolidation. The lines indexable in a 10 to 80 degree two-theta scan for the W-Ni-Fe/B_4C system after liquid-phase assisted consolidation includes W (110),(200),(211), W_2C (021),(002),(121),(102),(321),(302), FeWB (001),(112), W_2B(110),(002),(200),(211), Fe_3C (101), Fe_6W_6C (660),(822) and Ni_4B_3(211),(410),(403),(013). The intermetallic Fe_7W_6 (119)was also observed. The elemental Fe and Ni were fully reacted. These phases were not observed in the material consolidated completely in the solid state, where the maximum applied pressure of 420 MPa was insufficient to produce full densification.

Several of the carbide forming reactions are highly exothermic, and once triggered, these reactions occurring at multiple and distributed interface nodes can be expected to maintain the high temperature developed in the early stages of the processing. Indeed this processing cycle then takes on characteristics similar to those observed in Self-Propagating High-Temperature Synthesis of ceramic phases [11]. The reaction products so derived effectively transform the nature of the composite material introducing the attributes of the in-situ composites, in which the reinforcing phases are produced during processing.

As a clearer understanding develops of the complex physical metallurgy of the high-temperature matrix materials, in particular the new RSP aluminides, alternative approaches to the selection of reinforcement phases become crucial. Some guidelines for such approaches have been discussed by Fine et al [12], and are being applied to our continued effort in high-temperature metal matrix composites.

ACKNOWLEDGMENT

We thank Ralph Anderson and Sandy Shuleshko of Pratt and Whitney, Read Stewart of Superior Graphite, and Haskell Sheinberg of Los Alamos National Laboratories who provided the powders. Assistance with processing was provided by Ted Aanstoos and Jim Allen at CEM-UT. Mike Schmerling, H. Tello, H.-G. Chun, C.J. Lund, and Ming-Jy Wang assisted in the structure evaluation. This research was supported by DARPA/ARO Contract DAAL03-87-K-0073.

REFERENCES

1. P. K. Brindley in High-Temperature Ordered Intermetallic Alloys II, edited by N. S. Stoloff, C. C. Koch, C. T. Liu, and O. Izumi (Mater Res. Soc. Proc. 81,Pittsburgh, PA 1987) pp. 419 - 424.

2. A. G. Metcalfe in Interfaces in Metal Matrix Composites, Volume 1, A. G. Metcalf (ed.),(Academic Press, New York, NY, 1974) pp. 67-123.

3. C. G. Rhodes, A. K. Ghosh, and R. A. Spurling, Metallurgical Transactions A, Volume 18A, Dec. 1987, pp. 2151-2126.

4. H. Sheinberg, Int. J. of Refractory and Hard Metals, March 1983, pp.17 - 26.

5. H. Sheinberg, Int. J. of Refractory and Hard Metals, December 1986, pp. 230 - 237.

6. G. Elkabir, PhD Dissertation, The University of Texas at Austin, August 1987.

7. H. L. Marcus, D. L. Bourell, Z. Eliezer , C. Persad and W. F. Weldon, Journal of Metals, December 1987, pp. 6-10.

8. G. Elkabir , L. K. Rabenberg, C. Persad and H. L. Marcus, Scripta Metallurgica, 20 (10),1986 pp. 1411-1416.

9. H. L. Marcus, L. K. Rabenberg, L. D. Brown, G. Elkabir, and Y. M. Cheong, in ICCM VI/ECCM 2-Composite Materials, eds. F. L. Matthews, N. C. R. Buskell, J. M. Hodgkinson and J. Morton (Elsevier Applied Science, London, 1987) p. 2.459.

10. C.E. Price in Metals Handbook, 9th edition, V. 9, Metallography and Microstructures (ASM, Metals Park, OH, 1985) p. 151.

11. J. B. Holt and D. D. Kingman in Emergent Process Methods for High-Technology Ceramics, eds.R. F.Davis, H. Palmour III, and R. L. Porter (Plenum Press, New York, NY, 1984) p. 167.

12. M. E. Fine, D. L. Bourell, Z. Eliezer , C. Persad, and H. L. Marcus , submitted to Scripta Met., March 1988.

MICROSTRUCTURE/PROCESSING RELATIONSHIPS IN HIGH-ENERGY HIGH-RATE CONSOLIDATED POWDER COMPOSITES OF Nb-STABILIZED Ti_3Al + TiAl

C. Persad, B.-H. Lee, C.-J. Hou, Z. Eliezer and H.L. Marcus,
Center for Materials Science and Engineering,
The University of Texas at Austin, Austin, Texas 78712.

ABSTRACT

A new approach to powder processing is employed in forming titanium aluminide composites. The processing consists of internal heating of a customized powder blend by a fast electrical discharge of a homopolar generator. The high-energy high-rate "1MJ in 1s" pulse permits rapid heating of an electrically conducting powder mixture in a cold wall die. This short time at temperature approach offers the opportunity to control phase transformations and the degree of microstructural coarsening not readily possible with standard powder processing approaches. This paper describes the consolidation results of titanium aluminide-based powder composite materials. The focus of this study was the definition of microstructure/processing relationships for each of the composite constituents, first as monoliths and then in composite forms. Non-equilibrium phases present in rapidly solidified TiAl powders are transformed to metastable intermediates en route to the equilibrium gamma phase. The initial single phase beta in Nb-stabilized Ti_3Al is transformed to alpha two with an intermediate beta two phase. In composite blends of TiAl powders mixed with Nb-stabilized Ti_3Al powders a 10 μm thick interfacial layer is formed on the dispersed TiAl. Limited control of post-pulse heat extraction prevents full retention of the rapidly solidified powder microstructures.

INTRODUCTION

The Ti-Al system offers a rich variety of phases and microstructures. Many of its equilibrium phases are disordered solutions with wide composition ranges, or simple ordered structures based on the disordered solutions [1]. Non-equilibrium processing such as the production of powders and ribbons by rapid solidification alters the phase boundaries [2,3]. Alloying additions further complicate the precise prediction of phase fields and it becomes practical to adopt the use of a qualitative Ti-Al pseudo-binary [4].

At the focus of alloy design and development effort remain the binary intermetallics: TiAl (gamma) and the Ti_3Al (alpha two). Lipsitt has reviewed the history, progress, and potential uses of these materials in aircraft turbine engines [5,6]. The TiAl intermetallic is of lower density (3.76 vs 4.15- 4.70 gm/cm^3) but is also less ductile at room temperature (1-2 vs 2-5 percent elongation) than the Ti_3Al [5]. The density advantage of TiAl is enlarged when the influence of common ternary additions such as Nb, Mo, and Ta to Ti_3Al is taken into account. Powder-based composites of Ti_3Al + TiAl have therefore been designed to take advantage of the ductility of the Ti_3Al as a matrix and the low density of the TiAl as a dispersed constituent. In addition to the increased specific strength and potential thermal stability, these composites attempt to exploit the lattice parameter matching principles espoused by Fine et al. [7].

The phases of interest for these selected constituents are alpha, alpha two, beta, beta two, and gamma in the pseudo-binary Ti - Al phase diagram. The beta two phase is stabilized by the presence of Nb [1,4,8]. The characteristics of the phases are indicated below.

alpha	A3	hexagonal-close-packed (hcp) structure
alpha two	DO_{19}	ordered phase, based on hcp structure
beta	A2	body-centered-cubic (bcc) structure
beta two	DO3	ordered phase, based on bcc structure
gamma	$L1_0$	ordered phase, based on fcc structure

Mat Res Soc Symp Proc Vol 133 ©1989 Materials Research Society

EXPERIMENTAL PROCEDURE

Materials :Rapidly solidified titanium aluminide powders (- 80 mesh) were supplied by United Technologies Pratt and Whitney Division , FL. As-received TiAl powders (51 at.% Ti, 49 at.% Al) and Nb-stabilized Ti_3Al powders (65 at.% Ti, 11 at.% Nb, 24 at.% Al) were used.

Processing: The processing consists of internal heating of a customized powder blend by a fast electrical discharge of a homopolar generator. The high-energy high-rate "1MJ in 1s" pulse permits rapid heating of a conducting powder in a cold wall die. The underlying fundamental approaches to high-energy high-rate processing have been described [9]. The general details of the experimental apparatus and the pulse characteristics have also been reported [10,11].

In this study, 50g quantities of powders each of three groups of materials were processed. Group I consisted of TiAl powders. Group II consisted of Nb-stabilized Ti_3Al powders. Group III consisted of composite blends containing 10, 20, 30, 40, or 50 mass percent TiAl powders mixed with Nb-stabilized Ti_3Al powders (+ 200 mesh). The powders were loaded into insulated die cavities between copper electrodes faced with molybdenum foils. A pressure of 210 MPa was applied, and the compact was rapidly heated by a homopolar generator pulse discharge. Disks of 50 mm diameter were produced. Specific energy inputs ranged from 3200 kJ/kg to 4000 kJ/kg.

Microstructure Evaluation: Standard metallographic procedures were employed in the preparation of radial cross sections of each of the consolidated materials. Disk sectioning by water-jet machining minimized mechanical damage. Vickers microhardness measurements were performed at room temperature on both the as-received and consolidated materials to indicate the influence of structural changes on mechanical properties.

For the consolidated Ti_3Al, heat treatments of 24h at 1173K were used to determine the equilibrium microstructure. Unetched and etched cross-sections were examined in an optical microscope fitted with a Nomarski interference contrast system. This permits the polishing relief developed due to phases of different hardnesses to become readily apparent in color micrographs [12]. X-ray diffraction analyses were performed on a Phillips diffractometer fitted with a Cu tube and a graphite monochromator. The powder samples were held onto a glass slide with double-sided adhesive tape. Sufficient powder was used so that no signal was detected from the glass slide. A 200 kV JEOL-200CX instrument was used in the TEM studies conducted on fully dense disks sectioned and thinned by electropolishing [13] for observation.

RESULTS AND DISCUSSION

Consolidation Processing & Microhardness: The processing parameters used for these consolidation experiments were derived from previously developed densification maps for each powder. Densities greater than 95% of the theoretical values were obtained. The most identifiable solid state densification mechanism is powder forging. For the composition-optimized Ti-Al-Nb alloys, the best combination of strength and ductility by ingot metallurgy is obtained by forging above the beta transus and controlled cooling to produce a fine Widmannstatten microstructure [14]. Controlled cooling is also crucial to the production of crack-free Nb-stabilized Ti_3Al disks by high-energy high-rate consolidation. Like many other single-residence powder consolidation processes which attempt to maintain RS microstructures, the necessary large-strain deformation processing for metallurgical bonding and limited control of post-densification heat extraction can hinder both the desirable near-net-shape processing [15], and the maintenance of isotropic, homogeneous microstructures.

Table 1 compares the average room-temperature hardnesses for powders and consolidated materials. In every case the processed material shows a hardness increase of about ten percent. Material-specific microstructural changes which occur in response to the applied thermomechanical processing cycle account for these changes. These are discussed below.

Table 1: Comparison of the room-temperature microhardnesses for powders and consolidates.

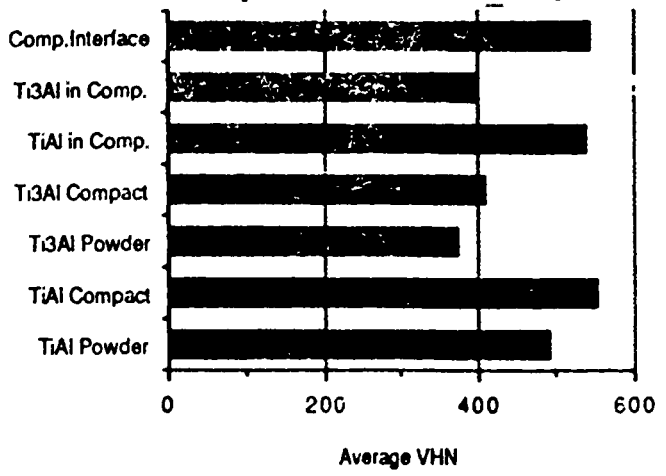

Microstructure and Chemistry

Group I : TiAl powders and consolidated monoliths: The as-received TiAl powder particles are largely two-phase. X-ray diffraction indicated that they were composed of the ordered TiAl (gamma) phase and the ordered Ti_3Al (alpha two) phase. This result is in agreement with those of Huang et. al. [3] for rapidly solidified ribbons of similar composition. A third contaminant phase, TiC, was also present. The relative ratios of Ti_3Al: TiAl, judged from X-ray peak intensities, varied from 5:4 in the coarse +200 mesh (>74 μm) powders to 5:1in the -325 mesh (<44μm) powders. The microstructure of the as-received powders is shown in Figure 1.

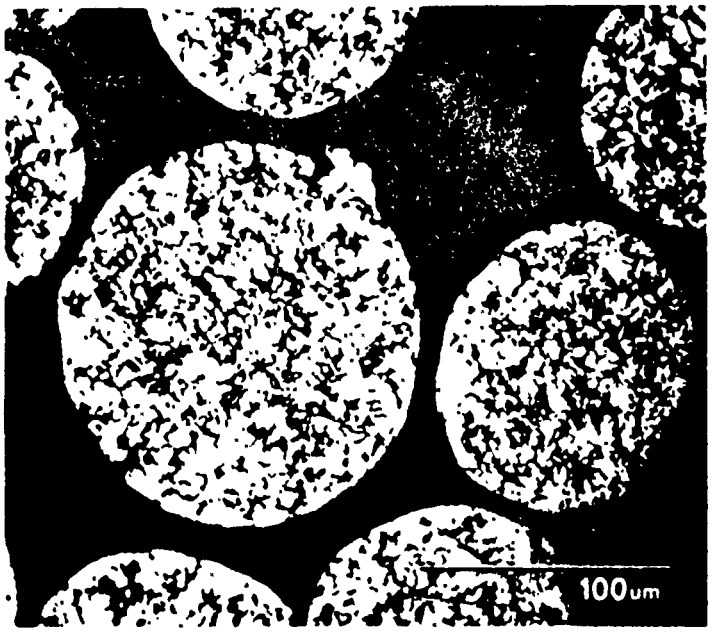

Fig.1.

Optical photomicrograph of polished and etched sections of as-received TiAl powders. A two phase structure is evident.

The consolidated compact has the same phases as the as-received particles but moves toward its equilibrium gamma phase during consolidation process. TEM studies indicated that the Ti_3Al appears as plates with submicron thicknesses distributed in the TiAl. The alpha two phase forms as semi-coherent plates within the the gamma phase. The microstructure of the consolidated material is shown in Figure 2.

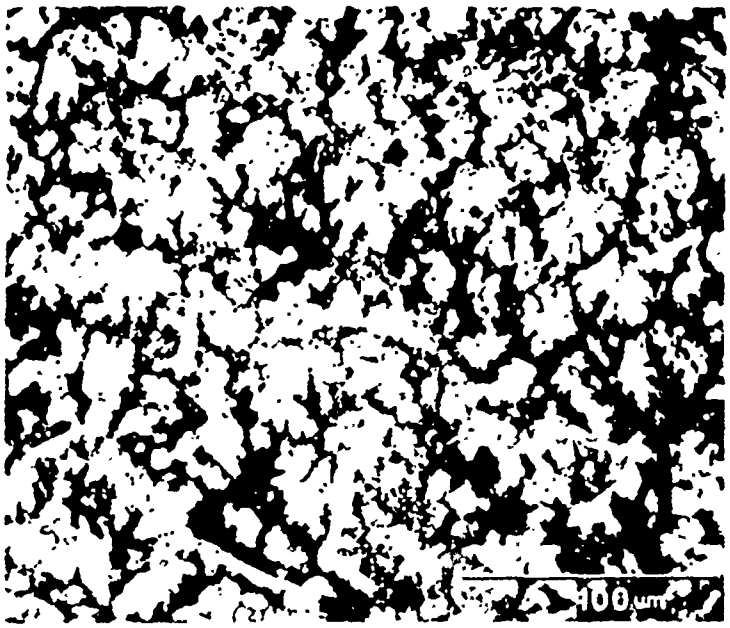

Fig.2.

Optical photomicrograph of a polished and etched radial cross-section of a disk produced from TiAl powders with an energy input of 3200 kJ/kg under 210 MPa applied pressure.

Group II: Nb-stabilized Ti_3Al powders and consolidated monoliths. The structure of the as-received powder particles appears to be single phase beta based on optical examination and X-ray diffraction study. Rapid-solidification-induced microstructural refinement in the as-received powders (Figure 3) is maintained in the fine grain size observed in the consolidated material (Figure 4). However, the consolidation cycle induces or completes the disorder-to-order transformation from the beta phase to the beta two phase. TEM of specimens from the consolidated disk showed tweed microstructures and anti-phase boundaries and some martensitic transformation from the beta two phase to the alpha two phase [16]. These microstructures were qualitatively similar to those observed by Jackson et al. in rapidly solidified Ti - 15 Al - 11Mo [17]. Complete transformation to the alpha two phase was observed after an 1173K, 24 hour heat treatment.

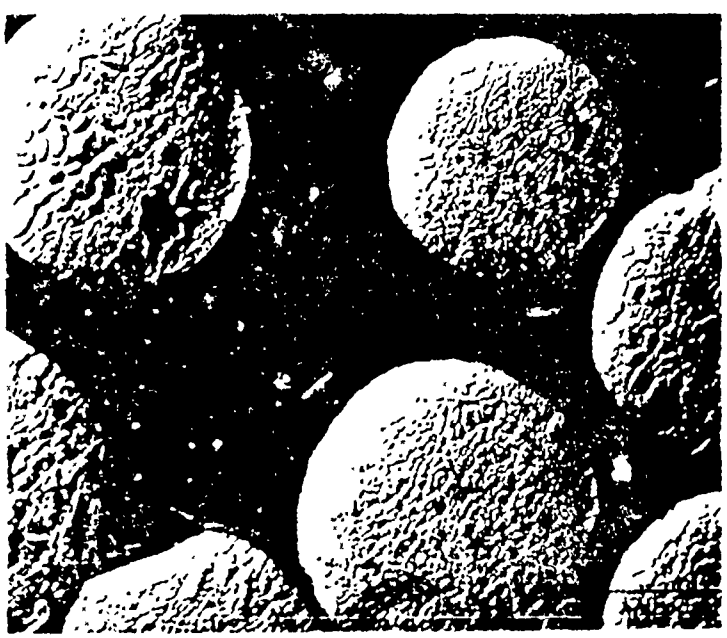

Fig.3.

Optical photomicrograph of polished and etched sections of as-received Nb-stabilized Ti_3Al powders. Grain sizes range from 5 to 50 µm.

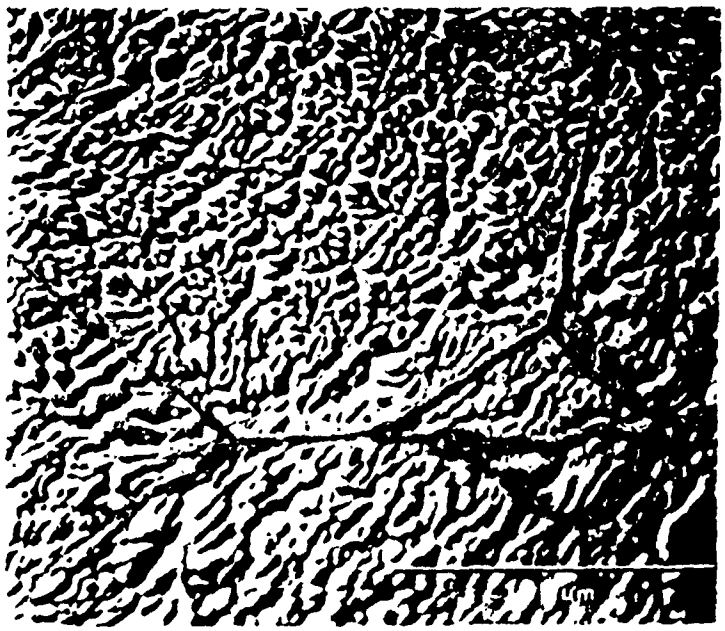

Fig.4.

Optical photomicrograph of a polished and etched radial cross-section of an Nb-stabilized Ti_3Al consolidated disk produced with an energy input of 3200 kJ/kg under 210 MPa applied pressure.

Group III: Composite blends of TiAl powders mixed with Nb-stabilized Ti_3Al powders.

High-energy high-rate consolidation produces fully dense composite bodies in which the TiAl powder particles remain largely intact and the Nb-stabilized Ti_3Al matrix flows to encapsulate them. Figures 5 and 6 provide typical overviews of the rapidly densified microstructures developed in the Nb-stabilized Ti_3Al + TiAl powder composite system. The Nb-stabilized Ti_3Al matrix is well consolidated, and excellent geometric conformability to the dispersed TiAl powders is observed.

A uniform interfacial layer is evident in Figure 6. The apparent width of the interfacial layer is about 10 μm. Phases similar to those observed in the consolidated Group I and Group II monoliths were observed. TEM studies also indicate the formation of an ordered othorhombic phase of the type described by Banerjee et al. [18]. Further TEM investigations of the phases present are currently underway. The extent of interfacial zone growth at elevated temperatures of 1173K and 1273K for periods of up to 100 hours is also being investigated.

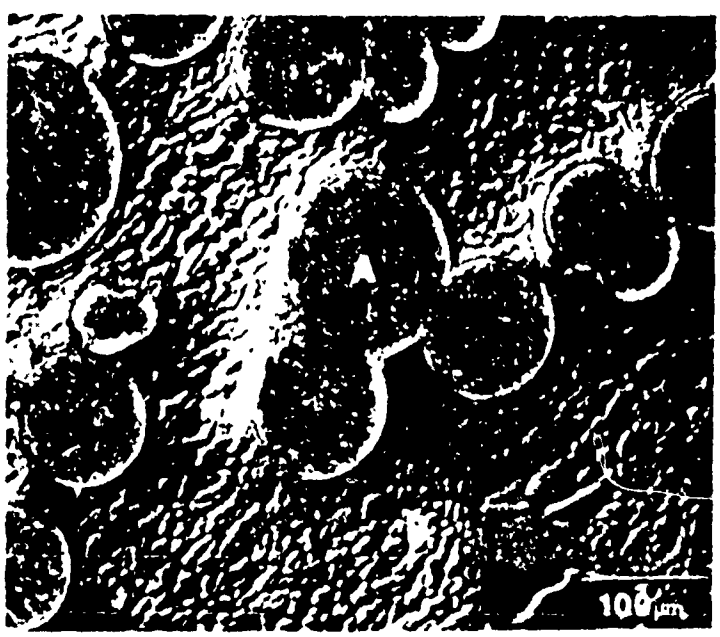

Fig.5.

Optical photomicrograph of an etched radial cross-section of a composite specimen produced with an energy input of 4000 kJ/kg under 210 MPa applied pressure. The macroscopic features are A-TiAl particles, B-Nb-stabilized Ti_3Al matrix.

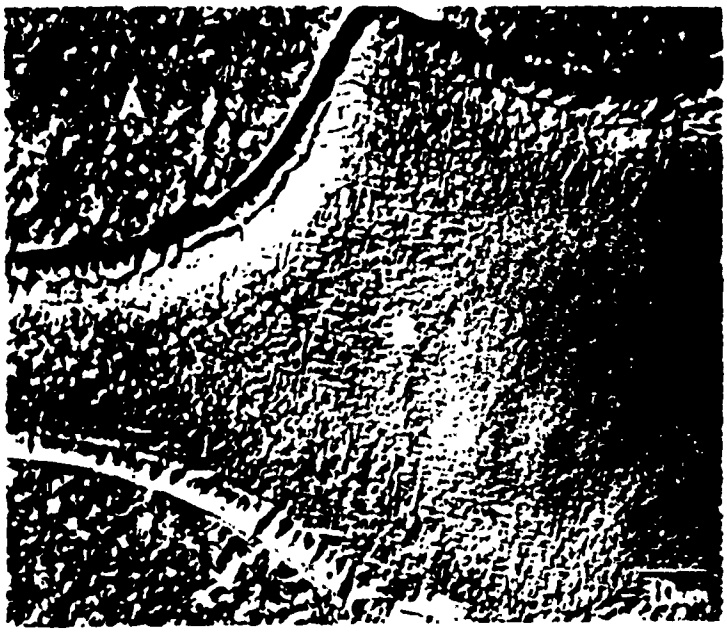

Fig.6.

Optical photomicrograph of specimen in Figure 5 at high magnification indicating the 10 μm dimension of the uniform interface between the TiAl particles (A), and the Nb-stabilized Ti_3Al matrix (B).

ACKNOWLEDGMENTS

We thank Ralph Anderson and Sandy Shuleshko of Pratt and Whitney, FL. who provided the powders. Assistance with processing was provided by Jim Allen at CEM-UT. M. J. Wang, L. K. Rabenberg, Mike Schmerling, and H.-G. Chun assisted in the structure evaluation. This research was supported by DARPA/ARO Contract DAAL03-87-K-0073.

REFERENCES:

[1] Joanne L. Murray, Met. Trans. 19A, 243 (1988).
[2] S. H. Whang, Z. X. Li, and D. Vujic in High-Temperature Ordered Intermetallic Alloys II, edited by N. S. Stoloff, C. C. Koch, C. T. Liu, and O. Izumi (Mater. Res. Soc. Proc. 81, Pittsburgh, PA 1987) pp. 151 - 156.
[3] S. C. Huang, E. L. Hall, and M. F. X. Gigliotti in High-Temperature Ordered Intermetallic Alloys II, op. cit., pp. 481 - 486.
[4] R. Strychor, J. C. Williams, and W. A. Soffa, Met. Trans. 19A, 225 (1988).
[5] H. A. Lipsitt, in High-Temperature Ordered Intermetallic Alloys, edited by C. C. Koch et. al., (Mater. Res. Soc. Proc. 39, Pittsburgh, PA 1985) pp. 351 - 364.
[6] H. A. Lipsitt, in Advanced High-Temperature Alloys: Processing and Properties, edited by S. M. Allen et al.(ASM, Ohio, 1986) pp.157 - 164.
[7] M. E. Fine, D. L. Bourell, Z. Eliezer, C. Persad and H. L. Marcus, Scripta Metallurgica, 22, 907 (1986).
[8] J. C. Williams, in Precipitation Processes in Solids, K. C. Russell and H. I. Aaronson, eds., (TMS-AIME, Warrendale, 1978) p. 191.
[9] H. L. Marcus, D. L. Bourell, Z. Eliezer, C. Persad and W. F. Weldon, Journal of Metals, 39, 6 (December 1987).
[10] G.Elkabir, L. Rabenberg, C.Persad and H.L.Marcus, Scripta Met. 20, 1411 (1986).
[11] D. R. Ervin, D. Bourell, C. Persad, L. Rabenberg, J. Mat. Sci. Eng. A102, 25 (1988).
[12] C.E. Price in Metals Handbook, 9th. edition, V. 9, Metallography and Microstructures (ASM, Metals Park, OH, 1985) p. 151.
[13] H. W. Rosenberg and W. D. Nix, Met. Trans. 1, 2962 (1970).
[14] P. R. Bridenbaugh, F. R. Billman, W. S. Cebulak, and G. J. Hildeman, in Advanced High-Temperature Alloys: Processing and Properties, op. cit., pp. 53-64.
[15] M. J. Blackburn and M. P. Smith, U. S. Patent No. 4 292 077 (29 September 1981).
[16] C. -J. Hou et al., presented at the 1988 TMS/AIME Fall Meeting, Chicago, IL, 1988.
[17] A. G. Jackson, K. Teal and F. H. Froes in High-Temperature Ordered Intermetallic Alloys II, op. cit., pp. 143 - 149.
[18] D. Banerjee, A. K. Gogia, T. K. Nandi and V. A. Joshi, Acta Metall. 36, 871 (1988).

MATRIX-REINFORCEMENT INTERFACE CHARACTERISTICS OF (Ti_3Al+Nb)-BASED POWDER COMPOSITES, CONSOLIDATED BY HIGH-ENERGY HIGH-RATE PROCESSING

Z. Eliezer, B.-H. Lee, C. J. Hou, C. Persad, and H.L. Marcus.

Center for Materials Science and Engineering,
The University of Texas, Austin, TX 78712.

Abstract

Intermetallic matrix composites containing discontinuous ceramic or intermetallic particulate reinforcements have been formed by high-energy high-rate powder consolidation. BCC-stabilized Ti_3Al powder matrices have been consolidated with second phases including AlN, TiB_2, and TiAl powders. Processing was accomplished by discharge of a single high electrical energy pulse through a powder blend under pressure. Control of energy input produced solid-state and liquid-phase-assisted consolidation. The high-temperature stability of the matrix/reinforcement interfaces was compared by annealing treatments of up to 100 hours at 1073K - 1273K. X-Ray diffraction, analytical electron microscopy, and microhardness profiling were employed in characterizing the interfacial phases.

This work was supported by DARPA under ARO Contract DAAL 0387-K-0073.

Metal & Ceramic Matrix Composites:
Processing, Modeling & Mechanical Behavior
Edited by R.B. Bhagat, A.H. Clauer, P. Kumar and A.M. Ritter
The Minerals, Metals & Materials Society, 1990

Introduction

It has been recently shown (1) that a broad variety of materials can be successfully consolidated by a process involving the deposition of a large amount of energy (megajoules) in a very short time (< 1 sec) into a powder mixture. In this High Energy High-Rate (HEHR) process, the short residence time at high temperature may provide the necessary mechanism for controlling the degree of microstructural coarsening and for limiting the number and size of deleterious interface structures in composites, a task that is very difficult to accomplish by conventional consolidation techniques. For these reasons, this high energy high rate processing method may be of particular interest in the consolidation of (Ti_3Al+Nb) - based metal matrix composites from initially rapidly solidified powders.

Preliminary results on the structure and properties of composites based on (Ti_3Al+Nb) as a matrix and SiC or TiAl as reinforcing dispersoids have been reported (2, 3). This article is aimed at discussing the matrix-reinforcement interface characteristics in three HEHR consolidated (Ti_3Al+Nb) - based metal matrix composites containing TiB_2, AlN, or TiAl reinforcing particles.

Experimental Procedure

Materials

Rapidly solidified Ti_3Al powders (65 at % Ti, 11 at % Nb, 24 at % Al) and TiAl powders (51 at % Ti, 49 at % Al) were supplied by United Technologies Pratt and Whitney Division, FL. The as-received Ti_3Al powders had a disordered bcc structure with a 3.25 Å lattice parameter and were spherical in form with diameters ranging from 10 to 150 microns. The TiAl powder had an ordered γ structure and were less than 100 μm in diameter. TiB_2 (<15 μm) and AlN single phase powders (<1 μm) were supplied by Herman C. Starck, West Germany, and Alfa Products, MA., respectively. Figs. 1-4 show the shapes and sizes of the as-received powders.

Fig. 1. SEM micrograph of as-received Ti_3Al+Nb powder.

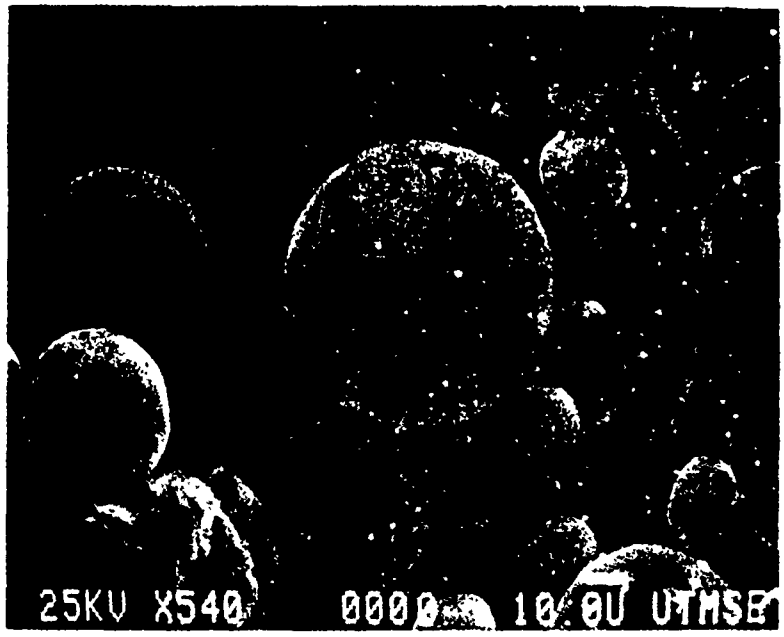

Fig. 2. SEM micrograph of as-received TiAl powder.

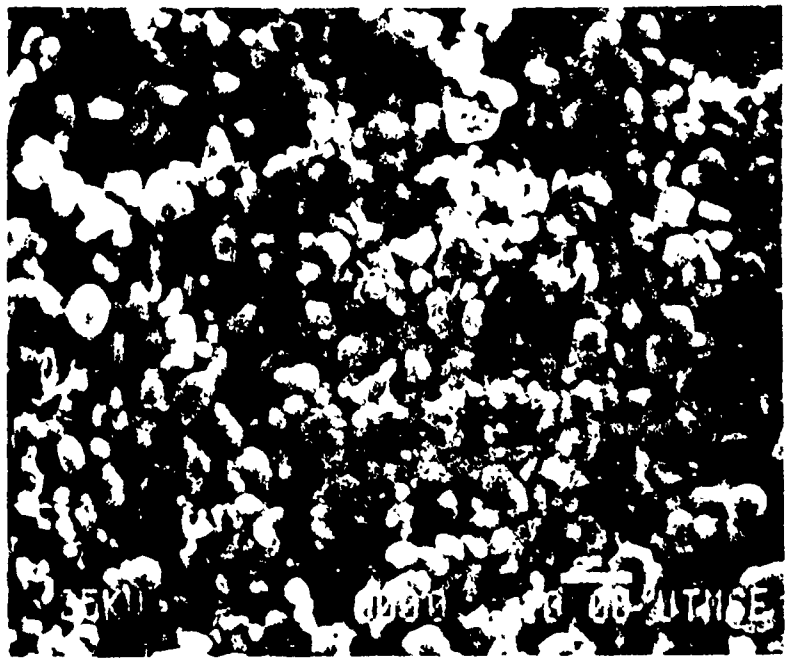

Fig. 3. SEM micrograph of as-received TiB_2 powder.

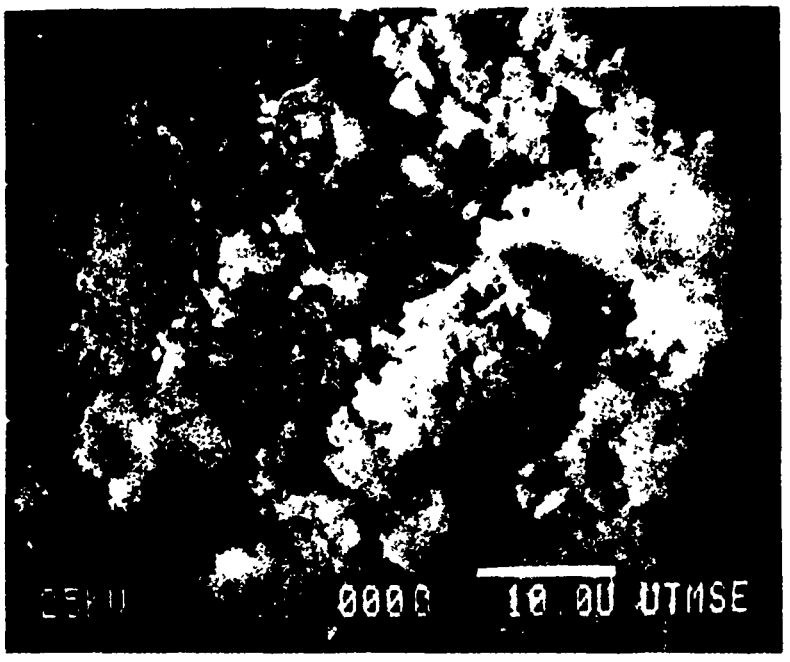

Fig. 4. SEM micrograph of as-received AlN powder.

Processing

Powder mixtures of Nb-stabilized Ti_3Al with TiB_2, AlN, or TiAl as reinforcements were processed by rapidly heating them in a cold wall die using a fast electrical pulse supplied by a homopolar generator (1). The mass of powder used was 12.5g for the TiB_2 and AlN mixtures, and 50g for the TiAl mixtures. The applied pressures varied between 210 and 420 MPa while the specific energy inputs ranged from 3200 to 4800 kJ/kg. The amounts of TiB_2, AlN, and TiAl in the three (Ti_3Al+Nb) - based composites were 10 w/o, 10 w/o and 20 w/o respectively.

Microstructural Evaluation

Standard metallographic procedures were employed in the preparation of radial cross sections of each of the consolidated materials. Vickers microhardness measurements were performed at room temperature on both the as-received and consolidated materials to assess the influence of structural changes on mechanical properties. Etched cross sections were examined with optical microscopes with or without Nomarski interference contrast system. X-ray diffraction analyses were performed on a Philips diffractometer fitted with a copper tube and a graphite monochromator. The powder samples were held onto an aluminum holder. Sufficient powder was used so that no signal was detected from the aluminum sample holder. A JEOL 35M scanning electron microscope was used for powder characterization. A 200 kV JEOL-200 CX instrument was used in the TEM studies, which were conducted on specimens taken from diametral slices of fully dense disks and thinned by electropolishing (4) for observation.

Results and Discussion

Consolidation Parameters

The processing parameters used for consolidation were derived from parameter sets previously developed for the unreinforced matrix materials. The most identifiable solid state densification mechanism is powder forging. Densities greater than 95% of the calculated theoretical values were obtained.

Microhardness

Table 1 shows the average room temperature microhardness values for the TiB_2 and AlN composites. The hardness values of the Ti_3Al+Nb matrix of both systems is quite close to the value of Ti_3Al+Nb monolith compact and approximately ten percent greater than the value of as-received powder. This is a result of the microstructural changes of the Ti_3Al+Nb matrix which occur in response to the applied thermomechanical processing cycle (5). In Ti_3Al+Nb/TiB_2 system, the interfacial region has a hardness value between the matrix and the reinforcements. In the case of Ti_3Al+Nb/AlN system, the width of the interfacial layer was too small for microhardness measurements.

Table 1. Average room temperature microhardness (VHN; 500g. load)

	(Ti_3Al+Nb)/TiB_2	Ti_3Al+Nb)/AlN	Ti_3Al+Nb Monolith	Ti_3Al+Nb Powder
Matrix	416	425	410	375
Interface	589	----	----	----
Reinforcements	1709	1013	----	----

Microstructure and Chemistry

(Ti_3Al+Nb/TiB_2 System. Figures 5 and 6 provide typical overviews of the rapidly densified microstructures in this system. The Nb stabilized Ti_3Al matrix is well consolidated and flows to encapsulate TiB_2 reinforcements. The difference in particle size of the matrix and reinforcement is responsible for the TiB_2 particle agglomeration on the matrix particle surface. In lower energy input samples (Fig. 5), the consolidation between TiB_2 reinforcements themselves is poor, and no new interfacial phases can be found. For higher energy samples, new interfacial phases begin to form along the matrix/reinforcement boundaries and good consolidation of TiB_2 particles is achieved (Fig. 6). Within a narrow specific energy input range (~5000 kJ/kg) good consolidation of TiB_2 particles without the formation of interfacial phases may eventually be achieved. Further consolidation experiments are underway. XRD analyses of the phases present in the processed composite reveal the likely reaction products to be TiB and AlB_2. The matrix has undergone the same microstructural changes as the Ti_3Al+Nb monolith compacts [3]. The AlB_2 has similar lattice parameters and same crystal structure as TiB_2. Higher energy input appears to increase the size of the interfacial phase region (Fig. 7).

(Ti_3Al+Nb)/AlN System. Fig. 8 is a typical overview of the microstructure of this system. Ti_3Al+Nb matrix flowed well to encapsulate individual AlN particles at the interface. The consolidation of reinforcement particles themselves is quite satisfactory. A thin interfacial layer less than 3 micron wide can be seen between matrix and reinforcement. XRD analyses of the processed composites showed that the likely reaction product is Ti_2N. Similar to the case of

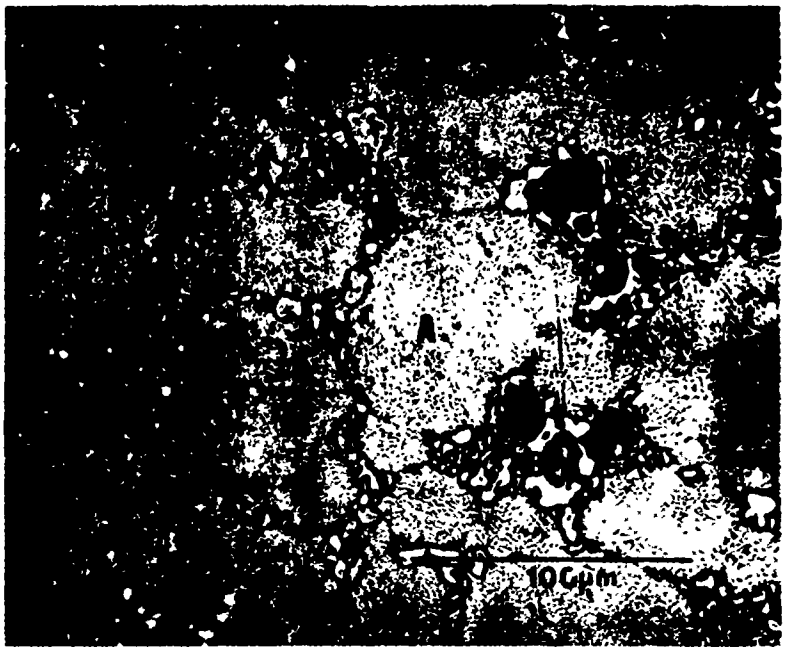

Fig. 5. Optical micrograph of an etched radial cross section of (Ti_3Al+Nb)/TiB_2 sample produced at relatively low energy input (3800 kJ/kg). A is the (Ti_3Al+Nb) matrix and B is the TiB_2 reinforcement. Dark regions denote TiB_2 particles pull-out.

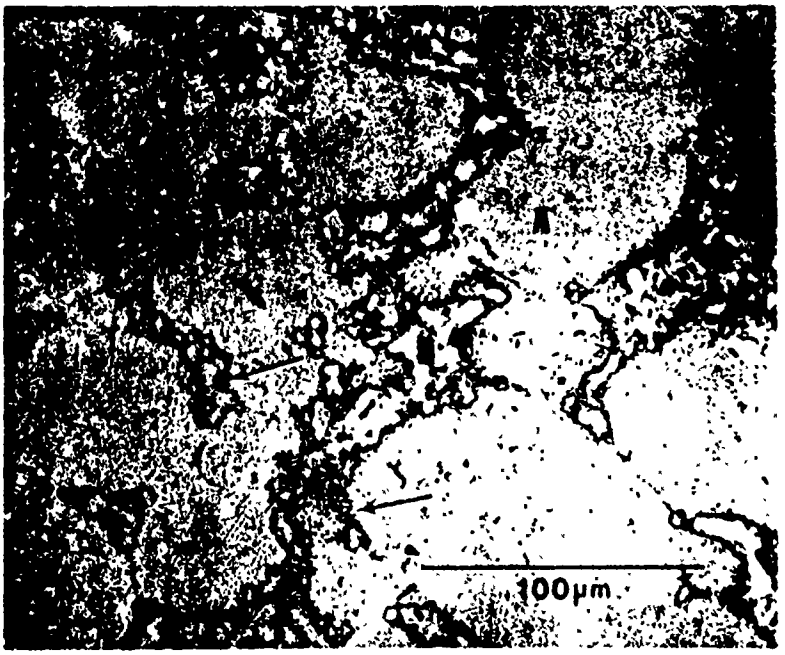

Fig. 6. Optical photomicrograph of an etched cross-section of (Ti_3Al+Nb)/TiB_2 sample produced at relatively high energy input (4200 kJ/kg). Arrows indicate the formation of interfacial reaction zones.

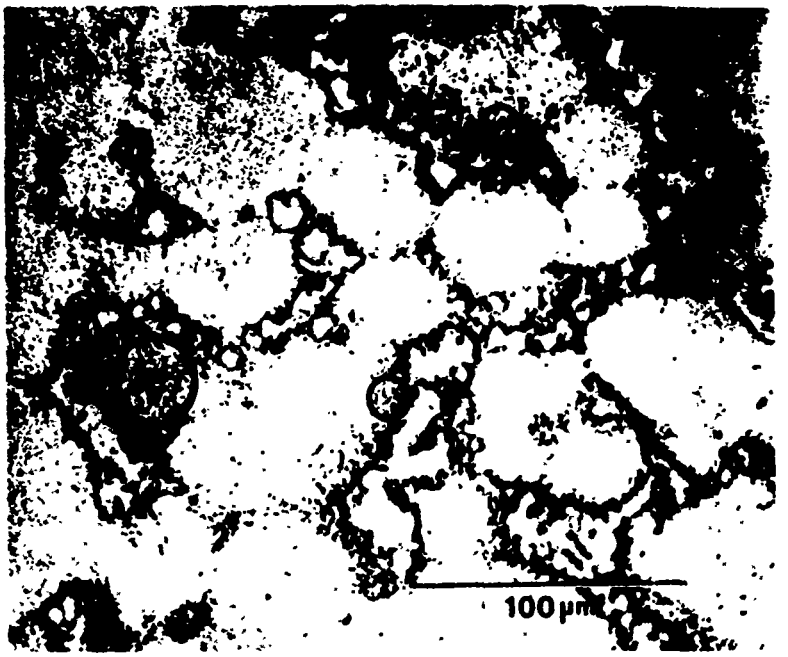

Fig. 7. Optical photomicrograph of an etched cross-section of (Ti_3Al+Nb)/TiB_2 sample produced at higher energy input (4600 kJ/kg). Extensive formation of an interfacial phase can be seen.

Fig. 8. Optical photomicrograph of an etched radial cross-section of (Ti_3Al+Nb)/AlN sample produced at relatively high energy input (4700kJ/kg). A is the (Ti_3Al+Nb) matrix and B is the AlN reinforcement. Arrow indicates the interfacial layer zone.

(Ti_3Al+Nb)/TiB_2 system, the consolidation of reinforcement particles themselves is very poor in lower energy input samples (Fig. 9).

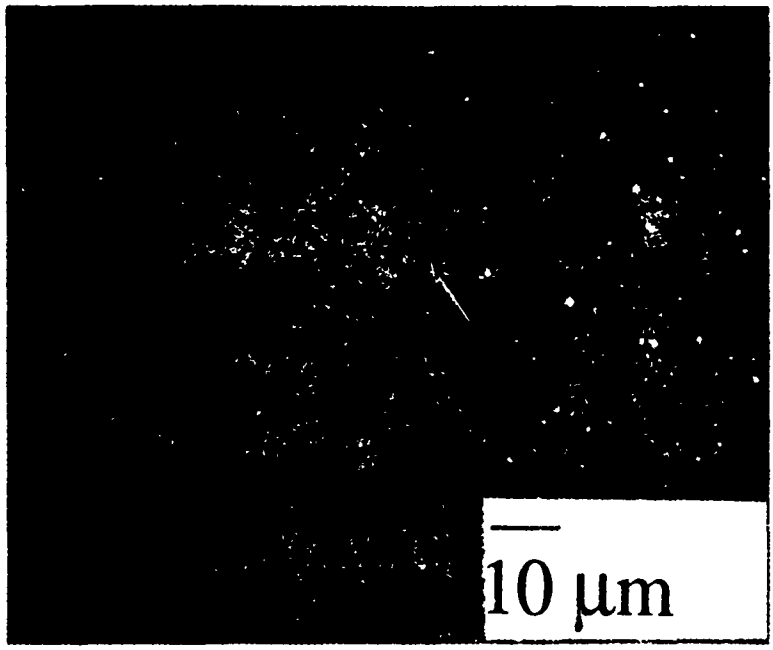

Fig. 9. Optical photomicrograph of an etched radial cross-section of (Ti_3Al+Nb)/AlN sample produced at relatively low energy input (4100 kJ/kg). A thin interfacial layer can still be seen.

(Ti_3Al+Nb)/TiAl System. Figure 10 is a typical overview of the microstructure of this sytem consolidated at a specific energy input of 4000 kJ/kg. The Nb stabilized Ti_3Al formed the matrix while the spherical TiAl particles were randomly distributed in the matrix. The phases present in the matrix and reinforcement particles after consolidation were analyzed by transmission electron microscopy. Lens-shaped alpha-two phase and residual untransformed disordered beta phase constituted the matrix (Figure 11). The constituent phases in the TiAl reinforcement after consolidation were ordered gamma and plate-shaped alpha-two (Figure 12). At the interface of matrix and the reinforcement, a 5 micron layer was formed (Figure 13). An electron diffraction pattern from this layer showed that alpha-two was the stable phase (Figure 14). The chemistry at this interface region was analyzed by micro energy dispersive spectroscopy (micro EDS) in a JEOL-1200 analytical electron microscope. X-ray spectra were taken from the matrix, reinforcement, and interface regions (Figure 15). Niobium peaks were observed in all three locations, but their intensities decreased from the matrix through the interface layer and into the reinforcing particles.

Evidently, the (Ti_3Al+Nb) regions close to the interface are depleted of Nb which in turn migrates to the initially Nb-free TiAl particles. As a result of this interparticle diffusion, the Nb-depleted zone transformed from the disordered β to the ordered α_2 structure (Figure 14). The width of the interface α_2 zone depends on the temperature developed at the interface during consolidation, and on the time at temperature. In our experiments a thickness of ~ 5 μm has been obtained (Figure 15). In principle, by optimizing the energy input, the Nb-depleted layer can be drastically decreased. Another possible route to reducing or eliminating the interface layer is the employment of Nb-rich TiAl particles. Under these conditions, the driving force for Nb diffusion from the matrix toward the reinforcing particles will disappear, and the brittle α_2 interface will not form.

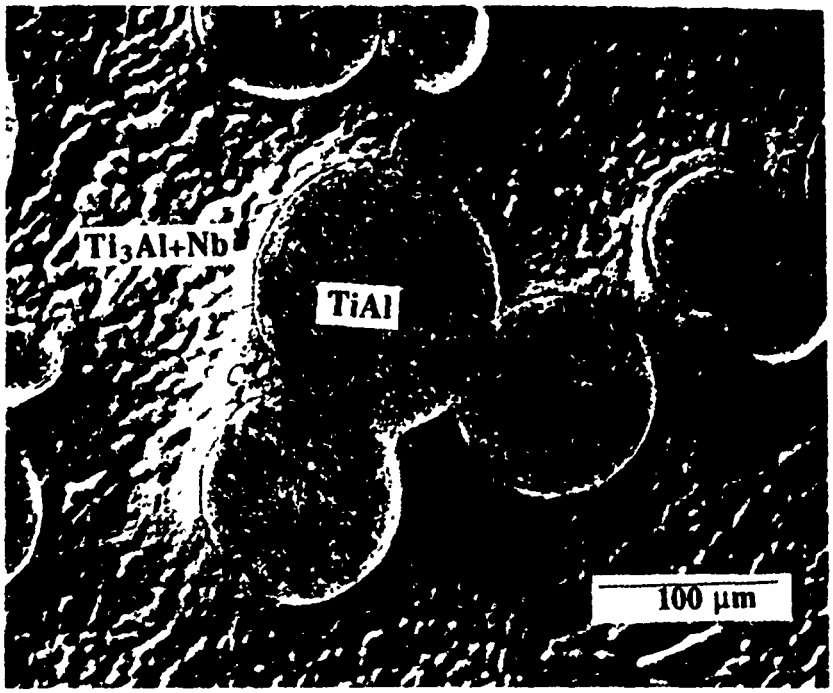

Fig. 10. Typical overview of consolidated (Ti_3Al+Nb)/TiAl composite. The matrix is Ti_3Al+Nb and the spherical particles are TiAl.

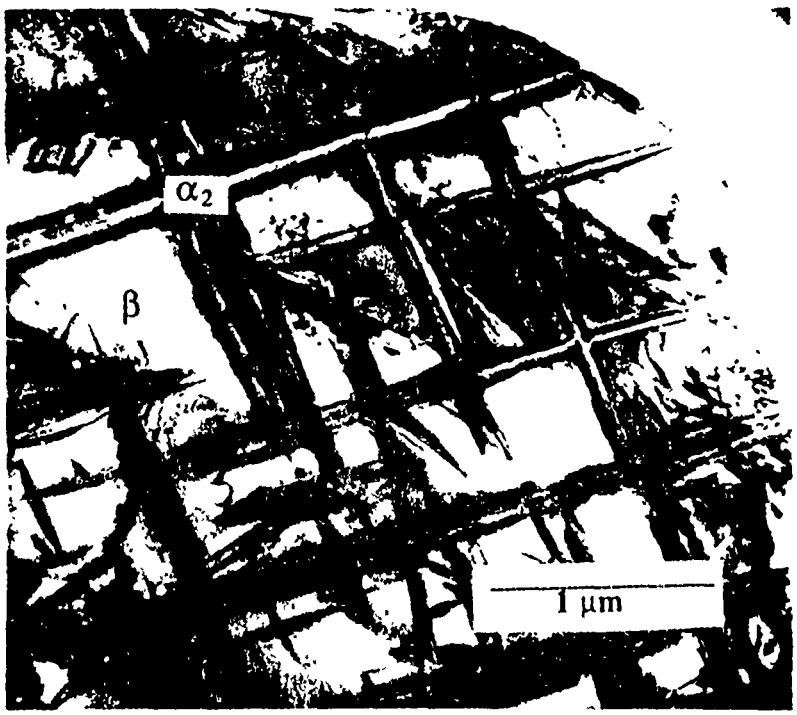

Fig. 11. Transmission electron micrograph of lens-shaped alpha-two phase in Ti_3Al+Nb region.

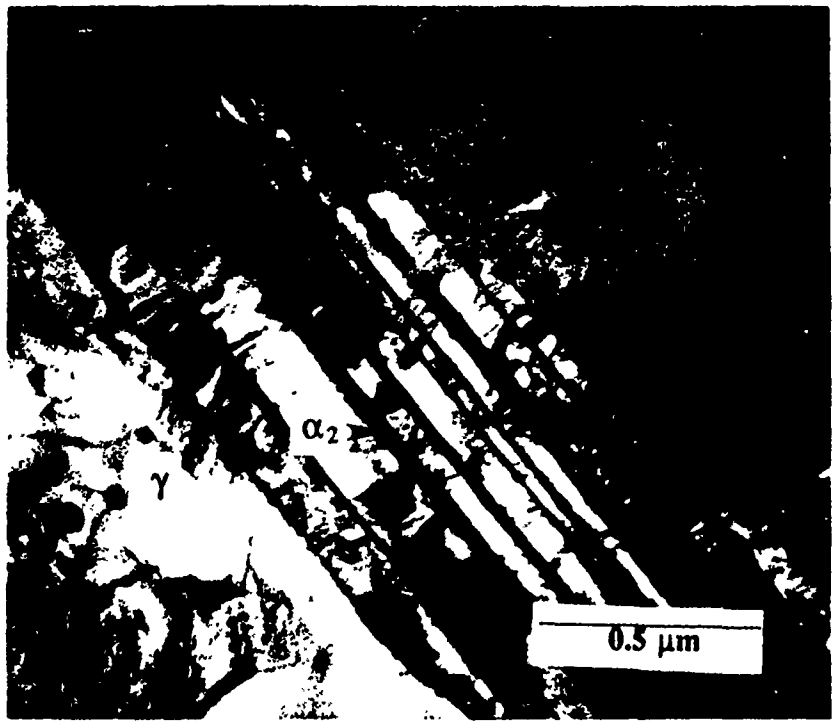

Fig. 12. Transmission electron micrograph of laminated alpha-two and gamma phases in TiAl region.

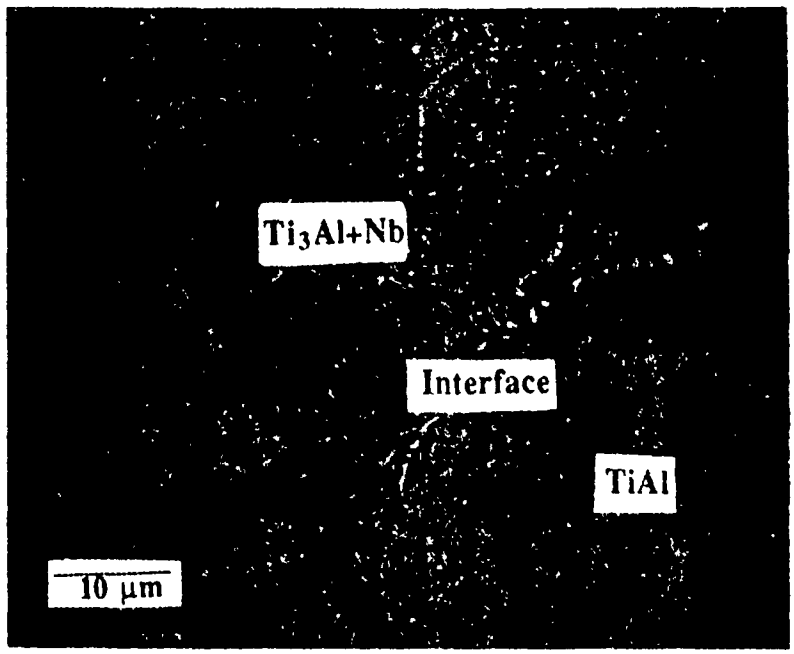

Fig. 13. Optical micrograph of consolidated (Ti_3Al+Nb)/TiAl composite showing an interface layer.

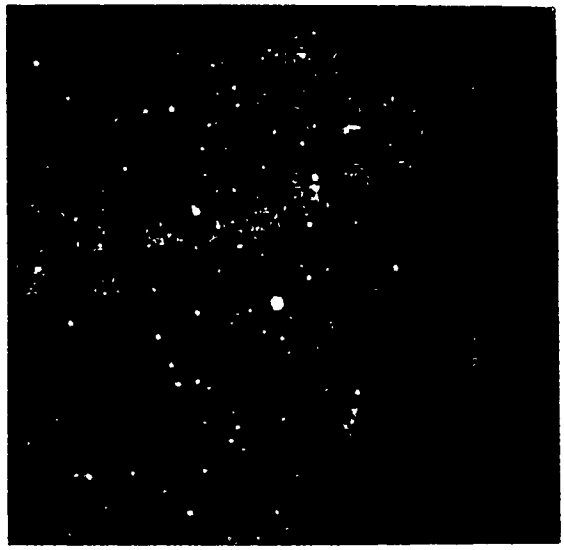

Fig. 14. Electron diffraction pattern of interface layer of Fig. 13, showing that the structure is alpha-two. The zone axis is [11$\bar{2}$0].

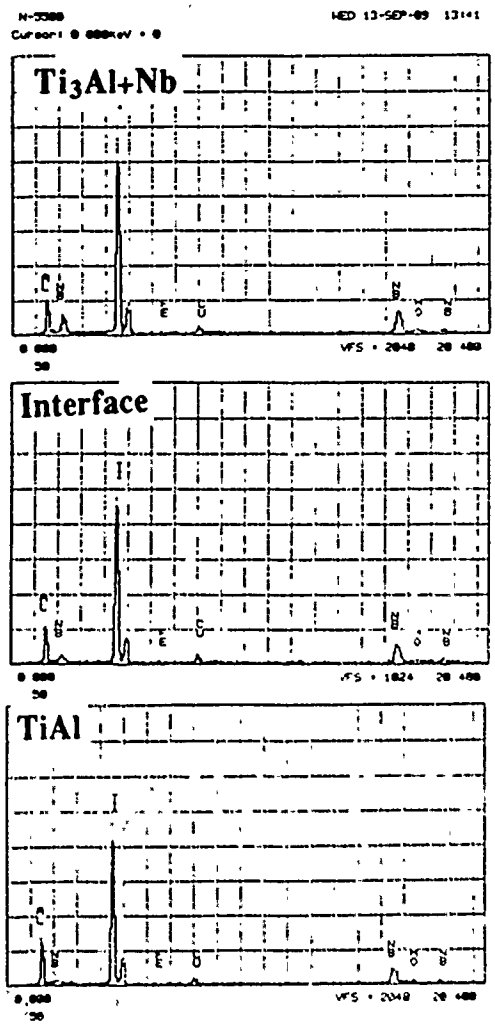

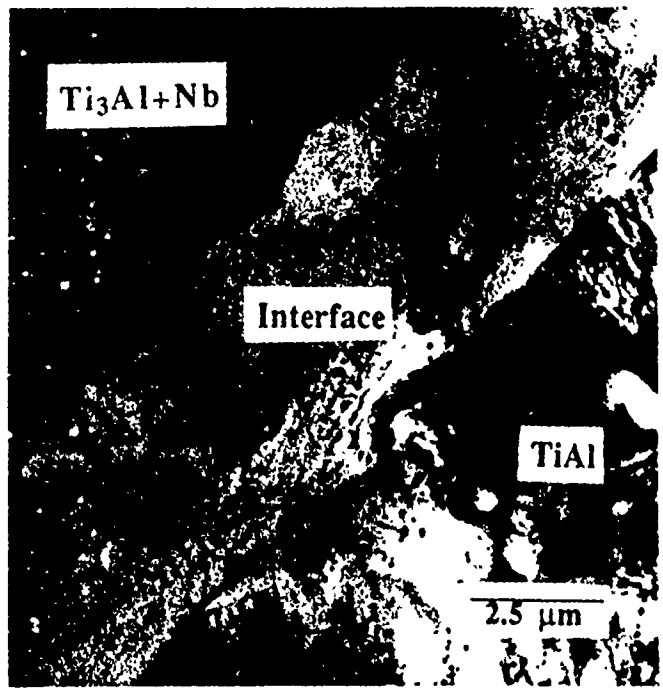

Fig. 15. Transmission electron micrograph and EDS spectra of matrix, interface, and reinforcement regions in consolidated (Ti_3Al+Nb)/TiAl system.

Conclusion

1. (Ti_3Al+Nb)-based composite with TiB_2, AlN, and TiAl particle reinforcements have been sucessfully produced by the High-Energy, High-Rate consolidation process.

2. The reaction products in (Ti_3Al+Nb)/TiB_2 seem to be TiB and AlB_2.

3. In the (Ti_3Al+Nb)/AlN system the likely reaction product is Ti_2N.

4. The (Ti_3Al+Nb)/ TiAl composite is characterized by an α_2 interface, with Nb migrating from the matrix, through the interface, and into the TiAl reinforcements.

Acknowledgments

We thank Sandy Shulesko and Ralph Anderson of Pratt and Whitney, Florida, who provided Ti_3Al+Nb and TiAl powder. Assistance with processing was provided by Jim Allen at CEM-UT. This research was supported by DARPA/ARO Contract DAAL03-87-K-0073.

References

1. H. L. Marcus, D. L. Bourell, Z. Eliezer, C. Persad and W. F. Weldon, Journal of Metals, (6) (1987), 39-.

2. C. Persad, S. Raghunathan, B.-H. Lee, D. L. Bourell, Z. Eliezer and H. L. Marcus, High Temperature/High Performance Composites, edited by F. D. Lemkey, S. G. Fishman, A. G. Evans, and J. R. Strife (Mater. Res. Soc. Proc. 120 Pittsburgh, PA, 1988) 23-28.

3. C. Persad, B.-H. Lee, C.-J. Hou, Z. Eliezer, and H. L. Marcus, High-Temperature Ordered Intermetallic Alloys III edited by C. T. Liu, A. I. Taub, N. S. Stoloff, and C. C. Koch (Mater. Res. Soc. Proc. 133 Pittsburgh, PA, 1989), 717-722.

4. H. W. Rosenberg and W. D. Nix, Met. Trans. 1A (1970), 2962.

5. C. J. Hou et al, paper presented at the 1988 TMS/AIME Fall Meeting, Chicago, IL.

APPENDIX D

COPPER-GRAPHITE

D-1. High-Energy/High-Rate Consolidation of Copper-Graphite Composite Brushes for High-Speed, High-Current Applications

D-2. A Novel Processing Technique for Metal/Ceramic Composites

D-3. Advanced Composite Materials for High-Performance Electrotribological Applications

HIGH-ENERGY/HIGH-RATE CONSOLIDATION OF COPPER-GRAPHITE COMPOSITE BRUSHES FOR HIGH-SPEED, HIGH-CURRENT APPLICATIONS

M. J. Wang[1], C. Persad[1], Z. Eliezer[1], and W. F. Weldon[2]

[1] The University of Texas at Austin
Center for Materials Science and Engineering
Austin, TX 78712

[2] The University of Texas at Austin
Center for Electromechanics
Austin, TX 78758

ABSTRACT

This paper reviews some of the important materials structure-property relationships that exist for copper-graphite composites, as they influence this class of materials in high current applications.

Commercial composite brushes fail in high-speed/high-current duty by loss of the low-melting-temperature, metallic binder, usually lead-tin, caused by the high flash temperature at the sliding interface combined with the softening due to I^2R heating.

The virtues of binderless copper-graphite brush materials have driven the development of a novel high-energy/high-rate processing approach employing a homopolar generator as a '1 MJ in 1 s' pulsed power source. The discharge of such an energy pulse through a powder mixture under pressure produces a dense product with improved mechanical and electrical properties compared to conventionally sintered commercial material.

The rapid processing minimizes internal oxidation, and the fast post-pulse cooling promotes the freezing of the copper matrix and tight micro-encapsulation of the graphite particles due to localized energy deposition at the copper-graphite interface. High and low speed testing have been used in the preliminary tribological evaluation. The behavior of these materials has compared favorably to commercial materials for pulsed high-speed, high-current duty.

Introduction

During the past ten years, a considerable amount of research effort has been dedicated to design and development of a solid-brush current collector system capable of reliably transferring large electrical currents through sliding contacts. One demand originated from the operating requirements for the homopolar generator energy transfer system, which is a pulsed power source for many advanced applications, such as electromagnetic launch [1], pulse resistance welding [2], and high energy high rate powder consolidation processing [3]. To date, studies show that metal (copper or silver)-graphite composites have the most satisfactory performance for solid brush materials [4-7], because they possess the basic properties required by the high current density collector at high sliding speed: a high melting temperature with sufficient mechanical strength and ductility; high thermal and electrical conductivities; and low friction coefficient and low wear rate. Based on the screening tests [4], it was observed that the total contact energy loss and wear rate were minimal when the brush metal mass fraction was around 0.8. Also, it has been suggested that if the electrical conductivity of the copper-graphite composite could be improved, substitution of a copper matrix for a silver matrix might reduce costs for some applications.

In order to maximize electrical conductivity in a copper-graphite composite material, a continuous three dimensional copper network must be formed [8]. Two main manufacturing techniques for conventional metal-graphite composites are by powder metallurgy and by solidification processing such as metal infiltration. Each technique has drawbacks in terms of efficiently utilizing the metal constituent. In the P/M technique, density differences between the metallic constituent and graphite make uniform mixing difficult. Thin, powdery graphite coatings on metal particles during mixing prevent direct metal to metal contact, reducing the strength of metal matrix as well. Differences in thermal expansion coefficients tend to produce discontinuities within the materials made by the infiltration technique.

A new approach which mixed the copper and copper-coated graphite powders for sintering was introduced by Yas et al. [9-10], and later researched by P. K. Lee [11]. In general, it only provides a high plating efficiency for large particle size (100-160 μm), and multiple platings are

needed for thick uniform coatings. For flaky graphite particles, uniform plating is hard to obtain due to the unavoidable agglomeration developed during electrolytic deposition. Further progress made by Lee showed that the sintered copper and copper-coated graphite material had a significant increase in electrical conductivity compared to the commercial material with the same composition. This result indicates that electrical resistivity of a copper-graphite composite can be reduced by forming a continuous copper matrix which is well sintered.

Due to the equilibrium immiscibility between copper and graphite at all temperatures, the interfacial bonds are weak; they can be improved most easily by adding low melting temperature metal binders, such as tin and lead. These increase the wetting between the matrix and graphite particles in the conventional sintering process. However, in the future high current, high speed applications the flash temperatures at the sliding contact interface are so high that the presence of such low melting temperature constituents in brush materials is extremely undesirable. In fact, the melting of the binder phase in a P/M copper-graphite brush was observed at the sliding speed around 220 m/sec at zero current [12]. In addition, the electrical conductivity of copper is very sensitive to impurities [13]. The large interfacial electrical power loss associated with high current density due to contact resistance can be partially reduced by minimizing the brush electrical resistivity, based on a recent contact resistance model [14].

For these reasons, it appears that a binderless copper-graphite composite with sufficient strength has excellent potential as a high current-high speed brush material.

High energy-high rate (HEHR) consolidation employing a pulsed homopolar generator (HPG) is an attractive alternative processing approach for such binderless copper-graphite composites based on the following characteristics: (1) extremely fast processing to minimize time for internal oxidation; (2) rapid heating and cooling rates associated with the pulsed Joule heating; (3) possible microencapsulation by preferential heating and local melting at copper-graphite interface; (4) a dense product with improved mechanical, electrical and thermal properties can be produced by a simultaneous forging action during the rapid heating cycle.

Recent studies on tribological characteristics of powder composite materials based on copper in high speed friction [15] showed that for sliding speeds up to 44 m/s, material containing at least 10 wt.% graphite is capable of forming a surface film which reduces the friction coefficient and can reliably protect the contacting surfaces against bonding; addition of sulfur and molybdenum disulfide in this case essentially did not affect the tribological characteristics.

It is evident now that for a binderless copper-graphite high current brush material, the graphite content should not be less than 10 wt.%, while the copper matrix mass fraction should be as high as possible so that total interfacial power loss (frictional plus electrical) can be minimized and the thermo/mechanical behavior of the interface improved by the elimination of low melting point constituents.

In this HEHR binderless copper-graphite composite brush consolidation, the graphite content is 11 wt.%. The copper and graphite powders used are the same as in a commercial P/M sintered composite which contains 5 wt.% tin and 2 wt.% lead as binders, and 11 w/o graphite. Selection of this composition allows the effects of "binder vs. binderless" and "conventional sintering vs. HEHR consolidation" to be compared directly.

The Consolidation Process

Figure 1 shows the schematic tooling configuration for the HEHR consolidation process. Investigations have involved the use of a 10MJ pulsed HPG as a power source and a modified vertical axis hydraulic press with a 100 ton force capacity. The general operating characteristics of the HPG are described elsewhere [2]. Powders were mechanically mixed and then loaded into the cavity of the die which was made of a dense alumina tube with an inner diameter of 32 mm. After compacting the powders to a desired pressure, the large energy pulse was discharged from the HPG, producing peak currents of ~100kA passing through the powder mixture.

Following the discharge, the pressure was maintained for 3 minutes. This holding period permits conductive heat transfer through the plungers to massive copper platens. The die was then unloaded and the consolidated disk-shaped compact was ejected. The current pulse length ranged

from 1 to 3 seconds, depending on both the magnitude of the stored energy (discharge rpm) and the external system resistance. The magnitude of peak current ranged form 31kA to 136kA, and is a function of the above two parameters. The external system resistance is mainly composed of the die electrode (plunger) resistance and the resistance of the compact. The interfacial resistances are considered negligible for the internally lubricated copper-graphite system within the applied pressure range (240-690 MPa).

Process Parameters

In the series of experiments described here, material variables were kept fixed, i.e., composition (11 wt.% graphite) and type of powders (proprietary copper and graphite powders). The subject of study was the effects of process parameters on the consolidated compact properties. The process parameters used are described in Table 1.

Results and Discussion

General Features of Consolidated Compacts

Three general features were observed for HEHR consolidated compacts:

(1) Preferred orientation. Based on x-ray diffraction patterns and microstructure examination the basal plane of graphite platelets was found to be normal to the compacting direction, except for the limited region near the edge, where back extrusion had occurred.

(2) Anisotropy (axial vs. radial). Electrical resistivity and hardness measurements showed anisotropy between axial and radial directions of the compact. This was attributed to density variation due to stress and temperature distributions [16-17] inside the die during the consolidation, which led to a greater degree of densification in the axial direction.

(3) Absence of oxidation. Although all the processing experiments were conducted in air, the short process time (1-3 seconds) appears to minimize the internal oxidation problems. An as-processed pure copper compact which had a near theoretical density showed an electrical conductivity of 91% of OFHC copper. Hydrogen annealing of this compact would further enhance the conductivity.

Table 1

THE PROCESS PARAMETERS EMPLOYED

COMPACTING PRESSURE:	241-689 MPa
HPG DISCHARGE RPM:	880-1300 (0.15-0.25 MJ)
DIE DIAMETER:	32 mm
POWDER MASS:	15g OR 30g
L/D RATIO:	0.1 OR 0.15
ELECTRODE:	ETP Cu OR 304SS

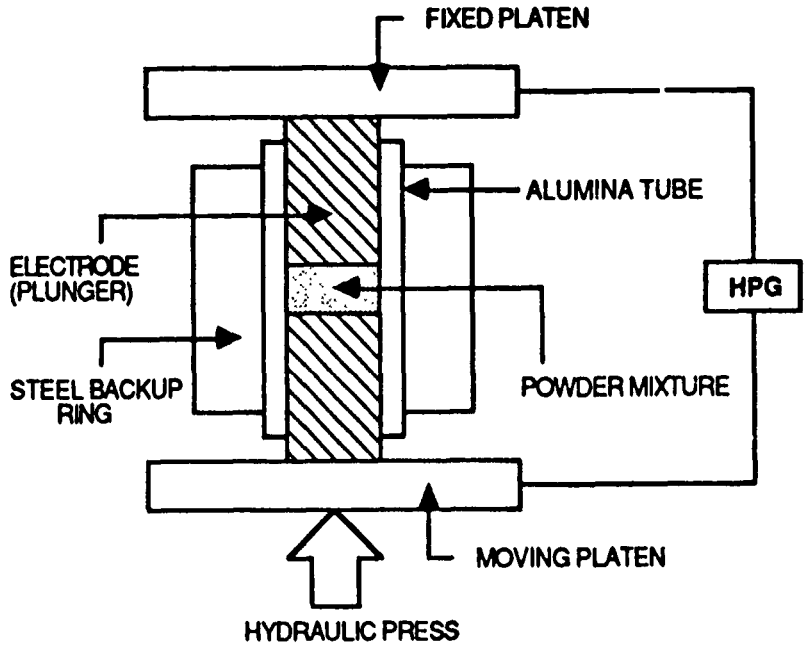

Figure 1 Schematic configuration of the HEHR consolidation process.

Effect of Process Parameters on Compact Properties

(1) Effect of Compacting Pressure

In Figure 2 a linear relationship between the final compact density and the compacting pressure is observed. As the pressure increases from 240 to 690 MPa, the compact density increases from 6.30 to 6.68 g/cm^3 which is 99.85% of the theoretical density. Figure 3 shows that the hardness, which is the average for the hardnesses measured along the radial direction on the compact end surfaces, also increases with the compacting pressure, as a result of density increase. It is obvious that the compacting pressure plays a key role in the copper-graphite composite consolidation when the discharge rpm is fixed, which corresponds to a constant energy input and a specific temperature profile during the discharge.

(2) Effect of Discharge RPM and Powder Mass

Plots of density vs. rpm and hardness vs. rpm are shown in Figures 4 and 5, respectively. A maximum in density or hardness is observed between 880 and 1300 rpm which covers a wide range of energy input (0.15 - 0.25 MJ). A 30g compact developed a higher density than the 15g compact. As discharge rpm increases, the heating rate of the compact becomes faster and the maximum temperature becomes higher due to the characteristics of the HPG pulsed Joule heating. This results in a higher strain rate during densification. On the other hand, a mass increase will cause a lower strain rate, due to a concomitant compact thickness increase. These combined effects indicate there is an optimal strain rate for maximum densification.

(3) Effect of Electrode

Most experiments were done with stainless steel electrodes rather than copper electrodes. This decision was based on the observation that when all other process parameters are the same, stainless steel electrodes produce a denser compact than copper electrodes. In addition, stainless steel can sustain a much higher compacting pressure without any noticeable plastic deformation, and it is therefore generally reusable. Furthermore, problems associated with adhesion between the surfaces of the compact and the electrode are much reduced when stainless steel is used. However, stainless steel consumes a large portion of the input energy due to its large electrical resistivity. The

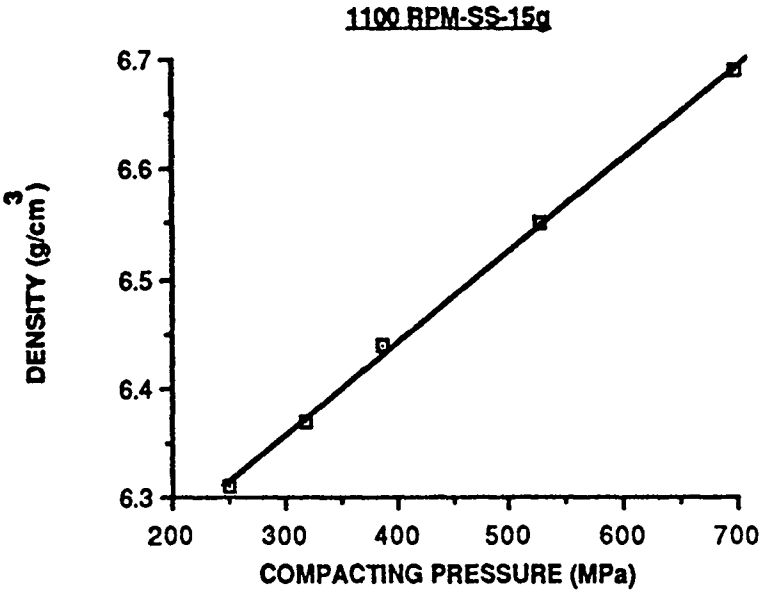

Figure 2 Compacting pressure effect on the compact final density.

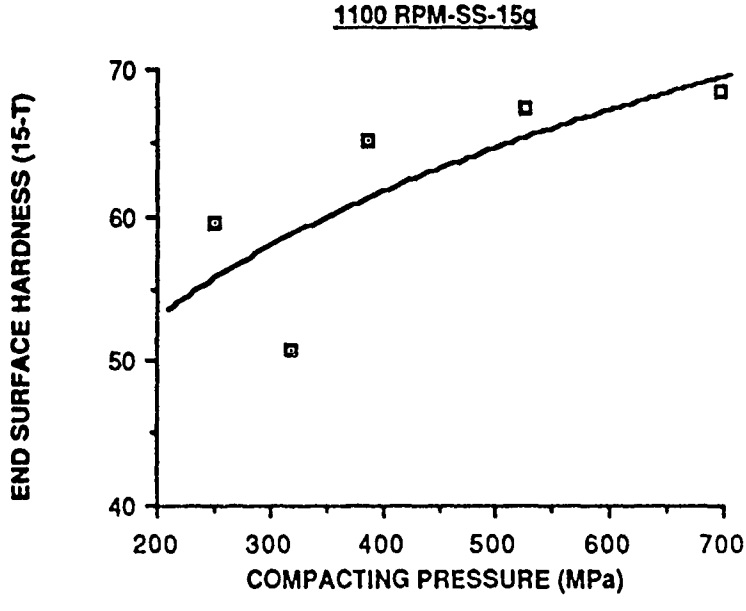

Figure 3 Compacting pressure effect on the compact end surface hardness.

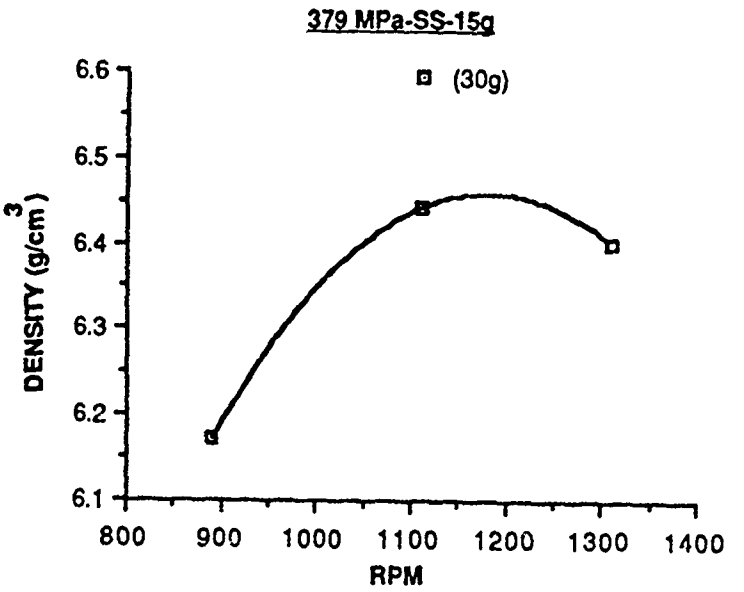

Figure 4 Discharge RPM effect on the compact final density.

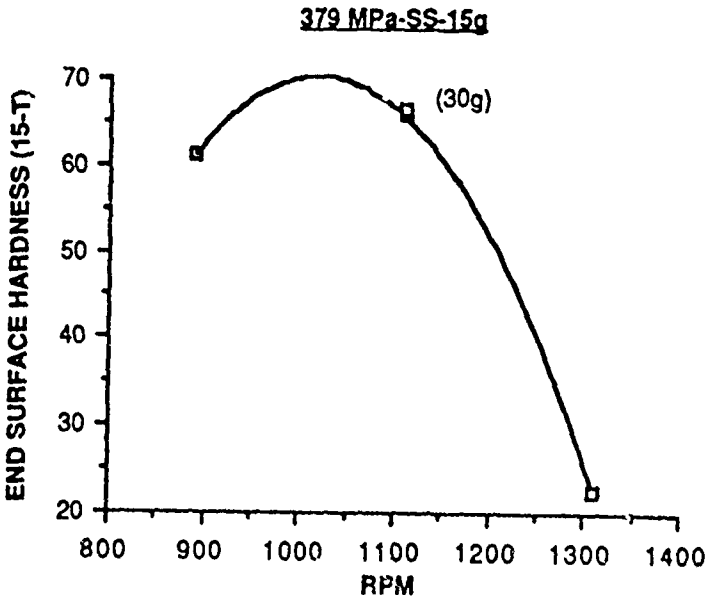

Figure 5 Discharge RPM effect on the compact end surface hardness

temperature rise of the electrodes caused by Joule heating has a very significant influence on the heat transfer at the electrode-compact interface. The high temperature developed in the electrodes has a favorable effect on the net densification by forging.

Figure 6 shows the microstructures of the copper-graphite composites consolidated using different types of electrodes. The retained porosity in the copper matrix after consolidation with copper electrodes is attributed to the rapid heat extraction by conductive heat transfer through the relatively cool copper electrodes.

Microstructures and Resistivity

All the consolidated compacts were sectioned in the radial direction, metallographically prepared, and then examined by SEM. In general, a fairly uniform microstructrue throughout the entire cross-section was observed. Localized recrystallization of copper matrix at the copper-graphite interface was seen in the relatively high density compacts. Dynamic recrystallization seems to have occurred during the process. The morphology and size distribution of the starting materials are shown in Figure 7. Dendritic copper powder with a large internal porosity and the flaky graphite powder are revealed in the micrographs. Microstructural changes with increasing compact density are demonstrated in Figures 8 through 10, which range from a green compact to a near-full density compact. The copper matrix becomes less porous as the density increases. Densification mainly occurs in the copper matrix by effectively closing the internal and inter-particle pores. A recrystallized region at copper-graphite interface can be clearly seen in Figure 10a. Geometric conformity between copper and graphite indicates an improved interfacial strength, as shown in Figure 6a and Figure 10. The strong contrast between Figure 8 and Figure 10 is indicative of the effectiveness of this rapid consolidation process in retaining a very fine microstructure.

Electrical resistivity in the axial direction is plotted against compact density in Figure 11. The theoretical value of electrical resistivity for copper-11 wt.% graphite is calculated based on the law of mixtures. Approximately one order of magnitude decrease in resistivity was attained through the HEHR consolidation. When the electrical conductivity is plotted against the compact density, it

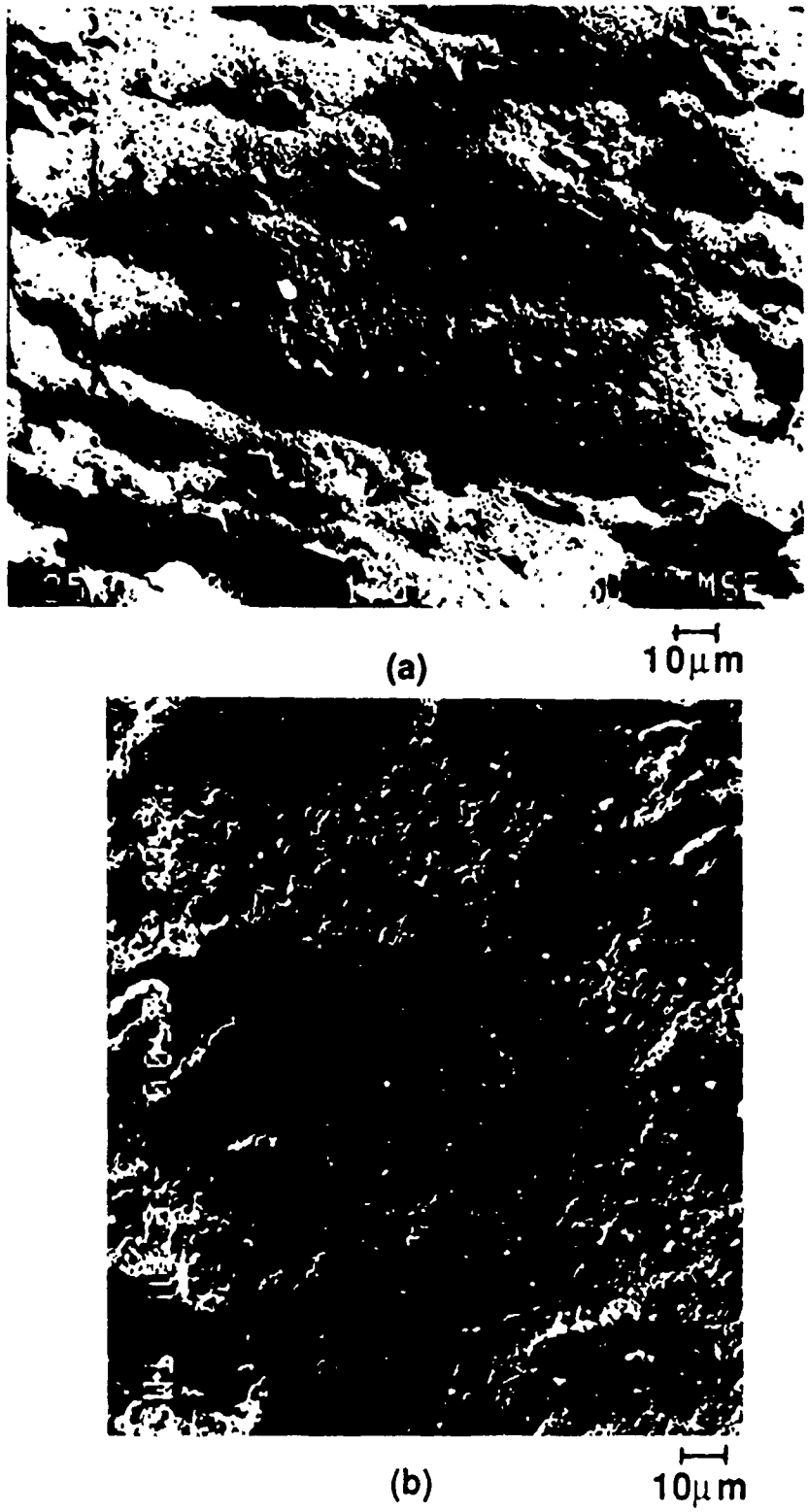

Figure 6 Effect of electrodes on compact microstructure and density
(a) using stainless steel, with a final relative density = 96.2%
(b) using copper electrode, with a final relative density = 92.2%
(compacting pressure = 379 MPa, RPM = 1100, mass = 15g)

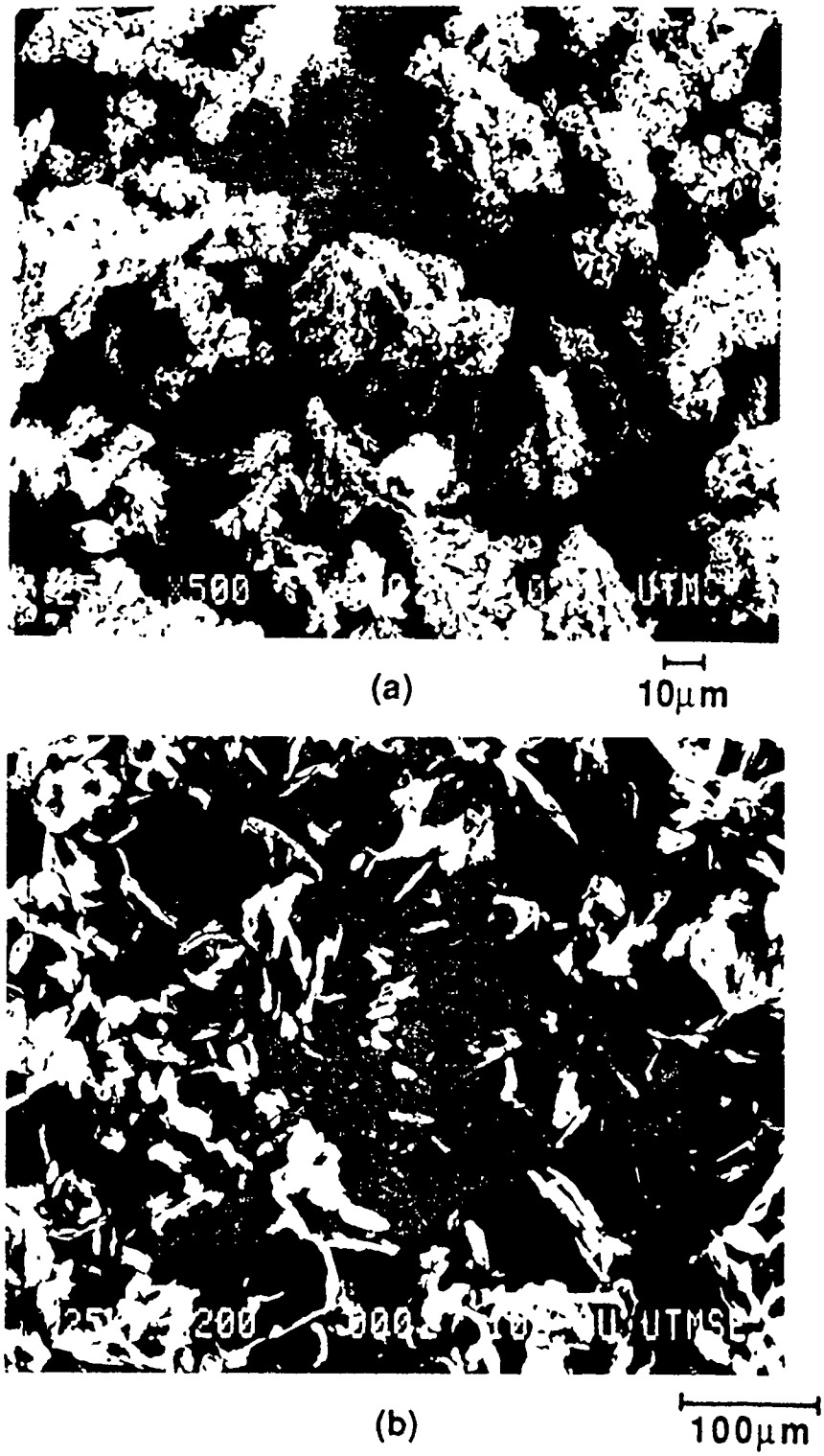

Figure 7 SEM micrographs of (a) dendritic copper powder and (b) flaky graphite powder.

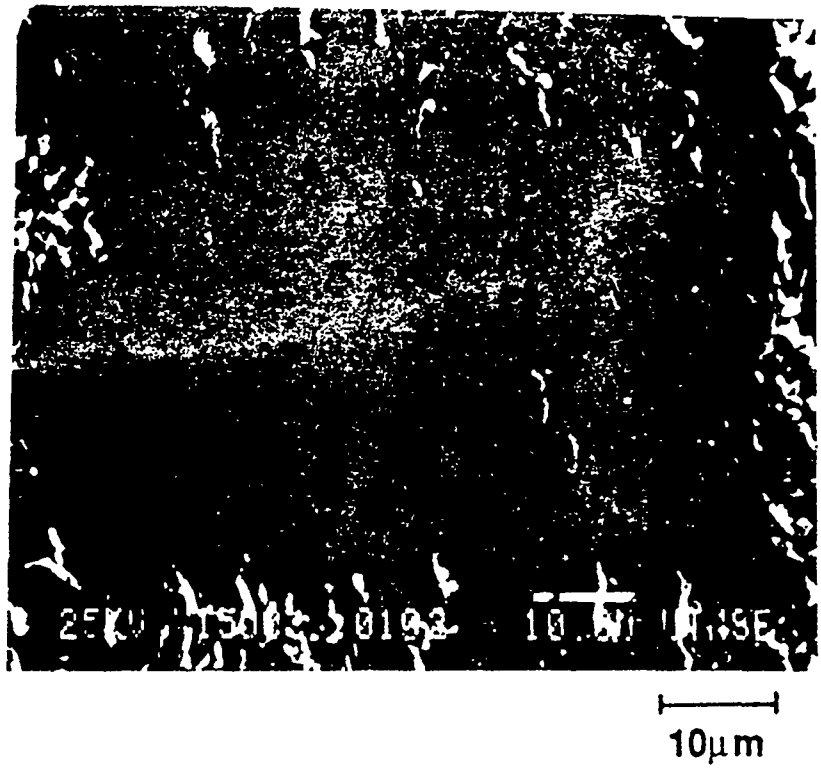

Figure 8 Microstructure of the cold compact (density = 87.6%, compacting pressure = 379 MPa).

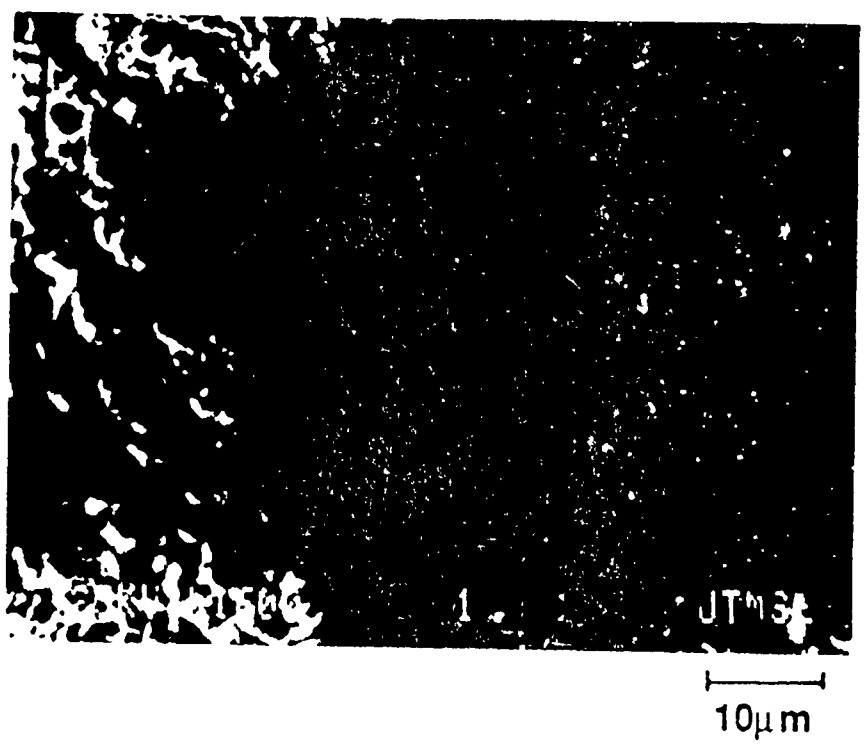

Figure 9 Microstructure of the compact with low energy input. (density = 92.2%, compacting pressure = 379 MPa).

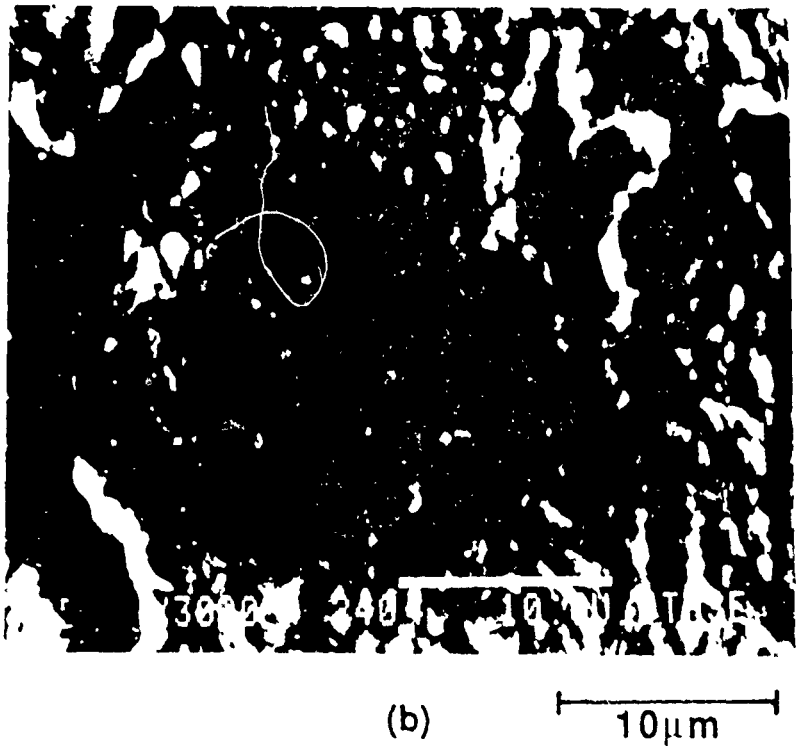

Figure 10 (a) Microstructure of the compact with intermediate energy input. (density = 99.85%, compacting pressure = 689 MPa)
(b) close-up of the copper matrix

is found that up to 6.43 g/cm^3, conductivity increases linearly with density. A similar relationship was observed by Taubenblat in sintered high conductivity copper compacts [18]. The increase of resistivity in the region above 6.43 g/cm^3 is thought to arise from the defects (dislocation) associated with large plastic deformation in the warm forging regime. Comparing the measured resistivity to the theoretical value, it indicates a continuous copper matrix was maintained and a porosity of about 10% was effectively eliminated within 3 seconds by the HEHR consolidation. A projected low resistivity for copper-11 wt.% graphite composite sintered by copper-coated graphite in Figure 5 of reference 11 has actually been achieved by using HEHR consolidation. The reference binder-containing commercial composite which is produced with the same powders, on the other hand, has a resistivity as high as 32 μΩ-cm, with a density of 5.5 g/cm^3, as indicated by the arrow in Figure 11.

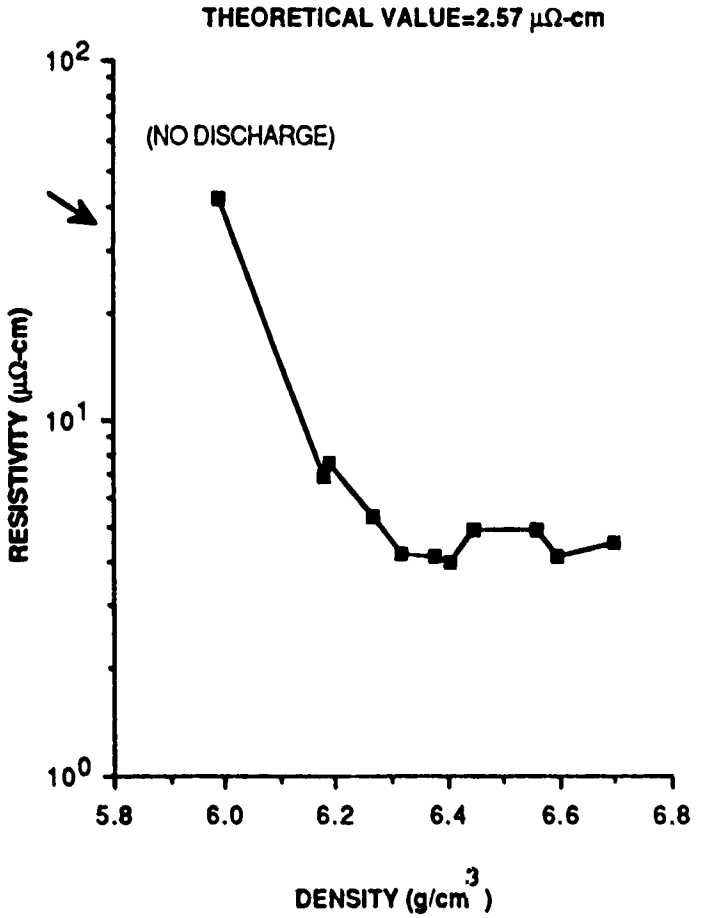

Figure 11 Relation between compact density and axial electrical resistivity.

Nature of Pulsed HPG Heating

In order to explore the nature of the pulsed Joule heating, which is closely related to the mechanism of HEHR consolidation, computer simulation of heat transfer during the process was attempted for the case using copper electrodes. An explicit finite difference method was taken to solve the Fourier equation for an axisymmetric system. Actual dimensions and power input were used. Calculation stability was maintained with a time increment of 1 millisecond. Preliminary results are shown in Figure 12 and 13. A random graphite orientation was assumed and pressure effects were neglected in this case. The total system resistance R was also plotted in Figure 12. T_1 is the temperature at the center of the compact mid-plane. T_3 is the temperature at the center of the compact end surface. T_2 is the temperature at the mid-point between the above two points. T_e is the average temperature of the copper electrodes. The nature of rapid continuous heating and cooling can be easily seen in Figure 12. The heating rate is around $5x10^4$ °C/sec, and the cooling rate is in the vicinity of 500°C/sec. It should be noted that the total resistance which decreases rapidly from the beginning reaches the minimum as the temperature of the compact rises to the peak, indicating the main densification can proceed only as the temperature continues to increase. The same phenomenon was observed in the sintering of fine thoria powder under continuous heating, and it was concluded that the plastic flow was the main densification mechanism [19]. The resistance rise after the minimum can be attributed to the effect of temperature rise in the electrodes. Figure 13 shows the change of temperature distribution on the mid-plane of the compact with time. The highest temperature quickly moves toward the center as the temperature increases. The center then remains at the highest temperature until the end of the discharge. Less heating near the edge results in a relatively low density region, which is confirmed by the hardness measurements.

Preliminary Tribological Evaluation

Preliminary evaluation of brush performance-related properties was accomplished by using three different types of testers for a wide range of sliding speeds (0-200 m/s). The HEHR

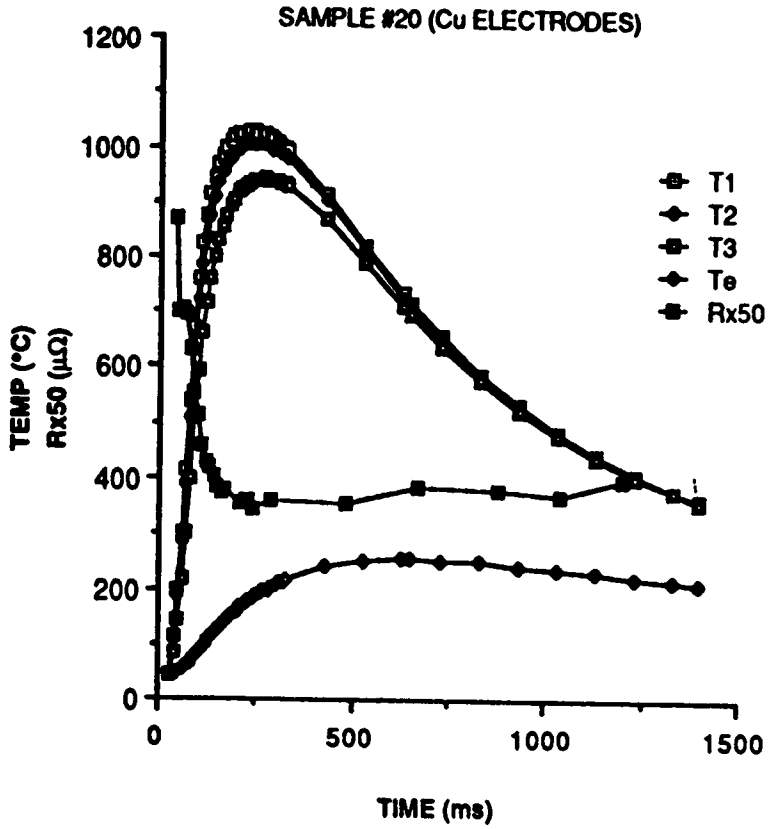

Figure 12 Simulated temperature change with time during powder consolidation process.

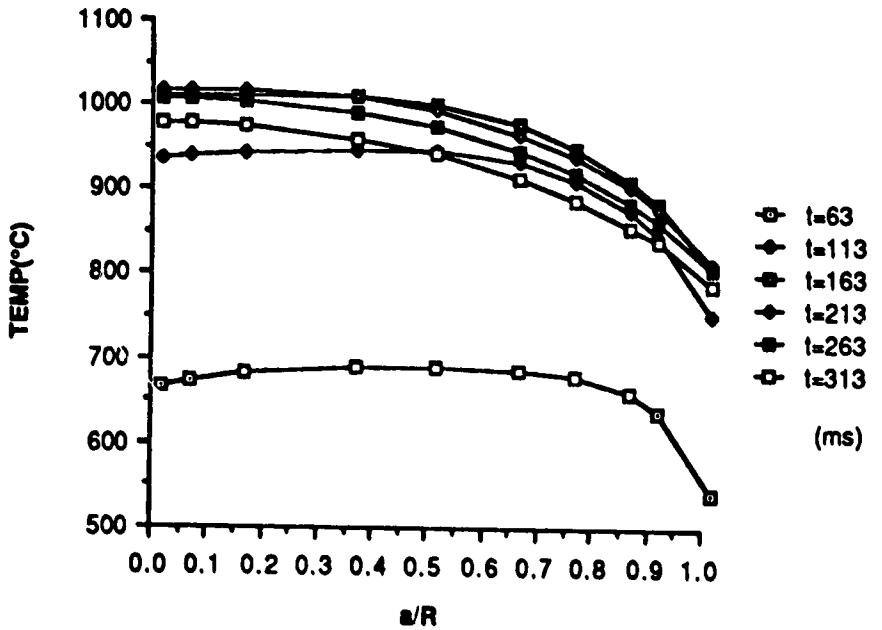

Figure 13 Simulated change of temperature distribution with time on the mid-plane of the compact.

consolidated composites of two different densities, i.e., 6.43 g/cm^3 (B) and 6.58 g/cm^3 (C), along with the commercial P/M composite A were tested.

Pin-On-Disc Tester

The testing conditions and test results are as stated in Table 2. In general, the steady state wear rates were very low. The frictional coefficient of the HEHR consolidated material was significantly lower than the reference material. Moreover, pin B showed an even lower wear rate than pin A, and no transferred copper was found on the wear track of the disc. Surface films were analyzed after the test. The film on pin A was found mainly composed of iron and graphite. This iron and copper interchange indicated that the surface film did not effectively prevent the interfacial bonding which resulted in high friction and relatively higher wear rate. The surface films consisting of copper and graphite on pin B and pin C were of different thicknesses. The higher wear rate and thicker film of pin C, which was consolidated under 517 MPa, were attributed to the internal cracking of graphite caused by this high compacting pressure. This reduced the strength of the graphite and the interfacial bonding between copper matrix and graphite.

The test results obtained here can be interpreted by the wear mechanism proposed by Eliezer et al. for composites [20]. Figure 14 shows the film formed on the pin sliding surface after the test. The EDS iron mapping of surface film on pin A is shown in Figure 15.

Pulsed HPG System Tester

The pulsed HPG system tester was designed as a test bed for HPG components. The composite brushes were discharged at 1000, 1200, and 2400 rpm in the ambient atmosphere without external cooling. For a 2400 rpm discharge, the brush sliding speed is 80 m/s. Due to the technical difficulties encountered during the tests, complete data collection was not accomplished for every discharge. Table 3 shows the test results obtained for 3 discharges. For the HEHR consolidated brushes, no appreciable wear was found when all the tests were finished. A high current density (up to 14 MA/m^2) capability at high sliding speeds was confirmed. A consistent low voltage drop and low contact resistance were observed at brush B.

Table 2

RESULTS FROM PIN-ON-DISC TESTER

DISC: 4340 STEEL (Rc=40)

SLIDING SPEED: 0.6 m/s

ENVIRONMENT: LAB AIR, WITHOUT EXTERNAL LUBRICATION

LOAD/AREA RATIO: 75 N/cm^2

PIN	A	B	C
FRICTION COEFF.	0.31	0.24	0.19
WEAR RATE (10^{-3} mm^3/km)	3.36	1.82	10.2
SURFACE FILM ON PIN	Fe-Gr THIN	Cu-Gr THIN	Cu-Gr THICK
SHAPE OF MAIN DEBRIS	FINE	FINE	FLAKY
COPPER SMEARED ON DISC	YES	NO	YES

Table 3

HIGH SPEED BRUSH TEST ON HPG SYSTEM TESTER

BRUSH DOWN FORCE = 31.2 N

BRUSH FACE AREA= 2.4 cm^2

DISCHARGE RPM	1000			1200			1200		
PULSE LENGTH(S)	5			3			3		
MACHINE VOLTS(V)	2.7			2.2			2.35		
MACHINE CURR(kA)	25			29			31		
TYPE OF BRUSH	A	B	C	A	B	C	A	B	C
BRUSH VOLTAGE DROP(V)	2.4	2.9	1.3	.55	.4	.55	.37	.18	.28
BRUSH CURR(kA)	--	--	--	2.8	3.4	2.04	--	--	--
TEMP(°C)	--	--	--	53	82	--	97	--	84

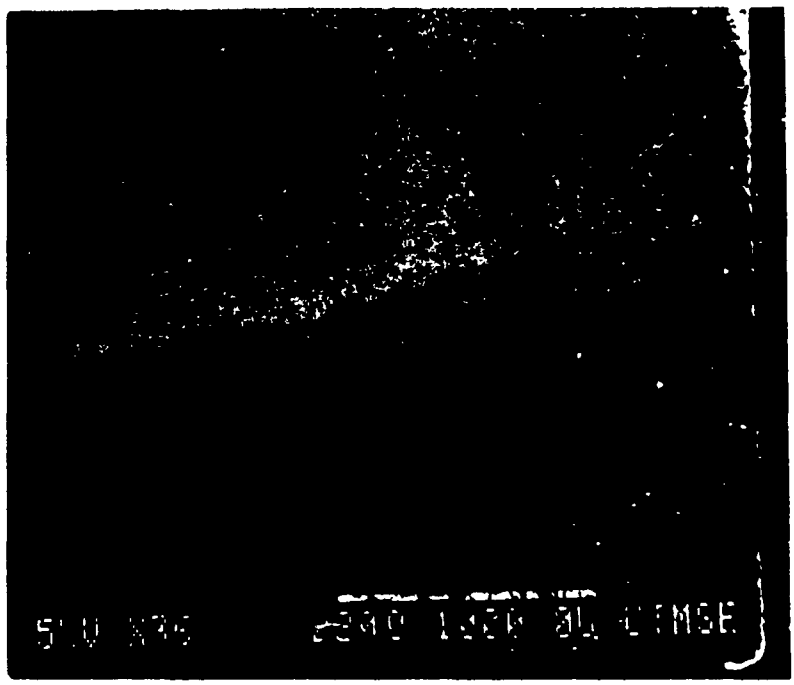

(a)

1000μm

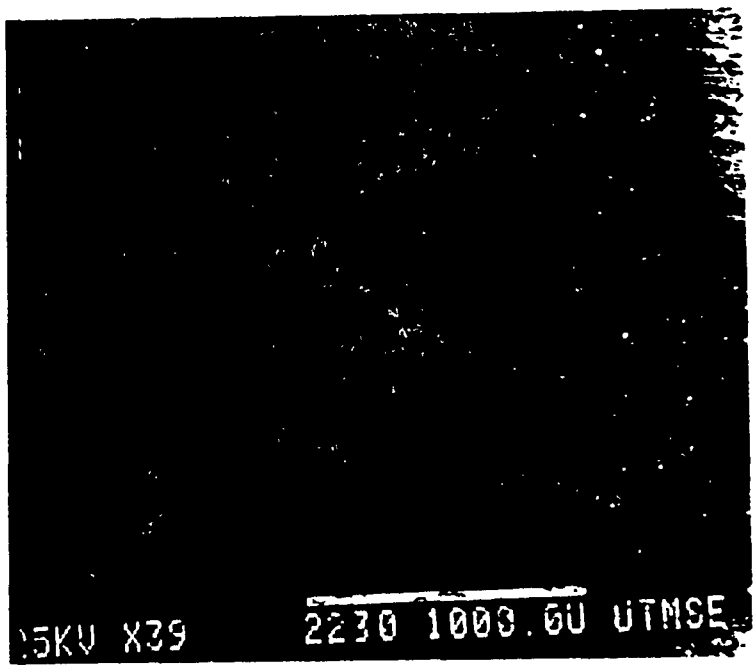

(b)

1000μm

Figure 14 Surface films formed after pin-on-disc test
(a) on pin A, which was a mixture of iron and graphite
(b) on pin D, which was a mixture of copper and graphite

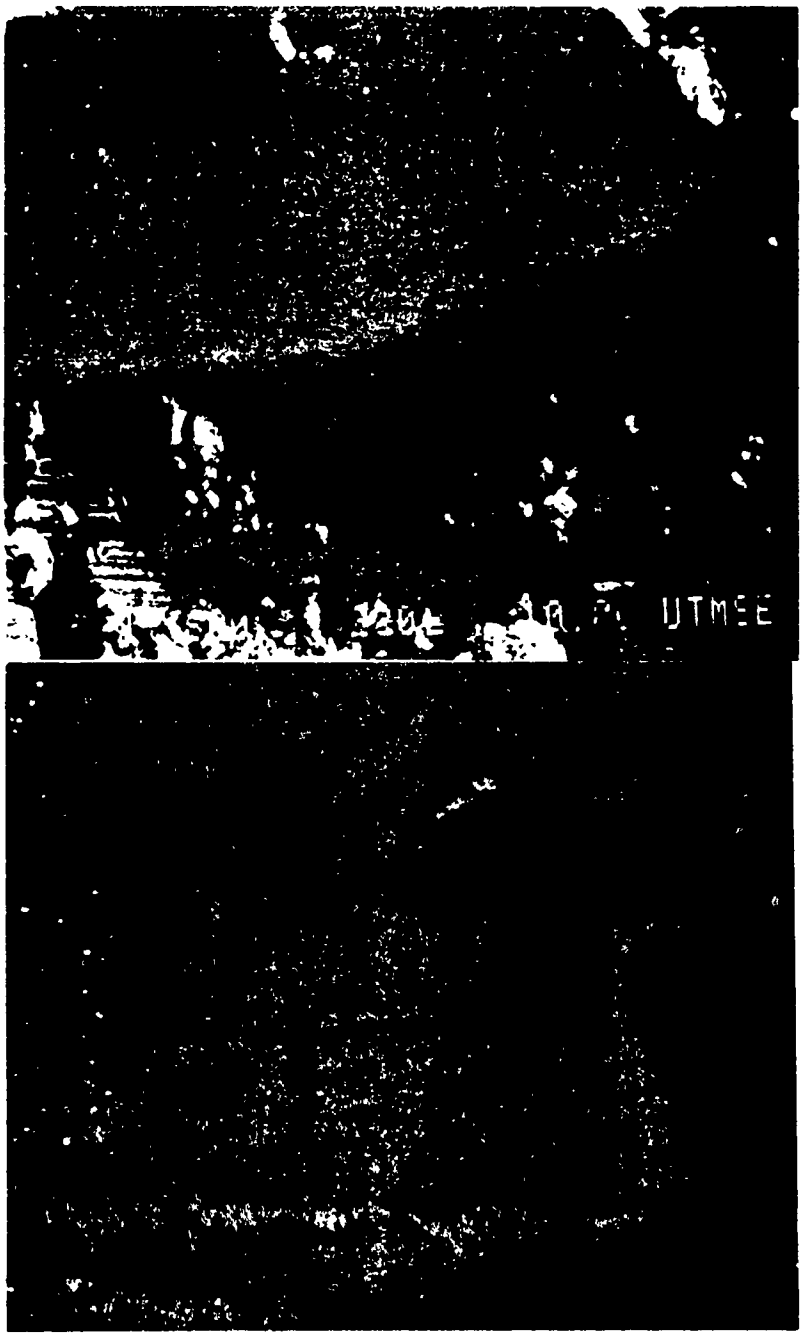

Figure 15 EDS iron mapping of surface film on pin A.

High-Speed Brush Tester

The high speed brush tester was mainly designed for investigation on flash temperature related phenomena. A thermal video imaging system was incorporated with the tester for real time temperature imaging. The HEHR consolidated composite brushes were tested at 50 m/s for 80 minutes and at 200 m/s for 1 minute at zero current. In Figure 16, the wear rates obtained from this test were plotted with those for the reference composite studied by Casstevens et al. [21]. The wear rates for these three composites obtained from the earlier pin-on-disc tester at 0.6 m/s are also plotted in this figure. Even though the load/area ratio is higher in the case of brushes B and C, their wear properties are quite comparable to the reference material A. As the speed goes up to 200 m/s, brushes C and D show only a slight increase over their wear rate at 50 m/s. However, the wear rate of the reference material shows a linear increase with sliding speed, and approximate by one order of magnitude increase in wear rate as speed increases from 50 m/s to 200 m/s. The HEHR consolidated copper-graphite composites clearly demonstrate their superior wear properties at high speeds.

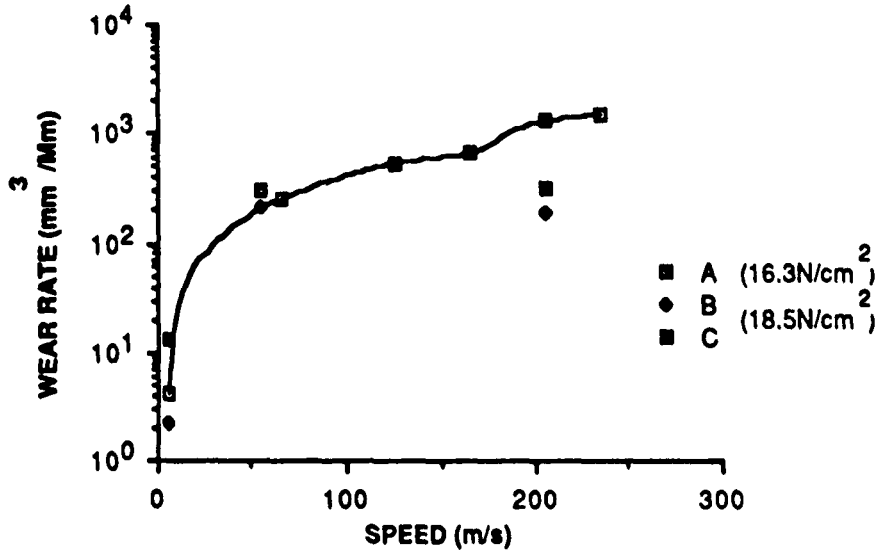

Figure 16 Comparison of wear behavior up to the sliding speed of 200 m/s.

From these experimental results and the electrical resistivity measurements mentioned earlier, the HEHR consolidation process can be developed into a viable alternative technique for producing binderless copper-graphite composite brushes for future, advanced, high-current, high-speed applications.

Conclusions

(1) The main densification mechanism for this P/M copper-graphite system is determined to be plastic flow.

(2) For high-speed, high-current applications, the high-energy/high-rate consolidation process is a promising technique for producing high density, and high electrical conductivity binderless copper-graphite composites with improved strength.

(3) Judicious combination of copper and stainless steel as heat transfer elements in consolidation dies can control the time at temperature and the densification kinetics of these materials.

(4) The tribological behavior of these materials appear especially promising at current densities of >10 MA/m^2 and sliding speeds > 100 m/s.

Acknowledgment

This work was part of M. J. Wang's doctoral dissertation and was supported by DARPA/NADC Contract N6-2269-85-C-0222 and by DARPA/ARO Contract DAAL03-87-K-0073. The authors also would like to thank T. Aanstoos and R. Laughlin for their assistance in processing and testing. Dr. F. L. Vogel and T. McCulfor of Intercal Company are greatly appreciated for the electrical resistivity measurements.

References

1. S. C. Rashleigh and R. A. Marshall, "Electromagnetic Acceleration of Macroparticles to High Velocities," J. App. Phys., 49, 2540 (1978).

2. J. B. Walters and T. A. Aanstoos, "Welding and Billet Heating with Homopolar Generators," Metal Progress 127, pp. 25-28 (1985).

3. K. C. Owen, M. J. Wang, C. Persad and Z. Eliezer, "Preparation and Tribological Evaluation of Copper-Graphite Composites by High Energy High Rate Powder Consolidation," Wear, 120 (1), p. 177 (1987).

4. J. L. Johnson and L. E. Moberly, "High-Current Brushes, Part I: Effect of Brush and Ring Materials," IEEE Trans. Components, Hybrids, Manuf. Technol., CHMT-1, pp. 36-40 (1978).

5. J. M. Casstevens, H. G. Rylander and Z. Eliezer, "Influence of High Velocities and High Current Densities on the Friction and Wear Behavior of Copper-Graphite Brushes at High Sliding Speeds," Wear 49, pp. 169-178 (1978).

6. P. C. Chan, "Materials for Advanced Electric Current Collecting Technique," M.S. Thesis, M.E. Department, Massachusetts Institute of Technology, May 1979.

7. E. Rabinowicz and P. C. Chan, "Wear of Silver-Graphite Brushes Against Various Ring Materials at High Current Density Electrical Contacts," Proc. 25th Holm Conf. on Electrical Contacts, pp. 123-127 (1979).

8. N. S. Dyadenko, A. I. Lunko and T. V. Kholopsteva, "Electrical Resistivity of Copper-Graphite Powder Composites," Porosh. Met., No. 12 (132), pp. 62-66 (1973).

9. D. S. Yas, L. A. Osvetimskii, N. S. Dyadenko, A. A. Zaporozhets, and N. A. Belentsova, "Copper-Graphite Materials with Copper-Clad Graphite Granule Additions I: Effects of Bare and Copper-Clad Graphite on the Strength Characteristics of Cu-Sr Materials," Porosh. Met. No. 5 (101), pp. 70-75 (May 1971).

10. D. S. Yas, V. I. Pavlenko, A. A. Zaporozhets, and N. S. Dyadenko, "Copper-Graphite Materials with Copper-Clad Graphite Granules," Porosh. Met., No. 4 (124), pp. 17-21 (April 1973).

11. P. K. Lee, "High Current Brush Material Development, Part I: Sintered Metal-Coated Graphite," IEEE Trans. Components, Hybrids, Manuf. Technol., CHMT-3, pp. 4-8 (1980).

12. J. M. Casstevens, H. G. Rylander and Z. Eliezer, "Friction and Wear Characteristics of Powder Metallurgy Copper-Graphite Brushes at High Sliding Speeds," Wear 49, pp. 169-178 (1978).

13. F. Pawlek and K. Reichel, Zeitschrift für Metallkunde 47, p. 347 (1956).

14. I. R. McNab and J. L. Johnson, "High-Current Brushes Part III: Performance Evaluation for Sintered Silver-Graphite Grades," IEEE Trans. Components, Hybrids, Manuf. Technol. CHMT-2, pp. 84-89 (1979).

15. I. M. Fedorchenko et al., "Tribological Characteristics of Powder Composite Materials Based on Copper in High-Speed Friction," Porosh. Met. No. 7 (283), pp. 52-56 (July 1986).

16. G. C. Kuczynski and I. Zaplatynky, "Density Distribution in Metal Powder Compacts," Trans. AIME 206, p. 215 (1956).

17. F. V. Lenel, "Resistance Sintering Under Pressure," Trans. AIME 203, p. 158-167 (1955).

18. P. W. Taubenblat, "Techniques for Measuring and Attaining High Electrical Conductivity with Copper Powder Compact," Int. J. of Powder Metallurgy 5 (2), pp. 89-95 (1969).

19. C. S. Morgan and C. S. Yust, "Material Transport During Sintering of Materials with Fluorite Structure," J. of Nuclear Materials 10(3), pp. 182-190 (1963).

20. Z. Eliezer, V. D. Khanna, and M. F. Amateau, "Wear Mechanism in Composites: A Qualitative Model," Wear, 51, pp. 169-179 (1978).

21. J. M. Casstevens, H. G. Rylander and Z. Eliezer, "Friction and Wear Properties of Two Types of Copper-Graphite Brushes Under Severe Sliding Conditions," Wear, 50, p. 376 (1978).

Paper presented at the International Ceramic Conference, Sydney, Australia, August 1988 and published in Ceramic Developments _ Edited by C. C. Sorrell and B. Ben-Nissan
Materials Science Forum Volumes 34-36 (1988)pp. 505-509
Trans Tech Publications Ltd., Switzerland.

A NOVEL PROCESSING TECHNIQUE FOR METAL- CERAMIC COMPOSITES

Z. Eliezer*, M. J. Wang, C. Persad, and J. Gully,
Center for Materials Science and Engineering
The University of Texas, Austin, TX 78712, USA.

INTRODUCTION

Powder-based metal-ceramic composites can be produced by a variety of methods including the use of large electrical currents. For over fifty years it has been known that the direct electrical resistance heating of conductive metallic powder materials can cause densification. The mechanism by which this densification proceeds is material specific and is related to time at temperature during processing. The interest in the use of electrical current for heating of powders has been sporadic [1-5] and has been handicapped by the absence of a well-matched power source.

Over the last decade, devices for the production of pulsed electrical power have enjoyed a developmental thrust. In particular, homopolar generators (HPG) based upon the Faraday disk have been successfully engineered and commercialized[6]. The availability of these machines as pulsed power sources has fostered the development of novel powder processing approaches for metal-ceramic composites.

At the University of Texas at Austin, powder processing powered by a homopolar generator has been developed as a high-energy high-rate (HEHR) materials processing technique[7]. The 1 MJ in 1s pulsed energy delivery from a 10 MJ HPG has been employed in a wide-ranging series of processing experiments. Metal-ceramic composite processing has been studied extensively [8-11]. The material systems characterized have included aluminum-silicon carbide[8], nickel-molybdenum boride[9], and copper-graphite[10, 11].

In what follows we will describe in detail the processing approach employed for the consolidation of copper-graphite composites, and the results of their evaluation as high temperature tribological materials.

In order to obtain a maximum electrical conductivity in a copper-graphite composite material, a continuous three dimensional copper network must be formed. Two manufacturing techniques for conventional copper-graphite composites are powder metallurgy and metal infiltration. In the conventional P/M technique, uniform mixing is difficult to achieve due to the large difference in density between the copper and graphite consituents. A thin graphite coating which develops on metal particles during the mixing prevents direct metal to metal contact, resulting in a low strength matrix. In the infiltration technique, the metal fillers may not be continuous in the porous graphite structure after cooling due to the differences in thermal contraction.

Due to the equilibrium immiscibility between copper and graphite at all temperatures, the interfacial bonds are weak; they can be improved most easily by adding low melting temperature metal binders, such as tin and lead. These increase the wetting between the matrix and graphite particles in the conventional sintering process. However, when used in high-current, high-speed sliding contact applications the flash temperatures at the sliding contact interface are so high that the low melting temperature constituents of the brush materials are extremely undesirable. In fact, the melting of the binder phase in a P/M copper-graphite brush was observed at the sliding speed of 220 m/s without carrying any current[12]. In addition, the electrical conductivity of copper is very sensitive to the impurities. The large interfacial electrical power loss associated with high current density and contact resistance can be partially offset by minimizing the brush electrical resistivity, as recently described in a contact resistance model[13].

For these reasons, binderless copper-graphite composites with sufficient strength are the most desirable candidates for high-current high-speed brush materials.

High-energy high-rate consolidation employing a homopolar generator is an attractive alternative processing approach for binderless copper-graphite composites based on the following characteristics: (1) extremely fast processing to minimize time for internal oxidation; (2) rapid heating and cooling rates associated with the pulsed Joule heating; (3) possible microencapsulation by preferential heating and local melting at copper-graphite interface; (4) a dense product with improved mechanical, electrical and thermal properties can be produced by simultaneous forging during the discharge.

EXPERIMENTAL APPROACH

Materials: Studies indicate that for a binderless copper-graphite high-current brush material, the graphite content should not be less than 10 w/o, while the copper matrix mass fraction should be as high as possible. In this HEHR binderless copper-graphite composite brush consolidation, the graphite content is thus selected as 11 w/o. The copper and graphite powders used are the same as in a commercial P/M sintered composite which contains 5 w/o tin, 2 w/o lead as binders, and 11 w/o graphite. The appearance of the starting powders is shown in figure 1, which indicates the morphology and size distribution of the dendritic copper powders and the flaky graphite.

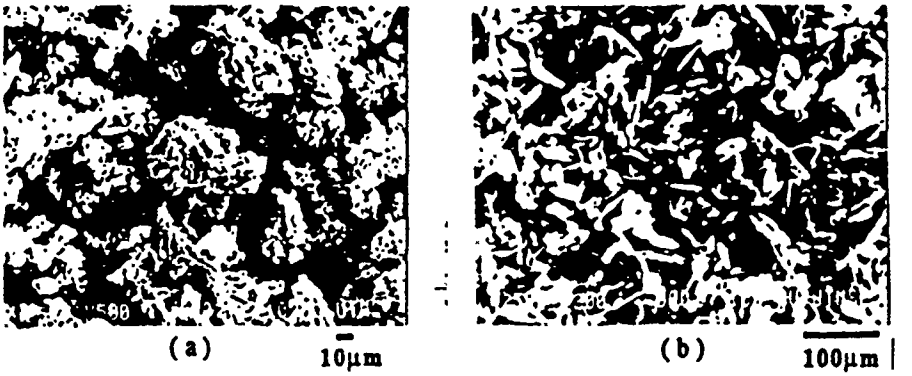

Figure 1 SEM micrographs of (a) dendritic copper powder and (b) flaky graphite powder.

The Consolidation Process: Figure 2 shows the schematic tooling configuration of the HEHR consolidation process. Investigations have involved the use of a 10 MJ pulsed HPG as a power source and a modified vertical axis hydraulic press with a 890 kN(100 ton force) capacity. The operating characteristics of the HPG are described elsewhere [14]. Powders are mechanically mixed and then loaded into the cavity of the die which was made of a dense alumina tube with an inner diameter of 32 mm. After compacting the powders to a desired pressure, the large current pulse was discharged from the HPG, passing through the powder mixture.

Following the discharge, the pressure was maintained for 180s. This holding period permits conductive heat transfer through the plungers to massive copper platens. The die was then unloaded and the consolidated compact was ejected The current pulse length ranged from 1 to 3 seconds, depending on both the discharge rpm and the external system resistance. The peak current ranged from 31kA to 136 kA, depending again on the above two parameters. The external system resistance was mainly composed of the electrode (plunger) resistance and the resistance of the compact. The interfacial resistances are considered negligible within the pressure range applied (241-689 MPa).

Table 1

THE PROCESS PARAMETERS EMPLOYED

COMPACTING PRESSURE:	241-689 MPa
HPG DISCHARGE RPM:	880-1300 (0.15-0.25 MJ)
DIE DIAMETER:	32 mm
POWDER MASS:	15g OR 30g
L/D RATIO:	0.1 OR 0.15
ELECTRODE:	ETP Cu OR 304SS

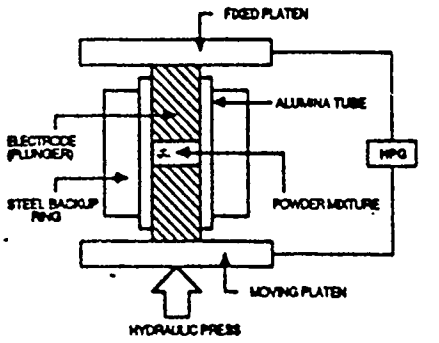

Figure 2 Schematic configuration of the HEHR consolidation process.

Process Parameters: In this series of experiments, material variables were kept fixed, i.e., composition (11 w/o graphite) and type of powders (proprietary copper and graphite powders). Emphasis was given to the effects of process parameters on the consolidated compact properties. The process parameters used are described in table 1.

RESULTS AND DISCUSSION

General Features of Consolidated Compacts: Three general features were observed for HEHR consolidated compacts:

(1) Preferred orientation : Based on x-ray diffraction patterns and microstructure examination the basal planes of graphite platelets were found to be normal to the compacting direction, except for the limited region near the edge which had been back extruded. The uniaxial compression with large height -to-diameter (L/D) ratio is responsible for this phenomenon.

(2) Anisotropy (axial vs radial) : Electrical resistivity and hardness measurements showed anisotropy between axial and radial directions of the compact. This was mainly attributed to density variation due to stress and temperature distributions inside the die during the consolidation, which led to a greater degree of densification in the axial direction [3,15].

(3) Absence of oxidation : Although all processing was conducted in air, the short process time at high temperature minimizes the degree of internal oxidation. An as-processed pure copper compact which had a near theoretical density showed a 91% electrical conductivity relative to OFHC copper. Hydrogen annealing of this compact would further enhance the conductivity.

Effect of Compacting Pressure: In figure 3 a linear relationship between the final compact density and the compacting pressure is observed. As the pressure increases from 241 to 689 MPa, the compact density increases from 6.30 to 6.68 g/cm^3 which is 99.85% of the theoretical density. Figure 4 shows that the hardness which is the average of the hardnesses measured along the radial direction on the compact end surfaces also increases with the compacting pressure, as a result of density increase. It is obvious that the compacting pressure plays a key role in the copper-graphite composite consolidation when the discharge rpm is fixed, which corresponds to a constant energy input and the development of specific temperature profile during the discharge.

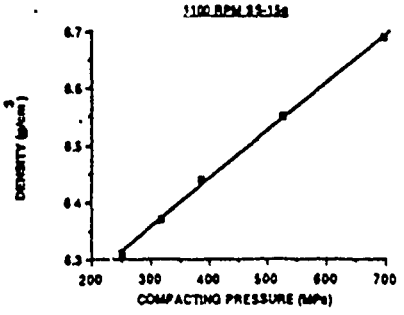

Figure 3 Compacting pressure effect on the compact final density.

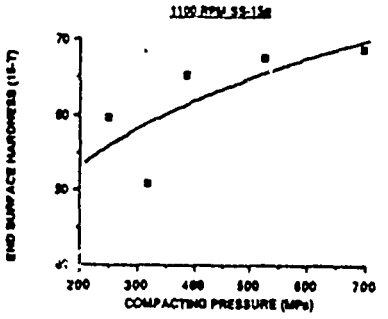

Figure 4 Compacting pressure effect on the compact end surface hardness.

Effect of Electrode Materials: Most experiments were done with stainless steel electrodes rather than copper electrodes. This is based on the fact that when all other process parameters are the same, stainless steel electrodes produce a denser compact than copper electrodes. Several factors account for this: a) stainless steel can sustain a much higher compacting pressure without any noticeable plastic deformation; b) while stainless steel consumes a large portion of the input energy due to its large electrical resistivity, the temperature rise of the electrodes caused by Joule heating has a very significant influence on the heat transfer at the electrode-compact interface, establishing a transient heat barrier for the compact during densification; c) the total amount of energy delivered to the load is higher in the case of stainless steel because the lower energy loss at brush-rotor interface associated with the smaller peak current and longer pulse length makes the energy conversion more efficient; d) the adhesion between the densified copper-graphite compact and the electrode is reduced; e) the electrodes are generally reusable.

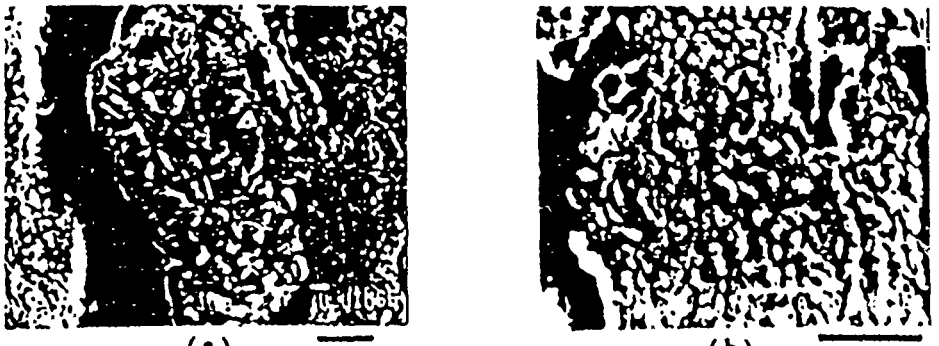

Figure 5 (a) Microstructure of the compact with intermediate energy input. (density = 99.85%, compacting pressure = 689 MPa) (b) close-up of the copper matrix

Microstructures and Resistivity: All the consolidated compacts were sectioned in the radial direction, metallographically prepared, and then examined by SEM. In general, a fairly uniform microstructure throughout the entire cross-section was observed. Localized recrystallization of copper matrix at the copper-graphite interface was seen in the relatively high density compacts. Dynamic recrystallization seems to have occurred during the process. Densification occurs in the copper matrix by effectively closing the internal and inter-particle pores. Excellent conformity between copper and graphite indicates an improved interfacial strength, as shown in figure 5. The microstructure in the densified composite material indicates the success of this rapid consolidation process in retaining very fine microstructure.

Electrical resistivity in the axial direction is plotted against compact density in figure 6. The theoretical value of electrical resistivity for copper-11 w/o graphite is calculated based on the law of mixtures. An order of magnitude decrease in resistivity was attained through the HEHR consolidation. When the electrical conductivity is plotted against the compact density, it is found that up to 6.43 g/cm^3, conductivity increases linearly with density. A similar relationship was observed by Taubenblat in sintered high conductivity copper compacts[16]. The increase of resistivity in the region above 6.43 g/cm^3 most likely results from the defects (high dislocation density) associated with large plastic deformation in the continuously cooled compacts. A comparison of the measured resistivity to the theoretical value indicates that a continuous copper matrix was maintained and a porosity of about 10% was effectively eliminated within 3 seconds by the HEHR consolidation. A projected low resistivity for copper-11 w/o graphite composite made from sintered copper-coated graphite [17] has been achieved by using HEHR consolidation. The reference commercial composite which is produced from similar powder stock has a resistivity of 37 μΩ-cm, with a density of 5.5 g/cm^3, as indicated by the arrow in figure 6.

Nature of Pulsed HPG Heating: In order to explore the effectiveness of the pulsed Joule heating, which is closely related to the mechanism of HEHR consolidation, computer simulation of heat transfer during the process was attempted. An explicit finite difference method was taken to solve the Fourier equation for an axisymmetric system. Actual dimensions and power input were used. Calculation stability was maintained with a time increment of 1 millisecond. The nature of rapid continuous heating and cooling can be easily seen in figure 7. The heating rate is around 5x10^4 K/s, and the cooling rate is in the vicinity of 500 K/s. It should be noted that the total resistance which decreases rapidly from the beginning reaches the minimum as the temperature of the compact rises to the peak,

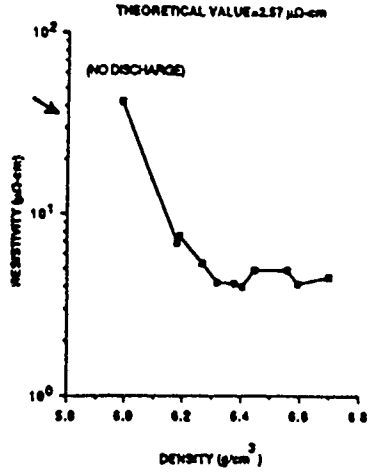

Figure 6 Relation between compact density and axial electrical resistivity.

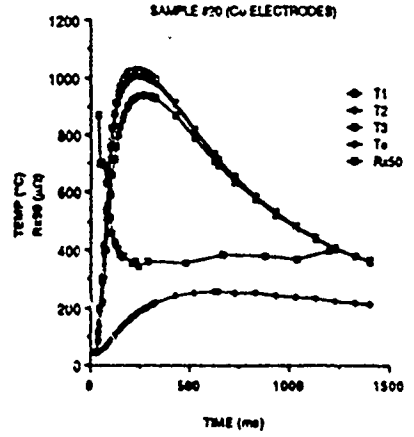

Figure 7 Simulated temperature change with time during powder consolidation process.

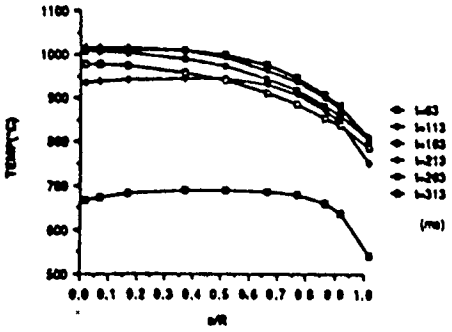

Figure 8 Simulated change of temperature distribution with time on the mid-plane of the compact.

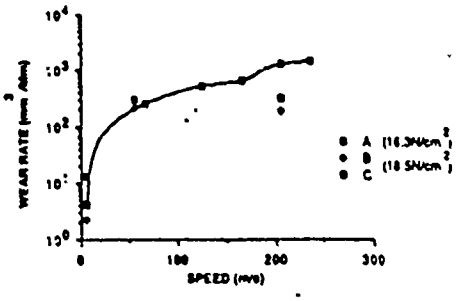

Figure 9 Comparison of wear behavior up to the sliding speed of 200 m/s.

indicating the main densification can proceed only as the temperature continues to increase. The same phenomenon was observed in the sintering of fine thoria powder under continuous heating, and it was concluded that plastic flow was the main densification mechanism[18]. The resistance rise after it reaches the minimum can be attributed to the effect of temperature rise in the electrodes. Figure 8 shows the change of temperature distribution on the mid-plane of the compact with time. The highest temperature quickly moves towards the center as the temperature increases. The center continues then to exhibit the highest temperature until the end of the discharge.

Tribological Evaluation: Preliminary evaluation of brush performance-related properties was accomplished by using testers with a wide range of sliding speeds (0-200 m/s). The HEHR consolidated composites of two different densities, i.e., 6.43 g/cm^3 (B) and 6.58 g/cm^3 (C), along with the commercial P/M composite (A) were tested.

(1) Pulsed HPG system tester : The pulsed HPG system tester was designed as a test bed for HPG components. It allows simulation of the operating environment of HPG brushes. Voltage drop, current and temperature were measured. The composite brushes were discharged at 1000, 1200, and 2400 rpm in air without external cooling. For a 2400 rpm discharge, the brush sliding speed is 80 m/s. Table 2 shows the test results obtained for 3 discharges. For the HEHR consolidated brushes, no appreciable wear was found when all the tests were finished. A high current density (up to 14 MA/m^2) capability at high sliding speeds was confirmed. A consistent low voltage drop and low contact resistance were observed at brush B.

Table 2

HIGH SPEED BRUSH TEST ON HPG SYSTEM TESTER

BRUSH DOWN FORCE = 31.2 N

BRUSH FACE AREA= 2.4 cm^2

DISCHARGE RPM	1000			1200			1200		
PULSE LENGTH(S)	5			3			3		
MACHINE VOLTS(V)	2.7			2.2			2.35		
MACHINE CURR(kA)	25			29			31		
TYPE OF BRUSH	A	B	C	A	B	C	A	B	C
BRUSH VOLTAGE DROP(V)	2.4	2.9	1.3	.55	.4	.55	.37	.18	.28
BRUSH CURR(kA)	—	—	—	2.8	3.4	2.04	—	—	—
TEMP(°C)	—	—	—	53	82	—	97	—	84

(2) High-speed brush tester : The high speed brush tester was mainly designed for investigation on flash temperature related phenomena. A thermal video imaging system was incorporated with the tester for real time temperature imaging. Continuous testing at speeds of up to 200 m/s at 6000 A is possible. The HEHR consolidated composite brushes were tested at 50 m/s for 80 minutes and at 200 m/s for 1 minute at zero current. In figure 9, the wear rates obtained from these tests were plotted with those for the reference composite studied by Casstevens et al.[19]. The wear rates for these three composites obtained from a pin-on-disk tester at 0.6 m/s are also plotted in this figure. Even though the load/area ratio is higher in the case of brushes B and C, their wear properties are quite comparable to the reference material A. As the speed goes up to 200 m/s, brushes B and C show only a slight increase over their wear rate at 50 m/s. However, the wear rate of the reference material A shows a linear increase with sliding speed, and exhibits approximately one order of magnitude increase in wear rate as speed increases from 50 m/s to 200 m/s. The HEHR consolidated copper-graphite composites clearly demonstrate their superior wear properties at high speeds.

ACKNOWLEDGMENT

This research received support from DARPA/ARO CONTRACT DAAL 0387-K-0073 and from the Texas Advanced Research Program under Grant No. 4357.

REFERENCES

1) Taylor, G. F. : Apparatus for Making Hard Metal Compositions, U. S. Patent 1,896,844, February 1933.
2) Ross, W. D. : Method and Apparatus for Making Solid Objects, U. S. Patent 2,355,954, August 1945.
3) Lenel, F. V. : J. of Metals, 1955, 7, 158.
4) Isserow, S. : Impulse Resistance Sintering of Compounds for Armor Applications, AMMRC-TR 73-43, 1973.
5) Persad, C., Marcus, H. L. and Weldon, W. F. : High-Energy High-Rate Pulsed Power Processing of Materials by Powder Consolidation and by Railgun Deposition, UTCMSE-87-02, March 1987.
6) Gully, J. H., Aanstoos, T. A., Nalty, K. and Walls, W. A. : IEEE Trans. Magnetics, 1986, 22, 1489.
7) Marcus, H.L., Bourell, D.L., Eliezer, Z., Persad, C. and Weldon, W. F. : J. of Metals, 1987, 39, 6.
8) Elkabir, G., PhD Dissertation, The University of Texas at Austin, August 1987.
9) Kim, Y.-W., PhD Dissertation, The University of Texas at Austin, December 1987.
10) Owen, K. C., MS Thesis, The University of Texas at Austin, August 1986.
11) Owen, K. C., Wang, M. J., Persad, C. and Eliezer, Z. : Wear, 1987, 120,177.
12) Casstevens, J. M., Rylander, H. G. and Eliezer, Z. : Wear , 1978, 49, 169.
13) McNab, I. R. and Johnson, J. L. : IEEE Trans. CHMT , 1979, CHMT-2, 84.
14) Walters, J. B. and Aanstoos, T. A. : Metals Progress, 1985, 127, 25.
15) Kuczynski, G. C. and Zaplatynky, I. : Trans. AIME, 1956, 206, 215.
16) Taubenblat, P. W. : Int. J. of Powder Metallurgy, 1969, 5, 89.
17) Lee, P. K. : IEEE Trans. CHMT , 1980, CHMT-3, 4.
18) Morgan, C. S. and Yust, C. S. : J. of Nuclear Materials, 1963, 10, 182.
19) Casstevens, J. M., Rylander, H. G. and Eliezer, Z. : Wear, 1978, 50, 376.

ADVANCED COMPOSITE MATERIALS FOR HIGH-PERFORMANCE ELECTROTRIBOLOGICAL APPLICATIONS

C. Persad, S.C. Sparks, D. Moore, M. Schmerling, Z. Eliezer

Center for Materials Science and Engineering

and

J. Gully, R. Carnes

Center for Electromechanics

The University of Texas at Austin

Austin, TX 78172

Abstract

Current collection in high-current electrical machines imposes severe electrotribological duty on sliding electrical contacts. Examples of such duty are found in the contacts in homopolar machines where velocities of 200 m/s and current densities of 2 kA/cm^2 must be sustained. Even more demanding are the requirements placed on solid armatures in electromagnetic accelerators, where velocities > 2000 m/s and current densities of 200 kA/cm^2 are desired. For these applications, self-lubricating composites with high electrical conductivity are being developed.

Binderless copper-graphite powder composites are promising materials for low-wear sliding electrical contacts at velocities of ~200 m/s and at current densities > 1 kA/cm^2. These materials are made by a process which employs "1 MJ in 1s" pulse resistive heating of a powder mass under pressure. Composites processed in this way have higher densities, hardnesses, and electrical conductivity than conventional commercial materials containing low temperature binders. The wear rate of the copper/graphite-on-steel couple at high sliding speeds (> 100 m/s) appears to be controlled by the size, volume fraction, and orientation of the graphite.

For solid armatures in electromagnetic accelerators, the state-of-the-art system consists of a high conductivity aluminum alloy sliding on copper. At velocities of 1000 m/s to 2000 m/s, this type of armature undergoes a hybridization process in which a fluid is formed at the sliding interface. Energy dissipation at the interface is increased as a consequence, and the net result is a decrease in efficiency of the conversion of electrical energy into kinetic energy. For this application, a variety of composite materials approaches are under development. These include an aluminum-alumina composite with graded electrical resistance; a copper-tungsten planar composite; a tungsten-copper powder composite; and a tungsten-tungsten carbide-carbon-copper composite with nanosized constituents.

Introduction

In this paper we describe several advanced composite materials being developed for current collection in two classes of high-performance electrical machines: homopolar pulse generators; and electromagnetic launchers. Current collection is performed under sliding conditions hence the use of the descriptor "electrotribological.".

Homopolar pulse generators transform rotational kinetic energy into electrical energy utilizing the Faraday effect. A low voltage, high impedance, megampere current source is obtained by rotating a metal disk in a magnetic field and harvesting the energy pulse during the braking of the disk to a stop. Pulsed power technology has enjoyed a recent resurgence and has been identified as a critical technology for the USA (1). The homopolar pulse generator technology is one of the enabling technologies for efficient pulsed power. More directly pertinent to this study is the recognition of homopolar generator current-collecting contacts (brushes) as a tribo-materials requirement for critical applications (2).

Electromagnetic launchers are capable of delivering high kinetic energy payloads such as those required for earth–to–space launch. Velocities >1 km/s are obtained by accelerating a solid armature between two conductors (or rails). Barber (3) has defined this as the hypervelocity sliding contact regime and has described some of the armature/rail interactions leading to the formation of a fluid interlayer. The fluid interlayer initiation has been reported to be a strong function of both the sliding velocity and the contacting materials (4).

The current density and velocity associated with the homopolar pulse generator and electromagnetic launcher applications are mapped in Figure 1. Their schematic operational arrangements are shown in Figure 2.

It is well established that a number of composite materials systems exhibit the characteristics necessary for high performance sliding electrical contacts. When based on

powder constituents, such composites provide some of the necessary product properties by selection and assembly of material at the microscopic level. The relationship between the tribological behavior of such contacts and their basic materials science is the subject of a large body of studies (5–15). A key issue is the value of the maximum temperature that can be sustained by the contact at the sliding interface, while maintaining the efficient energy transfer associated with solid-to-solid contact. In these applications, the complex electrotribological environments encountered provide multiple interface heating sources, as indicated in figure 2 (a) for a homopolar generator brush. Achieving the necessary performance demands novel approaches to the design, processing, characterization and laboratory testing of suitable materials.

Approach

A qualitative summary of the approach that we describe here includes the following steps:

- Design a material that can sustain maximum temperature at the sliding interface;

- Incorporate constituents that can provide the necessary physical properties: electrical conductivity, thermal conductivity, hardness, lubricity,etc.;

- Satisfy the technological demands of processability in the appropriate size and shape and at minimum cost.

The design of the new contact materials begins with the question: how do these materials normally fail? The simple answer is that they fail because the temperature at the sliding interface is too high. The high temperature is caused by localized dissipation of electrical and mechanical energy at the interface. The underlying theoretical limits have been described by Kuhlmann–Wilsdorf (16). How best to handle the high interface

temperature? Three possibilities are: eliminate the source; actively cool the contact: design a material that can survive the elevated temperature. The thrust of this work is to design materials that can survive the elevated temperatures developed in electrotribological duty.

Experimental Procedure

I. Materials Systems

A summary of the materials systems discussed in this paper is given in Table 1.

Table 1. Materials systems being investigated for high-performance electrotribological applications.

Contact Type/ Constituents	Development Status	Performance/Characteristics
Composite Brushes		
Cu-Gr-Sn-Pb	Commercial Material	Used in present generation of pulse homopolar machines. Fails at 220 m/s due to catastrophic wear.
Binderless Cu-Gr	Experimental Material	Proposed for use in future pulse homopolar machines. Hardness and conductivity exceed that of commercial material.
Composite Armatures		
W- Cu(90/10)	Experimental Material	Hardness and conductivity exceed that of the 90W-10Cu commercially available material.
W-WC-C-Cu	Experimental Material	Nanosized constituents increase population of potential contact spots.

For the solid armatures, the fabrication of a powder-based aluminum-alumina composite and a laminar copper-tungsten composite were described previously (17). The laminar

copper–tungsten composite was constructed from copper foils and tungsten mesh. These materials were stacked such that the controlled variation in spacing between the exposed tungsten fibers in the consolidated composite would yield a graded electrical resistivity.

II. The Consolidation Process

Two of the experimental materials are listed in Table 1 (the binderless copper-graphite for composite brushes and the tungsten-copper for solid armatures) were consolidated from powders using a single-residence materials processing technique developed in our laboratories (18). This high-energy high-rate processing technique has been successfully applied to a wide variety of single phase and composite materials (19–25). A 10 MJ homopolar generator (HPG) dedicated to industrial applications was the pulsed power source used in conjunction with a modified 100 ton vertical axis hydraulic press.

The dies and starting materials were initially at ambient temperature. Consolidation was performed in laboratory air at pressures of 300 to 400 MPa. After compacting the precursors to a desired pressure, a large current pulse was used to heat and consolidate the composite material. Following the discharge, the pressure was maintained for a brief holding period, thus permitting conductive heat transfer through the plungers to massive copper platens. The die was then unloaded and the consolidated compact was ejected.

The voltage drop across the compact and the magnitude of the current were recorded during the pulse. The product of these values was used to obtain the power curve during the pulse. The power curve was numerically integrated to produce the total energy input to the specimen. Division of the total energy input by the mass consolidated yields the specific energy input (SEI) in units of J/g. The SEI approximates the enthalpic heat input and provides data for finding an upper bound estimate of the bulk temperature reached during processing.

III. Evaluation

A. Properties and Microstructure

Density, hardness, and electrical resistivity measurements were used in the preliminary evaluation of these composites. Selected consolidated composite materials were sectioned in the radial direction, metallographically prepared, and then examined by scanning electron microscopy. Image analysis techniques by gray scale differentiation of the electron image were used to quantify the area fraction of graphite in the copper graphite brushes.

B. Tribological Evaluation

Low Speed Testing. The low speed tests were conducted in air on a pin-on-disk machine. Friction force and pin wear were monitored by a strain ring and a linear-displacement transducer respectively. An Apple II computer stored and plotted the data. The pin wear rate and friction coefficient were calculated from the plots. The applied load range was 2 to 20N, and the sliding velocity range was 220 to 670 mm/s.

High Speed Testing. Figure 3 shows the sliding electrical contact tester (SECT). This is a device which allows rapid evaluation of materials and cooling methods with respect to interface power dissipation and wear rate. Continuous testing at speeds of up to 180 m/s at 6000 A is possible. Electromagnetic displacement probes monitor brush wear, and a video thermal imaging system provides a time-temperature history of the slider, sliding interface, and rotor. The tests were performed dry in air. No active cooling was used. Constant down force of 100N was maintained during the temperature excursion tests. The specimen surfaces were prepared by polishing with a final polish using 600 grit silicon carbide paper. Prior to the test the contact and rotor surfaces were cleaned with high-purity ethyl alcohol.

Results and Discussion

I. Composite Brushes

A. Processing

The commercial composite is made by a proprietary method using conventional powder metallurgy techniques. No details of the processing are available. The binderless copper-graphite is produced by the high-energy high-rate technique (23-25). The degree of homogeneity of the distribution of the graphite in the copper matrix depends upon the mechanical mixing that is achieved prior to loading of the powder mixture into the die. The degree of mixing depends upon the relative densities and flow characteristics of the loose starting powders.

Since the single-residence processing occurs in the solid-state, the pressure and temperature conditions within the die during the processing control the degree of densification. The copper matrix is powder-forged to high densities, while the graphite undergoes intraparticle shear to accomodate the plastic flow of the matrix. Heating rates of 100 K/s to 500 K/s are used to rapidly bring the copper matrix to the warm processing range (0.4 to 0.6 Tm, where Tm is the melting temperature of copper = 1356K). While at temperature the composite densifies under an applied stress that is in excess of the flow stress within the powder volume.

B. Microstructure and Properties

The microstructures developed in these two material systems reveal the differences in their processng. Figure 4 shows the Cu-Gr-Sn-Pb material. The composition (in mass percent) of COM–A is 82 Cu, 11 graphite, 5 Sn, and 2 Pb. The tin was found to alloy

with the copper to form bronze. The lead formed small dispersoids which probably act as a low–temperature solid lubricant. There is virtually no interfacial strength between the matrix and graphite, resulting in very low hardness and low toughness. The bronze matrix helps increase the hardness somewhat, but it also decreases the conductivity.

Figure 5 shows the microstructure of the binderless copper-graphite composite consolidated by high-energy high-rate processing. Low magnification shows that the graphite is fairly well distributed, but a strong orientation has developed. Higher magnification shows the tight microencapsulation of the graphite in the copper matrix.

The measured values of density, hardness and electrical resistivity of the composite materials for brushes are listed in Table 2.

Table 2. Properties of composite materials for brushes.

	Cu-Gr-Sn-Pb	Binderless Cu-Gr
Density (g/cm^3)	5.5	6.30-6.68
(percent theoretical)	82.2	94.1-99.8
Average Hardness *	45	62 (Axial)
(Rockwell 15T)		50 (Radial)
Electrical Resistivity	37	3.82 (Axial)
(μ ohm-cm at room temp.)		8.95 (Radial)

* On this scale a fully dense copper powder compact has an average hardness of 70.7.

II. Composite Armatures

A. Processing

Copper–Tungsten. Copper–tungsten composites exploit the high temperature hardness and refractory nature of tungsten in combination with the ductility and electrical conductivity of copper and have been studied for hypervelocity contact applications such as the solid armature described earlier. In this research, four P/M processing approaches for these composites have been pursued: Cu infiltration of porous W; W + Cu blended elemental composites; Cu–W from H–reduced copper tungstate; and Cu–coated W powders, each processed by high energy high rate consolidation.

W–WC–C Nanosized Structures. Nanosized structures based on tungsten/tungsten carbide/graphite/copper systems are being developed to meet high-performance electrical sliding contact needs . These structures provide the needed abundance of current-collecting, refractory contact spots at the sliding interface. Sol-gel synthesis, large-strain deformation processing and high-energy high-rate powder consolidation are the main steps in the preparation of these novel microstructures.

The electrotribological potential is optimized by embedding a hard, wear-resistant tungsten or tungsten carbide layer into an electrically and thermally conductive copper substrate, while retaining a graphite surface layer to act as a boundary lubricant.

Tungsten oxide gel precursors allow the development of a nanosized grain structure (≈100 nm) in metallic tungsten (21). This creates a large amount of a-spots to act as conduction points on the sliding contact interface. The production of the tungsten oxide aerogel is preceded by the production of a hydrated tungstic oxide gel. This occurs by the following sequence:

1. Dissolution of sodium tungstate in dilute HCl:

   $Na_2WO_4 + 2HCl = WO_3 \cdot H_2O + 2NaCl$;

2. Hydrated tungstic oxide precipitates as an aquagel;

3. Alcohol substituted for water to form alcogel;

4. Alcohol removed using critical point drying to form aerogel.

This tungsten trioxide aerogel has the potential of undergoing reduction and carbothermic reactions to form metallic tungsten and tungsten carbide. A thin layer of such a material embedded on a conductive (copper) substrate would form an ideal sliding contact. Therefore the tungsten trioxide gel is mixed with colloidal graphite to form a 4:1 carbon-tungsten ratio. This mixture is coated onto the inside of a clean copper tube. The tube is next rolled flat to form a sandwich structure with the carbon-tungstic oxide mixture coated inside the flattened copper tube. The longitudinal tube edges are slit and the sandwich is hydrogen annealed at 800°C for 1 hour to convert the tungstic oxide to tungsten. The copper/tungsten sandwich is then placed between two electrodes connected to a HPG. Pressure is applied and a peak current flux of 50 kA/cm^2 is passed through the sandwich. This embeds the tungsten/graphite layer into the copper.

B. Microstructure and Properties

Copper–Tungsten. Results indicate that the density, hardness and electrical conductivity of the Cu–coated W consolidates are higher than those produced by the other three approaches. The density and hardness values are higher than those for commercial material produced by conventional sintering (1700K/ 1 hour in hydrogen). The values are given in Table 3.

A typical microstructure developed in the consolidated material is shown in Figure 6. The lighter phase is tungsten which has a wide particle size distribution allowing for efficient filling of space. The copper, though the minority phase, is the continuous phase and is responsible for the high level of plastic-flow induced densification.

Table 3. Properties of 90:10 W:Cu composite material

	This Process	Commercial Material
Density	14.8 g/cm3	14.0 g/cm3
Hardness (HRB)	81	70
Electrical Resistivity	11.2 μΩ-cm	n.a.

III. Electrotribological Performance

An effort to optimize contact performance requires an understanding of the pertinent materials science concepts, particularly as they apply to the control of processing. The powder metallurgy based composite materials that are described in this study have been prepared by novel processing routes. Electrotribological behavior of three different systems are described: (1) Copper and Graphite (2) Copper and Tungsten (3) W/WC/C and Cu layered composites.

Composite Brushes

In the past, unidirectional graphite fibers/copper matrix composites have been extensively studied for use as electrical brushes. Although their behavior in the absence of current proved to be satisfactory, t..e passage of high currents increased the friction coefficient and the wear rate to unacceptable values; apparently, the lubricating properties of the graphite fibers are inferior to those of bulk graphite. One possible reason for that may be the desorption of water vapor from the graphite fibers at high interface temperatures (26).

Preliminary results of the tribological characterization of the binderless copper and graphite powder-based composites were previously published by Owen et al (23), Wang et al (24), and by Eliezer et al (25). The low speed pin on disk tests (0.6 m/s) of the copper and graphite on 4340 steel showed friction coefficients in the range 0.133 to 0.207 versus an average value of 0.120 for the commercial Cu-Gr-Sn-Pb composite.

At high speeds the wear of the binderless composite is significantly lower than the commercial material. At 200 m/s values of 0.2-0.3 x 10^3 mm^3/Mm versus 2 x 10^3 mm^3/Mm, are obtained over 6 km sliding distances.

Everett (27) reported on the pulse duty (<3 seconds) performance of these binderless copper–graphite contact materials. An improvement in contact resistance was observed compared to commercial composite material (COM-A) at velocities of 20m/s to 90m/s. Current density comparisons at 100m/s and 160m/s showed the binderless material to have twice the current carrying ability of the commercial composite. When pulse loaded at 3kA/cm^2 at 160m/s, a nearly linear temperature rise of 100K/s was observed to a peak temperature of 420K.

From the results of the electrotribological testing described, several wear mechanisms are known to be active depending upon the nature of the reinforcing phase. One example is the apparent re-transfer of fine particles of graphite to the copper matrix, first transferred as a thin film from the brush to the rotor. The post-test wear surface exhibiting this effect is shown in Figure 7.

Composite Armatures

A graded resistance armature concept is based upon the two–dimensional model for current density distribution within a traveling solid armature developed by Long(28). It attempts to compensate for the observed tendency of the current to concentrate close to the

trailing edge of the armature by making that edge the most resistive part of the armature, thus forcing a more uniform distribution of the current.

The proposed design concepts have as a common objective the maintenance of armature/rail contact. However, controlling energy dissipation at the sliding interface poses another significant challenge as guns get longer and are driven harder. Performance suffers as solid armatures tend to be converted to hybrid (plasma/solid) armatures in bore during firing.

Figure 8 shows a SEM photomicrograph of the surface of the composite armature material after a high speed wear test on the sliding electrical contact tester. Diagonal wear tracks are evident. Plastic flow of the copper has produced wear tracks with a regular spacing of approximately 100 μm. This dimension corresponds to the machining marks on the rotor surface, and suggests that there may be geometry induced current concentration effects during sliding which led to localized heating of the contact. The peak temperature observed thermographically during the test was 560°C. (Test was conducted in air, uncooled, with 100N downforce. It was run for 60s at 100 m/s with zero current, then for 30s at 100 m/s with 1kA/cm^2. Nominal contact area was 20mm x 12.5 mm on turned 4340 steel rotor surface.)

Figures 9a, 9b, 9c show SEM photomicrographs of the wear surface of 100 μm thick W-WC-C layer on a copper substrate after a high speed wear test on the sliding electrical contact tester. At low magnification, the profile of the rotor surface appears to be replicated on the contact surface with a series of evenly spaced troughs running horizontally. At higher magnification, a loose wear particle with approximately 20 μm dimensions is visible at the bottom of the photo. A high magnification view of the bottom of a wear trough shows loose particles with 1-2 μm dimensions distributed on the substrate which has retained the original nanosized structural features.

IV. Combined Consolidation and Bonding

Due to the localized pulse resistive heating that develops at the interface between the metallic electrode and the consolidated material, this processing technique also allows an examination of the producibility of metal–ceramic joints. The sensitivity of contact materials such as copper to the presence of impurity elements is revealed in the large increments in electrical resistivity versus composition. For example, phosphorus in copper produces a two fold increase in resistivity at the 0.1 percent level. Phosphorus is a common constituent in brazing alloys for copper . Thus, it is advantageous to eliminate braze fillers in the attachment of contacts to copper straps. This is the motivation for the study of bonding of these materials to metallic copper using subsecond high temperature exposures in the high energy–high rate processing.

The tight interfacial bonds observed between the Cu electrode and the compact, Figure.10, suggests that such a joint would efficiently transfer heat and current. In this example, layer 3 is a binderless copper-graphite composite layer which transfers energy to a wrought copper disk via a copper powder composite layer. In practice the wrought material can be the brush strap and the copper powder then serves as an efficient conductive interlayer between the sliding interface and strap. This reduces the losses due to resistive heating of the brush, and eliminates the brazed joint between brush and strap, thus reducing a source of heating of the strap and allowing more efficient energy transfer across the brush/strap interface.

A final example of how the contact materials being developed might be incorporated into an actual device is shown in Figure 11. This is a schematic view of a partially hollowed-out cylindrical composite solid armature. This arrangement has been proposed for a 90 mm diameter solid armature (17). It consists of a thin outer layer of a W-WC-C nanosized composite embedded into a tubular section made of dispersion-hardened copper which is

fitted over a high-strength, high-conductivity aluminum core. This arrangement provides for a light-weight armature with a refractory skin. The tribological behavior of the outerlayer material is being investigated currently, as indicated in Fig. 9 (29).

For each of these systems, the key feature revealed in the testing is the high temperatures that are developed at the sliding interface. A more complete understanding of the electrotribological behavior under these conditions requires a detailed knowledge of the microstructure/property relationships for each of the materials systems at elevated temperature. This is an involved but essential task in the continued development of these advanced composite contact materials.

Conclusion

Findings are as follows:

1. A variety of sliding electrical contact powder composite materials can be successfully processed by high-energy high-rate processing utilizing high-current discharges from a homopolar pulse generator. The copper-graphite, tungsten-copper, and tungsten-tungsten carbide-carbon-copper composite systems have been described.

2. Microstructures of the copper-graphite and tungsten-copper composites show continuous copper matrices, and well-dispersed graphite, and tungsten, respectively.

3. Properties of the copper-graphite and tungsten-copper composites such as density, hardness, and electrical conductivity are superior to those of commercial composites made by conventional processing methods. This has been confirmed by our own comparative

studies of alternative processing methods such as roll-compaction followed by vacuum sintering.

4. Performance evaluations of each of these composites at high sliding velocities show improvements in wear behavior and the ability to sustain higher temperatures at the sliding interface than comparable conventionally-processed material. The superior electrical (and thermal) conductivity of these materials may contribute to such performance.

5. The more complex tailored structure in the tungsten-tungsten carbide-carbon-copper composite system is a novel response to the materials needs in hypervelocity sliding contacts. It matches materials to the thermal gradients observed in the analysis of such armatures: tungsten skeleton at the hot rail/armature interface, embedded in copper via which energy is transferred through a relatively cool aluminum core to the opposite hot interface. Such a construction also reduces the density penalty of using tungsten, the overall density being less than twenty percent greater than an all aluminum armature (3.2 gm/cm^3 vs 2.7 gm/cm^3).

6. Combined consolidation and bonding methods for incorporating these powder-based composites into contact components have been developed.

Acknowledgment

We thank Dick Mason of AMETEK, CT for providing the Cu-coated W powders, and Andrew Yeoh, Jim Gent, and Ghulam Husnain for their assistance in preparing the manuscript. This work was supported by DARPA under ARO Contract DAAL 0387-K-0073, by the Texas Advanced Research Program, Grant #4357, and by the Texas Advanced Technology Program, 1989-1991 Grant.

References

1. C. Norman, "How the United States Stacks up in Key Technologies",Science, Vol. 248, 1990, p.299.

2. Tribology of ceramics, Report of the Committee on the Tribology of Ceramics of the National Materials Advisory Board, Publication # NMAB-435, National Academy Press, 1988, p. 17.

3. J. P. Barber, "The Acceleration of Macroparticles in a Hypervelocity Electromagnetic Accelerator", Ph.D. Thesis, The Australian National University, 1972.

4. G. L. Jackson et al, " Electromagnetic railgun extended-life bore material tests results", IEEE Trans. on Magnetics, Vol. MAG-22, No. 6, Nov. 1986, pp. 1542–1545.

5. R. Holm, Electric Contacts, 4th. ed., Springer Verlag, Berlin/New York, 1967.

6. R. A. Marshall, " Design of Brush Gear for High Current Pulses and High Rubbing Velocities", IEEE Trans. on Power Apparatus and Systems, Vol. PAS 85, No 11, Nov. 1966, pp. 1177-1188.

7. J. L. Johnson and L. E. Moberly, " High Current Brushes, Part I: Effect of Brush and Ring Materials", IEEE Trans. on CHMT, Vol. CHMT-1, No. 1, March 1978, pp. 36–40.

8. J. P. Barber, D. P. Bauer, T. J. McCormick and D. E. Johnson" The Performance of High Current Density Metallic Conductors", in Proceedings of the CURRENT COLLECTOR CONFERENCE, Raleigh, NC. October 1985. pp. 228 - 235.

9. J. P. Barber, C. McDonald " Electric Contacts at High Velocity", in Proceedings of the CURRENT COLLECTOR CONFERENCE, Raleigh, NC. October 1985. pp.236-241.

10. C.J. Lund, C. Persad, Z. Eliezer, D. R. , and J. Hahne, " Composite Solid Armatures for Railguns", Paper #13, Proceedings of the 3rd. Int. Current Collector Conference, Austin, TX, Nov. 1987.

11. D. P. Ross, G. L. Ferrentino and F. J. Young, "Experimental Determination of the Contact Friction for an Electromagnetically Accelerated Armature," Wear, 78 (1982) pp. 189 - 200.

12. J. M. Casstevens, H. G. Rylander, and Z. Eliezer, "Influence of High Velocities and High Current Densities on the Friction and Wear of Copper-Graphite Brushes",Wear 48, p. 121 (1978).

13. M. Brennan . Z. Eliezer, W. F. Weldon, H. G. Rylander and H. H. Woodson," The Testing of Sliding Electrical Contacts for Homopolar Generators", IEE Trans. CHMT., Vol. CHMT-2, No. 1, March 1979.

14. R. A. Burton, "Materials for Sliding Contacts in the Twenty-first Century", Electrical Contacts -1988, Proc. of the 34th. IEEE Holm Conference, 1988, p. 257.

15. H. G. Rylander, J. H. Gully, Z. Eliezer, "Limiting Design Parameters for Future High Speed, High Current Density Sliding Electrical Contacts" Electrical Contacts - 1988, Proc. of the 34th. IEEE Holm Conference, 1988, p. 247.

16 D. Kuhlmann-Wilsdorf, "Flash Temperatures due to Friction and Joule Heat at Asperity Contacts," Wear, 105 (1985) pp. 187-198.

17. C. Persad, D. R. Peterson, and R. C. Zowarka, " Composite Solid Armature Consolidation by Pulse Power Processing: A Novel Homopolar Generator Application in EML Technology" IEEE Trans. on Magnetics, Jan. 1989, pp.429-432 .

18. C. Persad, H. L. Marcus, and W. F. Weldon, "High Energy High Rate Pulsed Power Processing of Materials by Powder Consolidation and by Railgun Deposition." Final Technical Report # UT–CMSE–87–02, March 1987, Gov. Reports Index # 732,954,NTIS Code AD–A179 289/4/GAR PC A07/MF A01.

19. D. E. Ervin, D. L. Bourell, C. Persad and L. Rabenberg, "Structure and Properties of High–Energy, High–Rate Consolidated Molybdenum Alloy TZM," Materials Science and Engineering A, 102, 1988, pp. 25–30.

20. Y. M. Kim, D. L. Bourell and C. Persad, "High Energy, High Rate Powder Processing of a Rapidly–Quenched Quaternary Alloy, $Ni_{56.5}Mo_{23.5}Fe_{10}B_{10}$", Materials Science and Engineering, A123, 1990, pp.99–115.

21. C. Persad, S. Raghunathan, A. Manthiram, M. Schmerling, D. L. Bourell, Z. Eliezer and H. L. Marcus, "Development and Control of Microstructure in P/M Tungsten by Synthesis and Reduction of Tungsten Trioxide Gels", Solid State Powder Processing", A. H. Clauer and J. J. de Barbadillo, eds., TMS, Warrendale, PA, 1990, pp. 357–364.

22. C. Persad, S. Raghunathan, B. -H. Lee, D. L. Bourell, Z. Eliezer and H. L. Marcus, "High -Energy High-Rate Processing of High Temperature Metal-Matrix Composites", MRS Symposia Proc. Vol. 120, F. D. Lemkey, A. G. Evans, S. Fishman, and J. R. Strife (eds.), MRS, Pittsburgh, PA, 1988, pp. 23 - 28.

23. K. C. Owen, M. J. Wang, C. Persad and Z.Eliezer, "Preparation and Tribological Evaluation of Copper-Graphite Composites by High-Energy/High-Rate Consolidation", Wear 120, 1987, pp. 117-121.

24. M. J. Wang, C. Persad, Z. Eliezer, and W.F.Weldon, "High-Energy / High-Rate Consolidation of Copper-Graphite Composite Brushes for High Speed, High Current Applications", Paper #20, Proceedings of the 3rd.Int. Current Collector Conference, Austin, TX, Nov.1987.

25. Z. Eliezer, M. J. Wang, C. Persad, and J. H. Gully," A Novel Processing Technique for Metal/Ceramic Composites", in Ceramic Developments, C. C. Sorrell and B. Ben-Nissan (eds),Materials Science Forum,Vol. 34-36, Trans Tech Publ., Switzerland, (1988) pp. 505-509.

26. Z. Eliezer, "Friction and Wear of Metal Matrix–Graphite Fiber Composites", in Friction and Wear of Polymer Composites, K. Friedrich (ed.), Elsevier, 1986.

27. J. Everett, MS Thesis, The University of Texas at Austin, Dec. 1988.

28. G. C. Long, "Railgun Current Density Distributions," IEEE Trans. on Magnetics, Vol. MAG-22, (Nov. 1986), pp. 1597-1602.

29. Z. Eliezer, C. Persad, S. Raghunathan, D. Barnes, D. Moore, S. C. Sparks, and J. H. Gully, "Nanosized Structures for High-Performance Tribological Applications", Poster Presentation at the 1989 TMS Fall Meeting, Indianapolis, IN., October 2-5, 1989.

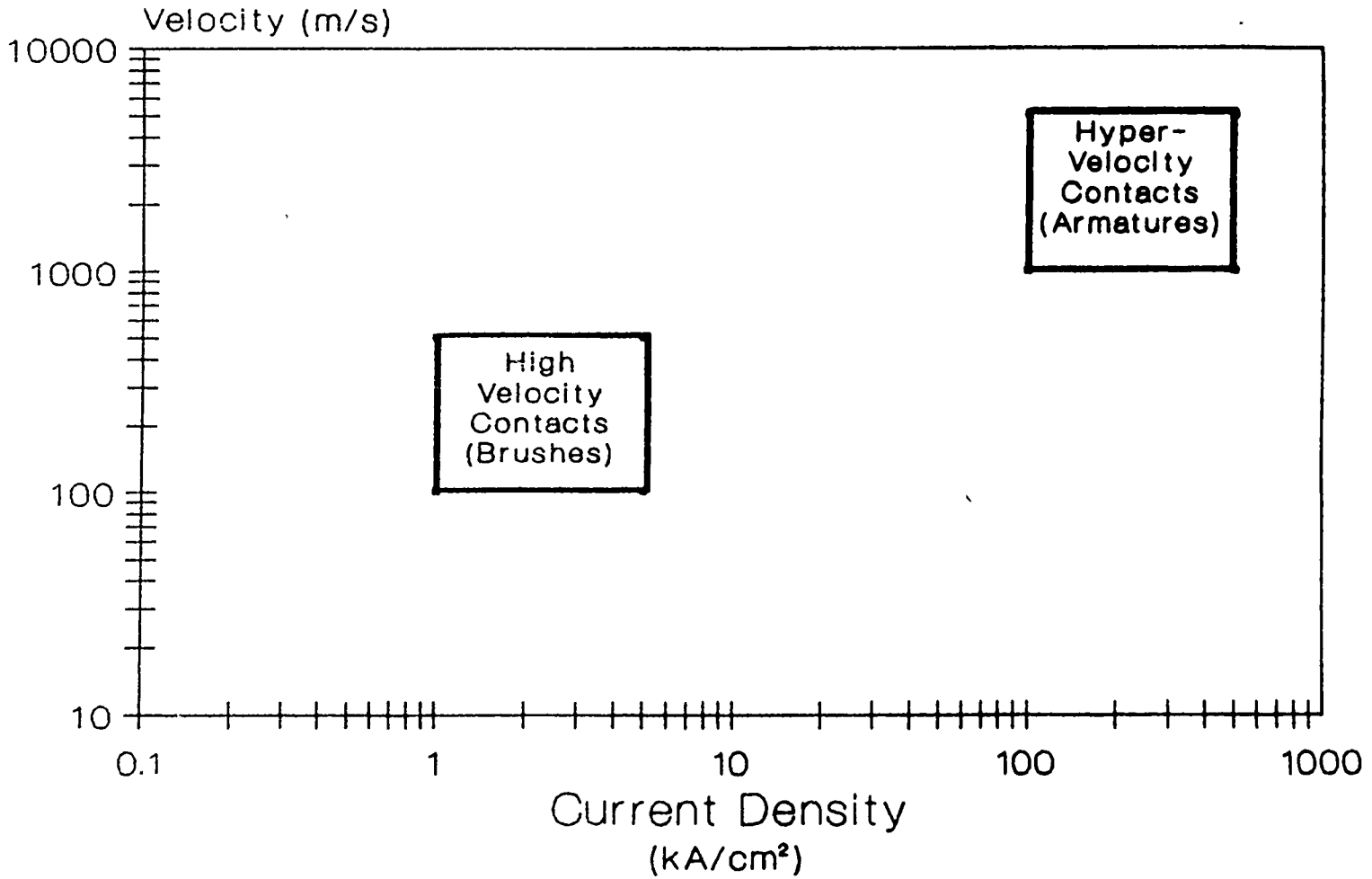

Fig. 1. Operating regimes for high velocity and hypervelocity sliding contacts shown on velocity/current density axes.

HEAT SOURCES IN A HOMOPOLAR BRUSH

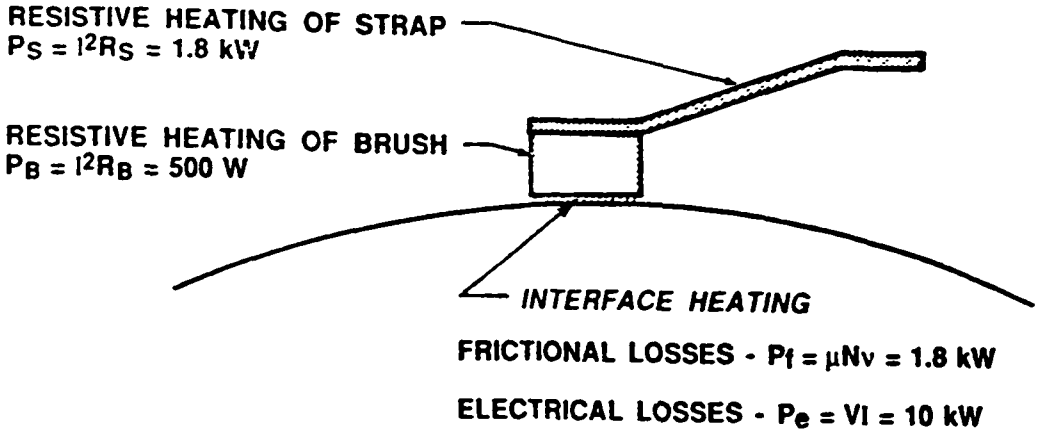

I = 5 kA	V = 2 V
v = 200 m/s	$R_B = 20\ \mu\Omega$
μ = 0.2	$R_S = 72\ \mu\Omega$
N = 45 N	

Electromagnetic Railgun

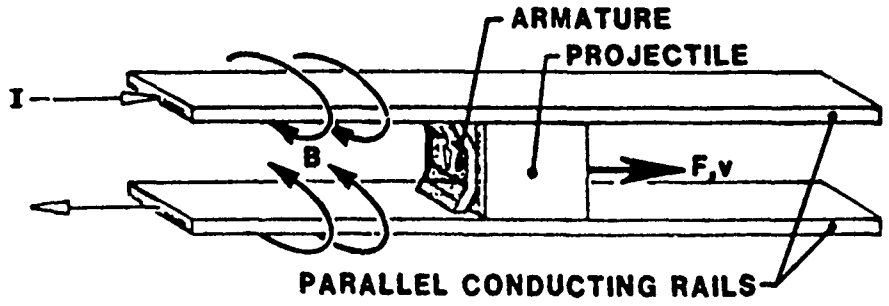

Fig. 2. Operating environment of (a) high velocity sliding contacts (brushes) and (b) hypervelocity sliding electrical contacts (armatures). In (a) the relative magnitudes of some of the heating sources of the contact are estimated using a typical set of parameters.

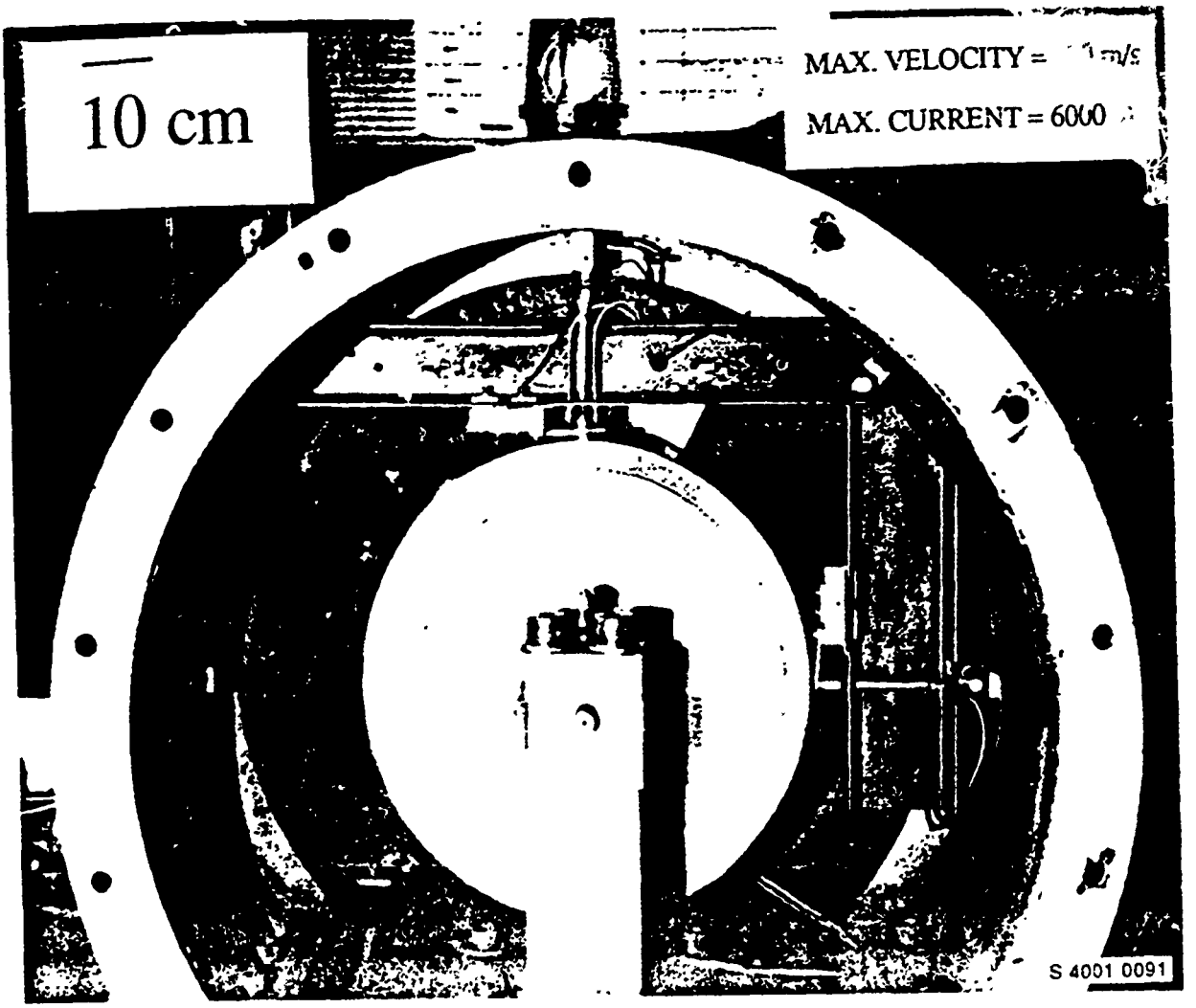

Fig. 3. Photograph of the sliding electrical contact tester. Inside the circular shroud is the rotor mounted on a horizontal shaft. The L-shaped frame provides a stiff support for the top-mounted test brush and the side-mounted return brush. Both brushes are actuated with pneumatic cylinders. The top-mounted test brush wear (heel and toe) is monitored by the two electromagnetic transducers located on either side of the pneumatic cylinder.

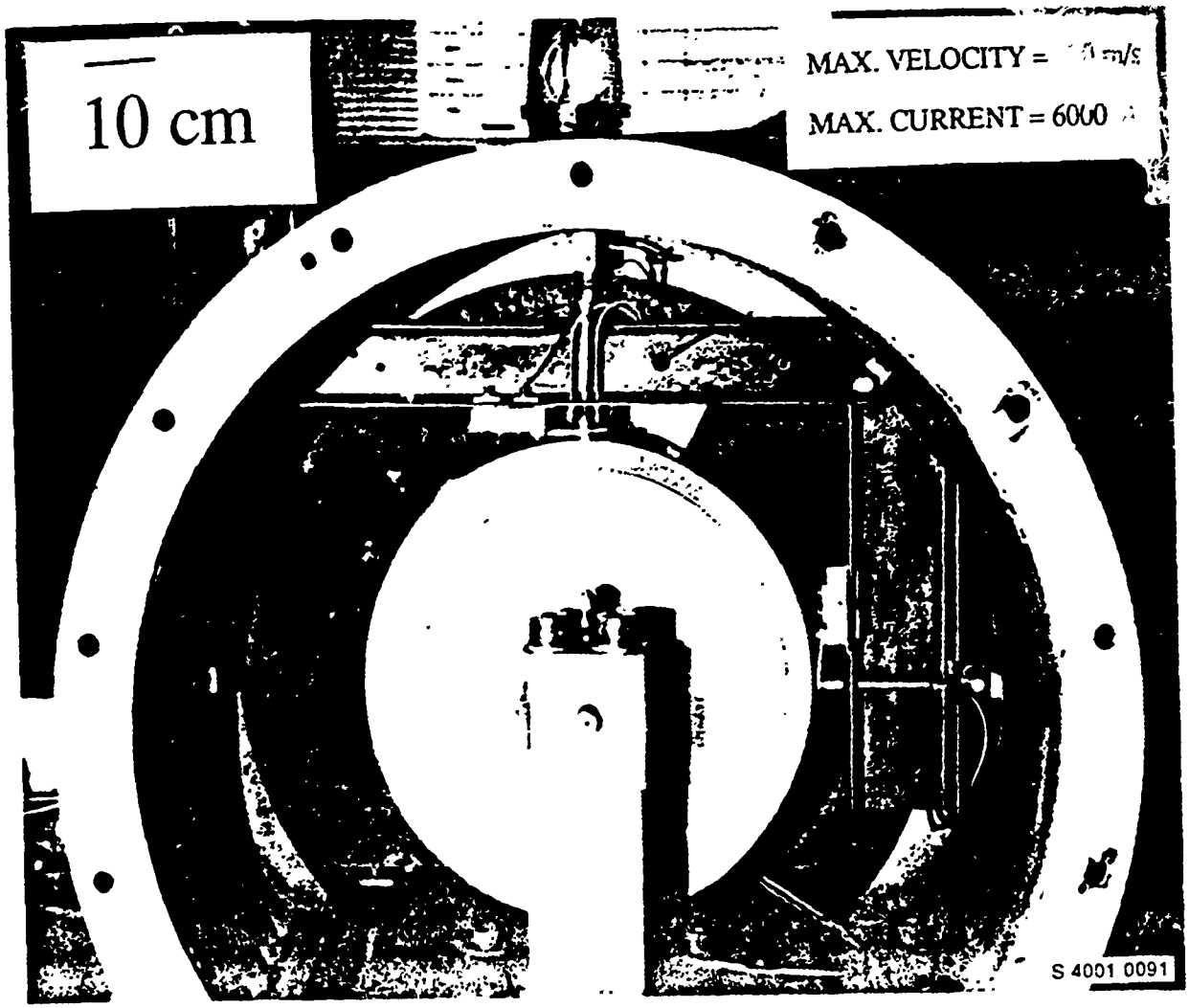

Fig. 3. Photograph of the sliding electrical contact tester. Inside the circular shroud is the rotor mounted on a horizontal shaft. The L-shaped frame provides a stiff support for the top-mounted test brush and the side-mounted return brush. Both brushes are actuated with pneumatic cylinders. The top-mounted test brush wear (heel and toe) is monitored by the two electromagnetic transducers located on either side of the pneumatic cylinder.

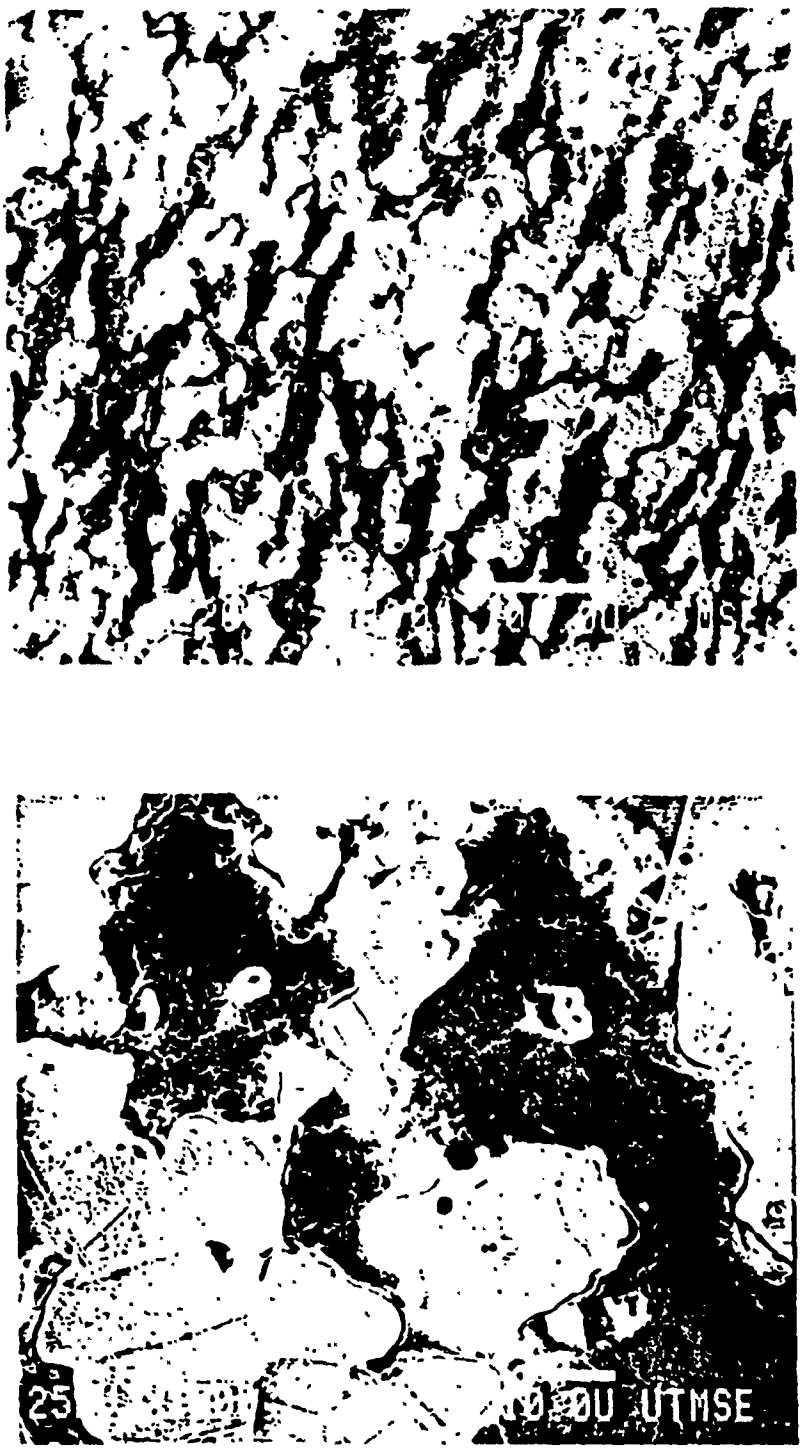

Fig. 4. Microstructure of the commercial Cu-Gr-Sn-Pb composite.
(a) Low magnification overview showing recrystallized structure in the initially "dendritic" copper powder. The copper matrix (light phase) is observed to be somewhat discontinuous in this 2-dimensional cross section.
(b) High magnification view showing the gaps between the copper matrix and the graphite.

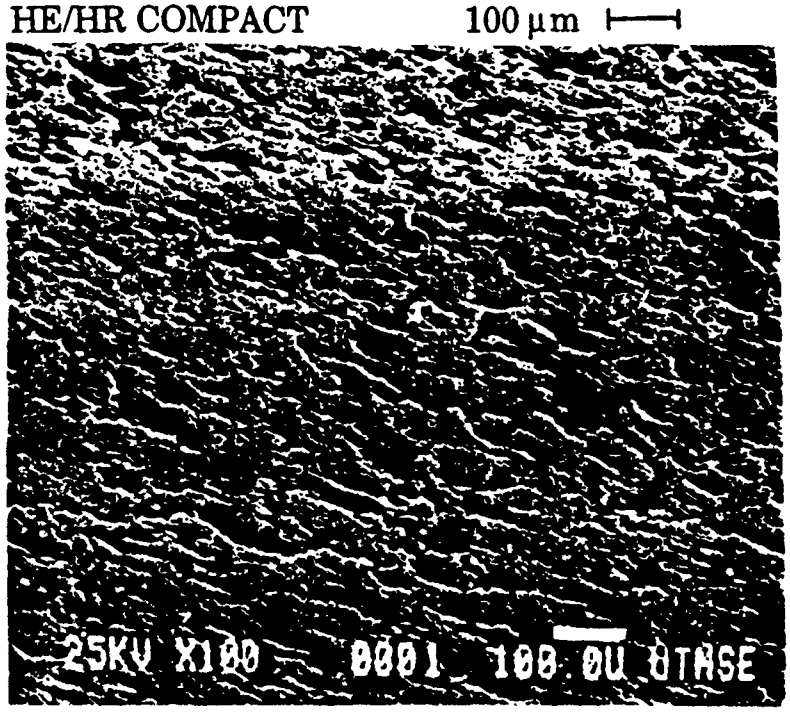

Fig. 5. Microstructure of the binderless copper-graphite composite consolidated by high-energy high-rate processing.
(a) Low magnification overview showing that the graphite is fairly well distributed but a strong orientation has developed.
(b) High magnification micrograph showing the tight microencapsulation of graphite in the copper matrix.

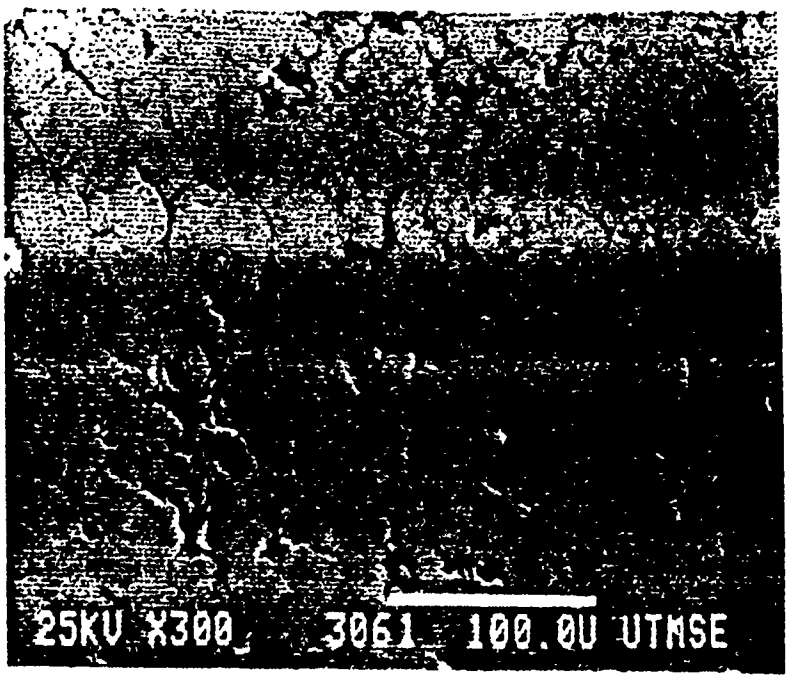

Fig. 6. Microstructure of a composite solid armature contact material made by consolidation of a copper-coated tungsten powder with a 90:10 tungsten : copper mass ratio. The lighter phase is tungsten which has a wide particle size distribution allowing for efficient filling of space. The copper, though the minority phase, is the continuous phase and is responsible for the high level of plastic-flow induced densification.

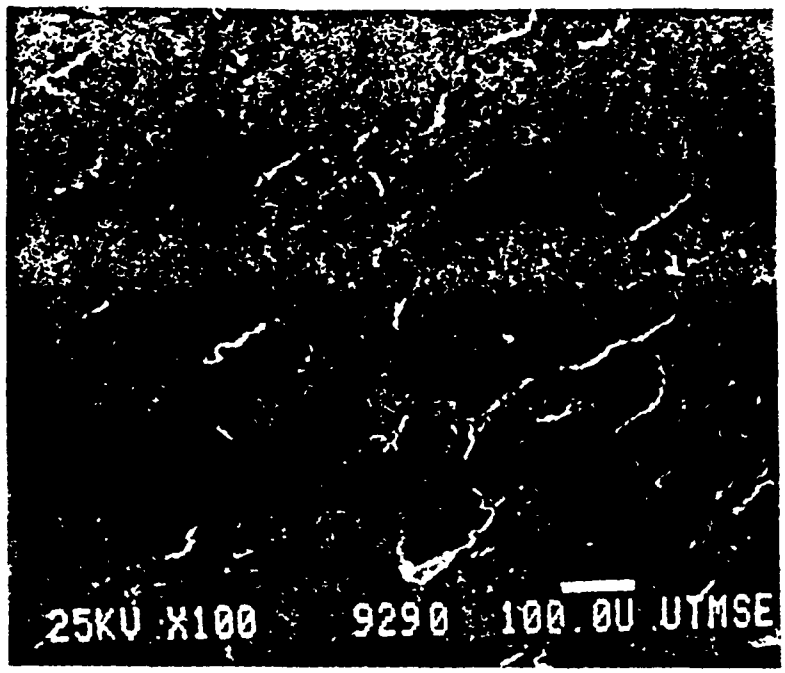

Fig. 7. SEM photomicrograph of the surface of the binderless copper-graphite composite after a high speed wear test on the sliding electrical contact tester. A graphite particle in the edge-on orientation is the dark lenticular shape located parallel to the wear tracks. Also visible are thin highly deformed laminar regions in the matrix and the decoration of the matrix surface with fine dark dots of graphite. (Test conducted in air, uncooled, with 100N downforce. Run for 60s at 100 m/s with zero current, then for 30s at 100 m/s with 1 kA/cm^2. Contact area 20 mm x 12.5 mm on turned 4340 steel rotor surface.)

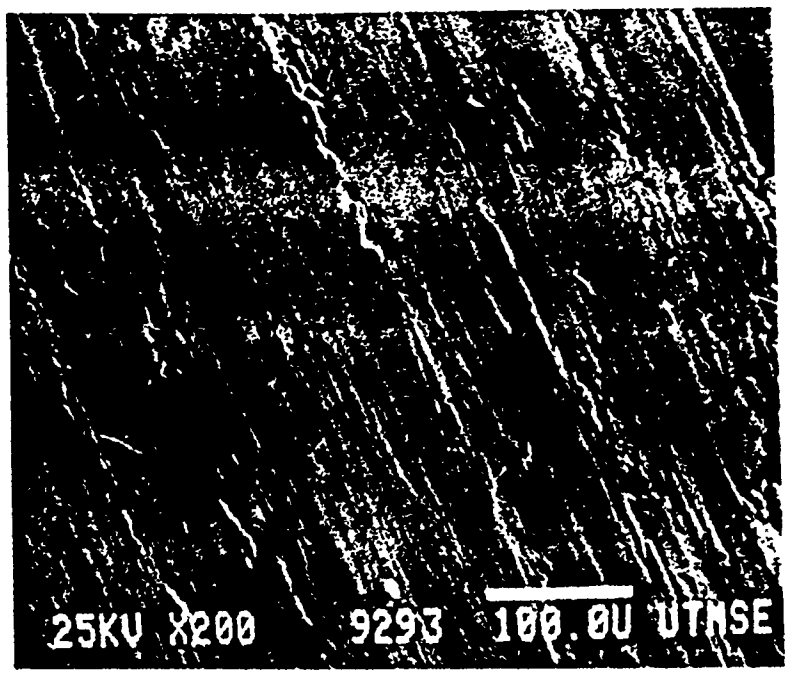

Fig. 8. SEM photomicrograph of the surface of the composite armature material after a high speed wear test on the sliding electrical contact tester. Diagonal wear tracks are evident. Plastic flow of the copper has produced wear tracks with a regular spacing of approximately 100 μm. This dimension corresponds to the machining marks on the rotor surface, and suggests that there may be geometry induced current concentration effects during sliding which led to localized heating of the contact. The peak temperature observed thermographically during the test was 560°C. (Test conducted in air, uncooled, with 100N downforce. Run for 60s at 100 m/s with zero current, then for 30s at 100 m/s with 1 kA/cm^2. Contact area 20 mm x 12.5 mm on turned 4340 steel rotor surface.)

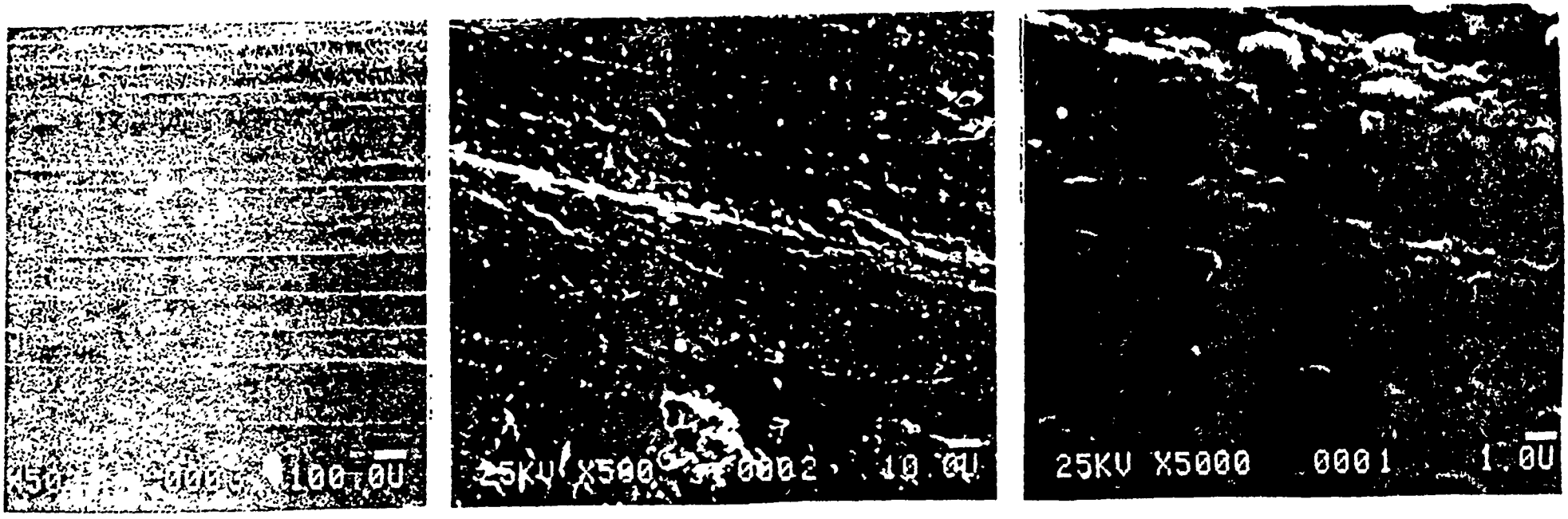

Fig. 9. SEM photomicrograph of the wear surface of 100 μm thick W-WC-C layer on a copper substrate after a high speed wear test on the sliding electrical contact tester.
(a) At low magnification, the profile of the rotor surface appears to be replicated on the contact surface with a series of evenly spaced troughs running horizontally.
(b) At higher magnification the wear track orientation is horizontal. A loose wear particle with approximately 20 μm dimensions is visible at the bottom of the photo.
(c) A high magnification view of the bottom of a wear trough showing loose particles with 1-2 μm dimensions distributed on the substrate which has the original nanosized structural features.

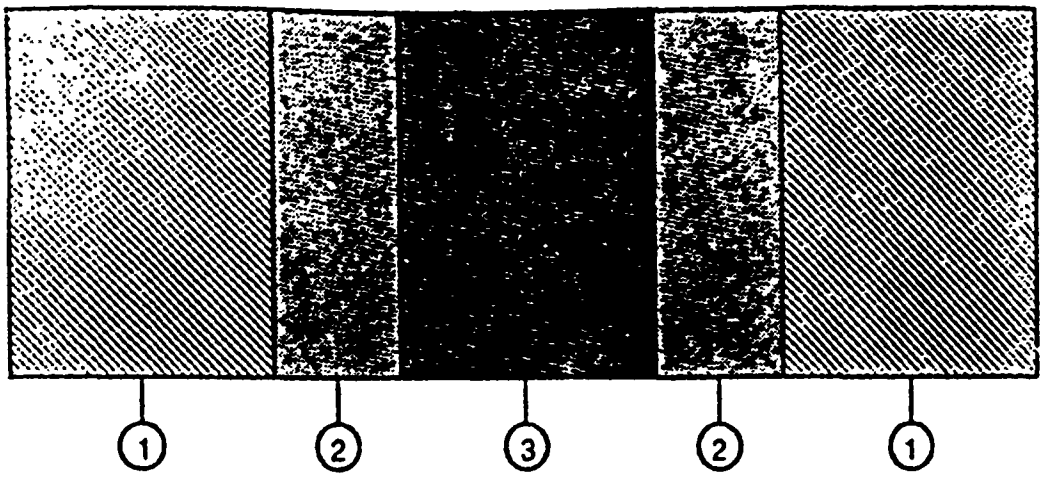

1) COPPER DISK LAYER

2) COPPER POWDER CONSOLIDATED LAYER

3) COPPER - GRAPHITE COMPOSITE LAYER

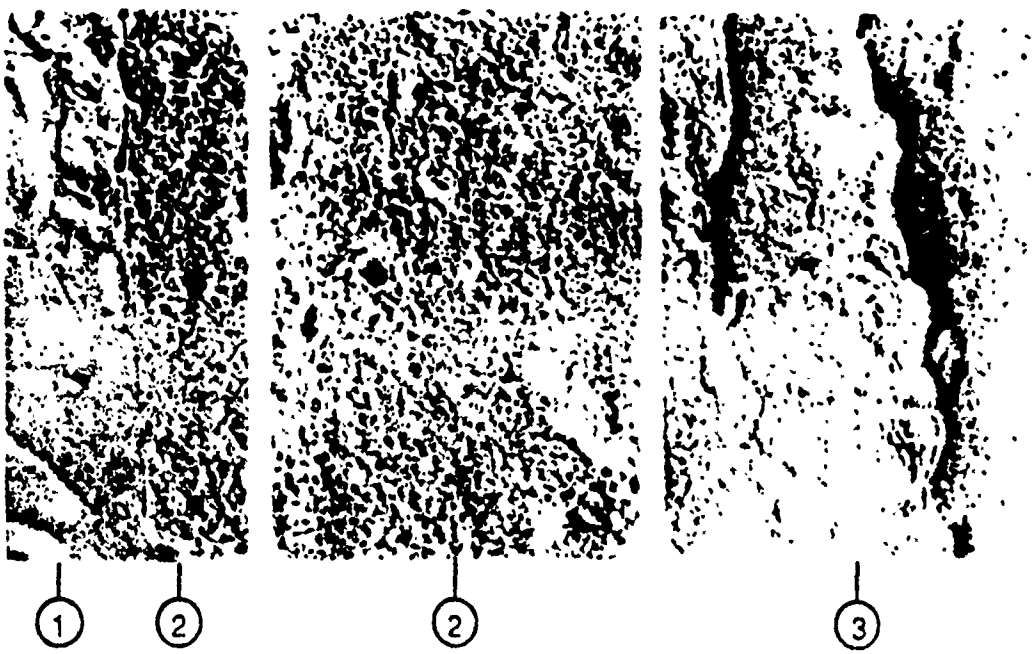

Fig. 10. Schematic and SEM photomicrographs of a method for and results of combined consolidation and bonding. Layer 3 is a binderless copper-graphite composite layer which transfers energy to a wrought copper disk via a copper powder composite layer. In practice the wrought material can be the brush strap and the copper powder an efficient conductive interlayer between the sliding interface and strap. This reduces the losses due to resistive heating of the brush, and eliminates the brazed joint between brush and strap, thus reducing a source of heating of the strap and allowing more efficient transfer of heat and current across the brush/strap interface.

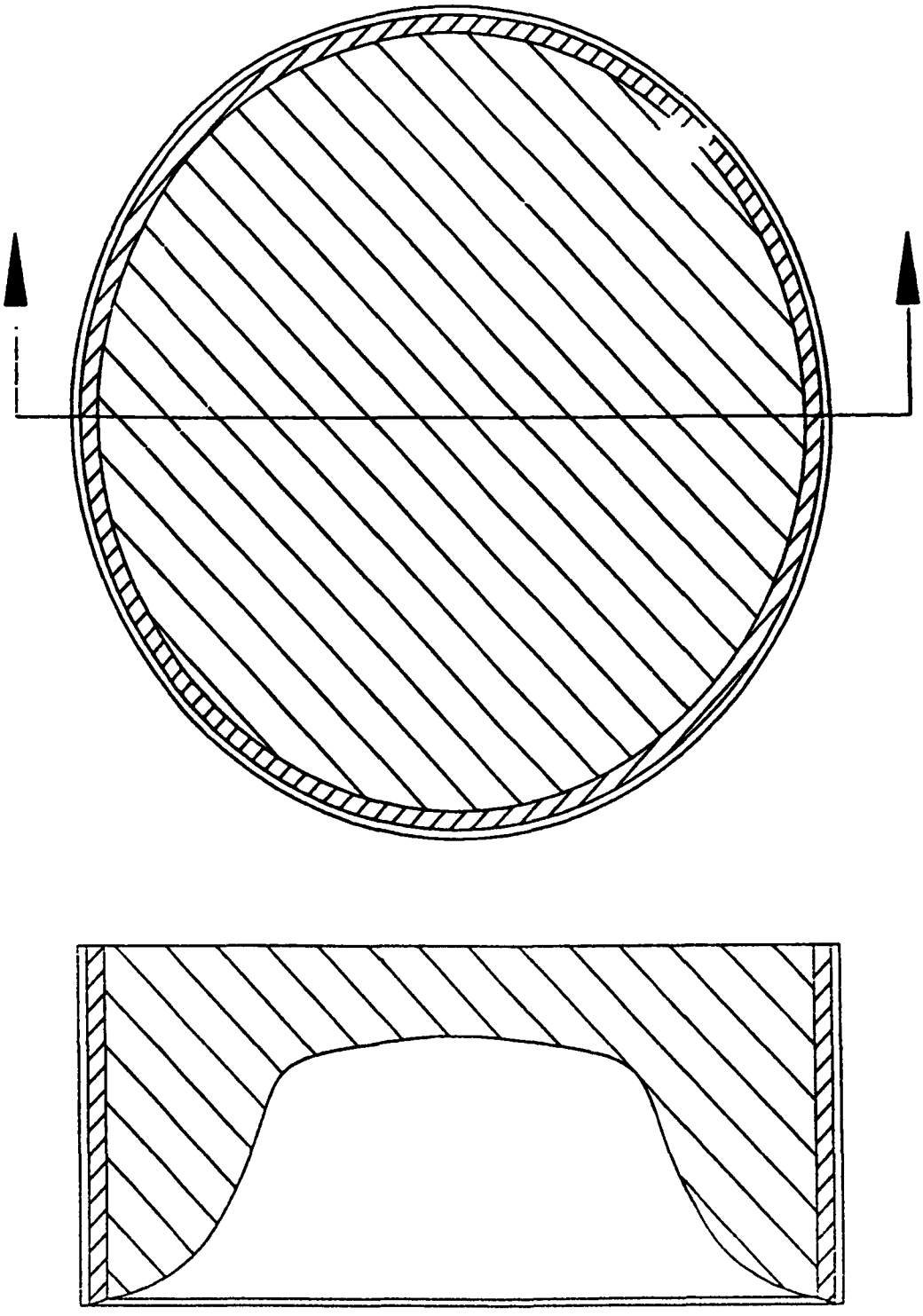

Fig. 11. Schematic and cross sectional views of a hollowed-out cylindrical composite solid armature. This arrangement has been proposed for a 90 mm diameter solid armature. It consists of a thin outer layer of a W-WC-C nanosized composite embedded into a tubular section made of dispersion-hardened copper which is fitted over a high-strength, high-conductivity aluminum core. This arrangement provides for a light-weight armature with a refractory skin. The outerlayer material behavior is being investigated as indicated in Fig. 9.

APPENDIX E

METALLIC GLASSES

E-1. Consolidation of Metallic Glass Ribbons using Electric Discharge Welding

E-2. Identification of an eta-Boride Phase as a Crystallization Product of a NiMoFeB Amorphous Alloy

E-3. High Energy-High Rate Powder Processing of a Rapidly-Quenched Quaternary Alloy, $Ni_{56.5}Mo_{23.5}Fe_{10}B_{10}$

Consolidation of Metallic Glass Ribbons Using Electric Discharge Welding

Y.W. KIM, D.L. BOURELL, and C. PERSAD

The purpose of this communication is to describe results of electrical discharge microwelding of metallic glass ribbon. The motivation for this undertaking was to study the feasibility of the technique in producing bulk geometries by joining thin ribbon metallic glass. Previous attempts reported in the literature include shock explosive compaction,[1] warm pressing,[2,3,4] and laser welding.[5] Characteristics associated with these lamination techniques are extensive crystallization, cracking, and interlayer oxidation.

A high voltage 510 μf capacitor discharge device was adapted to consolidate multiple layers of metallic glass ribbon. The potential of the capacitor bank was varied between 2.25 kV and 10 kV, corresponding to stored energies of 1.3 kJ to 25.5 kJ, respectively.* Two alloy foils were consolidated: iron-based METGLAS® 2605S-2 ($Fe_{78}Si_9B_{13}$) and cobalt-based METGLAS® 2705M ($Co_{69}Fe_4Ni_{1.5}Mo_{1.5}B_{12}Si_{12}$). Both were supplied by Allied Corporation in the form of 20 μm thick melt-spun ribbon. Four pieces of material 25 mm × 25 mm were stacked and pressed between electrodes to low (80 MPa) or high (200 MPa) pressure. The stack was assembled such that the longitudinal axes of the ribbon elements were each offset by a 90 deg rotation rela-

* For capacitance devices, $E = \frac{1}{2} CV^2$, where E is the stored energy, C the capacitance, and V the charge voltage.

Y. W. KIM, formerly a Graduate Research Assistant in the Materials Science and Engineering Program, The University of Texas at Austin, is Senior Research Engineer with Hyundai Motor Company, Seoul, Korea. D. L. BOURELL, Associate Professor, and C. PERSAD, Research Associate, are with The Center for Materials Science and Engineering, The University of Texas, Austin, TX 78712.

Manuscript submitted June 19, 1987.

tive to the element previously laid. The capacitor bank was then discharged across the laminate. No cracks were observed in the joined ribbon. The melt-spun ribbons exhibit the usual surface characteristics of one dull, wheel-side face and one shiny, air-side face. The welding response of the assemblage was not a function of the various contact combinations: air/air, air/wheel, wheel/wheel.

Qualitative mechanical testing was performed analogous to Mode I and Mode II crack opening displacements (Figure 1). In all cases, the interface between layers was stronger than individual ribbons, indicated by fracture crack propagation away from the interlayer interface.

By careful peeling, it was possible to expose small areas of the interlayer interface, although extensive tearing of individual ribbons occurred. Analysis using SEM illustrated the nature of the interlayer bonding. The main features are shown in Figure 2. Two layers of ribbon are shown at increasing magnification. Ribbon bonding is accomplished by widely spaced microspot welding, presumably between asperities of adjacent foils. Ligament features bridging the ribbon elements are apparent in Figure 2(b) A common characteristic of these ligaments was a weld splat or flash which outlined the periphery of most ligaments where they joined the ribbons (arrows in Figures 2(b) and 2(c)).

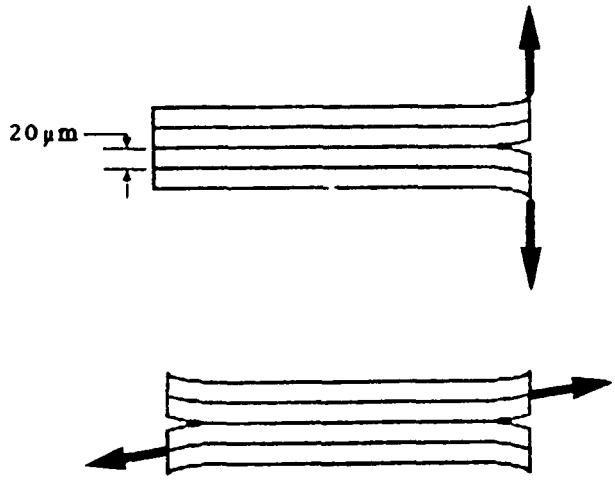

Fig. 1—Two mechanical test geometries used to assess the interface strength of the capacitor discharge welded four-foil assemblages. In all cases, the fracture path cut across individual ribbons rather than following the weld interface

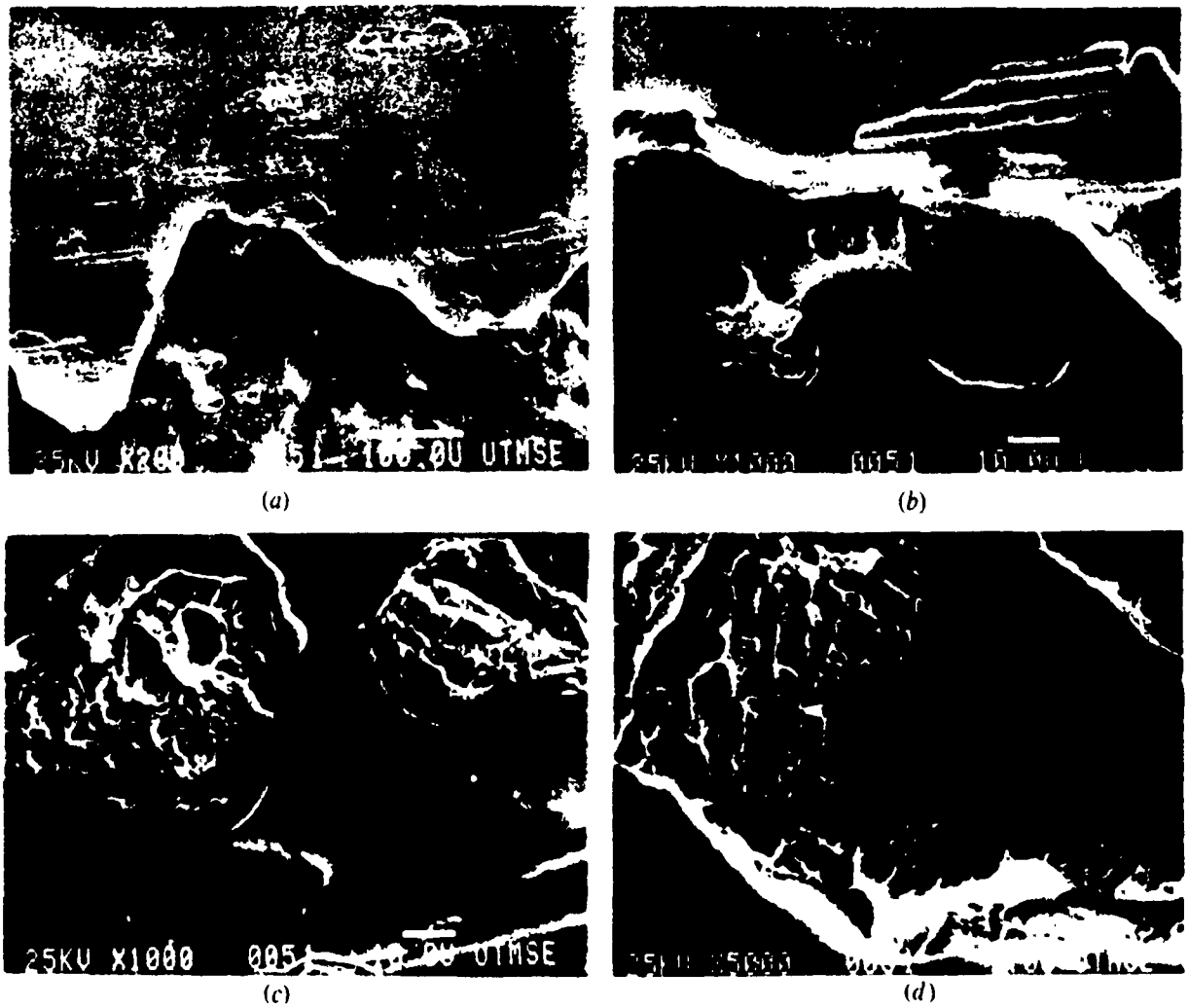

(a) (b) (c) (d)

Fig. 2—Progressive magnification SEM micrographs showing the following features of capacitor discharge welded cobalt based alloy 2705M processed at 2.25 kV (*a*) two ribbons and associated microwelds, (*b*) concave weld ligaments and "flash" (arrows), (*c*) a weld fracture close-up showing "flash" (arrows), and (*d*) a microweld interface showing a riverlike fracture appearance typical for amorphous metals

It is believed that the concave shape of these ligaments is due not only to surface energy effects but also due to a magnetic compression "pinch effect" during processing.[6,7] Figure 2(d) shows the river pattern on a microweld ductile fracture typical of amorphous metallic materials.[8,9]

The effect of processing voltage and pressure on weld size and spacing was studied. Figure 3 shows a carefully separated iron alloy interface after a voltage/pressure consolidation of 4 kV/80 MPa. Weld ligament diameter is estimated to be 3 μm (Figure 3(a)) and the spacing between welds is approximately 150 μm (Figure 3(b)). Separation of ribbons entailed fracture of the weld ligaments and occasional pull-out of parent metal (upper right weld in Figure 3(b)).

Increasing voltage to 8 kV/80 MPa produced the interface shown in Figure 4. The spacing between welds remains approximately 150 μm. Fracture is accomplished by pull-out exclusively, which complicated measurement of the weld diameter. A weld diameter of 15 to 20 μm is estimated. Increasing the pressure from 80 MPa to 200 MPa has no effect on weld size, spacing, or fracture mode, as shown in Figure 5 for the iron alloy joined at 8 '.

Figure 6 shows the interface of the iron alloy processed at 10 kV and 200 MPa. As for all previous weldments, the spacing remains at 100 to 200 μm. However, at this high input energy the weld zone now traverses more than two ribbons. Figure 6(a) illustrates an extreme case where careful separation left sections from all four ribbons at a weld spot. These sections span between 40 and 100 μm in diameter.

For both cobalt and iron based metallic glass, the weld ligament size increased with increasing capacitor discharge voltage and was not dependent on applied pressure during consolidation. The spacing between ligaments was approximately 150 μm for both alloy systems regardless of changes

(a) (b)

Fig. 3—(*a*) High and (*b*) low magnification SEM micrographs of iron based alloy 2605S processed at 4 kV and 80 MPa. Shown is the interface region after foil separation. Microwelds are present, of 3 mm diameter and 150 mm spacing

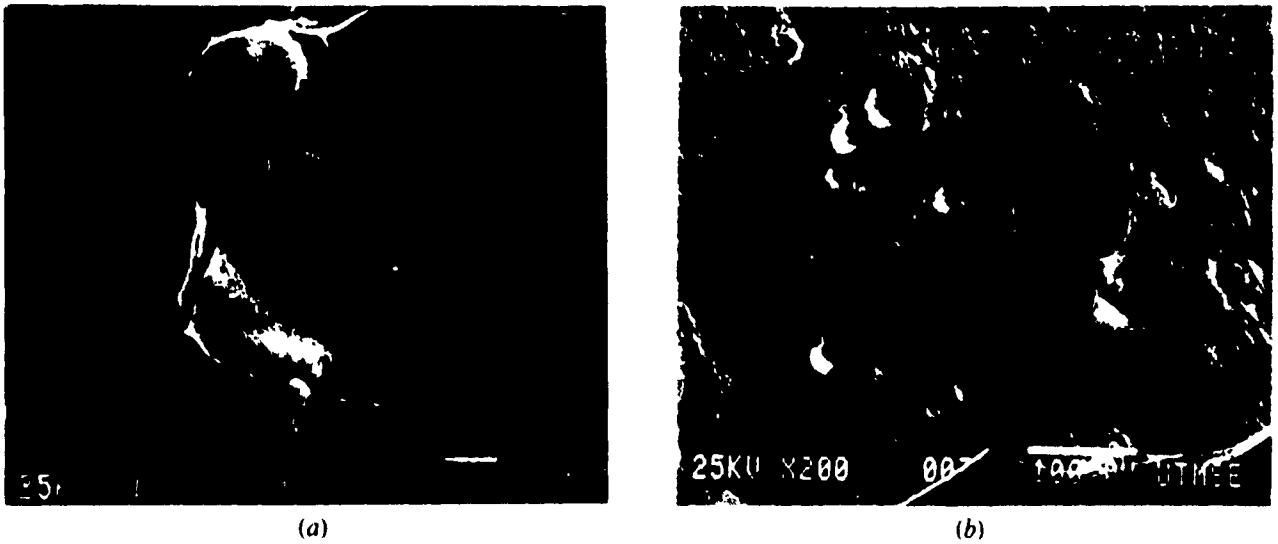

(a) (b)

Fig. 4—(*a*) High and (*b*) low magnification SEM micrographs of iron based alloy 2605S processed at 8 kV and 80 MPa. Foil cracking occurred during separation of foils to expose the interface region

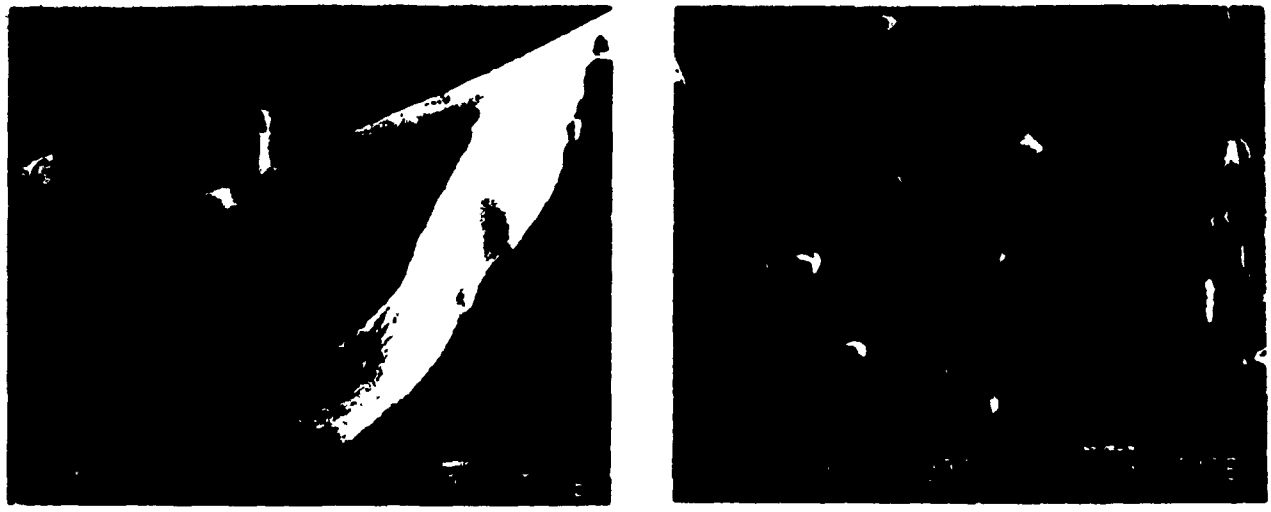

(*a*) (*b*)

Fig. 5—(*a*) High and (*b*) low magnification SEM micrographs of iron based alloy 2605S processed at 8 kV and 200 MPa. Foil material pull-out is evident. The effect of pressure is negligible: *cf*. 80 MPa, Fig. 4.

(*a*) (*b*)

Fig. 6—(*a*) High and (*b*) low magnification SEM micrographs of iron based alloy 2605S processed at 10 kV and 200 MPa. Shown is the interface region after foil separation. Foil cracking occurred during separation. Sections from all four foil layers are present in (a), supported by the schematic inset.

in the processing parameters. Weld ligament diameter of the Co alloy was much greater than that for the Fe alloy for identical processing conditions. Raybould and Diebold[4] have shown that METGLAS 2605S-2 can be consolidated by application of pressure and temperature. They observed similar asperity bonding, and determined *via* Auger spectroscopy that the bonds consisted of SiO_2 "glue". This differs from the ligament microwelds observed in the present study. Auger depth profiling of fractured microwelds in METGLAS 2605S-2 showed no evidence of silicon enrichment.

The degree of crystallization was assessed by X-ray analysis of the iron-based alloy processed at 4 kV and 80 MPa. The X-ray scan illustrated in Figure 7 confirms that the bulk remains in virtually the same state as the starting material.

In summary, cobalt and iron based amorphous metal foils have been successfully joined using capacitor discharge resistance welding. The microweld array between ribbon elements is generally stronger than the individual components.

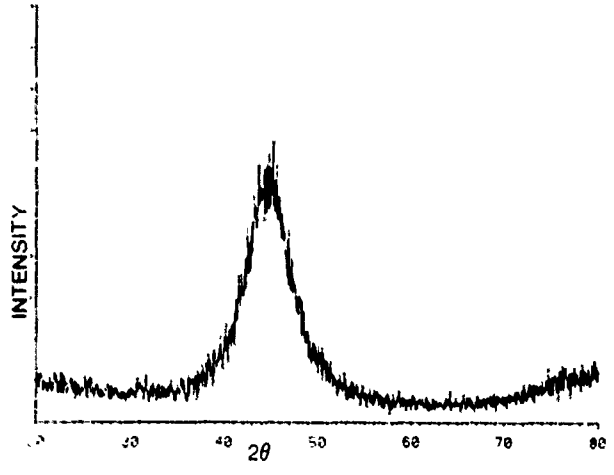

Fig. 7—X-ray analysis for the iron alloy 2605S assembly after joining (4 kV/80 MPa). The initial, amorphous structure is retained.

The strength and appearance of the joints were similar for air-side to air-side joints, wheel-side to air-side joints, and wheel-side to wheel-side joints. The size of each microweld is proportional to the discharge voltage and is independent of processing pressure between 80 and 200 MPa. The spacing of microwelds is 100 to 200 μm, independent of processing voltage and pressure. This joining technique does not produce measurable oxide formation or crystallization of the bulk.

The authors would like to thank the staff of the Center for Electromechanics, particularly Mr. R. Allen who assisted with fabrication and operation of the processing system. This research was funded by DARPA/NADC contract N6 2269-85-C-0222, DARPA/ARO contract DAAL03-87-K-0073, and by the State of Texas under an Academic Development Program in Magnetic Materials and Devices.

REFERENCES

1. A. H. Clauer, R. V. Raman, R. S. Carbonara, and R. E. Maringer: in *Rapid Solidification Processing, Principles and Technologies, II*, R. Mehrabian, B. H. Kear, and M. Cohen, eds., Claitor's Publishing Div., Baton Rouge, LA, 1980, p. 339.
2. J. L. Stempin and D. R. Wexell: U. S. Pat., 4298382, 1981.
3. H. H. Lieberman: in *Rapid Solidification Processing, Principles and Technologies, II*, R. Mehrabian, B. H. Kear, and M. Cohen, eds., Claitor's Publishing Div., Baton Rouge, LA, 1980, p. 393.
4. D. Raybould and A. C. Diebold: *J. Mat. Sci. and Eng.*, 1986, vol. 21, pp. 193-202.
5. N. B. Dahotre, C. Wakade, and K. Mukherjee: in *TMS-AIME Conf. Proc. on Laser Processing of Materials*, K. Mukherjee and J. Mazumder, eds., TMS-AIME, Warrendale, PA, 1985, pp. 101-15.
6. S. Clyens, S. T. S. Al-Hassani, and W. Johnson: *Int. J. Mech. Sci.*, 1976, vol. 18, pp. 37-44.
7. D. J. Williams and W. Johnson: *Powder Metallurgy*, 1982, vol. 25, pp. 85-89.
8. F. Spaepen and A. I. Taub: in *Amorphous Metallic Alloys*, F. E. Luborsky, ed., Butterworths, 1983, ch. 13, pp. 231-56.
9. T. W. Wu and F. Spaepen: in *Mechanical Behavior of Rapidly Solidified Materials*, S. M. L. Sastry and B. A. MacDonald, eds., TMS-AIME, Warrendale, PA, 1986, pp. 293-305.

Identification of an η boride phase as a crystallization product of a NiMoFeB amorphous alloy

Y. W. Kim,[a] L. Rabenberg, and D. L. Bourell
Center for Materials Science and Engineering, The University of Texas at Austin, Austin, Texas 78712

(Received 18 February 1988; accepted 17 June 1988)

A new, apparently metastable, Mo–Ni boride phase has been observed in transmission electron microscope samples of rapidly consolidated MoNiFeB metallic glass powders. The phase is cubic with lattice parameter 1.083 nm. Its space group as determined by electron diffraction is $Fd\bar{3}m$ and its approximate composition is Mo_3Ni_3B. Because its structure, its composition, and its role as a transition phase are analogous to those of η carbide (M_6C) in steels and cemented carbides, this phase has tentatively been named "η boride."

I. INTRODUCTION

In the course of an investigation of the feasibility of using a high current discharge to consolidate powders comminuted from melt spun metallic glass ribbons,[1] a previously unreported two-metal boride phase has been observed. This article describes identification and characterization of this new phase.

The new phase occurs as a transition state in the decomposition of a Ni-rich fcc solid solution, supersaturated with Mo and B, to a two-phase mixture of a fcc Ni solution and the equilibrium Mo_2NiB_2. As such, its metallurgical role is very similar to that of the η carbide (M_6C). The η carbide is a cubic ($Fd\bar{3}m$, $a_0 = 1.1$ nm) ternary intermetallic compound that occurs in W and Mo high-speed steels, austenitic stainless steels, and cemented carbides.[2] Originally described as W_2Fe_4B, it can vary in composition continuously to W_3Fe_3B. The η carbide can be formed from a variety of transition metal pairs including W–Ni, Mo–Ni, and Mo–Co. For this reason, and because this new boride phase seems to be isostructural with η carbide, it will be referred to as η boride.

II. EXPERIMENTAL DETAILS

An amorphous metallic alloy powder of nominal composition $Ni_{56.5}Mo_{23.5}Fe_{10.0}B_{10.0}$ (atomic percent) (Allied Corporation METGLAS® 7025) was rapidly consolidated using a homopolar generator. In this process, rotational kinetic energy is rapidly converted to a dc electrical current discharge; the current is caused to flow through a compact of the powder, resistively sintering it. The sintered body cools quickly as heat flows out of the sample into the surrounding platens.[3] Although this process, as currently implemented, has never been sufficiently rapid to retain the amorphous state in the dense body, it did produce a variety of microcrystalline states, as described elsewhere.[4] Specimens for phase identification were sliced from the consolidated alloys using an electrodischarge machine, encapsulated in evacuated (10^{-4} Torr) Vycor tubes, and annealed at 800 °C for 4 h and then 1100 °C for 2 h.

Phase identification and characterization were accomplished using a Philips automated powder diffractometer, a JEOL 200CX TEM, and a JEOL 1200EX TEM/STEM, equipped with energy dispersive x-ray spectroscopy (EDS) and electron energy loss spectroscopy (ELS). Electron transparent foils were prepared by electrodischarge machining 3 mm disks, then twin-jet electropolishing in an electrolyte of 3 parts nitric acid and 1 part methanol at -25 to -35 °C. Convergent beam electron diffraction (CBED) in TEM mode at 120 keV in the JEOL 1200EX was used to determine the symmetry of the η boride phase. The approximate composition of metallic elements in the η boride was determined using standardless analysis of EDS spectra obtained from particles embedded in the Ni-rich matrix in thin foil specimens using a conventional Be window detector. The presence of B and the absence of C in the η boride was confirmed using ELS.

III. RESULTS

The η boride occurred as a minor phase in many of the consolidated samples after aging for extended times at temperatures in the range 650 to 1100 °C.[4] Figure 1 shows an x-ray diffractometer (2θ) scan of a consolidated sample, subsequently used to coarsen the η phase particles. The strong lines are from the Ni-rich fcc solid solution and the equilibrium Mo_2NiB_2 phase. Several η lines have been indicated. Further aging at 1100 °C caused the η to be consumed by the growing Mo_2NiB_2 and fcc matrix phases. Because the largest η crystals obtainable were typically 1.0 μm in size, single-crystal x-ray work was effectively precluded.

The η generally precipitated at grain boundaries of the fcc Ni-rich solid solution (γ). A typical TEM micrograph and selected area diffraction pattern (SAD) appear as Fig. 2. After the structural analysis using CBED,

[a] Present address: Hyundai Advanced Engineering and Research Lab, 140-2 Ke-Dong, Jongro-gu, Seoul, 110 Korea.

 0884-2914/88/061336-06$01.75

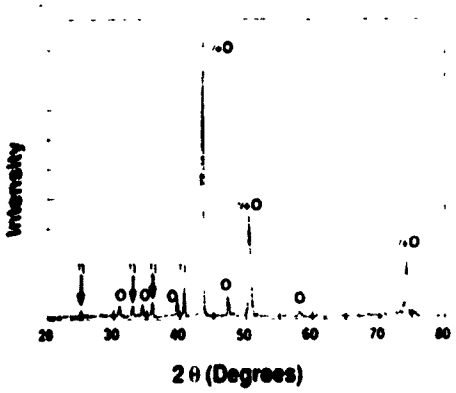

FIG 1 X-ray diffractometer (2θ) scan of a sample aged 4 h at 800 °C and 2 h at 1100 °C to coarsen the η particles. Here, "γ" refers to the Ni-rich matrix; "O" refers to the orthorhombic Mo_2NiB_2 phase. The four lines marked "η" correspond to the {111}, {400}, {331}, and {422} reflections of the η boride.

it could be determined that this SAD is typical of the η phase; such patterns indicate that the η commonly takes the following orientation relationship with respect to the γ grains:

$$(110)_\eta \| (110)_\gamma,$$

$$[1\bar{1}1]_\eta \| [1\bar{1}1]_\gamma,$$

$$[\bar{1}11]_\eta \| [1\bar{1}\bar{5}]_\gamma.$$

The lattice parameters of the η ($a_0 = 1.083$ nm) and the γ ($a_0 = 0.361$ nm) are such that the following lattice matches are observed:

$$\eta{:}d_{(111)} = \gamma{:}3d_{(111)},$$

$$\eta{:}d_{(1\bar{1}1)} = \gamma{:}9d_{(1\bar{1}\bar{5})}.$$

The η particles are commonly facetted, with large areas of $\{110\}_\eta$ in contact with $\{110\}_\gamma$.

Determination of the η phase point group was done by obtaining CBED patterns from the three prominent zone axes shown in Fig. 3. The analysis, as well as the notation and terminology, follows Buxton *et al.*[5] and Steeds.[6] The pertinent observations and results are summarized in Table I. The point group $m\bar{3}m$ is the only one listed for each zone axis, so $m\bar{3}m$ is the only point group that can give the observed diffraction symmetries. For point group $m\bar{3}m$, the *A* zone axis ($4mm1_R$) is an ⟨001⟩ axis, the *B* zone axis ($2mm1_R$) is an ⟨011⟩, and the *C* zone axis (6_Rmm_R) is a ⟨111⟩.

The Bravais lattice was determined by analysis of the radii of the higher-order Laue-zone (HOLZ) rings as indicated in Fig. 3 in conjunction with the x-ray powder pattern of Fig. 1. The x-ray pattern was indexed on the basis of a face-centered-cubic unit cell with $a_0 = 1.083$ nm. Calculation of the expected separation between the zero-order Lane zone (ZOLZ) and the HOLZ (H in Fig. 3) using the equations derived by Raghavan *et al.*[7] are consistent with that analysis. It is concluded that the η boride has a face-centered Bravais lattice.

The four space groups consistent with point group $m\bar{3}m$ and face-centering translations are $Fm\bar{3}m$, $Fm\bar{3}c$, $Fd\bar{3}m$, and $Fd\bar{3}c$. The "*d*" and "*c*" glides cause systematic absences under kinematic diffraction conditions, for dynamical electron diffraction, extinctions only occur for specific orientations of the electron beam relative to the specimen.[8] In particular, extinctions normally occur for two-dimensional diffraction if the beam is perpendicular to a glide plane. In this case, the {200} and {420} reflections are absent in the [001] zone, but the $\{1\bar{1}1\}$, $\{3\bar{1}1\}$, and $\{1\bar{3}3\}$ reflections are present in the [011] zone (Fig. 4). Thus, "*d*" glides normal to ⟨001⟩ are present, but there are no "*c*" glides normal to ⟨011⟩. Further verification is obtained using the [102] zone

FIG 2 (a) TEM micrograph of η boride particles (arrowed) at a grain boundary of the Ni-rich matrix. (b) A diffraction pattern that selects an area including one η particle and the lower Ni grain shows that both the η and the Ni are near the ⟨011⟩ orientation. The direction of the arrows is parallel to the common $[1\bar{1}1]$ direction.

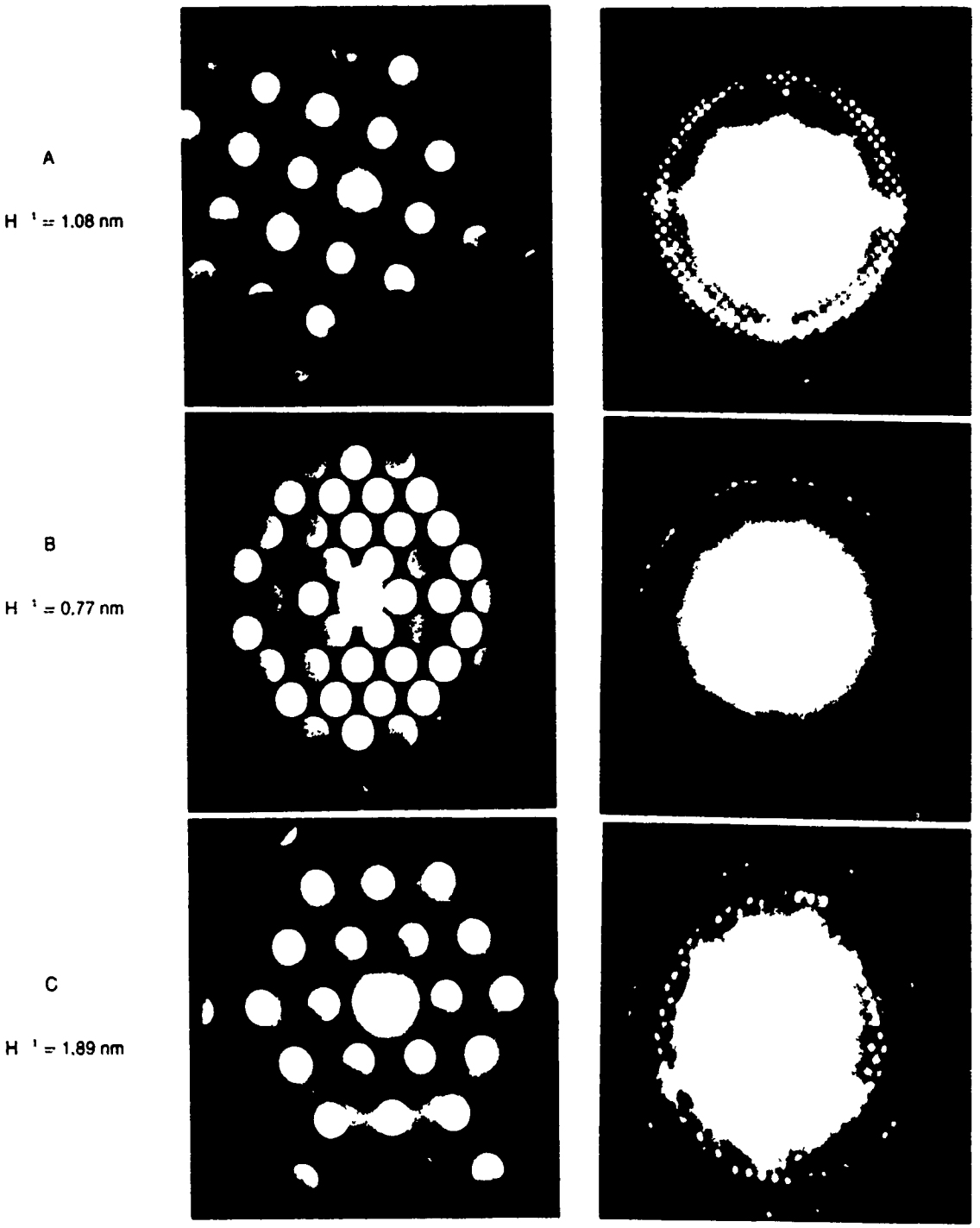

FIG. 3. CBED patterns from three prominent zone axes of a single η boride particle. *A*, *B*, and *C* are [001], [011], and [111] zone axes, respectively. The left and right columns show two different camera lengths.

axis in which the electron beam lies in the plane of one of the "*d*" glides (Fig. 5). The black line through the $(\bar{4}02)$ reflection is also indicative of a glide plane normal to [020]. The only space group consistent with these observations is $Fd\bar{3}m$.

The η boride decomposes into a Ni-based fcc solid solution and the stable orthorhombic Mo_2NiB_2 phase when aged for very long times. This fact made it impossible to grow large single crystals for a complete x-ray structure determination.

The chemical composition of the η phase as determined by EDS is 55% Mo, 39% Ni, and 6% Fe (atomic

TABLE I. Observed electron diffraction symmetries for the three zone axes of Fig. 3.

Zone axis	*A*	*B*	*C*
Bright field	$4mm$	$2mm$	$6mm$ or $3m'$
Whole pattern	$4mm$	$2mm$	$3m$
Possible diffraction groups	$4mm$ $4mm1_R$	$2mm$ $2mm1_R$	$3m1_R$ $3m, 6_R mm_R$
Possible point groups	$4mm$ $4/mmm$ $m\bar{3}m$	$mm2$ $6m2$ mmm $4/mmm$ $6/mmm$ $m\bar{3}$ $m\bar{3}m$	$6m2$ $3m$ $\bar{3}m$ $\bar{4}\bar{3}m$ $m\bar{3}m$

percent). Boron in the η phase was readily detected using ELS, but no attempt was made to obtain accurate quantitation. Typical EDS and ELS results are shown in Fig. 6. The overall composition of the η boride probably falls between $Mo_3(NiFe)_3B$ and $Mo_4(NiFe)_2B$.

IV. DISCUSSION

It is somewhat surprising that no metal-rich ternary boride similar to the one observed here has ever been reported. Such phases are well known to exist in carbon- or silicon-containing systems. The η carbides (M_6C, prototype W_3Fe_3C, $a_0 = 1.106$ nm, 114 atoms per unit cell, $Fd\bar{3}m$), the τ carbides ($M_{23}C_6$, prototype $Cr_{23}C_6$, $a_0 = 1.0638$ nm, 116 atoms per unit cell, $Fm\bar{3}m$), and the "G" silicide phases ($M_{22}Si_7$, prototype $Ti_{16}Ni_6Si_7$, $a_0 = 1.187$ nm, 116 atoms per unit cell, $Fm\bar{3}m$) are cubic, ternary, intermetallic compounds that can exist over a range of metal stoichiometries and with a variety of metal substitutions. It is reasonable to

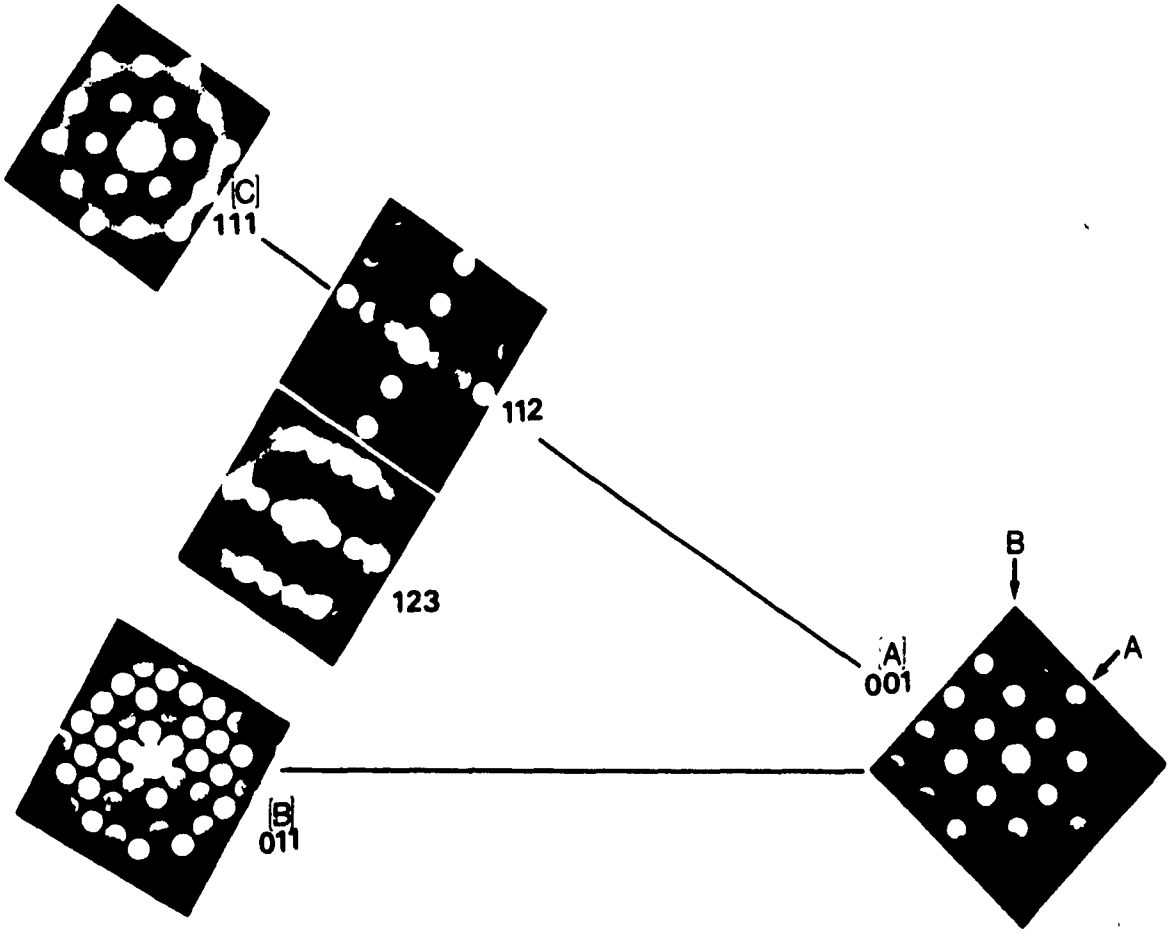

FIG. 4. Relative orientations of five different zone axes obtained from the same η boride particle (arranged as though on a stereographic projection.) Note that the (200) reflection occurs by double diffraction in the [011] but not in the [001].

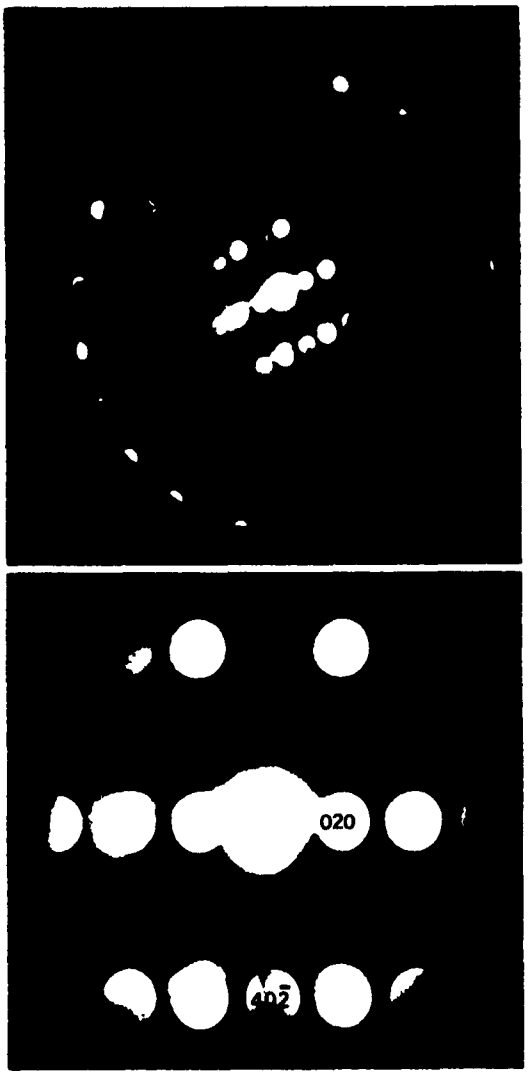

FIG. 5. CBED pattern from the η boride in the [102] orientation. The $(\bar{4}02)$ and $(40\bar{2})$ disks show radial black lines indicative of the presence of a glide plane normal to [020]. Upper and lower show two different camera lengths.

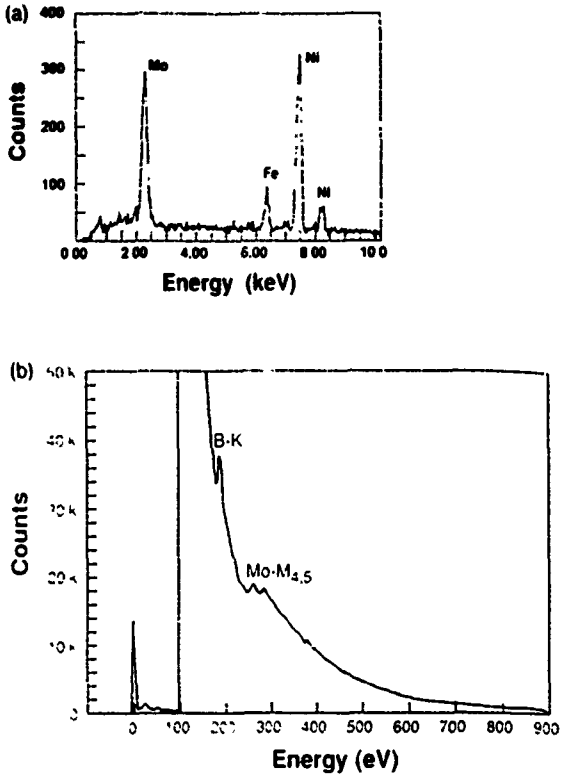

FIG. 6. (a) EDS spectrum and (b) ELS spectrum from the η boride.

expect that B might be able to substitute into one or more of these phases, especially since B tends to have properties intermediate between those of C and Si in metal-rich intermetallic compounds. Nevertheless, even though Goldschmidt[2] had already suggested more than 20 years ago that the transition from the η to the G phases might be a "fruitful subject of study," no one seems to have prepared and reported such a boride phase.

In this particular case, the $Fd\bar{3}m$ space group and the measured metal stoichiometries suggest that B has stabilized a structure isomorphous with the η carbides rather than with the G phases. If this is true, the B is in sixfold coordination, its nearest neighbors forming a trigonal antiprism. However, in the absence of a complete structure determination, these statements must remain somewhat tentative.

The η boride in this system is slightly unstable with respect to decomposition into the terminal solid solution and the orthorhombic Mo_2NiB_2 phases. Its existence here is made possible by the rapid thermal processing that allowed a relatively large B concentration to be metastably retained in the Ni matrix and by a slight competitive advantage in formation kinetics it may have over the Mo_2NiB_2. A small degree of stabilization by coherency effects may also be present. With regard to the kinetic aspects, the η phase is structurally more similar to the fcc Ni matrix than is the Mo_2NiB_2 in that the atomic occupancy of the {111} in the η phase is very similar to that of the {111} in the Ni-rich terminal solid solution. The atomic motions required for the formation of the η are probably less extensive than those required for the formation of Mo_2NiB_2. This idea has been invoked in descriptions of the metallurgical role of η carbide in high speed steels.[3] Evidence for coherency stabilization comes from the observation that the η boride takes specific orientation relationships and forms well-defined facets with the Ni-rich matrix. Presumably, the ability to form such low energy surfaces provides for more favorable conditions for the η phase. After coarsening, loss of coherency raises the specific surface energy of the η phase particles, eliminating the advantage that coherency provided and allowing the Mo_2NiB_2 to dominate.

Of broader interest is whether the η boride can be stabilized as a single phase by substitution of other transition metals. Using the idea that B is slightly larger than C, it seems appropriate to choose larger metallic species. Thus (Nb, Hf, or Zr)$_3$Fe$_3$B seems to be a prime candidate. Whether such alloys would, in fact, form a stable single phase must await experimental verification.

V. CONCLUSIONS

A new two-metal boride phase having space group $Fd\bar{3}m$ and $a_0 = 1.083$ nm has been observed and identified in crystallization products of a MoNiFeB metallic glass. Although this crystalline phase is marginally unstable with respect to decomposition into better-known phases, it represents the first of what might be a large class of ternary borides, some of which are probably stable.

ACKNOWLEDGMENTS

Metallic glass was provided by Dr. Derek Raybould of Allied Corporation. The assistance of Dr. C. Persad in coordinating the project is gratefully acknowledged. T. A. Aanstoos and J. Allen of The University of Texas Center for Electromechanics operated the homopolar generator; their efforts are greatly appreciated.

This work was supported by DARPA/NADC Contract No. N62269-85-C-0222 and DARPA/ARO Contract No. DAAL03-87-K-0073.

REFERENCES

[1] H. L. Marcus, D. L. Bourell, Z. Eliezer, C. Persad, and W. Weldon, J. Metals **39**, 6 (1987).
[2] H. J. Goldschmidt, *Interstitial Alloys* (Plenum, New York, 1967).
[3] J. B. Walters and T. A. Aanstoos, Met. Prog. **127**, 25 (1985).
[4] Y. W. Kim, Ph. D. dissertation, The University of Texas at Austin, 1987. Available from University Microfilms, Ann Arbor, MI.
[5] B. F. Buxton, J. A. Eades, J. W. Steeds, and G. M. Rackham, Proc. R. Soc. London **281**, 171 (1976).
[6] J. W. Steeds, in *Introduction to Analytical Electron Microscopy*, edited by J. J. Hren, J. I. Goldstein, and D. C. Joy (Plenum, New York, 1979), pp. 387–422.
[7] M. Raghavan, J. C. Scanlon, and J. W. Steeds, Met. Trans. A **15A**, 1299 (1984).
[8] J. Gjønnes and A. F. Moodie, Acta Cryst. **19**, 65 (1965).

Materials Science and Engineering, A123 (1990) 99–115

High Energy, High Rate Powder Processing of a Rapidly Quenched Quaternary Alloy, $Ni_{56.5}Mo_{23.5}Fe_{10}B_{10}$

Y. W. KIM*, D. L. BOURELL and C. PERSAD

Center for Materials Science and Engineering, The University of Texas at Austin, Austin, TX 78712 (U.S.A.)

(Received July 7, 1989)

Abstract

Nickel-based metallic glass powder has been successfully consolidated using high energy, high rate (HEHR) processing. Processing involved compaction pressures of 250–400 MPa and electrical energy densities of 1830–2460 J g^{-1}. Over 95% of the energy was deposited in less than 1 s. Consolidates were structurally inhomogeneous, with fine borides near the surface and coarse borides in a central sample nugget zone. Microhardness tests correlated with boride particle size. All compacts crystallized during HEHR consolidation, forming a fine Ni–Mo–Fe f.c.c. solid solution, Mo_2NiB_2 and, in some cases, a CuPt-type structure of unidentified composition. The thermal stability of HEHR processed consolidates was assessed by annealing for up to 100 h at 650 °C. New phases appeared, including Ni_3Mo, $M_{23}C_6$-type boride and M_6C-type boride. On monotonic heating, the crystallization sequence for $Ni_{56.5}Mo_{23.5}Fe_{10}B_{10}$ was determined to be amorphous phase → phase separation → glass transition of a high temperature amorphous phase → partial crystallization of the Ni–Mo–Fe f.c.c. solid solution → complete crystallization (Mo_2NiB_2). The activation energy for the low temperature crystallization, 290 kJ mol^{-1}, equals the interdiffusion value for molybdenum in nickel. The activation energy for the high temperature crystallization, 390 kJ mol^{-1}, compares favorably with the activation energy for molybdenum self-diffusion. Two peaks on the HEHR power curves during processing are interpreted to reflect changes in powder resistivity associated with the crystallization events.

1. Introduction

There has been sustained interest in bulk consolidation of rapidly quenched metallic materials for engineering applications [1–6]. More recently, these materials have been identified as potential precursor materials for microcrystalline composites [7]. Cahn [8] has outlined a parallel approach for making microcrystalline ceramics from specially formulated oxide glasses, using the Pyroceram processes developed around 1960. In the last 6 years, several new metallic glasses have been formulated, combining transition metals and metalloids [9–12]. Several of these materials retain some ductility and high strength after devitrification.

These materials are bulk consolidated from powders or thin ribbons by numerous processing approaches which minimize structural degradation by limiting the time at an elevated temperature. These include plasma spraying [13], laser welding [4], swaging [14], warm deformation processing [5, 15] and explosive or dynamic compaction [16–21]. Success is limited since these materials form low toughness phases when they crystallize at a relatively low temperature. Typically $T_g \approx 0.5 T_m$ where T_g is the glass transition temperature and T_m is the liquidus temperature [22]. Bulk processing of these materials by hot pressing or extrusion is possible. However, the high temperature exposure generally induces thermal degradation and microstructural coarsening [23].

High energy, high rate (HEHR) processing is an alternative method for consolidating microcrystalline particulate materials. It attempts to take advantage of pulse heating above T_g, which can increase nucleation rates by orders of magnitude [24]. The heating takes place under an

*Present address: Hyundai Advanced Engineering and Research Laboratory, 140-2 Ke-Dong, Jongro-gu, Seoul 110, Korea.

0921-5093/90/$3.50

applied stress which accelerates nucleation as well as volume-diffusion-controlled growth [24].

HEHR power sources and processing have been described elsewhere for a variety of materials [25]. The purpose of this investigation was to assess the feasibility of HEHR processing in bulk consolidation of microcrystalline composite materials by devitrification of metallic glass precursors. A 10 MJ capacity homopolar generator (HPG) power source was used to consolidate metallic glass powder by direct pulse electrical resistance heating under pressure. The energy deposited in the powder mass was of the order of 2000 J g^{-1}, over 95% of which was deposited in less than 1 s.

2. Experimental procedure

Metglas ®7025 ($Ni_{56.5}Mo_{23.5}Fe_{10}B_{10}$) powder and ribbon were obtained from the Allied Corporation. The ribbon was produced by planar flow casting; as-received (AR) powder (−140 mesh) was comminuted from the ribbon. The near-amorphous state of the $Ni_{56.5}Mo_{23.5}Fe_{10}B_{10}$ (AR) was confirmed via X-ray diffraction and transmission electron microscopy (TEM) (Fig. 1). Powder was preprocessed by annealing to produce starting materials differing from the as-received material. Some powder was heat treated in vacuum (10^{-4} Torr) at 515 °C for 1–3 h and some at 800 °C for 1 h. These preprocessed materials are referred to as follows: partly crystallized powder, $Ni_{56.5}Mo_{23.5}Fe_{10}B_{10}$ (I); fully crystallized powder, $Ni_{56.5}Mo_{23.5}Fe_{10}B_{10}$ (II).

As-received and preprocessed powders were consolidated in 50 g lots using a 10 MJ capacity HPG. The HPG is an electrical machine which converts stored rotational kinetic energy into electrical energy using the Faraday effect [26]. It is a low voltage, high current device operated in a pulsed mode. Typical energy delivery parameters for this research were 2.5–4 V and 40–70 kA. A powder mass was placed in a steel-backed alumina sleeve of 25 mm inside diameter. Copper plunger-electrodes were installed on each end and the powder mass was pressurized. The HPG was discharged across the powder mass via the copper electrodes. No protective atmosphere was used. During processing, the variations in electric current and voltage across the powder mass were continuously monitored using an oscillographic recorder. Energy dissipation was calculated by integration of the product of the curves.

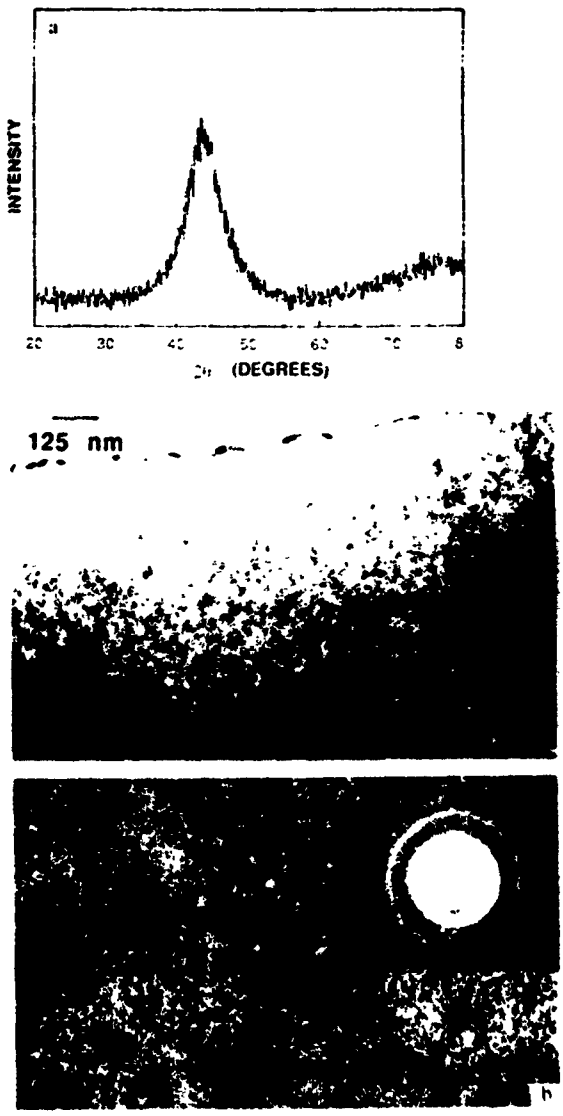

Fig. 1. a. X-ray diffraction pattern of the as-received $Ni_{56.5}Mo_{23.5}Fe_{10}B_{10}$; b. TEM micrographs and electron diffraction pattern of the as-received $Ni_{56.5}Mo_{23.5}Fe_{10}B_{10}$.

Structural homogeneity was assessed by microhardness testing: 500 g Knoop and diamond pyramid tests were performed on selected samples. Optical metallography was accomplished after mechanical polishing and etching using a solution of 2 g of Cr_2O_3, 400 ml of HCl and 80 ml of H_2O.

Scanning electron microscopy (SEM) was performed using a JEOL-35C scanning electron microscope. The SEM image was somewhat improved by sputtering a thin layer of gold on the sample surface. Specimens for TEM were prepared by twin-jet thinning in a Fischione cell using a solution of 3 parts of methanol and 1 part

of nitric acid at between −32 and −25 °C. Some TEM samples were prepared by ion milling using a Gatan twin miller, argon gas, an excitation voltage of 5 kV and a current of 0.1 A. A removal rate of approximately 1 μm h^{-1} was obtained. A JEOL-1200EX scanning transmission electron microscope operated at 120 kV was used for analytical microscopy. Energy-dispersive (X-ray) spectroscopy (EDS) and electron energy loss spectroscopy (EELS) were performed.

Differential scanning calorimetry (DSC) and, above 725 °C, differential thermal analysis (DTA) were used to detect crystallization exotherms. A Perkin–Elmer series 7 differential scanning calorimeter and a differential thermal analyzer 760 were used. The heating rate was varied between 40 and 160 K min^{-1}, and a nitrogen atmosphere was used (20 ml min^{-1}). The peak and transition temperatures were recorded. X-ray diffraction was performed using a Philips diffractometer with a copper tube operated at 35 kV with a nickel window.

3. Results

3.1. *High energy, high rate processing*

Table 1 lists the HEHR processing parameters for consolidation of powders. The energy inputs ranged beween 1830 and 2460 J g^{-1}. Figure 2(a) shows typical power distributions for $Ni_{56.5}Mo_{23.5}Fe_{10}B_{10}$ (AR) processed at various energy inputs, and Figs. 2(b) and 2(c) those for the three starting materials processed at less than 2000 J g^{-1} and greater than 2000 J g^{-1} respectively. All electrical energy was deposited in less than 1.5 s. The peak power ranged between 100 and 200 kW. All consolidations of $Ni_{56.5}Mo_{23.5}Fe_{10}B_{10}$ (AR) exhibited power curves with three peaks, at approximately 80, 200 and 300 ms. These power curve peaks were better articulated at high energy inputs. The second peak was absent for compacts of $Ni_{56.5}Mo_{23.5}Fe_{10}B_{10}$ (I). For $Ni_{56.5}Mo_{23.5}Fe_{10}B_{10}$ (II), only the first peak was present.

Microstructural examination of HEHR processed specimens revealed complete densification but varying degrees of structural inhomogeneity. This is evident in the etching behavior of specimen cross-sections shown in

TABLE 1 High energy, high rate processing parameters

Specimen	*Specific energy input* J g^{-1}	*Pressure* MPa	*Aspect ratio*[a]	*Powder condition*[b]
721	1850	393	0.45	AR
820	1970	251	0.23	AR
752	2285	327	0.23	AR
158	–	266	–	AR
757	2395	251	0.23	AR
766	1830	251	0.23	I
765	2120	251	0.23	I
824	1900	251	0.23	II
827	2460	251	0.23	II

[a]Post-processed height-to-diameter ratio.
[b]AR, as-received powder; I, powder partly crystallized by annealing at 515 °C for 1–3 h; II, powder fully crystallized by annealing at 800 °C for 1 h

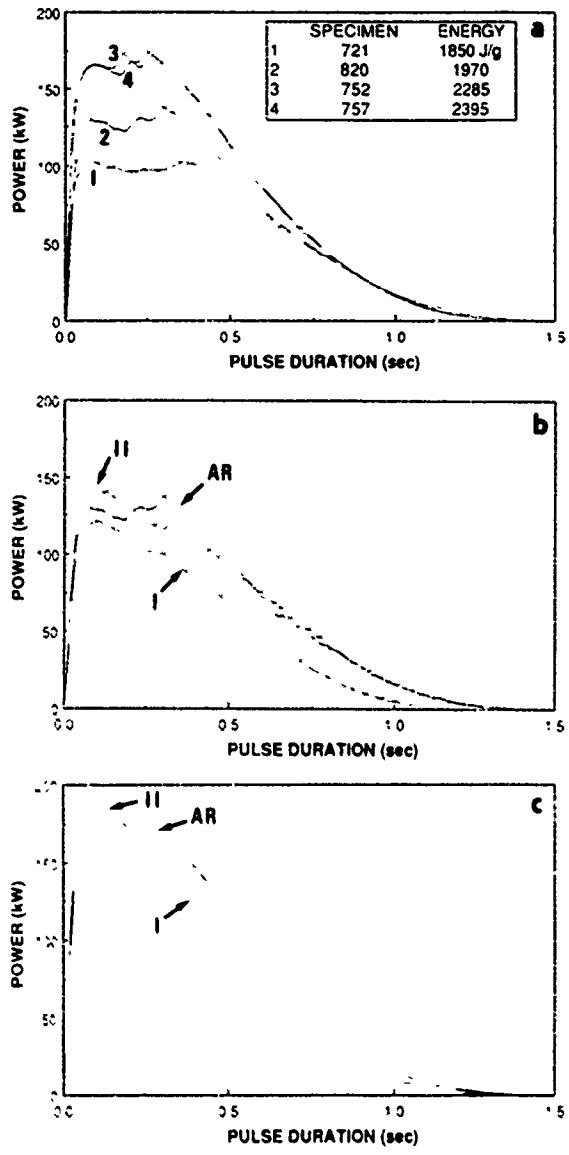

Fig. 2. Power spectra of the a as-received powder consolidates, b low less than 2000 J g^{-1} input energy samples 820 AR, 766 I and 824 II and c high more than 2000 J g^{-1} input energy samples 757 AR, 765 I and 827 II.

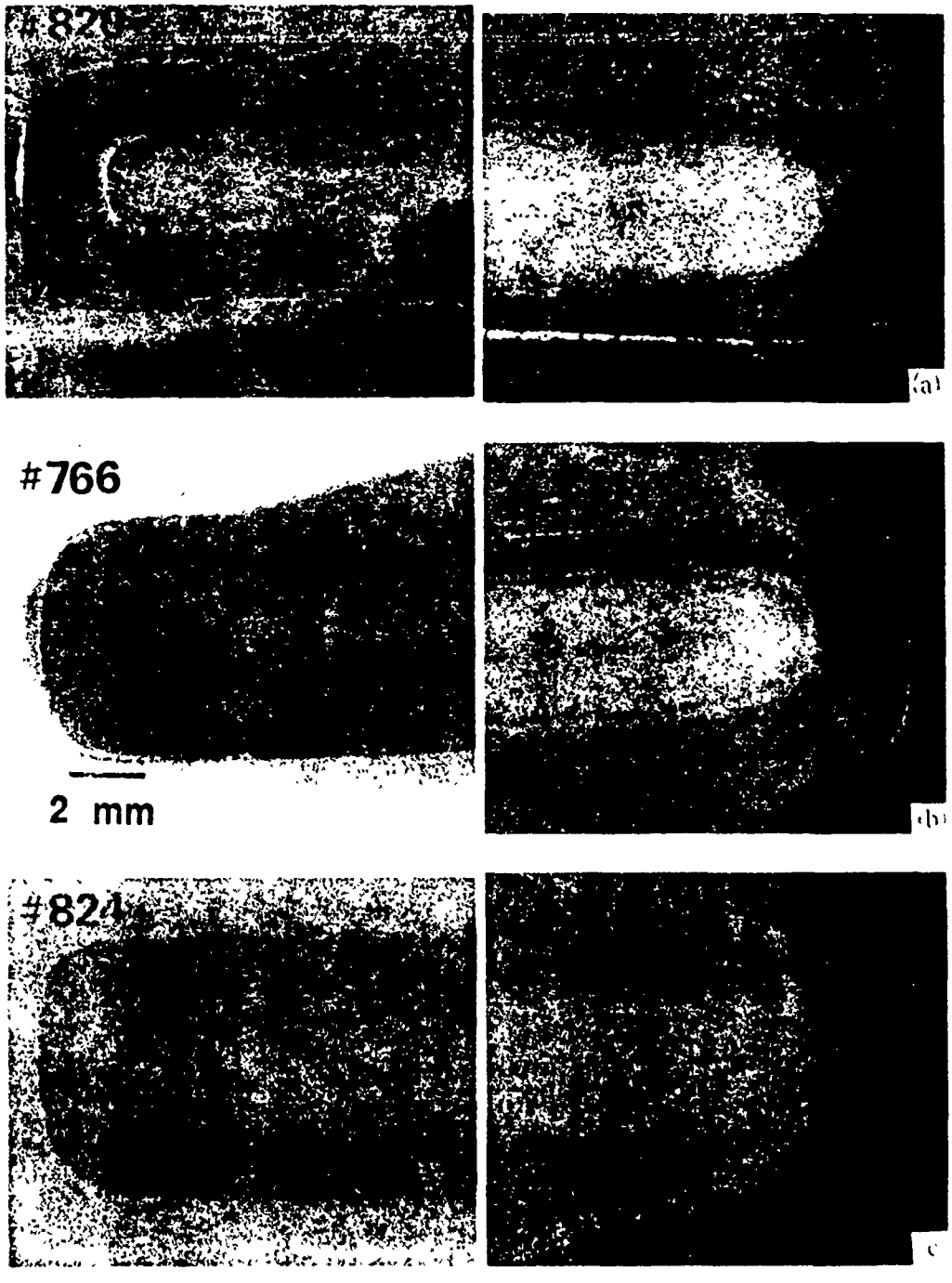

Fig. 3. Heterogeneous macrostructures with different input energy shown by the left-hand (low input energy) and right-hand (high input energy) columns: (a) the as-received powder consolidates, (b) the crystallized powder consolidates annealed at 515 °C for 1 h, (c) the crystallized powder consolidates annealed at 800 °C for 1 h. Structural inhomogeneity, evidenced by the etching response, is minimized for low energy input in fully crystallized powder sample S24.

Fig. 3. The axis of symmetry for each specimen is coincident with the vertical line splitting the left- and right-hand columns. The left-hand column represents low energy inputs (less than 2000 J g^{-1}) and the right-hand column high energy inputs (greater than 2000 J g^{-1}). The three rows are for $Ni_{78}Mo_{2.5}Fe_5B_{14.5}$ AR, I and II. It appears that structural homogenization is

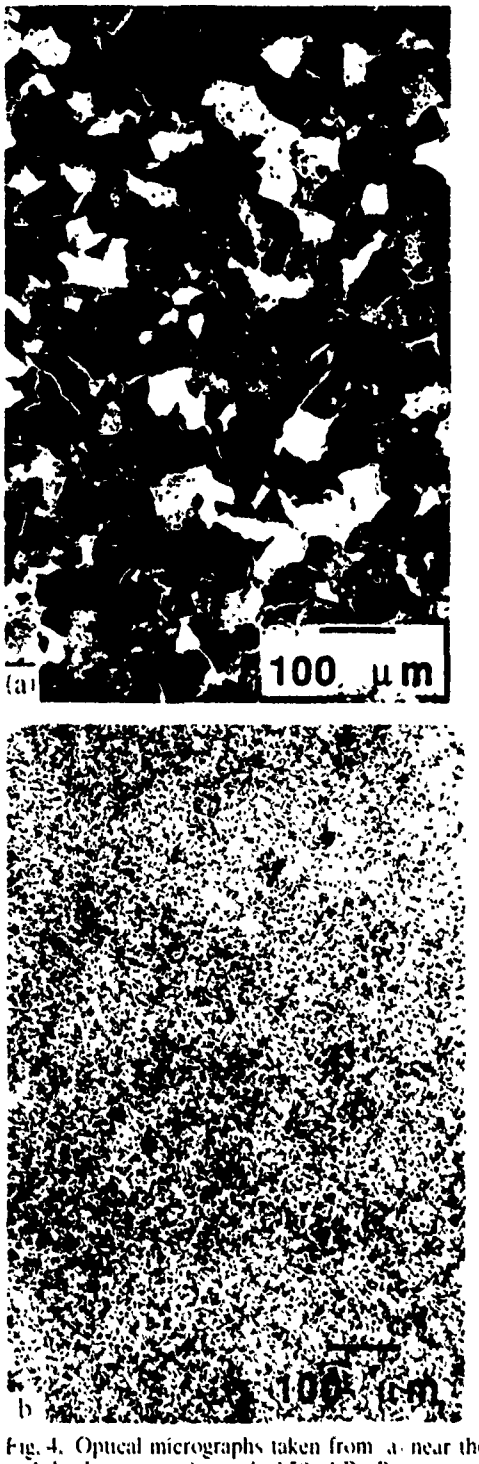

Fig. 4. Optical micrographs taken from (a) near the surface and (b) the center of sample 158 AR. Prior particle boundaries are visible near the surface and some voids are present. Fine borides dominate the central region of the specimen

improved by low energy density consolidation and structurally stable starting material. Figure 4 shows optical micrographs of the microstructures of a low energy input, HEHR processed $Ni_{56.5}Mo_{23.5}Fe_{10}B_{10}$ (AR) specimen in the dark-etching region near the copper electrode during consolidation (Fig. 4(a)) and in the light-etching region near the center of the specimen (Fig. 4(b)). At low magnifications the specimen appears unaffected after processing near the surface, retaining the powder particle boundaries. The central "nugget" region of the specimen was structureless except for a well-distributed second phase of dark-etching particles. SEM micrographs of over-etched specimens at a higher magnification are shown in Figs. 5(a) and 5(b). The particles, identified as the Mo_2NiB_2 reaction product in an Ni–Mo solid solution matrix, are less than 0.1 μm in size near the surface specimen and are coarsened to approximately 1 μm in the central nugget core. The boride was present in all HEHR processed materials. Its size in the dark-etching surface region was 0.1 μm or less for all specimens, although the boride distribution was more uniform when the starting material was $Ni_{56.5}Mo_{23.5}Fe_{10}B_{10}$ (I) (*cf.* Figs. 5(a) and 5(c)). Specimens which tended toward macroscopic homogeneity exhibited less boride coarsening. This is shown in Figs. 5(c) and 5(d), SEM micrographs taken from the surface and nugget region respectively of $Ni_{56.5}Mo_{23.5}Fe_{10}B_{10}$ (I) HEHR processed at a low energy input. Some coarsening occurred in the central region of this specimen relative to the surface, but the extent is significantly less than in the $Ni_{56.5}Mo_{23.5}Fe_{10}B_{10}$ (AR) HEHR processed at high energy density (Fig. 5(b)).

Axial inhomogeneity was further characterized by microhardness testing. Figure 6 shows a typical hardness traverse. The nugget zone containing coarse borides was significantly softer than the dense coarse-grained surrounding material containing the fine borides. Hardness profiles for the six specimens in Fig. 3 appear in Fig. 7. The diamond pyramid hardness of the central nugget zone was consistently 500 DPH for the four specimens exhibiting this feature. The primary effect of increased energy density was to expand the size of the nugget zone without substantive change in surface hardness 700–800 DPH.

HEHR processed specimens subjected to microstructural and hardness characterization were re-evaluated after annealing at 650 °C for 20, 50 or 100 h. The hardness profiles and Mo_2NiB_2 morphology were unchanged by this post-processing annealing.

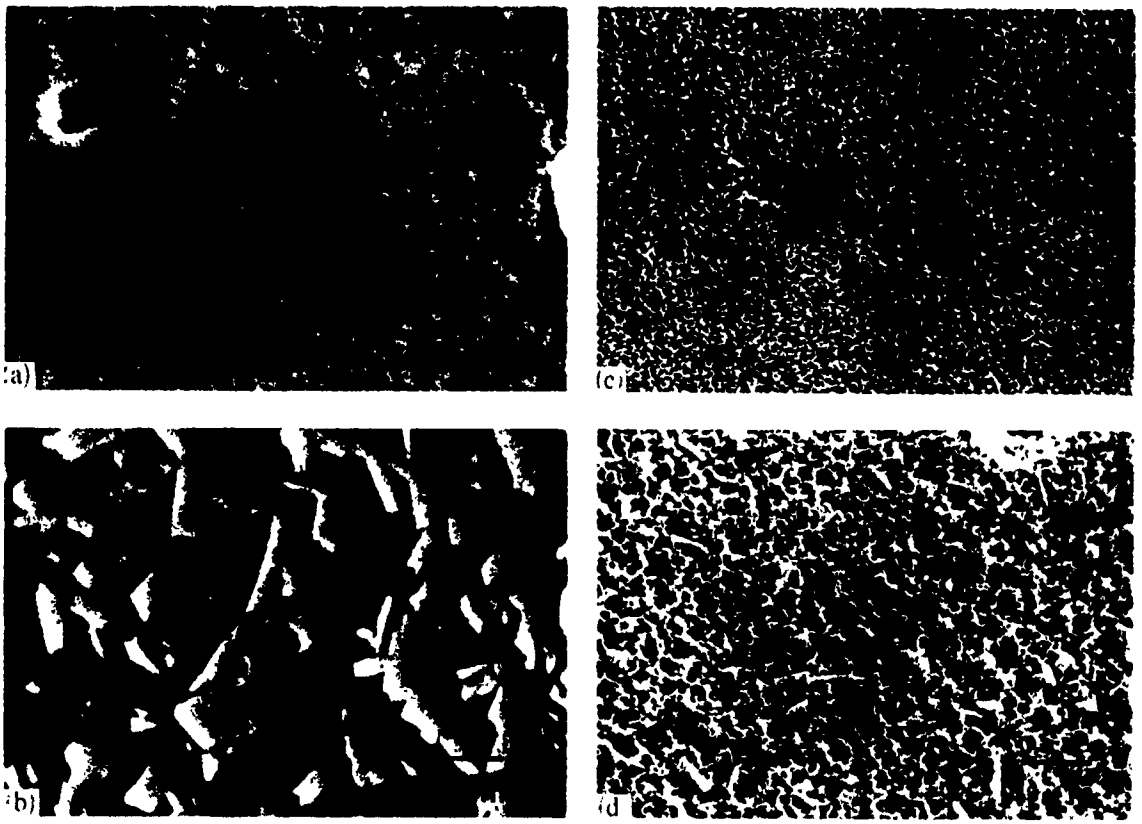

Fig. 5. SEM micrographs taken from (a), (c) near the surfaces and (b), (d) near the centers of (a), (b) sample 757 (AR) and (c), (d) sample 766 (I). The Mo_2NiB_2 particles are coarsened in the center of the samples but remain fine and well distributed in the dark-etching surface region.

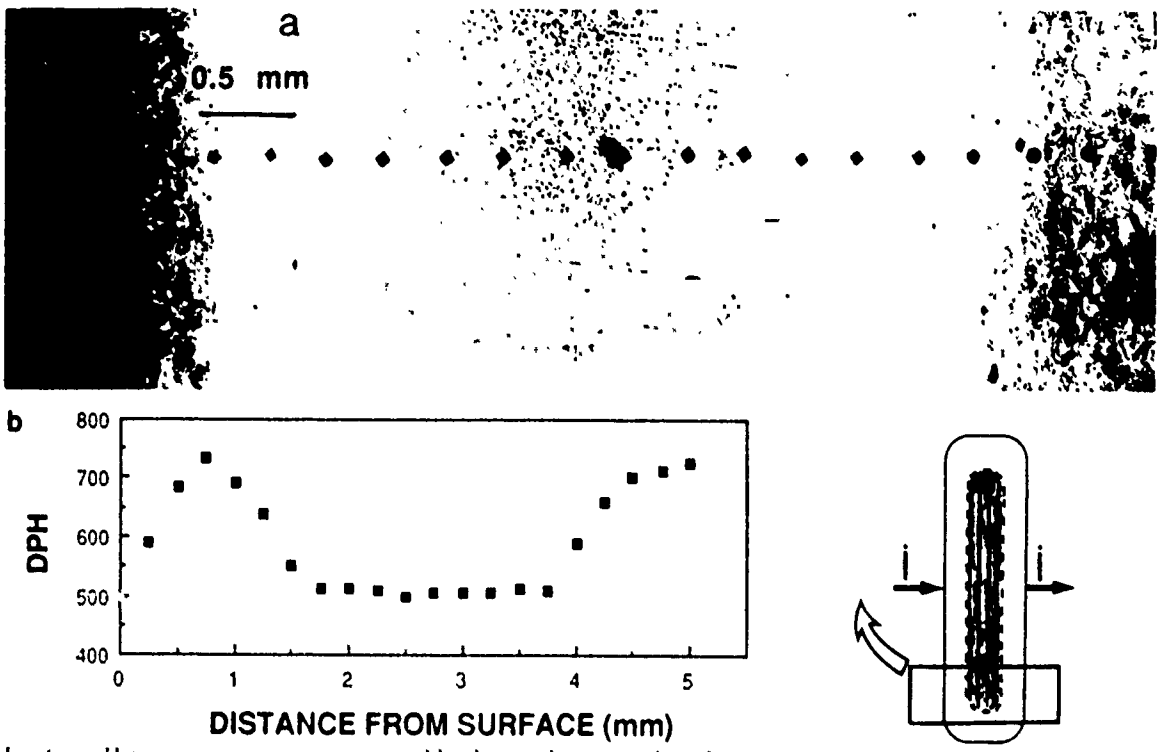

Fig. 6. a Heterogeneous macrostructure and hardness indentations along the axial dimension for sample 158 as shown in the schematic cross-section. The arrows indicate the direction of current flow during consolidation. b Diamond pyramid hardness values for the indentations.

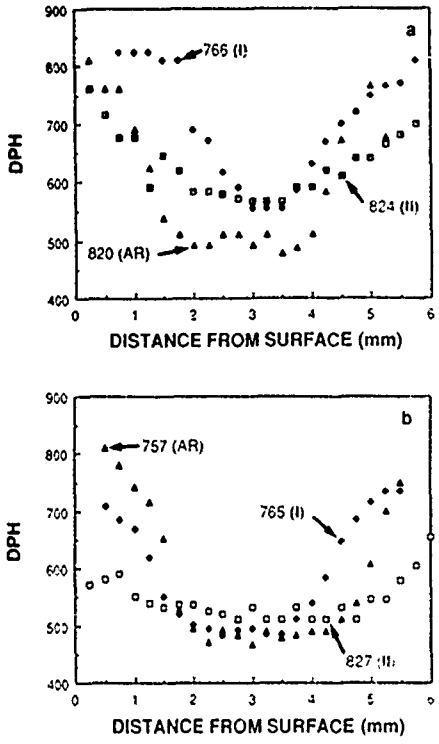

Fig. 7. Axial hardness profiles of the a low and b high input energy samples. The extent of the light-etching nugget zone of Fig. 3 corresponds to the central 500 DPH hardness plateau.

3.2. *Crystallization behavior*

The crystallization of $Ni_{56.5}Mo_{23.5}Fe_{10}B_{10}$ was probed using thermal analysis (DSC and DTA), X-ray diffraction and analytical electron microscopy. The structure of ribbon from which the powder was comminuted is shown in Figs. 1(b), 8(a) and 8(b), for the as-received condition, after heating in a DSC chamber to 537 °C at a rate of 40 K min^{-1}, and after heating in a DSC chamber to 677 °C at a rate of 40 K min^{-1} respectively. The diffraction patterns confirm the presence of amorphous material in all cases. The as-received material (Fig. 1(b)) is mottled with fine particle features approximately 5 nm in diameter. The material heated to 537 °C shows similarly sized particles now superimposed in a compositionally modulated matrix. The light areas in Fig. 8(a) are nickel rich; the dark areas are iron and molybdenum enriched. Material heated to 677 °C (Fig. 8(b)) partially crystallized with particles 10–15 nm in diameter. At the lower magnification the modulated structure is still imaged but is less distinct than the material illustrated in Fig. 8(a).

The effect of powder preprocessing is shown in Fig. 9 for as-received (AR), partially crystallized (I) and fully crystallized (II) powder. The as-

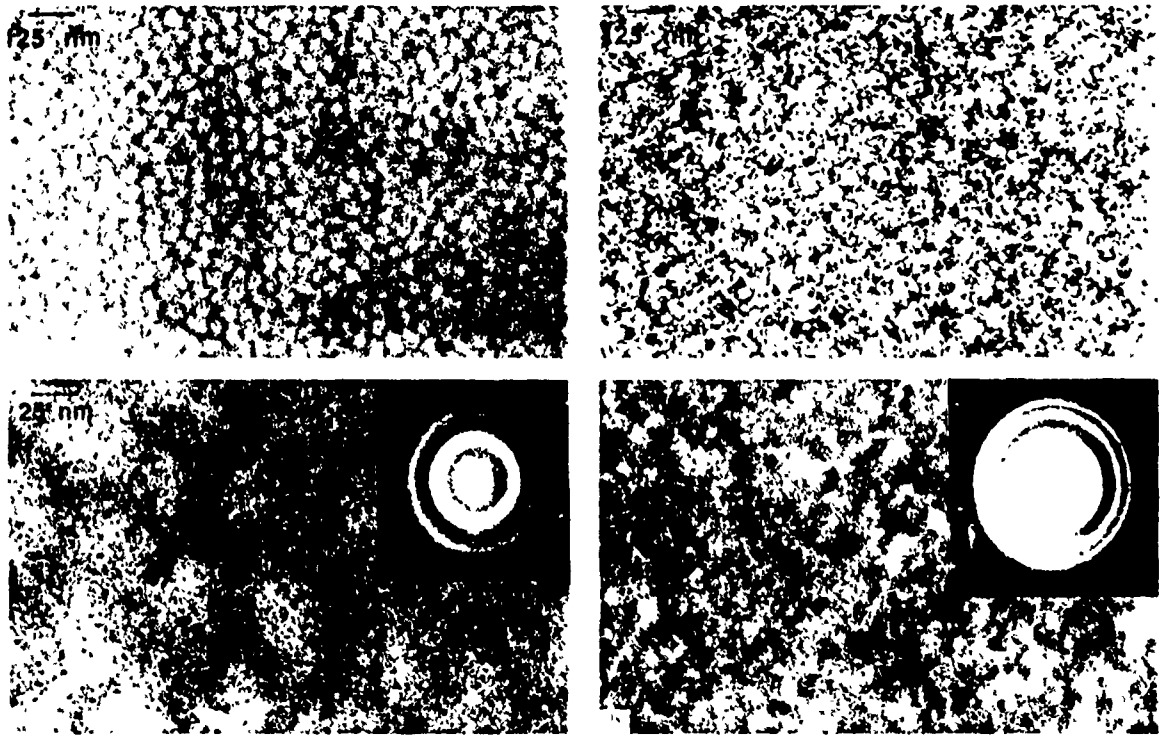

Fig. 8. TEM micrographs and electron diffraction patterns of as-received ribbon scanned by DSC at 40 K min^{-1} up to a 537 °C and b 677 °C. A modulated structure and some amorphous material are present in both cases. Fine particles are visible in the high magnification micrographs.

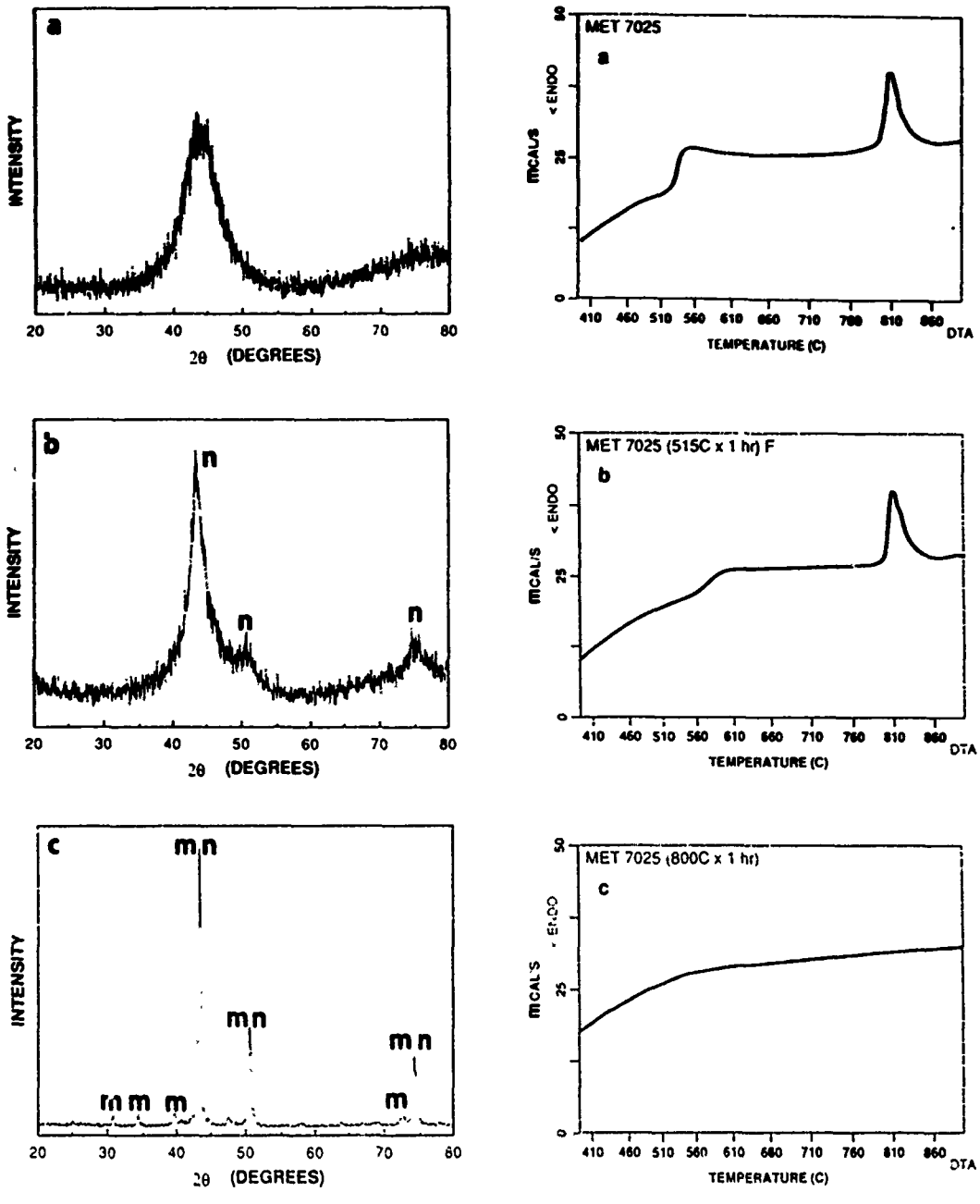

Fig. 9. X-ray diffraction patterns and DTA thermograms from a the as-received powder (AR), (b) powder annealed at 515 °C for 1 h (F) and (c) powder annealed at 800 °C for 1 h (H).

received material shows a single broad X-ray peak indicative of its amorphous nature. DTA of the $Ni_{56.5}Mo_{23.5}Fe_{10}B_{10}$ (AR) is typified by two exothermic crystallization peaks at 531 and 815 °C for a heating rate of 40 K min^{-1}. The $Ni_{56.5}Mo_{23.5}Fe_{10}B_{10}$ (F) (515 °C for 1 h) Fig. 9 b shows three diffraction peaks labelled n, which correspond to f.c.c. Ni–18at.%Mo solid solution of lattice parameter 0.36 nm*[27]. The first DTA crystallization peak is absent and the high temperature crystallization peak is still present.

*EELS and EDS results of phase identification from HEHR consolidated sample 158 (AR) and sample 166 (F) yield matrix compositions of Ni–23at.%Mo–10at.%Fe and Ni–20at.%Mo–10at.%Fe respectively. This phase is referred to as the "f.c.c. solid solution".

Based on DSC results, the inflection at 575 °C is thought to be associated with a glass transition in the high temperature amorphous material. $Ni_{56.5}Mo_{23.5}Fe_{10}B_{10}$ (II) (800 °C for 1 h) exhibits two sets of sharp diffraction peaks, the n peaks for the f.c.c. solid solution and a set of m peaks which were indexed as Mo_2NiB_2. The (211)–(310), (121) and (231) Mo_2NiB_2 peaks are coincident with the (111), (200) and (220) f.c.c. solid solution peaks respectively. The associated DTA run also indicates complete crystallization by the absence of any exotherm.

DSC of the first crystallization period in the as-received powder delineated a combined broad endothermic peak and a sharp exotherm (Fig. 10). These peaks are associated with a superposition of the glass transition at T_g and the crystallization at T_x as shown schematically in Fig. 10(b). Unlike the exothermic peak, the endothermic peak appeared to be suppressed at high heating rates and was reversible if high temperature crystallization was avoided (*cf.* Fig. 9(b)).

Kissinger [28] plots of the two crystallization events were obtained by plotting T_x^2/β *vs.* $1/T_x$ on logarithmic scales (Fig. 11) where T_x is the peak temperature of the exotherm and β is the

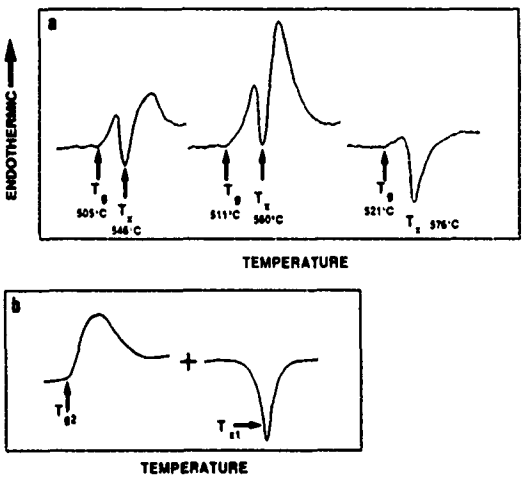

Fig. 10. (a) DSC thermograms of the as-received powder with different heating rates (40, 80 and 160 K min^{-1}); (b) schematic thermogram decomposed into a glass transition peak for a high temperature amorphous phase and superimposed crystallization peak for a low temperature amorphous phase.

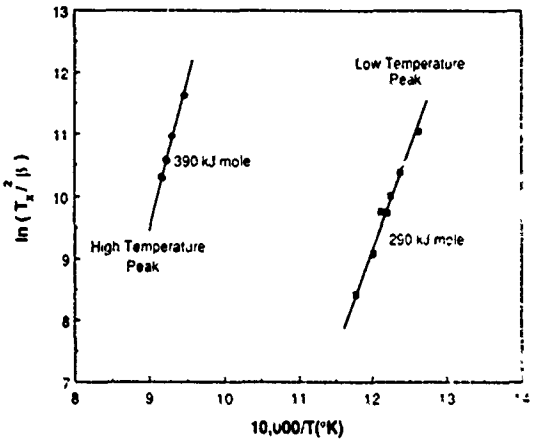

Fig. 11. Kissinger plot of both crystallization events in $Ni_{56.5}Mo_{23.5}Fe_{10}B_{10}$: open symbols are DSC data; full symbols are DTA data. The activation energy for the low temperature crystallization correlates with interdiffusion of molybdenum and/or iron in nickel. The activation energy for the high temperature crystallization equals that for molybdenum self-diffusion.

TABLE 2 Phases identified in high energy, high rate processed $Ni_{56.5}Mo_{23.5}Fe_{10}B_{10}$ in as-processed and post-processed annealed conditions

Condition	*Phases identified*		
	As-received powder $Ni_{56.5}Mo_{23.5}Fe_{10}B_{10}$ (AR)	*Partly crystallized powder* $Ni_{56.5}Mo_{23.5}Fe_{10}B_{10}$ (I)	*Fully crystallized powder* $Ni_{56.5}Mo_{23.5}Fe_{10}B_{10}$ (II)
As processed	f.c.c. solid solution*; Mo_2NiB_2; CuPt structure	f.c.c. solid solution, Mo_2NiB_2	f.c.c. solid solution, Mo_2NiB_2
Annealed at 650 °C for 20 h	f.c.c. solid solution; Mo_2NiB_2; Ni_4Mo; CuPt structure; $M_{23}C_6$ structure	f.c.c. solid solution, Mo_2NiB_2, η-boride	f.c.c. solid solution; Mo_2NiB_2; η-boride
Annealed at 650 °C for 50 h	f.c.c. solid solution, Mo_2NiB_2, Ni_4Mo; CuPt structure; η-boride	f.c.c. solid solution, Mo_2NiB_2, η-boride	f.c.c. solid solution; Mo_2NiB_2; η-boride
Annealed at 650 °C for 100 h	f.c.c. solid solution; Mo_2NiB_2, Ni_4Mo dissolving; CuPt structure, η-boride	f.c.c. solid solution, Mo_2NiB_2; η-boride	f.c.c. solid solution, Mo_2NiB_2; η-boride

*Ni = 18–23 at.%, Mo = 10 at.%, Fe, based on X-ray diffraction, EDS and EELS.

heating rate. The activation energy of the low temperature crystallization is 290 kJ mol^{-1}, while that for the high temperature crystallization is 390 kJ mol^{-1}.

The major phases in all HEHR processed materials (Table 2) are the f.c.c. solid solution and Mo_2NiB_2, as reported in the calorimetric studies of the powder. The Mo_2NiB_2 has a chunky shape (Fig. 5) and is embedded in the f.c.c. matrix. It is coarse in the center section of HEHR consolidates but it appears with the f.c.c. solid solution as a complex fine-scale microconstituent near the surface (Fig. 12).

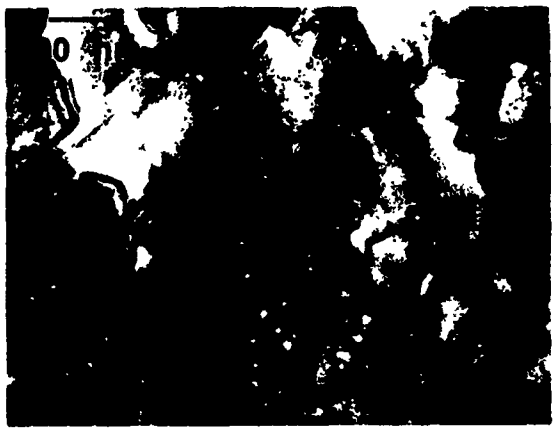

Fig. 12. Fine Mo_2NiB_2 particles approximately 30 nm in size, in an f.c.c. solid solution matrix. The TEM foil was taken from the near-surface region of as-consolidated sample 158 AR.

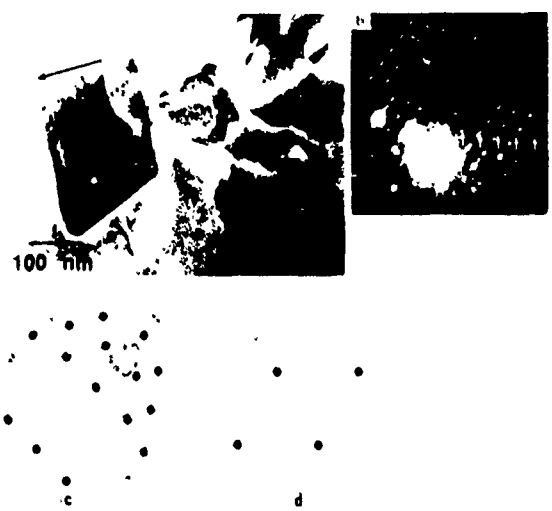

Fig. 13. As-consolidated sample 158 AR: a CuPt-type phase with selected-area diffraction of CuPt 011 orientation. The arrow shows the CuPt 111 direction. b The selected-area diffraction of the CuPt-type phase. The white arrows indicate twin spots in the CuPt-type phase. c Distribution of atoms at the composition CuPt, from 29. The alternate 111 planes are the copper ○ and platinum ● positions. d Distribution of atoms on a single Cu 111 plane, at the composition Cu Pt, from 29.

A third phase was detected in the HEHR processed samples from as-received powder (Fig. 13). The diffraction pattern of the planar defect area of the diamond-shaped crystal shows additional spots at $\frac{1}{3}(111)_{fcc}$ and $\frac{1}{3}(200)_{fcc}$. The matrix spots show streaking along [111]. This diffraction pattern is interpreted as due to an ordered CuPt-type superlattice D_{3d}^5 ($R\bar{3}m$). As shown in Fig. 13(c), a stoichiometric composition consisting of alternating copper (lighter element) and platinum (heavier element) positions on (111) planes is consistent with the diffraction spots at $\frac{1}{3}(111)_{fcc}$. In the case of CuPt, it is known that, if the composition is off-stoichiometric (more than 50% Pt), platinum positions appear on the Cu(111) plane (Fig. 13(d)). This causes a secondary ordering which is the origin of the $\frac{1}{3}(200)_{fcc}$ diffraction spots. Final arrangement of this ordering would be complete in a compound of stoichiometry, Cu_3Pt_5 [29]. The composition was undetermined; however, this phase is thought to be a binary or ternary NiMoFe compound, possibly (Mo, $Ni)_3Fe_5$. Twin spots are also observed in the diffraction pattern in Fig. 13(b) (arrows). Twin spots aligned with $\frac{1}{3}(111)_{fcc}$ spots on the sixth streaked plane.

The thermal stability of HEHR processed $Ni_{50.5}Mo_{23.5}Fe_{10}B_{16}$ was assessed by annealing consolidates for various times at 650 °C. After 20 h, two new phases were detected in HEHR processed as-received powder. The first was a finely distributed Ni_2Mo ordered phase (Fig. 14). Ni_2Mo forms near the Mo_2NiB_2 interface and on dislocations. The diffraction pattern of this area shows additional $\frac{1}{3}(420)$ spots on the $[\bar{1}22]$ zone axis selected-area diffraction, consistent with Ni_2Mo crystallographically aligned with the matrix. Mottled strain contrast can be seen on the bend contour, simultaneous with a diffused halo on the diffraction pattern. The Ni_2Mo ordered phase has the orthorhombic D_{2h}^{25} ($Immm$ superlattice. The c axis of Ni_2Mo can be aligned parallel to $100_{\gamma\gamma}$ with a and b directed along approximate $110_{\gamma\gamma}$. This gives rise to six independent variants. In Fig. 15 the diffraction pattern of the $\bar{1}12_{\gamma\gamma}$ zone axis shows two additional spots dividing $420_{\gamma\gamma}$ along one of the g $420_{\gamma\gamma}$ into three equal sections. Additional spots are similarly arranged along $220_{\gamma\gamma}$ and $311_{\gamma\gamma}$. Bright field and dark field taken from $311'_{\gamma\gamma}$ and $402_{\gamma\gamma}$ micrographs Figs.

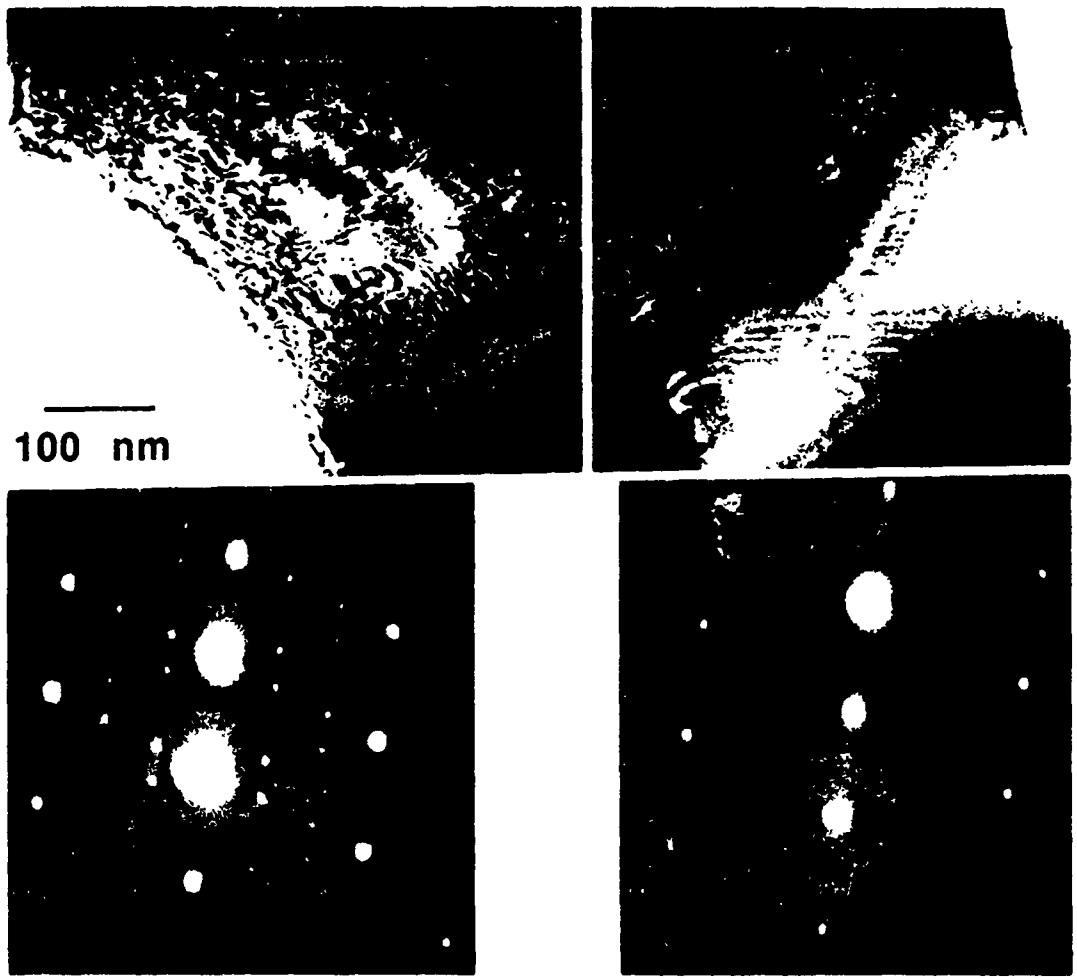

Fig. 14. Sample 158 (AR) annealed at 650 °C for 20 h, showing the Ni_2Mo ordered phase (left) and stacking fault (right) with selected-area diffraction of the [122] orientation.

15(a)–15(c)) reveal two different variations of Ni_2Mo.

The second phase observed on annealed HEHR processed specimens from as-received powder was a boride of $M_{23}C_6$ type, shown in Fig. 16 as grain boundary precipitates. On the diffraction pattern, ordered Ni_2Mo spots appear with additional spots dividing $\boldsymbol{g}\ 001_{Ni_2Mo}$ by three. This is a typical $M_{23}C_6$ orientation [30]. The $M_{23}C_6$-type boride is frequently observed in two metal boride systems [31, 32] with the habits

$$\{111\}_{M_{23}C_6} \parallel \{111\}_{\gamma}$$

$$\{110\}_{M_{23}C_6} \parallel \{110\}_{\gamma}$$

$$a_{M_{23}C_6} = 3a_{\gamma}$$

After annealing for 50 h at 650 °C, a new metastable phase appeared, identified as η-boride (Fig. 17) [33]. These well-defined faceted η-boride particles were typically located at matrix grain boundaries. The Ni_2Mo particles were not present in the vicinity of the η-borides. Strain contrast on the lateral side of the coarsened Ni_2Mo particles indicated that coherency distortion of the matrix on the long interface of the Ni_2Mo increased as the Ni_2Mo coarsened.

After aging for 100 h at 650 °C, the Ni_2Mo ordered phase had coarsened to about 150 nm. The first evidence for Ni_2Mo decomposition was evident after this thermal treatment, indicated in Fig. 18 by particle ledging and disruption of the grain boundary.

The long-term stability of the various phases present in HEHR processed samples from as-received powder was assessed by annealing at 800 °C for 4 h followed by a 2 h anneal at 1100 °C. Figure 19 shows typical structures. Present are Mo_2NiB_2 particles 500–800 nm long

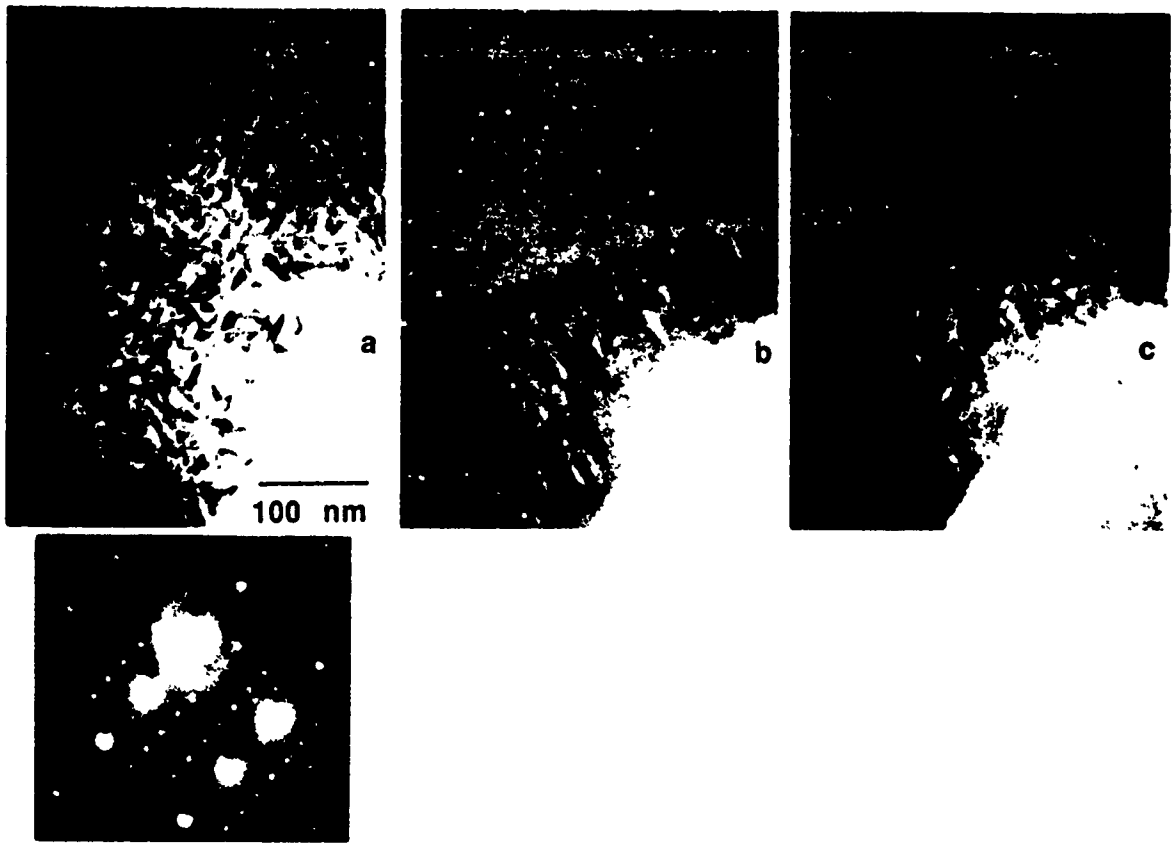

Fig. 15. Sample 158 (AR) annealed at 650 °C for 20 h, showing the Ni_4Mo ordered phase with different variations: the selected-area diffraction is in the $\{112\}_{fcc}$ orientation: (a) bright field, (b) dark field from $g = \{311\}_{fcc}$, (c) dark field from $g = \{402\}_{fcc}$.

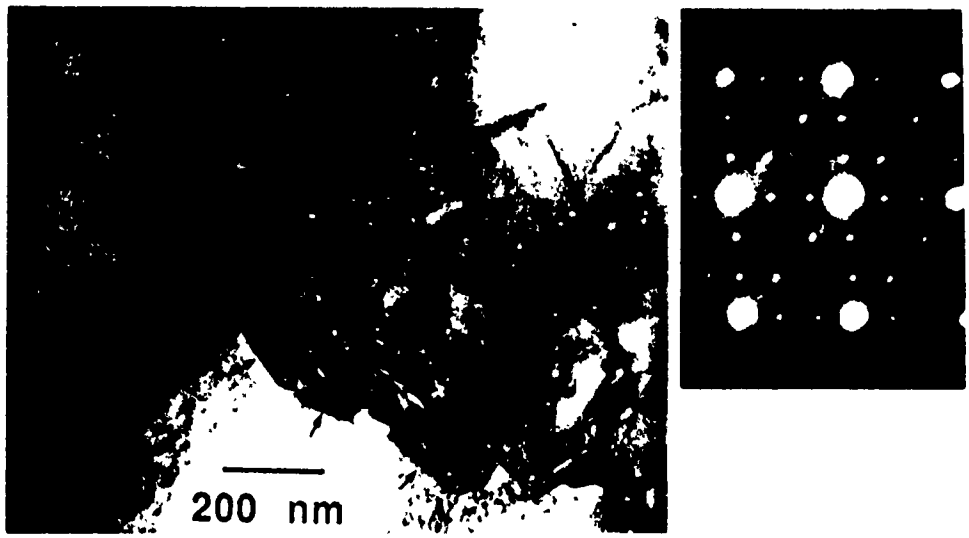

Fig. 16. Sample 757 (AR) annealed at 650 °C for 20 h, showing the Ni_4Mo ordered phase precipitated on dislocations, and M_6C-type boride (arrows) precipitated at the grain boundary; the selected-area diffraction is in the 001 orientation.

in a matrix of the f.c.c. solid solution with an occasional η-boride particle now coarsened to over 1 μm in size. No Ni_4Mo was observed.

The structural stability of specimens HE-HR processed from partly crystallized and fully crystallized powder was similar and less complex than the HE-HR processed as-received powder. All specimens after processing were fully crystallized.

Fig. 17. Sample 158 (AR) annealed at 650 °C for 50 h, showing η-boride (black arrows) on a grain boundary and the Ni_2Mo ordered phase (white arrow) near an Mo_2NiB_2 particle.

Fig. 18. Sample 158 (AR) annealed at 650 °C for 100 h. The decomposing Ni_2Mo ordered phase exists near the grain boundary where several ledges are seen.

consisting of 1 μm grains of f.c.c. matrix with 100–200 nm Mo_2NiB_2 particles loosely clustered along f.c.c. grain boundaries. Annealing at 650 °C for times between 20 and 100 h produced no change in the as-consolidated structure, excepting formation of η-boride after annealing for 20 h. Typical microstructures appear in Fig. 20 for partly crystallized I, Fig. 20(a) and fully crystallized II, Fig. 20(b) starting powder. For the most part, η-borides appeared among the clustered Mo_2NiB_2 microstructures typical for these materials.

4. Discussion

4.1. High energy, high rate power curves

The power curves in Fig. 2 are interpreted as reflecting the electrical resistance state of the material. The first peak at 80 ms is associated with the pulse characteristics of the homopolar generator. An origin for the second peak at 200 ms is the reduction in powder mass resistance associated with the low temperature crystallization. For an average heating rate β of 4000 K s^{-1}, this temperature is approximately 750 °C based on extrapolation of the data in Fig. 11. This interpretation is supported by the suppression of the second peak for HEHR processing of partly or fully crystallized material.

The third peak in the power curves is associated with the high temperature crystallization with concomitant resistance drop. This peak is present for the fully amorphous and partly crystallized starting material but is absent when the starting powder is fully crystallized. For an average heating rate of 4000 K s^{-1}, the crystallization temperature is estimated to be 1120 °C. Both process crystallization temperatures are significantly higher than the values recorded in the low heating rate 40 K min^{-1} calorimetry experiments, 531 °C and 815 °C respectively.

4.2. Crystallization behavior of $Ni_{50.5}Mo_{23.5}Fe_{10}B_{16}$

On monotonic heating, the crystallization sequence in $Ni_{50.5}Mo_{23.5}Fe_{10}B_{16}$ involves a two-stage process. The amorphous metal first undergoes a compositional phase separation. A glass transition of a high temperature amorphous phase takes place at approximately 520 °C, concurrent with crystallization of a low temperature amorphous phase to form an Ni–18–23 at.%Mo–10at.%Fe solid solution. On the basis of the overall composition, this involves mass transport of molybdenum away from the crystallizing phase. The activation energy for this crystallization, 290 kJ mol^{-1}, closely matches the activation for interdiffusion of molybdenum in nickel, 280 kJ mol^{-1} [34], suggesting that diffusion of molybdenum from the nickel-rich crystal might be the rate-limiting step for low temperature crystallization.

At approximately 800 °C, the high temperature amorphous phase crystallizes to form Mo_2NiB_2 in a network surrounding the f.c.c. solid solution. The activation energy for crystallization is 390 kJ mol^{-1}, which corresponds to the self-diffusion activation energy for molybdenum [35].

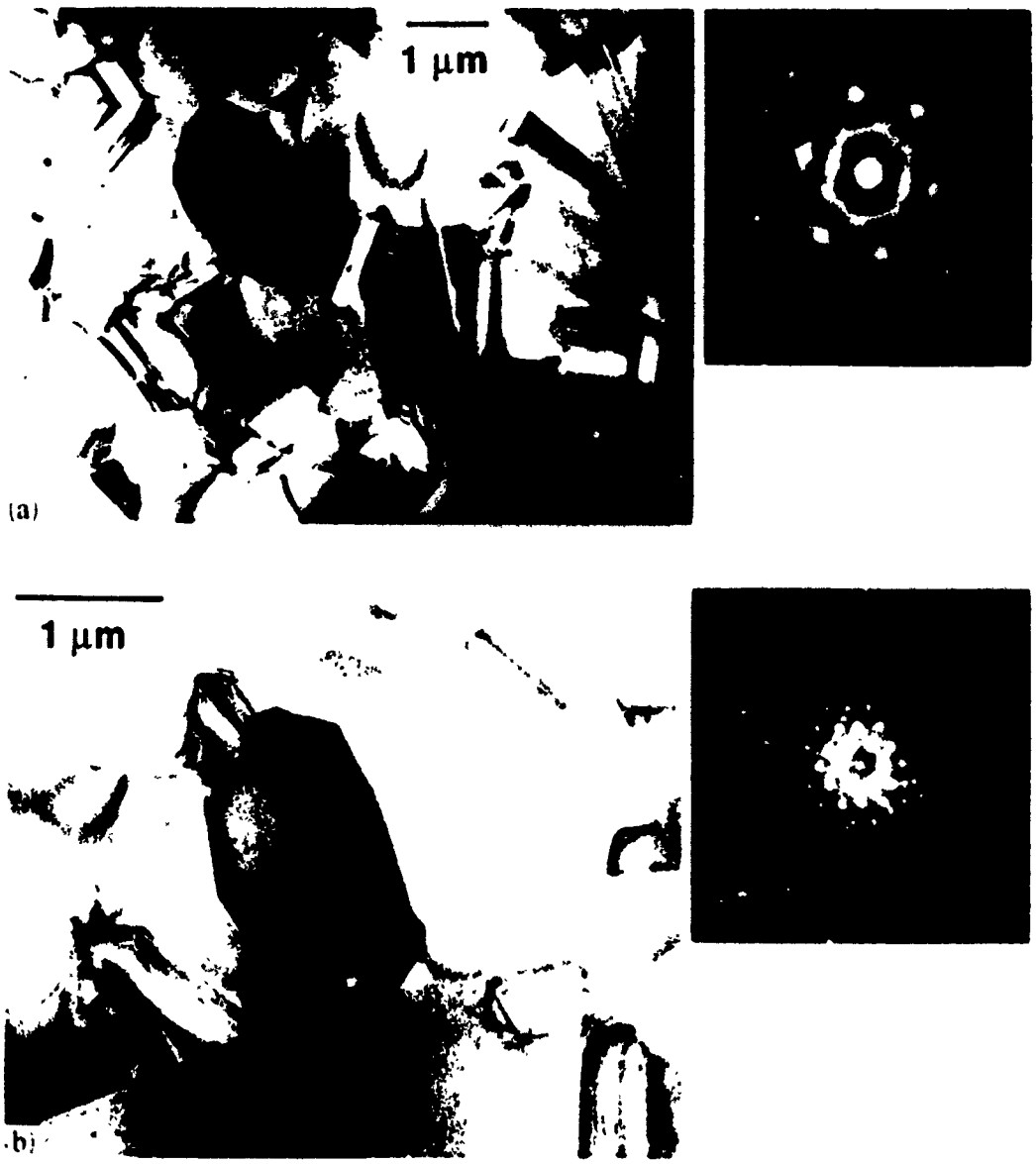

Fig. 19. Sample 158 AR annealed at 800 °C for 4 h, followed by 1100 °C for 2 h. a Faceted Mo_2NiB_2 particles in the f.c.c. solid solution matrix are shown. The selected-area diffraction is in the 114_{γ} orientation of the dark-contrast f.c.c. solid solution grain. Long-term thermal exposure induces coarsening of the Mo_2NiB_2 and f.c.c. phases and dissolution of Ni_2Mo. b Coarsened η-boride dark contrast and defect Mo_2NiB_2 particles. The selected-area diffraction is in the 111_{γ} orientation.

4.3. Structural stability of high energy, high rate processed material

Salient macroscopic features of HEHR processed $Ni_{56}Mo_{23.5}Fe_{10}B_{10}$ are a central light-etching nugget surrounded by a surface dark-etching region (Fig. 3). The origin of the nugget is the high processing temperature associated with the internal material removed from the metal platens–electrodes. The nugget region is typified by coarse Mo_2NiB_2, which correlates with the duration of the high temperature excursion during processing. The amount of coarsening is greater for higher input energy processing. The coarsening gradient is diminished by crystallization prior to HEHR processing. The formation of the nugget probably involves melting of the alloy ($T_m = 1250$ °C). On solidification, the first phase to appear is Mo_2NiB_2, followed by matrix solidification of the f.c.c. solid solution.

The inherently rapid consolidation in the HEHR processing induces a non-equilibrium state owing to lack of time for the species to

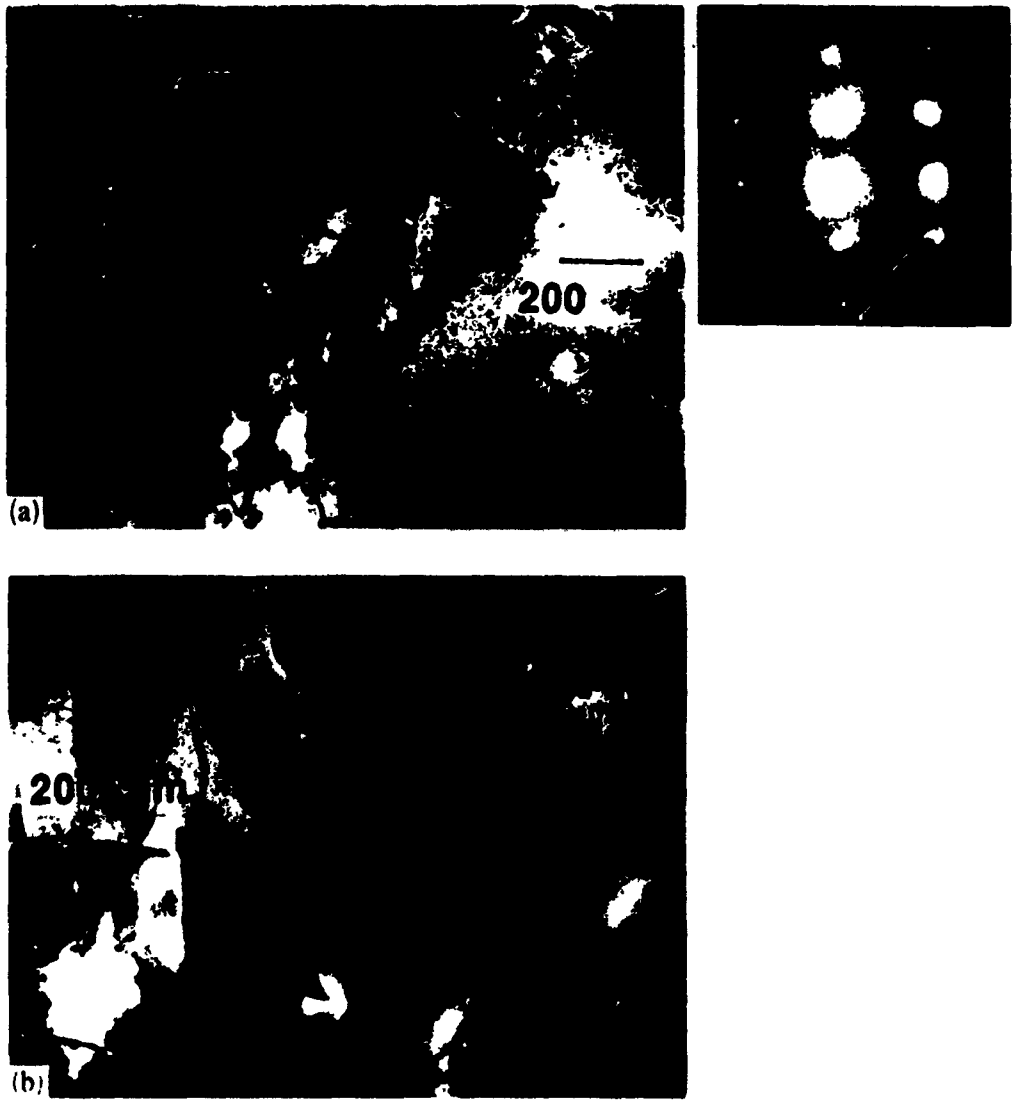

Fig. 20. (a) Sample 766 (1) annealed at 650 °C for 20 h, showing fine Mo_2NiB_2 along the grain boundary with selected-area diffraction of the $\bar{1}12_{fcc}$ orientation. Diffuse $1/3\{0\}$ short-range order spots are seen. The size of borides along the grain boundary is comparable with that in the grain. (b) Sample 827 (II) annealed at 650 °C for 20 h. Boride phases are observed along a grain boundary.

diffuse to achieve an equilibrium state. The non-equilibrium states, usually manifested by a supersaturated solid solution, transform into the equilibrium state by precipitation of some second phase under an environment of sufficient temperature and time for atomic transport to occur.

Annealing treatments of the non-equilibrium structure induced by HEHR consolidation result in several intermediate precipitates: Ni_2Mo ordered phase, CuPt-type phase, $M_{23}C_6$-type boride and M_6C-type η-carbide boride. The same composition consolidated by hot isostatic pressing or hot extrusion does not show such precipitates even with the same annealing condition [12]. There are several variables which influence the size and distribution of these precipitates. Preheat treatment of powder before consolidation changed the precipitation sequence significantly as indicated in Table 2. Consolidates from the as-received powder generated all precipitates while, for consolidates of powders partially or fully crystallized, the Ni_2Mo and CuPt-type phases were not observed. The formation of the Ni_2Mo ordered phase in the HEHR processed, fully amorphous powder is believed to arise from compositional variations associated with the first

crystallization and in some cases from the generation of a dislocation structure in the f.c.c. solid solution.

5. Summary and conclusions

Amorphous $Ni_{56.5}Mo_{23.5}Fe_{10}B_{10}$ on rapid heating crystallizes through a two-step process. The first crystallized phase is an Ni–Mo–Fe solid solution and, at higher temperatures, a second phase, Mo_2NiB_2, crystallizes. The f.c.c. solid solution has a primary crystallization mode where molybdenum interdiffusion in nickel is responsible for the kinetics of crystallization. Following the first crystallization, molybdenum segregates to the periphery of the f.c.c. solid solution crystallites. At higher temperatures, molybdenum and boron adjacent to the f.c.c. solid solution crystallize to Mo_2NiB_2, forming a network structure. The activation energy of the second crystallization matches that of molybdenum self diffusion.

A glass transition from the molybdenum-rich amorphous phase was detected in DSC independent of the first crystallization. This is an indication that the Mo_2NiB_2 is not a solid state precipitation but a real product of the crystallization from the amorphous phase.

The crystallization sequence of $Ni_{56.5}Mo_{23.5}Fe_{10}B_{10}$ is summarized as amorphous phase → phase separation → glass transition of the high temperature amorphous phase → partial crystallization (f.c.c. solid solution) → complete crystallization (Mo_2NiB_2).

$Ni_{56.5}Mo_{23.5}Fe_{10}B_{10}$ powders in the fully amorphous, partly crystallized and fully crystallized conditions were HEHR consolidated to produce dense, fully crystalline two-phase compacts of f.c.c. solid solution and Mo_2NiB_2. A nugget formed in the middle of each consolidate. Coarse Mo_2NiB_2 was present inside the nugget area, showing a low hardness. Solid state consolidation was operative near the surface to produce finer Mo_2NiB_2 and higher hardness. The degree of crystallinity of the preprocessed powder and the input energy are dominant factors for nugget formation and the related hardness variation. The elimination of the crystallization exotherms by preconsolidation annealing decreased the nugget size significantly and increased the hardness.

The crystallizations were monitored through *in situ* variation of the electrical data. During HEHR consolidation the perturbations on the power spectra by the two crystallizations are manifest as distinct peaks. These peaks originate from the decrease in the contact resistance component of the total resistance due to the increased contact area between powders, and from specific intrinsic resistivity changes from first and second crystallizations during the HEHR consolidation.

Consolidates from fully amorphous powder evolved several transition phases during post-consolidation annealing. The f.c.c. matrix precipitated an Ni_2Mo ordered phase along with a CuPt-type superlattice structure as transition phases. As the transition phases disappeared, an η-boride phase formed on grain boundaries as one of the final phases in this annealing regime. Consolidates from crystallized powder did not evolve Ni_2Mo or CuPt-type structures on annealing; only the η-boride phase appeared.

Acknowledgments

The authors gratefully acknowledge Dr. L. Rabenberg and Dr. M. Schmerling for their assistance with the electron microscopy. Dr. Manthiram was instrumental in facilitating the use of the thermal analyzer. The metallic glass ribbon and powder were generously provided by Mr. Derek Raybould of the Allied Corporation. T. A. Aanstoos and J. Allen of The University of Texas Center for Electromechanics operated the HPG; their efforts are greatly appreciated.

This research was supported by Defense Advanced Research Project Agency–U.S. Naval Air Development Center under Contract N62269-85-C-0222 and Defense Advanced Research Project Agency–U.S. Army Research Office under Contract DAAL03-87-K-0073.

References

1 W. Klement, R. H. Willens and P. Duwez, *Nature (London), 187* (1960) 869.

2 D. Raybould and A. C. Diebold, *J. Mater. Sci., 21* (1986) 193.

3 A. H. Clauer, R. V. Raman, R. S. Carbonara and R. E. Maringer, in R. Mehrabian, B. H. Kear and M. Cohen eds., *Proc. 2nd Int. Conf. on Rapid Solidification Processing, Principles and Technologies*, Claitor's Publishing Division, Baton Rouge, LA, 1980, p. 339.

4 N. B. Dahotre, C. Wakade and K. Mukherjee, in K. Mukherjee and J. Mazumder eds., *Proc. Conf. on Laser Processing of Materials*, Metallurgical Society of AIME, Warrendale, PA, 1985, p. 101.

5 J. L. Stempin and D. R. Wexell, *U.S. Patent 4298382*, 1981.

6 H. H. Lieberman, in R. Mehrabian, B. H. Kear and M. Cohen (eds.), *Proc. 2nd Int. Conf. on Rapid Solidification Processing: Principles and Technologies*, Claitor's Publishing Division, Baton Rouge, LA, 1980, p. 393.
7 R. Ray, *J. Mater. Sci.*, *16* (1981) 2924.
8 R. W. Cahn, *Annu. Rev. Mater. Sci.*, *12* (1982) 51.
9 S. K. Das and D. Raybould, in S. Steeb and H. Warlimont (eds.), *Rapidly Quenched Metals*, North-Holland, Amsterdam, 1985, p. 1787.
10 D. Raybould, *Met. Powder Rep.*, *39* (1984) 282.
11 S. K. Das, L. A. Davis, J. R. Y. Wang and D. Kapoor, *Proc. 3rd Int. Conf. on Rapid Solidification Processing: Principles and Technologies*, National Bureau of Standards, Washington, DC, 1982, p. 559.
12 S. K. Das, K. Okazaki and C. M. Adam, *Proc. Conf. on High Temperature Alloys: Theory and Design*, Metallurgical Society of AIME, Warrendale, PA, 1984, p. 451.
13 B. C. Giessen, N. M. Madhava, R. J. Murphy, R. Ray and J. Surette, *Metall. Trans. A*, *8* (1977) 346.
14 J. C. Smith, J. H. Perepezko, D. H. Rasmussan and C. R. Loper, *U.S. Patent 4282034*, 1981.
15 F. Spaepen and D. Turnbull, *Scr. Metall.*, *8* (1974) 563.
16 V. Panchanathan, in B. H. Kear and B. C. Giessen (eds.), *Rapidly Solidified Metastable Materials*, *Materials Research Society Symp. Proc.*, Vol. 28, Elsevier, New York, 1984, p. 407.
17 T. Vreeland, Jr., P. Kasiraj and T. J. Ahrens, in B. H. Kear and B. C. Giessen (eds.), *Rapidly Solidified Metastable Materials*, *Materials Research Society Symp. Proc.*, Vol. 28, Elsevier, New York, 1984, p. 139.
18 P. Kasiraj, D. Kostka, T. Vreeland, Jr., and T. J. Ahren, *J. Non-Cryst. Solids*, *61–62* (1984) 967.
19 C. F. Cline and R. W. Hopper, *Scr. Metall.*, *11* (1977) 1137.
20 D. G. Morris, in B. H. Kear and B. C. Giessen (eds.), *Rapidly Solidified Metastable Materials*, *Materials Research Society Symp. Proc.*, Vol. 28, Elsevier, New York, 1984, p. 145.
21 T. Vreeland, Jr., P. Kasiraj, A. H. Mutz and N. N. Thadhani, in L. E. Murr, K. P. Staudhammer and M. A. Meyers (eds.), *Metallurgical Applications of Shock Wave and High Strain Rate Phenomena*, Dekker, New York, 1986, Chapters 11, 12.
22 L. A. Davis, Metallic glasses, in R. I. Jaffee and B. A. Wilcox (eds.), *Fundamental Aspects of Structural Alloy Design*, Plenum, New York, 1977, p. 431.
23 J. W. Sears, B. C. Muddle and H. L. Fraser, in B. H. Kear and B. C. Giessen (eds.), *Rapidly Solidified Metastable Materials*, *Materials Research Society Symp. Proc.*, Vol. 28, Elsevier, New York, 1984, p. 163.
24 U. Koster, Microstructure of partially crystalline metallic glasses, in P. R. Sahm, H. Jones and C. M. Adam (eds.), *Science and Technology of the Undercooled Melt*, Martinus Nijhoff, Dordrecht, 1986, p. 258.
25 H. L. Marcus, D. L. Bourell, Z. Eliezer, C. Persad and W. F. Weldon, *J. Met.*, *39* (1987) 6.
26 J. B. Walter and T. A. Anstoos, *Met. Prog.*, *127* (1985) 25.
27 R. E. W. Casselton and W. Hume-Rothery, *J. Less-Common Met.*, *7* (1964) 212.
28 H. E. Kissinger, *J. Res. Natl. Bur. Stand.*, *57* (1956) 217.
29 C. S. Barrett and T. B. Massalski, *Structure of Metals*, McGraw-Hill, New York, 1966, Chapter 11.
30 J. K. Lai, D. J. Chastell and P. E. J. Flewitt, in H. Aaronson, D. E. Laughlin, R. F. Sekerka and C. M. Wayman (eds.), *Proc. Int. Conf. on Solid–Solid Phase Transformations*, Metallurgical Society of AIME, Warrendale, PA, 1982, p. 781.
31 H. J. Goldschmidt, *Interstitial Alloys*, Plenum, New York, 1967, Chapter 3.
32 G. Geoffroy, F. Dutlos and A. Lasalmonie, in B. H. Kear and B. C. Giessen (eds.), *Rapidly Solidified Metastable Materials*, *Materials Research Society Symp. Proc.*, Vol. 28, Elsevier, New York, 1984, p. 295.
33 Y. W. Kim, L. Rabenberg and D. L. Bourell, *J. Mater. Res.*, *3* (6) (1988) 1336.
34 S. D. Gertsriken, I. Ya. Dekhtyar and V. S. Mikhalenov, *Metallurgiya i Metallovedenie*, Akademii Nauk S.S.S.R., Moscow, 1958, p. 279.
35 J. Askill and D. H. Tomlin, *Philos. Mag.*, *8* (1963) 997.

APPENDIX F

ELECTROTRIBOLOGY

F-1. Composite Solid Armatures for Railguns

F-2. Composite Solid Armature Consolidation by Pulse Power Processing: A Novel Homopolar Generator Application in EML Technology

F-3. Wear of Conductors in Railguns: Metallurgical Aspects

F-4. Nanosized Structures in Cu-W-WC-C Composites for Electrotribological Applications

COMPOSITE SOLID ARMATURES FOR RAILGUNS

C. J. Lund[1], C. Persad[1], Z. Eliezer[1], D. Peterson[2], J. Hahne[2]

[1]The University of Texas at Austin
Center for Materials Science and Engineering
Austin, TX 78712

[2]The University of Texas at Austin
Center for Electromechanics
Austin, TX 78758

ABSTRACT

Solid armatures used for electromagnetic launchers may be considered as single-duty high speed sliding contacts. The design and fabrication of these are the subject of an ongoing research program at The University of Texas at Austin. Highly time dependent conditions at the high-velocity (> 1km/s), high current density (> 10^5 A/cm^2) sliding interface are characteristic of the operation of these armatures. In railguns, the residue left by the traveling armature influnces the multi-shot performance possibilities, making an understanding of wear phenomena crucial.

Wear phenomena are described for three multi-leaf graded resistance armatures. These armatures were comprised of Cu-Mo-Ti (6-4), Cu-Mo-Ti (CP), and Cu-Al-Ti (CP). Each of these armatures were sliding against flame sprayed molybdenum.(Mo) on copper (Cu) rails.

For a sucessful railgun shot, the bore dimensions must be maintained within close tolerences. Through an understanding of the wear mechanisms occuring during a railgun shot, the wear rate of the sliding couple can be reduced. A reduction of the wear products could make the multi-shot armature railgun a reality. At present, wear debris makes reconditioning of the bore a necessity after only a few shots.

INTRODUCTION

Before railgun technology develops its full potential, several problems must be confronted. One of the most perplexing is the problem associated with the rail-armature sliding couple. The armature may be considered as a single-duty high-speed sliding electrical contact. However, even as a single-duty unit, the wear and subsequent wear products associated with the sliding couple must be minimized. Wear products alter the bore dimensions and render insulators ineffective. This reduces the operating efficiency of the gun. The wear process necessitates the refinishing of the bore to remove metallic wear products from the insulators, restore uniform bore dimensions, and custom fitting of an armature to the new dimensions. The design and fabrication of these armatures to reduce wear and increase performance are the subject of an ongoing research program at The University of Texas at Austin.

SOLID ARMATURES

The primary goal of an armature in a railgun is to propel a projectile. The solid armature propels the projectile through direct mechanical stresses. The armature is subjected to high current densities ($>10^5$ A/cm^2), high mechanical stress and severe resistive heating. The solid armature, as opposed to a non-solid armature, possesses many desirable attributes. The armature-projectile pair can be integrated into one unit. Solid armatures have been predicted to be more efficient at velocities less than 10 km/s. They also have shown lower rail wear than non-solid armatures. Finally, their behavior is intrinsically easier to model than non-solid armatures.[1] They can, however, develop into non-solid (hybrid) type armatures through the wear process at the sliding interface.

The wear process associated with the sliding couple limits the multi-shot potential of the railgun. Two processes have been proposed as major contributors to the wear process. They are pulsed joule heating and arc erosion. Abrasive wear, adhesive wear, fatigue wear, and erosion are mechanisms that manifest themselves as a result of these two processes. Pulsed joule heating is sometimes referred to as the skin effect because a fast rising current pulse travels in a region close to the surface of a conductor. The skin effect has been shown to result in surface melting and resolidification.[2] Arc erosion results from electrical arcing. The arc strikes from the rail to a conductor causing material vaporization and subsequent condensation. It has been reported that the function between arc distance and severity is an inverse relationship.[3]

ARMATURE CONSIDERATIONS

The rise in temperature due to thermal loading has been believed to limit the armature performance. Therefore, parameters such as density, heat capacity, and resistivity have been grouped to form what is called an action constant. The action constant, g, is a measure of the loading that an armature can sustain without melting. Barber defines the action constant as

$$g=\int_{T_0}^{T_0+\Delta T}\frac{pCp}{\xi}\,dt$$

and goes into detail deriving an equation for minimum mass.[4] Although thermal loading is by far the most critical, Barber also presents data for temperature rise associated with velocity, current density, and pressure. Barber's underlying assumption for minimum

mass is that the current carrying cross section carries a uniform current density. The velocity skin effect negates this assumption. The velocity skin effect states that all of the current will flow in the rear of the armature when the armature is moving. There are two options to control the velocity skin effect. The first is varying the material resistivity and the second is varying the size of the conductors.[5] Both in essence make the rear of the armature more resistive and force the current to flow forward of the rear of the armature.[6]

EXPERIMENTAL SET-UP

Preliminary studies were conducted using a one meter long, 12.5 mm x 12.5 mm square closed bore railgun (Figure 1). The railgun was connected to 10 discharge capacitance banks with a total available energy of 600 kJ. These banks can be charged to the desired energy level and fired in a predetermined sequence. The firing sequence is based upon a calculated desirable acceleration profile. The rail material was flame sprayed molybdenum on ETP copper. The molybdenum was used because it was believed to possess desirable physical properties and resistance to arc erosion.[7] The armature sliding against the rails was composed of chevrons of 3 different materials (Figure 2). The most resistive material was at the rear of the armature. The least resistive was at the front. The three armatures tested were as follows:

Armature Materials	Resistances (microhm-cm)
Cu-Mo-Ti(6-4)	1.67 - 5.20 - 170.0
Cu-Mo-Ti(CP)	1.67 - 5.20 - 24.1
Cu-Al-Ti(CP)	1.67 - 2.65 - 24.1

The "graded resistance" design of the armatures was used to force a more uniform current distribution in the armature during flight. The design used an interference fit of up to 0.508

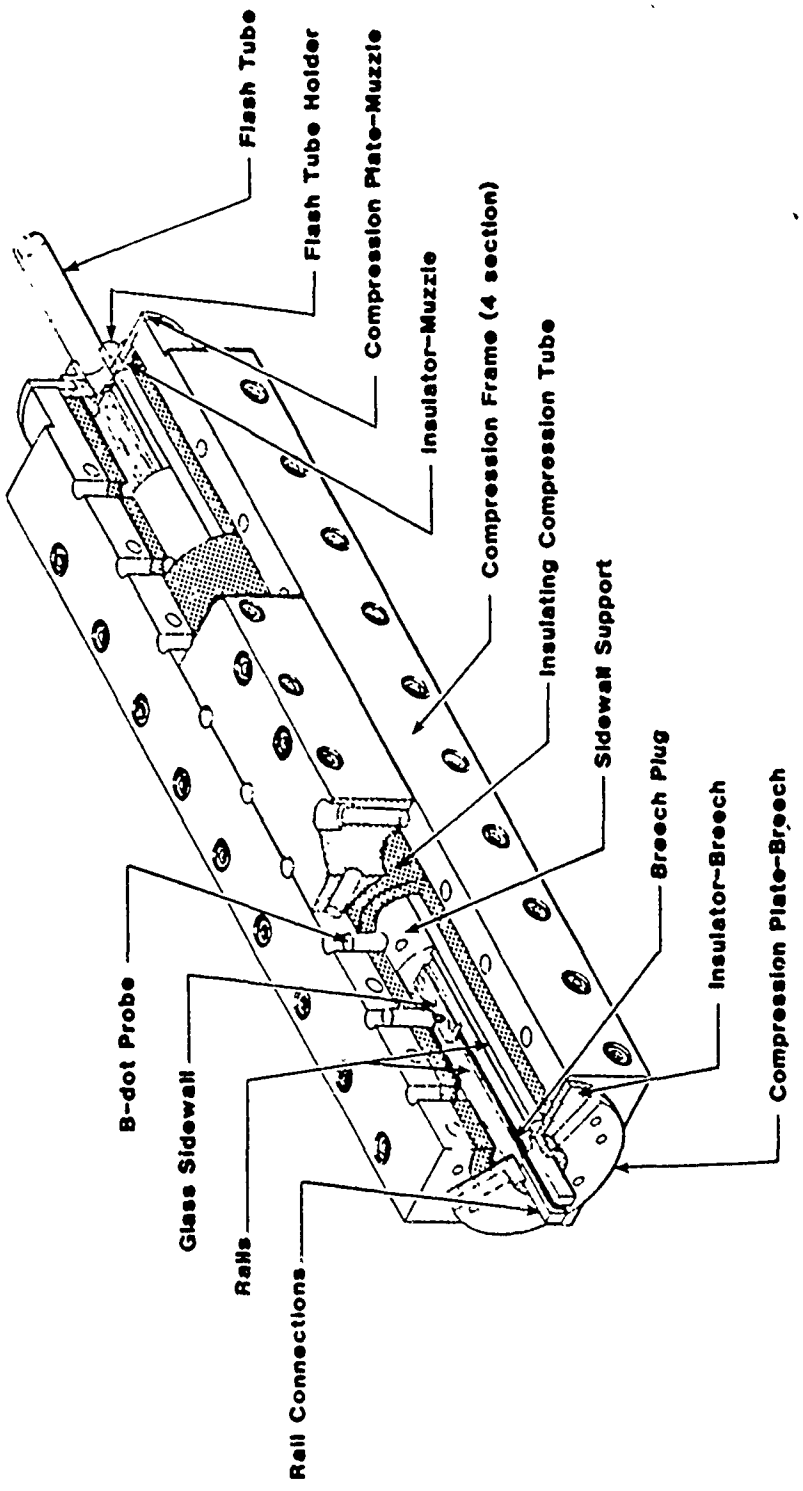

Figure 1: Schematic of Railgun Used in Experiments.

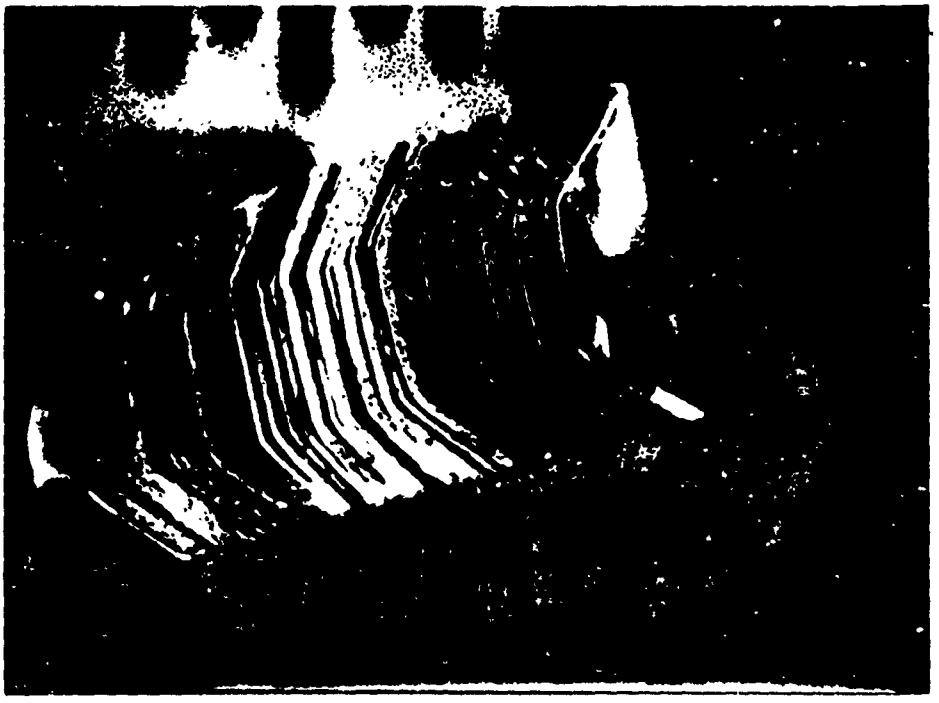

Figure 2: Armature Design.

mm to ensure contact of the armature to the rails. For solid armatures contact to the rails is of primary importance. If the interference fit is minimal and the armature loses contact with the rails, severe arc damage results. If the interference fit is too large the armature may weld to the rails. The design also incorporates the "leaves" of the armature shaped in the form of a "C". An armature with square edges at the rail/armature interface will cause the current to be concentrated there, resulting in severe heating and possible local material removal.[8]

RESULTS

The experiments were conducted using a bolted armature and flame sprayed molybdenum on copper rails. The molybdenum coating was 1.016 mm thick. The first armature, Cu-Mo-Ti(6-4) had a 0.508 mm interference fit. The projectile broke apart inside of the gun and the recovered pieces were studied. The following can be observed. The copper leaves show abrasive wear tracks suggesting thermal softening of the material. (Figure 3, top) The molybdenum leaves show extensive damage. Melted and resolidified droplets of molybdenum appear on the surface of the trailing titanium leaves. (Figure 3, bottom) There is some evidence of melting of the molybdenum leaves, possibly due to a premotion microwelding of the molybdenum leaves to the molybdenum rail coating (Figure 3, middle). The titanium leaves do not show any evidence of damage. Heavy debris accumulation suggests that these leaves acted as a mechanical scavenging device .

The bolt connecting the leaves together was the only part of the armature to become accelerated out of the bore of the gun. It was hypothesized that the titanium was too resistive and the current never flowed in it. Because there was not current flow in them they were not being accelerated and resulted in the armature being pulled apart.

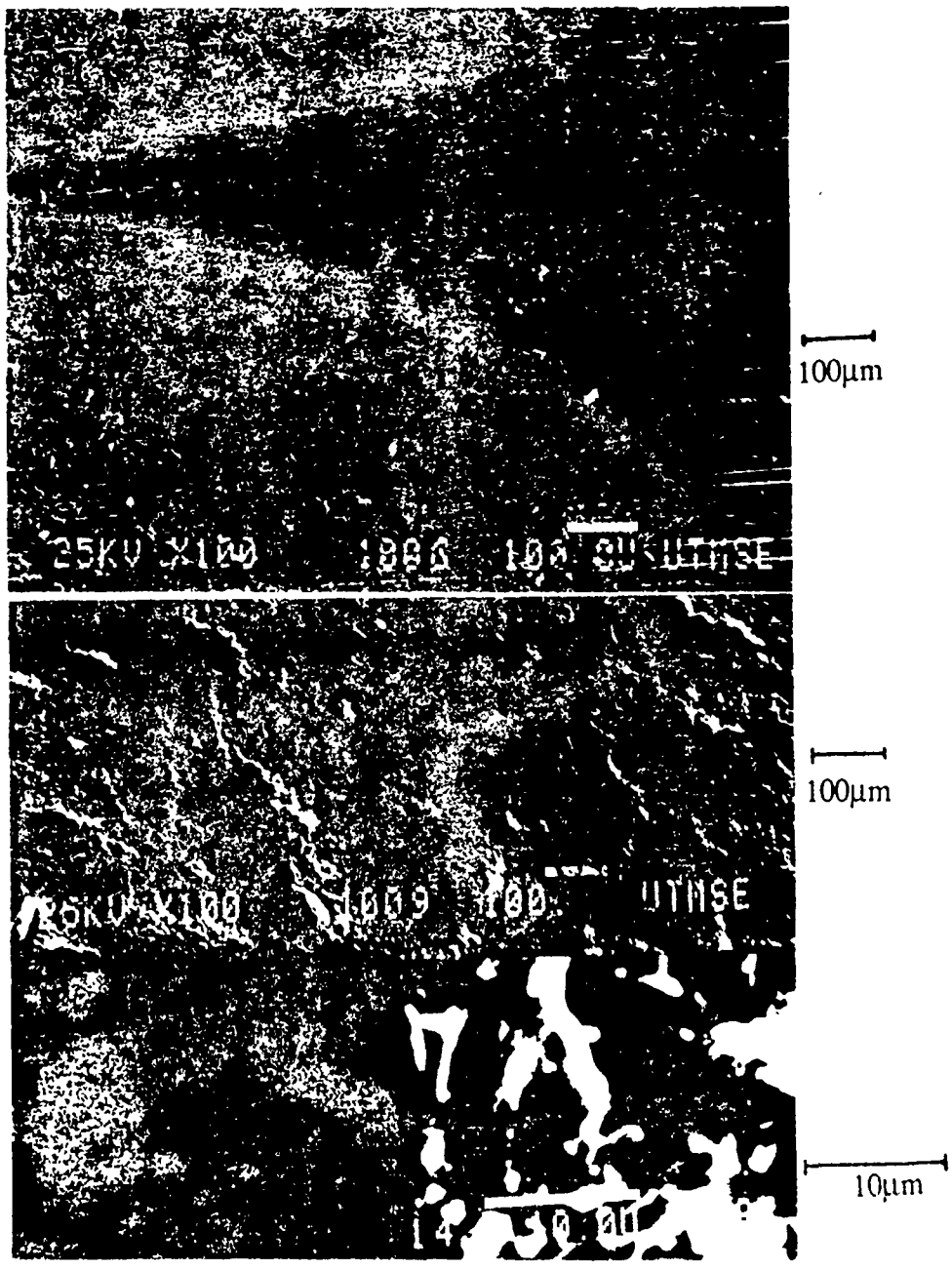

Figure 3: Wear Surfaces of Copper, Molybdenum, and Titanium.

The second armature, Cu-Mo-Ti(CP), was used as an improvement over the first. By changing only the type of titanium (to a lower resistivity) and reducing the interference fit to 0.254 mm a comparison could be drawn. The second armature behaved identically as the first. The bolt was again accelerated out of the railgun, leaving behind the material that it held together.

The last experiment of the "graded resistance" armatures was one that changed the strength of the bolt and substituted aluminum for molybdenum. The bolt was changed because the armature was believed to be breaking apart due to the failure of the bolt and the molybdenum was changed to alleviate the microwelding problems. The interference was reduced to 0.01905 mm. The minimal interference fit was used to reduce inhibition to movement, but led to the melting of the armature due to severe arc damage. Debris inside of the bore was recovered and examined. Also, armature fragments were recovered outside of the gun and observed.

Some of the features common to all of the "graded resistance" armatures is severe wear of the molybdenum coating corresponding to the at rest position of the armature, failure of the bolt due to thermal loading, and unacceptable oxidation formation of the molybdenum rail coating exposed to the atmosphere. It was decided that the best way to tackle these problems was to use an armature that did not need to be bolted together and to eliminate the molybdenum coating and use plain ETP copper rails.

ARMATURE DEVELOPMENT

Due to the findings of the previously described experiments, two items become important with respect to the design of the armature. First, the armature must remain in contact with the bore of the gun. Second, the armature should not rely on the mechanical

bonding of the different materials together. Another concept that still held favor was the idea of graded resistance. Two such graded resistance armatures are under development at The University of Texas. The first is the "contact assured" armature that varies the number of conductors to grade the resistance and the second is a metal-ceramic composite composition of which is continuously varied to achieve a graded resistance.

The contact-assured armature is produced by inter-leaving a tungsten mesh between copper foils. The schematic geometry is shown in Figure 4. As shown, the interfiber spacing is dictated by the weave of the mesh material. The inter-weave spacing can be varied to any distance needed. Varying the inter-weave spacing allows the resistance to vary continuously from the back to the front of the armature. The tungsten mesh is a 60 x 60 mesh with a fiber diameter of 0.0508 mm. This stack up of materials has been consolidated using a homopolar generator in conjunction with a consolidation press fixture. The homopolar generator passes a large current through the material. The copper softens and flows around the tungsten fibers forming a solid piece of material. The material system of copper and tungsten was chosen because of the absence of copper-tungsten intermetallics and the favorable physical properties of copper. After the material is consolidated, the faces in contact with the rails are etched to reveal the fibers. A five minute nitric acid etch was used to remove the copper and expose the fibers. Varying the etchant time allows more or less fiber to be exposed. The exposed fibers are the mechanism assuring the contact to the rail material. Figure 5 shows such an exposed sliding surface.

The second solid armature under development is a combination of metal and ceramic. The metal is aluminum and the ceramic is alumina. The original form of the materials is a powder. By mixing different percentages of alumina into aluminum and layering the blended powders, a solid piece of material can be processed. Again the

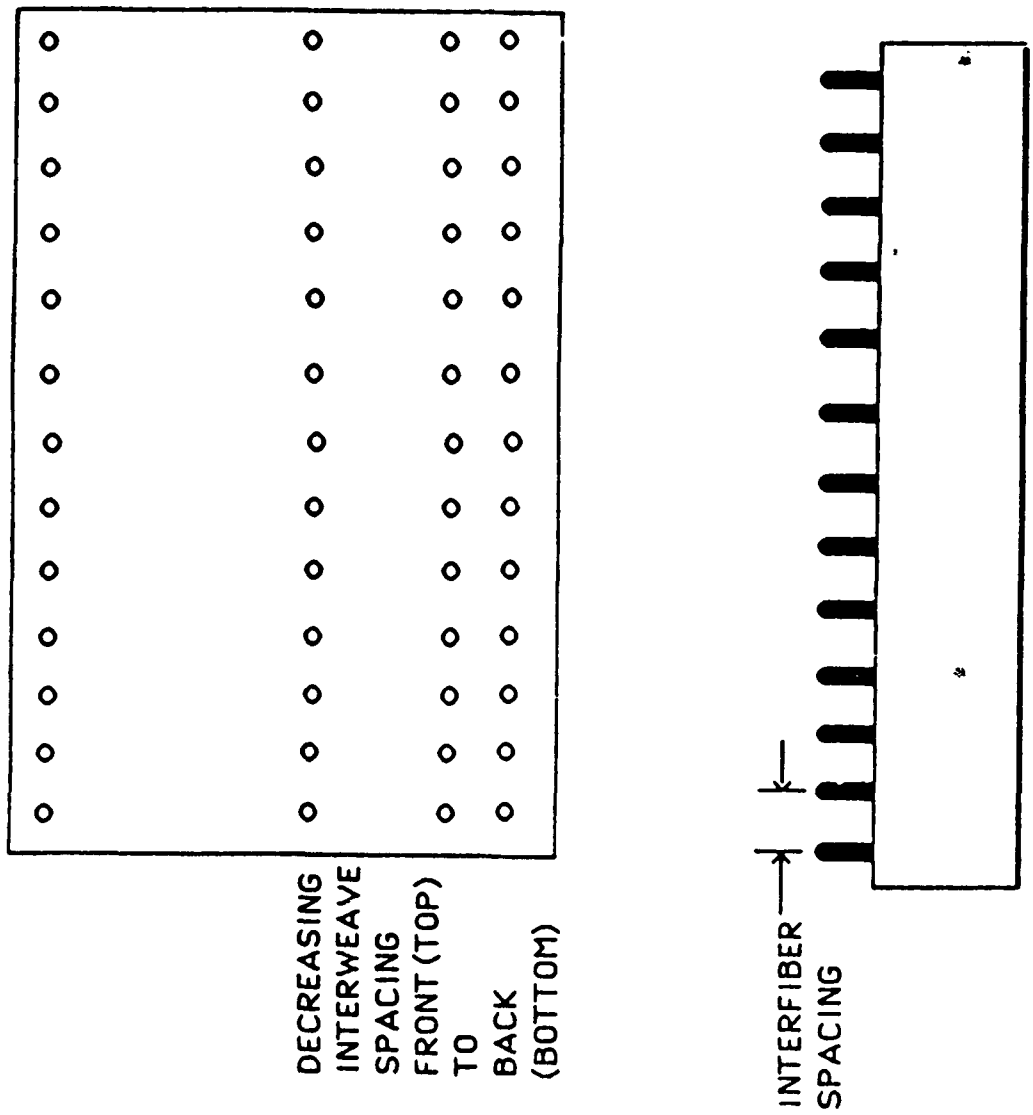

Figure 4: Foil and Mesh Combination

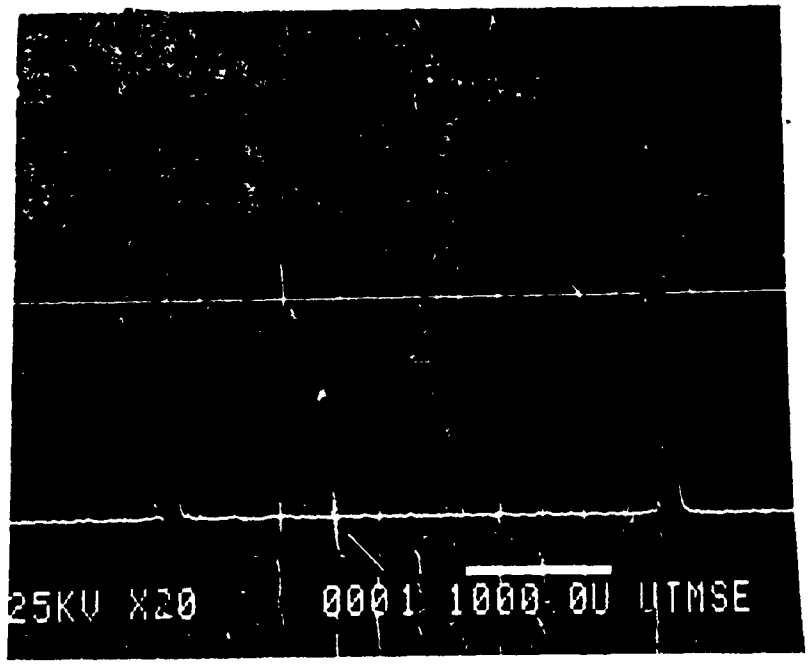

Figure 5: Copper and Tungsten Consolidation

mechanism of consolidation is the homopolar generator and consolidation press fixture. The combination of a low and high melting temperature material allows the aluminum to soften and flow without affecting the ceramic. This solid piece of material would have to be machined into a leaf design incorporating an interference fit. Preliminary proof-of-principle experiments have indicated that both these approaches have the potential to produce graded resistance composite solid armatures.

Acknowledgments

This research was funded partially by the following contracts: DARPA/NADC # N62269-85-C-0222,ARDEC/SETA # DAAA21-86-C-0259, ARDEC # DAAA21-86-C-0251, and DARPA/ARO # DAAL-03-87-K-0073. The authors would also like to thank Dr. M. Schmerling for his assistance with the microscopy and the entire CEM technical staff for their help in conducting the experiments.

REFERENCES

1. Barber, J.P., "The Role of Armature Losses in Railgun Performance," Presented at EM Armature Workshop, Elgin AFB FL, 24-26 June 1986.

2. Persad, C., Peterson, D.R., "High Energy Rate Surface Modifications of Surface Layers of Conductors," Electromagnetic Launch Technology, 3rd Proceeding, April 1986, Institute of Electrical and Electronics Engineering, Inc., New York. Pp. 203-205. IEEE Transactions on Magnetics, Vol. MAG-23. November 1986.

3. Bedford, A. J., "Rail Damage in a Small Calibre Railgun," IEEE Transactions on Magnetics, Vol. Mag-20, No. 2, March 1984.

4. Barber, J. P., "Metal Armature Critical Issues," Presented at EM Armature Workshop, Elgin AFB FL, 24-26 June 1986.

5. Condit, B., and Stachowski, R., "Velocity Skin Effect: Solid and Plasma Armatures," Presented at EM Armature Workshop, Elgin AFB FL, 24-26 June 1986.

6. Long, G. C., "Railgun Current Density Measurements," 3rd Symposium Proceeding, April 1986, Institute of Electrical and Electronics Engineering, Inc., New York. IEEE Transactions on Magnetics, pp. 1597-1602. November 1986.

7. Donaldson, A. L., et al., "Electrode Erosion in High Current, High Energy Transient Arcs," 3rd Symposium Proceedings, April 1986, Institute of Electrical and Electronics Engineering, Inc., New York, IEEE Transactions on Magnetics, pp. 1441-1447, November 1986.

8. Long, G. C., Ph.D. Dissertation, The University of Texas at Austin, 1987.

COMPOSITE SOLID ARMATURE CONSOLIDATION BY PULSE POWER PROCESSING : A NOVEL HOMOPOLAR GENERATOR APPLICATION IN EML TECHNOLOGY

C. Persad, D. R. Peterson, and R. C. Zowarka
Center for Electromechanics,
The University of Texas at Austin,
Austin, TX 78758.

ABSTRACT

Some of the desirable characteristics for the solid armatures used in railguns appear feasible through the use of composite materials. Graded electrical resistance, and assured sliding contact are among these characteristics. Metal-metal, metal-ceramic, and metal-polymer composites are generic types of potential solid armature materials. Copper-tungsten and aluminum-alumina are example composite systems, of the metal-metal and metal-ceramic types respectively, which have been employed in the demonstration of the versatility of the Homopolar Generator as a materials processing tool for composites. Powder metallurgy and laminate bonding approaches have been utilized. In conventional processing, energy deposition is prolonged and the bulk heating which results often destroys the structural and chemical integrity of the starting materials. Composite solid armature materials have been consolidated with subsecond high temperature exposure. Densification in the solid state proceeds by a warm/hot forging mechanism and fully dense composites are obtained by a combined application of pressure and a controlled energy input.

INTRODUCTION

Performance evaluation of railguns depends on availability of suitable solid armatures. Rail/armature combinations which promote efficient energy transfer also minimize bore damage. Less flexibility exists in the choice of rail materials than in armatures. In the search for optimum performance, it is therefore logical to focus on alternative armature designs, and on methods for their processing and fabrication.

A broad-based, integrated approach to solid armature development has evolved over the last several years. At the Center for Electromechanics at the University of Texas (CEM-UT), predictive electrothermal models have been developed and successfully applied to actual armature performance. The models have confirmed the desirability of conductivity grading for improving the current distribution within these ultrahigh speed, variably-loaded sliding contacts. The requirements can probably best be met by composite armatures.

The underlying concepts have been tested in a series of preliminary experiments [1]. These experiments employed a macro-composite solid armature constructed of leaves of materials with different electrical conductivities. Subsequently, fabrication techniques for a more controlled and customized grading of electrical conductivity were proposed. Solid armatures from powder-based metal-ceramic microcomposites, and from metal-metal laminar composites were candidates.

Such composites have been produced by a novel experimental approach which employs a homopolar generator in a pulse-powered materials consolidation system. The feasibility of this approach has been demonstrated for a wide variety of engineering materials [2,3]. A relevant composite system is the binderless copper-graphite composite brush material, which shows application potential for high-speed, high-current duty [4,5].

EXPERIMENTAL PROCEDURE

The Consolidation Process

Figure 1 shows the schematic tooling configuration of the consolidation process. A 10 MJ homopolar generator dedicated to industrial applications was the pulsed power source used, in conjunction with a modified 100 ton vertical axis hydraulic press. The operating characteristics of the HPG as a powder processing tool are described elsewhere [2].

For the powder-based metal-ceramic composite consolidation, powders were mechanically mixed in batches, with ceramic mass fractions of 1% to 10%. Predetermined amounts of each batch were loaded into the cavity of the die to produce an eleven layer stack with graded composition (0% to 10% ceramic mass fraction). The insulated die cavity was lined with a dense alumina tube with an inner diameter of 50 mm.

The laminar copper-tungsten composite was constructed from copper foils and tungsten mesh. These materials were stacked such that the controlled variation in spacing between the exposed tungsten fibers in the consolidated composite would yield a graded electrical resistivity. The concept is illustrated in Figure 2.

The dies and starting materials were initially at ambient temperature. Consolidation was performed in laboratory air. For consolidations performed at pressures ≤ 300 MPa (45 ksi), copper electrode/plungers were used for energy/pressure transfer to the precursors. For pressures > 300 MPa (45 ksi) AISI 416 stainless steel electrodes were employed.

After compacting the precursors to a desired pressure, the large current pulse was used to heat and consolidate the composite material. Following the discharge, the pressure was

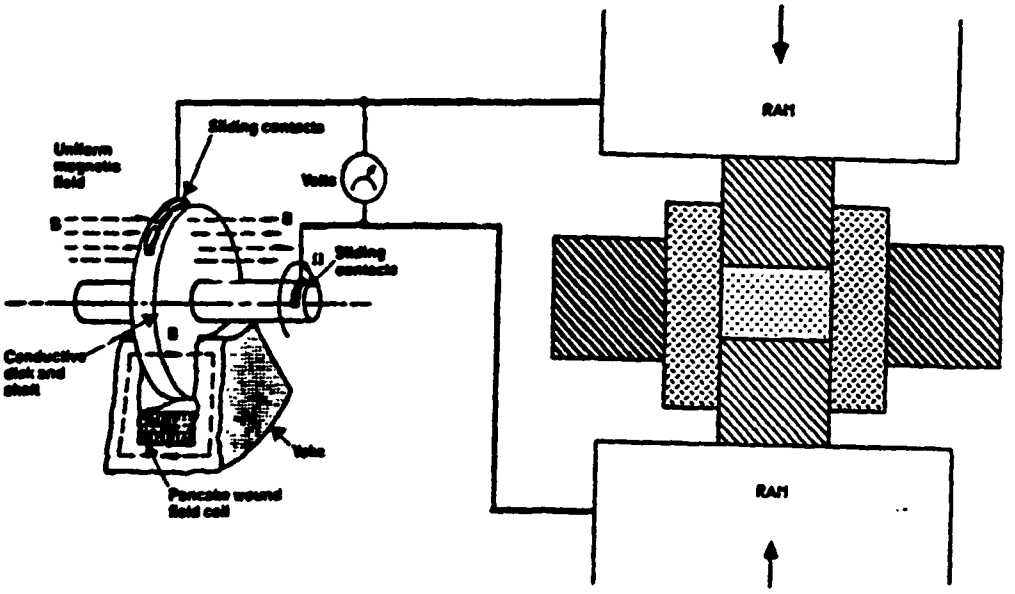

Figure 1. Schematic of the arrangement of the HPG powered consolidation apparatus.

maintained for a holding period, permitting conductive heat transfer through the plungers to massive copper platens. The die was then unloaded and the consolidated compact was ejected.

The voltage drop across the compact and the magnitude of the current were recorded during the pulse. The product of these values was used to obtain the power during the pulse. The power was numerically integrated to produce the total energy input to the specimen. Division of the total energy input by the mass consolidated yields the specific energy input (SEI) in units of J/g. A set of curves for a copper-tungsten consolidation are shown in Figure 3.

Evaluation

Microstructure and density measurements were used in the preliminary evaluation of these composites. The consolidated composite materials were sectioned in the radial direction, metallographically prepared, and then examined by scanning electron microscopy.

RESULTS AND DISCUSSION

Microstructures

Highly dense microstructures were observed throughout the cross-sections of the consolidated composite materials examined by SEM as shown in Figure 4 for the copper-tungsten composite. Excellent conformity between copper and tungsten indicates the potential for a highly conductive interface. An etched cross section is shown at three magnifications in Figure 4 (a), (b), and (c). Figure 4 (c) also indicates the retention of the interfiber spacing of the starting material.For both material systems, densities greater than 95% of theoretical were achieved in the preliminary experiments.

Alternative precursors

One potential difficulty with these materials in high speed sliding duty is the relatively large scale of the constituents. The apparent sliding contact behavior, fn which 5-20 point contacts actively carry current at any instant [6], suggests that more finely dispersed structures may produce better performance. Furthermore, in the refractory-metal skeleton systems, such as copper-infiltrated tungsten, where the vaporization of the infiltrant effectively controls wear, the need is for many micro-islands of tungsten each surrounded by copper.

These difficulties may be resolved by the adoption of novel materials engineering approaches. For the refractory-metal-based systems, the ultrafine filamentary composites described by Bevk [7] is an attractive technical alternative. These materials are

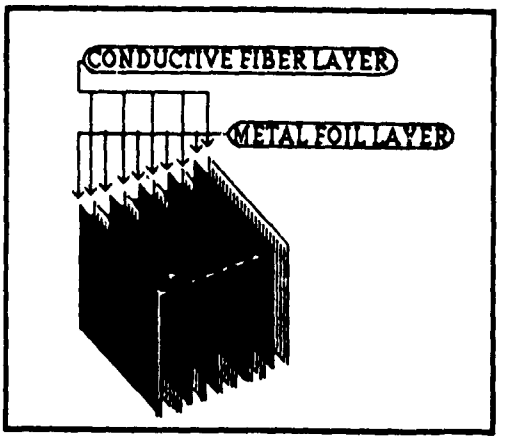

Figure 2. Schematic showing the interleavi concept applied to the copper foil/ tungst weave composite starting materials.

aracterized by dense and uniform dispersions 10^6 to $10^{10}/cm^2$) of fine filaments (5 to 100 nm ick). In this approach a powder metallurgy oduct may be used as the starting material. is material is deformation-processed by olling, swaging, drawing, or extrusion to very rge strains until the *in-situ* formed ilaments are sufficiently small.

Another approach to microstructural refinement is to derive the metal powder blend from the reduction of a complex metal oxide precursor. Suitable copper tungstates and copper molybdates for this purpose have been identified. The challenge is then to consolidate these finely distributed, homogeneous powder blends into useful forms without structural coarsening. This is a task to which the high-energy high-rate consolidation processing may be well matched.

In the case of the aluminum-alumina system, two alternative approaches may be taken to distribution of the alumina in the metal matrix. One is by heat treatment of air-atomized powder particles after compaction to intermediate densities (≈85%). This leads t spheroidization of the alumina in a continuous aluminum matrix, which can then be consolidated to full density. The second approach is by mechanical alloying. The continuous welding and fracturing of an aluminum powder assemblage, and the rapid oxidation of the freshly-fractured surfaces leads to a fine and uniform dispersion of the alumina [8]. These composite powder particles could then be consolidation processed into desired shapes.

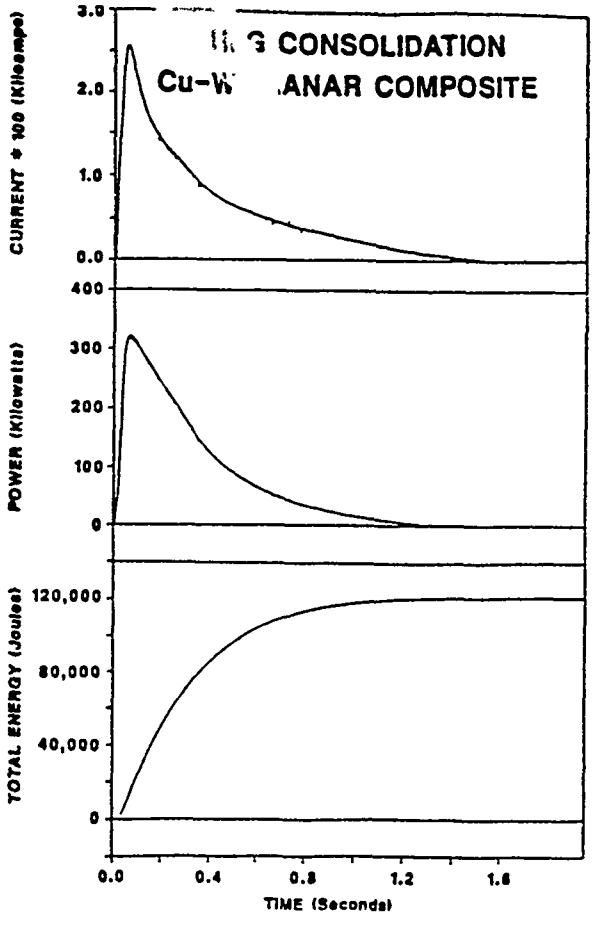

Figure 3. Current, power and total consolidation energy waveforms applied to the copper foil/ tungsten weave composite starting materials.

Metal-polymer composites

The widespread use of polycarbonate cubes as the accelerated load in plasma-driven railguns indicates the survival potential of polmer-on-metal sliding couples in the hypervelocity regime. Recent advances in conducting polymers raise the question of the potential benefit of the incorporation of such materials into solid armatures. It has been reported that on a mass basis a new, iodine-doped polyacetylene polymer is as conductive as copper. More recently, Lockheed has developed the polyanilines which in large scale production may be dollar-a-pound material. These materials are claimed to be less difficult to process than other conducting polymers and they do not ignite upon exposure to air [9].

The potential exists to incorporate these advances in polymer technology into the development of a composite solid armature design which matches the high-speed, high-current duty demanded of these components. One approach may be the use of a tubular skeleton made of a fine tungsten powder, infiltrated with a suitable conducting polymer and fitted over an aluminum or aluminum-alumina composite core. Such an arrangement takes advantage of the tribological and conducting properties of the polymer, the high melting temperature of the tungsten, and the low mass of the core. Other interesting possibilities exist for grading the mechanical, electrical and tribological properties in the radial and longitudinal direction.

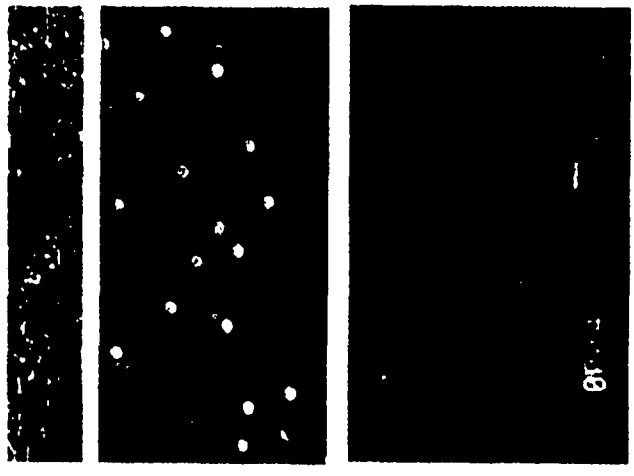

Figure 4. Scanning electron micrographs at (a) low (b) intermediate and (c) high magnification of an etched cross section of a copper foil/ tungsten weave based planar composite.

SUMMARY

Some of the desirable characteristics for the solid armatures used in railguns appear feasible through the use of composite materials. Graded electrical resistance, and assured sliding contact are among these characteristics. Metal-metal, metal-ceramic, and metal-polymer composites are generic types of potential solid armature materials. Copper-tungsten and aluminum-alumina are example composite systems, of the metal-metal and metal-ceramic types respectively, which have been employed in the demonstration of the versatility of the Homopolar Generator as a materials processing tool for composites.

ACKNOWLEDGMENT

This research received early support from SETA Contract DAAA- 86-C-0259. The latter stages were supported by DARPA/ARO Contract DAAL 0387-K-0073. The authors thank Ted Aanstoos and Jim Allen for their assistance with the processing. Chris Lund and M-J. Wang assisted with the microstructural evaluation. This work is part of a collaborative effort between the Center for Materials Science and Engineering and the Center for Electromechanics at The University of Texas at Austin. We thank them for their cooperation.

REFERENCES

1. C.J. Lund, C. Persad, Z. Eliezer, D. R. Peterson, and J. Hahne, " Composite Solid Armatures for Railguns", Paper #13, Proceedings of the 3rd. Int. Current Collector Conference, Austin, TX, Nov. 1987.

2. H. L. Marcus, D. L. Bourell, Z. Eliezer, C. Persad, and W. F. Weldon, "High-Energy High-Rate Processing", Journal of Metals, December 1987, pp 6-10.

3. H. L. Marcus, C. Persad, Z. Eliezer, D. L. Bourell, and W. F. Weldon, High-Energy High-Rate Processing of Composites", Proceedings of the AIME Northeast Meeting, Hoboken, NJ, May 1987.

4. K. C. Owen, M. J. Wang, C. Persad and Z.Eliezer, "Preparation and Tribological Evaluation of Copper-Graphite Composites by High-Energy/High-Rate Consolidation", Wear 120, 1987, pp. 117-121.

5. M. J. Wang, C. Persad, Z. Eliezer, and W.F.Weldon, "High-Energy / High-Rate Consolidation of Copper-Graphite Composite Brushes for High Speed, High Current Applications", Paper #20, Proceedings of the 3rd.Int. Current Collector Conference, Austin, TX, Nov. 1987.

6. I. R. McNab, " Pulsed High Power Brush Research II. Interpretation of Experimental Data", in High Power-High Energy Pulse Production and Application, ed. E.K. Inall, Australian National University Press, (Canberra) 1978. pp 201-215.

7. J. Bevk, "Ultrafine Filamentary Composites", in Annual Reviews of Materials Science, 13, 1983 edited by R. A. Huggins, R. H. Bube, and D. A. Vermilyea (Annual Reviews Inc., Palo Alto, CA) pp. 319-338).

8. P. S. Gilman and W. D. Nix, "The Structure and Properties of Aluminum Alloys Produces by Mechanical Alloying: Powder Processing and Resultant Powder Structures", Metall. Trans., 12A, May 1981, pp. 813-824.

9. T.S. Kuan,'Conducting Plastics Sell for $1 a Pound', in SUPERCONDUCTIVITY Flash Report, Vol. 1, No. 9, Jan. 11, 1988. p.8.

WEAR OF CONDUCTORS IN RAILGUNS:

METALLURGICAL ASPECTS

C. Persad, C.J. Lund, Z. Eliezer,

Center for Materials Science and Engineering,

University of Texas, Austin, TX 78712

and

D.R. Peterson, J. Hahne, R. Zowarka,

Center for Electromechanics,

University of Texas, Austin, TX 78758

ABSTRACT

The wear of metallic rail conductors influences the performance of electromagnetic railguns in which initially solid armatures (sliding electrical contacts) are accelerated to high velocities. Vapor and fine liquid droplets formed at the armature/rail interface reduce the multishot operating efficiency.The experimental focus in this study was the analysis of wear debris generatedby an aluminum alloy armature sliding on copper rails. The experimental parameters were set to maximize armature velocity. Preliminary rail and armature wear observations were documented as part of a database for solid armature development. A variety of debris collection and characterization approaches were used. Both in-bore debris and muzzle- exit debris were collected for size and chemical analysis. Debris constituents were copper rich and the compound Cu_9Al_4 was observed in the splat-quenched muzzle debris. The approach and method are detailed to indicate the potential of wear studies in defining the activity at the sliding interface. Some implications of rail surface roughening on zero wear measurements are also discussed and the adoption of wear mechanism maps is proposed.

INTRODUCTION

Wear processes which occur in railguns are characteristic of sliding electrical contacts [1,2]. These processes are complex and appear to be system specific. From a metallurgical viewpoint it is interesting to view a high-speed solid armature as a vehicle for surface modification of rails. Such an approach is potentially important for predicting performance in the multi-shot operating environment where successive changes in the surface state and chemistry of the rails can drastically alter the mode in which the current is distributed in the near-surface regions. This in turn changes the coupling into the solid sliding armature.

When a particular armature/rail couple is subjected to an electro-thermo-mechanical loading spectrum the metallurgical response is only qualitatively predictable based upon enlightened empiricism. The difficulties associated with more precise predictions are evident when the range of contributing phenomena is considered. Important metallurgical effects include alloy formation due to elevated temperatures developed at the sliding interface between dissimilar material pairs; material exchange between the armature and the rail; chemical reactions between the environment and the freshly re-exposed rail surfaces; and the embedding of debris produced in the forward section of the solid armature and pushed into the softened rail surface by the high pressures in the rear section. Muzzle arc debris produced at armature exit further complicates the metallurgical analysis.

The temperature and pressure changes at the sliding interface are particularly important to armature performance. Pressure effects originate in mechanical preload and in magnetic pressure. The temperature effects have been analyzed by Kuhlmann-Wilsdorf [1]. Pressure effects have been included in the analysis by Ross et. al. [2].

The flash temperature solutions proposed by Kuhlmann-Wilsdorf allow heat evolution at contact spots. Joule heating is assumed to be velocity-independent, while friction heat is proportional to the relative velocity. Contributions to Joule heating include film resistance heating and constriction resistance heating. Qualitative accomodation of the continuous quenching of the armature slider by cold rails make these temperature predictions upper-bound solutions.

The dynamic friction force calculations of Ross et al. are translated into friction coefficients (μ) through constant normal contact force Copper -on -copper sliding at up to 0.20 km/s yields a nearly linear drop in μ from 0.40 to 0.10 [2]. These coefficients are low at velocities > 0.10 km/s. Uncertainties in the value of the inductance per unit length, L' (assumed constant), and in contact force (also assumed constant) are suggested reasons for the low values.

These reviews indicate that existing quantitative predictive models are still incomplete. A single parameter predictor such as interface temperature remains attractive. The difficulty lies in ascertaining the contributions of each of the multiple and coupled heat-generating sources. Potentially more difficult is the prediction of the conditions where impact-generated stresses and consequent localized energy absorbtion can push the temperatures sufficiently high to cause solid-to-hybrid conversion of armatures. It is apparent that bore smoothness, bore straightness, and bore stiffness concepts being incorporated into the present generation of EM guns may contribute to extended bore life by reducing or eliminating some of the sources of impact-generated stresses.

In this paper, we focus upon wear debris analysis for a monolithic aluminum alloy armature sliding between ETP (electolytic tough pitch) copper rails. The experimental parameters were set to maximize armature velocity. Preliminary rail and armature wear observations were documented as part of a database for solid armature development. A variety of debris collection and characterization approaches were used. Both in-bore debris and muzzle- exit debris were collected for size and chemical analysis. The approach and method are detailed to indicate the potential of wear studies in defining the activity at the sliding interface.Some implications of rail surface roughening on zero wear measurements are also discussed and the adoption of wear mechanism maps is proposed.

EXPERIMENTAL APPROACH

EML System

Details of the 7050 aluminum alloy 'fishbone' solid armature and of the 1m long, 12.7 mm square bore railgun used for solid armature development are given by Price et. al. [3]. The current waveform for the experiment selected for detailed analysis was roughly semi-sinusoidal in shape with a peak current of 320 kA at 0.75 ms in a pulse of total length 1.9 ms. The armature was cooled in liquid nitrogen to reduce the insertion force due to its interference fit. In the interval between loading and firing, the armature returned to room temperature. The armature was sized 0.3 mm greater than the rail-to-rail dimension. The armature was accelerated to a muzzle exit velocity of 1100 m/s.

Debris Collection

Post-shot debris collection employed a 1 m long, 6mm diameter stainless steel tube connected to a sealed glass jar for in-bore vacuum scavenging. This technique combines a small mechanical action of the tube tip and vacuum suction to remove loose in-bore debris. The muzzle-exit debris was stripped from the arc chutes. The arc chutes are two steel flats inclined at a 45 degree angle relative to the rail surfaces, and positioned ≈10mm above and below the rail surfaces at the muzzle exit.

Debris Analysis

The scanning electron microscopy examination was conducted in a JEOL 35M instrument operated at 25 kV. Chemical analysis was performed by energy dispersive spectroscopy in the SEM. This provided the size and overall chemistry information. X-ray diffraction data were obtained on a Phillips diffractometer. This allowed confirmation of the crystal structure of the phases present.

RESULTS AND DISCUSSION

Wear Related Observations

The condition of railgun exterior (i.e. the steel structural envelope) was documented as was the state of gun bore surfaces viewed by a borescope from the breech and from the muzzle ends. The pertinent observations are summarized below.

Exterior: The arc chutes were covered with a splat-quenched deposit which had a metallic copper-aluminum appearance. The top chute which was located slightly closer to the bore had a larger and thicker deposit. The rounded rail edges at the muzzle exit appeared to be heavily eroded. There was no evidence of any black powdery soot normally associated with carbonaceous debris production.

Gun Bore: The general appearance of the bore was dominated by an aluminum-colored coating, with occasional gold-colored streaks. The deposit was not uniformly distributed on the top and bottom rails or along the gun length. The lower rail was more heavily coated with a clearer transition from a thick to a thin deposit. The thickness of the deposit was greater at the breech end and became progressively thinner towards the muzzle.

The process by which the material is transferred from the armature to the rail is not entirely clear. It may be 1) smeared while the armature is in the heat-softened solid state, 2) transferred from a liquid interlayer to the rails in a mode qualitatively similar to planar flow casting or 3) spray deposited as a fine debris driven off a transient molten layer and entrained in a debris plume which spreads the debris well away from its source. It appears likely that as the initially solid armature progresses down the bore and the sliding interface temperature rises, the dominant process changes from 1) to 2) to 3). However, non-uniform longitudinal and lateral temperature distributions make it possible for these processes to operate simultaneously, as evidenced by the streaking of the transferred material.

These observations indicate that the degree of wear of a solid armature produced by armature /rail interaction is indeed a function of the energy dissipated during the residence time of the armature at a particular location. This confirms the desirability of measures taken to avoid armatures starting from rest in a railgun bore. Typically the motivation is to reduce rail damage. Pre-acceleration might produce the added benefit of reduced wear of the solid armature.

Debris Analysis.

SEM analysis shows the in-bore debris dimensions to range from tens of microns to submicron. Figure 1 shows a typical high magnification view of the extracted, loose, in-bore debris mounted

Figure 1. Scanning electron photomicrograph of loose in-bore debris.

in colloidal graphite. The large paricles appear to be agglomerations of small particles. We focus upon the micron-sized particles which appear to be the building blocks of the debris. This particle morphology leads us to hypothesize that these particles were spheroidized in flight in the bore. They were deposited onto a more tightly adhered and already oxidized wear layer which made them easier to vacuum scavenge out of the bore. Two different debris chemistries are evident in the EDS scans given in Figures 2a &b. In figure 2a, Cu-Al- Zn rich debris is evident. The source of the zinc is the 7050 alloy chemistry (weight percent 6.2 Zn, 2.25 Mg, 2.3 Cu, 0.12 Zr, Bal. Al) . In Figure 2b, taken from the "gold-colored" debris, the Zn is absent.

The muzzle exit debris is 80 μm to 100 μm thick covering areas of 200-400 mm^2.The spectrum of elemental constituents is graphically detailed with micrograph inset in Figure 3. The X-ray diffraction studies focused on the muzzle exit debris. Copper X-ray diffraction lines were present in each of the two-theta diffraction spectra. The line broadening observed was attributed to the residual strains associated either with a supersaturation of aluminum or with rapid splat quenching. In addition to the copper-rich matrix, the intermetallic compound Cu_9Al_4 was found to be present. Cu_9Al_4 had been previously observed in a railgun deposition environment by DeLuca in his studies of the quenching of exploded aluminum foil onto a copper substrate [4].

Properties of the Sliding Pair Al/Cu

Bore wear analysis requires that the physical properties of the armature/rail material pair be understood, since the severe wear observed appears to be dominated by large-scale material transfer. This section reviews the equilibrium phase diagram, and examines the influence of alloy chemistry on fluidity and resistivity.

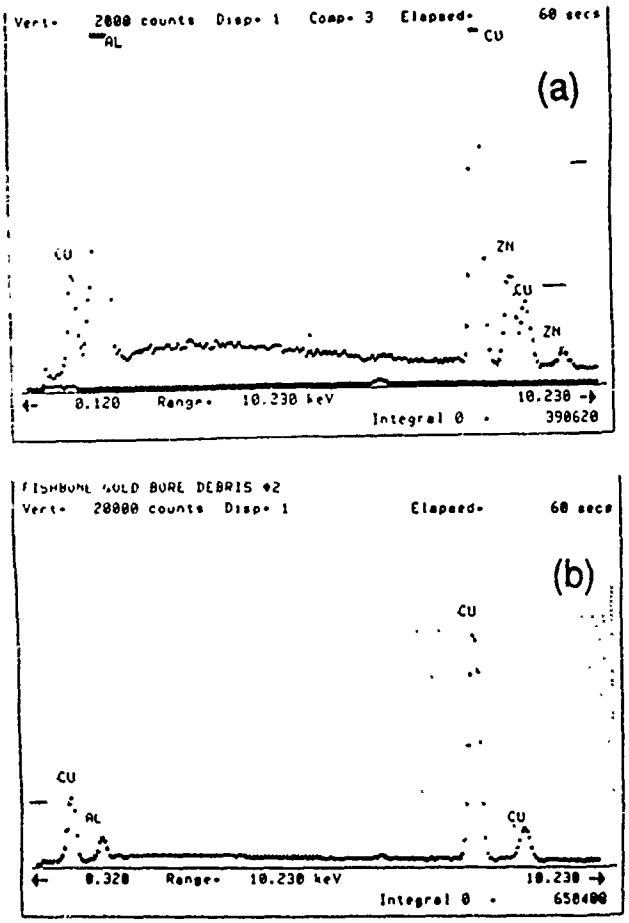

Figure 2. Energy Dispersive Spectroscopy (EDS) Plots indicating the chemistry of the loose in-bore debris (a) Cu-Al-Zn rich (b) Cu-Al rich.

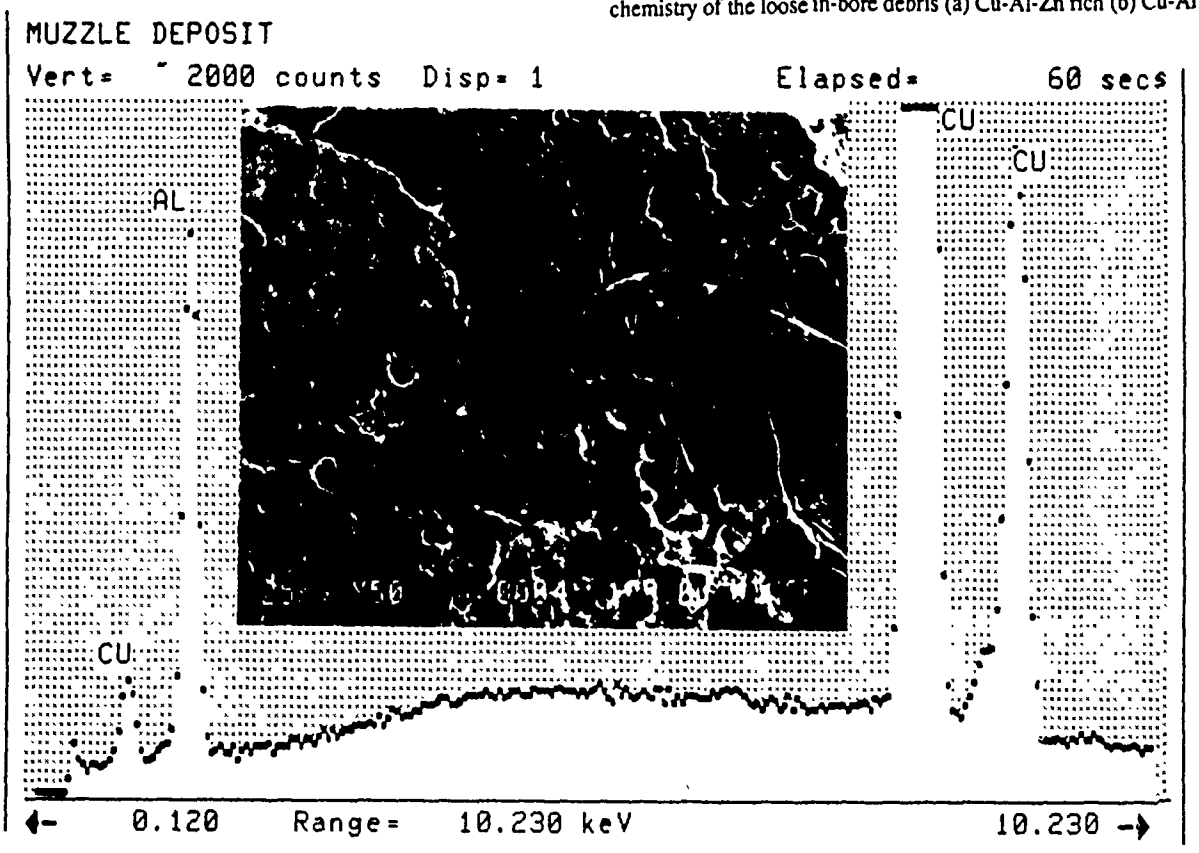

Figure 3. Energy Dispersive Spectroscopy (EDS) Plot indicating the chemistry of the muzzle exit debris is Cu-Al rich. The appearance of the debris is shown in the inset photomicrograph.

Phase Diagram

The equilibrium binary phase diagram for the system Al-Cu is shown in Figure 4, taken from reference [5] in which the characteristics of this system are detailed. Pertinent to this discussion is the described multiplicity of complex solid state reactions. Here we focus on the source of the Cu_9Al_4 . Cu_9Al_4, based on the gamma-brass structure, is the gamma-1 phase which exists over the compositional range of 62.5 to 69 at. % Cu. Its source appears to be the stable high-temperature ß phase which melts at 1322K. A two phase [(Cu) + ß] field exists between the eutectic temperature and the eutectoid reaction ß -> gamma-1 + (Cu) at 850K. The gamma-1 phase has also been observed in diffusion couples annealed at 773K [5]. The presence of Cu_9Al_4 in the splat-quenched muzzle debris is a clear indication of an alloy liquid phase formation. From the phase diagram it may also be observed that the eutectic Al-Cu alloy melts at 112K lower than Al. The formation of this eutectic may place an effective limit for the temperature increase ΔT in the solid-to-solid sliding regime, the liquid thresholdbeing its formation rather than the melting of Al.

Fluidity

For aluminum-copper binary alloys, fluidity decreases rapidly as the copper is added, reaching a minimum at ≈10 mass percent copper. As the alloy composition approaches the eutectic (33 mass

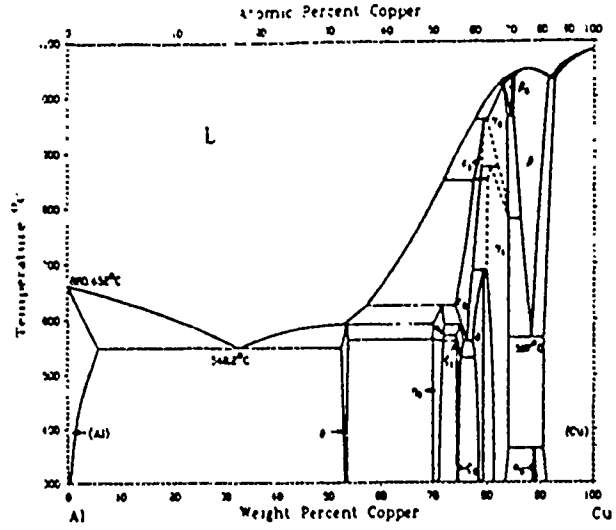

Figure 4. The equilibrium binary phase diagram for the system Al-Cu

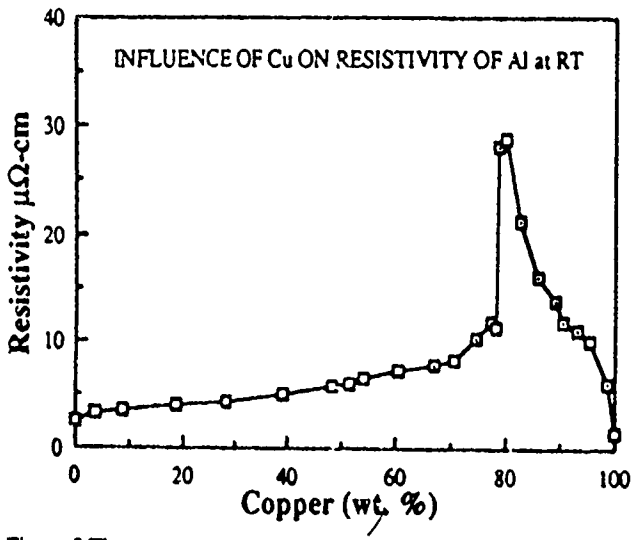

Figure 5.The room-temperature resistivity of aluminum as a function of mass of copper added {data from reference (7)}.

percent copper) fluidity increases significantly. The eutectic fluidity is higher than that of pure aluminum [6]. Fluidity and chemistry in the Al-Cu system are important in explaining the the smearing of alloy debris in the bore and the possibilities for development of a superheated transient thin liquid film layer as a friction reducing phenomenon at the armature/rail interface.

Resistivity

The room-temperature resistivity of aluminum as a function of mass of copper added is shown in Figure 5, which is a plot of data from reference [7] . Resistivity is observed to rise steadily with increasing copper content, and to increase significantly in the range of 70 to 95 mass % Cu. If the interface voltage drop is to be correctly predicted for an armature which develops a liquid surface, then the resistivity changes due to alloy formation must also be taken into account. Furthermore, if such alloys are formed and are a residual deposit on the rail surface, then the implications for advantageous current redistribution also need analysis.

Impact Energy Dissipation - Gouging

The potential roles of electrical and frictional energy dissipation at the sliding interface have been mentioned. The discussion now includes the least well-understood wear phenomenon: gouging due to impact energy dissipation. In uncoated copper rails, postfiring observations reveal gouges appearing in clusters of up to six small pits, 1 mm to 3 mm in diameter. Their appearance is easily distinguishable from arc damage, which, in copper rails, takes the form of small, densely-packed craters 10um to 100um in diameter. Clusters of gouges appear on alternate sides of the bore in a distinctive repeating pattern. The distance between successive clusters increases with increasing armature velocity, suggesting the presence of a secondary transverse perturbation of constant frequency superimposed upon the primary accelerating force.

The phenomena of gouging due to intermittent grazing impact at velocities > 1 km/s has been reported previously [8]. It was observed that material ejected from the gouge was deposited in the form of a metallic spray forward of the gouge pits. In early railgun research [9], it was reported that for copper sliding on copper, gouging begins at 0.6 km/s and increases in severity with velocity. Indium, rhodium, and gold plating of copper rails were each found to marginally reduce gouging. In our research, the use of a 0.5 mm thick, flame-sprayed molybdenum coating on copper rails was found to eliminate the gouging phenomenon. The absence of a fundamental understanding of gouging prevents a rationalization of this finding. At the present time quantitative data on bore damage is scarce. Qualitatively, the degree of bore damage appears sensitive to a variety of experimental conditions. These include: the bore finish and fit of the armature and the general integrity of the structural envelope. Straightness, smoothness and stiffness are desirable attributes and may be crucial to delaying the onset of gouging.

Crack Formation

Wear processes are likely to be influenced by large fluctuating stress conditions as a result of both magnetic pressure and thermal changes. Pressures on the order of 40 ksi [10] , and thermal gradients of 1000K over 200 microns are not uncommon [11]. These conditions have led to surface microcracking of the rails and insulator side walls [12]. The continued effect can result in surface failure and break-up into wear particles.

In pulsed joule heating experiments at 1 to 10 MW/mm^2, metallic conductors were found to undergo a variety of surface transformations [11].The effect of pulsed joule heating alone, in the absence of arc tracking or high speed sliding contact, was sufficient to produce surface melting and microcracking. It appears that these effects were aggravated by the presence of non-metallic, second-phase inclusions in commercial purity materials. Such inclusions presumably cause constrictions in surface current flow and may contribute to localized surface melting. The development of directionally resolidified grain structure [13,14] may also influence crack resistance.

The 'Zero Wear' Artifact

Reports of 'zero wear' in railgun bores in which several MJ of energy have been dissipated have become disturbingly common. The abundant production of wear debris, whether in spectacular muzzle exit debris or the more common 'railgunner's soot', suggests a need for re-interpretation of these results. Two 'invisible' sources of wear debris have come to our attention: the first is the micro-roughening due to liquid droplet impact or to microparticle or ion clusters being plucked from the rail surfaces; the second is the wear material removal which accompanies the rounding of the rail corners, where both theory and experiment indicate that the current density is at its maximum. These wear phemonena may not change the rail-to-rail dimensions but do alter the surface roughness. These phenomena have been non-destructively checked through the use of surface replication techniques used in fractography [15].

The 'zero wear limit' is used in the Bayer-Ku sliding wear theory [16]. Adopting a similar definition for railgun rail conductors, the 'zero wear limit' will be the point in the life of a railgun when its surface roughness median has been depressed to half the depth of the initial peak-to-valley finish, as illustrated in Figure 6 adapted from Engel [17]. Such a definition allows accomodation of the fact that microscopic changes in asperity dimensions precede the development of distinguishable wear. This 'zero wear limit' will be important in future analytical treatments of rail wear, since it marks the start of a measurable wear rate: a process which is crucial to accurate bore life prediction. At this time, it is possible that not many experimental EML systems have undergone sufficient cycles to produce measurable wear by these criteria. However, the potential pitfall is the behavior within the 'zero wear limit' being extrapolated.

Wear Mechanism Maps

The wear mechanism mapping approach proposed by Ashby's group [18] is potentially useful. For rail wear, appropriate axes might be mass removed vs energy dissipated. Since energy dissipation is itself a function of current, velocity, sliding pair materials, etc., a series of sub-plots will be required. Models which predict energy dissipation are currently being developed and await experimental verification. When these are implemented, wear mechanism maps can be used to graphically define the transitions at the sliding interface and to point the directions for wear control in railguns.

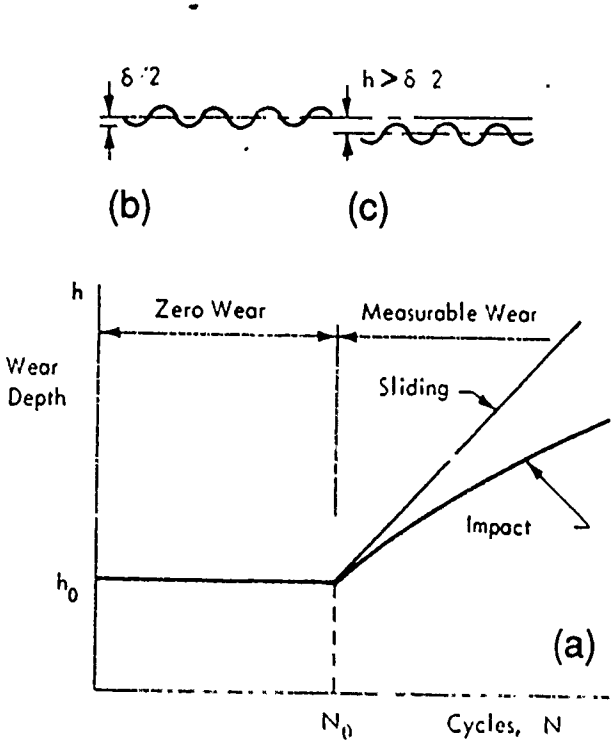

Figure 6. Zero wear and measurable wear: (a) a log-log schematic for wear data (b) zero wear (c) measurable wear

ACKNOWLEDGMENT

This research received early support from SETA Contract DAAA-86-C-0259. The latter stages were supported by DARPA/ARO Contract DAAL 0387-K-0073. The authors thank Drs. M-J. Wang and M. Schmerling for their assistance with the microstructural evaluation. This work is part of a collaborative effort between the Center for Materials Science and Engineering and the Center for Electromechanics at The University of Texas at Austin. We thank them for their cooperation.

REFERENCES

1. D. Kuhlmann-Wilsdorf, "Flash Temperatures due to Friction and Joule Heat at Asperity Contacts," Wear, 105 (1985) pp. 187-198.
2. D. P. Ross, G. L. Ferrentino and F. J. Young, "Experimental Determination of the Contact Friction for an Electromagnetically Accelerated Armature," Wear, 78 (1982) pp. 189 - 200.
3. J.H. Price, C. W. Fulcher, M. Ingram, D. Perkins, D. R. Peterson, R. C. Zowarka, Jr., and J. A. Pappas, "Design and Testing of Solid Armatures for Large-Bore Railguns", Distributed at Proc. of the 4th. EML Conf., Austin, TX, April, 1988.
4. R. J. DeLuca, MS Thesis, The University of Texas at Austin, May 1987, p. 30, p.79.
5. J. L. Murray, Binary Alloy Phase Diagrams, T. B. Massalski (ed.), ASM, Ohio,1986, pp. 103-108.
6. F. R. Mollard, M. C. Flemings, and E. F. Niyama, "Aluminum Fluidity in Casting," J. of Metals, (Nov. 1987), p.35.
7. Handbook of Resistivity of Binary Alloys, K. Schroder (ed.), CRC Press, Boca Raton, FL., 1983, p.79.
8. K.F. Graff and B.B.Detloff, " The Gouging Phenomenon between Metal Surfaces at High Sliding Speeds," Wear 14 (1969), pp 87-97.
9. R.A. Marshall, "Moving Contacts in Macro-Particle Accelerators", in High Power-High Energy Pulse Production and Application, ed. E.K. Inall, Australian National University Press, (Canberra) ,1978.
10. R.F.Davidson,W.A.Cook, D.A.Rabern, N.M. Schnurr, "Predicting Bore Deformations and Launcher Stresses in Railguns", IEEE Transactions on Magnetics, Vol. MAG-22, (Nov. 1986), pp. 1435-1440.
11. C. Persad and D. R. Peterson , "High Energy Rate Modification of Surface Layers of Conductors", IEEE Trans. on Magnetics, Vol. MAG-22, (Nov. 1986), pp. 1658-1661.
12. D. R. Peterson, D. A. Weeks, R. C. Zowarka, R. W. Cook , and W. F. Weldon, "Testing of a High Performance, Precision Railgun," IEEE Transactions on Magnetics, Vol.MAG-22, (Nov. 1986), pp. 1662-1668.
13. A.J. Bedford, "Rail Damage in a Small Calibre Railgun," IEEE Transactions on Magnetics, Vol. Mag-20, No. 2, (March 1984), pp.348-351 .
14. R. F. Askew, B. A. Chin, B. J. Tatarchuk, J. L. Brown, and D. B. Jensen, "Rail and Insulator Erosion in Rail Guns," IEEE Trans. on Magnetics, Vol. MAG-22, (Nov. 1986), pp. 1380-1385.
15. Metals Handbook: Fractography and Atlas of Fractographs, H. E. Boyer (ed.), 8th. ed., Vol. 9, ASM, Ohio, 1974, p.56.
16. R. G. Bayer, A. T. Shalkey, and A. R. Wayson, " Design for Zero Wear," Machine Design, 41 (1) (Jan. 1969) pp. 142-151.
17. Peter A. Engel, Impact Wear of Materials, Elsevier, New York, NY, 1978, p. 182.
18. S. C. Lim, M. F. Ashby, and J. H. Brunton, 'Wear -Rate Transitions and their Relationship to Mechanisms', Acta Metall., (June 1987), 35 (16), pp. 1343-1348.

BINDERLESS COPPER-GRAPHITE AND NANOSIZED STRUCTURES IN Cu-W-WC-C COMPOSITES FOR ELECTROTRIBOLOGICAL APPLICATIONS:

C. Persad, M. Schmerling, Z. Eliezer,

Center for Materials Science and Engineering,
University of Texas, Austin, TX 78712

and R. Carnes, J. Gully

Center for Electromechanics,
University of Texas, Austin, TX 78712

Abstract

Sliding speeds, current densities, and useful operating lifetimes are key parameters for electrical contacts in future high-performance pulsed power machines. For homopolar pulse generator brushes, infiltration of Pb-Sn into a copper-graphite powder composite skeleton is a conventional fabrication route. This composite fails at v>220 m/s by loss of the low melting temperature binder. Binderless copper-graphite materials operate at higher temperatures. However, speeds > 200 m/s at current densities > 2 kA/cm^2 produce interface temperatures > 500°C. Results will be presented on a recent novel materials science approach to handling of such high interface temperatures. Contact layers containing a tungsten aerogel-type skeleton structure with 100 nm-sized contact points, and with nanosized WC and colloidal graphite particles have been fabricated. Sol-gel synthesis, carbothermic reduction, large-strain deformation processing, and high-energy, high-rate powder consolidation were the main steps in the processing of these nanosized structures. The processing/microstructure/properties base for these nanosized composite structures was related to the observed high-speed, high-current, electrotribological performance.

This work was supported by the Texas Advanced Research Program, Grant # 4357, 1988-1990, the Texas Advanced Technology Program, 1989-1991 Grant, and by DARPA under ARO Contract DAAL 0387-K-0073.

Introduction

Pulsed power and hypervelocity phenomena are critical emerging technologies (1). These technologies are undergirded by a variety of hardware. Among these are powerful electrical machines. Their powerfulness is derived in part from high operating speeds and extremely large electrical currents. Examples of such machines are homopolar pulse generators and electromagnetic launchers. Sliding electrical contacts are integral current collecting components in these machines. They must perform under extreme conditions as depicted in Figure 1. In homopolar pulse generators, the brushes must harvest electrical currents in the megampere regime at sliding speeds > 100 m/s. In electromagnetic launchers, the solid armatures must drive payloads by megampere-induced Lorentz forces to velocities in excess of 1 km/s. Schematic diagrams of each of these devices are shown in Figure 2.

High performance composite materials are being developed to meet these needs. The brushes are being fabricated as a powder metallurgy composite of copper and graphite. These constituents provide the conductivity and lubricity sought in this device (2). The solid armatures are being designed as a hybrid composite component with special attention to the sliding interface (3). These "electrotribological" systems are so designated because of the combined sliding and current-carrying duty.

It is well established that a number of composite materials systems exhibit the characteristics necessary for high performance sliding electrical contacts (4). When based on powder constituents, such composites provide some of the necessary product properties by selection and assembly of material at the microscopic level. The relationship between the tribological behavior of such contacts and their basic materials science is the subject of a large body of studies (5–15). A key issue is the value of the maximum temperature that can be sustained by the contact at the sliding interface, while maintaining the efficient energy transfer associated with solid-to-solid contact. In these applications, the complex electrotribological environments encountered provide multiple interface heating sources, as indicated in figure 2 (a) for a homopolar generator brush. Achieving the necessary performance demands novel approaches to the design, processing, characterization and laboratory testing of suitable materials.

Sliding at high speeds while carrying large currents causes combined mechanical and electrical energy dissipation at the sliding interface. The contact surface becomes hot. In the case of solid armatures, the contact surface becomes hot enough to melt metallic conductors such as aluminum (16). In electromagnetic launcher terminology, the onset of melting leads to a change in electrical performance described as "transitioning". During "transitioning" a fluid interlayer (liquid, vapor or plasma) develops at the sliding interface and a solid armature then becomes a hybrid armature showing some of the characteristics of a plasma armature at the interface while the bulk remains a softened solid. Hybrid armatures perform unpredictably. It is therefore desirable to design solid armatures that remain solid during use (17).

Experimental Procedures

Materials

1. Composite Brushes. The binderless copper-graphite was produced by the high-energy high-rate technique (18–20). The degree of homogeneity of the distribution of the graphite in the copper matrix depended upon the mechanical mixing that is achieved prior to loading of the powder mixture into the die. The degree of mixing depends upon the relative densities and the flow characteristics of the loose starting powders. Since the single-residence processing occurred in the solid-state, the pressure and temperature conditions within the die during the processing control the degree of densification. The copper matrix was powder-forged to high densities, while the graphite was subjected to intraparticle shear to accommodate the plastic flow of the matrix. Heating rates of 100 K/s to 500 K/s were used to rapidly bring the copper matrix to the warm processing range (0.4 to 0.6 Tm, where Tm is the melting temperature of copper = 1356K). While at temperature the composite densified under an applied stress that was in excess of the flow stress within the powder volume.

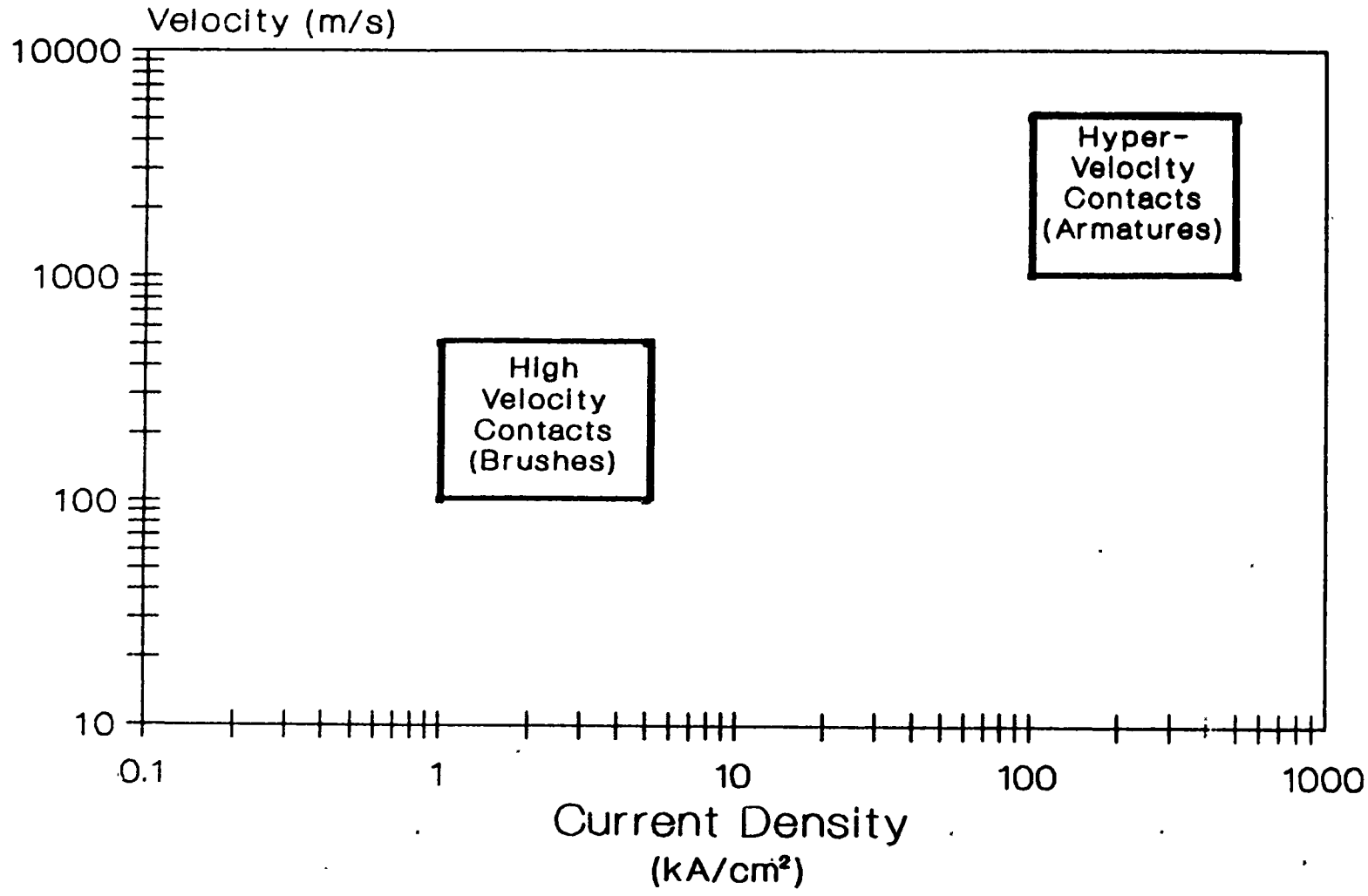

Fig. 1. Operating regimes for high velocity and hypervelocity sliding contacts on velocity/current density axes

HEAT SOURCES IN A HOMOPOLAR BRUSH

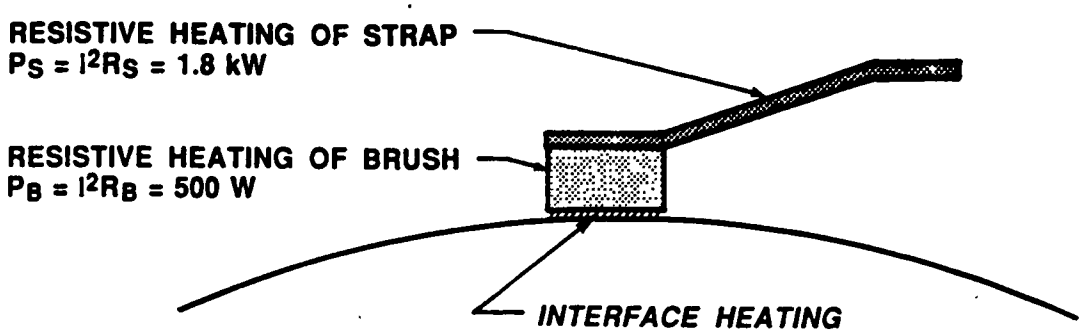

I = 5 kA	V = 2 V
v = 200 m/s	$R_B = 20\ \mu\Omega$
$\mu = 0.2$	$R_S = 72\ \mu\Omega$
N = 45 N	

(a)

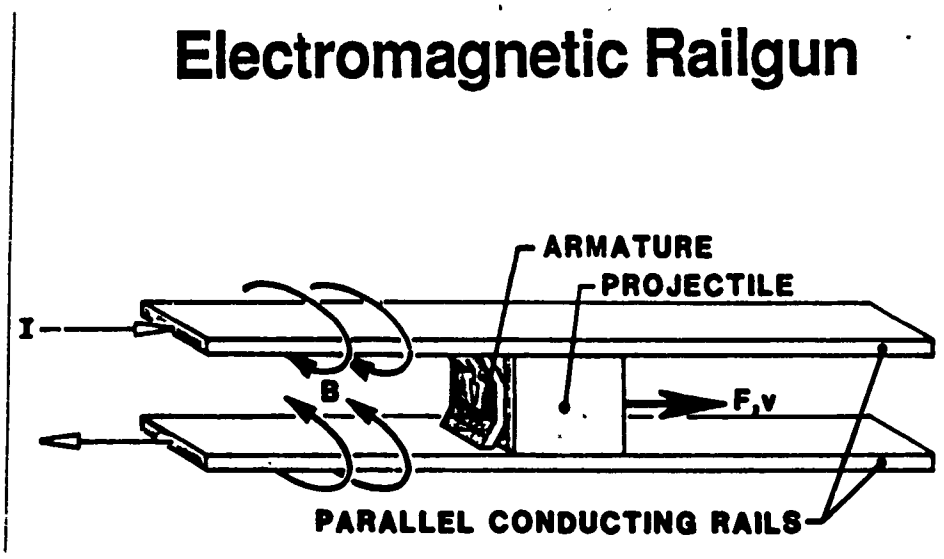

(b)

Figure 2 - Operating environment of (a) high velocity sliding contacts (brushes) and (b) hypervelocity sliding electrical contacts (armatures). In (a) the relative magnitudes of some of the heating sources of the contact are estimated using a typical set of parameters.

The measured values of density, hardness and electrical resistivity of the binderless copper-graphite composite material for brushes are listed in Table I.

Table I. Properties of binderless copper-graphite composite materials for brushes.

	Binderless Cu-Gr
Density (g/cm^3) (percent theoretical)	6.30-6.68 94.1-99.8
Average Hardness * (Rockwell 15T)	62 (Axial), 50 (Radial)
Electrical Resistivity (μ ohm-cm at 300K)	3.82 (Axial), 8.95 (Radial)

* On this scale a fully dense copper powder compact has an average hardness of 70.7.

II. Composite Armatures. The composite material designed for solid armatures consists of a 100 μm thick W/WC/C layer embedded into copper. The objective was to produce a sliding interface capable to simultaneously withstand and reduce the high interface temperature (21, 22). This W/WC/C layer was synthesized by a technique consisting of synthesis of tungstic acid gel, precursor blending with colloidal graphite, followed by spreading of a thick film of the blended precursor onto copper. The W/WC/C layer was formed by carbothermic reaction and embedded into copper by flat rolling followed by pulsed joule heating under pressure. W/WC/C coated copper rectangles (20 mm x 12 mm) were then cut and mounted for testing and evaluation. Figure 3 shows the structure of the blended precursor thick film.

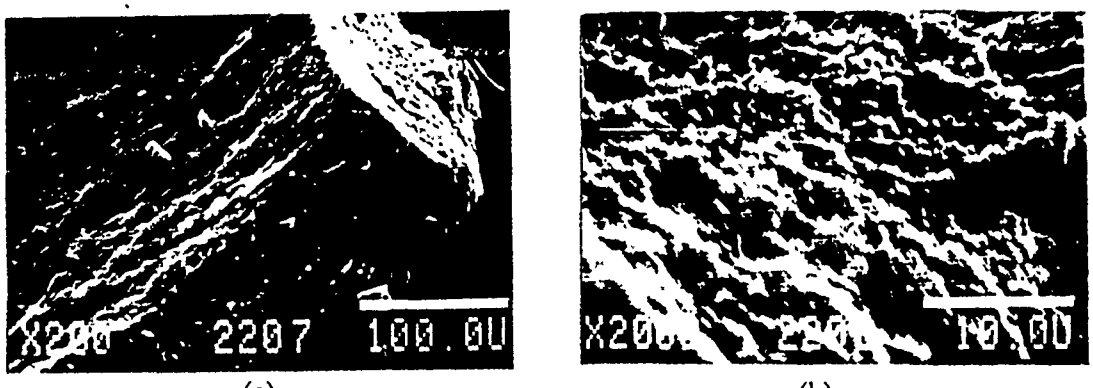

(a) (b)

Figure 3 - SEM photomicrograph of a vacuum dried composite film synthesized from a tungstic acid/colloidal graphite blend.
(a) low magnification showing the corner edges of a 100 μm thick layer.
(b) high magnification view of a fracture surface of the composite film in (a) showing the ultrafine particle microstructure.

Materials Evaluation

Low Speed Testing. The low speed tests were conducted in air on a pin-on-disk machine. Friction force and pin wear were monitored by a strain ring and a linear-displacement transducer respectively. An Apple II computer stored and plotted the data. The pin wear rate and friction coefficient were calculated from the plots. The applied load range was 2 to 20N, and the sliding velocity range was 220 to 670 mm/s.

High Speed Testing. The sliding electrical contact tester (SECT) is a device which allows rapid evaluation of materials and cooling methods with respect to interface power dissipation and wear rate. Continuous testing at speeds of up to 180 m/s at 6000 A is possible. Electromagnetic displacement probes monitor brush wear, and a video thermal imaging system provides a time-temperature history of the slider, sliding interface, and rotor. The tests were performed dry in air. No active cooling was used. Constant down force of 100N was maintained during the temperature excursion tests. The specimen surfaces were prepared by polishing with a final

polish using 600 grit silicon carbide paper. Prior to the test the contact and rotor surfaces were cleaned with high–purity ethyl alcohol.

Post-Test Evaluation. Following tribological evaluation, the contact surfaces were examined in the scanning electron microscope to determine the response of the wear surface to electrotribological loading.

Results and Discussion

A. Binderless Copper-Graphite Composite Brush Material

Preliminary results of the tribological characterization of the binderless copper and graphite powder-based composites were previously published by Owen et al (18), Wang et al (19), and by Eliezer et al (20, 23). The low speed pin on disk tests (0.6 m/s) of the copper-graphite composite on 4340 steel showed friction coefficients in the range 0.133 to 0.207.

At high speeds the wear of the binderless composite is significantly lower than the commercial composite material now being used. At 200 m/s values of 0.2-0.3 x 10^3 mm^3/Mm versus 2 x 10^3 mm^3/Mm, are obtained over 6 km sliding distances. The peak interface temperatures observed by video thermography during these tests were 450 °C to 620 °C in the downforce range of 44.8 N to 134.4 N.

Based upon previous work in our laboratory, Everett (24) reported on the pulse duty (<3 seconds) performance of these binderless copper–graphite contact materials. An improvement in contact resistance was observed compared to commercial composite material (COM-A) at velocities of 20m/s to 90m/s. Current density comparisons at 100m/s and 160m/s showed the binderless material to have twice the current carrying ability of the commercial composite. When pulse loaded at 3 kA/cm^2 at 160 m/s, a nearly linear temperature rise of 100 K/s was observed to a peak temperature of 420K.

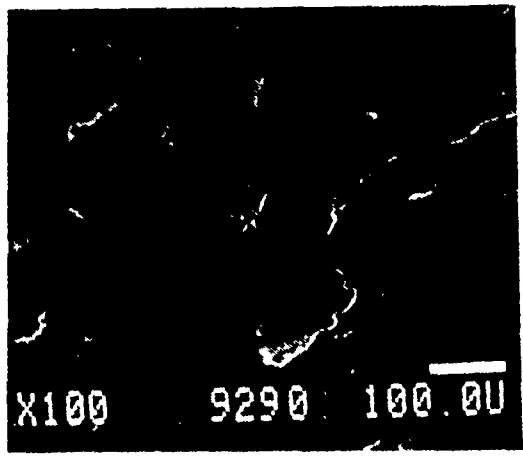

Figure 4 - SEM photomicrograph of the surface of the binderless copper-graphite composite after a high speed wear test on the sliding electrical contact tester. A graphite particle in the edge-on orientation is the dark lenticular shape located parallel to the wear tracks. Also visible are thin highly deformed laminar regions in the matrix and the decoration of the matrix surface with fine dark dots of graphite. (Test conducted in air, uncooled, with 100N downforce. Run for 60s at 100 m/s with zero current, then for 30s at 100 m/s with 1 kA/cm^2. Contact area 20 mm x 12.5 mm on turned 4340 steel rotor surface).

From the results of the electrotribological testing described, several wear mechanisms are known to be active depending upon the nature of the reinforcing phase. One example is the apparent re-transfer of fine particles of graphite to the copper matrix, first transferred as a thin

film from the brush to the rotor. A post-test brush wear surface exhibiting this effect is shown in Figure 4.

B. Solid Armatures Containing Tungsten Contact Points

A graded resistance armature concept is based upon the two–dimensional model for current density distribution within a traveling solid armature developed by Long(25). It attempts to compensate for the observed tendency of the current to concentrate close to the trailing edge of the armature by making that edge the most resistive part of the armature, thus forcing a more uniform distribution of the current. Armatures incorporating this gradation have been fabricated and evaluated by Persad et al. (3).

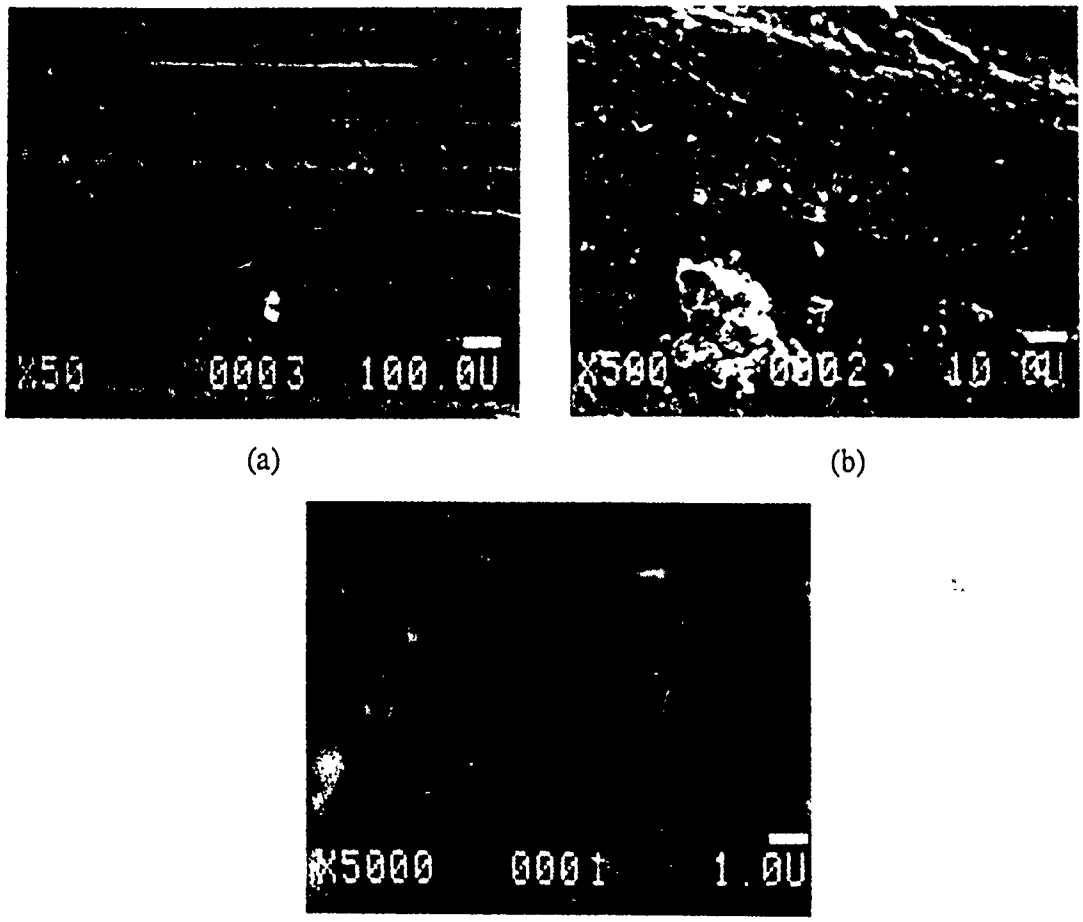

(a) (b)

(c)

Figure 5 - SEM photomicrograph of the wear surface of 100 µm thick W-WC-C layer on a copper substrate after a high speed wear test on the sliding electrical contact tester. (a) At low magnification, the profile of the rotor surface appears to be replicated on the contact surface with a series of evenly spaced troughs running horizontally. (b) At higher magnification the wear track orientation is horizontal. A loose wear particle with approximately 20 µm dimensions is visible at the bottom of the photo. (c) A high magnification view of the bottom of a wear trough showing loose particles with 1-2 µm dimensions distributed on the substrate which has the original nanosized structural features.

These proposed design concepts have as a common objective the maintenance of armature/rail contact. However, controlling energy dissipation at the sliding interface poses another significant challenge as guns get longer and are driven harder. Performance suffers as solid armatures tend to be converted to hybrid (plasma/solid) armatures in bore during firing. This hybridization can be delayed by use of a W-WC-C layer at the sliding interface.

Figures 5a, 5b, 5c show SEM photomicrographs of the wear surface of 100μm thick W-WC-C layer on a copper substrate after a high speed wear test on the sliding electrical contact tester. At low magnification, the profile of the rotor surface appears to be replicated on the contact surface with a series of evenly spaced troughs running horizontally. At higher magnification, a loose wear particle with approximately 20 μm dimensions is visible at the bottom of the photo. A high magnification view of the bottom of a wear trough shows loose particles with 1-2 μm dimensions distributed on the substrate which has retained the original nanosized structural features.

A major concern in the operation of high speed sliding contacts remains the control of temperature at the sliding interface. While many of the heating sources are identifiable, it is less clear how this heating influences contact performance especially at the microstructural level of contact spots. Wear mechanism maps (26) need to be developed to clarify the regimes in which phenomena such as oxidation and melt lubrication are likely to operate. This work contributes some data towards the eventual development of such maps for devices fabricated from high performance composite materials.

Acknowledgements

We thank Jim Allen and Alber Walther for their assistance in fabricating and testing these contacts, and A. Yeoh, S. Raghunathan, and G. Husnain for their assistance in evaluation of these materials and preparation of this manuscript. This work was supported by the Texas Advanced Research Program, Grant # 4357, 1988-1990, the Texas Advanced Technology Program, 1989-1991 Grant, and by DARPA under ARO Contract DAAL 0387-K-0073.

References

1. C. Norman, "How the United States Stacks up in Key Technologies", Science, 248 (1990), 299.

2. Tribology of ceramics, Report of the Committee on the Tribology of Ceramics of the National Materials Advisory Board, Publication # NMAB-435 (National Academy Press, 1988), 17.

3. C. Persad, D. R. Peterson, and R. C. Zowarka, "Composite Solid Armature Consolidation by Pulse Power Processing: A Novel Homopolar Generator Application in EML Technology" IEEE Transactions on Magnetics, Jan. (1989), 429-432 .

4. Z. Eliezer et al,. "Advanced Composite Materials for High-Performance Electrotribological Applications" (To be published in ASM International's Conference on Tribology of Composite Materials Proceedings), Oak Ridge May 1-3, 1990.

5. R. Holm, Electric Contacts, 4th. ed., (Springer Verlag, Berlin/New York, 1967).

6. R. A. Marshall, " Design of Brush Gear for High Current Pulses and High Rubbing Velocities", IEEE Transactions on Power Apparatus and Systems, PAS 85(11)(1966), 1177-1188.

7. J. L. Johnson and L. E. Moberly, " High Current Brushes, Part I: Effect of Brush and Ring Materials", IEEE Transactions on CHMT, CHMT-1(1)(1978), 36-40.

8. J. P. Barber, D. P. Bauer, T. J. McCormick and D. E. Johnson" The Performance of High Current Density Metallic Conductors", in Proceedings of the CURRENT COLLECTOR CONFERENCE (Raleigh, NC. October 1985), 228-235.

9. J. P. Barber, C. McDonald " Electric Contacts at High Velocity", in Proceedings of the CURRENT COLLECTOR CONFERENCE (Raleigh, NC. October 1985), 236-241.

10. C.J. Lund, C. Persad, Z. Eliezer, D. R. , and J. Hahne, " Composite Solid Armatures for Railguns", Paper #13, Proceedings of the 3rd. Int. Current Collector Conference (Austin, TX, Nov. 1987)

11. D. P. Ross, G. L. Ferrentino and F. J. Young, "Experimental Determination of the Contact Friction for an Electromagnetically Accelerated Armature," Wear, 78(1982), 189- 200.

12. J. M. Casstevens, H. G. Rylander, and Z. Eliezer, "Influence of High Velocities and High Current Densities on the Friction and Wear of Copper-Graphite Brushes", Wear 48(1978), 121.

13. M. Brennan , Z. Eliezer, W. F. Weldon, H. G. Rylander and H. H. Woodson," The Testing of Sliding Electrical Contacts for Homopolar Generators", IEE Transactions CHMT., CHMT-2(1)(1979).

14. R. A. Burton, "Materials for Sliding Contacts in the Twenty-first Century", Electrical Contacts -1988, Proc. of the 34th. IEEE Holm Conference, (1988), 257.

15. H. G. Rylander, J. H. Gully, Z. Eliezer, "Limiting Design Parameters for Future High Speed, High Current Density Sliding Electrical Contacts" Electrical Contacts -1988, Proc. of the 34th. IEEE Holm Conference, (1988), 247.

16. C. Persad, C. J. Lund, Z. Eliezer, D. Peterson, J. Hahne, R. C. Zowarka, "Wear of Conductors in Railguns: Metallurgical Aspects", IEEE Transactions on Magnetics, (Jan. 1989), 433-437.

17. R. C. Zowarka, R. W. Cook, A. Y. Yu, C. Persad, H. Patterson, and H. Liu, "Advanced Armature Program - Task 1", Final Technical Report, AFATL TR 88-58, (August 1988).

18. K. C. Owen, M. J. Wang, C. Persad and Z.Eliezer, "Preparation and Tribological Evaluation of Copper-Graphite Composites by High-Energy/High-Rate Consolidation", Wear 120(1987), 117-121.

19. M. J. Wang, C. Persad, Z. Eliezer, and W.F.Weldon, "High-Energy / High-Rate Consolidation of Copper-Graphite Composite Brushes for High Speed, High Current Applications", Paper #20, Proceedings of the 3rd.Int. Current Collector Conference (Austin, TX, Nov.1987).

20. Z. Eliezer, M. J. Wang, C. Persad, and J. H. Gully," A Novel Processing Technique for Metal/Ceramic Composites", in Ceramic Developments, C. C Sorrell and B. Ben-Nissan (eds), Materials Science Forum, (Trans Tech Publ., Switzerland), 34-36(1988), 505-509.

21. D. Kuhlmann-Wilsdorf, "Flash Temperatures due to Friction and Joule Heat at Asperity Contacts," Wear 105(1985), 187-198.

22. Z. Eliezer, C. Persad, S. Raghunathan, D. Barnes, D. Moore, S. C. Sparks, and J. H. Gully, "Nanosized Structures for High-Performance Tribological Applications", (Poster Presentation at the 1989 TMS Fall Meeting, Indianapolis, IN., October 2-5, 1989).

23. Z. Eliezer, "Friction and Wear of Metal Matrix–Graphite Fiber Composites", in Friction and Wear of Polymer Composites, K. Friedrich (ed.), Elsevier, (1986).

24. J. Everett, (MS Thesis, The University of Texas at Austin, Dec. 1988).

25. G. C. Long, "Railgun Current Density Distributions," IEEE Transactions on Magnetics, MAG-22(Nov. 1986), 1597-1602.

26. S. C. Lim and M. F. Ashby, "Wear-Mechanism Maps", Act. Metall. 35(1)(1987), 1-24.

APPENDIX G

OTHER SYSTEMS

Scripta METALLURGICA Vol. 22, pp. 907-910, 1988
Printed in the U.S.A.

BASIC PRINCIPLES FOR SELECTING PHASES FOR HIGH TEMPERATURE METAL MATRIX COMPOSITES: INTERFACIAL CONSIDERATIONS

M. E. Fine, D. L. Bourell, Z. Eliezer, C. Persad and H. L. Marcus

Department of Mechanical Engineering and Center for Material Science & Engineering
The University of Texas at Austin
Austin, TX 78712

(Received March 9, 1988)

It has become increasingly recognized that interfacial considerations will ultimately determine the success or failure of a particular metal matrix composite (MMC, broadly interpreted to include precipitation as well as dispersion strengthened alloys) consisting of phases selected on the basis of attractive properties of the homogeneous phases alone. While each basic principle for selecting phases to give the desired interfacial properties may be well known, there has not been a concise discussion of all of them in any one place nor has there been a general discussion of how one might achieve these desired interfacial properties. The desired interfacial properties are, of course, high strength, absence of brittleness, and thermal stability.

A successful high temperature alloy must be resistive to chemical attack in the atmosphere such as air to which it is subjected or an effective protective coating is required. This is a large important field of alloy development study but the principles of oxidation or other chemical attack prevention will not be discussed here. If the alloy needs an outer protective coating, we will assume such a coating has already or can be developed.

Thermal stability requires that the phases do not react to form undesirable phases and that the structure does not excessively coarsen during fabrication or at the temperature of application. The safest approach is to start the MMC design with phases that are in equilibrium with each other.

High strength, of course, requires strong bonding across the interface. Absence of brittleness at the interface between phases would seem to be best achieved by having the bonding be to a large degree metallic in nature. This means there should be a high degree of metallic bonding in the phases themselves, i.e., they should be metallic solid solutions or intermetallic compounds.

For a number of reasons interfacial energy is a key property which must be taken into consideration. As is well known, the fracture energy to make a unit area of fracture at the interface is

$$\gamma_F = \gamma_\alpha + \gamma_\beta - \gamma_{\alpha\beta} \qquad (1)$$

where γ_α and γ_β are the surface energies of a unit area of each phase while $\gamma_{\alpha\beta}$ is for the interface. Small $\gamma_{\alpha\beta}$ is desired to make γ_F large. Thus dispersions of high interface energy particles are expected to be more subject to interfacial fracture. Such particles are often microvoid initiators during creep or cyclic loading leading to early fracture.

If dispersion strengthening is part of the design of the MMC then the spacing between particles must be small because the stress to force dislocations between particles in the absence of thermal activation is approximately

$$\tau_{bp} \sim Gb/l \qquad (2)$$

where G is the shear modulus, b is the dislocation's Burgers vector, and l is the spacing between particles along the dislocation line. For τ_{bp} to be large, l must be very small, approximately 100 times b or approximately 30 nm. This must be achieved in the microstructure to obtain the desired dispersion strengthening. Such values of l require rather small particles even if the volume fraction is large. Thus

0036-9748/88 $3.00 + .00

excessive particle coarsening at the temperature of application cannot be tolerated. Such coarsening may be accelerated by stress application.

Interfacial energy drives dispersed particle coarsening (Ostwald ripening). If the rate is controlled by volume diffusion (VDC) in the matrix, then the LSW theory (1) tells us that the average particle size $\bar{r}$ varies with time t as follows:

$$\bar{r}^3 \sim \frac{\varphi \gamma_{\alpha\beta} \bar{v}^{\beta 2} D_B C_B}{kT} t \qquad (3)$$

where D_B is the volume diffusivity of the rate controlling component in the matrix and C_B is its solubility in the matrix at absolute temperature T. $\bar{v}^{\beta}$ is the partial atom volume of B component in the dispersed phase. Later modifications of this theory (2,3) take account of volume fraction of β due to overlap of diffusion fields of neighboring particles. Another factor φ is introduced which increases with the volume fraction (V_f) of β. Thus for small coarsening rate and for microstructural stability, the product $\gamma_{\alpha\beta} D_B C_B$ is important and needs to be small.

Alternatively, the reaction at the interface (1) may control the coarsening rate (IRC),i.e., the rate at which atoms attach themselves to the growing particles is slower than the slowest solute diffusion rate. Then the diffusion gradient near the particle is very small and no or very small effect of V_f on coarsening rate is expected. In any respect the slowest process controls the coarsening rate.

Coherent particles often grow by the ledge mechanism. Ledges commonly occur on the interface and growth occurs by ledge movement (4). Most particles have curved interfaces with the matrix while coherence requires planar interfaces. Thus a macroscopically curved interface must be made up of small planar areas terminating in ledges and there is a very large number of ledges to facilitate growth. In the authors' opinion interface growth by the ledge mechanism is most often rapid and not rate controlling in the absence of impurity segregation. However, impurity segregation may be an effective way to slow coarsening by "poisoning" the ledges causing interface drag.

There is still another reason why low interfacial energy is desirable in an MMC. High interfacial energy particles tend to be located at grain boundaries. The change in interfacial energy to form such segregated particles is

$$\Delta\gamma \equiv 2\gamma_{\alpha\beta} - \gamma_{gb}. \qquad (4)$$

Thus if $\gamma_{\alpha\beta}$ is high, it is energetically very favorable for the particles to be located at grain boundaries rather than within the grains. As is well known high interfacial energy particles at grain boundaries are particularly effective initiators of failure due to cavitation under creep or fatigue loading at high temperatures. Further, diffusion is more rapid along grain boundaries so excessive Ostwald ripening may be a problem if C_B is not low.

What are the possibilities for achieving low energy, strong, and ductile interfaces between phases that will not transform or react to form undesirable phases during processing or at the high temperature of application? As already mentioned metallic solid solutions and intermetallics would seem most promising for giving strong ductile metallic type bonding across the interface and equilibrium between phases is desired, i.e., phases which are present in the same phase field of the phase diagram.

One way of lowering the interfacial energy is by Gibbs adsorption. The Gibbs adsorption equation,

$$d\gamma = \sum_i \Gamma_i \, d\mu_i \qquad (5)$$

tells us that segregation of a solute at the interface will lower the interfacial energy. In Eq. 5 Γ_i is the number of adsorbed atoms of component i per unit area of interface and μ_i is the chemical potential of the matrix or dispersed phase. Of course such segregation must not cause embrittlement such as by increasing the ionic or covalent character of the interface bonding, rendering the doped alloy unusable. The interfacial energy may be

reduced through reduction in misfit energy by Gibbs adsorption without changing the character of the metallic binding. The preferred way to achieve a low energy interface is by having planes of similar structure and nearly the same atomic spacing face each other across the interface. Interfacial considerations are also important in achieving an oxidation resistant coating for a high temperature alloy but this is another subject.

What are the possibilities for achieving these desirable interfacial properties in a real system? The classical example is the Ni based superalloys which are naturally formed metal matrix composites, that is by solutioning and precipitation heat treatment. The $L1_2$ structured dispersed phase is coherent and coplanar with the A1 structured Ni based solid solution matrix, i.e.,

$$\{100\}_{A1} \parallel \{100\}_{L1_2} \text{ and } <100>_{A1} \parallel <100>_{L1_2}.$$

and the habit plane is {100}. Both have F-type unit cells. This is the most successful series of high temperature alloys to date, but, of course, lower density and higher operating temperature without sacrificing stiffness or even with increased stiffness are goals which underpin much current research. There are other examples of coherent-coplanar $L1_2$ structural precipitates in aluminum structured matrices. Al_3Li, Al_3Zr, Al_3Ti, $Al_3(Zr,V)$, and $Al_3(Zr,Ti)$ (5) in aluminum alloy matrices are examples, but unfortunately all of these $L1_2$ phases are metastable.

An interesting case of a similar orientation relation occurs with $MgFe_2O_4$ precipitates in MgO (6). The former has the $H1_1$ (spinel) structure while the latter has the B1(NaCl) structure. Both also are based on cubic F-type unit cells and again $\{100\}_{B1} \parallel \{100\}_{H1_1}$ and $<100>_{B1} \parallel <100>_{H1}$ but the interface plane is {111} in both phases in contrast to {100} for the A1-$L1_2$ case. The origin of this difference is not known.

The relationship between the A2 and B2 structures which have I unit cells is identical to that between the A1 and $L1_2$ structures, i.e., coplanar-coherent interfaces may be achieved if the lattice parameters are nearly the same and of course many metals have the A2 structure and B2 is a very large class of compounds. Precipitation of NiAl in Fe has this property and again the interface is {100} in both phases (7). NiAl has a higher melting temperature than Ni_3Al (γ), 1640 compared to 1387°C and Fe has a higher melting temperature than Ni, 1538 compared to 1455°C. Thus Fe based superalloys are a worthwhile objective (for example, alloyed with Cr to stabilize the A2 structure and give oxidation resistance). Chromium (also B2 structured) melting at 1863°C is almost 400° higher than that of Ni and perhaps is worthy of further study as the basis for a useful high temperature alloy.

While lattice parameter matching with similar structures is one way to obtain low energy interfaces, there may be special orientation relations which give interface matching even though the lattice parameters and structures are different. The classical example in the metallurgical literature is the Kurdjumow-Sachs relation, $\{111\}_{A1} \parallel \{110\}_{A2}$ and $<110>_{A1} \parallel <111>_{A2}$ between martensite and ferrite. Another example is $\{111\}_{A1} \parallel (0001)_{A3}$ and $<110>_{A1} \parallel <2110>_{A3}$ between the A1 and A3 structured phases in cobalt. While the interface plane in cobalt is the close packed plane in both phases, $\{111\}_{A1}$ and $(0001)_{A3}$, in the steel case to achieve lattice matching the undistorted-unrotated habit plane (the interface plane) is different than the parallel planes. It is $\{225\}_{A1}$ in medium carbon steels.

The low energy interface plane examples cited have all been prepared by solid state phase transformation. Rapid solidification processing gives the alloy designer much greater freedom in selecting phases and systems. The best high temperature aluminum alloy developed to date is a rapidly solidified alloy based on the Al-Fe system with Si and V additions (8). During processing the compound α-$Al_{12}(Fe_{.9}V_{.1})Si$ forms in the matrix. This is complex I lattice cubic with 138 atoms per unit cell, but the lattice parameter is 1.261 nm which is 3.1 times that of Al. The dispersed particles are thermodynamically stable, spherical and coherent with the matrix. The $Al_3(Zr,V)$ and Al(Zr,Ti) dispersion strengthened aluminum alloys referred to earlier were also made by rapid solification processing.

If the dispersed phase is put into a MMC by mechanical mixing then reorientation of the particles to reduce the interfacial energy is not expected unless recrystallization, coarsening of the particles, or liquid phase sintering has been made to occur. High energy rate processing (9) may possibly give reorientation of the matrix and particles because very high temperatures are achieved for very short periods of time. Also reactive sintering of the elements or precursors to give an MMC alloy may possibly lead to low interfacial energy orientation relations. Therefore, the authors believe it is worthwhile to consider what kinds of phases might give low energy interfaces, assuming that phase reorientation can be achieved, when the processing starts with mechanical mixing or alloying rather than melting.

The Ti-Al system has much current interest because Ti melts at 1672°C and these alloys have the possibility of low density combined with high melting point. Further, Nb stabilizes the A2 structure in Ti and raises the melting temperature still higher (10). The intermetallic "TiAl" has the $L1_0$ structure but the c/a ratio is 1.02 so it is nearly cubic (11). One might anticipate a K-S relation between ß stabilized Ti and $L1_0$ "TiAl", alloyed to lower the c/a ratio, because the interatomic spacing in TiAl and the A2 structured Ti-Nb solid solution are both approximately 0.28 nm. An interface plane close to that in steel might also be expected.

Alloy theory is progressing to the point where the stability of alloy phases may be predicted. Nb_3Si has the $L1_2$ structure but alas it is only stable between 1783 and 1953°C (12). If it could be further stabilized by ternary additions (adding or subtracting electrons), then it becomes an attactive combination with Nb for a refractory metal based superalloy. Since Nb has the A2 structure, again the K-S relations may be made to occur.

Many metalloid intermetallics like NbC, NbN, TiC, TiN have the B1 structure. In adding a carbide, nitride, boride or oxide to a metallic matrix it is important to select a compound which is more stable than the solvent in the matrix. A case in point is SiC added to aluminum where a reaction to Si and Al_4C_3 may occur which embrittles the interface (13). TiC or TiN are more promising from this point of view (14).

In forming a dispersion between an A2 metal plus a metal interstitial compound care must be taken to assure that the interstitial compound does not dissociate with some of the interstitial dissolving in and embrittling the matrix. Again, a compound should be selected with a lower free energy of formation versus T curve than that of the interstitial with the matrix. For example TiN has such a relation with chromium nitride and would be a candidate for dispersion strengthening of Cr (14).

The lattice parameters of the B1 structured metal carbides and nitrides are larger than those of the A2 metals (11); however, if the 100 plane of the A2 metal is rotated 45° with respect to the 100 plane of the B1 compound so that $\{100\}_{A2} \parallel \{100\}_{B1}$ and $<110>_{A2} \parallel <100>_{B1}$, then good matching between the 100 face of the F cell so defined for the A2 metal and a 100 face of the B1 compound may be achieved. For example, a <110> for Cr is 0.407 nm and that for cubic $(Re_{.6}W_{.4})C_{.6}$ is 0.406 nm (11).

Many, many more examples can no doubt be found, but these suffice to illustrate the principles which have been discussed.

Acknowledgment

Partial support for this work was provided by DARPA/ARO under contract DAAL03-87-K-0073.

References

1. C. Wagner, Z. Elektrochem., 65, 581-591 (1961).
2. A. D. Brailsford and P. Wynblatt, Acta Metall., 27, 489-497 (1979).
3. P. W. Voorhees and M. E. Glicksman, Metall. Trans. A, 15A, 1081-1088 (1984).
4. G. J. Shiflet and J. A. Hawk, 1988 TMS Annual Meeting, Phoenix, AZ, 25 January 1988. Conference volume to be published, Y. W. Kim and W. M. Griffith, editors.
5. M. S. Zedalis and M. E. Fine, Metall. Trans. A, 17A, 2187-2198 (1986).
6. G. P. Wirtz and M. E. Fine, J. Amer. Ceram. Soc. 51, 402-410 (1968).
7. H. Calderon and M. E. Fine, Materials Science and Engineering 63, 197-204 (1984).
8. D. J. Skinner, R. L. Bye, D. Raybould and A. M. Brown, Scripta Met. 20, 867-872 (1986).
9. H. L. Marcus, D. L. Bourell, Z. Eliezer, C. Persad, and W. Weldon, Journal of Metals, Dec. 1987, 6-10.
10. J. L. Murray, "TiAl and TiNb" Phase Diagrams, in "Binary Alloy Phase Diagrams," American Society for Metals. Metals Park, Ohio, T. B. Massalski, editor-in-chief, 1986.
11. W. B. Pearson, "Handbook of Lattice Spacing and Structures of Metals," Vol 2, Pergamon Press Ltd., Oxford, England, 1967.
12. A. G. Knapton, "Metals Handbook," 8th Ed. Vol. 10, Metals Park, Ohio, 1973, p. 283.
13. H. L. Marcus and L. K. Rabenberg, "Interface Characteristics and Mechanical Properties of Metal-Matrix Composites," Office of Naval Research Contract N00014-84-K-0687, Technical Report UTCMSE-87-3, pp. 160-165, 1987; G. Elkabir, "High Energy-High Rate Powder Processing of Aluminum Silicon Carbide Metal Matrix Composites" (Ph.D. Thesis, University of Texas, Austin, TX, August 1987).
14. T. Rosenquist, "Principles of Extractive Metallurgy." McGraw-Hill Inc., USA 1974, pp. 516-534.

CONSOLIDATION OF POWDERS OF THE OXIDE SUPERCONDUCTOR $YBa_2Cu_3O_x$ BY HIGH ENERGY - HIGH RATE PROCESSING.

C. Persad*, S. -J. Lee, D.R. Peterson**, J. S. Swinnea*, M. Schmerling*,

K.M. Ralis*, H.L. Marcus* and H. Steinfink*

*Center for Materials Science and Engineering

and **Center for Electromechanics,

The University of Texas at Austin,

Austin, Texas 78712.

ABSTRACT

The consolidation response of powders of the superconducting compound $YBa_2Cu_3O_{7-\partial}$ is reported. Cu, Ag, Sn and Cu-based metallic glass infiltrants have also been employed in preliminary fabricability studies. The processing approach relies on short duration (< 1s), high current density (10^4 A/cm^2), pulse resistive heating of powders under applied pressures of 200 MPa to 400 MPa. Powders and fabricated disk compacts were characterized by X-ray diffraction, optical and scanning electron microscopy, and resistivity measurements. X-ray diffraction comparisons of starting powder and consolidated material show retention of the single phase 1-2-3 structure and the development of a preferred orientation. In the consolidated pure $YBa_2Cu_3O_{7-\partial}$, T_c onsets of 87K were accompanied by broad transitions. Iodometric analyses indicated oxygen depletion in the as-consolidated disks. Observed oxygen content profiles across the sample thickness had values $0.11 < \partial < 0.35$. The variation in the peak processing temperature within the disk was found to correlate with the oxygen content profile.

INTRODUCTION

It is evident that the promise of the new high-temperature ceramic superconductors will not be realized without an intense materials science and engineering effort focused on converting these oxide powders into useful bulk forms. The general limitations of the conventional press and sinter ceramic processing approach (1) are likely to be amplified by the sensitivity of the superconductivity transitions to oxygen content(2).

It has been shown that the composition $YBa_2Cu_3O_x$ has values $6<x<7$ (3,4). The superconducting orthorhombic phase exists over a range of x near 7 while a semiconducting, tetragonal structure exists for x=6. Indeed the narrow stoichiometric limits for oxygen in the '90K' superconducting, orthorhombic structure appear to be a major challenge in the processing of these materials. It has been observed that post sintering reoxygenation of the material is a useful tool in assuring the return of the '90K' superconductivity (4). However, the practical fabrication of bulk forms and composite bulk forms will require post-shaping annealing in a controlled atmosphere and over a narrow temperature range.

Useful, small-section forms have been successfully fabricated at a number of laboratories. In particular, the fabrication of wires , tapes , and coils has been reported (5-7). In this work, we report the preliminary results on the consolidation of thin disks from $YBa_2Cu_3O_x$ powders by the use of a novel high energy high rate approach employing subsecond high-current pulses from a homopolar generator or capacitor bank.

EXPERIMENTAL

Yttrium-barium-copper-oxide disks 54 mm in diameter and 0.6 mm thick were produced by consolidating seven-gram quantities of the oxide powders. Powder blends of the elemental powders of Cu, or Ag , or Sn with the $YBa_2Cu_3O_x$ were consolidated into disks 25mm or 50 mm in diameter with masses of 10g to 50g.The metal:oxide ratio was varied from 5% to 50% by mass. In a third approach, preconsolidated disks were infiltrated with a Cu-based metallic glass (mass % 77Cu, 6 Ni, 10 Sn, 7 P).

Two types of pulsed power sources were employed in the processing. A 510 μF, 1. kV capacitor bank was used for the low energy consolidations, and a 10 MJ homopolar generator for the high energy consolidations. Both sources produce high-current pulses with subsecond duration. The capacitor bank discharge developed a peak current of ≈100 kA at 100 μs. Energy inputs at the 100 J/g level were used. The homopolar generator developed peak currents of ≈60 kA at 200 ms to deliver the 5000 J/g energy level chosen. Consolidation was performed in insulated dies under applied pressures of 30 ksi (207MPa) to 75 ksi (517MPa). Details of the general procedure have been reported elsewhere (8).

Figure 1 shows the processing parameter matrix employed for the $YBa_2Cu_3O_x$ powders. The dies and powders were initially at ambient temperature. Consolidation was performed in laboratory air (72°F, 50%RH). Specimens A, B, C and D, consolidated by the short-pulse capacitor discharge, are referred to as low-energy consolidations. Specimens E and F, consolidated by the homopolar generator discharge, are referred to as high-energy

pressures ≤ 300 MPa (45 ksi), copper electrode/plungers were used for energy/pressure transfer to the oxide powders. For pressures > 300 MPa (45 ksi) AISI 416 stainless steel electrodes were employed. The voltage drop across the compact and the magnitude of the current were recorded during the pulse. The product of these values was used to obtain the power curve during the pulse. The power curve was numerically integrated to produce the total energy input to the specimen. Division of the total energy input by the mass consolidated yields the specific energy input (SEI) in units of J/g. A set of curves for specimen E is shown in Figure 2.

RESULTS AND DISCUSSION

A. Processing Response

Specimens A, B and C, consolidated at low energy and under increasing pressure, all retained the original powder structure, judged by a comparison of the pre-consolidation and post-consolidation x-ray diffraction profiles of the single-phase, orthorhombic $YBa_2Cu_3O_x$. Post-consolidation analysis of specimen D showed $BaCO_3$ contamination. We speculate that this was due to moisture (H_2O) pick-up prior to consolidation. All these low energy consolidated disks exhibited the Meissner effect at liquid nitrogen temperature. This was considered a qualitative confirmation of the high T_c properties of the post-consolidated $YBa_2Cu_3O_x$.

The in-process voltage drop across the compacts in this pressure range, which is roughly proportional to the resistance, showed a continued decrease with increasing pressure. As indicated in Figure 3, the rate of decrease in room-temperature resistance vs pressure also

diminishes with increasing pressure. A value of 2 milli-ohm is reached at 517 MPa (75 ksi). The low energy consolidations (A, B, C and D) defined the processability of the material using the high energy-high rate approach. Parameters for specimens E and F were set to seek the high energy threshold for pulse resistive heating of the material. Specimen E exhibited limited solid-state infiltration of the copper electrode into the compact due to softening at the compact/electrode interface. Back-extruded flash developed on the periphery of specimen F consolidated with a specific energy input of 5,500 J/g.

E. Structure/Processing

The morphology of the as-consolidated $YBa_2Cu_3O_x$ is shown in Figure 4. The pre-consolidated powder particle shapes are retained in the low-energy consolidated material, Figure 4(a). At high energy, Specimen F, a melted and resolidified surface morphology is evident, Figure 4(b). The resolidified material shows extensive cracking. This cracking may be due to thermal shock or to the volumetric change during resolidification.

In DTA studies of $YBa_2Cu_3O_7$ heated at 20 deg/min. in air, we observed a melting/decomposition endotherm at 1030 °C. The threshold for this endotherm should be shifted higher by the heating rate of $\cong 10^5$ deg/min. in the homopolar generator consolidation possibly allowing short-time higher temperature processing. Our studies of these high heating rate effects on the stability of the superconducting orthorhombic structure are expected to provide insights into the usefulness of these materials for potential application as pulse-loaded elements in

high energy storage devices. Elements such as switches will be incorporated into circuits containing metallic conductors. Efficient energy transfer at metal-ceramic superconductor interfaces becomes critical. Due to the localized pulse resistive heating that develops at the interface between the metallic electrode and the consolidated material, this processing technique also allows an examination of such metal-ceramic joints. The apparent sensitivity of the $YBa_2Cu_3O_7$ chemistry to prolonged 1000 °C exposure limits the use of conventional techniques for the study of bonding of this material to metallic copper (T_m=1083 °C). The subsecond high-temperature exposures in the high energy-high rate processing makes it an attractive approach for such a study.

The tight interfacial bonds observed in Specimen E, between the Cu electrode and the $YBa_2Cu_3O_x$ compact, Figure 5, suggest that the metal-oxide eutectic bonding mechanism (9) known to exist in the copper-oxygen system may be operative. The mechanism involves the formation of a Cu-O liquid eutectic at 1065 °C. It has been reported that strong bonding to copper has been achieved via this mechanism for a number of single oxides (10).

C. Metal-oxide composites

Sn- $YBa_2Cu_3O_x$ In this system layered structures developed and severe crazecracking was observed. XRD indicated that a variety of tin oxides were formed, along with an oxygen-depleted 1-2-3 orthorhombic phase.A Tc onset of 80K was observed, followed by a slow decrease in resistance to 77K. Figure 6 shows the resistance measurements on the as-consolidated material.

Cu- $YBa_2Cu_3O_x$ A homogeneous structure was obtained in this system through controlled processing with low energy inputs but oxygen depletion was still evident.In the as-processed condition, a superconductive transition is observed at 98K following semiconductive behavior, as shown in Figure 7. Upon annealing, the copper-rich regions tranformed to copper oxides. These oxides appear to inhibit a transition to complete superconductivity (zero resistance), as indicated in Figure 8.

Ag- $YBa_2Cu_3O_x$ In this system, some internal cracking was evident and a small amount of a Cu-Ag eutectic phase wass formed. A Tc transition is observed at 90K, as shown in Figure 9.

Cu-based Metallic glass- $YBa_2Cu_3O_x$ The infiltration arrangement and the microstructure developed are shown in Figure 10. The low melting temperature of the infiltrant (920K) and its high electrical resistivity in the glassy state (188 $\mu\Omega$-cm) aid in the production of a fully dens product.

In each of the four composite systems, fully dense structures with mechanical integrity were obtained. However, in each case the superconductive properties were adversely affected. The major common reason for this appears to be oxygen depletion of the $YBa_2Cu_3O_7$.

ACKNOWLEDGMENT

We thank the Center for Electromechanics management for their assistance in facilitating the processing experiments. R. Allen, T. A. Aanstoos D. Badger, and R.

W. Cook operated the pulsed power sources and data acquisition systems. A. Manthiram assisted with the chemical analyses and DTA work. This research was supported by the Center for Materials Science and Engineering. JSS and HS acknowledge support from the R. A. Welch Foundation, Houston, Texas and from NSF DMR 8520028. DARPA/ARO contract DAAL03-87-K-0073 provided support for part of the processing and characterization work.

REFERENCES

1. M. Paulus, "The Influence of Powder Synthesis Techniques on Processes Occurring During Compact Formation and Its Sintering" in Emergent Process Methods for High-Technology Ceramics, eds. R. F. Davis, H. Palmour III, and R. L. Porter, Plenum Press, New York (1984) pp. 177-192.

2. J. M. Tarascon, W. R. McKinnon, L. H. Greene, G. W. Hull,B. G. Bagley, E. M. Vogel and Y. LePage. Proceedings of the Materials Research Society Symposium High-temperature Superconductors with T_c over 30K". 1987. Materials Research Society, Pittsburgh, PA, 15237.

3. J. S. Swinnea and H. Steinfink, J. Materials Research, July/August, 1987.

4. A. Manthiram, J. S. Swinnea, Z. T. Sui, H. Steinfink, and J. B. Goodenough, Journal of the American Chemical Society,1987, In press.

5. D. W. Johnson, Jr., E. M. Gyorgy, W. W. Rhodes, R. J. Cava,L. C. Feldman and R. B. Van Dover, Materials Research Society Meeting, April 21-24, 1987, Anaheim, CA.

6. S. Jin, R. C. Sherwood, R. B. van Dover, T. H. Tiefel, and D. W. Johnson, Jr., Appl. Phys. Lett., 1987, In press.

7. F. Fletcher, J. of Metals, V.39,#5, May 1987 p.9.

8. G. Elkabir, C. Persad, L. K. Rabenberg, H. L. Marcus, "Microstructure in High Energy High Rate Consolidation of P/M Al X7091", Scripta Metallurgica, October 1986 p.1411-1416.

9. A. C. D. Chadlaker, A. M. Armstrong and S. K. Misra, J. Am.Chem. Soc., **51**, 630 (1968).

10. M. Wittmer, MRS Symposium on Electronic Packaging Materials Science, Boston, MA, 1984, MRS Symposia Proc. **40**, 393 (1985)

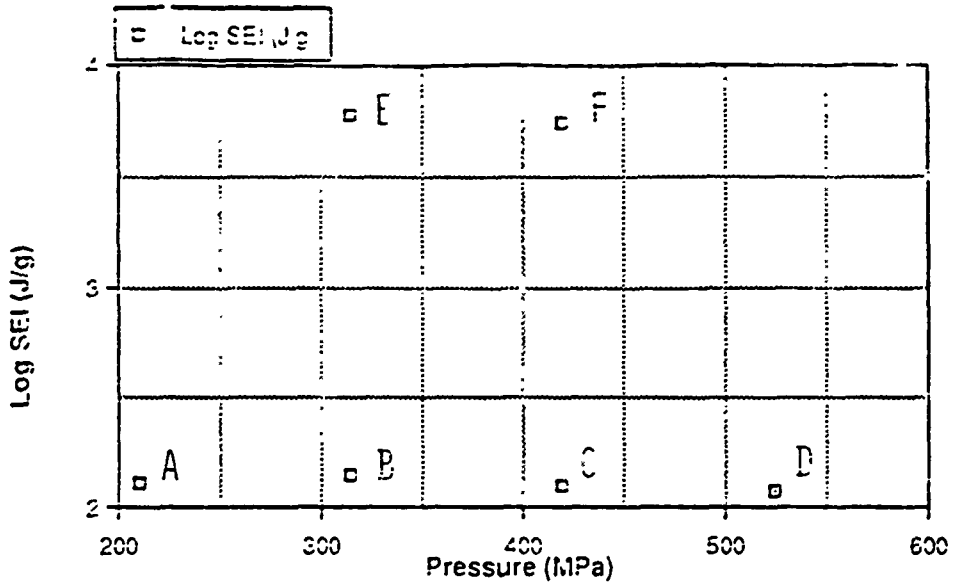

Figure 1: The processing parameter matrix employed in the consolidation of $YBa_2Cu_3O_x$ powders, showing the pressure/SEI coordinates used in processing. Specimens A, B, C,and D are capacitor bank (I_{peak} at 100 μs) consolidations, E and F are homopolar generator (I_{peak} at 200 ms) consolidations.

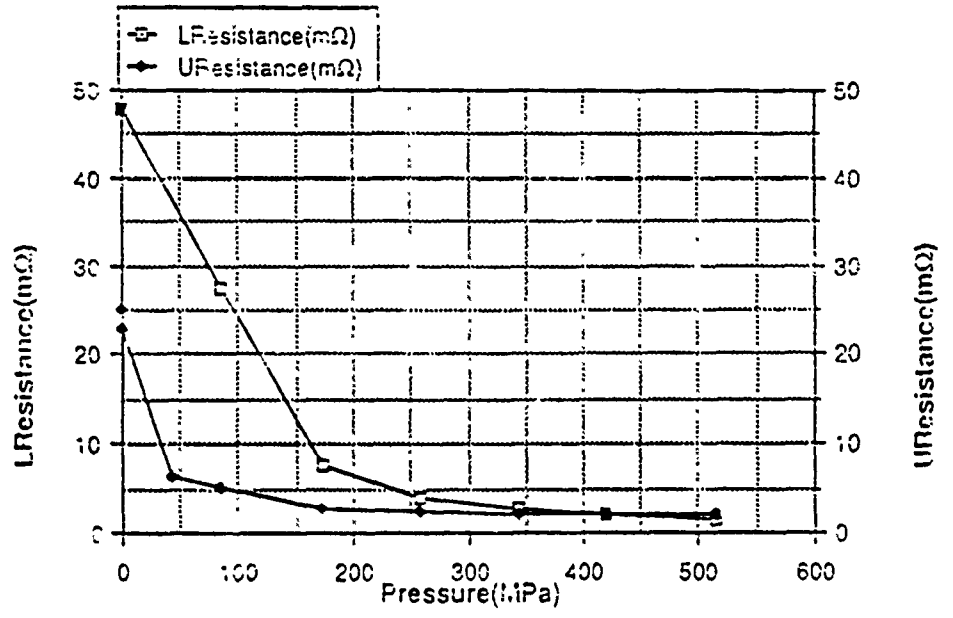

Figure 3: Resistance of Specimen D vs Pressure during pressurizing (LResistance) and depressurizing (UResistance) cycle.

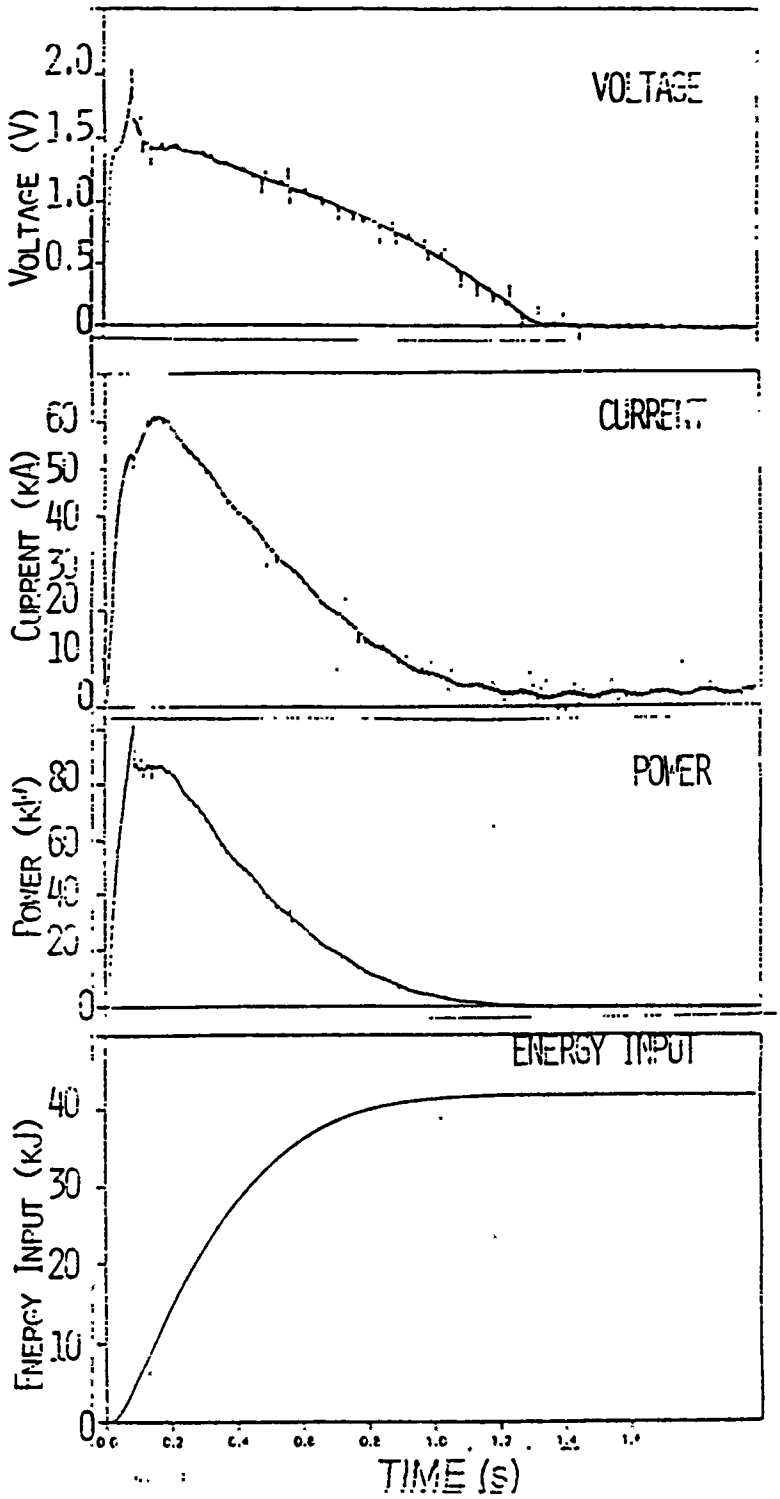

Figure 2: Curves indicating the pulse characteristics of the homopolar generator discharge employed for consolidating Specimen E.

a) Voltage vs Time b) Current vs Time

c) Power vs Time d) Cumulative energy input vs Time

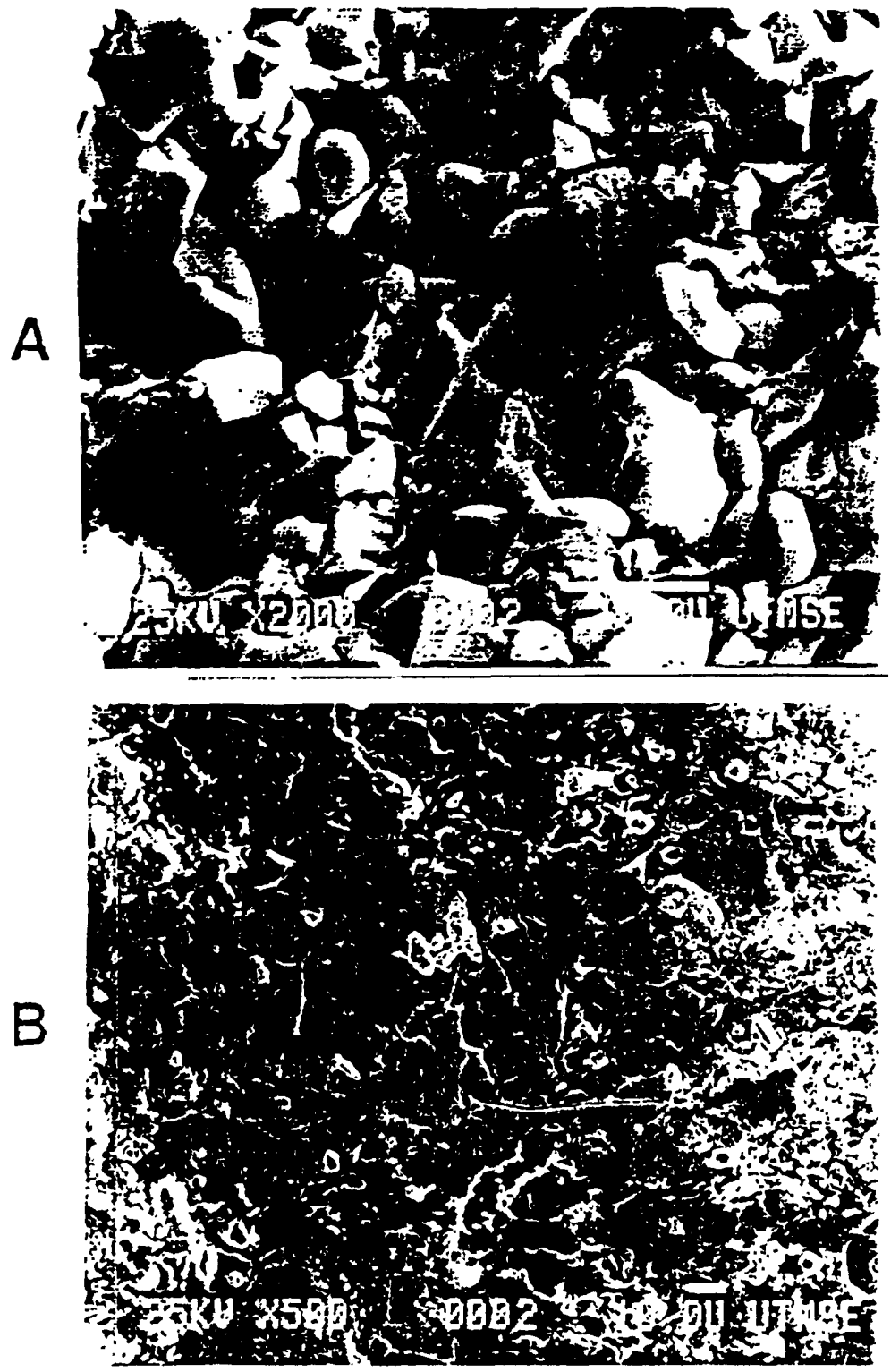

Figure 4: SEM Photomicrographs of surfaces of $YBa_2Cu_3O_x$ consolidations.

a) Fracture surface of Specimen D.

b) Melted and resolidified region on surface of Specimen F.

SIMULTANEOUS CONSOLIDATION AND BONDING

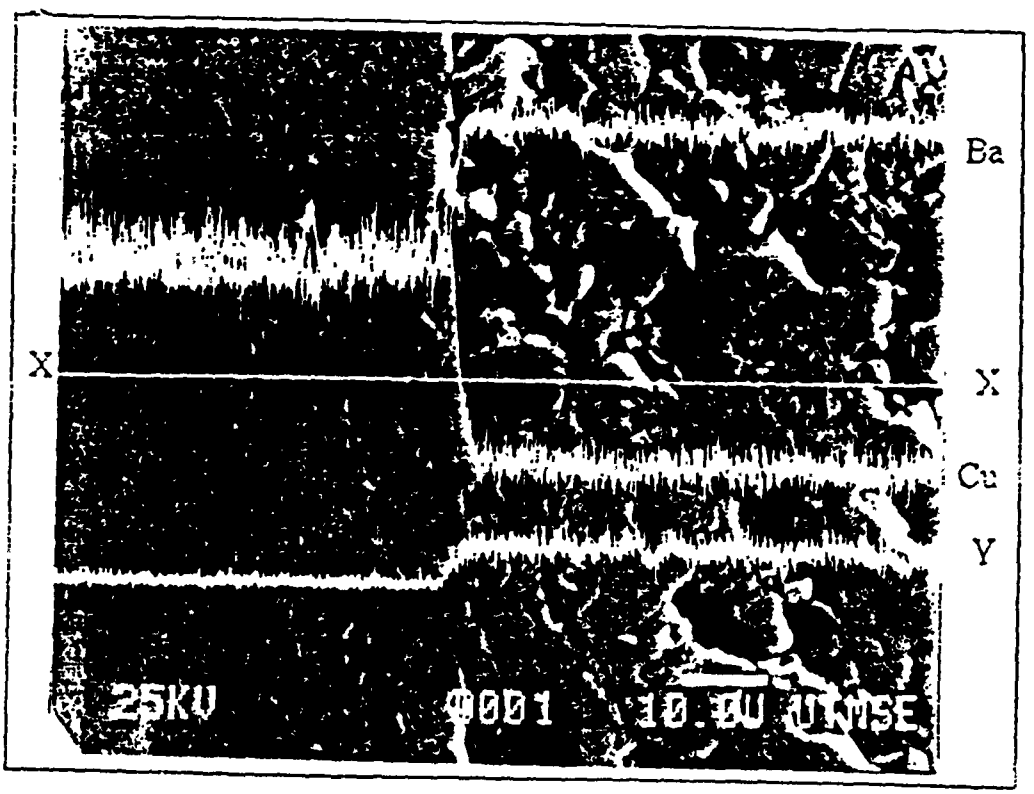

Figure 5: SEM Photomicrograph of polished cross-section of Specimen E. An Energy Dispersive Spectroscopy scan across line XX reveals the elemental concentration discontinuities at the interface between the copper electrode (left) and the $YBa_2Cu_3O_x$ compact.

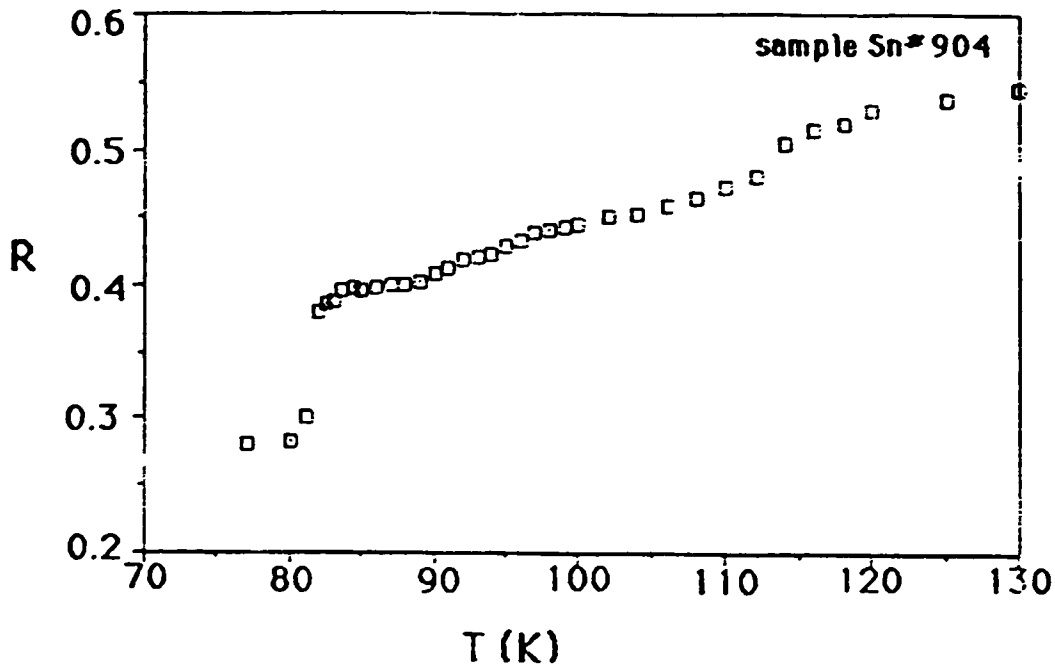

Figure 6: Resistive transitions in an as-consolidated Sn-$YBa_2Cu_3O_x$ composite.

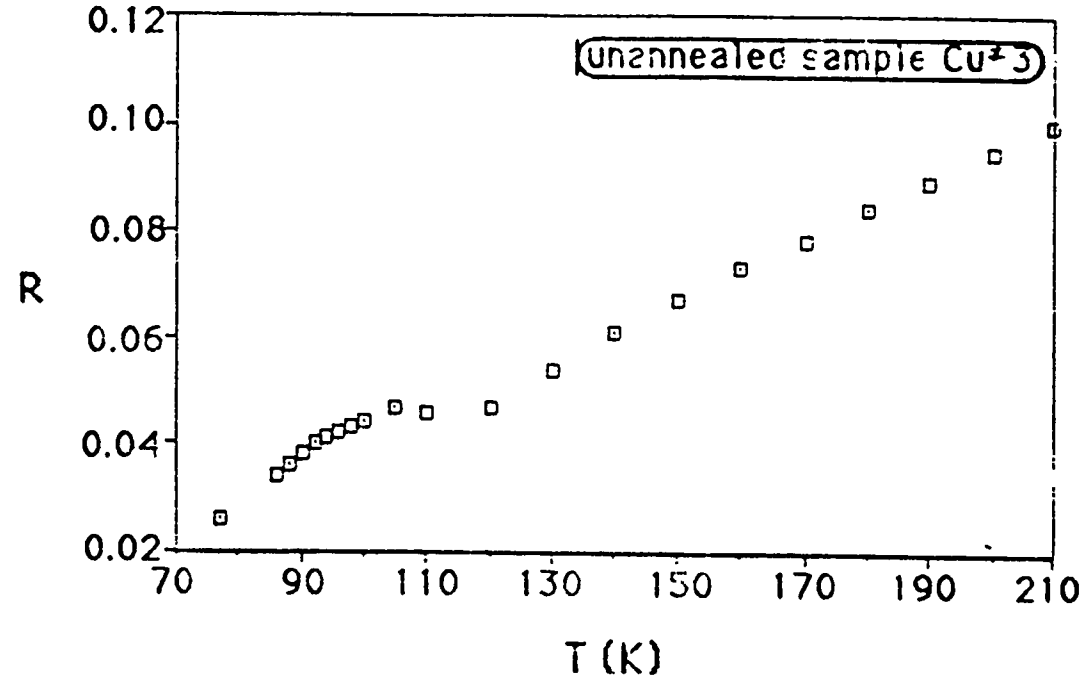

Figure 7: Resistive transitions in an as-consolidated Cu-$YBa_2Cu_3O_x$ composite.

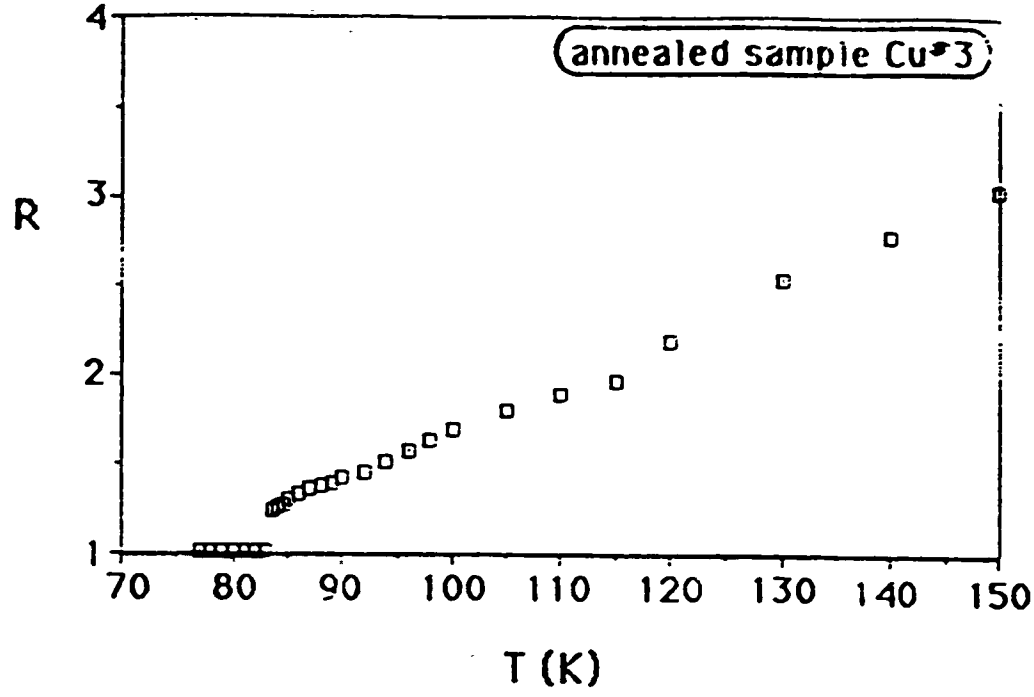

Figure 8: Resistive transitions in an annealed Cu-$YBa_2Cu_3O_x$ composite.

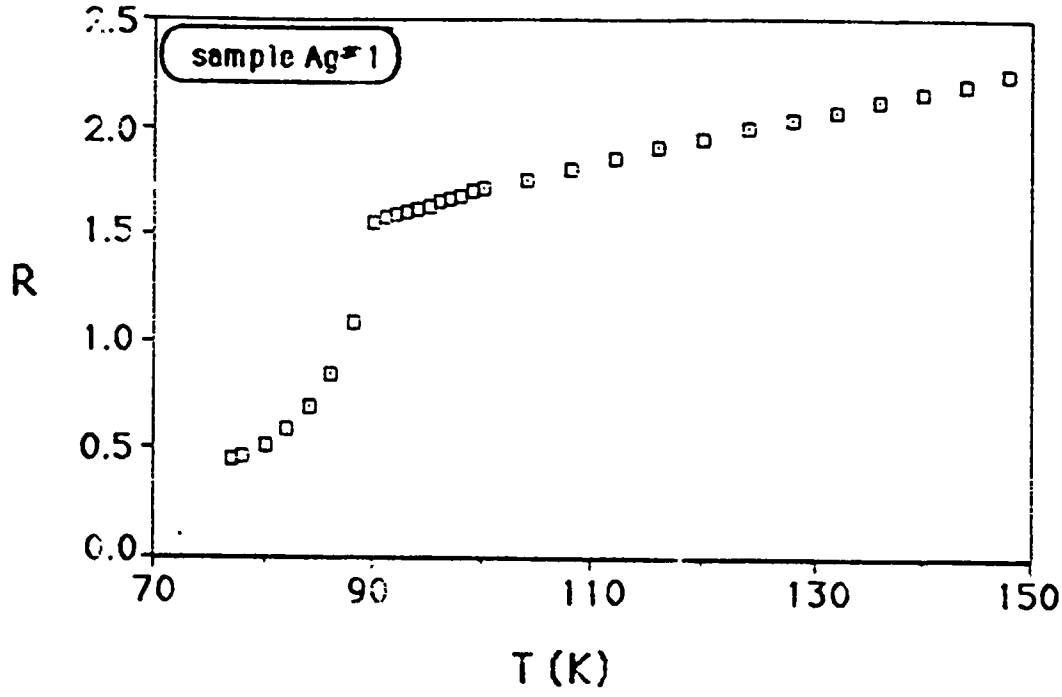

Figure 9: Resistive transitions in an as-consolidated Ag-$YBa_2Cu_3O_x$ composite.

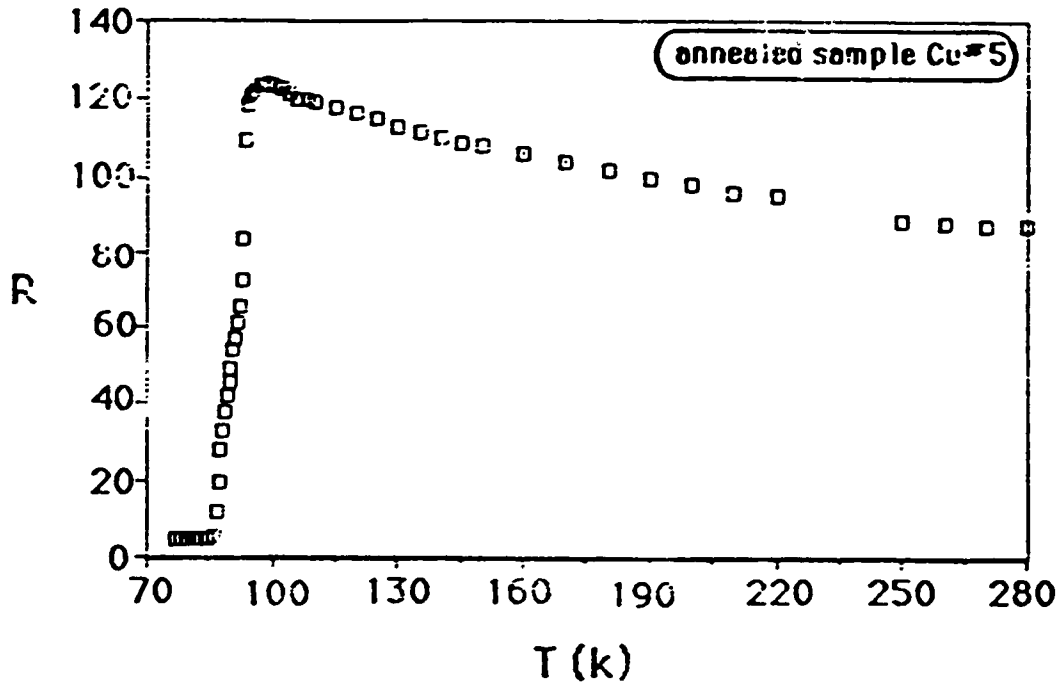

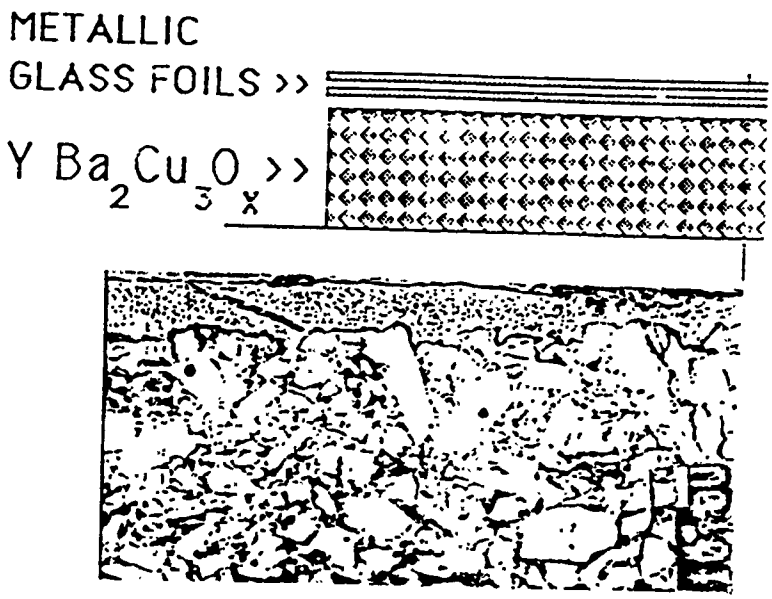

Figure 10: Processing and microstructure of a Cu-based metallic glass infiltrated $YBa_2Cu_3O_x$ composite (A) Arrangement for infiltration processing (B) Microstructure of an unetched cross-section of a composite disk.

HIGH-ENERGY HIGH-RATE DEFORMATION PROCESSING OF P/M ALUMINUM-SILICON CARBIDE COMPOSITES

H.M. Tello, C. Persad, H.L. Marcus, D.L. Bourell
Center for Materials Science and Engineering
The University of Texas at Austin
Austin, TX 78712.

ABSTRACT

High-Energy High-Rate (HEHR) deformation processing was used to form near-full density metal-matrix composites (MMC's) of rapidly solidified Al-Fe-Ce powders and SiC particulates. Near-full density was achieved by open die forging of HEHR consolidated compacts, and by extrusion of a premixed powder blend. The uniformity of the SiC distribution in the matrix was found to be strongly dependent upon the amount of deformation. Critical values for forging reduction and extrusion ratio were determined. The HEHR process uses a high-current pulse to rapidly heat the material being processed. The elevated temperature exposure time for the HEHR process is usually less than 1 second. This high-rate process minimizes the microstructural coarsening of the rapidly solidified matrix powders.

INTRODUCTION

The advances in rapidly solidified (RS) powder processing have resulted in a vast amount of work directed toward the development of new alloys and processing techniques which take advantage of rapidly solidified microstructures. Several dispersion-strengthened aluminum alloys have been developed for use at temperatures higher than those used for ingot metallurgy alloys [1,2]. One particular group of RS alloys which have shown promise are alloys composed of Al-Fe-M (M = Mo, V, Ce, Co, Ni). These alloys have high volume fractions of dispersoids which remain stable at high temperatures. In particular, the Al-Fe-Ce alloys remain stable to 316°C [1]. Metal-matrix composites (MMC's) of these aluminum alloys and SiC are of considerable interest because of their high strength, high temperature stability, and specific stiffness (3,4).

The Al-Fe-Ce alloys can not be processed by conventional powder metallurgy (P/M) techniques. Typical degassing temperatures of 400-500°C can not be used because the dispersoids coarsen rapidly in this temperature range [5]. The hydrated surface oxide layer present on each powder prevents good metallurgical bonding and results in materials which fracture predominantly along prior particle boundaries. The effect of the surface oxide on the mechanical properties is reduced with the amount of hot working done after consolidation. Forging reductions of 80% or more are required to achieve optimal ductility and fracture toughness [6].

High-Energy High-Rate (HEHR) powder consolidation processing employs a fast rising, high-current pulse from a 10 MJ homopolar generator (HPG) to consolidate the powders being processed (7,8). The consolidation process occurs by pulse resistive heating of the particle interfaces while under pressure, leading to particle-particle bonding. The advantage of HEHR processing is that the time at processing temperature is very short, typically less than 1 second. The fine RS structure of the powders is maintained and dispersoid coarsening is kept to a minimum. The density of the consolidated composite is typically in the range of 90-98% of the theoretical density.

In order to achieve near-full density, HEHR deformation processing was used. The techniques used were open die forging and extrusion of consolidated compacts and premixed powder blends. HEHR deformation processing simply involves rapid pulse resistive heating of the material followed by application of high pressures to induce plastic flow. The processing time for HEHR deformation processing is typically around 1 to 2 seconds.

The ability to conduct low voltage (≈ 10 V), kiloampere currents through the powders is essential for the HEHR process. The total bulk resistivity of the powder blend depends upon several factors [9] including the:

- type of matrix material and its related surface oxide layer.
- electrical properties and chemical composition of the reinforcement.
- volume fraction and uniformity of distribution of the reinforcement in the matrix.
- amount of porosity of the packed powder blend prior to the current pulse.

EXPERIMENTAL PROCEDURE

The powder composite system used for this HEHR deformation processing study was an Al-8.6Fe-3.7Ce (wt pct) alloy matrix with 10 vol% α-SiC particle reinforcement. The alloy powders were air atomized by Alcoa. The chemical composition of the alloy is given in Table 1. The alloy powders ranged in size from 3 to 44 μm with an average particle size of 14 μm. The α-SiC particles were supplied by Norton Co. They were designated as 1200 grit "black", with an average size of 3 μm and a narrow size distribution. SEM photomicrographs of the starting matrix and reinforcement powders are shown in Figure 1.

Table I. Chemical Composition of the RS Al-Fe-Ce Alloy (wt pct).

Fe	Ce	Si	Cu	Mg	Zn	Ni,Co,Cr	Al
8.63	3.74	0.13	0.02	0.02	0.05	<0.01	bal

Figure 1. Al-Fe-Ce starting powders (a), and SiC reinforcement particles (b).

Powder Consolidation

HEHR powder consolidation was used to provide a reference microstructure and for the production of specimens for the open die forging experiments. Powder consolidation was achieved by placing the powders in an alumina sleeve as shown in Figure 2. A compressive force was applied by the ram followed by a high-current pulse. The consolidated compacts had densities of 90 to 95% of the theoretical density. Figure 3 shows a cross-sectional view of a consolidated compact. The photomicrograph shows that there is some particle-to-particle bonding, but no significant deformation of individual powders.

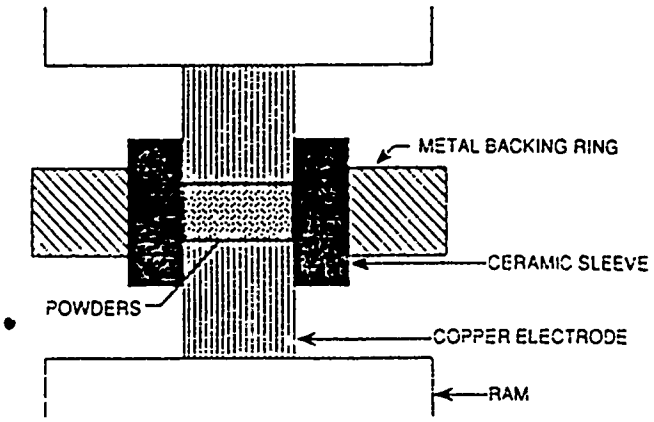

Figure 2. HEHR Powder Consolidation apparatus.

Open Die Forging

HEHR forging was achieved by placing a powder filled container, or a circular disk, of the material to be forged between two graphite-coated platens. A compressive force was applied, then the high-current pulse from the HPG, followed by a forging stress. A two step application of pressure was employed in some of the experiments where the material was heated before being forged. This was accomplished by setting the initial pressure to < 145 MPa (21 ks), and increasing the pressure to between 215 and 500 MPa (31.2-72.5 ksi) a short time after pulse initiation, typically 0.1 to 0.3 second. The reduction of thickness of the forged specimens ranged from 40 to 75 %.

Three procedures were used for the HEHR open die forging. Procedure A achieved consolidation and forging in a single step process. A premixed powder blend was packed to approximately 65% full density inside a can. The can was constructed of a stainless steel ring having an outer diameter of 25.4 mm (1 inch) and a wall thickness of 0.89 mm (0.035 inch). Thin stainless steel sheets were adhesively bound to the top and bottom of the ring to enclose the powders. The canned powder assembly was HEHR forged as described earlier.

Procedures B and C used HEHR consolidated compacts. Procedure B involved forging of an unconstrained HEHR consolidated compact. For Procedure C, the diameter of HEHR consolidated compacts were ground to 23.67 mm (0.932 inches). Each compact was then shrunk-fit into a stainless steel ring. The assembly was then HEHR forged.

Figure 3. Short-transverse (S-T) cross-section micrograph of HEHR consolidated Al-Fe-Ce+SiC.

Extrusion Processing

HERR extrusion processing involved a single residence process in which premixed powders were consolidated and extruded. The powders were placed in an extrusion assembly shown schematically in Figure 4. A small pressure, <145 MPa, was applied to the ram to compact the powders in the alumina sleeve. The powders were then subjected to a high-current pulse from the HPG. A short time after pulse initiation, 0.1 to 0.3 second, the pressure applied by the ram was increased to 500 MPa, and the compressed, heated powders were then extruded through the die. Experiments were performed using extrusion ratios of 12:1, 10:1, and 7:1.

Results and Discussion

The microstructure of the composite processed by Procedure A is shown in Figure 5. As evident from the photomicrograph, the density of the specimen is higher than that of the consolidated specimen of Figure 3. Some porosity remains, and there is still no significant deformation of individual powder particles. This sample also shows that matrix powder bonding only occurs where SiC particles are absent. A substantial amount of agglomeration of SiC particles is seen throughout the forged specimens.

The microstructures of the specimens processed by Procedures B and C are very similar. However, only small samples, < 20 mm in diameter, can be forged without edge cracking on the circumference by Procedure B. Figure 6 for Procedure C, shows that the matrix powders have been deformed substantially and that there is some orientation of the SiC particles in the radial direction. This specimen was taken from a disk forged to 70% reduction in thickness. Near-full density was achieved by Procedures B and C when the forging reduction was approximately 50% or greater.

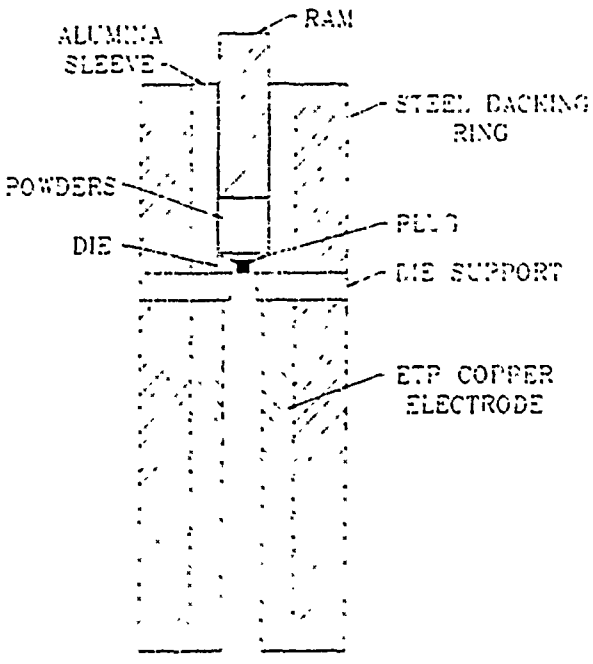

Figure 4. Schematic diagram of the extrusion die assembly.

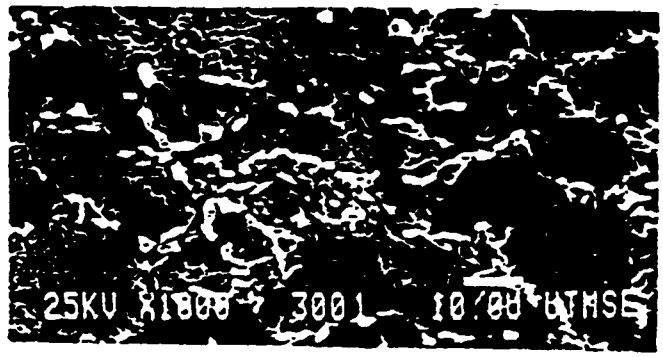

Figure 5. S-T cross-section of Al-Fe-Ce+SiC composite processed by Procedure A.

Figure 6. S-T cross-section of Al-Fe-Ce+SiC composite processed by Procedure C.

The photomicrographs in Figure 7 show that powder extrusion results in a microstructure similar to that of the forged specimens. Near-full density is achieved with extrusion ratios of 10:1 or larger. Partial alignment of the SiC in the extrusion direction is observed.

The distribution of SiC in the matrix appears to be strongly dependent upon the amount of deformation. This is seen in Figure 8a which shows SiC particles outlining matrix powder boundaries for a sample processed by Procedure A. The samples forged by Procedures B and C do not show this feature in regions where the matrix powders have been substantially deformed, Figure 8b. The amount of deformation appears to promote a more uniform distribution of SiC in the matrix. The uniformity of distribution of SiC particles in the matrix is a major contributor to the strength and fracture toughness of the composite [10]. The large strains associated with the open die forging and extrusion processes, combined with the predicted abrasiveness of the SiC particulates, should result in a substantial break up and redistribution of the Al-Fe-Ce surface oxide layer.

The samples processed by Procedure C were given isothermal and isochronal anneals. The results of microhardness tests are given in Figure 8. The plots show that 1 hour exposures to temperatures of 300 and 400°C do not result in a significant decrease in microhardness. After 6 hours at 350°C the microhardness was decreased by approximately 20%. This indicates that the strengthening contribution of the matrix dispersoids is reduced during the 350°C, 6 hr. to 24 hr. heat treatment, presumably due to dispersoid coarsening. The microhardness of the extruded powders was the same as that of the material processed by Procedure C.

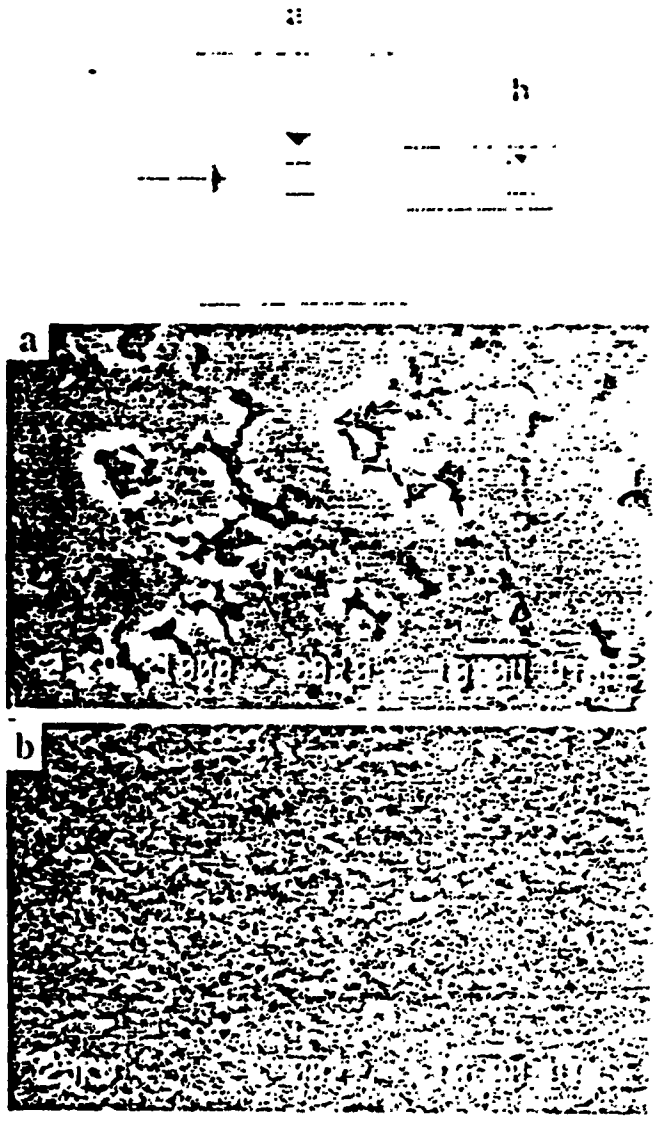

Figure 7. Microstructure of Al-Fe-Ce+SiC composite before (a) and after extrusion (b).

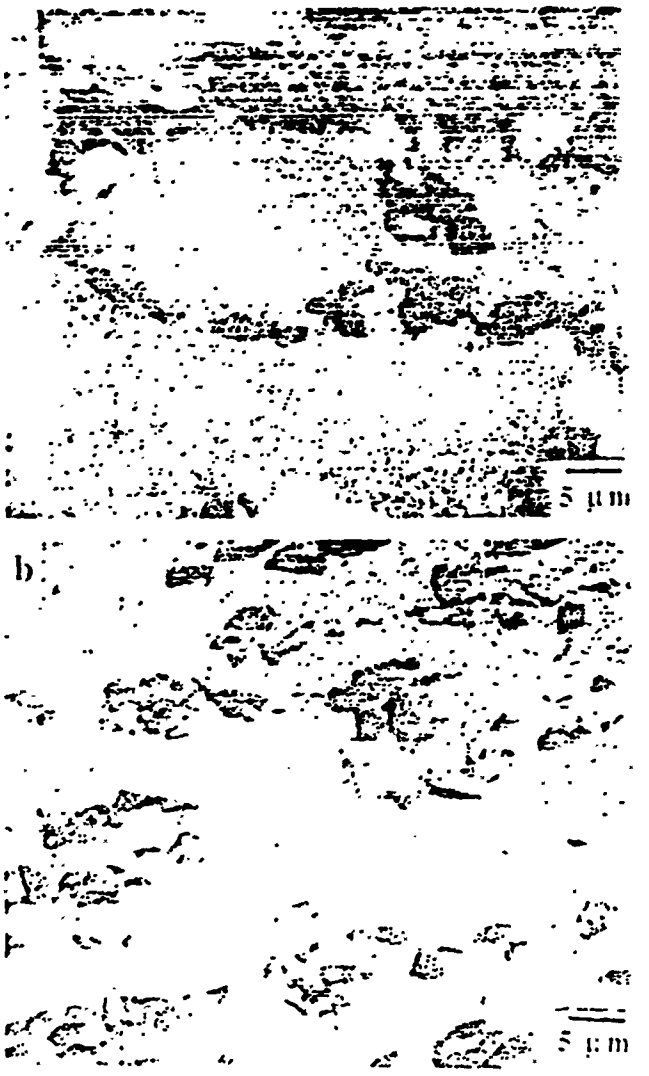

Figure 8. Change in SiC distribution as shown for composite processed by Procedure A (a), and by Procedure C (b).

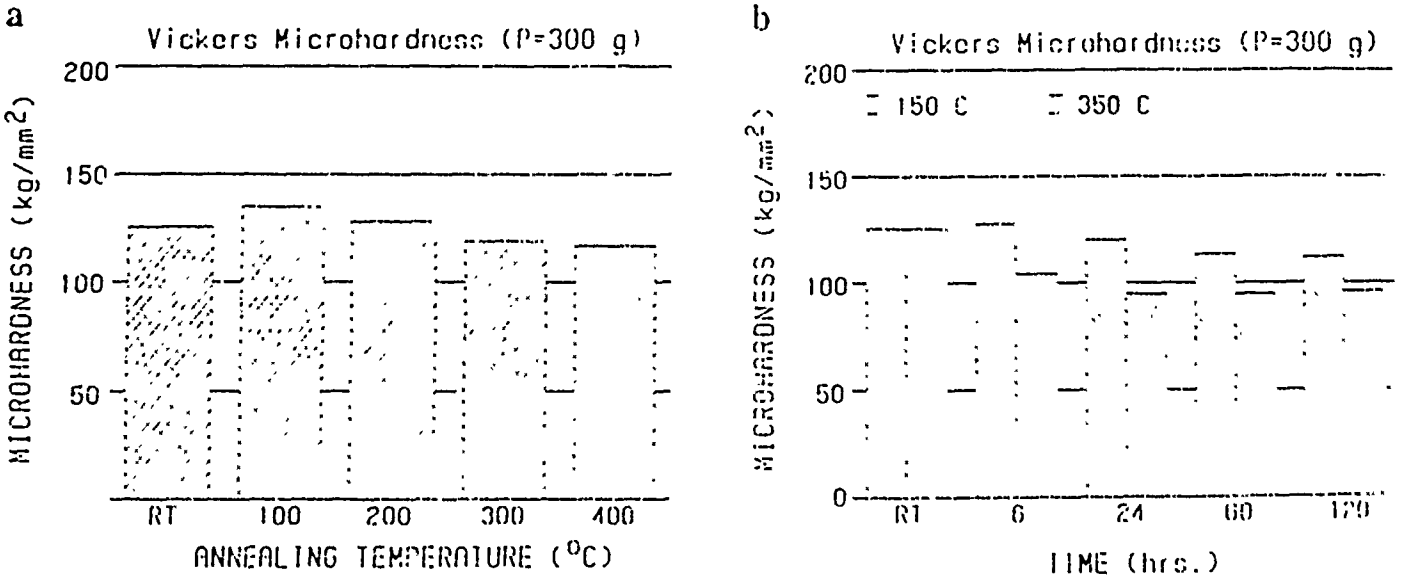

Figure 9. Room temperature microhardness after isochronal (a) and isothermal (b) annealing of Al-Fe-Ce+SiC composites processed by Procedure C.

CONCLUSION

Near-full density composites of Al-Fe-Ce+SiC were formed by HEHR deformation processing. The flow of the matrix promotes a more uniform distribution of the SiC in the matrix which should result in improved strength and fracture toughness. The combination of deformation and abrasiveness of the SiC particulates should adequately break up the surface oxide layer of the matrix powders. It appears that large strain HEHR deformation processing by forging or extrusion can be successfully combined with powder consolidation with the retention of the RS powder structure.

ACKNOWLEDGEMENTS

The authors would like to acknowledge the assistance of Mr. Jim Al[illegible] of The Balcones Research Center, Center for Electromechanics. This work was supported by DARPA under ARO Contract DAAL 0387-K-0073.

REFERENCES

1. W.M. Griffith, R.E. Sanders, Jr. and G.J. Hildeman. "Elevated Temperature Aluminum Alloys for Aerospace Applications". High Strength Powder Metallurgy Alloys. M.J. Koczak, G.J. Hildeman, eds., Warrendale: TMS-AIME, 1982.
2. S.L. Langenbeck, W.M. Griffith, G.J. Hildeman, and J.W. Simon. "Development of Dispersion-Strengthened Aluminum Alloys". Rapidly Solidified Powder Aluminum Alloys. M.E. Fine and E.A. Starke, Jr., eds., Philadelphia: ASTM Publication 890, 1986.
3. F.H. Froes and J.R Pickens. "Powder Metallurgy of Light Metal Alloys for Demanding Applications". J. Metals, vol. 36, no. 1, 1984.
4. Erich, Donald L. "Metal Matrix Composites: Problems, Applications, and Potential in the P/M Industry". Int. J. of Powder Metall., vol. 23, no 1, 1987.
5. Y.W. Kim and W.M. Griffith. "Annealing Behavior and Tensile Properties of Elevated Temperature P/M Aluminum Alloys". Rapidly Solidified Powder Aluminum Alloys. M.E. Fine and E.A. Starke, Jr., eds., Philadelphia: ASTM Publication 890, 1986.
6. Y.W. Kim, W.M. Griffith, and F.H. Froes. "Surface Oxides in P/M Aluminum Alloys". J. of Metals, vol. 37, no. 9, 1985.
7. G. Elkabir, L. Rabenberg, C. Persad and H.L. Marcus. "Microstructural Evaluation of a High-Energy High-Rate P/M Processed Aluminum Alloy". Scripta Metall, vol. 20, no. 10, (1986).
8. H.L. Marcus, D.L. Bourell, Z. Eliezer, C. Persad, and W.F. Weldon. "High-Energy, High-Rate Materials Processing". J. of Metals, vol. 39, no. 12, 1987.
9. G. Elkabir, Ph.D. Dissertation, The University of Texas at Austin, 1987.
10. J.J. Lewandowski and C. Liu. "Microstructural Effects on the Fracture Mechanics in 7XXX Al P/M-SiC Particulate Metal Matrix Composites". Processing and Properties of Powder Metallurgy Composites. P. Kumar, K. Vedula, and A. Ritter, eds., Warrendale: TMS-AIME, 1988.

ELECTRICAL CHARACTERISTICS OF HIGH ENERGY-HIGH RATE CONSOLIDATED METAL-MATRIX COMPOSITES.

G. Elkabir +, C. Persad and *H. L. Marcus
Center for Materials Science and Engineering
The University of Texas at Austin
Austin, TX 78712
(512) 471-3188

Abstract

Discontinuous silicon carbide reinforced aluminum metal-matrix composites (MMC) were made by consolidating powder constituents using a novel, high energy-high rate process which employs a fast-rising high-current pulse. The powder mixtures were contained in an insulated die, under pressure, and were rapidly densified during the discharge from a homopolar generator (HPG), in a processing time of about one second. The electrical properties of the metallic/ceramic mixture were found to be very sensitive to the relative concentration of the constituents. Use of graphite-enriched β-SiC enabled an increase in the volume fraction of the ceramic reinforcing phase due to a better electrical conductivity associated with the graphite enriched particle surfaces. Optimum results were obtained by using a multiple electrical pulse technique, discharging the first pulse at low pressure (≤ 120 MPa) and stepping up the pressure to about 300 MPa on the second pulse.

+ Present Address : 27 Weizmann Street
Nahariya 22404 ISRAEL

*Please send all correspondence to H. L. Marcus at the address listed above.

I. INTRODUCTION

Powder consolidation by the high energy-high rate method is an electrical energy pulse resistive heating type of process, described in more detail elsewhere [1,2]. The metallurgical bonding mechanism stems from the selective energy deposition at the interparticle contacts. The bonding between metallic particles such as aluminum can be achieved by local break-up of the oxide film (incurred at the compaction stage or during the discharge), or through the oxide film. The latter mechanism is possible due to high local electrical field across the thin interparticle oxide interface, resulting in a breakdown of the oxide layer. The transport mechanism that leads to the very high rate of densification which seems to be related to excess plastic deformation is not yet clear and was not pursued in this study.

The ability to conduct the low voltage (~ 10V), hundred kilo-ampere current, supplied by the homopolar generator (HPG), is an essential condition for this process to operate. The total bulk conductivity of the compact before, during and after consolidation depends on a number of factors such as:

1. Type of matrix material (aluminum alloy in this case) and its related surface oxide and hydrated-oxide layer.
2. Reinforcement agent (type, grade, size, shape, size distribution, thermal and electrical properties and chemical composition).
3. The volume fraction of the ceramic reinforcement phase within the metal matrix.
4. The uniformity of distribution of the ceramic-phase particles throughout the volume of the metal-matrix composite.
5. The fraction of pores existing within the compact under the predetermined applied

pressure, related to the potential packing efficiency of the particular powder blend.

6. The local temperature which is developed at particle surfaces during discharge.

7. The specific energy imput (SEI) into the powder mixture during pulse discharge.

The present study was undertaken to examine the electrical characteristics of a system comprising a metallic/ceramic mixture and its relationships to the high energy-high rate consolidation processing parameters.

II. EXPERIMENTAL METHODS

Selected characteristics of the powders used in this study are presented in Table 1. More detailed characterization has been documented elsewhere [3]. The major components of the processing equipment included:

1. A 10 MJ capacity, disc-type, single rotor, iron core, pulse-duty HPG.

2. A vertical-axis, 890-kN (100 ton force) capacity hydraulic press.

The HPG serves as the pulse power source which produces the electrical current responsible for the powder consolidation. The hydraulic press maintains the powders under pressure in a closed die, allowing pre-pulse compaction of the powder mixture, ensuring a threshold value of the electrical conductivity of the compact, and facilitating rapid thermomechanical densification of the powder compact .

In-process electrical data measurements (current and voltage) were recorded by using oscillographic chart records during the pulse duration time. Two separate current paths led from the HPG through the press, and then to the ground. Both loops were fitted with current measuring capability, using the Rogowski coil method [4].The voltage drop is proportional to the time derivative of the total current passing through through the die, irrespective of the spatial distribution of that current. For voltage measurements, a

connection was placed on each platen. The voltage drop across the material during consolidation was measured using a fast-response DC voltmeter. This enables the determination of the instantaneous values of impedance during current pulses.

The total electrical energy introduced into the workpiece during the discharge period can be determined from the following equation:

$$\text{Total Energy} = \int_{t=0}^{t=t} [V(t) \cdot I(t)]\, dt$$

where, V(t) and I(t) represent the instantaneous voltage and current, respectively. Since the analytical functions for the voltage and current are not known, the above integral can be solved numerically by using the signal plots for the voltage and current versus time. From these data, specific energy input (kJ/kg) calculations were generated, along with the peak parameter values.

III. RESULTS

This section contains experimental data which reflect selected electrical characteristics of aluminum alloy based metal matrix composites. Data is presented which describe the influence of a variety of pre-processed materials conditions. For various aluminum alloy powder matrices, the results show the influence of volume fraction of α-SiC reinforcement, effect of reinforcement type, effect of graphite content on the surface of β-SiC reinforcement, and the responses due to variations in resistivity of the graphite used for surface enrichment of the beta-SiC. In addition, the potential of a multiple pulse technique in achieving powder composite consolidation by rapid thermomechanical deformation is presented.

Volume Fraction of Reinforcement

As the volume fraction of the reinforcement phase was increased, an increase in compact resistivity occurred, reducing the current flow during consolidation. This is demonstrated in Figure 1 which is based on data taken from Al-8Fe-4Ce, reinforced with 5 and 10 vol. % α-SiC-1200 grit "black". The peak current drops from about 190 kA (MMC with 5 vol. % reinforcement) to 100 kA (MMC with 10 vol. % reinforcement).

Effect of Reinforcement Type

Figure 2 shows the comparison of the instantaneous transmitted current during the total consolidation period (1.5 - 2 seconds) for four different MMC systems, based upon the same Al-matrix (CW67) with different types of reinforcement (TiB_2, pure graphite, β-SiC enriched with 0.5% graphite and α-SiC "green"). All four MMC systems were processed with the same parameters: 25 vol. % of reinforcing phase, applied pressure of 210 MPa and HPG shaft speed of 1,500 rpm. Figure 2(a) shows a very large change in both peak current values and the peak rise-times. Both TiB_2 and graphite-reinforced CW67Al MMCS show very high current peaks (~ 170 kA) after 0.2 second of the discharge. The β-SiC containing 0.5% graphite has a maximum current peak of about 80 kA (after ~ 1 second) while the α-SiC "green" reinforced material sustains maximum current of ~ 50 kA (after ~ 0.7 second). These results are in agreement with the relative resistivities of these reinforcing phases as shown in Figure 2(b).

Graphite content on reinforcement surface

Metal-matrix composites, reinforced with β-SiC which have been enriched with a

different graphite content (1% vs. 5%) resulted also in noticeable changes in the electrical properties, as shown in Figures 3(a) and 3(b). Figure 3(a) illustrates the current vs. time for 1% and 5% graphite-enriched β-SiC (reinforcing CW67Al) and Figure 3(b) compares the instantaneous resistivities.

Influence of graphite resistivity

Another experiment was undertaken in order to evaluate the influence of the grade of graphite used to enrich the β-SiC powder particles. The MMC system which was selected for this experiment was CW67Al+ 25 vol. % β-SiC enriched with 5% graphite of two different grades. The first type is known as "4739" which is a natural graphite having an electrical resistivity between 130-160 μΩ-cm. The other type of graphite is trademarked under "9039" which is produced from a petroleum cake and has a higher electrical resistivity, relative to the natural graphite, 220 to 250 μΩ-cm. The plots of the instantaneous current and in-process resistivity are both shown in Figure 4(a) and 4(b), respectively. It can be seen from these plots that the MMC reinforced with the natural graphite-enriched SiC (the grade with higher conductivity) ends up with a significantly higher current peak, when compared with the compact reinforced with the more resistive type of graphite (100 kA vs. 80 kA). The resistivity plot, Figure 4(b), also shows the same trend of behavior. It should be mentioned that this particular measurement is based only on one experiment. However, these results are in agreement with the trends from the experiments described previously. In data gathered from similar experiments where identical compacts were consolidated, the scatter range for peak current was ±10%, which is less than the difference detected in this experiment.

Multiple pulse technique

A multiple electrical pulse technique was found to be advantageous in densifying those compacts which contained a high volume fraction of SiC powder (usually greater than 20 vol. %), having a relatively high initial resistance. Because of the change in resistance of the compact during processing, the current developed during the consolidation pulse varies considerably. The rate of change in resistance during consolidation decreased in the second and later pulses in a multiple pulse process, suggesting a more uniform current distribution and therefore restriction of "current channeling" along preferred paths.

The peak instantaneous power input introduced into the MMC compact by the HPG during consolidation typically occurred after approximately 0.15 second in the second step of a two-pulse consolidation. This is the point in which the main densification of the powder compact occurred, as noticed from the rapid drop in the resistivity seen in Figure 5. Figure 5 also demonstrates the effectiveness of double discharge on densification processing, as illustrated by the resistivity drop from about 450 μΩ-cm to 250 μΩ-cm at the onset of the current peak. This results from the fact that the first pulse, done at relatively low energy (corresponding to 1000 rpm HPG shaft speed), reduces the green compact resistivity by a factor of 2 (from 1000 μΩ-cm to 500 μΩ-cm), as shown in Figure 3. Only then, while the compact was still warm, a second, higher-energy pulse (at 1,500 rpm) was applied, which accomplishes the final consolidation.

In the two-pulse method, the best results are obtainable by discharging the first pulse with the compact at low pressure (≤ 120 MPa) and stepping up the pressure to approximately 300 MPa during the second pulse. Another benefit gained by using this technique is an increased amount of forging, as detected from the total stroke of the upper electrode, due to the fact that during the second pulse the compact is still warm. In actual

experiments it was found that for the same compact composition and applied pressure, a typical total forging stroke for a single discharge consolidation process of a 10 mm thick compact is about 2mm. After double pulsing it is increased to 3 mm . The clear disadvantage of this technique is the fact that the total en . .y input is increased, with the possible adverse effects on the matrix material microstructure due to the longer time at elevated temperature.

IV. DISCUSSION

The discussion focuses on characteristics of high energy - high rate processed MMCs. When a second-phase, such as SiC particulate, is introduced in a mixture with an aluminum alloy powder for powder composite making two major consequences follow:

1. The bulk resistivity of the whole compact is significantly increased since the resistivity ratio of SiC to metallic Al is on the order of 10^8. As a result, compacts containing high level of ceramic reinforcement phase do not pass sufficient current to be consolidated.
2. The flow characteristics of the composite material system changes, which in turn affects the nature of powder mixing, as well as powder compaction (or densification) under the applied pressure.

The insulating SiC particles present obstacles to the current which cannot pass through them, and therefore current will flow through the Al-matrix and along SiC/Al interfaces, as can be seen schematically in Figure 6. Modification of the surface electrical properties of the reinforcement agent changes the total capacity of the compact to conduct current. This was demonstrated by the following experiment: two different compacts were processed, having the same parameters (type of Al powder, reinforcement content, pressure, etc.), in which the only variable was the free carbon (in graphite form) present on

the SiC surface (1% vs. 5%). Evaluation of both consolidations showed that the resistivity of the compact which contained the lower level of graphite within the SiC was three times higher, in comparison to the 5%-graphite enriched SiC. This suggests that the surface conductivity of the SiC plays a significant role in this process. Figure 7 illustrates the change in resistivity of both compacts during the consolidation period. Figure 8 shows schematically the influence of a conductor-coated ceramic phase on the current distribution within the metal-matrix composite. The current is able to flow through the graphite-rich interface without requiring continuity in the aluminum thus producing an increase in the total bulk conductivity of the compact. The significant differences in the electrical resistivities of compacts containing the 1% and 5% graphite-enriched β-SiC, as shown in Figure 3 support this view. This phenomenon could be exploited by further enrichment or coating of SiC particulates in order to increase the processing-limited volume fraction of the ceramic-reinforcement phase above 20 vol. %, which seems to be the approximate upper threshold for uncoated α-SiC. Aluminum-coated SiC particles may be a good choice for Al-SiC systems since the aluminum not only possesses good electrical properties, but can produce stronger interface bonds than graphite can. In these experiments the metal/insulator size ratio was about 5. The conductivity limits imposed by relative particle sizes were not explored. However, percolation effects in thick film resistors indicate that a larger volume of metal is required for conduction when the metal and insulator grains are of comparable size. In a copper/polyvinylchloride system with a 1/35 size ratio a 4 percent fraction of copper was found to be sufficient for conduction [5].

The sharp cut-off in conductivity might lead to the conclusion that an anisotropic percolation conduction problem is playing a role. This conclusion finds support from the experimental data which show a significant increase in the threshold value for graphite-enriched SiC. It is believed that the modified powder flow characteristics during the blending and green compaction processes, due to the graphite on the surface, result in a more uniform distribution of the SiC particles within the Al-matrix, as can be observed

from the very low angle of repose, while mixing the Al/SiC powders. The percolation threshold for the system, therefore, will increase and allows higher volume fraction of the ceramic phase to be added to the conductive Al-matrix.

V. SUMMARY AND CONCLUSIONS

The primary conclusion drawn from the experiments done is that the surface-related electrical properties of the ceramic-reinforcing phase play a significant role in the processing of MMCs by high energy-high rate consolidation.

The electrical properties of materials consisting of a mixture of metals and dielectrics are, as would be anticipated, an extremely sensitive function of the relative concentration of the components, and the manner in which they are distributed throughout the volume of the material. Thus it seems that such systems will conduct electrically when the concentration of the conducting matrix (Al) exceeds a critical minimum value. For a three-dimensional system, this would correspond to a critical volume fraction and to a critical cross-section area fraction. McLachlan [6] has proposed that for binary resistor networks, the number of contacts multiplied by their areas - an effective contact area per unit volume fraction, may be is a more accurate representation of a continuous conducting host component with embedded insulator grains. Using the graphite-enriched β-SiC enabled an increase in the volume fraction of the ceramic reinforcing phase. This was due to a better electrical conductivity associated with the graphite on its surfaces. The influence of graphite lubricity on cold packing may have also contributed to this conductivity improvement.

ACKNOWLEDGEMENTS

The authors wish to express their appreciation to Jeff Becker and Stephen Cheng for their technical assistance, and to Read Stewart of Superior Graphite for providing the C-enriched SiC powders. Processing experiments were performed at the University of Texas at Austin Center for Electromechanics with the collaboration of Jim Allen and Ted Aanstoos. This research was supported by DARPA/ARO Contract DAAL 0387 - K- 0073.

REFERENCES

1. Elkabir, G., Rabenberg, L., Persad, C., Marcus, H. L, Scripta Metall., 20:1411-1416 (1986).

2. Marcus, H. L, Bourell, D. L.,Eliezer, Z., Persad, C., and Weldon, W. F., J. of Metals, 39, No. 12:6-10 (1987)

3. Elkabir, G., High Energy-High Rate Powder Processing of Aluminum-Silicon Carbide Metal-Matrix Composites, Ph.D. Dissertation, The University of Texas at Austin, 1987.

4. Marton, L., Methods of Experimental Physics, New York, NY:Academic Press (1971).

5. Newnham, R. E., Ann. Rev. Mater. Sci., 16, 47-68, (1986)

6. McLachlan, D.S., J. Phys. C: Solid State Phys., 20, 865-877 (1987).

Table 1: Characteristics of Powders Used in this Study*

Designation	Material	Supplier	Features/Dimensions
Matrix A	Aluminum Alloy (CW 67)	ALCOA	Air-atomized Classified to - 325 mesh APD = 14μm
Matrix B	Aluminum Alloy (Al-8Fe-4Ce)	ALCOA	Air-atomized Classified to - 325 mesh APD = 14μm
Reinforcement A	Black α-SiCp	Norton	1200 grit - (~3μm)
Reinforcement B	β-SiCp	Superior Graphite	500 grit (17μm)
Reinforcement C	Green α-SiCp	Norton	1200 grit (~3μm)
Reinforcement D	TiB_2 Grade D	H. C. Starck	<1000 grit
Reinforcement E	Graphite No. 4935	Superior Graphite	1000 grit (5μm)
Reinforcement F	Graphite "4739" enriched β-SiCp	Superior Graphite	1000 grit (5μm)
Reinforcement G	Graphite "9039" enriched β-SiCp	Superior Graphite	1000 grit (5μm)

*More detailed microstructural characterization of these materials is reported in Ref. 3.

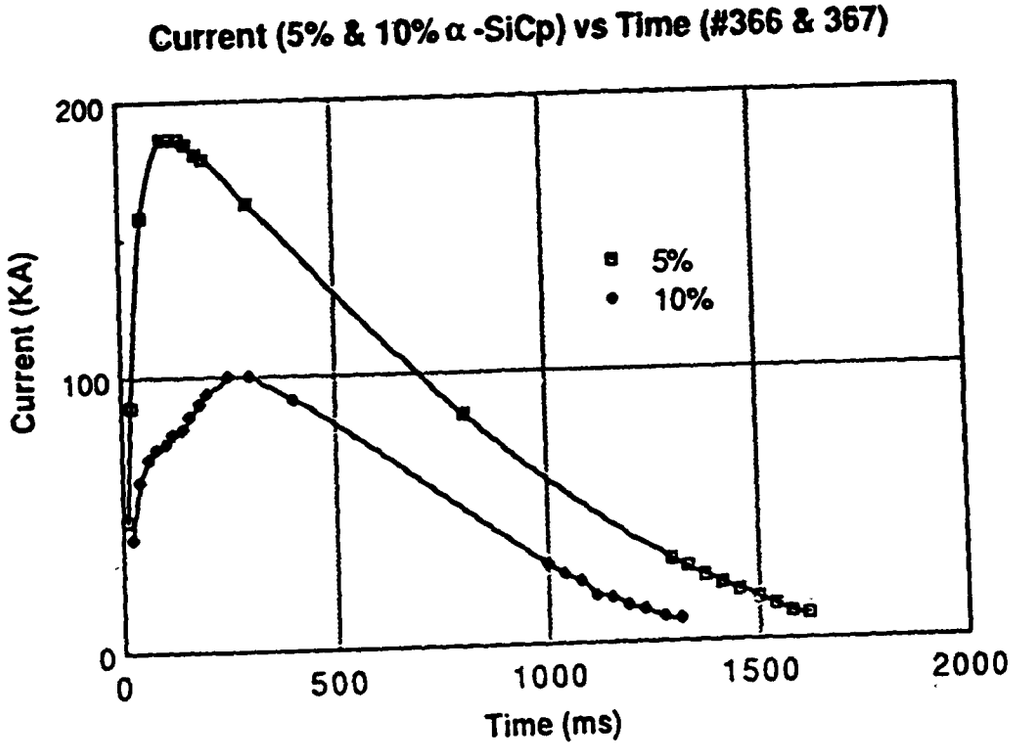

Figure 1: Comparison of the effect of volume fraction of reinforcement on current vs time curves for Matrix A reinforced with 5% and 10% volume fractions of Reinforcement A processed with equal amounts of stored energy.

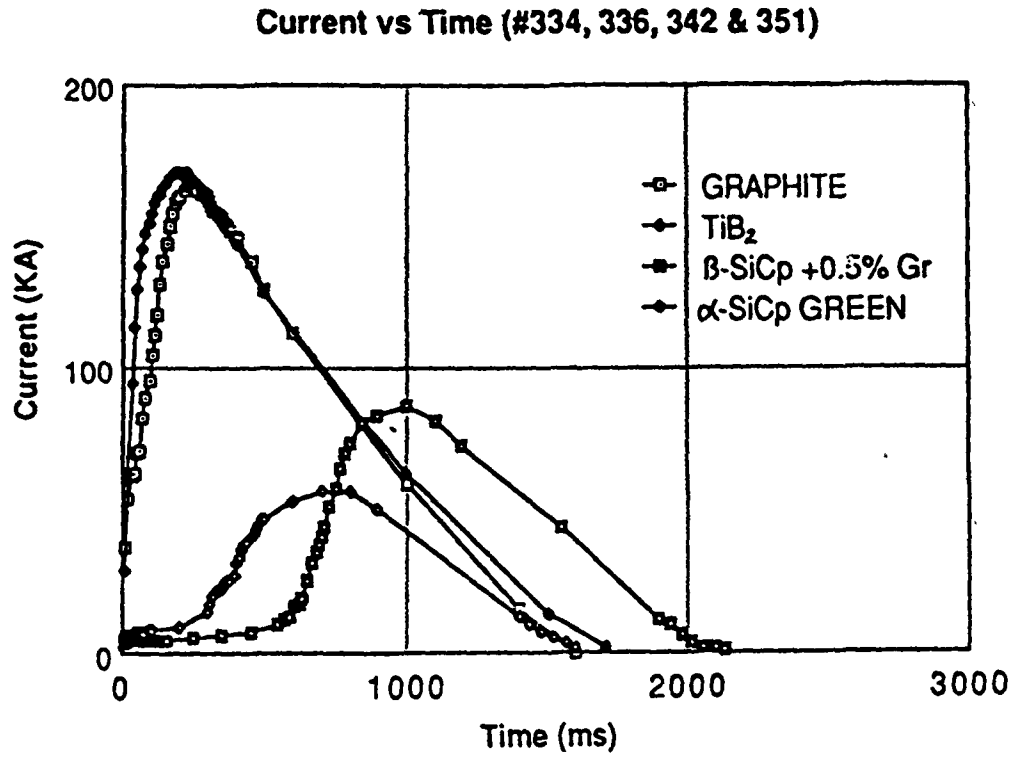

Figure 2: a) Comparison of the influence of reinforcement types on the current traces for 25 volume percent of Reinforcements B, C, D, E in Matrix A processed with equal amounts of stored energy.

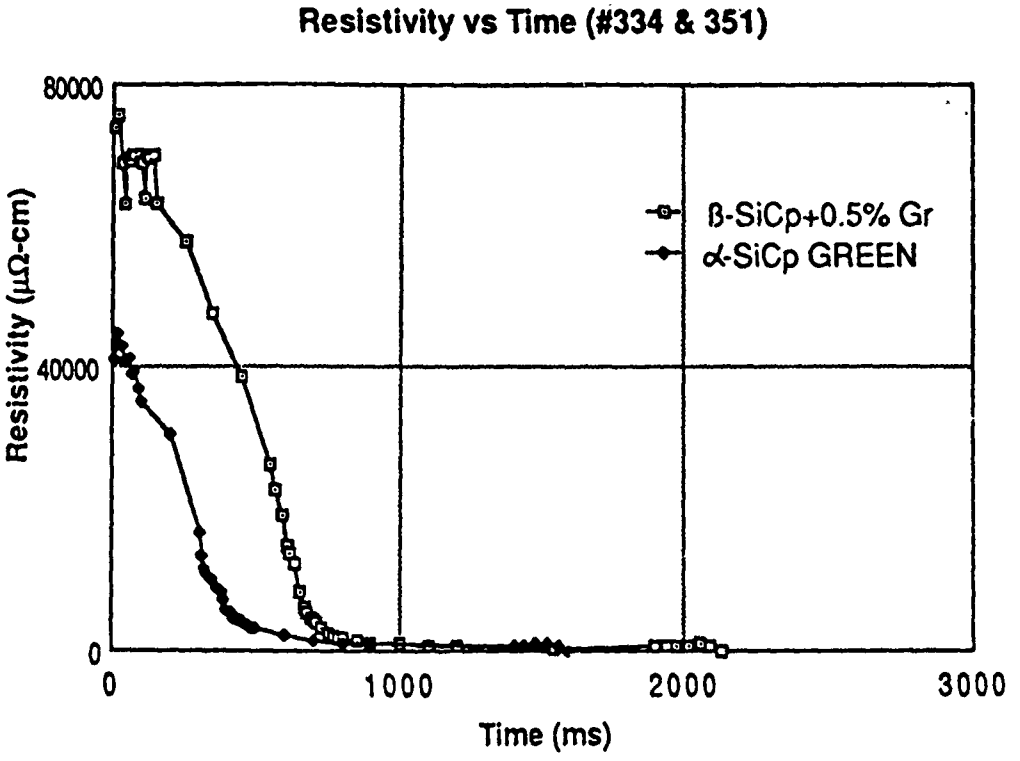

b) Comparison of the resistivities during processing of the composites in 2(a) with the SiCp Reinforcements B and C.

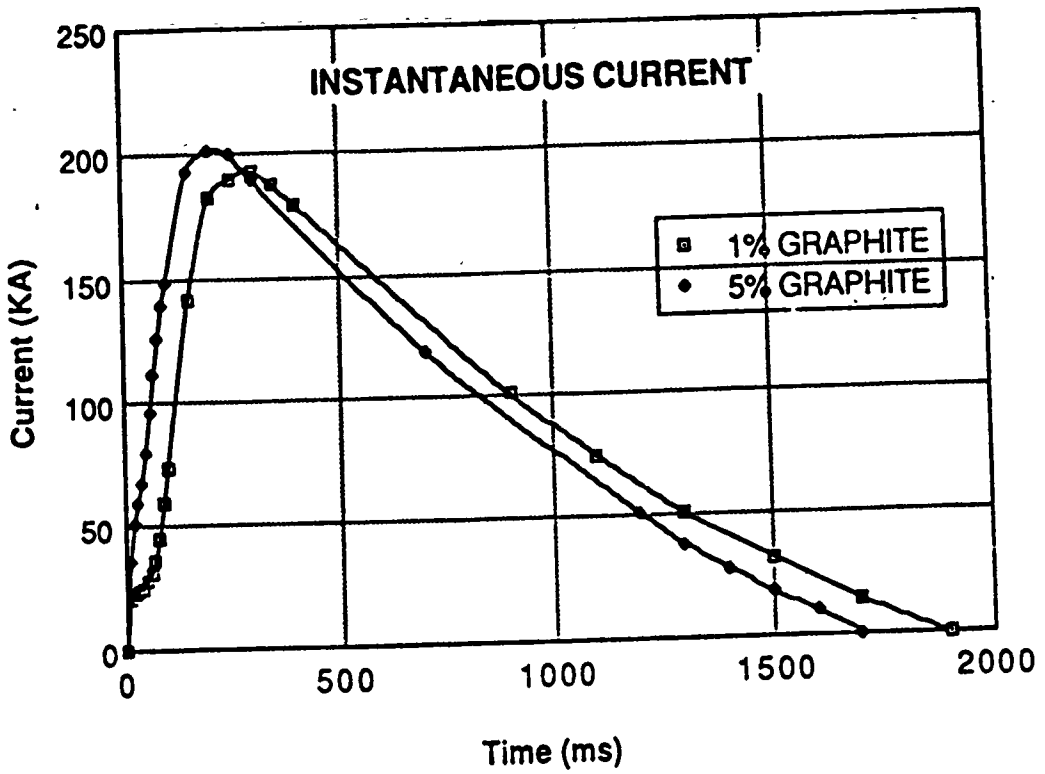

Figure 3: a) Influence of surface graphite content on the current flow. The composite consisted of Matrix A with 25 volume percent of β-SiCp with 1% or 5% graphite.

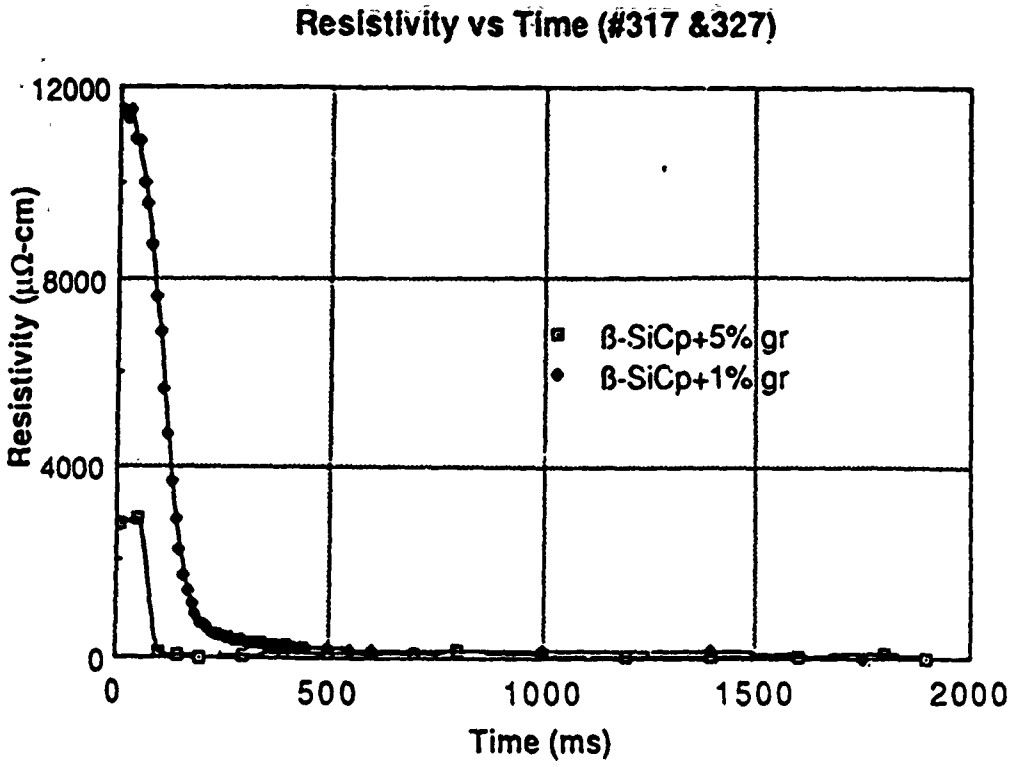

b) Comparison of the resistivities of the composites in 3(a) during the process.

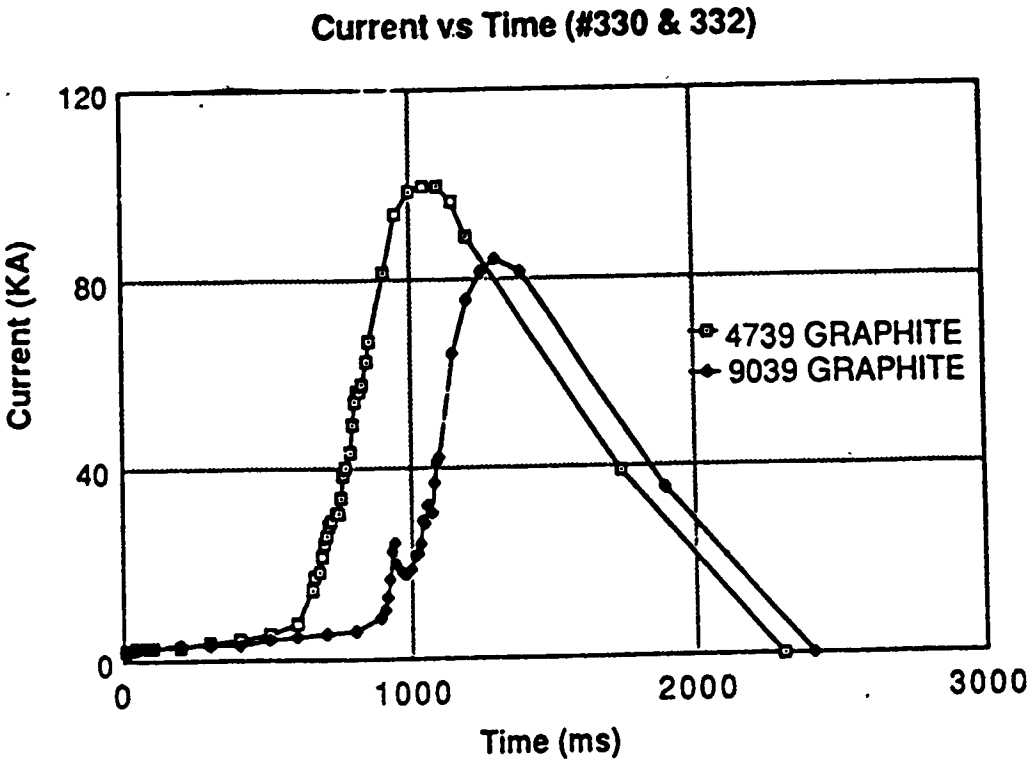

Figure 4: a) Comparison of the influence of the type of graphite on the current flow. The composite consisted of Matrix A + 25 volume percent of Reinforcements F and G.

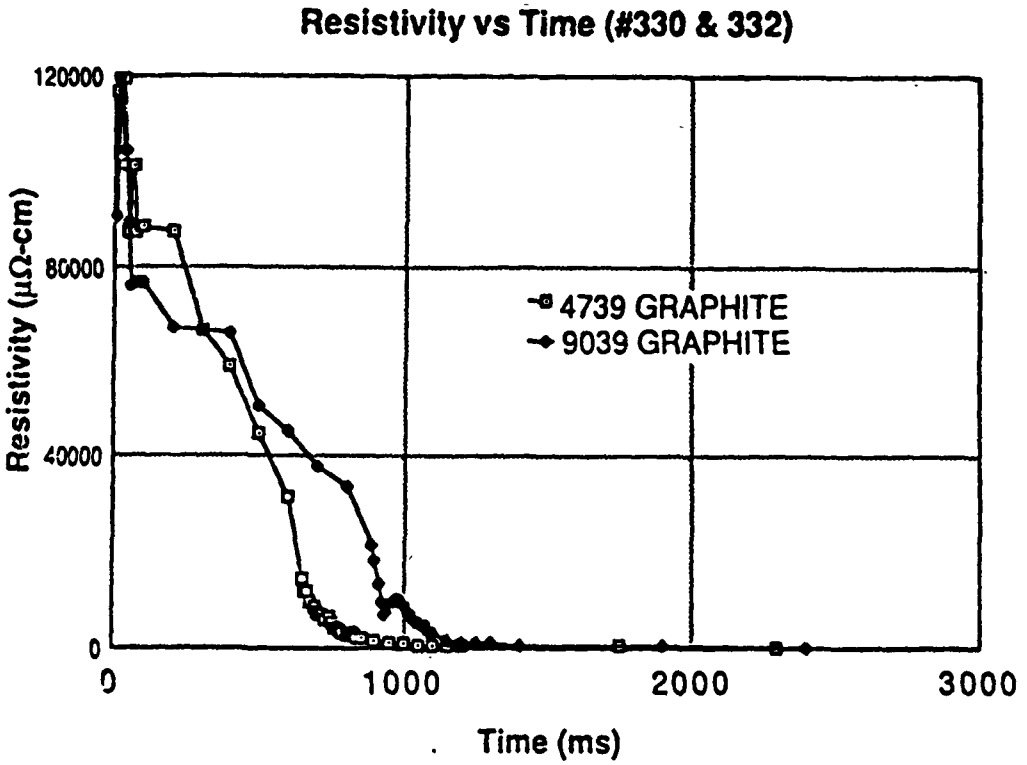

b) .Comparison of the resitivities of the composites in 4(a) during the process.

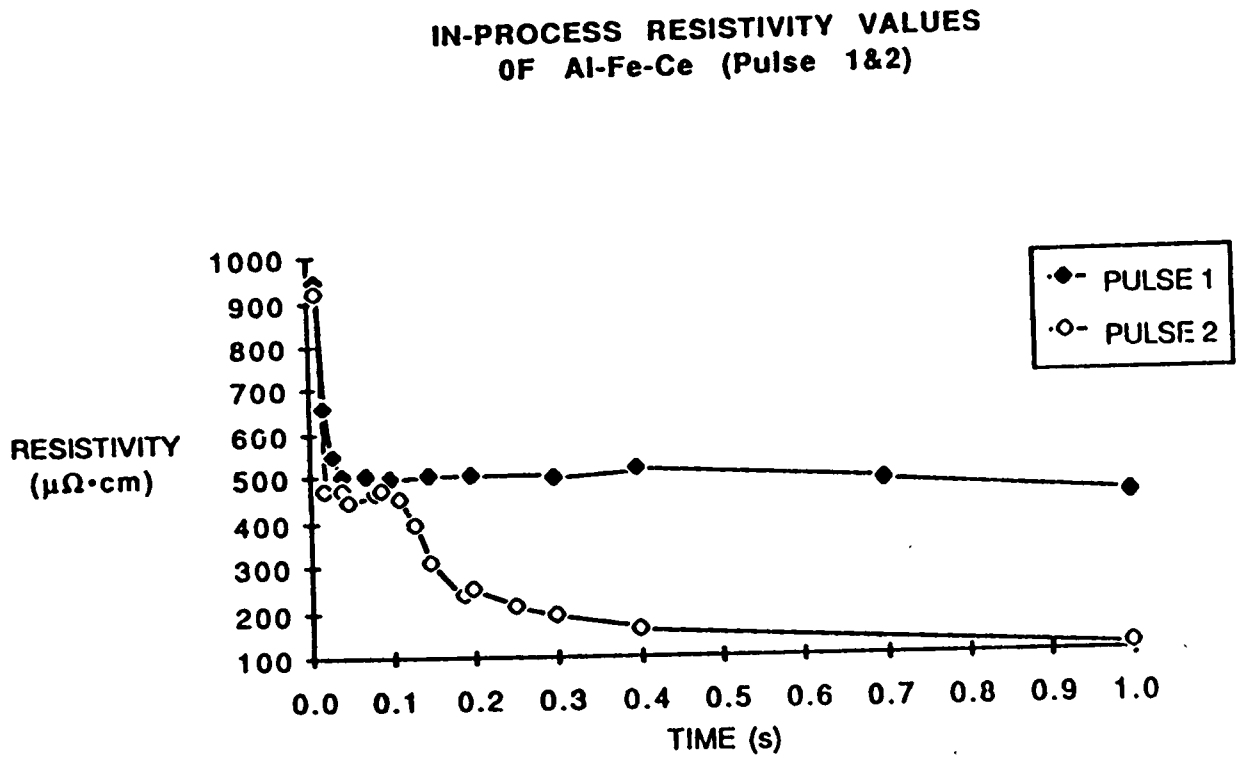

Figure 5: Resistivity vs time plots for Matrix B powders without reinforcement consolidated by the double pulse technique.

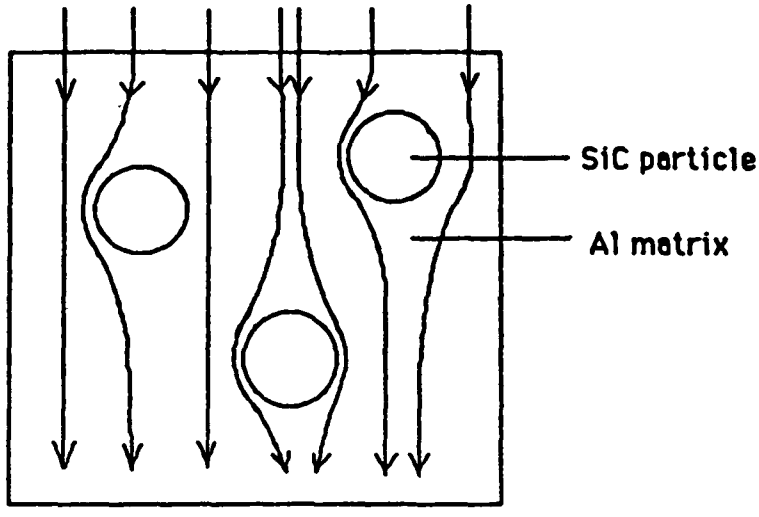

Figure 6: Schematic of the effect of SiC particles on the current flow path during consolidation processing.

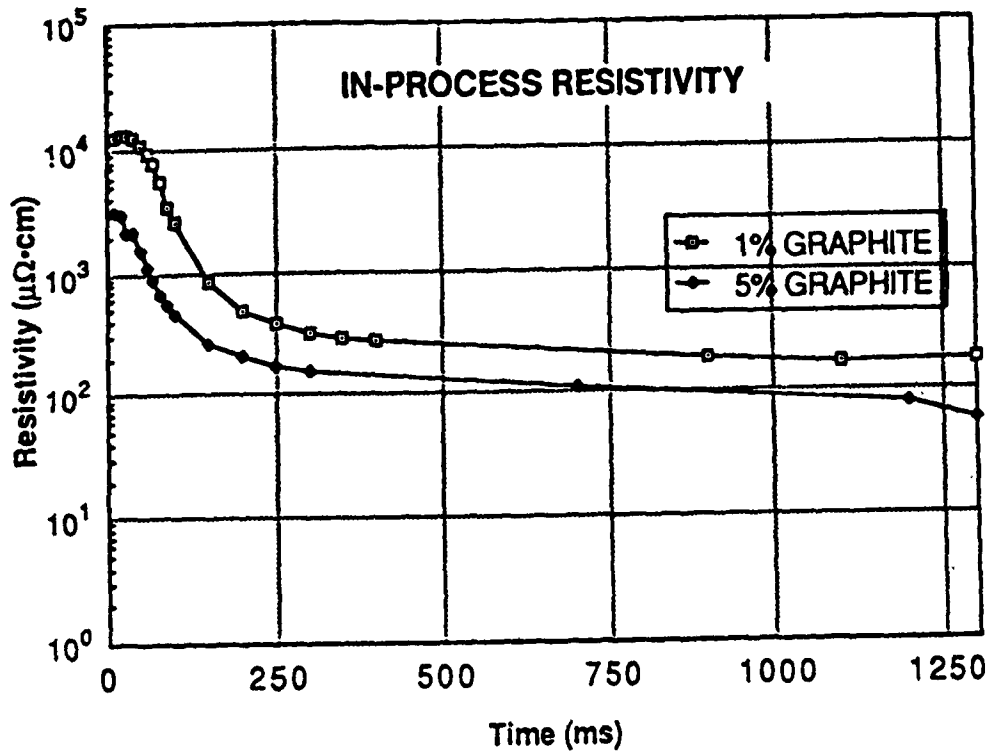

Figure 7: Comparison of the in-process resistivities of composites consisting of Matrix A + 25 volume percent β-SiCp enriched with 1% and 5% graphite. (Note the resistivity is plotted on a log scale).

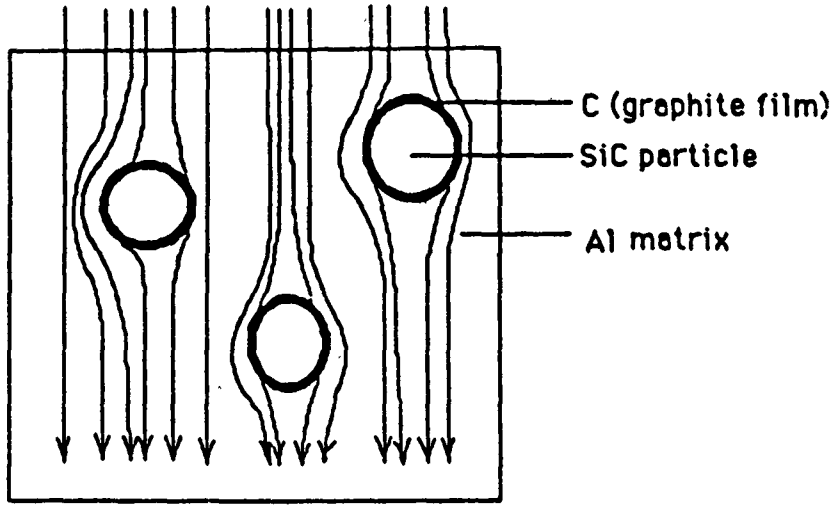

Figure 8: Schematic of the effect of a conductive layer (graphite) on the current flow path in an Al + SiC composite.

ABSTRACT

HIGH RATE CONSOLIDATION OF FERROMAGNETIC Co-Fe-B POWDERS

by

UDAYKUMAR LAKSHMINARAYAN B. Tech.

SUPERVISING PROFESSOR: Dr. H.L.Marcus.

High energy high rate consolidation processing using the Homopolar Generator is a novel approach to make sputtering targets and bulk ferromagnetic materials. In this study, mixtures of elemental cobalt, iron and boron in differnt proportions were consolidated. Since this process involves very rapid heating of the compact by a fast electrical discharge, the microstructure of the original powder is retained in the compact. The effect of subsequent heat treatment in vacuum on the properties of the compact will also be discussed. Densities of upto 93% were obtained. Using these consolidates as sputtering targets, thin magnetic films have been grown and the characteristics of these films will be discussed.

THESIS

MASTER OF SCIENCE IN ENGINEERING

THE UNIVERSITY OF TEXAS AT AUSTIN

MAY 1989